

ECIO 2008

European Conference on Integrated Optics

Eindhoven University of Technology, Netherlands

Collected Manuscripts

(c) Copyright 2008 The ECIO Board. All rights reserved.

Contents

ID	Author	Title
We1	R. Alferness	(Invited) The Next Wave of Photonic Integration for Optical Networks
We2	R.M. De La Rue	(Invited) Photonic integration: the other wavelengths, the other material system, the other applications
We3	E. Yablonovitch	(Invited) Photonic Crystal based nanophotonic integration
WeA1	P. Viktorovitch	(Tutorial) Photonic Crystal based nanophotonic integration
WeA2	A.A.M. Kok, J.J.G.M. van der Tol	Pillar photonic crystal for polarization filtering
WeA3	P.E.K El-Kallassi1, S. Balog1, L	Local tuning of the optical response of two dimensional photonic crystals
WeB1	A. Poustie	(Invited) Hybrid Integration for advanced photonic devices
WeB2	L. Zimmermann1, T. Tekin2, H. Sc	ePIXpack – Advanced Smart Packaging Solutions for Silicon Photonics
WeB3	N. Galler, H. Ditlbacher, A. Hoh	Waveguide intensity modulators based on electrically actuated elastomers
WeB4	B.M.P. Romeira1, J.M.L. Figueire	Optoelectronic Integration of a Resonant Tunneling Diode and a Laser Diode
WeB5	N. Bamiedakis1, R.V. Penty1, I.H	Cost-Effective Polymer Multimode Directional Couplers for High-Speed On-Board Optical Interconnects
WeC1	C. Chang-Hasnain	(Invited) High-index contrast grating integrated VCSELs
WeC2	L. Balet1, M. Francardi2, A. Ger	Quantum dot photonic crystal membrane LED at 1.3 μm
WeC3	H. Wang, J. Yuan, S. Anantathana	Butt-joint integrated InAs/InP quantum dot Fabry-Perot laser devices emitting at 1.5 μm
WeC4	M.J.R. Heck1, A. Renault2, E.A.J	Passively mode-locked quantum dot laser diodes at 1.53 μm with large operating regime
WeC5	S. McMaster, J.J. Bregenzer, M.	Monolithic Integration of a Compact Passive Polarisation Converter within a Laser Diode
WeD1	V. Pruneri1, D. Janner1, D. Tull	(Invited) Integrated electro-optic modulators in micro-structured LiNbO3
WeD2	L. Gui, H. Hu, M. Garcia-Granda,	Ferroelectric Microdomains in Plasma-Etched Ridges on X-Cut Lithium Niobate
WeD3	H. Hui, W. Sohler, R. Ricken	Etching of Lithium Niobate: From Ridge Waveguides to Photonic Crystal Structures
WeD4	M. Garcia Granda1, H. Hu1, W. So	Novel structures for broadband electrooptic modulators in LiNbO3
WeD5	S.M. Kostritskii, A.A. Dikevich,	Performance of Waveguide FPI with Si-on-LiNbO3 Bragg Gratings under Temperature Gradient
WeE1	G. Roelkens, L. Liu, J. Brouckae	(Invited) Wafer bonding and heterogenous Integration : III-V/Silicon Photonics
WeE2	D.L. Huffaker	(Invited) Long wavelength lasers on Silicon
WeE3	F. Bordas1, G. Roelkens2, E.J. G	Compact Grating Coupled MMI on DVS-BCB Bonded InP-Membrane
WeE4	A. Bennecer1, R.V. Penty1, I.H.	Monolithic Directly-Modulated Multi-Wavelength-Channel GaInAsP/InP Micro-Ring Laser Array
WeF1	M.J. van der Hoek	(Invited) Sensors and photonic integration
WeF2	C. Dongre1, R. Dekker1, H.J.W. H	Fluorescence sensing with femtosecond laser written waveguides in a capillary electrophoresis chip for monitoring molecular separation
WeF3	L.J. Kauppinen, H.J.W.M. Hoekstr	Grated Waveguide Optical Cavity as a Compact Sensor for Sub-nanometre Cantilever Deflections
WeF4	K. Florjanczyk1, P.C. Cheben2, S	Multiaperture Fourier transform arrayed waveguide spectrometer

WeF5	N. Ismail, E.J. Klein, G. Sengo,	Multi-Waveguide Based Collector for the Detection of Backscattered Light from Highly Scattering Media
Th2	R. Nagarajan, M. Kato, S. Corzin	(Invited) InP-based photonic integration
Th3	H. Atwater	(Invited) Active plasmonic materials and divices
ThA1	R.A. Griffin	(Invited) Integrated InP devices for advanced optical modulation formats
ThA2	M. Nikoufard, L. Xu, X.J.M. Leij	High bandwidth waveguide photodetector based on an amplifier layer stack on an active-passive semi-insulating InP at 1.55 μm
ThA3	O.R. Raz, Y.S. Oei, H.J.S. Dorre	All Optical Wavelength Conversion Based on Injection Locking in InP Ring Laser
ThA4	N. Calabretta1, S. Beri2, L. Gel	Experimental investigation of bistable operation of semiconductor ring lasers under optical injection
ThA5	L.M. Augustin, J.J.G.M. van der	Method for polarization effect suppression in semiconductor optical amplifiers
ThB1	S. Tanzilli, S. Tascu, P. Abouss	(Invited) Advances in quantum communication using integrated optics
ThB2	S. Longhi	(Invited) Quantum mechanics with curved photonics structures
ThB3	I.L. Garanovich1, A. Szameit2, A	Light localization at surfaces of modulated photonic lattices
ThB4	N. Le Thomas1, J. Jágerská1, R.	Probing the dispersion properties of 1D nanophotonic waveguides with far-field Fourier optics
ThP01	E. Cantelar1, R. Rodenas1, A. Be	CW laser oscillation in Nd:YAG ceramic waveguides fabricated by femtosecond laser writing
ThP02	B.W. Tilma, E.A.J.M. Bente, X.J.	Design of an Integrated Electro-optically Tunable Filter for Tunable Laser purposes
ThP03	I. Akca1, , A. Dâna1, A. Aydinli	Electro-optic Modulation of InAs Quantum Dot Waveguides
ThP04	M.F. Ferrario1, R.B. Bratovich1,	Local Reconstruction of Birefringence in Bent Waveguides by Polarization-Sensitive Optical Low-Coherence Reflectometry
ThP05	P. Muellner1, N. Finger2, R. Hai	Resonance characteristics of rib-type slot waveguides
ThP06	I. Barbu1, H.H.J.E. Kicken1, P.A	Liquid crystal-infiltrated nanocavity and waveguide in deeply etched InP-based photonic crystals
ThP07	R.B. Bruck, R.H. Hainberger	Efficiency enhancement of grating couplers for single mode polymer waveguides through high index coatings
ThP08	A. Melloni1, G. Cusmai1, F. Mori	Design on tolerances in integrated optics
ThP09	M. Yan1, L. Thylen1, M. Qiu1, D.	Deep-Subwavelength Optical Waveguides Based on Near-Resonant Surface Plasmon Polariton
ThP10	S.H Hisatake, Y.T. Takemoto, K.T	Phase velocity estimation of a modulation wave in a quasi-velocity-matched electro-optic phase modulator using electro-optic sampling system
ThP11	E. Martín Rodríguez1, M. Quintan	Confocal optical techniques to study channel waveguides in LiNbO3
ThP12	M. Rossetti, P. Bardella, M. Gio	Carrier Transport Effects in Multi Layer Quantum Dot Lasers and SLDs
ThP13	M.N. Passaro, M. Lagioia, F.D.L.	Design of nonlinear SOI slot waveguides
ThP14	A.V. Tsarev	Passive polarization rotator in anisotropic LiNbO3 graded-index waveguide
ThP15	L. Huang, K.C. Tsang, E.Y.B. Pun	Sm3+ doped polymers for planar optical waveguide amplifiers
ThP16	J.V. Galan Conejos, P. Sanchis K	Horizontal slot waveguide-based efficient fiber couplers suitable for silicon photonics
ThP17	M.A. Vincenti1, D. De Ceglia2, M	Surface Plasmon Generation in a Subwavelength Slit in metal: a Palladium-Based H2 Leak Detection Sensor
ThP18	X. Cui, D. Erni	Nanorice Chain Waveguides Based on Low and High Order Mode Coupling
ThP19	G. Lévêque1, E.P.R. O’Reil	Theoretical study of plasmonic propagation on a chain array

ThP20	X. Zhang1, J. Rosas-Fernandez1,	Transfer Matrix Analysis of Spectral Response of Even-Row Microring Resonator Arrays
ThP21	B.A. Usievich, V.V. Svetikov, J.	Surface waves on the boundaries of photonic crystals and their coupling
ThP22	F. De Leonardis1, V.M.N. Passaro	Stimulated Raman Scattering in Membrane Silicon Waveguides
ThP23	C. Habib1, P. Muñoz1, L. Chen2,	Design of a Monolithically Integrated All-Optical Label Swapper for Spectral Amplitude Code Labels Using Cross-Gain Modulation
ThP24	K. Solís Trápala, R.W. Smink, J.	High-Q whispering-gallery mode quantum-dot microdisk lasers
ThP25	A.M. Hatta1, T. Farrell1, N.M.I.	Design of the optical core of an integrated ratiometric wavelength monitor
ThP26	G. M. Manzacca, G. Cincotti	Quantum optical effect for switching and slow light applications
ThP27	A.V. Tsarev	New thin heterogeneous optical waveguides on SOI for reconfigurable optical add/drop multiplexers
ThP28	P. Bardella, I. Montrosset	BPM Validation of the Modal Gain Measured with the Segmented Contact Method
ThC1	M.K. Kim, M.K. Seo, S.H. Kim, Y.	(Invited) Photonic crystal microlasers
ThC2	H. Benisty1, C. Cambournac1, M.	Functional photonic-crystal mini-stopband demux integrated in emitting and detecting devices
ThC3	O. Bouchard1, A. Monmayrant1, O.	Photonic Crystal DFB laser array and fine emission wavelength engineering
ThC4	O. Bouchard1, S. Bonnefont1, O.	CW electrical operation of single-mode all photonic crystal DFB-like laser
ThC5	L. O’Faolain, T.P. White,	Efficient Injectors for Slow light Photonic Crystal Waveguides
ThD1	A. Samarelli1, M. Gnan1,2, R.M.	Low propagation loss photonic wire and ring resonator devices in silicon-on insulator using hydrogen silsesquioxane electron-beam resist
ThD2	A. Kazmierczak1, L. Vivien2, K.B	Optical microring resonators in Si3N4/SiO2
ThD3	M. Waldow, M. Först, H. Kurz	Analysis of Raman lasing in integrated small-volume silicon-on-insulator racetrack resonators
ThD4	A. Brimont1, F.Y. Gardes2, P. Sa	Design of a micro-ring resonator electro-optical modulator embedded in a reverse biased PN junction
ThD5	F. Morichetti, C. Ferrari, L. Fl	Wavelength routing and dispersion compensation in a narrow-band integrated resonant router
ThD6	Z. Zhang1, M.D. Dainese2, L.W. W	High-quality-factor micro-ring resonator in amorphous-silicon on insulator structure
Fr1	K. Kuipers	(Invited) Ultrafast tracking of slow photonics and plasmons
Fr2	T. Umeki1, M. Asobe1, T. Yanagaw	(Invited) Widely tunable mid-infrared DFG using apodized c(2) grating and its application to gas spectroscopy
FrA1	A. Fiore	(Tutorial) Semiconductor Quantum Dots
FrA2	A. Albores-Mejia, T. De Vries, E	Scalable Quantum Dot Amplifier Based Optical Switch Matrix
FrA3	H. Wang1, E.T. Aw1, M.G. Thompso	Integrated Quantum Dot 2×2 Switch for Uncooled Switching Applications
FrB1	T. Clapp1, J.V. DeGroot2	(Invited) Polymer Devices in Integrated Optics
FrB2	A. Subramanian1, J. Oton1, Rober	Er:Ta2O5 waveguide optimization & spectroscopy
FrB3	S.K. Selvaraja, W. Bogaerts, D.	Fabrication of Uniform Photonic Devices Using 193 nm Optical Lithography in Silicon-on-Insulator
FrB4	L. Martínez1, S. Giurgola2, P. V	Thermally stable ultra thin metal transparent electrodes
FrB5	J.S. Schrauwen1, D. Van Thourhou	Trimming of silicon ring resonator by electron beam induced compaction
FrC1	H. Schmid, P. Cheben, S. Janz, J	Subwavelength Structures in Silicon-on-Insulator Waveguides for Modification of Facet Reflectivity and Efficient Fiber-Chip Coupling
FrC2	D. Szymanski1, B.D. Jones1, D. O	Ultrafast all optical switching in AlGaAs photonic crystal waveguides

FrC3	D.M. Beggs, T.P. White, L. O&#82	Design and fabrication of a photonic crystal directional coupler for use as an optical switch
FrC4	T. Stomeo1, T.F. Krauss2, D. Van	Successful fabrication and integration of multifunctional photonic-crystal devices on bonded InP membrane chip
FrC5	I. Bayn1, B. Meyler1, A. Lahav1,	Photonic crystals (PC) in diamond: Ultra-high-Q nanocavity design, analysis and fabrication
FrC6	K. Van Acoleyen, M.Q. Qiu	Investigation of photonic crystal cavities sandwiched in a grating structure
FrD1	A. Melloni, F. Morichetti, A. Ca	Deeply inside tunable CROW delay lines
FrD2	W. Bogaerts, L. Vanholme, P. Bra	Closed-loop Modeling of Silicon Nanophotonics: From Design to Fabrication and Back Again
FrD3	J.L. Ito, I.K. Iwamoto, T.H. Tsu	Design of a Waveguide-Type Polarization Beam Splitter Incorporating Trenches Filled with Low-Refractive Index Material
FrD4	K. Kashiwagi1, S. Yamashita1, K.	Temperature Insensitive Silicon Slot Waveguides with Air Slot
FrD5	A. Delâge1, P.J. Bock1, P. Chebe	A Demultiplexer with Blazed Waveguide Sidewall Grating
FrPD1	A. Martin1, V. Cristofori3,1, P.	Integrated optical source of polarization entagled photons at 1310 nm
FrPD2	L. Ferrier, G. Le Gac, O. El Dai	Near field properties of vertical emitting laser based on 2D photonic crystal heterostructures
FrPD3	A.R. Md Zain, N.P. Johnson, M So	High-Quality Factor Suspended-Wire 1D Photonic Crystal Micro-cavity in Silicon-on-Insulator
FrPD4	L. Xu, X.J.M Leijtens, P.J. Urba	InP-based Monolithic Integrated Colorless Reflective Transceiver

The Next Wave of Photonic Integration for Optical Networks

Rod C. Alferness

Bell Laboratories, Alacatel-Lucent, Murray Hill, New Jersey

Abstract. *Photonic or optical integration is firmly established as a key technology that has enabled optical networks that underpin global and local communication networks. Key components/circuits include modulators, wavelengths mux/demux, line conditioning devices and ROADMs. Ubiquitous video is ramping bandwidth needs that will need higher per channel bit rates that require new modulation formats. Further in the future, optical packet switching and WDM access networks appear to offer potentail solutions to growing capacity needs that are extending to the home. All offer important opportunities and challenges for the next wave of photonic integration applications.*

Photonic Integration: the other wavelengths, the other material systems, the other applications

Richard M. De La Rue

Optoelectronics Research Group, Department of Electronics and Electrical Engineering,
University of Glasgow, Glasgow G12 8QQ, Scotland U.K.

Abstract: Recognising the importance of hybrid integration, alongside the prospects offered by the use of monolithic integration, this presentation will range widely over the topic of photonic integration. It will also range widely over the optical spectrum, as implied by the title of this paper. While the words 'other wavelengths' may suffice for some purposes, the recognition that these words also automatically suggest other material systems (than silicon or indium phosphide) and other applications – than fibre telecomm – will shape the presentation.

Introduction

Because of the importance of fibre-optical telecommunications for the infra-structure of the world, it is often assumed by those working in the corresponding parts of integrated photonics research and development that the most important activity is oriented towards telecommunications. It is certainly of great interest to observe how both silicon photonics and indium-phosphide based photonic integration have progressed in recent years. We may also believe that, despite the current wave of financial incompetence that has struck some of the leading economies in the world, there will be a serious revival in fibre-based telecoms development, particularly at the LAN, MAN and FTTH levels.

Working to a title that includes 'the other wavelengths' has the primary problem that the territory is embarrassingly rich. We have the whole of the visible spectrum to consider – and can now legitimately include a substantial part of the ultra-violet spectrum in our territory of interest. Likewise, going only a short way beyond the fibre telecom wavelength bands around 1.55 μm opens up the longer wavelength parts of the near infra-red spectrum, before we proceed to consider the mid- and far- infra-red.

Hybrid Integration: Display Devices and Laser Pointers

Taking a broad view of the meaning of photonic integration, and allowing for various levels of hybridity, opens up, for example, the vastly important area of display devices - and the much less important territory of the laser pointer.

The liquid crystal display (LCD) is now all-pervasive. Although the plasma-display provides significant competition, it is primarily the LCD that is now used in place of the cathode-ray tube for displays in consumer optoelectronics such as televisions and computer monitors. The LCD, on all size-scales, is intrinsically a strongly hybrid photonic/optoelectronic component. Although molecularly oriented liquid crystal films lie at the heart of the display, the active layer must be sandwiched between transparent plates of glass, which additionally support patterned conductive layers, colour selective and polarising films - and arrays of driver transistors in thin-film (i.e. amorphous silicon) format. Furthermore, the approximately white light source required for the LCD must be provided separately – and distributed as evenly as possible across the entire active display region. Edge-mounted sources that distribute light via leaky/scattering

waveguide layers provide one route to LCD illumination. A possible alternative approach uses back-lighting from an array of discretely distributed high-brightness white or UV light-emitting diodes (LEDs). The latter approach offers an interesting opportunity for the application of photonic crystal or photonic quasi-crystal light extraction structures integrated into the LEDs, with the multiple objectives of enhancing the extraction efficiency and the overall 'wallplug' (conversion) efficiency of electric power into useful light – and of controlling the shape of the emitted beam of low-coherency light.

The blue semiconductor diode laser, as exemplified by its application in Blu-ray disc consumer electronics, has become the pre-dominant species of laser - in terms of absolute numbers manufactured and sold, being produced annually in quantities measured in hundreds of millions. It is by no means certain that optical disc-based memory technology will prevail, because of trends in purely electronic storage, magnetic disc memory and direct (streaming) production of audio and video information via the internet, but it seems likely that the blue semiconductor diode laser, followed fairly closely by the ultra-violet semiconductor diode laser will be used in a progressively wider range of applications. Integration of grating structures to realise DFB and DBR lasers in the blue and ultra-violet spectrum will make it possible to have accurately controlled emission wavelengths, together with a measure of tunability.

The laser pointer provides an interesting example of a mass-produced device that makes use of clever hybrid integration techniques at the miniature/micro-optics level. We may characterise the laser pointer as being a compact device that produces coherent light in the visible part of the electromagnetic spectrum, has good beam quality - and low enough electrical power consumption and sufficiently high efficiency to be conveniently operated in hand-held mode.

While currently available red laser pointers use direct conversion of electron flow into photons, i.e. injection electroluminescence, in red light emitting semiconductor diode lasers, green laser pointers use a more complex combination of components. For green laser pointers, the process begins with light generation at approximately 850 nm in an infra-red emitting semiconductor diode laser, followed by (frequency) down-conversion to 1.06 μm through pumping of a neodymium-doped (Nd-doped) crystal chip and then second harmonic generation (SHG) of green light at 530 nm, via a chip of potassium titanyl phosphate (KTP). The greater complexity involved in the green laser pointer does indeed imply greater intrinsic cost, perhaps by as much as an order of magnitude in comparison with the red laser pointer.

Laser pointers for light at other, longer, wavelengths than the green, such as the yellow at 577 nm or 593 nm, also use wavelength conversion, but the process involves optical pumping (again starting from an infra-red semiconductor diode laser) in a disc of semiconductor gain medium, with the intermediate step of second harmonic generation of the light from the infra-red semiconductor laser. Finally, in currently available and (quite probably) all future manifestations, the blue laser pointer goes back to being simply an edge-emitting semiconductor diode laser, together with collimating/patterning optics. Post-finally, it seems plausible to suggest that there will soon be ultra-violet laser pointers that will take advantage of the intrinsic invisibility of the ultra-violet light beam, even when propagating through scattering media, and that will rely on the fluorescence of many materials for visibility where required. Safety and ethical issues

are likely to impact on the availability of ultra-violet laser pointers to the general public, but legitimate applications of the same kind of technology, with suitable operating restrictions, will surely be found.

Projection TV and Coherence Issues

An application that is fairly closely related to both laser pointers and to displays is the topic of scanning laser-based projection TV – and cinema. The development of compact and efficient lasers with the appropriate combinations of semiconductor diode lasers and solid-state (typically single-crystal) gain and frequency conversion components for specific colours in the red-green-blue (RGB) parts of the visible spectrum will make it possible to create high quality images that are generated by rapid scanning (and switching) of the constituent laser beams.

An important issue in the use of intrinsically coherent light sources such as lasers for display and optical memory applications is the generation of speckle. Speckle is the direct result of random scattering of coherent light from typical more-or-less rough surfaces. Because of coherence the scattered laser light has strong interference effects that degrade image quality in a visually unacceptable manner. To overcome the speckle problem it becomes necessary to destroy the coherence of the laser light in an appropriate way. For the possible use of lasers in display back-lighting, specific forms of integrated screen that have the right combination of transparency and diffusivity are required. For semiconductor diode lasers used in reading compact discs, saturable absorption is typically integrated with the laser stripe – in order to produce fluctuating (and therefore functionally less coherent) light via Q-switching behaviour.

OLEDs: a possible alternative display technology

Returning to the issue of basic approaches to display technology, we now turn briefly to consideration of the organic light-emitting diode (OLED) based display. In contrast to the LCD approach, OLED displays involve intrinsically light emitting semiconductors that are based on electron and hole injection and recombination in layers of electrically conducting organic chemicals. These chemicals may take the form of oriented molecules, of polymers or dendrimers. Different molecules emit light at different colours. OLED displays offer significant potential advantages, by comparison with LCDs, in terms of substantially simpler construction, mechanical flexibility and ruggedness – and even in terms of overall efficiency. Although the issue of reliability has not yet been definitively dealt with, it is now reasonably likely that OLED displays will push into the territory of LCDs, beginning at the bottom end.

Compact Tunable Lasers in the Visible/Ultra-Violet spectral range

The various examples of photonic integration that have been described and discussed above certainly have a largely hybrid nature – and definitely conform to the ‘other wavelengths’ definition through being mostly concerned with light in the visible part of the spectrum. One plausible direction for future work is the extension of the micro-chip laser approach through the use of a wider range of materials, both classical ‘solid-state’ (often single crystal) media for gain and frequency conversion and semiconductors diodes or optically-pumped semiconductor structures. 1D and 2D Photonic crystal structures integrated into microchip lasers that use broad-spectrum gain media, such as titanium doped sapphire (Ti:Al2O3), offer the opportunity to produce widely tunable (many tens of nanometres of wavelength range) visible-wavelength coherent light

sources - through second harmonic generation selected by careful matching between the fundamental and second-harmonic band-structures of the photonic crystal [1]. Arguably there is a 'crying need' for such lasers, which could reduce the costs and size of tunable coherent light sources by several orders of magnitude – in comparison with the current generation of lasers that consume large amounts of electrical power and occupy a substantial fraction of a large optical table. With integrated saturable absorption, peak powers could be usefully large, e.g. one Watt – and many potential applications, e.g. in molecular spectroscopy, should not require more than a few milliWatts of tunable coherent light.

DFB and DBR lasers at other wavelengths – and further levels of integration complexity

Up to this point, our discussion has deliberately emphasized the use of hybrid approaches to photonic integration – and it has also not made any attempt to restrict the definition of integration to the use of planar optical waveguides in 'integrated optical circuits. Let us now take on board the recent large advances in essentially monolithic waveguide device integration based on silicon VLSI technology and the complex, monolithically integrated structures that have been realised in epitaxial heterostructures based on indium phosphide. Recent progress towards low cost integrated components for telecomm applications - at levels from chip interconnect, via LAN and FTTH and on up to long-haul - has been most impressive. The issue of the 'silicon laser' seems likely to be solved within a few years – and is not a central problem, because it can already be solved through hybrid integration with a III-V semiconductor gain chip. Alternatively the primary light source for a circuit may be an off-chip 'conventional' semiconductor laser that provides enough power to drive the whole integrated photonic chip.

Even if we generalise the definition of (fibre) telecomm wavelengths to cover all of the plausible wavelength ranges – such as those around 850 nm, 980 nm, 1300 nm and 1550 nm – there remain large areas of the optical spectrum that will or must be exploited for applications other than telecomm ones. If we select the blue/ultra violet spectral region, the need for monolithic integration arises from the desire to have efficient blue light sources with controlled coherence, including narrow emission lines that can be tuned over several nanometres. The integrated waveguide photonic component required for this functionality is a multi-section DFB or DBR laser based on large band-gap nitride semiconductor diodes. Basic large band-gap nitride laser diodes are typically (in-plane) edge-emitters and can be produced on intrinsically semi-conducting substrates that include single crystal gallium nitride platelets or thick layers of hydride vapour phase grown material. But such nitride lasers may also use the insulating (single-crystal) sapphire substrates that have largely been used in blue LEDs. A degree of justifiable additional, opto-electronic, complexity could then come from the use of similar epitaxial material as the medium for electronic components such as drive transistors linked to the laser. An arguably more interesting extension of this degree of complexity might come from the monolithic integration of micro-fluidic structures on the same substrate, with applications such as integrated bio-sensor chips being addressed.

Going away from the telecomm wavelength bands, but now moving to longer wavelengths, bring us to the quantum cascade (QC) laser. It is of some interest to note that successful introduction of the QC laser concept was based on epitaxially grown III-V semiconductor structures with many hundreds of thin layers. An important point is

that, because only electron-transport between sub-band states is involved, it has been possible to use a larger range of semiconductors for QC lasers than would be considered for lasers based on electron-hole pair recombination across the electronic band-gap. Tunable DFB and DBR versions of QC lasers will surely find a range of applications at wavelengths in the range from 2 to 20 μm. Etch and re-growth of local regions on the same substrate as the QC laser could again allow electronic drive transistors to be monolithically integrated. Enclosed channels for flowing gases to be probed spectrally, through the in-plane emitted mid-IR radiation, would add further to the complexity of the monolithic integration that was achieved. The European Community FP6 project Nitwave has explored the use of large band-gap nitride semiconductors for inter-sub-band transition based devices over a range of infra-red wavelengths [2].

Conclusions

This summary has unavoidably been shaped by the need to understand developments in, and the possibilities generated, by light sources based on semiconductor diodes. For many purposes, the semiconductor diode is the primary light generator of choice, being typically the most efficient and compact way of performing the task of converting electric power into optical power. This superior performance holds good for light sources over a large range of optical spectrum – from the deep ultra-violet, through the visible and near infra-red - and well on into the mid-IR. But the summary has also endeavoured to explore some of the possibilities for integration, of both a hybrid nature and a monolithic nature, across this range of wavelengths.

References

[1] J. Torres, D. Coquillat, R. Legros, J.P. Lascaray, F. Teppe, D. Scalbert, D. Peyrade, 'Giant second-harmonic generation in a one-dimensional GaN photonic crystal', *Phys. Rev. B*, **69**, 085105 1-8, (2004).

[2] L. Nevou, N. Kheirodin, M. Tchernycheva, L. Meignien, P. Crozat, A. Lupu, E. Warde, F.H. Julien, G. Pozzovivo, S. Golka, G. Strasser, F. Guillot, E. Monroy, T. Remmele, M. Albrecht , "Short-wavelength electro-absorption modulation based on electron tunneling between GaN/AlN coupled quantum wells", *Appl. Phys. Lett.*, **90**, 223511, (2007).

NanoPhotonics: From Photonic Crystals to Plasmonics

Eli Yablonovitch

Electrical Engineering & Computer Sciences Dept.
eliy@eecs.berkeley.edu
University of California, Berkeley, USA, 94720-1770

Abstract. *Engineering design is sometimes inspired by Nature. The natural world is filled with crystals, periodic structures that interact with electron waves. Drawing on this analogy, photonic crystals are artificial periodic structures that are intended for electromagnetic waves instead. Such nano-photonic structures are now being designed and patterned into Silicon-on-Insulator (SOI) to provide for commercial nano-photonic integration, as a component part of conventional CMOS circuits.*

Further optical frequency miniaturization will take us toward nano-plasmonics, metallic-wired electrical circuits, running at optical frequencies.

Photonic Crystal based photonic Integration

Pierre Viktorovitch
Institut des Nanotechnologies de Lyon, CNRS, Ecole Centrale de LYON, Ecully, France
Pierre.Viktorovitch@ec-lyon.fr

Abstract. *Fundamental properties of Photonic Crystals, as well as the basic physical concepts which are relevant to their practical exploitation are presented. The tutorial focuses on two dimensional Photonic Crystals (2DPC), which are shown not only to have a great potential in the prospect of the development of 2D Microphotonics in the wave-guided in-plane configuration, but to open the way to other brilliant developments, where 2D Microphotonics is extended to out of plane operation.*

Introduction

The principal motivations for the emergence of Photonic Crystals can be summarized in one single word, that is "λ-Photonics", whose definition could be *the control of photons within the tiniest possible space during the longest possible time*: this implies to structure space at the wavelength scale, which means in the sub-micron range, for the optical domain.
The next section will present a brief overview of the basic concepts which underlie Photonic Crystals, with a special emphasis on two-dimensional Photonic Crystals (2DPC), which have been the matter, so far, of most of the new applications in terms of device demonstrations. It will be shown in the subsequent section that 2DPC have definitely entered within the realm of practical devices. A special attention will be given to surface addressable devices, which have been the matter of very recent developments. In that respect, the concepts of 2.5 Microphotonics based on 2DPC, which can be considered as a major extension of planar technology through exploitation of the third ('vertical') dimension, will be presented.

Photonic crystals : a brief overview of basic concepts

What are photonic crystals?
A Photonic Crystal is a medium which the optical index shows a periodical modulation with a lattice constant on the order of the operation wavelength. The specificity of Photonic Crystals inside the wider family of periodic photonic structures, lies in the high contrast of the periodic modulation (generally more than that 200%): this specific feature is central for the control of the spatial-temporal trajectory of photons at the scale of their wavelength and of the their periodic oscillation duration.
We will restrict the rest of this paper to 2DPC, which have been the matter of most of the recent developments in the field of Micro-Nano-Photonics and are far more accessible than 3DPC [1], from the fabrication point of view.
A real 2DPC consists in considering a 2D structuration of a planar dielectric waveguide where photons are "index guided", that is to say vertically confined by the vertical profile of the optical index. In the rest of this chapter we will concentrate on the so called membrane approach, where the vertical confinement is strong: guiding of light is

achieved in a high index semiconductor membrane surrounded with low index cladding or barrier layers (for example an insulator like silica or simply air). In monomode operation conditions, the thickness of the membrane is very thin, around a fraction of µm; it results that low loss coupling schemes with an optical fiber are not easily achievable, but, the positive counterpart lies in the relaxed technological constraints for the fabrication of the 2D PC (holes with a shape ratio around unity). Also, the strong vertical confinement, leading to a reduced volume of the optical modes, lends itself to the production of very compact structures, which is essential for active devices to operate at the cost of very low injected power. It should be mentioned, at this stage, that most of the recent achievements reported in the literature in terms of device demonstrations, are based on the membrane approach. For passive devices silicon is often used for the membrane material, especially in the silicon on insulator (SOI) configuration, which is fully available in the world of microelectronics. For active devices, III-V semiconductor membranes have been principally used so far: the thin membrane is generally bonded by the molecular bonding procedure on the low index material, such as silica on silicon substrate [2]. This approach presents a definite advantage: it lends itself to heterogeneous integration of active III-V optical devices with silicon based passive optical devices and microelectronics.

Why photonic crystals?

Refraction phenomena have been widely used in opto-electronics for the guiding of photons or for their confinement within micro-cavities. The control of photon "trajectory" is based upon the total internal reflection that they experience at the boundary between the external world and the higher index medium where they are meant to be confined. Photonic crystals offer a new strategy for optical mode confinement based on diffraction phenomena. The new avenue opened up by Photonic Crystals lies in the range of degrees of freedom which they provide for the control of photon kinetics (trapping, slowing down), in terms of angular, spatial, temporal and wavelength resolution.

Photonic crystals : how does it work?

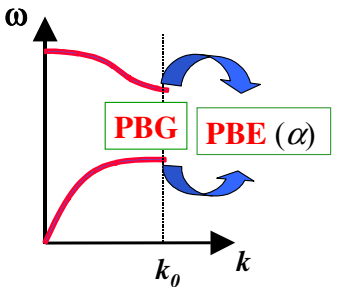


Figure 1 : schematic representation of a photonic band gap (PBG) and of related photonic band edges (PBE) in the dispersion characteristics of a photonic crystal.

In photonic crystals, which are strongly corrugated periodic structures, strong diffraction coupling between waveguided modes occurs; these diffraction processes affect significantly the surface dispersion characteristics, or the so called band structure, according to the solid state physics terminology. The essential manifestations of these disturbances consist in (figure 1):

- The opening of multidirectional and large photonic band gaps (PBG)
- The presence of flat photonic band edge extremes (PBE), where the group velocity vanishes, with low curvature (second derivative) $\alpha \approx \frac{1}{PBG}$.

These are the essential ingredients which are the basis of the two optical confinement schemes provided by photonic crystals (PBG / PBE confinement schemes) and which make them the most appropriate candidates for the production of a wide variety of compact photonic structures.

PBG confinement scheme using localized "defect" or cavity modes

In the PBG scheme, the propagation of photons is forbidden at least in certain directions. This is in particular true when they are trapped in a so called localized defect or micro-cavity and the related optical modes are *localized*: in this case the propagation of photons is fully prohibited. Opening of large PBG (in the spectral range) provided by the PC, allows for a very efficient trapping of photons, which can be made strongly localized in free space.

PBE confinement scheme using delocalized slow Bloch modes

In the PBE scheme, the PC operates around an extreme of the dispersion characteristics where the group velocity of photons vanishes. It should be noted however that the dispersion characteristics apply strictly for infinite periodic structure and time and that the concept of zero group velocity is fully true only under these particular extreme conditions. The real common world is actually finite and transitory. It is therefore more appropriate to speak in terms of *slowing down* of optical modes (so called Bloch modes for a periodical structure), which remain however *de-localized.* It can be shown that the lateral extension of the area *S* of the slowing down Bloch mode during its lifetime τ is proportional to $\alpha\tau$ [3]. As mentioned above, one essential virtue of PC is to achieve very low curvature α at the band edge extremes, thus resulting in very efficient PBE confinement of photons.

The most efficient confinement of photons can be achieved with the PBG scheme. The PBE scheme provides weaker confinement efficiency than with the PBG approach, while resulting in an improved control over the directionality or spatial/angular resolution.

The issue of vertical confinement in 2DPC: below and above light-line operation

It has been explained earlier in this contribution that the vertical confinement of photons is based on refraction phenomena. However, full confinement of photons in the membrane wave-guiding slab is achieved only for those optical modes which operate below the light-line. This mode of operation is restricted to devices which are meant to work in the sole wave-guided regime, where wave-guided modes are not allowed to interact or couple with radiated modes. This is the territory of 2D micro-photonics. For wave-guided modes whose dispersion characteristics happen to lie above the light line,

coupling with the radiated modes is made possible, the wave-guided "state" of the related photons is transitory, and the photonic structure can operate in both wave-guided and free space regimes. This is the world of 2D-3D microphotonics, which we will quote later in this paper as 2.5D microphotonics.

Photonic Crystals: devices

Following the pioneering and triggering contributions of E. Yablonovitch [1], it took quite a few years for the modeling and technological tools to reach the degree of maturity requested by the production of the first elementary building block devices, essentially based on 2DPC. This gradual start has been followed, around 2000, by an ever growing wave of new device demonstrators, so much so that it may be stated, to day, that Photonic Crystals have entered within the realm of practical devices.
In order to help the reader to find his way within this jungle, we choose to classify the wide range of devices produced so far into four main categories, depending upon whether they operate singly in the wave-guided regime or not, and upon whether they make use of the PBG or of the PBE confinement scheme.

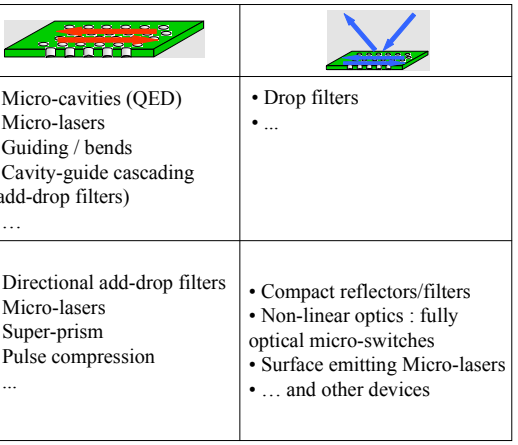


Figure 2: classification of 2D PC based devices in four main categories.

This classification is further detailed in the table of figure 2, which provides a non-exhaustive list per category of the principal device structures demonstrated so far. In the following sections we emphasize devices making use of slow Bloch modes along the PBE confinement scheme and specifically those devices belonging to the fourth category, that is to say devices operating in the wave-guided regime while being also opened to the third direction of space: these devices include in their functionality the coupling of wave-guided to radiated modes.
Photonic devices based on 2D PC have been principally aimed, so far, at forming the basic building blocks of integrated photonics and are usually designed for in plane wave-guided operation. We remind that the operation of photonic integrated circuits based on 2D PC may be deeply affected by optical losses resulting from unwanted diffractive coupling of waveguided modes with the radiation continuum.

Instead of attempting to confine the light entirely within waveguide structures, the 2D structures can be deliberately opened to the third space dimension by *controlling* the coupling between wave-guided and radiation modes. In this approach, the exploitation of the optical power is achieved by accurately tailoring the optical radiation into free space.

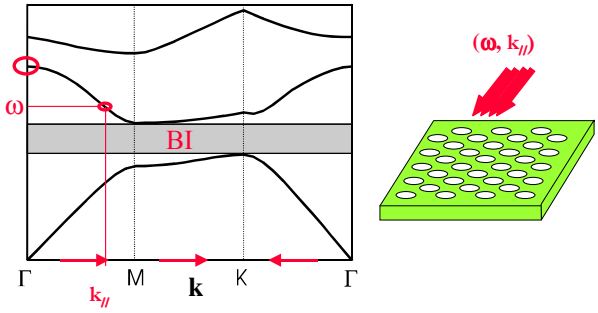


Fig.3. Illustration of the resonant coupling between a waveguided mode and a radiated mode.

A simple illustration of this approach is the use of a plain Photonic Crystal Membrane as a wavelength selective transmitter / reflector: when light is shined on this photonic structure, in an out-of-plane (normal or oblique) direction, resonances in the reflectivity spectrum can be observed. These resonances, so called Fano resonances [4], arise from the coupling of external radiation to the guided modes in the structures, whenever there is a good matching between the in-plane component of the wave vector of the incident wave and the wave vector of the guided modes (figure 3). Accurate tailoring of the spectral characteristics of the Fano resonances (shape, spectral width) is made possible by the design of the 2DPC membrane (type of 2DPC, membrane thickness,…). In addition and very importantly, the ability of high index contrast PC to slow down photons and to confine them laterally, especially at the high symmetry points (or extremes) of the dispersion characteristics, allows for the production of very compact, yet very efficient, devices.

A variety of passive as well as active devices has been demonstrated in the recent literature. For example, very compact passive reflectors showing a large bandwidth (a few hundreds of nanometers) and consisting in a plain 2DPC membrane formed in Silicon on silica have been reported [5].

The 2DPC membrane can be also designed in such a way as to result in very strong Fano resonances, that is to say with a very narrow spectral bandwidth. Use of such strong Fano resonances has been made for the demonstration of very low threshold and very compact surface emitting Bloch mode laser [6]. The photonic crystal consists in a graphite lattice (figure 4), which can be viewed as an array of H_1 coupled cavities, formed in a triangular lattice.

The graphite lattice 2D PC active membrane used for surface laser emission is very generic and can apply for a large variety of other types of active devices, at the very cheap expense of slight changes in the design of the 2DPC. Along this line spectacular demonstrations of diverse devices have reported recently, including optical amplifiers and fully optical micro-switches [7, 8]. For the latter it is made use of electronic Kerr

effect, via photo-injection of carriers in quantum wells, to manipulate the Fano resonance wave-length.
All these devices are convincing illustrations of a planar technological approach resulting in 2DPC devices freed from the bi-dimensional universe.

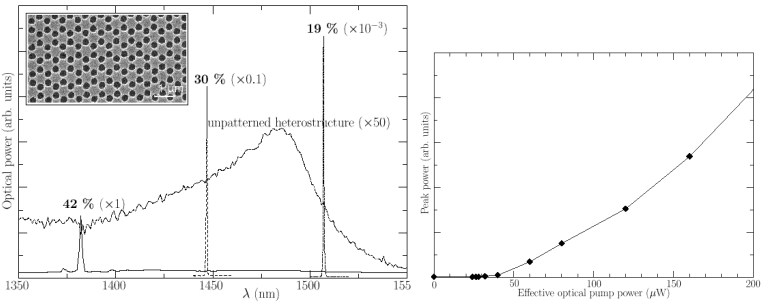


Fig.4. Emission spectra of the surface emitting laser formed in a graphite lattice 2D PC, for different hole filling factors (f). The plot of the emitted power versus the pumping power indicates a threshold power of 40 μW for f = 19%.

Towards 2.5D Micro-Nano-Photonics

It has been proposed a major extension of planar technology, through exploitation of the third (« vertical ») dimension by using a so-called multi-layer approach, where the lateral high index contrast patterning of layers would be combined with the vertical 1D high index contrast patterning : it is here more appropriate to think in terms of « 2.5 dimensional » photonic structures, in which an interplay between wave-guided-confined photons and radiated photons propagating through the planar multilayer structure occurs [3]. The simplest illustration of this approach is the use of a plain Photonic Crystal Membrane as discussed in the previous section. If one considers now a multilayer structure, the strong vertical 1D modulation of the optical index, allows for a fine and efficient « carving » of the density and vertical field distribution of radiated modes, using a limited number of layers. As a result the variety of coupling schemes between optical modes is considerably widened, thus opening large avenues toward new photonic functionality.
The technology schemes to be adopted are compatible with technological approaches which are normally describable as planar and are familiar to the world of silicon microelectronics.
The 2.5D Microphotonics approach has been successfully applied recently for the production of very low threshold power microlasers [9] and of a new class of optical bistable devices based on the Kerr effect [10].
The basic common building block for these devices is shown is figure 5. It consists in a graphite lattice 2D PC active membrane, similar to that presented in the previous section, bonded on to the top of a Bragg reflector formed by high index contrast SiO_2-Si quarter wavelength pairs. The thickness t_G of the top SiO_2 “gap” layer, which supports the bonded 2D PC membrane, is essential for the performances of both types of devices, in terms of the requested threshold power : the coupling rate of wave-guided photons with the radiation continuum is inhibited for t_G on the order of an odd integer number

of quarter wavelength, which results in an increased strength of the slow Bloch mode Fano resonance and, therefore, in a significantly reduced threshold power of the device (and *vice versa* for t_G on the order of an integer number of half wavelength).

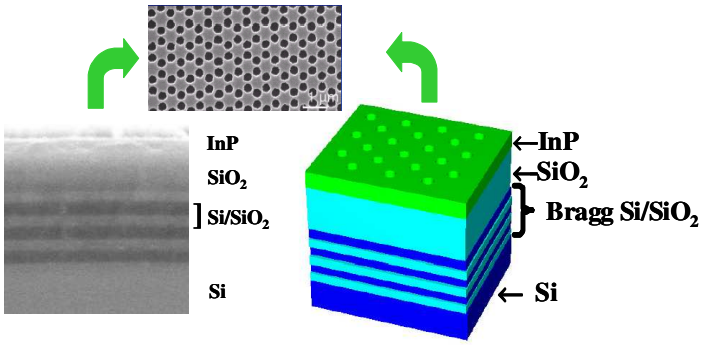


Fig.5. Photonic Crystal membrane bonded on top of a Bragg

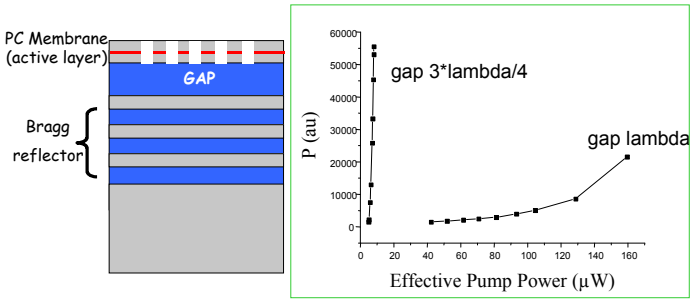


Fig.6. 2.5D Photonic Crystal micro-laser: the thickness of the top silica "gap" layer has a wide impact on the threshold power of the micro-laser

This is illustrated in a spectacular manner in figure 6, which shows the gain characteristics of the micro-laser for the two (quarter-wavelength or half wave-length) t_G values. Optical bistabity could be demonstrated, as expected, for the sole quarter-wavelength t_G case, corresponding to the strongest mode confinement (inhibition of coupling to the radiation continuum). It should be pointed out that the only difference between these two categories of devices lies in the particular design of the 2D graphite PC: needless to say, therefore, that the building block shown in figure 5 is very generic.
Other domains of photonics should take advantage of the 2.5D microphotonics approach. For example, the introduction of 2D PC in MOEMS (Micro Opto Electro Mechanical) devices shows great promises in terms of widening of the spectrum of (electromechanically actuable) optical functions, achievable with further enhanced compactness structures.

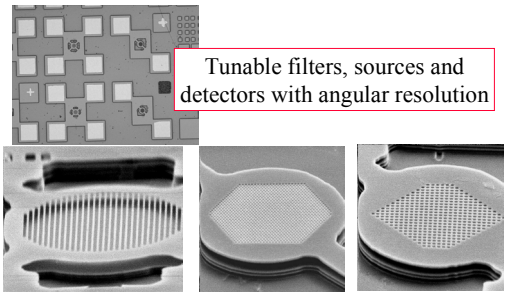


Fig.7. New class of MOEMS devices: structures including several InP membranes suspended in air, with a 1D and 2D PC formed in the top membrane (SEM view).

Figure 7 shows examples of such 2.5 dimensional MOEMS structures. These new types of photonic structures should be applied in various domains, including Optical Telecommunications (tunable or switchable wavelength selective devices, taking advantage of the extra angular resolution provided by the in-plane 1D-2D PC). Highly selective and widely tunable 2.5D MOEMS filters have been demonstrated recently [11]. Also, a new family of hybrid VCSEL, where one of the traditional Bragg reflectors is replaced by a PC membrane reflector, has been reported both in the GaAs and InP systems [12, 13].

Conclusion

The flow of innovations, whose threshold has been initiated in the late 1980 by the introduction of the concept of photonic crystals [1], is still very close to its source and will inflate in the future to an extent which is certainly beyond our full consciousness. We hope that the reader will have been convinced that 2D PC are fully engaged in the process of innovation and that we are living, in that respect, a true microphotonic revolution. We have shown, in particular for the so called 2.5D microphotonics, where 2D PC are deliberately opened to the third dimension of space, convincing demonstrations of their ability to generate, in the short run, a wide range of photonic devices (« killer applications »), combining compactness, spatial (angular) and spectral resolution, and whose fabrication meets the standards of the planar technology, familiar to the world of microelectronics.

This work was partly supported by the EC FP6 network of excellence ePIXnet.

References

[1] E. Yablonovitch, "Inhibited spontaneous emission in solid – state physics and electronics", Phys. Rev. Lett., vol. 58, pp. 2059-2062, 1987.

[2] C. Monat, C. Seassal, X. Letartre, P. Viktorovitch, P. Regreny, M. Gendry, P. Rojo-Romeo, G. Hollinger, E. Jalaguier, S. Pocas and B. Aspar, "InP 2D photonic crystal microlasers on silicon wafer : room temperature operation at 1.55µm", Electron. Lett. vol. 37 pp. 764-766, 2001.

[3] X. Letartre, J. Mouette, C. Seassal, P. Rojo-Romeo, J.-L. Leclercq, P. Viktorovitch, "Switching devices with spatial and spectral resolution combining Photonic Crystal and MOEMS structures", Journal of Lightwave Technology, vol. 21, pp. 1691-1699, 2003.

[4] VN Astratov, DM Whittaker, LS Culshaw, RM Stevenson, MS Skolnick, TF Krauss and RM De La Rue. "Photonic band-structure effects in the reflectivity of periodically patterned waveguides", Phys. Rev. B, vol. 60 pp. R16255-R16258, 1999.

[5] S. Boutami; B.B. Bakir; H. Hattori; X. Letartre; J.-L. Leclercq; P. Rojo-Romeo; M. Garrigues; C. Seassal; P. Viktorovitch, "Broadband and compact 2-D photonic crystal reflectors with controllable polarization dependence", Photonic Technology Letters, vol. 18, 835-837, 2006.

[6] J. Mouette, C. Seassal, X. Letartre, P. Rojo-Romeo, J.-L. Leclercq, P. Recgreny, P. Viktorovitch, E. Jalaguier, P. Perreau, H. Moriceau, "Very low threshold vertical emitting laser operation in InP graphite photonic crystal slab on silicon", Electron. Lett vol.39, pp. 526-528, 2003.

[7] Crina Cojocaru, F. Raineri, P. Monnier, C. Seassal, X. Letartre, P. Viktorovitch, A. Levenson, R. Raj, "Ultrafast nonlinear dynamics of a two-dimensional InP-based photonic crystal response", Appl. Phys. Letters, vol. 85, pp. 1880-1882, 2004.

[8] F. Raineri, G. Vecchi, A. M. Yacomotti, C. Seassal, P. Viktorovitch, R. Raj, A. Levenson, "Doubly resonant photonic crystal for efficient laser operation: Pumping and lasing at low group velocity photonic modes", Appl. Phys. Letters vol. 86, pp. 011116-118, 2005.

[9] B. Ben Bakir, Ch. Seassal, X. Letartre, P. Viktorovitch, M. Zussy, L. Di Cioccio, And J. M. Fedeli, "Surface-emitting microlaser combining two-dimensional photonic crystal membrane and vertical Bragg mirror", Appl. Phys. Lett. Vol. 88, pp. 081113-115, 2006 and Virtual Journal on Nanoscale Science & Technology, 13 n°10, 2006.

[10] A. M. Yacomotti, F. Raineri, G. Vecchi, R. Raj, A. Levenson, B. Ben Bakir, C. Seassal, X. Letartre, P. Viktorovitch, L. Di Cioccio, J. M. Fedeli, "All-optical bistable band-edge Bloch modes in a two-dimensional photonic crystal", Appl. Phys. Lett. vol. 88, pp. 231107-109 2006.

[11] S. Boutami, B. Ben Bakir, J.-L. Leclercq, X. Letartre, P. Rojo-Romeo, M. Garrigues, P. Viktorovitch, I. Sagnes, L. Legratiet, And M. Strassner, "Highly selective and compact tunable MOEMS photonic crystal Fabry-Perot filter", Optics Express, vol. 14, pp. 3129-3137, 2006.

[12] C. Y. Huang, Y. Zhou, and C. J. Chang-Hasnain, "A surface-emitting laser incorporating a high-index-contrast subwavelength grating", Nat. Photonics vol. 1, pp. 119-122, 2007.

[13] S. Boutami, B. Ben Bakir, J.-L. Leclercq, P. Viktorovitch, "Compact and polarization controlled 1.55µm vertical-cavity surface emitting laser using sinble-layer Photonic Crystal mirror", Appl. Phys. Lett. vol. 91, pp. 071105-107, 2007.

Pillar photonic crystal for polarization filtering

A.A.M. Kok, J.J.G.M. van der Tol, E.J. Geluk, F. Karouta and M.K. Smit

COBRA Research Institute, Eindhoven University of Technology,
Den Dolech 2, P.O. Box 513, 5600 MB, Eindhoven, The Netherlands
j.j.g.m.v.d.tol@tue.nl

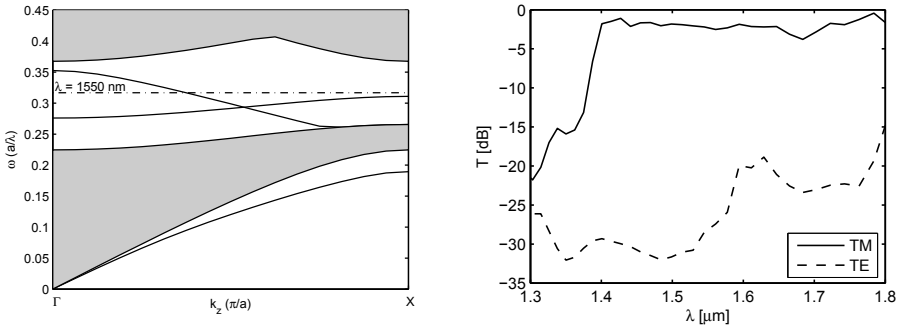
Abstract *- The strong polarization dependence of two-dimensional photonic crystals is exploited for polarization filtering. The device with a length of 3.9 μm is integrated in a photonic integrated circuit based on InP waveguide technology. The average transmissions in the EDFA-window are* -8.7 *dB for TM polarization and* -26.5 *dB for TE polarization.*

Introduction

Two-dimensional photonic crystals (2D PhCs) have been subject to extensive research in the past years, offering a huge potential for integration in photonic integrated circuits. They can be used to miniaturize existing integrated optical devices, e.g. bends, microcavities, add-drop filters and band edge lasers. Furthermore, their special properties can be used to design devices based on new principles. An example of such a device is a polarization filter. The polarization sensitivity of photonic crystals makes it possible to significantly reduce the foot print of polarization filters.
Photonic integrated circuits can be realized in different material systems, depending on the applications. However, indium phosphide (InP) technology is the only platform to monolithically integrate active and passive devices for use in the EDFA window (1530 – 1570 nm), the operating range for telecom applications. The classical waveguides of InP photonic integrated circuits are based on total internal reflection; light is confined to the indium gallium arsenide phosphide (InGaAsP Q[1.25]) core, which has a higher refractive index than the InP cladding layers ($n_{\mathrm{InGaAsP}} = 3.3640$ and $n_{\mathrm{InP}} = 3.1693$). In 2D PhCs, the in-plane confinement is created by the photonic band gap properties of the crystal, whereas the light is confined out-of-plane by total internal reflection.
TM-polarized light has its electric field vector parallel to the pillars, normal to the plane of the chip, and TE-polarization has its electric field vector in the plane of the chip. The strong polarization dependence of 2D photonic crystals ([1]) is used to investigate a TE polarization filter based on a pillar photonic crystal waveguide in a square lattice of high-index pillars. The device is integrated in a classical photonic integrated circuit on an InP substrate with a 500-nm-thick InGaAsP core layer and a 1-μm-thick InP top cladding. The layer stack of the pillar photonic crystal is compatible with that of the classical photonic integrated circuit, and so is the fabrication technology.

Design of the TE filter

A waveguide based on a line defect in a pillar PhC can serve as a TE filter if the TE polarized light does not couple into the PhC waveguide (either if this waveguide has a TE band gap or if the coupling efficiency for TE is very small) or if the TE polarized light is not confined by the crystal, in which case it radiates away from the line defect. The



(a) (b)

Figure 1: Modeling of a photonic crystal waveguide consisting of a line of larger pillars in a square lattice: a) band diagram showing the TM modes of the waveguide, where the lattice constant is 491 nm, the radius of the rods is 123 nm and that of the defect pillars is 210 nm, and b) the calculated transmission of an 8-period-long waveguide for both TM and TE polarization.

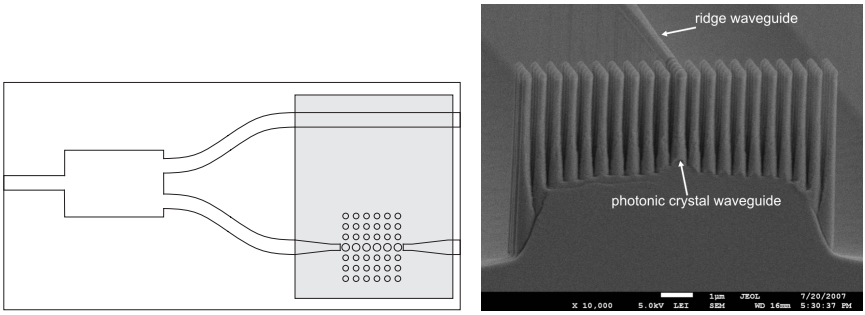
transmission of TM polarized light should be high. Therefore the line defect was first optimized for TM transmission.

Based on 2D band solver calculations, and using the effective index method to account for the third dimension, the background PhC was chosen to have a lattice constant $a = 491$ nm and a radius $r = 0.25a$. The introduction of a line defect of larger pillars along the ΓX-direction creates two guided TM modes inside the PhC band gap. Fig. 1(a) shows the projected band diagram of a PhC waveguide based on a line defect with radius $r_{\mathrm{d}} =$ 210 nm. The mode that increases in frequency, having a positive slope, is a mode with odd symmetry. The mode with a negative slope is a mode with even symmetry. At the wavelength of operation, i.e. in the range from 1530 to 1570 nm, the waveguide only supports the even symmetry mode.

The light is coupled from a conventional ridge waveguide to the PhC waveguide and vice versa by placing the waveguides next to each other as is schematically shown in Fig. 2(a). The ridge waveguide is first adiabatically tapered down to a width that is equal to the diameter of the defect pillars, i.e. 420 nm. The gap between the end facet of the ridge waveguide and the first PhC pillar results in the highest transmission if it chosen in such a way that the ridge end facet is located exactly at the mirror plane between the first defect pillar and its virtual neighbor; this optimal gap is given by $g_{\mathrm{opt}} = 0.5(a - 2r_{\mathrm{d}})$.

In Fig. 1(b) the calculated transmission is shown for a PhC waveguide that is 8 periods long (based on a 3D FDTD calculation). The transmission for TM polarized light is -2.3 dB with an extinction ratio better than 25 dB around $\lambda = 1550$ nm. The good performance of this device is mainly due to a high coupling efficiency of the TM polarization at the transitions between the ridge waveguides and the PhC waveguide, while the TE polarization has a poor coupling from the access ridge waveguide to the PhC waveguide. The length of the polarization filter is only 3.9 μm (eight times the lattice constant).

The optical circuit design, as schematically shown in Fig. 2(a), on the chip consists of a 2-μm-wide input ridge waveguide, followed by a 1×2 multimode interference coupler



(a) (b)

Figure 2: a) Schematic drawing of the chip layout, and b) SEM image of a cross-section of a photonic crystal waveguide connected to a classical ridge waveguide on an InP substrate.

(MMI) splitting the light into two branches. In the reference branch, the light propagates through a conventional ridge waveguide towards the output side of the chip. The other branch contains a PhC waveguide. This configuration has two advantages. First, the coupling into the input waveguide can easily be optimized using the reference arm, even if the PhC waveguide has high losses. Second, the transmission of the PhC waveguide can directly be calculated from a comparison with the transmission of the reference arm.

Fabrication

The ridge waveguides and the MMIs are defined by optical lithography, whereas the photonic crystals are defined by electron beam lithography to have sufficient control over the critical dimensions. At the transition between the optically defined waveguides and the e-beam lithography areas the waveguides are 0.8 µm wide. The waveguide pattern, including the PhCs, is first defined in a 50-nm-thick chromium masking layer by a series of lithography steps. This pattern is transferred into a 430-nm-thick silicon dioxide layer by reactive ion etching (RIE) using a CHF_3 chemistry. Finally, the deep etch to create the waveguides is performed by inductively coupled plasma (ICP) RIE using a $Cl_2 : Ar : H_2$ chemistry [2]. Fig. 2(b) shows a scanning electron microscope (SEM) image of the PhC structure after the ICP etch. The pillars are ~ 3.0 µm deep. According to simulations this should be enough to prevent the light from coupling to the substrate modes. Lateral dimensions of the PhC are well under control with this fabrication process [3].

Transmission measurements

Light from a tunable laser source is coupled into the input waveguide using a microscope objective. The polarization is fixed to TM or TE by use of a polarizer. At the output side, the transmitted light is collected with a lensed fiber. The collected light is measured by a photoreceiver. After optimization of the in- and outcoupling alignment at $\lambda = 1550$ nm, the tunable laser scans the wavelength from 1530 to 1570 nm in steps of 0.1 nm.
The cleaved facets of the chip introduce Fabry-Pérot fringes on the measured spectrum. These are averaged out by taking a running average over 10 data points of the spectrum. From the averaged spectra of both the branches, the transmission of the photonic crystal

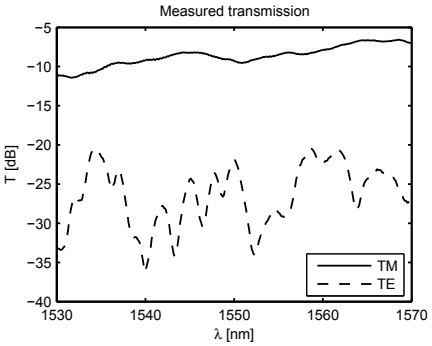


Figure 3: Measured transmission of a photonic crystal waveguide for both polarizations.

from 0.8 µm width down to the diameter of the defect pillars, the coupling to and from the photonic crystal waveguide and the propagation loss of the photonic crystal waveguide. The measured transmission for both TM and TE polarization is shown in Fig. 3. The average transmission for TM polarized light is -8.7 dB. The losses are higher than was calculated in the 3D simulation, probably due to scattering and to the non-vertical sidewalls of the pillars, which can cause large substrate leakage. Both can be reduced by an optimization of the fabrication technology. The TE transmission is -26.5 dB, which is in agreement with the simulated transmission. The modulation on the TE polarization is due to the reflections at the transitions between the ridge waveguides and the PhC waveguides, and to the reflections at the transitions between the optically defined waveguides and the e-beam defined ones. The latter reflections can be eliminated by adapting the design of the chip. The average transmission for TE polarization is -26.5 dB, whereas that of TM polarized light is -8.7 dB. This implies that an extinction ratio of about 18 dB should be feasible if the reflections are reduced.

Conclusions

A very short TE polarization filter can be realized in a pillar photonic crystal. The fabrication process is compatible with that of a photonic integrated circuit based on conventional waveguide technology. The device with a length of 3.9 µm has a transmission of -8.7 dB for TM polarization and -26.5 dB for TE polarization. The high losses are probably due to fabrication issues which can be solved by further optimization of the technology.

This research is supported by NanoNed, a technology programme of the Dutch Ministry of Economic Affairs via the foundation STW.

References

[1] John D. Joannopoulos, Robert D. Meade, and Joshua N. Winn. *Photonic crystals: molding the flow of light*. Princeton university press, Princeton, 1995.

[2] B. Docter, E.J. Geluk, M.J.H. Sander-Jochem, F. Karouta, and M.K. Smit. Deep etched DBR gratings in InP for photonic integrated circuits. In *Proc. IPRM*, pages 226–228. Matsue, Japan, 2007.

[3] A.A.M. Kok, E.J. Geluk, B. Docter, J.J.G.M. van der Tol, R. Nötzel, M.K. Smit, and R. Baets. Transmission of pillar-based photonic crystal waveguides in InP technology. *Appl. Phys. Lett.*, 91:201109, November 2007.

Local tuning of the optical response of two dimensional photonic crystals

P. El-Kallassi[1], S. Balog[2], L. Balet[2,3], L. H. Li[2], R. Ferrini[1], R. Houdré[2], A. Fiore[3] and L. Zuppiroli[1]

[1]Laboratoire d'Optoélectronique des Matériaux Moléculaires, EPFL, 1015 Lausanne, Switzerland
pascale.el-kallassi@epfl.ch
[2]Institut de Photonique et d'Electronique Quantique, EPFL, 1015 Lausanne, Switzerland
[3]Eindhoven University of Technology, P.O. Box 513, NL-5600 MB Eindhoven, The Netherlands

Abstract. *Local tuning of the optical response of GaAs-based two dimensional photonic crystals (PhCs) is reported. A selective polymer infiltration technique was developed. Scanning electron microscopy and optical measurements were used to characterize the filled PhC structures.*

Over the past decade, photonic crystals (PhCs) have been intensively studied as a new platform for the realization of integrated optical devices such as waveguides, filters and switches [1]. On one hand, these devices are classically fabricated by omitting, modifying the size or the position of the air holes [2]. On the other hand, several theoretical studies suggested that selective filling of photonic crystal holes can provide a novel platform for ultracompact photonic integrated circuits and open the way up to create components such as single mode waveguides, broadband low-reflection waveguide bends, crossings, splitters [3] and ultrahigh-*Q* cavities [4]. Therefore PhC infiltration with organic materials [5-8] has a great potential for the realization of PhC devices provided that a selective filling procedure is achieved. For instance, F. Intonti *et al.* have demonstrated local microinfiltration of liquids via hollow submicron size pipettes [9], and C. Smith et *al.* have used a similar technique to create a PhC double heterostructure [10]. Moreover, D. Erickson et *al.* have used nanofluidic targeting to infiltrate a single row of holes within a planar PhC using fluids with different refractive indices [11].

In this communication, we present a selective polymer infiltration technique to trim the optical properties of GaAs-based planar PhC membranes. Our technique has several advantages with respect to micro-/nano- pipetting and nanofluidic procedures: it is fast, simple, easily reproducible and enables the control of the size of infiltrated PhC region (from 1 to 10 μm) [12].

Experiment

The sample, grown by molecular beam epitaxy, consists of a 320-nm-thick GaAs membrane on top of a 1.5 μm $Al_{0.7}Ga_{0.3}As$ sacrificial layer. A single layer of self-assembled InAs quantum dots (QDs) (high aerial density:100-150 dots/μm^2) emitting at 1.3 μm is embedded in the middle of the membrane. PhC nanocavities were fabricated using e-beam lithography and CHF_3 plasma etching of a hard SiO_2 layer which eventually serves as a mask for the pattern transfer onto the GaAs layer by $SiCl_4/O_2/Ar$ reactive ion etching [13]. The sacrificial layer is then selectively etched in a diluted HF

solution to release the GaAs membrane. As a result, a PhC structure is obtained at the center of a 12 μm diameter suspended membrane. A L3 defect cavity was formed by omitting three holes along the ΓK direction at the center of the PhC triangular slab. The lattice constant and the holes diameter are a=330 nm and d~193nm, respectively [Fig. 1(a)]. This provides an air filling factor of 0.31 that corresponds to a photonic bandgap for the TE polarization at wavelengths around 1.3 μm. For the selective infiltration experiments we used a polymer with a refractive index n=1.502±0.005 at λ=1.3 μm. Details on the filling procedure are given in reference 12.

Results

Scanning electron microscopy (SEM) top view images of (a) empty and (b)-(c) locally infiltrated L3 cavities are shown in Figure 1, respectively. The size of the infiltrated PhC region can be controlled at the micrometer scale (i.e. corresponding to tens of air holes): e.g. 5.2 μm and 1.2 μm in figures 1(b) and 1(c) respectively.

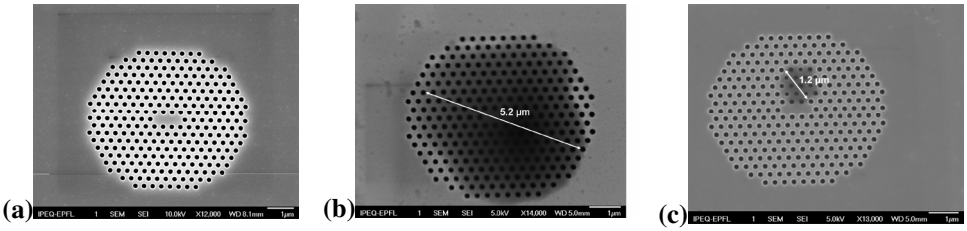


FIG. 1. Scanning electron microscopy top view images of (a) empty and (b)-(c) locally infiltrated L3 cavities. The dark regions are the polymer-filled areas.

Optical measurements were performed with an internal light source technique with frontal collection [14]. A helium-neon laser at 632.8 nm was used to excite the QD luminescence in the membrane. The frontal emitted signal is collected through the same objective and then coupled to a multimode fiber which is connected to a spectrometer providing a spectral resolution of 0.1 nm. The results are shown in Figures 2 (a) and (b). When the empty cavity is excited, a resonance peak appears at λ~1248 nm that corresponds to a cavity mode of the L3 cavity. Fitting the measured resonance wavelength with a two-dimensional plane wave expansion (2D-PWE) calculation, a filling factor value of 0.31±0.01 is obtained, which agrees with SEM measurements. The full width at half maximum of the peak resonance yields a quality factor Q ≈ 435.

Once the cavity boundaries are globally infiltrated [Fig. 1(b)], the resonance peak red-shifts due to the reduced refractive index difference between the holes and the substrate (Δλ=44 nm) [Fig. 2(a)]. The 2D-PWE fit of this energy peak provides the refractive index value of the infiltrated holes that is consistent with the polymer refractive index measured by ellipsometry. After the infiltration, the cavity quality factor decreases due to the reduced reflectivity of the PhC boundaries (Q' ≈ 199).

When the cavity is locally infiltrated [Fig. 1(c)], the resonance peak slightly red-shifts (Δλ=4 nm) [Fig. 2(b)]. This shift is consistent with the 2D-PWE calculation for the same polymer distribution as in Fig. 1(c). The cavity quality factor slightly decreases with respect to the empty state (Q' ≈ 360).

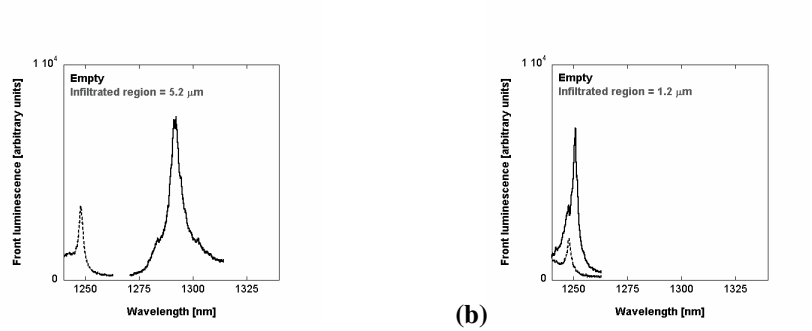


FIG. 2. Front luminescence spectra of the locally infiltrated L3 cavities shown in figure 1 (solid lines). The diameter of the polymer-filled region is (a) 5.2 μm and (b) 1.2 μm, respectively. The resonance peaks for the corresponding empty cavities are shown as reference (dashed lines).

The authors thank N. Le Thomas, M. Schär from the Ecole Polytechnique Fédérale de Lausanne (EPFL, Switzerland) and M. Hofmann from 3D systems (Marly, Switzerland) for their help. This work was performed within the framework of the European Network of Excellence on Photonic Integrated Components and Circuits (ePIXnet-contract 004525) and the Swiss National Center of Competence in Research (NCCR) in Quantum Photonics.

References

[1] K. Busch, S. Lölkes, R.B. Wehrspohn, and H. Föll, Photonic Crystals, Weinheim: Wiley-VCH, 2004.
[2] B-S. Song, S. Noda, T. Asano and Y. Akhane, "Ultra-high-*Q* photonic double-heterostructure nanocavity", Nature Materials, vol. 4, pp. 207-210, 2005.
[3] S. Mingaleev, M. Schillinger, D. Hermann and K. Busch, "Tunable photonic crystal circuits: concepts and designs based on single-pore infiltration", Optics Letters, vol. 29, pp. 2858-2860, 2004.
[4] S. Tomljenovic-Hanic, C. Martijn de Sterke and M.J. Steel, "Design of high-*Q* cavities in photonic crystal slab heterostructures by air-holes infiltration", Optics Express, vol. 14, pp.12451-12456, 2006.
[5] J. Martz, R. Ferrini, F. Nüesch, L. Zuppiroli, B. Wild, L.A. Dunbar, R. Houdré, M. Mulot and S. Anand, "Liquid crystal infiltration of InP-based planar photonic crystals", Journal of Applied Physics, vol. 99, 103105, 2006.
[6] R. Ferrini, J. Martz, L. Zuppiroli, B. Wild, V. Zabelin, L.A. Dunbar, R. Houdré, M. Mulot, and S. Anand, "Planar photonic crystals infiltrated with liquid crystals: tuning and optical characterization of molecule orientation", Optics Letters, vol. 31, pp. 1238-1240, 2006.
[7] P. El-Kallassi, R. Ferrini, L. Zuppiroli, N. Le Thomas, R. Houdré, A. Berrier, S. Anand, and A. Talneau, " Optical tuning of planar photonic crystals infiltrated with organic molecules," Journal of the Optical Society of America B, vol. 24, pp. 2165-2171, 2007.
[8] R. van der Heijden, C-F. Carlström, J. Snijders, R. W. van der Heijden, F. Karouta, R. Nötzel, H. Salemink, C. Kjellander, C. Bastiaansen, D. Broer, and E. van der Drift, "InP-based two dimensional photonic crystals filled with polymers," Applied Physics Letters, vol. 88, 161112, 2006.
[9] F. Intonti, S. Vignolini, V. Türck, M. Colocci, P. Bettotti, L. Pavesi, S.L. Schweizer, R. Wehrspohn and D. Wiersma, "Rewritable photonic circuits", Applied Physics Letters, vol. 89, 211117, 2006.
[10] C. L. C. Smith, D. K. C. Wu, M. W. Lee, C. Monat, S. Tomljenovic-Hanic, C. Grillet, J. Eggleton, D. Freeman, Y. Ruan, S. Madden, B. Luther-Davies, H. Giessen and Y-H. Lee, "Microfluidic photonic crystal double heterostructures", Applied Physics Letters, vol. 91, 121103, 2007.
[11] D. Erickson, T. Rockwood, T. Emery, A. Scherer and D. Psaltis, "Nanofluidic tuning of photonic crystal circuits", Optics Letters, vol. 31, pp. 59-61, 2006.

[12] P. El-Kallassi, S. Balog, L. Balet, L.H. Li, R. Ferrini, R. Houdré, A. Fiore and L. Zuppiroli, "Local tuning of the optical response of two-dimensional photonic crystals", Applied Physics Letters, submitted.
[13] A. Gerardino, M. Francardi, L. Balet, C. Monat, C. Zinoni, B. Alloing, L.H. Li, N. Le Thomas, R. Houdré and A. Fiore, "Fabrication and characterization of point defect photonic crystal nanocavities at telecom wavelength", Microelectronic Engineering, vol. 84, pp. 1480-1483, 2007.
[14] R. Ferrini, D. Leuenberger, M. Mulot, M. Qiu, J. Moosburger, M. Kamp, A. Forchel, S. Anand, and R. Houdré, "Optical study of two-dimensional InP-based photonic crystals by internal light source technique", IEEE Journal of Quantum Electronics, vol. 38, pp. 786-799, 2002.

Hybrid Integration for Advanced Photonic Devices

A. Poustie

CIP Ltd., B55 Adastral Park, Martlesham Heath, Ipswich, IP5 3RE, U.K.
alistair.poustie@ciphotonics.com

Abstract. *Hybrid photonic integration with passive assembly techniques allows compact optical modules to be realised with high optical performance and low packaging cost. Recent advances in integrating semiconductor optical amplifiers into practical all-optical signal processing circuits is described, with advanced applications from optical memory to sophisticated burst-mode optical regenerators.*

Introduction

The ability to easily combine different optical components via photonic integration is widely recognised as one of the key strategic technologies for the future. Within photonics, it is also acknowledged that using one material system for monolithic integration is not always viable for all the required optical functions. In addition, the optical performance of monolithically integrated devices is often compromised to some degree and this has been a barrier to commercial realisation of devices. In other words, compactness on its own is not sufficient for practical use of integrated devices – optical performance is also vitally important. To address this, CIP has pioneered a photonic integration approach using hybrid integration technology that allows different high-performance optical components (active and passive) to be combined into integrated modules [1]. This is achieved by using precision design and fabrication techniques that allow the different component piece parts (as shown in Figure 1) to be simply pushed together via passive assembly. We believe that this approach not only offers the necessary precision for low-loss coupling of single-mode optical components, but will also lead to greater module scalability, flexibility and lower cost manufacturing in the future.

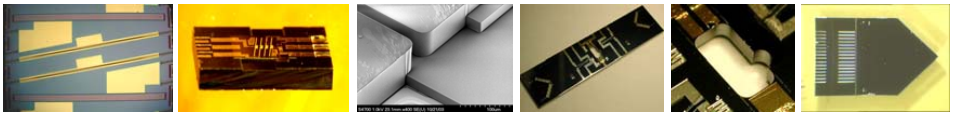


Figure 1: Photographs of the hybrid integration platform piece parts (L to R: precision cleaved semiconductor optical amplifier (SOA) monolithic twin chip, Si daughterboard, polymer precision edge stops, PLC, recess in PLC for SOAs, fibre ribbon clip).

In this paper, recent advances in the passive assembly hybrid integration platform are described. In particular, its use in combining InP actives (SOAs) and passive devices (optical isolator) with planar silica waveguides to create advanced optical signal processing circuits is demonstrated. These modules use the nonlinear optical properties of SOAs to allow one light beam to be switched with another [2]. SOAs are attractive components because they are compact (~mm size), can be electrically powered, provide optical gain and require very low switching energies (<100fJ). To operate at high switching speeds (>40Gb/s), the SOAs typically have to be incorporated into a compact optical interferometer, such as a Mach-Zehnder device, in order to exploit the cross-phase as well as the cross-gain dynamics of the optical switching. These types of

integrated interferometric devices are well suited to hybrid integration of the active SOAs with low-loss, passive planar silica waveguide interferometers. The planar silica waveguides allow other optical functions, such as wavelength selective combiners/splitters, to also be included in the module [3] and provides a scalable path to compact arrays of 40Gb/s regenerator devices.

Hybrid Integration Platform

CIP has been developing a hybrid integration platform over many years that is based on passive assembly for low cost. The basic principle of this platform is that the active and passive devices are designed together so that the complete integrated circuit is optimised, rather than just the individual components. For example, the active InP chips (e.g. SOAs) are designed with optical mode expansion and mechanical precision cleave features that make the overall chip size larger, but allows the chip to be passively aligned to the planar lightwave circuit (PLC). The PLC ($\Delta \sim 0.75\%$) also has some mode expansion to minimise coupling loss and retains the attractive silica waveguide features of low transmission loss (<0.1dB/cm) and high thermal stability. The active chips are aligned to the PLC by mounting the chip on a silicon submount (or 'daughterboard') and then mounting the assembled daughterboard onto the PLC (or 'motherboard') so that the active InP components fit into precision machined or etched holes in the motherboard, as schematically shown in Figure 2. The lateral position of the daughterboard is defined by precision polymer (SU-8) stops that are lithographically defined on the motherboard. Vertical position is defined by the height of the silica cladding above the silica waveguides in the PLC. These processes can give micron scale alignment accuracy which is sufficient to align single-mode optical elements with <1dB in coupling loss.

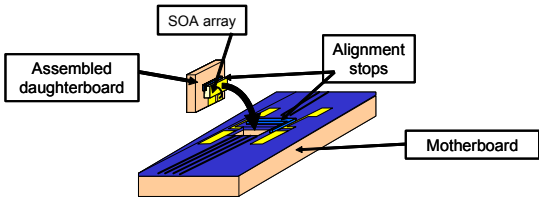


Figure 1: Schematic diagram of the CIP hybrid integration platform with passive assembly.

Active Devices

One of the advantages of the hybrid integration approach is that the active InP devices used in the platform can be optimized without regard to epitaxial or processing compatibility with the other optical parts of the integrated circuit. Hence, we use advanced InP multiple quantum well (MQW) SOA devices in a buried heterostructure device geometry since these offer very high performance [4] and are manufacturable. These SOAs achieve state-of-the-art performance by also incorporating optical mode expanders, tilted facets and coatings to reduce the residual facet reflectivity to $<10^{-5}$ and hence maintain high optical gain (>30dB) at high injection currents. This performance is vital to achieve the very fast gain recovery lifetimes required for high-speed optical processing modules [5]. These SOAs can be produced in monolithically integrated,

precision cleaved arrays, as shown in figure 3, for one-step assembly into hybrid integrated devices.



Figure 3: Photograph of monolithic SOA chips (single, twin, quad and octo).

Passive Devices

The PLC is used in the integration platform to interconnect the relevant active devices with waveguide structures such as interferometers and couplers. A typical PLC is shown in figure 4, which comprises 4 parallel Mach-Zehnder interferometers, Y-branch combiners, thermo-optic heaters and a parallel (12 way) fibre clip connection on each end. The 2 holes in the PLC are to accommodate the assembly of two monolithic quad arrays of SOA devices.

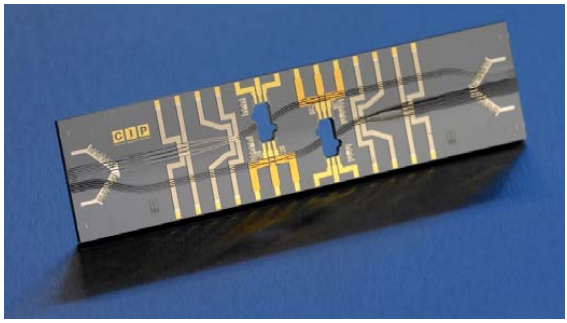


Figure 4: Photograph of a 4 channel SOA-MZI motherboard PLC.

In addition to waveguide devices, other passive optical element can be designed to fit with the hybrid platform. Figure 5 shows an example of a passively assembled optical isolator that uses the same assembly approach to provide on-chip isolation for the optical circuits.

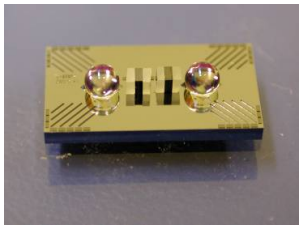
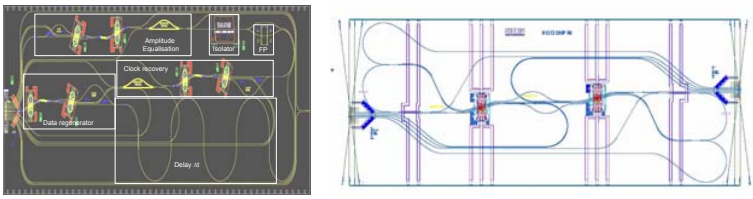


Figure 5: Photograph of a passively assembled optical isolator for the hybrid integration platform.

Hybrid Integrated Optical Circuits

By combining the functionality of the various active and passive components of the hybrid integration platform, it is relatively easy to form advanced optical circuits. Two different designs are shown in figure 6 for a 40Gb/s time-of-flight optical memory and a 40Gb/s burst-mode receiver (BMR) [6]. Each circuits uses common optical piece parts, with only the waveguide circuitry differing to define the interconnections and hence the circuit functionality.



(a) *(b)*

Figure 6: Waveguide design layouts for (a) 40Gb/s BMR and (b) optical memory.

The fabricated BMR circuit and package is shown in figure 7, and comprises 9 different assemblies of SOA arrays, fibre arrays, optical isolator and a Fabry-Perot filter.

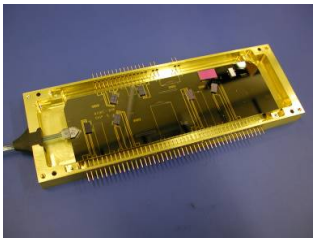


Figure 7: Photograph of the fabricated 40Gb/s BMR circuit.

Up-to-date results on these circuits and other details of the hybrid integration platform will be given during the conference presentation.

References

[1] G. Maxwell, "*Low-cost hybrid photonic integrated circuits using passive alignment techniques*", invited paper MJ2, *IEEE-LEOS Annual Meeting*, Montreal, Canada (2006).

[2] A. J. Poustie, "*SOA-based all-optical processing*", invited tutorial OWF1, *OFC*, Anaheim, U.S.A. (2007).

[3] G. Maxwell et al, "*WDM enabled, 40Gb/s hybrid integrated all-optical regenerator*", paper Th4.2.2, *ECOC*, Glasgow, U.K. (2005).

[4] J. Sakaguchi, F. Salleras, K. Nishimura and Y. Ueno, "*Frequency-dependent electric dc power consumption model including quantum conversion efficiencies in ultrafast all-optical semiconductor gates around 160 Gb/s*", *Optics Express*, **15**, p.14887 (2007).

[5] A. Poustie, "*Integrated devices for all optical signal processing*", invited paper 4.3.1, *ECOC*, Berlin, Germany (2007).

[6] G. T. Kanellos, D. Petrantonakis, D. Tsiokos, P. Bakopoulos, P. Zakynthinos, N. Pleros, D. Apostolopoulos, G. Maxwell, A. Poustie and H. Avramopoulos, "*All-Optical 3R Burst Mode Reception at 40 Gb/s using 4 integrated SOA-MZI switches*", *IEEE J. of Lightwave Technol.*, **25**, p.184 (2007).

ePIXpack - Advanced Smart Packaging Solutions for Silicon Photonics

L. Zimmermann[1], H. Schröder[2], P. Dumon[3], W. Bogaerts[3], T. Tekin[2]

[1] TU Berlin, HFT 4, Einsteinufer 25, D-10587 Berlin, Germany, Tel: +49 30 314 25670, Fax: +49 30 314 24626
Lars.Zimmermann@TU-Berlin.DE
[2] Fraunhofer Institute for Reliability and Microintegration (IZM), G.-Meyer-Allee 25, 13355 Berlin, Germany
[3] Ghent University – IMEC, INTEC, Sint-Pietersnieuwstraat 41, 9000 Gent, Belgium

Abstract. *We introduce two Silicon photonics packages to be used in future applications requiring multiple optical & electrical i/o. One package is based on a fiber array to assure small footprints. The other package provides configurable optical & electrical connectivity. Both packages are built using commercially available parts.*

Introduction

Silicon photonics is a rapidly advancing field with a strong potential for applications in integrated photonics. These applications comprise a wide spectrum ranging from optical sensors to optical data & telecom sub-modules. The most prominent merit of Silicon photonics is the use of highly advanced microelectronics process technologies. This allows for the fabrication of ultra-compact and low loss Silicon waveguide devices (photonic nanowires) in a CMOS-compatible fashion, opening the way for a true convergence of electronics and photonics.

Nanowires pose a challenge for optical coupling to the outside world due to the large mismatch in mode size between conventional single-mode fibers (SMF) and the waveguides. Conventional butt-coupling techniques yield insertion loss figures in excess of 20dB, rendering such approaches infeasible in real applications. The problem has been researched intensively and various solutions have been proposed and demonstrated. Our work is based on coupling via waveguide gratings. Gratings offer clear advantages such as compatibility with planar processing, the possibility for wafer-level testing, and relatively large alignment tolerances. However, gratings also evoke the need for entirely new smart packaging solutions due to the effect of out-of-plane coupling. New approaches are required to handle issues of mechanical stability, and reliability while preserving at least partially the compactness of the underlying devices. At the same time, these approaches should be derived from micro-electronic packaging to keep costs as low as possible.

To be clear, the goal of this work was not the development application specific packages, but rather to study some generic aspects that will become of central importance in Silicon photonics packaging. In the following paper we shall introduce two new Silicon photonic packages. The first package offers a compact solution for an 8-port fiber array interface. The second package provides a generic and configurable optical & electrical interface to a standardized Silicon photonic chip. This chip is offered by the Silicon Photonics Platform of the European Network of Excellence ePIXnet [1]. Both packages are under development by the Photonic Packaging Platform ePIXpack [2], which is also one of the activities of ePIXnet.

Optical coupling to photonic wire waveguides via gratings

Coupling to silicon photonic wires through high-index contrast gratings is attractive because of the relaxed alignment tolerances compared to facet coupling while using standard single mode fibers. Because of the high index contrast, the grating can be short (25 periods) and achieve a relatively large bandwidth.

Simple one-dimensional grating couplers with a uniform fill factor, etched into a broad waveguide, achieve a coupling efficiency of around 30% with a 40nm 1dB bandwidth (per

coupler) for a single polarization [3]. Detuned gratings with a coupling angle of 8º to 10º are used in order to avoid coupling to the wrong direction. The alignment tolerance for a 1dB loss penalty is over ±2µm.

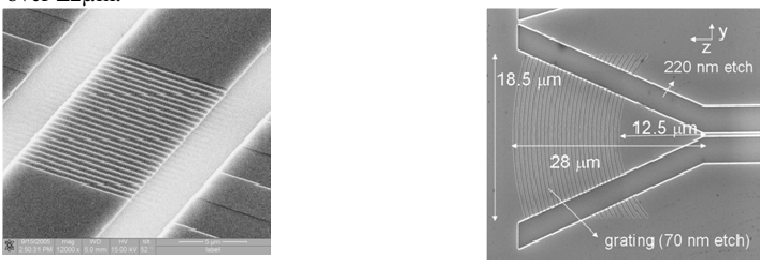


Figure 1: (a) Uniform fiber couplers etched in a 10µm wide SOI waveguide.[3] (b) Focusing grating coupler with similar efficiency but more compact footprint [5]

In addition, a two-dimensional grating coupler simultaneously splits the two incident polarizations and can be used in a polarization diversity scheme [4]. Simple 2D couplers achieve similar efficiency and bandwidth as one-dimensional couplers, but have a more strict alignment tolerance in order to achieve polarization independent circuits.
The grating couplers can be optimized in various ways to improve the efficiency or size. Focusing couplers achieve the same efficiency on a much smaller footprint, as with the regular coupler one still has to taper down the broad waveguide [5]. By using non-uniform fill factors, much lower coupling losses can be obtained. The efficiency can be further boosted by decreasing the vertical symmetry of the structure or adding bottom mirrors [3]. With an overlay, highly efficient couplers can be obtained that even couple light vertically instead of detuned [6].

Examples of optical & electrical packages

As packaging is necessary to achieve a reliable device on basis of the silicon photonic chips the challenge is to couple in the light into a fiber array maintaining the advantage of size and coupling efficiency. This so called interconnection bottleneck has to be overcome by a packaging concept providing standard optical interfaces. Alignment, reliability, standardization, and mass production suitability are the most important issues. Two first approaches using the standard sized chips described above are described in the following sections compact fiber array package. The compact fiber array package is a smart packaging approach for all optical functionality of the chip without any need of electrical wiring. The optical fibers are arranged in one row and serve as input and output fibers for the chip. A central requirement for Silicon photonics packages is compactness. Our first package focuses on this aspect. The concept is depicted in Fig. 2.

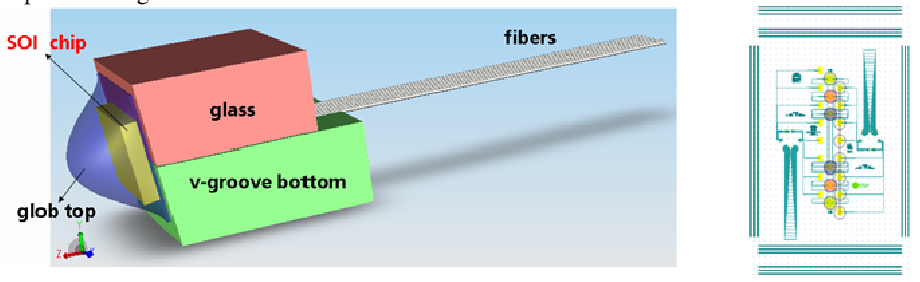


Figure 2 (a) Fiber array based package for Silicon photonic chip (SOI chip). Stability of the package is based on the actual fiber array mount, which consists of a V-groove bottom & a glass lid. The SOI chip contains a number of equally spaced grating couplers (optical i/o-ports). An example of a corresponding layout is shown in (b). The couplers are indicated by the circles shaded in color.

The package uses a commercial fiber array connector as a base to mount the Silicon photonic chip. Such arrays provide up to 32 i/o-ports without the need for a dedicated fiber array design. Glass lid and V-groove bottom are polished to provide the correct angle for coupling. The chip is sealed by an appropriate glob top encapsulation. A very compact package with multiple optical ports can be realized in this way.
A less compact but very flexible approach is taken for the second Silicon photonics package, which is depicted in Fig. 3.

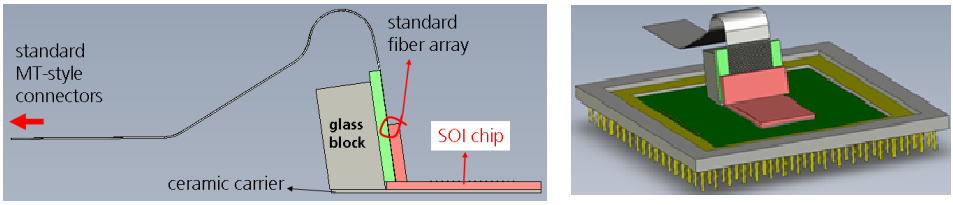


Figure 3: Configurable Silicon photonics test package. The cross section in (a) shows the ceramic carrier that acts as a base for the fiber array connector & the SOI chip. The carrier also contains the respective electrical fanout structures that route the connection to the underlying standard PGA (b).

The package can be configured to provide only electrical, only optical, or both electrical and optical connectivity. It is based on an SOI chip design, which uses standardized pitches for grating couplers and bond pads. The necessity of more generic & flexible test packages arises mainly in the R&D environment, where configurable electrical & optical connectivity is preferred to compact & qualified packages.

Experimental results

Fig. 4 shows a fiber array based package without and with glob top encapsulation. The SOI chip is mounted face down on the fiber array. The chip alignment is optimized by active alignment using two monitoring ports on the SOI chip. After active alignment the position of the chip is fixated by a UV-curing epoxy.

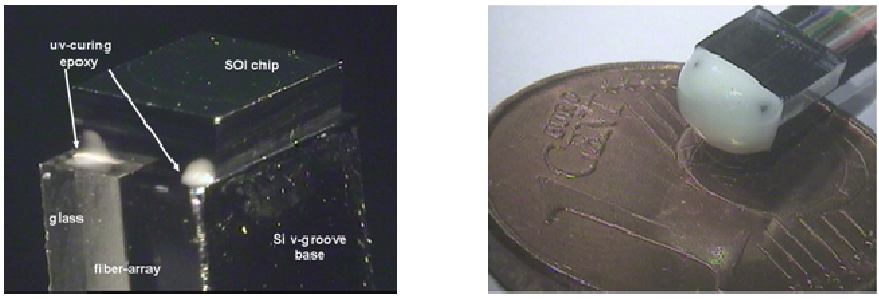


Figure 4: (a) Fiber array based package without glob top. The SOI chip is mounted face down on the fiber array. (b) Encapsulated SOI chip on fiber array (8 fibers) in comparison to 1 Euro Cent coin.

Our first experiment coupled to an array of 6 couplers that were cross-connected (i.e. shortened) in pairs by photonic wire waveguides. This configuration allowed for a simple test of the optical coupling concept. Fig. 5 (a) depicts the coupling characteristics of an aligned fiber in the package as a function of wavelength, which shows the wavelength dependence of the grating coupler. Fig. 5 (b) shows the transmission characteristics of the fiber-chip coupling in the dependence of lateral displacement of fiber array to the chip. Due to the fiber core/cladding concentricity <0.5µm and due to tolerances within the v-groove ±1µm, the coupling uniformity is expected to be <0.5dB.

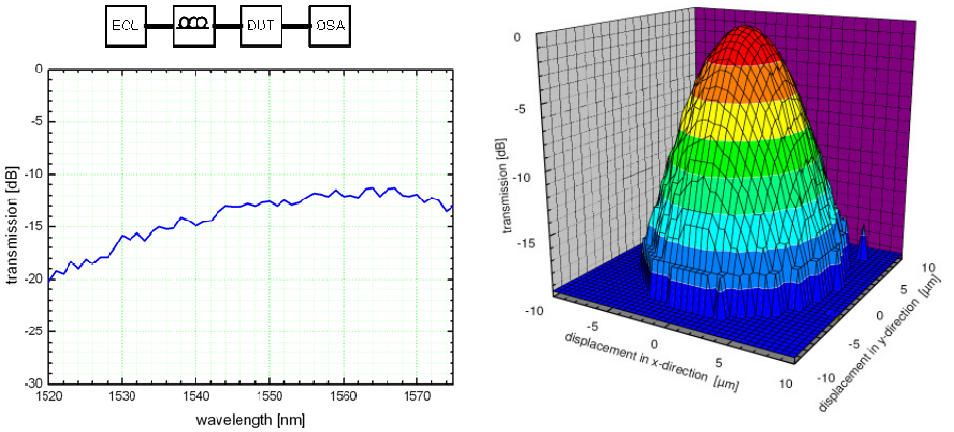


Figure 5: (a) Wavelength dependence of transmission through 2 shortened grating couplers. (b) Transmission characteristic of fiber-to-grating coupler in the dependence of lateral displacement.

Conclusions

Two new Silicon photonic packages have been presented. Both packages provide a solution for fiber array coupling to high-index contrast photonic wire waveguide gratings. Using standardized SOI chip designs and commercial assembly parts, the packages allow for small footprint or flexible use in an R&D environment.

Acknowledgements

This article is the result of cooperations in the frame of the Network of Excellence ePIXnet, and of the Packaging Platform ePIXpack. The responsibility for this publication is held by the authors only. The authors would like to thank S. Marx, G. Lang, J. Krissler for fruitful discussions.

References

[1] http://www.epixnet.org

[2] http://epixpack.eu

[3] D. Taillaert, F. Van Laere, M. Ayre, W. Bogaerts, D. Van Thourhout, P. Bienstman, R. Baets, “Grating couplers for coupling between optical fibers and nanophotonic waveguides”, Jap. J. Appl. Physics 45 (8A), p. 6071-6077 (2006)

[4] D. Taillaert, H. Chong, P. Borel, L. Frandsen, R.M. De La Rue, R. Baets, “A compact two-dimensional grating coupler used as a polarization splitter”, Photonics Technology Letters 15 (9) p. 1249-1251, 2003

[5] F. Van Laere, T. Claes, J. Schrauwen, S. Scheerlinck, W. Bogaerts, D. Taillaert, L.O’Faolain, D. Van Thourhout, R. Baets, “Compact focusing grating couplers for silicon-on-insulator integrated circuits”, Photonics Technology Letters 19 (23), p. 1919-1921, 2007

[6] G. Roelkens, D. Van Thourhout, R. Baets, “High efficiency grating couplers between silicon-on-insulator waveguides and perfectly vertical optical fibers”, Optics Letters 32 (11) p. 1495-1497.

Waveguide intensity modulators based on electrically actuated elastomers

N. Galler, H. Ditlbacher, A. Hohenau, D.M. Koller, J.R. Krenn, A. Leitner and F.R. Aussenegg

Institute of Physics and Erwin Schrödinger Institute for Nanoscale Research, Karl-Franzens-University, 8010 Graz, Austria

nicole.galler@uni-graz.at

Abstract *- We present a new concept for optical waveguide intensity modulators, based on the thickness change in an elastomer in a parallel plate capacitor, squeezed due to the attractive forces exerted by the capacitor electrodes when charged.*

Introduction

Integrated polymer optics is of broad interest due to advantages like low costs and ease of fabrication and there are several components already commercially available. There is a variety of waveguide materials which can be structured, e.g., by photo lithography and which form waveguides with optical losses as low as 0.01 dB/cm [1]. Also available are organic light emitting diodes (OLEDs) [2] as well as organic photo-diodes [3]. In modulators and switches electro-optical (EO) polymers are used reaching a modulation bandwidth up to 100 GHz [4]. Thermo-optical (TO) modulators use the temperature dependent refractive index of polymers and achieve modulation speed in the range of a few kHz, significantly lower than that of EO-modulators. Nevertheless TO-waveguide modulators are discussed for applications in optical communication networks, for example in optical routing [5]. However, TO-modulators also significantly consume power for switching, with values of several mW for one element [5]. The small optical path length changes that can be induced by both the EO and TO effect require interaction length in the range of several mm to cm for both modulator types. Therefore, there is a clear demand for novel modulator principles that allow for short interaction lengths to reduce the size of optical chips.

Modulator Concept

Here we report on an electro-mechanical modulator relying on the properties of an elastomer as the dielectric medium in a parallel plate capacitor. The attractive forces between the differently charged capacitor electrodes compress that layer, representing a special type of electrostrictive effect [6]. The system of metallic electrodes with an elastomer in-between forms a metal-insulator-metal (MIM) optical waveguide, whose propagation properties can be tuned by the thickness of the elastomer layer and thus by the voltage applied to the electrodes. When optically coupled to a dielectric waveguide this MIM waveguide can act as a modulator. The thickness change of the elastomer in the MIM-waveguide directly affects the coupling conditions between the waveguide modes in the dielectric and in the MIM-waveguide. It causes a change in the maximum optical power which is transferred from the dielectric to the MIM-waveguide and a change of the coupling length (i.e. the distance within this transfer takes place). The achievable modulation depth can be optimized by two parameters, the initial thickness of the elastomer and the length of the MIM-waveguide, see Fig. 1.

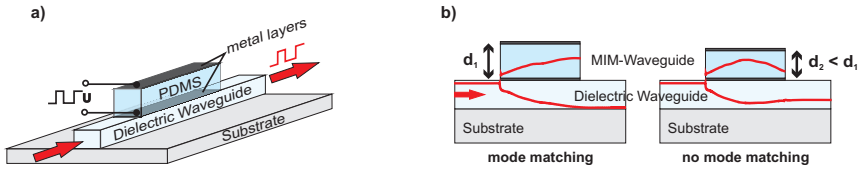


Fig. 1: Sketch of the proposed modulation device (a), PDMS is the squeezable elastomer in the MIM-waveguide and U is the voltage applied to the metal electrodes. Coupling between the dielectric and the MIM-waveguide (b). The arrow indicates the direction of the propagating light. The curves in the dielectric waveguide and the elastomer indicate the decrease and increase of guided optical power in the two waveguides due to coupling between them but also due to absorption in the bottom-electrode.

Realization

So far we investigated i) the coupling between the dielectric waveguide and the MIM-waveguide for an extended layer system and ii) the temporal behavior of the deformation of the elastomer in the MIM-system to estimate the response times of the modulator.

Coupling between dielectric and MIM-waveguide

To analyze the feasibility of mode matching between the dielectric and the MIM-waveguide we performed calculations using stratified media theory and compared them to angle resolved reflectance measurements.
Our model layer system consists of a Cytop layer (low refractive index fluoropolymer provided by Asahi Glass; used as the bottom cladding of the dielectric waveguide) on glass substrate. We used SU8-3010 (epoxy resin, MicroChem) for the dielectric waveguide, silver as bottom- and gold as top-electrode and for the elastomer we used polydimethylsiloxan (PDMS), namely a blend of Sylgard 527 and Sylgard 184 (provided by Dow Corning). We calculated the reflectivity of the layer system sketched in Fig. 2a (microscope cover slide / 500 nm Cytop / 370 nm SU8 / 40 nm Ag / PDMS / 40 nm Au) in dependence of the thickness of the PDMS-layer and the effective mode index N (Fig. 2b) which is related to the angle of incidence φ by $N = N_{glass} \sin\varphi$. The calculations were done for TM-polarized light of 633 nm wavelength.

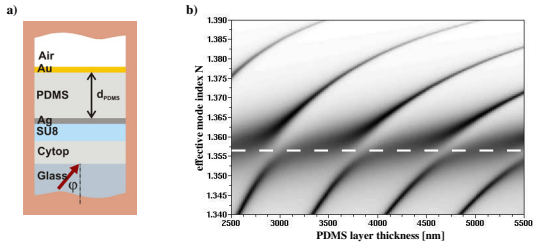


Fig. 2: Sketch of the layer system (a). φ is the angle of light incidence. Gray scale plot of the calculated reflectance against PDMS-thickness and effective mode index N (b).

The dark traces are reflectivity minima which display the guided modes in the dielectric

and the MIM-waveguide. The dashed line refers to the mode in the dielectric waveguide, which intersects with the modes in the MIM-waveguide (sloping dark lines). For PDMS thicknesses where the dark lines are anticrossing the modes in the dielectric and the MIM-waveguide are perfectly matched.
Angle resolved reflectance measurements were performed for samples with PDMS thickness of about 3700 nm (mode matching case) and 4100 nm (no mode matching) and compared with calculated curves, see Fig. 3.
Sample preparation was done by spin coating Cytop onto a microscope cover slide. Before SU8 was spin casted, the Cytop surface was treated with an air plasma for 1 min to ensure adhesion. Onto the SU8 layer the MIM-system was produced by thermally evaporating silver, layer deposition of the PDMS by spin coating and thermally evaporating gold. Before evaporation of the 40 nm thick gold top-electrode the PDMS surface was treated with an air plasma for 20 s to prevent diffusion of the gold atoms into the polymer [7].
Fig. 3 shows experimental (dots) and calculated (line) angle resolved reflection curves for the two PDMS thicknesses. The reflectivity minima which are quite narrow correspond to the waveguide modes in the MIM-waveguide and the broad minimum in Fig. 3a correspond to the dielectric waveguide mode. When the dielectric waveguide mode and a mode in the MIM-waveguide are matched (Fig. 3b), the width of and the distance between the coupled minima are changed. That is, that the maximum optical power which can be transferred and the coupling length are changed. We found good agreement between measurements and theory.
First simulations using beam propagation method (BPM) suggest, that device lengths of tens of μm are sufficient for such a modulation unit if a possible thickness change of 10 % is assumed.

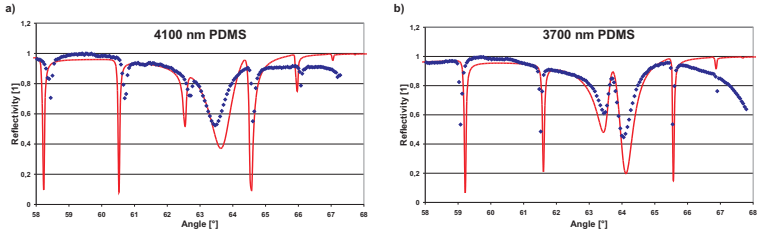


Fig. 3: Experimental (dots) and calculated (line) angle resolved reflection curves (λ=633 nm, TM-polarization) for the layer system depicted in Fig. 2a. (a) no mode matching, (b) mode matching case.

Response times

As an elastomer is practically incompressible the electrodes must be laterally confined to get a significant thickness change of the elastomer. The elastomer has to be ”squeezed” to the area outside the electrodes (see Fig. 4). We investigated two different geometries: samples with bottom electrode structured only (Type 1) and samples where the whole layer system was structured by reactive ion etching (Type 2). Measuring the time dependent thickness changes of the PDMS we found response times in the order of 100 μs

and thickness changes up to 7% for an initial elastomer thickness of 5 μm and an applied voltage of 120V, for details concerning sample preparation as well as experimental setup see [8].

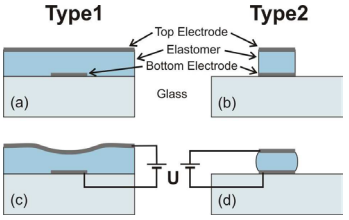


Fig. 4: Scheme of the two different geometries for time response measurements. (c) and (d) sketch the deformation which is induced by an applied voltage.

Conclusion

To summarize we could show that for an extended layer system coupling between a dielectric and the MIM-waveguide is indeed possible. We found response times of our modulation unit in the order of 100 μs and possible thickness changes of about 7 %.
Such types of modulators may find application in the field of (low cost) integrated polymer opto-electronics. There are several advantages of the proposed modulator concept as compared to TO-modulators: Comparable switching times with a negligible power consumption on device length of mm instead of cm.

Acknowledgments

This work is supported within the project cluster ISOTEC of the national Austrian nanoinitiative.

References

[1] L. Eldada and L.W. Shacklette, "Advances in Polymer Integrated Optics", *IEEE J. Sel. Top. Quantum Electron.*, vol. 6, pp. 54-68, 2000.

[2] G. Grem, G. Leditzky, B. Ullrich and G. Leising, "Realization of a blue-light-emitting device using poly(p-phenylene)", in *Adv. Mater.*, vol. 4, pp. 36-37, 1992.

[3] C.W. Tang, "Two-layer organic photovoltaic cell", *Appl. Phys. Lett.*, vol. 48, pp. 183-185, 1986.

[4] D.T. Chen, H.R. Fetterman, A.T. Chen, W.H. Steier, L.R. Dalton, W.S. Wang and Y.Q. Shi, "Demonstration of 110 GHz electro-optic polymer modulators", *Appl. Phys. Lett.*, vol. 70, pp. 3335-3337, 1997.

[5] N. Keil, H.H. Yao, C. Zawadzki, K. Lösch, K. Satzke, W. Wischmann, J.V. Wirth, J. Schneider, J. Bauer and M. Bauer, "Hybrid polymer/silica thermo-optic vertical coupler switches", *Appl. Phys. B*, vol. 73, pp. 469-473, 2001.

[6] R.E. Pelrine, R.D. Kornbluh and J.P. Joseph, "Electrostriction of polymer dielectrics with compliant electrodes as a means of actuation", *Sens. and Act. A*, vol. 64, pp. 77-85, 1998.

[7] H. Hillborg, J.F. Ankner, U.W. Gedde, G.D. Smith, H.K. Yasuda and K. Wikström, "Crosslinked polydimethylsiloxane exposed to oxygen plasma studied by neutron reflectometry and other surface specific techniques", *Polymer*, vol. 41, pp. 6851-6863, 2000.

[8] N. Galler, H. Ditlbacher, B. Steinberger, A. Hohenau, M. Dansachmüller, F. Camacho-Gonzales, S. Bauer, J.R. Krenn, A. Leitner and F.R. Aussenegg, "Electrically actuated elastomers for electro-optical modulators", *Appl. Phys. B*, vol. 85, pp. 7-10, 2006.

Optoelectronic Integration of a Resonant Tunneling Diode and a Laser Diode

B. Romeira[1], J. M. L. Figueiredo[1], T. J. Slight[2], L. Wang[2], E. Wasige[2] and C. N. Ironside[2]

[1]Centro de Electrónica, Optoelectrónica e Telecomunicações, Universidade do Algarve, Campus de Gambelas, 8005-139 Faro, Portugal
bmromeira@ualg.pt
[2]Department of Electronics and Electrical Engineering, University of Glasgow, Glasgow G12 8LT, United Kingdom

Abstract. *We report on a hybrid integration of a resonant tunneling diode laser diode driver configuration that operates as a self-oscillating circuit and can be described as a Liénard's oscillator. When externally perturbed it is capable of frequency division, chaos generation and synchronization with potential novel functions for optical communications systems.*

Introduction

Recent work on Opto Electronic Integrated Circuits (OEICs) has shown that it is possible to monolithically integrate a resonant tunnelling diode (RTD) with an optical waveguide electroabsorption modulator (RTD-EAM) [1] and a RTD with a laser diode (RTD-LD) [2]. Crucially the RTD introduces negative differential resistance (NDR) into the electrical characteristics of the RTD-EAM and the RTD-LD. RTDs have attracted much attention due to their strong nonlinear current-voltage (*I-V*) characteristic, wide-bandwidth NDR region, and high frequency operation [3].

This paper presents recent work on a hybrid optoelectronic integrated circuit (OEIC) consisting of a RTD driving a communication laser diode (LD) that produce various optical outputs including self-sustained oscillations, frequency division and chaos in electrical and optical domains [4]. The circuit preserves the nonlinear dynamical behavior of the RTD increasing laser diode functionality with several potential advantages, such as low modulating voltage, ultrahigh speed operation, and significant reduction in the complexity of chaotic optical carriers generators needed for optical communications [5]. The RTD-LD circuit operation can be described by Liénard's oscillator theory. Numerical simulations also show optical chaotic synchronization in two identical resonant tunneling diode – laser diode circuits operating as an unidirectional driven coupled system. We anticipate that this circuit will lead to new applications in optical communications including clock recovery, clock division and data encryption using synchronized chaos.

Circuit Description and Operating Principle

Figure 1(a) shows the schematic diagram of the RTD-LD hybrid OEIC. The shunt capacitor was used to decouple the DC from the AC circuit. The RTD detailed structure is described in [1]. The LD was an optical communications laser fabricated by Compound Semiconductor Technologies (Scotland); it has a threshold current of 6 mA, 20 GHz bandwidth, and operates at 1550 nm with average output power of 5 mW. The room temperature *I-V* characteristics of the RTD, LD, and the RTD-LD are shown in

Fig. 1(b). The circuit electrical output was taken across the RTD-LD series, Fig. 1(a); the laser optical output was coupled to a lensed optical fibre and detected by a 45 GHz IR New Focus Photo-detector.

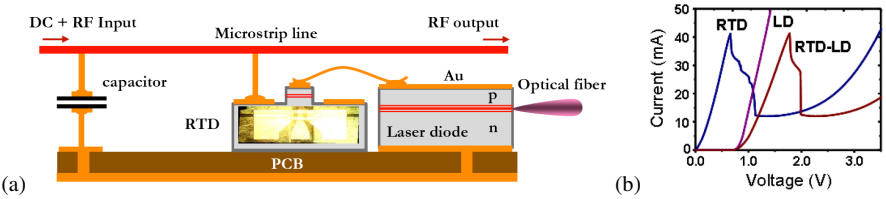


Fig. 1 (a) Schematic of the RTD-LD OEIC; (b) *I-V* characteristics of RTD, LD and RTD-LD.

When DC biased in the NDR region the experimental circuit represented by Fig. 1(a) produces self-sustained oscillations at frequency around 560 MHz, determined mainly by the wire bonding inductance and intrinsic RTD-LD capacitance. The LD optical output is modulated by the current oscillations induced by the RTD, producing an optical output with the same harmonic content of the electrical oscillations.

Theory and Numerical Model

The nonlinear dynamics behavior of the RTD-LD module can be analyzed using the lumped circuit shown in Fig. 2(a). The physics-based RTD $f(V)$ current-voltage description given in [6] was used, Fig. 2(b). When operated above the threshold, the laser can be modeled using an ideal diode in series with a voltage source V_{TH} and a current limiting resistor R_S. From Fig. 2(c) we obtain $V_{TH} = 0.84$ V and $R_S = 11\ \Omega$.

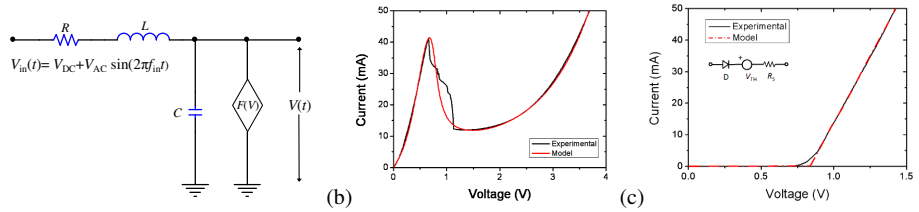


Fig. 2 (a) Equivalent lumped circuit of circuit shown in Fig. 1(a); (b) Experimental and fitting of RTD *I-V* curves; (c) Experimental *I-V* characteristics of the laser diode and model.

For a given DC bias voltage, V_{DC}, the voltage output across the RTD-LD series, $V(t)$, Fig. 1(a), can be described by a nonlinear system known as Liénard's oscillator:

$$V''(t) + H(V)V'(t) + G(V) = V_{AC}\sin(2\pi f_{in}t), \qquad (1)$$

where $G(V)$ is a nonlinear "force", $H(V)V'(t)$ and $V_{AC}\sin(2\pi f_{in}t)$ are the damping factor and the externally applied forcing signal, respectively. $H(V)$ and $G(V)$ are given by:

$$H(V) = \frac{R}{L} + \frac{1}{C}\frac{df(V)}{dV}; \quad G(V) = \frac{V(t)}{LC} + \frac{R}{LC}f(V) - \frac{V_{DC}}{LC}. \qquad (2)$$

The laser diode optical output was modeled using the laser diode single mode rate equations for the electron density $N(t)$ and the photon density $S(t)$:

$$N'(t) = \frac{I(t)}{q\vartheta} - \frac{N(t)}{\tau} - g_0\left(N(t) - N_0\right)\frac{S(t)}{1+\varepsilon S(t)} \quad (3)$$

$$S'(t) = g_0\left(N(t) - N_0\right)\frac{S(t)}{1+\varepsilon S(t)} - \frac{S(t)}{\tau_p} + \frac{\beta N(t)}{\tau}, \quad (4)$$

where $I(t)$ is the current through the laser diode given by Liénard's model (1), q is the electron charge, ϑ is the active region volume, τ and τ_p are the spontaneous electron and photon lifetime, respectively; β is the spontaneous emission factor; g_0 is the gain coefficient, N_0 is the minimum electron density required to obtain a positive gain and ε is the value for the nonlinear gain compression factor.

Self-sustained oscillations

In Fig. 3(a) we show the electrical output of the RTD-LD in the self-oscillating mode (V_{AC}=0 V); also represented is numerical output given by the Liénard's model [equation (1)]. In Fig. 3(b) we show the laser optical output experimental data fitted with the calculated light intensity as a function of the injection current $I(t)$ using the rate equations [equations (3) and (4)] with typical parameters of communication laser diode.

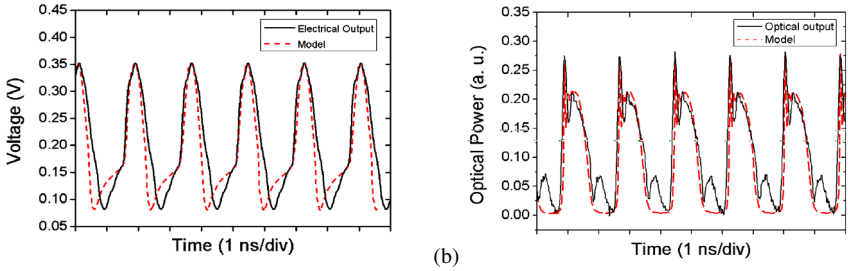


Fig. 3 (a) Experimental and modeled electrical signals at voltage of 1.8 V, both with fundamental frequency oscillation around 560 MHz. The circuit parameters used in the model are L=8.0 nH, C=5.0 pF, R=6.2 Ω and V_{DC}=1.8 V, V_{AC}=0.0 V; (b) The corresponding photo-detected signal and the model output.

The comparison between the experimental results with the numerical simulation shows that the theory of the Liénard's nonlinear differential equation can be used to model the RTD based driver circuit of an optical communications laser diode.

Frequency Division, Chaotic Behavior and Synchronization

Frequency division in a hybrid optoelectronic integrated RTD-LD circuit has been investigated numerical and experimentally when an external sinusoidal voltage signal is applied. Figure 4 shows experimental and numerical results of frequency division by 2 and 5 in the laser optical output induced by low driving AC voltages. The bifurcation diagram representing the amplitude peaks heights of RTD-LD output voltage oscillations, $V(t)$, as a function of the excitation frequency f_{in}, obtained numerically shows period-adding bifurcation in a sequence of quasi-periodic (unlocked) and periodic (locked) oscillations [4]. In the quasi-periodic regions, depending on parameters conditions, route to chaos behavior is expected [3][4].

We have also analyzed the electrical and optical synchronization of two identical coupled chaotic RTD-LD oscillators using the Liénard's oscillator and the

synchronization diagrams of the evolution of output signals of the transmitter vs. receiver show chaos synchronization between the RTD-LD coupled circuits.

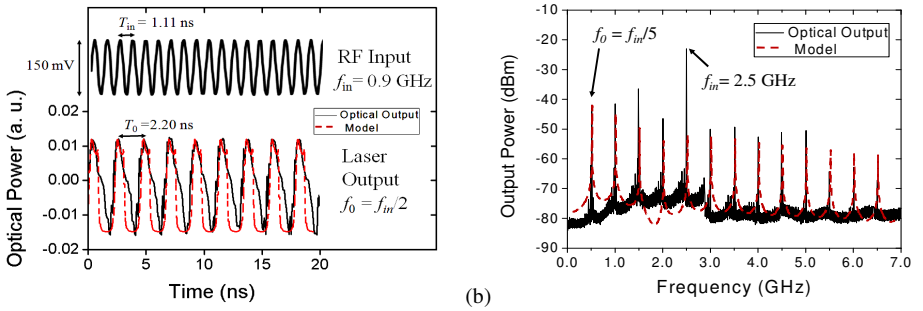


Fig. 4 (a) Laser output showing frequency division by 2 when V_{AC}=150 mV at 0.9 GHz and model; (b) Spectrum of the laser output showing frequency division by 5 when V_{AC}=150 mV at 2.5 GHz and model.

Conclusions

A RTD-LD circuit acting as an oscillator producing self-sustained oscillation and frequency division both in the electrical and optical outputs was demonstrated. The self-sustained behavior can be a simple way to convert fast, short electrical pulses into fast sharp optical pulses. The sub-harmonic locking can be used for dynamic frequency division with a selectable dividing ratio. We also have shown that the electrical and optical operation of the circuit can be described by Liénard's oscillator theory.

Although the hybrid RTD-LD circuit presented here operates at relatively low frequencies compared to modern optical communication systems, recent work by the authors has shown that with reduced RTD-LD bond wire inductance, voltage controlled oscillation frequencies in the range of 1.9 GHz to 2.1 GHz can be achieved. With fully integrated versions we anticipate much higher operating frequencies in the region of 10 Gbits or higher - data rates more appropriate for present day and future optical communication systems.

Acknowledgments

B. Romeira acknowledges the support of the Fundação Calouste Gulbenkian, Portugal.

References

[1] J. M. L. Figueiredo *et al.*, "Electric field switching in a resonant tunneling diode electroabsorption modulator", IEEE Journal of Quantum Electronics, vol. 37, pp. 1547-1552, 2001.

[2] T. J. Slight and C. N. Ironside, "Investigation into the integration of a resonant tunnelling diode and an optical communications laser: Model and experiment", IEEE Journal of Quantum Electronics, vol. 43, pp. 580–587, 2007.

[3] K. Maezawa *et al.* "Direct Observation of High-Frequency Chaos Signals from the Resonant unneling Chaos Generator", Japanese Journal of Applied Physics, vol. 43, pp. 5235–5238, 2004.

[4] B. Romeira, *et al.*, "Observation of Frequency Division and Chaos Behavior in a Laser Diode driven by a Resonant Tunneling Diode", accepted in Proceedings of the Conference on Lasers and Electro-Optics (CLEO 08).

[5] A. Argyris *et al.*, "Chaos-based communications at high bit rates using commercial fibre optic links", *Nature*, vol. 438, pp. 343–346, 2005.

[6] J. N. Schulman, H. J. D. Santos, and D. H. Chow, "Physics-based RTD current-voltage equation", IEEE Electron Device Letters, vol. 17, pp. 220–222, 1996.

Cost-Effective Polymer Multimode Directional Couplers for High-Speed On-Board Optical Interconnects

N. Bamiedakis[1], R. V. Penty[1], I. H. White[1], J. V. DeGroot Jr.[2] and T. V. Clapp[2]
[1]Electrical Engineering Division, University of Cambridge, Cambridge, UK
nb301@cam.ac.uk
[2]Dow Corning Corporation, Midland, Michigan, USA

Abstract: *Cost-effective polymer multimode directional couplers suitable for high-speed on-board optical interconnects are presented. Power splitting ratios from 30 to 75% are achieved, symmetric behaviour is obtained for both input arms and robust performance in terms of input misalignment is demonstrated. No special fabrication steps are required for patterning the devices.*

Introduction

Polymer multimode waveguides have become increasingly of interest for use in short reach optical interconnects in recent years as they offer a promising solution to the bottleneck imposed by conventional electronic circuitry [1,2]. Their main advantage consists of low-cost and simple fabrication processing compatible with the existing manufacturing process of electronic printed circuit boards (PCBs). The siloxane materials reported in this work exhibit excellent thermal and mechanical properties and are able to withstand the in excess of 250^{o}C temperatures that are required for solder reflow processes [3]. Moreover, owing to their reduced alignment tolerances, multimode waveguides allow for reduced cost connectorisation and packaging. Yet further cost advantages and increased functionality could be achieved by directly forming passive components in the polymer guides.

Interconnection architectures comprising an optical bus and various optical stations or cards require the use of passive add/drop devices (Fig. 1). The majority of multimode devices, however, offer only a 3dB power splitting ratio as a result of mode mixing and power redistribution between the large numbers of modes inside the guides [4-5]. Being able to control the power splitting ratio is therefore an important attribute for any passive component to be employed in such add/drop applications. In this paper we report the fabrication and characterisation of directional multimode coupler devices patterned by conventional photolithographic techniques on FR4 substrates which are suitable for use in on-board optical interconnects. Despite the multimode nature of the guides and the low potential cost of the devices, good performance is achieved even in the presence of significant input misalignments.

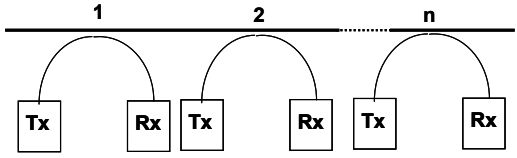


Fig.1 Optical bus architecture with passive add/drop devices.

Device design and fabrication

The devices are fabricated on a FR4 substrate by conventional photolithographic techniques from silicone OE4140 (core) and OE4141 (cladding) polymer materials. The

waveguide cross section is 50×50 μm^2 so as to match standard 50/125 μm multimode fibre systems (MMF) while the waveguide separation is chosen to be 250 μm to comply with conventional fibre ribbon, VCSEL and photodiode array spacing. The intrinsic waveguide loss is measured to be 0.03-0.05 dB/cm at an 850 nm wavelength.
The couplers consist of a pair of 6 mm long raised-cosine S-bends and a middle interaction section whose length L_{mid} is varied from 0 to 4.5 mm. The total length of the device is 20 mm. Fig. 2a shows a schematic of the coupler design. It should be noted that the two coupler arms are in contact so that no separation gap exists in the interaction section. Due to the large index step between the core and cladding material ($\Delta n \sim 0.02$), the separation distance that is required to ensure efficient power coupling between the two guides, is in the order of a few microns (~5 μm) – a value much smaller than the height of the core polymer layer (H=50 μm). Standard low-cost photolithographic techniques fail to efficiently produce features of such an aspect ratio as vertical sidewall deformation occurs (Fig. 2b-2c). By merging the two arms together at the interaction region, no extra fabrication steps (i.e. etching process) are required in order to create the necessary narrow gap, allowing thus an easier patterning and simplified fabrication. Nevertheless, the convergence of the arms will eventually create similar defects near the junction points (points A-B in Fig. 2a) at both the input and output sides of the device, inducing as a result additional excess loss.

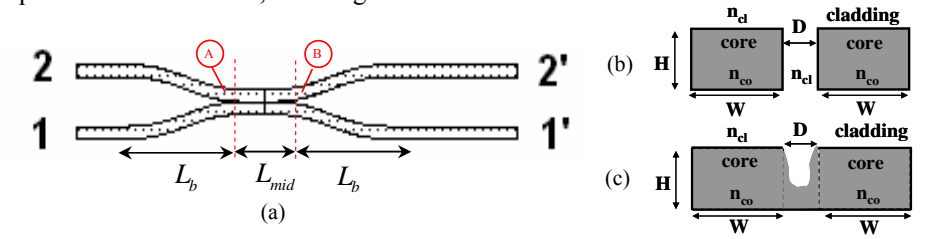


Fig.2. Schematic of (a) a polymer coupler and (b-c) illustration of the cross section of fabricated parallel waveguides in the case of (b) a large ($D / H >> 0.5$) and (c) a small ($D / H < 0.5$) feature aspect ratio.

The multimode polymer coupler can be treated as a multimode interference (MMI) device [6] which, in this case, has multimoded input and output arms. The power coupled to each one of the guided modes inside the interaction region depends on the power distribution and the relative phases of the modes of each one of the input arms (point A), while the power coupled to each one of the output arms depends on the interference between the modes of the interaction region at the output arms-interaction region interface (point B). Therefore the operation of the device and, more specifically the power splitting ratio between the output arms, depends strongly on the length of the interaction region and the mode distribution inside the input arms. Furthermore, the input and output S-bend regions affect the device behaviour as their converging input and diverging output waveguides result in additional mode coupling between the arms of device. Our goal is to investigate the performance of the device in the case of an overfilled launch into each arm of the device and evaluate the robustness of the splitting power ratio in the presence of input misalignments (which are expect to be likely in low-cost integrated optical systems). Therefore, multimode fibre (MMF) launches are employed in order to create a mode power distribution at the input arms as uniform as possible while representing an input configuration scenario that could be met in real-world applications (e.g. a fibre ribbon – polymer optical board interface).

Characterisation studies

A standard 850 nm multimode VCSEL source is used as a transmitter while a standard cleaved 50/125 μm MMF patchcord is used to couple light into each of the device's input arms. A 62.5/125 μm butt- coupled MMF is used to collect the light at each output arm and deliver it to an optical power meter. Index matching gel is used at both waveguide ends to maximise coupling efficiency. The excess loss of the devices is 0.8 dB for a 50/125 μm MMF input and can be attributed to the bending loss induced by the input and output S-bends and the acute point at the convergence region of the input and output arms (points A and B).

In fig. 3 the variation of the splitting ratio of output power (fraction of output power coupled into the antisymmetric port: 1→2' and 2→1') as a function of the length of the interaction section L_{mid} of the device is shown. A symmetric response is obtained for both input arms while the percentage power coupling varies from 30 to 75% depending on the interaction length L_{mid}. Moreover, similar behaviour is observed for both multimode fibre input configurations. The same black fit line is shown in both plots in order to simplify the comparison. The observation indicates the robustness of the operation of the multimode couplers on launch conditions as long as those are kept close to being overfilled. Owing to the multimode nature of the devices, complete power coupling into the antisymmetric port cannot be achieved. The minimum coupled power percentage obtained is approximately 30% for a nominal interaction section length of L_{mid} =2 mm. Larger interaction lengths lead gradually to a smaller power coupling fraction variation due to the mode mixing occurring inside the interaction region.

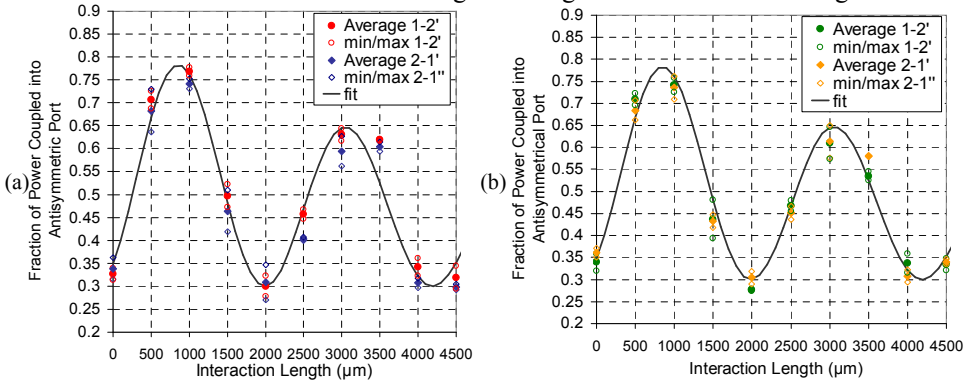
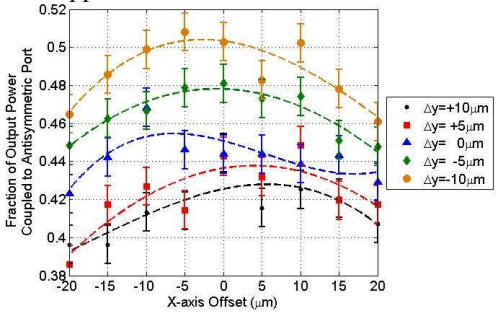


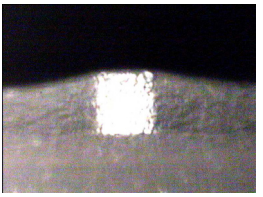
Fig. 3. Fraction of output power received at the antisymmetric port as a function of interaction length L_{mid} for a (a) 50 μm and a (b) 62.5 μm MMF input.

For each device and for each input port, the worst-case behaviour scenario is implemented by adjusting the position of the input fibre with a 3D translation stage so as to maximise the power received in one of the output arms of the device. The input fibre is kept constant while recording the power received at the other output. The maximum variation of the splitting ratio for every device can be obtained providing thus an indication of the robustness of the device performance. The non-filled points in Fig. 3 represent the minimum and maximum power fractions achieved by this technique. The average variation for all devices under investigation obtained is ±2.5% while the maximum value recorded is approximately ±5% for the device #4 (4th device in Fig. 2) with an interaction section length of L_{mid} =1.5 mm.

To further investigate the effect of input misalignment to the operation of the couplers, the performance of the device #4 exhibiting the greatest power splitting ratio variation is studied in more detail. The received power at the device's two output arms is recorded while offsetting the input MMF both in the horizontal and vertical direction (Fig. 4a). It can be noticed that for horizontal misalignment a symmetric behaviour is obtained while the maximum power splitting variation is smaller than 5% (±2.5%) for an input offset of ±10 μm for all vertical input positions. Vertical misalignment however leads to an asymmetric behaviour and slightly greater variation. Offsetting the fibre towards the substrate leads to a small change in the splitting ratio (< 3%) whereas an upward input fibre movement has a greater effect. This can be attributed to the asymmetry of the cross section of fabricated waveguides in the vertical dimension (Fig. 4b). Increasing the thickness of the top cladding layer is expected to overcome this issue. Overall, the observed power splitting variation due to input misalignment of this "worst-case" coupler is relatively small, demonstrating thus the potential of the use of the devices in real-world applications.

(a)





(b)

Fig. 4. (a) Fraction of output power received at the antisymmetric port as a function of horizontal input offset for different input vertical positions for device #4 and (b) photograph of one of the output waveguide facets of the device when illuminated with the VCSEL source.

Conclusion

Low cost polymer multimode directional couplers fabricated on FR4 substrate exhibiting a power splitting ratio between 30 and 75% are presented. Despite being highly multimoded structures, symmetric behaviour for both input arms and robust performance are achieved, even in the presence of input misalignment in the order of 10 microns in both horizontal and vertical directions. The devices are suitable candidates for use in high-speed on-board optical interconnection schemes.

References

[1] R. T. Chen, et al., "Fully embedded board-level guided-wave optoelectronic interconnects", in Proceedings of the IEEE, vol. 88, pp. 780–793, 2000.

[2] C. Berger, et al., "Optical links for printed circuit boards", in Proceedings of IEEE Laser and Electro-Optics Society 2003, vol. 1, pp. 61-62.

[3] J. D. Ingham, et al, "Multimode siloxane polymer waveguides for robust high-speed interconnects", in Proceedings of Conference on Lasers and Electro-Optics 2006, paper CThS4.

[4] R. Griffin, et al., "Asymmetric Multimode Couplers", Journal of Lightwave Technology, vol. 9, pp. 1058-1517, 1991.

[5] S. Musa, et al., "Low-cost Multimode Waveguide Couplers for Multimode Fibre-Based Local Area Networks", in IEEE Lasers and Electro-Optics Society Annual Meeting 2000, vol. 2, pp. 468-469.

[6] L.B. Soldano, et al., "Optical Multi-Mode Interference Devices Based on Self-Imaging: Principles and Applications", Journal of Lightwave Technology, vol. 13, pp. 615-627, 1995.

High-index contrast grating integrated VCSELs

C. Chang-Hasnain
University of California, BERKELEY, United States of America

Quantum dot photonic crystal membrane LED at 1.3 µm

L. Balet[1,2], M. Francardi[3], A. Gerardino[3], N. Chauvin[2], D. Bitauld[2], L.H. Li[1], B. Alloing[1], and A. Fiore[2]

[1]Institute of Photonics and Quantum Electronics, EPFL, Lausanne, Switzerland
laurent.balet@epfl.ch
[2] COBRA Research Institute, TU Eindhoven, The Netherlands
[3]Institute for Photonics and Nanotechnologies-CNR, via Cineto Romano 42, 00156 Roma, Italy

Abstract. *Electrical pumping of InAs QD's in a photonic crystal membrane nanocavity is demonstrated at 1.3 µm through the observation of cavity modes with quality factors around 2600.*

Introduction

The control of light at sub-micrometer scale is the focus of intense interest, both for fundamental science and for applications. [1] Photonic crystals (PhCs) provide a flexible platform for light manipulation through high quality cavities and waveguides. On the other hand, the atom-like behavior and wavelength adjustability of semiconductor quantum dots (QDs) make them perfect candidates as single photon sources for quantum optics or quantum cryptography and lasers with low thresholds currents. [2] They can also be straightforwardly embedded into PhC structures, leading to the control and enhancement of spontaneous emission, thus to higher efficiency and emission rates. [3] Whereas most of the experiments found in the literature are performed under optical excitation, a mature device needs to work under electrical pumping. We present here a structure which combines a photonic crystal nanocavity with electrical injection, leading to cavity-enhanced emission at telecommunication wavelengths.

Sample fabrication

The sample is grown by molecular beam epitaxy (MBE) and consists of a 370 nm thick GaAs membrane on top of a 1.5 µm $Al_{0.7}Ga_{0.3}As$ sacrificial layer. The top of the membrane is p-doped and the bottom is n-doped. A single layer of low areal density InAs QDs with emission at 1.3 µm at liquid helium temperature is embedded in the middle of the membrane.

The sample is wet-etched in diluted H_3PO_4 / H_2O_2 / H_2O to form ~300 nm high mesas with diameter between 8 to 10 µm. The bottom n-contact, a 200 nm layer of insulating Si_3N_4 and the top p-contact are then deposited. An aperture is left in the top contact for the PhC cavity. The holes are etched by a $SiCl_4$ / O_2 / Ar reactive ion etching (RIE) and the membrane is then released in diluted HF. The cavity is formed at the center of the mesa by not etching three holes in the ΓK direction. The air filling factor was measured to be around 27%. The first holes on each side are shifted outwards by 15% and rescaled to 61% of the unperturbed holes diameters, following [4], [5] [6].

The modified L3 cavity is clearly visible at the center of the SEM image in figure 1. The border of the mesa is apparent through the gold top contact, which also serves as a

cover to block photons emitted outside the PhC region and the side of the mesa. On the top of the image, the n-contact looks darker, since it is covered by the insulating Si_3N_4.

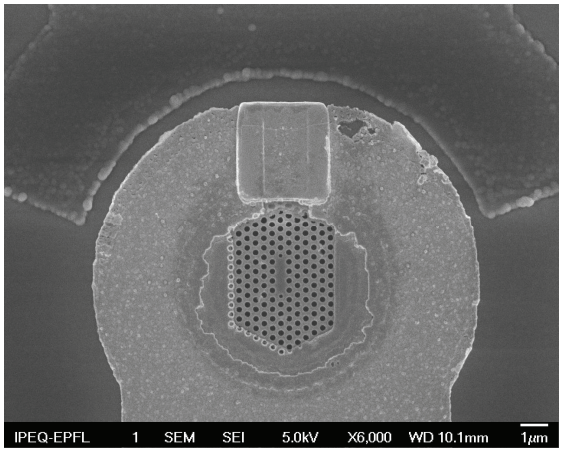


FIG. 1 : Scanning Electron Microscopy (SEM) image of a modified L3 photonic crystal cavity on a suspended membrane. Electrons are injected through the dark semi-circular contact on the top of the image, whereas holes are fed by the annular clear contact.

Measurement and results

The sample was measured in a cryogenic probe station at liquid helium (LHe) and liquid nitrogen (LN_2) temperature. The light was collected into a single mode fiber and dispersed by a spectrometer onto a LN_2 cooled InGaAs array. IV-curves were recorded, showing clear diode behavior and a relatively low threshold voltage of 2 V, which proves the high quality of the process.

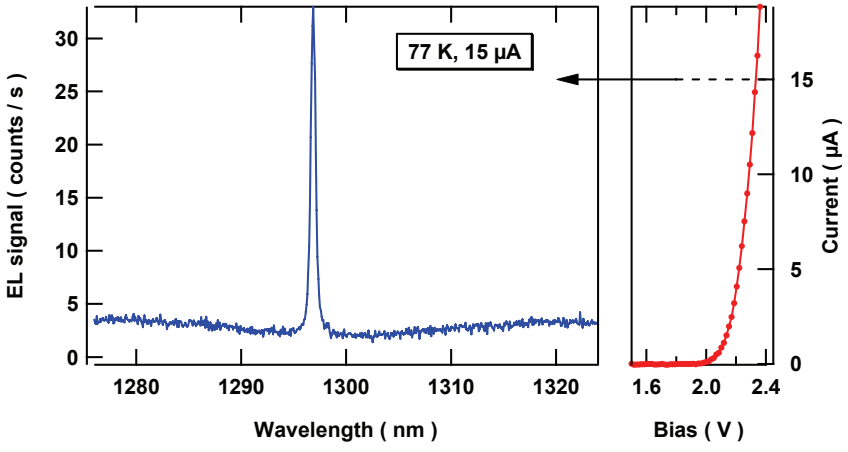


FIG. 2 : *a)* Electroluminescence spectrum under 15μA excitation and *b)* IV-curve of a modified L3 photonic at 77 K

The electroluminescence spectrum presented in figure 2 was performed at 77 K on a device with PhC lattice parameter a = 231 nm under 15 µA continuous current. A cavity mode is clearly observed, with a measured quality factor (Q) above 2600. This shows that this structure and process approach lead to PhC cavities with low optical loss, despite the presence of doped layers and metal contacts. It is therefore suitable for the long-sought demonstration of Purcell-enhanced emission under electrical injection. Pulsed electroluminescence measurements on these structures are under way and will be presented at the conference.

Conclusion

We demonstrated successful electrical pumping of InAs QD's in PhC membrane modified L3 nanocavity under continuous bias at LN_2 and LHe temperature. Time resolved experiments are under way.

References

[1] P. Bhattacharya, J. Sabarinathan, J. Topol'ancik, S. Chakravarty, P.-C. Yu, W. Zhou, Proceedings of the IEEE **93**, 1825 (2005)

[2] B. Ellis, I. Fushman, D. Englund, B. Zhang, Y. Yamamoto, and J. Vučković, Appl. Phys. Lett. **90**, 151102 (2007)

[3] L. Balet, M. Francardi, A. Gerardino, N. Chauvin, B. Alloing, C. Zinoni, C. Monat, L. H. Li, N. Le Thomas, R. Houdré, and A. Fiore, Appl. Phys. Lett. **91**, 123115 (2007)

[4] Y. Akahane, T. Asano, B. S. Song, and S. Noda, Nature **425**, 944 (2003).

[5] M. Francardi, L. Balet, A. Gerardino, C. Monat, C. Zinoni, L. H. Li, B. Alloing, N. L. Thomas, R. Houdré, and A. Fiore, phys. stat. sol. (c) **3**, 3 (2006).

[6] M. Francardi, A. Gerardino, L. Balet, N. Chauvin, D. Bitauld, C. Zinoni, L.H. Li, B. Alloing, N. Le Thomas, R. Houdré and A. Fiore, Microelectron. Eng., in press (2008)

Butt-joint integrated InAs/InP quantum dot Fabry-Pérot laser devices emitting at 1.5 µm

H. Wang, J. Yuan, S. Anantathanasarn, P.J. van Veldhoven, T. de Vries, E. Smalbrugge, E.J. Geluk, E.A.J.M. Bente, Y.S. Oei, M.K. Smit, and R. Nötzel

COBRA Research Institute, Eindhoven University of Technology, 5600 MB Eindhoven, The Netherlands
h.wang@tue.nl

Abstract. *Butt-joint integrated extended cavity InAs/InP (100) quantum dot (QD) Fabry-Pérot laser devices emitting around 1.55 µm are demonstrated. Continuous wave lasing at room temperature is realized with devices of different lengths. The threshold currents, transparency current density, and external differential quantum efficiency are all comparable to those of all-active QD lasers. The Butt-joint reflectivity for straight waveguides is below – 40 dB. Light versus current curves and lasing spectra reveal that for low current, lasing starts on the QD ground state transition, while excited state lasing sets in with increasing current.*

Monolithically integrated quantum dot (QD) laser devices for photonic integrated circuits have been realized in the InAs/GaAs materials system by selective area – and regrowth techniques [1,2]. We demonstrate the first Butt-joint active-passive integrated QD laser device in the InAs/InP (100) materials system emitting in the technologically important 1.55 µm wavelength region for fiber based optical telecommunication systems. The extended cavity Fabry-Pérot QD laser operates in continuous wave (CW) mode at room temperature (RT) on the QD ground state (GS) transition. The threshold current, transparency current density, and external differential quantum efficiency are comparable to those of our all-active Fabry-Pérot QD lasers [3]. The Butt-joint reflectivity is below – 40 dB for straight waveguides. Double-state lasing on the QD GS and excited state (ES) is observed with increasing injection current, which is caused by the inter-level relaxation rate of carriers typical for QDs [4].

Device fabrication: The integrated QD laser structure was grown by Metal-Organic Vapor Phase epitaxy (MOVPE) in a three-step process [5]. In the first epitaxy step, the active layer was grown on n-doped InP (100) substrate. It consists of a stack of five QD layers embedded in the center of a 500 nm thick $\lambda = 1250$ nm lattice-matched InGaAsP (Q1.25) layer. The average QD diameter, height, and density are 50 nm, 5.6 nm, and 2×10^{10} cm^{-2}, and the Q1.25 separation layers are 40 nm thick. The emission wavelength of the 3-monolayers (MLs) InAs QDs was tuned into the 1.55 µm wavelength region through insertion of ultrathin (1.3 MLs) GaAs interlayers underneath the QDs [6]. Then a p-doped 200 nm thick InP layer was grown. Active mesa blocks were defined by photolithography using a 100 nm SiN_x layer as etching mask. The mesa blocks are 30 µm wide and spaced apart by 250 µm with lengths varying from 200 to 2000 µm. The future passive areas were etched wet chemically 50 nm below the active layer, thus 560 nm were etched for regrowth. An overhang below the SiN_x mask prevents the lateral overgrowth at the Butt-joint. Then undoped Q1.25 and InP layers were regrown by selective area MOVPE using the same SiN_x mask. The thicknesses of both layers are matched to the original thicknesses. The SiN_x mask was removed and the 1.5 µm gradually p-doped InP top cladding and compositionally graded p-doped InGaAsP

contact layer were grown. After growth, straight ridge waveguides with a width of 2 µm were fabricated by reactive-ion dry etching 100 nm into the Q1.25 layer. The structure was planarized by polyimide and Ti/Pt/Au contact layers were fabricated on the active region and the back side. The extended cavity laser structures under investigation have a total length of 2250 µm. The active waveguide with length of 1450, 1200 and 750 µm in different devices is connected to one passive waveguide with length of 800, 1050 and 1550 µm, respectively. The integrated laser structures are terminated by cleaved mirrors on both ends, as shown in Fig 1.

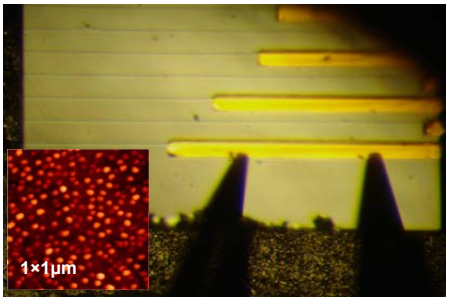


Fig. 1: Photograph of the integrated extended cavity InAs/InP (100) quantum dot (QD) laser devices. The two current probes contact the laser with 1450 µm long active and 800 µm long passive waveguides. Inset: atomic force microscopy (AFM) image of uncapped QDs.

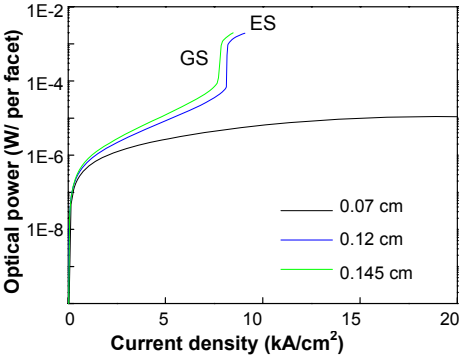


Fig. 2 light versus current (LI) curves of the integrated QD laser devices with different length of the active waveguides taken in continuous wave (CW) mode at room temperature (RT). The regimes of QD ground state (GS) and excited state (ES) lasing are indicated.

Results: Figure 2 shows the light versus current (LI) curves of the integrated laser structures with different length of the active waveguides. For the 1450 and 1200 µm long active waveguides, lasing occurs in CW mode at RT. The respective threshold currents are 0.198 A （6.76 kA/cm^2） and 0.195 A （8.13 kA/cm^2）and the external differential quantum efficiencies are 7.26 and 2.75, similar to those of our all-active Fabry-Pérot QD lasers [3]. This confirms a low Butt-joint loss, which has been previously evaluated to be 0.1 – 0.2 dB in passive-passive structures [5]. From the length dependence of the threshold current, a transparency current density of 116 A/cm^2, i.e., 23.2 A/cm^2 per QD layer is estimated..The device with 700 µm long active waveguide does not show laser operation.

Lasing starts on the QD GS transition at 1.53 µm while ES lasing at shorter wavelength (1.50 µm) sets in with increasing current due to QD GS saturation. This leads to the characteristic step-like output power increase in the LI curves and is confirmed by the lasing spectra of the device with 1200 µm long active waveguide shown in Fig 3. When the current is increased from 0.192 A to 0.194 A, the GS emission intensity increases strongly while the ES emission intensity almost keeps constant. For further increase of the current from 0.20 A to 0.220 A, the GS emission intensity saturates, whereas the ES emission intensity steeply increases. Such double-state lasing phenomena are often

observed for self-assembled QD lasers, and caused by the carrier inter-level relaxation and recombination processes typical for QDs [4].

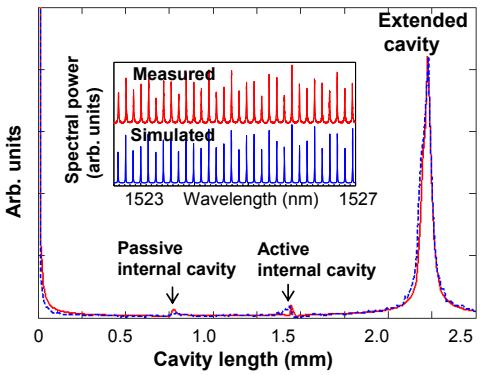


Fig. 3: Fourier Transforms of the experimental and fitted sub-threshold emission spectra. Inset: high resolution emission spectra. The active waveguide is 1450 µm.

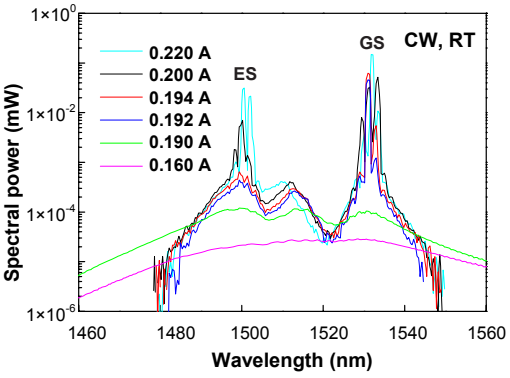


Fig. 4. Lasing spectra of the integrated QD laser with 1200 µm long active waveguide for various currents (0.160 A, 0.190 A, 0.192 A， 0.194 A, 0.200 and 0.220 A). QD GS and ES transitions are indicated.

In addition to low Butt-joint absorption, a low Butt-joint reflectivity is essential for stable operation of photonic integrated devices and circuits. The Butt-joint reflectivity is measured based on the analysis of sub-threshold emission spectra which are recorded by an Optical Spectrum Analyzer (APEX AP2040) with a very high resolution of 0.16 pm [5]. By fitting the calculated sub-threshold mode structure to the recorded data, values of the reflectivity are extracted. Figure 4 depicts the Fourier Transforms of the experimental and fitted emission spectra, which are shown in the inset. In addition to the dominant peak in the Fourier Transform due to the extended cavity, small peaks are visible originating from the passive and active internal cavities formed by the cleaved mirrors and the Butt-joint. The extracted Butt-joint reflectivity is – 42 dB (6×10^{-5}). This is similar to the reflectivity of our Butt-joints examined with bulk active region extended cavity lasers and can easily be reduced to below – 50 dB using waveguides entering the Butt-joint under an angle [7].

Conclusion: We have demonstrated Butt-joint active-passive integrated extended cavity Fabry-Pérot laser devices based on InAs/InP (100) quantum dots (QDs) emitting around 1.55 µm. Continuous wave lasing at room temperature on the QD ground state transition was achieved. The threshold current was comparable to all-active Fabry-Pérot QD lasers. With increasing current, double-state lasing occurs which is typical for QDs due to the specific carrier inter-level relaxation and recombination processes. A Butt-joint reflectivity < – 40 dB for straight waveguides was determined. Hence, compatibility of our InAs/InP (100) QD gain material with Butt-joint active-passive integration is demonstrated paving the way for QD based photonic integrated devices

and circuits operating in the technologically important 1.55 μm wavelength region for fiber based optical telecommunication systems.

References

[1] S. Mokkapati, H.H. Tan and C. Jagadish, 'Integration of an InGaAs quantum-dot laser with a low-loss passive waveguide using selective-area epitaxy', IEEE Photon. Technol. Lett., vol. 18, pp. 1648-1650, 2006.

[2] J. Yang, P. Bhattacharya and Z. Wu, `Monolithic integration of InGaAs-GaAs quantum-dot laser and quantum-well electroabsorption modulator on silicon`, IEEE Photon. Technol. Lett., vol. 19, pp. 747-749, 2007.

[3] S. Anantathanasarn, R. Nötzel, P. J. Veldhoven, F. W. M. Otten, Y. Barbarin, G. Servanton, T. Vries, E. Smalbrugge, E. J. Geluk, T. J. Eijkemans, E. A. J. M. Bente, Y. S. Oei, M. K. Smit and J. H.Wolter, 'Lasing of wavelength-tunable (1.55 μm region) InAs/InGaAsP/InP (100) quantum dots grown by metal organic vapor-phase epitaxy', Appl. Phys. Lett. vol. 89, pp. 073115, 2006.

[4] L.W. Shi, Y.H. Chen, B. Xu, Z.C. Wang and Z.G. Wang, 'Effect of inter-level relaxation and cavity length on double-state lasing performance of quantum dot lasers', Physica E: Low-dimensional Systems and Nanostructures, vol. 39, pp 203-208, 2007.

[5] Y. Barbarin, E.A.J.M. Bente, T. de Vries, J.H. den Besten, P.J. van Veldhoven, M.J.H. Sander-Jochem, E. Smalbrugge, F.W.M. van Otten, E.J. Geluk, M.J.R. Heck, X.J.M. Leijtens, J.G.M.van der Tol, F. Karouta, Y.S. Oei, R. Nötzel and M.K. Smit, `Butt-joint interfaces in InP/InGaAsP waveguides with very low reflectivity and low loss`, in Proc. IEEE/LEOS Symp. Benelux Chapter 2005, pp. 89-92.

[6] S. Anantathanasarn, R. Nötzel, P. J. Veldhoven, F. W. M. Otten, T.J. Eijkemans and J.H. Wolter, `Stacking and polarization control of wavelength-tunable (1.55-μm region) InAs/InGaAsP/InP (100) quantum dots`, Appl. Phys. Lett. vol. 88, pp. 063105, 2006.

[7] Y. Barbarin, E.A.J.M. Bente, C. Marquet, E.J.S. Leclère, J.J.M. Binsma and M.K. Smit., 'Measurement of Reflectivity of Butt-Joint Active-Passive Interfaces in Integrated Extended Cavity Lasers', IEEE Photon. Technol. Lett., vol 17, pp. 2265-2267, 2005.

Passively mode-locked quantum dot laser diodes at 1.53 μm with large operating regime

M.J.R. Heck[1,2], A. Renault[2], E.A.J.M. Bente[1], Y.S. Oei[1], M.K. Smit[1], K.S.E. Eikema[2], W. Ubachs[2], S. Anantathanasarn[1] and R. Nötzel[1]

[1]COBRA Research Institute, Technische Universiteit Eindhoven, Eindhoven, the Netherlands
m.heck@tue.nl
[2]Laser Centre Vrije Universiteit, Amsterdam, the Netherlands

Abstract. *Passive mode-locking in two section InAs/InP (100) quantum dot lasers emitting around 1.53 μm is observed over a large operating regime. For absorber voltages of 0 V down to -3 V and for amplifier currents of 750 mA up to 1 A the fundamental RF-peak is over 40 dB above the noise floor.*

Introduction

Sources of picosecond or femtosecond optical pulses with a wavelength around 1550 nm have many applications in optical telecommunications. They can be used as pulse sources for time-domain multiplexed systems and as synchronized pulse sources or multi-wavelength lasers for wavelength-division multiplexed systems. Moreover the optical spectrum is a frequency comb and may be used in e.g. arbitrary pulse generation. An important requirement for many of these applications is a broad coherent optical bandwidth of the output of the source, which may well exceed 1 THz. Also the operation regime should be robust for practical implementation.

For reasons of stability, compactness, and fabrication costs, mode-locking of semiconductor laser diodes is an attractive option for generating picosecond pulses at 1.55 μm [1]. The material system of choice for fabricating these mode-locked laser diodes (MLLDs) is InP/InGaAsP, using either bulk or quantum well gain material. The bandwidth of these MLLDs is however limited to between 1 nm – 5 nm [1,2].

Quantum dot (QD) gain material is promising for the application in MLLDs due to its broad gain spectrum. Sub-picosecond pulse generation down to 0.4 ps with a bandwidth of 14 nm has been achieved with InAs/GaAs QD material operating at wavelengths around 1.3 μm [3]. These lasers are shown to have robust operating regimes [4].

In this paper a study of the ranges for absorber voltage and amplifier current for passive mode-locked operation of 4.6-GHz monolithic two-section InAs/InP (100) QD lasers is presented. These devices operate at wavelengths of around 1.53 μm. Some first results have been published in [5].

Design and fabrication

The QD laser structure is grown on n-type InP (100) substrates by metal-organic vapor-phase epitaxy (MOVPE), as presented in [6]. In the active region five InAs QD layers are stacked. These are placed in the center of a 500 nm InGaAsP optical waveguiding core layer. The bottom cladding of this laser structure is a 500-nm thick n-InP buffer and the top cladding is a 1.5-μm p-InP with a compositionally graded 300-nm p-InGaAs(P) top contact layer. This layerstack is compatible with a butt-joint active-passive integration process for possible further integration.

Two-section Fabry-Pérot-type laser devices have been designed and realized. The ridge waveguides have a width of 2 μm and are etched 100 nm into the InGaAsP waveguiding

layer. To create electrical isolation between the two sections, the most highly doped part of the p-cladding layer is etched away. The waveguide and isolation sections are etched using an optimized CH_4 / H_2 two-step reactive-ion dry etch process. The structures are planarized using polyimide. Two evaporated and plated metal pads contact the two sections to create two contacts. The backside of the n-InP substrate is metallized to create a common ground contact for the two sections.
The structures are cleaved to create the mirrors for the FP cavity. No coating is applied. The two-section devices are operated by forward biasing the longer gain section, creating a semiconductor optical amplifier (SOA) and by reversely biasing the shorter gain section, creating a saturable absorber (SA). The devices are mounted on a copper chuck, p-side up, which is kept at a temperature of 10 ˚C. The total length of the devices is 9 mm. In this paper we study two two-section devices with SA lengths of 270 µm and 540 µm respectively. A 9-mm one-section device (i.e. an SOA with cleaved mirrors), fabricated on the same wafer, is used for reference purposes.

Experimental results

The laser with a 270-µm SA section has lasing threshold current values of 660 mA to 690 mA for SA reverse bias voltages of 0 V to -4 V respectively. Passive mode-locking is first studied by recording the electrical power spectrum using a 50-GHz photodiode and a 50-GHz electrical spectrum analyzer. The RF-spectra obtained for this laser show clear peaks at the cavity roundtrip-frequency of 4.6 GHz. In Fig. 1 the height of these RF-peaks over the noise floor is given as a function of the operation parameters, i.e. the SA bias voltage and the SOA injection current. A large, robust operating regime with RF-peak heights over 40 dB is found for values of the injection current of 750 mA up to 1.0 A and for values of the SA bias voltage of 0 V down to -3 V.

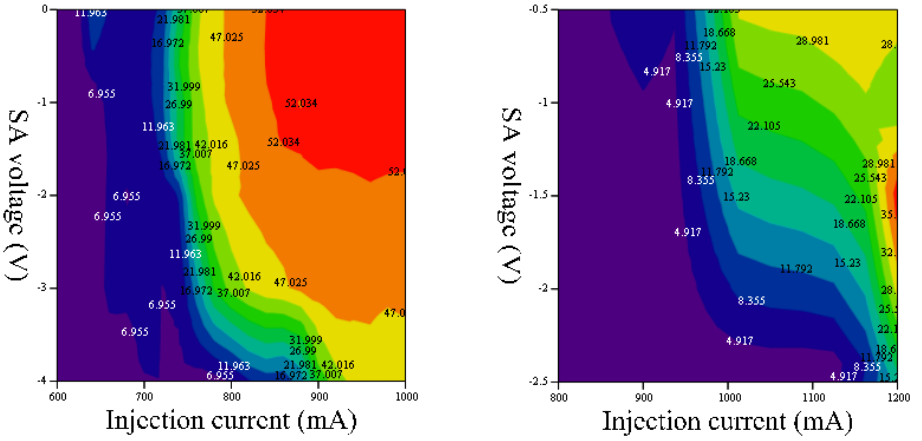


Fig. 1 RF-peak heights (over the noise floor, dB-scale) for a 9-mm laser with a 270-µm SA (left) and a 540-µm SA (right). The electrical bandwidth used to obtain the RF-spectra is 50 kHz. An external SOA was used before the 50-GHz photodiode to boost the optical output power of the 270-µm laser by about 6 dB – 7 dB. The 540-µm laser was directly connected to the photodiode, without an SOA.

The width of this RF peak is narrow, i.e. 0.57 MHz at -20 dB (for I_{SOA} = 900 mA and V_{SA} = -1 V). Also the position of this RF-peak, which is centered around 4.599 GHz, is stable within 3 MHz for the operating regime mentioned above. In MLLDs based on

bulk gain material minimum RF-linewidths of 2.5 MHz at -20 dB have been reported, with a stability of the roundtrip frequency of about 50 MHz over their operating regime [2]. So a clear improvement of the 'longer term' laser stability is observed by using QD gain material instead of bulk gain material.

The laser with a 540-μm SA section has lasing threshold current values of 830 mA to 910 mA for SA reverse bias voltages of -0.5 V to -2.5 V respectively. This increase of the threshold current as compared to the 270-μm laser is caused by the increased SA length and the correspondingly increased absorption in the laser cavity.

The RF-spectra obtained for this laser show that mode-locking only sets in at relatively high values of the injection current, i.e. around 1.0 A. For the SA bias voltages of -2.0 V down to -2.5 V mode-locking sets in close to 1.2 A. This is the upper limit for our measurement setup, since above this value of the injection current the detrimental effect of the device heating causes the output power to drop.

For comparison we studied the 9-mm one-section QD-laser. The threshold current of this device is 380 mA. The electrical spectrum shows no distinct peak at the roundtrip frequency. This can be expected based on the well-known mechanisms of passive mode-locking in laser diodes with bulk or quantum-well gain material, where the SA plays a crucial role [1,2]. However one-section quantum-dash lasers emitting at 1.56 μm have been reported to show passive mode-locking, without the aid of an SA [7].

Timing jitter has been studied by evaluating the single-sideband phase noise signal around the fundamental RF-peak, using an integration interval of 10 kHz - 80 MHz. The timing jitter has been evaluated for the 270-μm SA device at a fixed injection current of 900 mA. The value is (35±3) ps for a low SA bias voltage of -0.5 V and increases slightly to (39±3) ps for an SA bias voltage of -2 V. For the 540-μm SA device (evaluated at 1100 mA) this increase of the timing jitter is larger, going from (36±4) ps to (53±7) ps for SA bias voltages of -0.5 V and -2 V respectively. We note that the mode-locking in the 540-μm device is weaker, as can be seen in Fig. 1.

These values of the timing jitter are relatively large as compared to e.g. MLLDs based on bulk gain material [2]. Compared to the results obtained for the width of the RF-peak, which has a relatively small value of 0.57 MHz at -20 dB, we conclude that the 'short-term' jitter is relatively large in the QD-lasers and the 'long-term' jitter is relatively small as compared to bulk or quantum-well MLLDs.

A typical optical spectrum of a 9-mm two-section laser is given in Fig. 2. The spectrum is broad, i.e. 6 nm – 7 nm, as can be expected from the inhomogeneously broadened gain of QD-lasers [6]. As was already measured in [5], this output spectrum is coherent. However the output pulses of these lasers are very elongated, i.e. well over 100-ps duration, and heavily up-chirped, with a chirp value of about 20 ps/nm. In this paper we confirm this observation by compressing the pulses, using standard single-mode optical fiber (SMF). The second order dispersion of SMF is in the order of 16 – 20 ps/(nm·km), meaning that 1.0 – 1.2 km of SMF should be able to compensate the chirp of these pulses. In Fig. 3 the autocorrelator traces are shown for different lengths of SMF after the 270-μm SA laser output. As can be seen the pulse is compressed to a minimum duration with 1500 m of SMF. However the strong peak in the center indicates an increased compression of part of the pulse. This partial compression can either be caused by a non-linear part of the chirp (or higher order SMF-dispersion), or by the non-Gaussian shape of the optical spectrum (Fig. 2). No autocorrelator traces could be obtained without SMF [5].

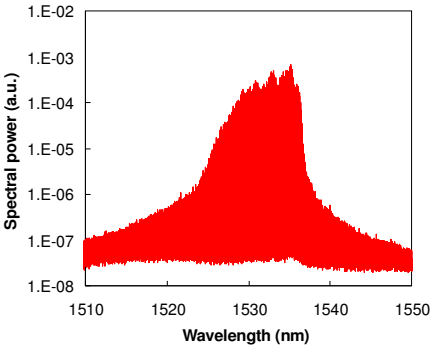


Fig. 2 Optical spectrum obtained for the 270-µm SA device. Injection current is 900 mA and SA bias voltage is -1 V. The optical bandwidth used to obtain the spectrum is 0.16 pm.

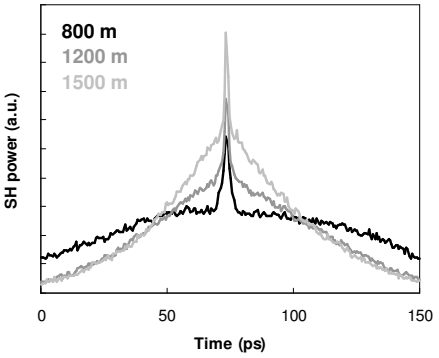


Fig. 3 Autocorrelator traces (second harmonic power given) obtained with a 270-µm SA device. Injection current is 900 mA and SA bias voltage is -1 V. The length of SMF between the device and the autocorrelator is indicated.

Conclusion

In this paper we have presented 4.6-GHz, two-section QD-lasers emitting around 1530 nm. Their operation is shown to be tolerant against variations in operation parameters. For a device with a 270-µm SA section, passive-modelocking with an RF-peak of 40 dB above the noise floor, was shown over a large operating regime of SOA injection currents of 750 mA up to 1.0 A and of SA bias voltages of 0 V down to -3 V. The variation of the roundtrip frequency within this operating regime is limited to below 3 MHz. This large and robust operating regime is essential for practical implementation of MLLDs.

The timing jitter values are relatively large, but the presence of an SA in the devices allows for possible hybrid mode-locking. This technique can severely decrease the timing jitter.

These QD-lasers have been realized with a fabrication technology that is compatible with further photonic integration. As such these devices can perform the function of e.g. a mode-comb generator in a complex photonic chip. The output spectrum is however not usable for ultrashort (sub-picosecond) pulse generation using common pulse compression techniques.

This work was supported by the Netherlands Foundation of Scientific Research (NWO), by the NRC Photonics Grant and by the Smartmix program MEMPHIS.

References

[1] R. Kaiser and B. Hüttl, IEEE J. of Sel. Top. Quant. Electr. vol. 13, pp. 125-135, 2007.
[2] Y. Barbarin et al., Optics Express, vol. 14, pp. 9716-9727, 2006.
[3] E.U. Rafailov et al., Appl. Phys. Lett., vol. 87, 081107, 2005.
[4] J.-P. Tourrenc et al., 15th International Conference on Ultrafast Phenomena, paper WC9, 2006.
[5] M.J.R. Heck et al., Optics Express, vol. 15, pp. 16292-16301, 2007.
[6] S. Anantathanasarn et al., Appl. Phys. Lett., vol. 89, 073115, 2006.
[7] C. Gosset et al., Appl. Phys. Lett., vol. 88, 241105, 2006.

Monolithic Integration of a Compact Passive Polarisation Converter within a Laser Diode

S. McMaster, J. J. Bregenzer, M. Sorel, B. M. Holmes and D. C. Hutchings

Department of Electronics and Electrical Engineering, University of Glasgow, Glasgow, G12 8LT, Scotland, UK,

s.mcmaster@elec.gla.ac.uk

Abstract. *We report on the realisation of a short, GaAs-AlGaAs unstrained double quantum well based passive waveguide polarisation converter monolithically integrated within a Fabry-Perot laser cavity. The observed transverse magnetic (TM) polarisation purity at the output is greater than 80 % for a converter section length of 20 μm at an operating wavelength of 867.1 nm.*

Introduction

The ability to control or indeed convert the polarisation state of light in guided wave devices is paramount to the development of current and future photonic integrated circuits. One such device is the proposed monolithically integrated optical isolator [1]; wherein polarisation selectivity is required in order to reciprocally rotate the input polarisation state by 45°. In *III-V* material systems, passive waveguide polarisation converters, also commonly referred to as polarisation rotators, may be used as a means to convert transverse electric (TE) to transverse magnetic (TM) polarised modes or vice versa [2]. In this paper we demonstrate the integration of a reciprocal polarisation mode rotator integrated within a semiconductor ridge waveguide laser, allowing for a device that emits predominantly TE or TM polarised light from each facet respectively.

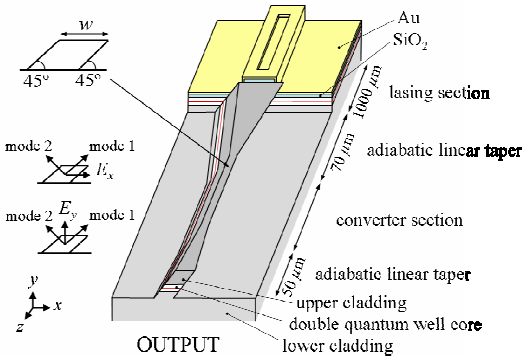


Fig. 1. Schematic representation of the integrated device (not to scale). Also shown are the mode configurations in the asymmetric waveguide section.

Converter design and fabrication

By introducing asymmetry into the waveguide design, as in our angled sidewalls geometry, the optical axes of the guide are effectively offset with respect to the *x* and *y* coordinates as shown in Fig. 1. When a linearly polarised TE_0 light wave - from the

integrated laser - enters the asymmetric section via a 70 μm long linear adiabatic taper, both orthogonally polarised fundamental modes are excited (mode 1 and 2). Mode beating occurs as they propagate along the length of the device (Fig. 2(b)). At each half beat length, $L_{Beat/2} = \pi / \Delta\beta$, the polarisation is effectively rotated by 90°. Note that $\Delta\beta$ is determined from the difference in propagation constants, β_1 and β_2, of the two zeroth order modes and is a characteristic dependant on the geometrical structure of the waveguide and the refractive index contrast between the epitaxial guiding and cladding layers.

The proposed structures were first simulated using a fully vectorial mode solver package in order to ensure single mode operation and to predict the section length required for a full TE to TM conversion. These computations resulted in a converter waveguide width of 680 *nm* and $L_{Beat/2} = 22$ μm as shown in Fig. 2. (a) and (b), respectively. A degree of mode beating begins in the angle-etched tapers, and therefore simulations also indicate that the appropriate ideal length of the narrow waveguide rotator section should be about 16 μm.

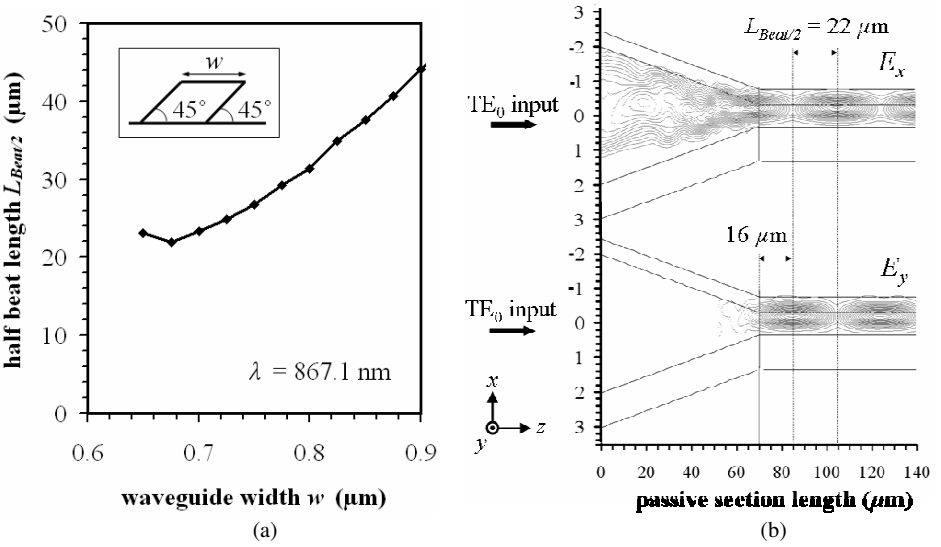


Fig. 2. (a) Half beat length $L_{Beat/2}$ versus the width w of the waveguide cross section for an operating wavelength λ of 867.1 nm. The cut off of the excited second lowest order mode (mode 2) takes place at a waveguide width w just smaller than 680 nm. (b) Top view of the simulated contour plot of both the E_x (TE) and E_y (TM) component of a TE_0 mode launched from the gain section into the passive converter section.

The material structure used here is an unstrained double quantum well GaAs-AlGaAs heterostructure grown by metal organic chemical vapour deposition (MOCVD), lattice matched to an n-doped GaAs substrate. The deeply etched converter waveguides were fabricated using a novel, single-step dry etch process [3]. After lithographic patterning, the etching process is carried out in a reactive ion etch (RIE) system using a $SiCl_4$ plasma and a custom designed sample holder that enables the chip to be aligned at various angles to the incident ion flux, without distorting the positive ions sheath and

hence maintaining the directionality of the incident reactive ions. A scanning electron microscope (SEM) image of a waveguide formed using this technique is shown in Fig. 3.

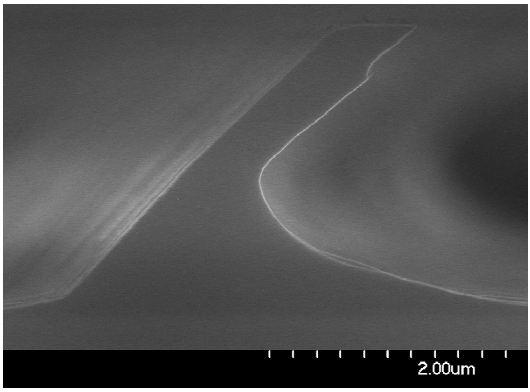
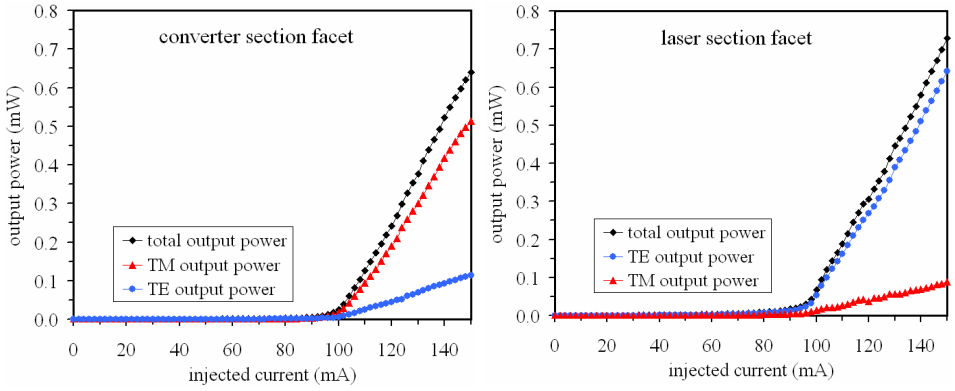


Fig. 3. SEM image of a deep etched angled waveguide section.

Results

Characterisation of the integrated device was performed using a continuous wave current source to drive the laser, with the output from each facet being separated via a polarising beam splitting cube. This enabled both the TE and TM components of the emitted beams to be individually detected using an InGaAs large area photo diode. The light-current (LI) characteristics at both the converter section facet and the laser section facet were measured and are shown in Fig. 4. (a) and (b), respectively. For injection currents above 130 mA it is observed that the converter facet emits predominantly TM polarised light with a polarisation purity, defined as $E_f = P_{TM} / (P_{TM} + P_{TE})$ x 100 % with P_{TE} and P_{TM} denoting the TE and TM output powers respectively, of greater than 80 %. In contrast, however, output from the laser facet shows, as expected due to the interband transitions, mainly TE polarisation with a TM purity of approximately 12 %. It is most likely due to fabrication tolerance that ~100 % conversion efficiencies at the converter facet end are not achieved. However, with simple adjustments to the post growth processing procedure, outputs designed with any mixture of TE and TM (including ~100% TM) should be readily obtainable. As there is no carrier injection in the rotator section, some excess optical loss will be evident, but polarisation mode conversion by mode beating occurs in a sufficiently short length that lasing threshold currents are observed to be only around double that of equivalent laser devices with no converter section. Furthermore, these optical losses may be negated by extending the top ohmic contact such that carrier injection occurs over the entire length of the device, by using a grating structure as one of the laser mirrors or by employing quantum-well intermixing in the passive section [4].



(a) (b)

Fig. 4. Measured L-I curves of the realised device showing the total output power and the separated TE and TM output powers for both (a) the converter section facet (OUTPUT in Fig. 1.) and (b) the lasing section facet.

Conclusions

In conclusion, we have demonstrated, to the best of our knowledge, the first monolithically integrated passive polarisation converter and semiconductor laser diode. This device emits predominantly TM and TE polarised light from the converter and laser facets, respectively. The single-section rotator is fabricated using a novel single-step RIE process, forming a waveguide structure with two angled sidewalls; allowing for a 90° polarisation state rotation without recourse to longitudinal periodic variation. Such integration technology could be useful in establishing a polarisation rotation of only 45° by adaptation of the converter section length, in order to contribute to the realisation of a monolithically integrated optical isolator.

References

[1] D. C. Hutchings, “Prospects for the implementation of magneto-optic elements in optoelectronic integrated circuits: a personal perspective”, Journal of Applied Physics, vol. 36, pp. 2222-2229, 2003.

[2] H. El-Refaei, D. Yevick, and T. Jones, “Slanted-Rib Waveguide InGaAsP-InP Polarization Converters”, Journal of Lightwave Technology, vol. 22, no. 5, pp. 1352-1357, 2004.

[3] J. J. Bregenzer, B. M. Holmes, M. Sorel, and D. C. Hutchings, “Realization of a single-section passive polarization converter using a single-step etch process,” in Proc. IEEE LEOS, 2004, pp. 161-162.

[4] O. P. Kowalski et al., “A universal damage induced technique for quantum well intermixing,” Applied Physics Letters, vol. 72, no. 5, pp. 581-583, 1998.

Integrated electro-optic modulators in micro-structured $LiNbO_3$

D. Janner[1], D. Tulli[1], M. Belmonte[2], and V. Pruneri[1,3]

[1] ICFO-Institut de Ciencies Fotoniques, Mediterranean Technology Park, 08860 Castelldefels (Barcelona), Spain
[2] R&D, Avanex Corporation Sede Secondaria, via Fellini 4, 20097, San Donato Milanese (MI), Italy
[3] ICREA - Institució Catalana de Recerca i Estudis Avançats, 08010, Barcelona, Spain

Abstract *- We review recent advances in micro-structuring $LiNbO_3$ crystals and demonstrate the achievement of large bandwidths and lower driving voltages using domain inversion. We will report on a domain engineered Mach-Zehnder modulator for 10Gb/s transmission with ∼2V switching voltage driven by inexpensive Si-Ge drivers.*

Introduction

Optical networks as main carriers of information are continuously growing in importance due to the ever increasing demand in bandwidth. External $LiNbO_3$ modulators are still extremely effective [1], in particular for long haul and metro applications. With respect to e.g. semiconductor based modulators, $LiNbO_3$ market share could even become larger if performance, integration and cost further improve. Indeed, even though the use of velocity matched (VM) traveling wave electrodes configurations [1, 2] greatly increase the modulation bandwidth (BW), the potential of $LiNbO_3$ in terms of modulation efficiency has been far from being exploited. The frequency dependent microwave loss limits the bandwidth (BW) making it inversely proportional to active length L, similarly to the switching voltage (V_π), so that a trade-off exists between V_π and BW and the ratio BW/V_π is used as a figure of merit. To obtain improved efficiency (increase in BW/V_π), improved interaction (overlap integral) between microwave and optical fields is required. To this end, different solutions have been proposed [3, 4, 5] which, although effective in some cases, rely on sophisticated techniques, not ideal for a large scale production environment.

Domain inversion (DI) in ferroelectrics, such as $LiNbO_3$, has been widely exploited in many all-optical processes, even though its use in electro-optics, has been mostly limited to quasi-velocity-matching for nonlinear processes or to achieve a desired chirp value for high-frequency and broadband modulators [6]. More recently, domain engineering of z-cut $LiNbO_3$ structures has been proposed to produce large bandwidth and very low voltage modulators in single drive configuration [7]. With respect to previous modulating structures in single domain crystal, the proposed DI symmetric scheme allows to achieve at the same time maximum-efficiency, chirp-free and single-drive operation all at once. As a demonstration of the impact of our approach, we report the design, fabrication and test of a DI modulator with 15 GHz bandwidth and ∼2 V switching voltage suited for the use with inexpensive Si-Ge drivers.

Improvements in micro-structured domain inverted modulators

Recently, we have demonstrated that by using DI in $LiNbO_3$, an efficient modulator can be designed and produced [7]. The cross section of the proposed modulator highlighting

the working principle is shown in Fig. 1c. Note that there is a silica based buffer layer between the hot electrode and lithium niobate crystal. This layer ensures at the same time low optical loss by keeping the evanescent optical field low in the lossy metal electrodes and velocity matching between the traveling optical and microwave fields.

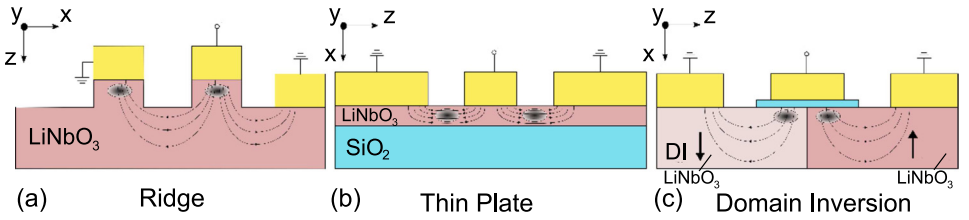


Figure 1: Comparison between different modulator schemes: a) ridge, b) thin plate, c) domain inverted push-pull

With respect to previous structures of coplanar waveguide (CPW) modulator [1, 6] the proposed layout offers several advantages, and with respect to the other approaches including ridge modulators [4, 5] or thin plate [3], it offers greater feasibility, even though the performance in some cases is slightly lower. The comparison between classical and more different schemes is summarized in table 1, where the characteristic parameters are considered: switching voltage ($V_\pi L$), microwave-optical overlap (Γ as defined in [2]), residual chirp factor (α) and RF drive configuration. Driving voltages (for similar device length) are close to those offered by dual drive structures (two waveguides under two hot electrodes driven by opposite sign voltages), with the advantage of being single drive, hence in the absence of any synchronization issue between two microwave lines. On the other hand the typical single-drive structure in single-domain z-cut has one of the two waveguides under the ground electrode, which induces a lower electro-optic effect due to field spreading compared to the other waveguide under the narrower hot electrode. The result is that the typical driving voltage is about 1.5 times that of a dual-drive structure and 1.4 times that of the proposed geometry.

Table 1: Comparison of the performances of different configurations

Structure	$V_\pi \cdot L$ (V· cm)	Γ	Chirp (α)	RF drive
$LiNbO_3$ physical limit	≈ 3.6	1	0	Single
Standard CPW [1]	≈ 12	0.3	$\neq 0$	Single
Dual drive CPW [1]	≈ 8	0.45	arbitrary(=0)	Dual
CPW with longitudinal DI [6]	≈ 12	0.3	≈ 0	Single
Domain inverted push-pull	≈ 9	0.4	0	Single
Ridge [4, 5]	≈ 6	0.6	≈ 0	Single
Thin plate [3]	≈ 9	0.4	≈ 0	Single

As an experimental demonstration of this type of modulator, we have fabricated a single-drive Mach-Zehnder with an active length of ~ 40 mm. To obtain the required inverted domain structure, high-voltage (>10 kV) pulsed poling is performed after Ti indiffused waveguide fabrication on the 0.5-mm thick crystal [8].

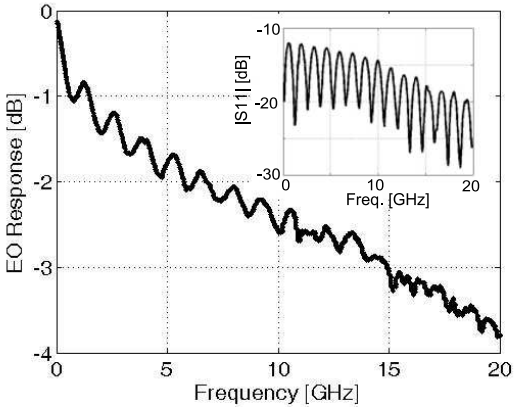


Figure 2: Domain engineered modulator electro-optic response (|S21|) and electrical reflection parameter (|S11| in the inset). The power reflected is below 10 dB over all the frequency range.

After DI, the modulator chip undergoes standard fabrication, e.g. silica buffer layer deposition, electroplated thick electrode, etc. In Fig. 2 we show the microwave reflection coefficient (|S11|) and the corresponding electrical frequency response (|S21|). From the figure one can see that the electrical reflection is always below -10 dB and the -6 dB electrical bandwidth is 15 GHz, which also is the expected value for the -3 dB electro-optic bandwidth.
The corresponding switching voltage is $\sim$ 2 V (measured at 1 kHz). The modulator could therefore easily be driven with significant extinction by a low-cost driver which typically provides less than 3 V for 10 Gb/s bit rate, thus allowing to use inexpensive Si-Ge electro-absorption drivers to modulate. We carried out system measurements for a typical low-voltage modulator driven by a Inphi 1015EA driver. The eye opening showed a performance suitable for standard optical communication at 10 Gb/s, with a dynamic extinction ratio $>$13 dB.

Conclusions

We have reported on micro-structured electro-optic waveguide $LiNbO_3$ modulators which are based on the use of domain inversion in order to enhance the BW/V_π figure of merit. We have experimentally demonstrated the feasibility of a modulator with a switching voltage of $\sim$2 V and a bandwidth of 15 GHz, suitable for inexpensive ultra low-voltage Si-Ge drivers. Besides, system measurements demonstrate the good performance in term of extinction ratio ($>$13 dB) and eye opening that make the device suited for 10 Gb/s transmission.

Acknowledgments

We acknowledge support from the Spanish national programs Plan Nacional no. TEC 2007-60185 and Juan de la Cierva.

References

[1] L. Wooten, K.M. Kissa, A. Yi-Yan, E.J. Murphy, D.A. Lafaw, P.F. Hallemeir, D. Maack, D.V. Attanasio, D.J. Fritz, G.J. McBrien, D.E. Bossi, *IEEE J. Sel. Top. Quantum* Electron. **6**, 69–82 (2000).

[2] R. C. Alferness, *IEEE Trans. Microwave Theory Tech.*, **30**, 1121–1137 (1982).

[3] K. Aoki, J. Kondo, A. Kondo, T. Ejiri, T. Mori, Y. Mizuno, M. Imaeda, O. Mitomi, M. Minakat, *J. Lightwave Technol.*, **24**, 2233–2237 (1982).

[4] N. Anwar, S. S. A. Obayya, S. Haxha, C. Themistos, B. M. A. Rahman, and K. T. V. Grattan, *J. Lightwave Tech.*, **20**, 826–833 (2002).

[5] M. Garcia Granda, H. Hu, *OptoEL*, MOI-13, (2007).

[6] N. Courjal, H. Porte, J. Hauden, P. Mollier and N. Grossard, *J. Lightwave Technol.* **22**, 1338–1343 (2004).

[7] F. Lucchi, D. Janner, M. Belmonte, S. Balsamo, M. Villa, S. Giurgola, P. Vergani, V. Pruneri, *Opt. Exp.*, **15**, 10739–10743 (2007).

[8] D. Janner, D. Tulli, F. Lucchi, P. Vergani, S. Giurgola and V. Pruneri, Appl. Phys. A, **91**, 319-321 (2008).

Ferroelectric Microdomains in Plasma-Etched Ridges on X-Cut Lithium Niobate

L. Gui[1], H. Hu[1], M. Garcia-Granda[1], W. Sohler[1], G. Berth[2] and A. Zrenner[2]

[1]Angewandte Physik, Universität Paderborn, 33098 Paderborn, Germany
lgui@mail.uni-paderborn.de
[2]Experimentalphysik, Universität Paderborn, 33098 Paderborn, Germany

Abstract. *The fabrication and investigation of (periodic) microdomains in the body of a ridge on X-cut Lithium Niobate (LN) is demonstrated. A 3-dim investigation with a non-linear Confocal Laser Scanning Microscope (CLSM) reveals a strong contrast of inverted and non-inverted sections of the ridge.*

Introduction

To enhance the efficiency of nonlinear interactions in optical waveguides, smaller cross section and higher index contrast are required leading to a stronger enhancement of the guided mode intensity. Therefore, "photonic nanowires" are currently developed [1]. If ferroelectric materials like Lithium Niobate (LN) are considered, a periodic domain inversion is required to enable quasi phase matching (QPM) for second order nonlinear processes. Ridge waveguides represent a first step towards photonic nanowires; they can be fabricated with excellent properties on Z-cut LN by chemical etching [2].
In this contribution we report the fabrication of ridges also on X-cut LN, using inductively coupled plasma (ICP) etching. Moreover, periodic domain inversion, localized in the body of the ridge only, is demonstrated - similar to the recent work of Généreux et al. [3]. The resulting domain structure is investigated in three dimensions using a nonlinear confocal Laser Scanning Microscope (LSM) [4]. It reveals a strong contrast between inverted and non-inverted sections of the ridge; however, the origin of this contrast has still to be explored.

Ridge fabrication and electrode definition

A Cr film of 220 nm thickness was deposited by sputtering on the –X face of a LN substrate of 1 mm thickness. Using optical contact lithography with an e-beam written mask and wet etching with a Cerium Sulfate solution, Cr stripes of 10 µm width were defined. The Cr stripes served as etch mask for the successive ICP (inductively coupled plasma) etching of LN with an etching ratio of 1:10. It was performed in an Oxford Plasmalab System 100 with an ICP 180 plasma source. The etching gas was a mixture

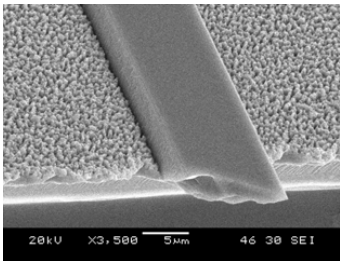


Fig. 1: SEM micrograph of an etched ridge of 2.4 µm height and 9.0 µm width on X-cut LN.

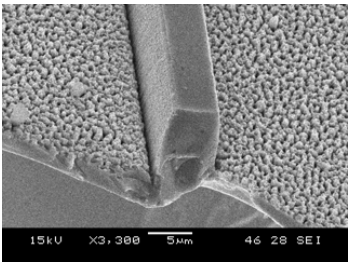


Fig. 2: SEM micrograph of an etched ridge of 5.8 µm height and 5.0 µm width on X-cut LN.

of 15 sccm C_4F_8 and 15 sccm He. After 4 minutes, the sample was taken out and cleaned in SC-1 solution (70% H_2O, 20% H_2O_2, 10% NH_4OH) for 1 minute to remove a brown layer, probably carbon polymers; then the etching was continued. This process was repeated 5 times until the etching depth was ~ 2 µm. Finally, the remaining Cr stripe was removed by a Cerium Sulfate solution and the sample was carefully cleaned. By using thicker Cr stripes, higher and smaller ridges could be fabricated with a height of up to 5.8 µm and a width of 4.0 µm. They can be doped by Ti to get optical guiding also in the depth [5]. Figs. 1 and 2 show SEM micrographs of etched ridges on X-cut LN of 2.4 µm (5.8 µm) height and 9.0 µm (5.0 µm) width, respectively.
A scheme of the poling configuration for a ridge on X-cut LN is depicted in Fig. 3. Comb like electrodes are placed on the Z-faces of the ridge enabling to generate periodic microdomains in the body of the ridge only. To fabricate such electrodes of 16.6 µm periodicity, we used lift-off lithography of a vacuum-deposited, 100 nm thick Ti layer. Fig. 4 presents a top view of the electrode structure on both sides of a 2.0 µm high ridge of 10 µm width. However, it turned out that the electrode fingers on both side walls were not as perfect as desired; only on one side the ridge wall was coated by the electrode fingers. On the other side, they terminated just in front of the ridge on the X-face of the substrate. Therefore, the electric field is higher at the bottom of the ridge; consequently, domain inversion should start here before growth to the top of the ridge, but also deeper into the substrate sets in.

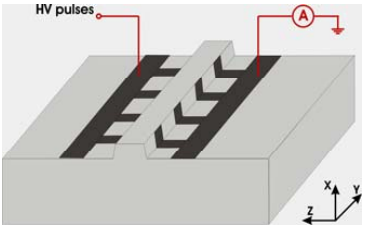


Fig. 3: Scheme of the poling configuration for a ridge on X-cut LN.

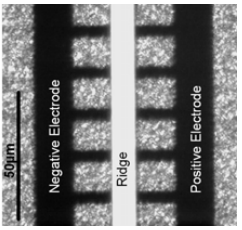


Fig. 4: Top view (optical micrograph) of the electrode structure of 16.6 µm periodicity on both sides of a 10 µm wide ridge.

Electric field assisted poling

In order to simulate the electric field distribution generated by the electrodes, the static electric potential distribution was calculated in the cross section of the ridge between the electrodes using a finite difference method. Afterwards, a numeric derivation was made on a non-uniform grid of 512x512 points in an area of 60x50 µm around the ridge, yielding as result the profile of the relevant component (E_z) of the electric field distribution. Fig. 5 presents as example lines of constant E_z in a ridge of 2.0 µm height and 10µm width, assuming 1 V applied to the left electrode. As the coercive field is ~ 20 kV/mm or 20 MV/m, respectively, the applied voltage should approach 200 V to start domain inversion. The highest field and, therefore, first nucleation are expected at the edges of the ridge assuming a symmetric field distribution as sketched in Fig. 5 (but see the comments given above).
The poling experiments have been done in an oil bath to maintain a high resistance between the two electrodes and to avoid any surface currents. Rectangular high voltage pulses have been applied for poling. The accumulated charge for each pulse was calculated and plotted as function of the pulse number. Fig. 6 shows as an example the

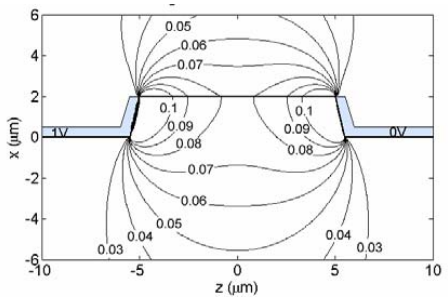


Fig. 5: Calculated lines of constant E_z (in MV/m) in a ridge of 2.0 μm height and 10 μm width, assuming 1 V applied to the left electrode.

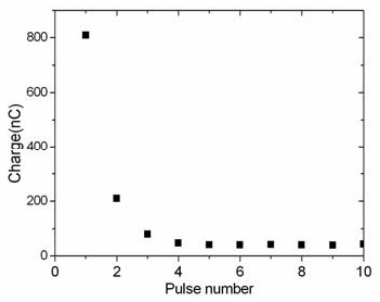


Fig. 6: The accumulated charge per rectangular poling pulse of 270 V as function of the pulse number.

charge evolution for a peak voltage of 270 V. The pulse duration was 10 ms and the interval time between consecutive pulses was 100 ms. We observe that the largest charge is accumulated during the first pulse; it decreases fast with increasing pulse number indicating that most of the domain inversion has been achieved by the first pulse alone. Such a behavior has already been observed previously [6].

Characterization by nonlinear confocal laser scanning microscopy

Preferential chemical etching, linear and nonlinear confocal laser scanning microscopy (CLSM) have been used to investigate the domain inverted structures. Etching with $HF:HNO_3$ (20 min.) attacks the -Z-face(s) of the ridge only; in case of a successful periodic domain inversion a corresponding pattern should become visible also from top. Therefore, we studied the processed ridge at the surface with a CLSM operated in the linear optical reflection mode; however, only a slight indication of a periodical modulation of the edges of the ridge is observable (Fig. 7, left). It might be that the domains did not grow up to the surface though expected from the calculated (ideal) electric field profile. However, operating the CLSM in the nonlinear (Second Harmonic Generation, SHG) mode with the polarization parallel to the Z-axis, a periodic pattern of strong contrast became visible at the surface of the ridge (Fig. 7, right). We were also able to observe the domain structure as function of the depth in the ridge down into the substrate; the pattern became weaker and broader in both dimensions with signatures under the electrode positions as well, before it completely disappeared in a depth of ~ 7 μm. The (nonlinear) CLSM was operated with a Ti-sapphire laser (λ_c = 800 nm, 20 fs pulses @ f_R= 80 MHz) with a depth resolution of ~1.0 μm. The generated SH-signal was detected in backward direction by a single photon counting module (avalanche photo diode) [4].

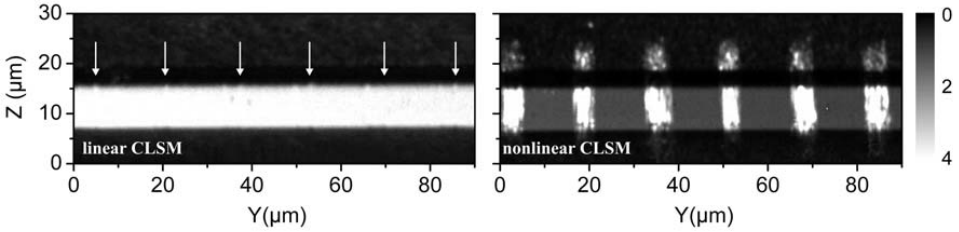


Fig. 7: Linear CLSM image of the X-face of a 10 μm wide ridge of 2.0 μm height; the faint periodic edge modulation is indicated (left). SH-signal generated by the nonlinear CLSM from the same surface (right). A grey scale of both, the fundamental- and SH-intensities, is given on the right.

Discussion

As already shown by Flörsheimer et al. [7], a relatively strong SH-signal can be expected from an X-face of LN, if the polarization is oriented parallel to the Z-axis. And domains of antiparallel orientation should yield the same SH-intensity, which drops to zero, if the focus of the LSM is shifted deeper into the substrate. The domain boundaries should become visible as fine dark lines at the surface and as bright lines in the bulk [7]. However, the behaviour we observe is quite different. Though the surface of the ridge gives a SH-signal in the non-inverted sections, which drops to zero in the depth, a much stronger signal is observed from the inverted sections (Fig. 7, right). The difference to [7] is that the investigated domain has a finite depth of several micrometers only. At the moment we can only speculate, why such a high nonlinear contrast arises. It might be due to the second nonlinear interface in the volume (or underneath) of the ridge. Or it might be due to a strong filamentation of the ferroelectric domains, which seem to be uniform, but might consist of many (not resolved) needle-like inverted filaments as already indicated in [7]. This could lead to an enhanced nonlinear contribution of the larger number of domain boundaries. By investigating cross sections of the ridges and by corresponding theoretical modelling we hope to be able answering this question.

Conclusions

ICP-etching allows fabricating ridges and ridge waveguides of good quality also in X-cut LN. By depositing electrodes on the side walls of the ridge, a fabrication of (periodic) microdomains in the body of the ridge becomes possible. In this way relatively low voltages of ~270 V are sufficient for ferroelectric domain inversion. A 3-dim investigation of the periodically poled ridge structure with a nonlinear CLSM reveals a strong contrast of inverted and non-inverted sections within the ridge. The origin of this contrast has still to be explored.

References

[1] M. A. Foster, A. C. Turner, M. Lipson, and A. L. Gaeta: "Nonlinear Optics in Photonic Nanowires", Optics Express **16**, 1300-1320 (2008).

[2] H. Hu, R. Ricken, W. Sohler, and R. B. Wehrspohn: "Lithium Niobate Ridge Waveguides Fabricated by Wet Etching", IEEE Photon. Technol. Lett., **19**, 417–419 (2007).

[3] F. Généreux, G. Baldenberger, B. Bourliaguet, and R. Vallée: "Deep Periodic Domain Inversion in X-Cut $LiNbO_3$ and its use for Second Harmonic Generation near 1.5 μm", Appl. Phys. Lett. **91**, 231112 (2007).

[4] Berth, V. Quiring, W. Sohler, and A. Zrenner: "Depth-Resolved Analysis of Ferroelectric Domain Structures in Ti:PPLN Waveguides by Nonlinear Confocal Laser Scanning Microscopy", Ferroelectrics **352**: 78-85 (2007).

[5] H. Hui: to be published

[6] D. Hofmann: "Nichtlineare, integriert optische Frequenzkonverter für das mittlere Infrarot mit periodisch gepolten Ti:LiNbO3 –Streifenwellenleitern", Ph. D.-thesis, University of Paderborn, 2001.

[7] M. Flörsheimer, R. Paschotta, U. Kubitscheck, Ch. Brillert, D. Hofmann, L. Heuer, G. Schreiber, C. Verbeek, W. Sohler, and H. Fuchs: "Second-Harmonic Imaging of Ferroelectric Domains in $LiNbO_3$ with Micron Resolution in Lateral and Axial Directions", Appl. Phys. **B 67**, 593-599 (1998).

Etching of Lithium Niobate: From Ridge Waveguides to Photonic Crystal Structures

H. Hui, R. Ricken and W. Sohler

Angewandte Physik,, Universität Paderborn, 33098 Paderborn, Germany
sol_hu@physik.upb.de

Abstract. *Recent progress of wet etching of Z-cut LN, of inductively coupled plasma (ICP-) etching of X-cut LN, and of ICP-etching of proton-exchanged X-cut LN is reported to fabricate low loss ridge guides, micromechanical, and photonic crystal structures.*

Introduction

The development of lithium niobate ($LiNbO_3$, LN) integrated optical devices requires etching techniques for a reliable fabrication of deep (sub-) micrometer structures. Examples are ridge guides, Bragg gratings, and photonic crystal structures. The existing etching methods can be classified into two categories: wet (chemical) etching and dry (ion) etching. Wet etching is generally performed in a mixture of HF and HNO_3, which attacks the –Z-face of the crystal, whereas the +Z-face is hardly affected. Therefore, selective chemical etching can either be achieved by depositing a metallic mask of the structure to be fabricated on the –Z-face [1] or by defining the structure first by a corresponding domain inversion [2]. Wet etching can also be applied to proton-exchanged or ion-implanted LN to form (sub-) micrometer structures in the surface of the crystal [3, 4]. In dry etching, plasma etching, ion beam milling and focussed ion beam etching are generally used [5, 6, 7]. In this contribution we report our recent progress of wet etching of Z-cut LN to fabricate low loss ridge guide and micromechanical structures, of inductively coupled plasma (ICP-) etching of X-cut LN to get ridges and other microstructures, and of ICP-etching of proton-exchanged X-cut LN to develop photonic crystal structures.

Wet etching of Z-cut LN: ridge waveguides and micromechanics

Wet etching of Z-cut LN with HF/HNO_3 proved to be a simple and reliable method to fabricate low loss Ti-doped ridge waveguides with TE propagation losses of 0.3 dB/cm only [4]. To get optical guiding, the ridges were defined in a planar $Ti:LiNbO_3$ waveguide. Cr-stripes have been used as etch masks.

Here we report a modified procedure yielding ridge guides of propagation losses nearly one order of magnitude lower (TE). They were fabricated in three steps using undoped (congruent) Z-cut LN as substrate: *1. Ridge fabrication*: Using a Cr-mask on the –Z surface of the LN substrate 4 to 12 μm wide ridges were fabricated by wet chemical etching in a mixture of 21 ml HF (40% concentration), 14 ml HNO_3 (100% concentration) and 5 ml ethanol, following the procedure described in [1]. A ridge of 6.5 μm (10 μm) height (top width) is shown in Fig. 1 (left); it is aligned parallel to the X-axis. *2. Ti-stripe definition:* A novel photolithographic process was developed, which allows coating the surface of a ridge selectively. Spin-coating of the sample with photo-resist results in an inhomogeneous thickness distribution with a thinner layer on top of the ridge. This is exploited by the following flood exposure (5 seconds), which leads to full exposure only on top of the ridge. By the subsequent development the photo-resist on

the top of the ridge is totally removed, while a thin layer remains besides the ridge and on the ridge walls. After lift-off a Ti-stripe is precisely defined on top of the ridge only (see Fig. 1-middle). *3. Ti-indiffusion:* The Ti-stripe can now be indiffused using conventional parameters (1060 ^{o}C @ 8.5 hrs in Ar (7.5 hrs) and O_2 (1 hr) atmosphere, respectively). The result is a Ti-doped ridge waveguide as shown in Fig. 1 (right); the edges are rounded and the surface roughness is reduced (see Fig. 1-right).

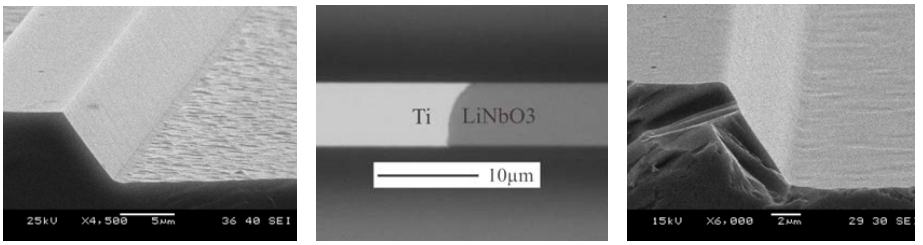


Fig. 1: Wet etched ridge on Z-cut LN, (left), Ti-coated ridge before indiffusion (middle), and after indiffusion (right). The height (top width) of the ridge is 6.5 μm (10 μm), aligned parallel X.

Therefore, also the propagation losses of the ridge guides, monomode up to a top width of 9 μm, are significantly lower than previous results [1]. They were measured using the Fabry-Perot resonance method at 1.55 μm wavelength. Both, the TE and TM losses decrease with increasing width. For TE-polarization the loss drops from 0.22 dB/cm at 5 μm width to 0.05 dB/cm at 7 μm width. For TM-polarization the losses are 1.3 and 0.36 dB/cm at 5 μm and 9 μm widths, respectively. They are significantly larger than TE-losses, though the TM mode is smaller than the TE-mode with lower field strength at the ridge walls. An explanation for the strongly polarization-dependent losses might be that due to the growth of Cr_2O_3 under the mask and due to outdiffusion of Li_2O the concentration of Li and O might vary near the surface leading to corresponding fluctuations of the extraordinary index of refraction (the ordinary index would remain nearly unaffected). Such index fluctuation would lead to scattering losses of the TM-mode alone.

It was even possible to control the slope of the ridge walls by adjusting the etching temperature. This allows getting even steeper walls and to fabricate micromechanical structures such as the interdigital fingers given as example in Fig. 2. It was etched at a temperature of 8 ^{o}C. The lamellas have a width of 2.6 μm with a separation of 2.8 μm. The etching depth is 7.7 μm.

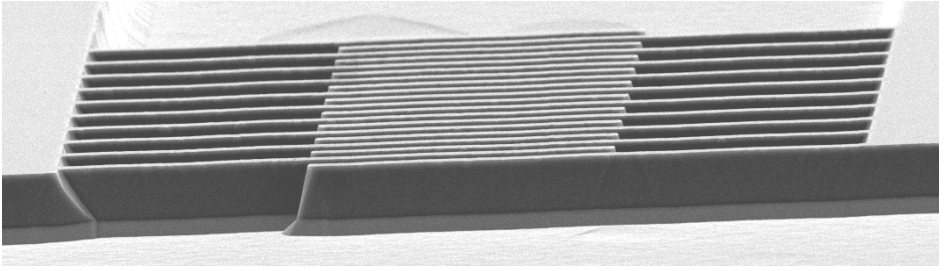


Fig. 2: Wet etched interdigital lamellas of 2.6 μm width and of 2.8 μm separation on Z-cut LN. The etching depth is 7.7 μm.

ICP-etching of X-cut LN: ridges and microstructures

Plasma etching is a very controllable process and has the advantage of being highly anisotropic. Plasmas based on fluorine gases are generally used for plasma etching of LN due to the good volatility of fully fluorinated niobium species at temperatures around 200 °C. However, a problem is the formation and re-deposition of LiF, which has a melting temperature of more than 800 °C. It will be deposited on all surfaces and will lower in this way the etching rate. Therefore, if re-deposition dominates the process, vertical side walls, which are necessary for the definition of small structures, can hardly be obtained. Our solution for this problem is as follows: at first, the sample with a Cr layer defining the structure to be fabricated is ICP-etched for several minutes in a C_4F_8/He (1:1) plasma. Then the etching process is stopped and the sample is cleaned in SC-1 solution (70% H_2O, 20% H_2O_2, 10% NH_4OH) for 1 minute to remove the deposition, before ICP-etching is continued. These two steps are repeated several times until the desired etching depth is reached. Fig. 3 shows as an example etched ridges in X-cut LN, aligned along the Y-direction; the ridges have a height (width) of 5.8 µm (8 µm). On the right of Fig. 3 more complicated microstructures of the same height are shown demonstrating that even small connections between the squares can be fabricated in a reproducible way with nearly vertical walls.

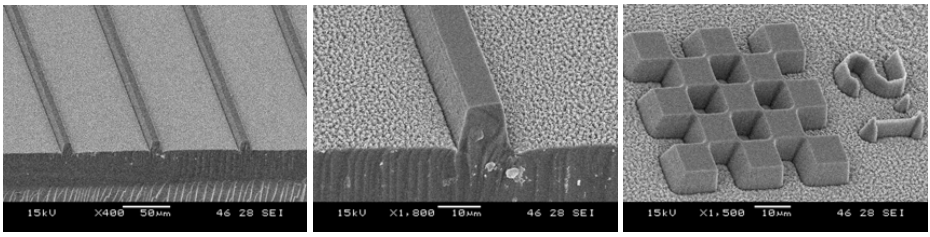


Fig. 3: ICP-etched ridges on X-cut LN of 5.8 µm height and 8 µm width (left and middle). Further microstructures of the same height with nearly vertical side walls (right).

ICP-etching of H^+-exchanged X-cut LN: photonic crystal structures

Another way to reduce the problem of LiF re-deposition is to lower the Li concentration in LN by a proton exchange (PE) process [8]. Thus, the rate of LiF re-deposition will be significantly reduced in comparison to etching of pure LN. As a consequence, the etching rate will be increased and the etch profiles will be improved. We demonstrated the realization of this concept be performing first a PE of congruent X-cut LN to a depth of 1.4 µm. Then the surface of the PE-LN was covered by a 110 nm thick Cr film deposited by sputtering and coated with a 120 nm thick photo-resist layer. Using conventional optical contact lithography, photonic crystal structures were defined in the

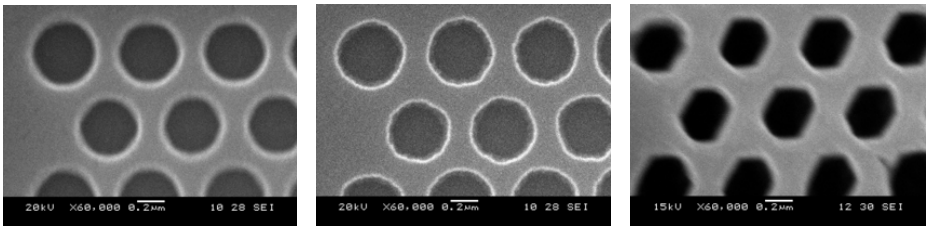


Fig. 4: Holes of a photonic crystal structure defined in photo resist (left), transferred by wet etching in the Cr film (middle) and by ICP-etching into the LN substrate.

photo-resist (Fig. 4, left). The smallest lines have a width of 170 nm. By wet etching these structures were transferred into the Cr film (Fig. 4, middle). Then the sample was ICP-etched for several minutes, and cleaned afterwards in SC-1 solution to remove all depositions. This process was repeated several times until the desired etching depth in the PE-LN was reached (Fig. 4, right). Fig. 5 shows the photonic crystal structure as a whole together with some details in higher magnification.

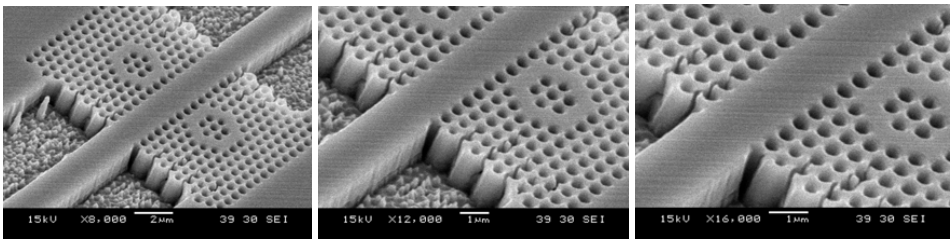


Fig. 5: Photonic crystal structure in PE-LN as a whole (left) and with more details in higher magnification (middle and right).

Proton exchange is also used for the fabrication of single polarization waveguides, as it increases only the extraordinary index of refraction. A subsequent reverse proton exchange (RPE) can even increase the Li concentration again to form buried waveguide profiles.

Conclusions

In conclusion, significant progress has been achieved to improve wet etching of Z-cut LN, ICP-etching of X-cut LN, and ICP-etching of proton-exchanged X-cut LN allowing a reliable fabrication of integrated optical devices with deep (sub-) micrometer structures. As examples ridge guides of very low propagation losses, micromechanical, and photonic crystal structures have been demonstrated.

References

[1] H. Hu, R. Ricken, W. Sohler, and R. B. Wehrspohn, "Lithium Niobate Ridge Waveguides Fabricated by Wet Etching", IEEE Photon. Technol. Lett., vol. 19, pp. 417–419, Mar. 2007.

[2] I. E. Barry, G. W. Ross, P. G. R. Smith, and R. W. Eason, "Ridge waveguides in lithium niobate fabricated by differential etching following spatially selective domain inversion," Appl. Phys. Lett., vol. 74, pp. 1487–1488, Mar. 1999.

[3] T.-L. Ting, L. -Y. Chen, and W.-S. Wang, "A novel wet-etching method using joint proton source in $LiNbO_3$", IEEE Photon. Technol. Lett., vol. 18, pp. 568–570, Feb. 2006.

[4] D. M. Gill, D. Jacobson, C. S. White, Y. Shi, W. J. Minford, and A. Harris, "Ridged $LiNbO_3$ modulators fabricated by a novel oxygen-ion implant/wet-etch technique", J. Lightwave Technol. vol. 22, pp. 887–894, Mar. 2004.

[5] Masashi Tamura, Shinzo Yoshikado, "Etching characteristics of $LiNbO_3$ crystal by fluorine gas plasma reactive ion etching", Surface and Coatings Technology, Vol. 169 –170, pp. 203–207, 2003.

[6] P. Rabiei and W. H. Steier, "Lithium niobate ridge waveguides and modulators fabricated using smart guide," Appl. Phys. Lett., vol. 86, Art. No. 161115, 2005.

[7] F. Lacour, N. Courjal, M.-P. Bernal, A. Sabac, C. Bainier, M. Spajer, "Nanostructuring lithium niobate substrates by focused ion beam milling", Optical Materials, Vol. 27, pp. 1421–1425, 2005.

[8] H. Hu, A. P. Milenin, R. B. Wehrspohn, H. Herrmann, and W. Sohler, "Plasma etching of proton-exchanged lithium niobate", J. Vac. Sci. Technol. A, vol. 24, pp. 1012-1015, Jul./Aug., 2006

Novel structures for broadband electrooptic modulators in $LiNbO_3$

M. García Granda[1,2], H. Hu[1], W. Sohler[1], J. Rodríguez García[2]

[1]Universität Paderborn. Angewandte Physik. Paderborn, Germany
[2]Universidad de Oviedo. Laboratorio de Óptica Integrada y Optoelectrónica. Oviedo, Spain
ggranda@mail.upb.de

Abstract. *Real data of wet-etched ridge waveguide in Z-cut $LiNbO_3$ is combined with two new electrode structures to improve the performance of Mach-Zehnder electrooptic modulators. Calculations show improvements up to 50% in driving voltage in comparison with commercial and published devices in the 40GHz range. Simulation results and fabrication state is shown.*

Introduction

External modulators based on lithium niobate ($LiNbO_3$) are being developed for high-speed and long-distance optical fiber transmission systems. Nowadays, they offer a modulation bandwidth exceeding 10 GHz combined with a low driving voltage, typically in the range of 5 V, with a voltage-length product ($V_\pi L$) in the order of 20 to 30 V·cm.
To enable higher bit rates and reduce the cost of modulator operation, lower voltages are required due to the restrictions of electrical instruments, in particular electrical driving amplifiers. Therefore, reduction of the driving voltage of a $LiNbO_3$ modulator is an extremely important issue for realizing future high-speed optical transmission systems. At the same time, the waveguide geometry and travelling-wave electrode structure must be optimized in order to reach high bandwidth performance and impedance matching.
Ridge waveguides in $LiNbO_3$ in combination with a proper geometric design of electrodes and dielectric buffer layer promise high bandwidth with low driving voltage [1-3]. Our proposed designs are based on real ridge waveguides made by Ti indiffusion in $LiNbO_3$ and wet etching techniques. They are evaluated regarding how the geometric design changes the main modulator parameters (overlap factor, effective index, characteristic impedance and frequency response). Also, fabrication possibilities are considered.

Modeling of Mach-Zehnder modulators

In a Mach-Zehnder (MZ) type interferometric modulator, an applied electric field changes the refractive index, creating a phase shift between the waves propagating through both arms of the interferometer.
Z-cut $LiNbO_3$ together with travelling-wave Coplanar Waveguide (CPW) electrodes for the microwave (MW) modulating signal are used to create a push-pull effect in both arms, producing therefore an enhanced phase shift. A dielectric buffer layer is necessary to avoid absorption of the optical field in the metal surface.
The broadband electrode structure must be designed in such a way that the effective index of the CPW line matches the effective index of the optical waveguide and the electrode impedance is similar to that of the rest of the electronic drive circuit, usually 50 Ω. Furthermore, the overlap between optical and controlling MW fields must be optimized in order to get a low drive voltage.

With these objectives in mind, the characteristics of ridge Mach-Zehnder modulators were studied when two different electrode structures are used:
On one side, the CPW on ridge structure (figure 1, left) is the most direct way to use a traditional CPW electrode on a ridge. Nevertheless, the electrodes on the walls of the waveguides lead to a non-optimal use of the vertical component of the electric field and the different levels of the electrodes make more difficult the accurate fabrication of these devices. Therefore, the new Surface-Compact CPW (SCCPW) structure is proposed here, combining an alternative design of the CPW electrode together with ridge waveguides below the $LiNbO_3$ surface (figure 2, right).

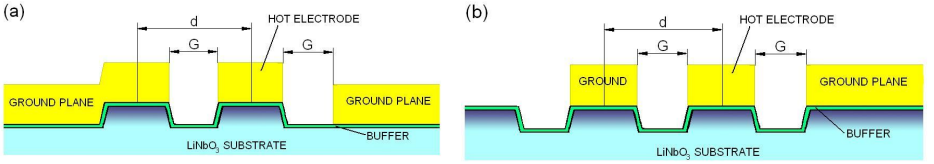


Figure 1: Cross section of the CPW structure on ridge (a) and the new proposed SCCPW (b).

The waveguide design was based on experimental results of wet-etched ridge waveguide fabrication on $LiNbO_3$ [4]. Mode profiles were simulated using a finite difference commercial software with Ti indiffusion index profiles calculated from the fabrication parameters [5]. Mode comparison with experimental results showed a good agreement.
The overlap integral for each waveguide (Γ_i) was calculated using own software.
From the electric capacitance of the structure, the electrode impedance (Z) and the microwave effective index (n_{eff}^{MW}) are also calculated.
In order to evaluate the transmission of the MW signal along the interaction length, the voltage signal at each x point along the electrode in a time t is taken as following:

$$V(x,t) = V_0\, 10^{\frac{-\alpha(f_{MW})L}{10}} \cos\left(\beta_{MW}x - \omega_{MW}t + \phi_0\right), \qquad (1)$$

where V_0 is the applied voltage, β_{MW} is the microwave propagation constant in the electrode, ω_{MW} is the microwave frequency, ϕ_0 is the initial phase and $\alpha(f_{MW})$ is the frequency dependent microwave loss along the electrode calculated as $\alpha(f_{MW}) = \alpha_0\sqrt{f_{MW}}$, where 0.4 dB cm^{-1} $GHz^{-1/2}$ is taken as usual value for α_0. The modulated signal was evaluated after four reflections on the active length edges regarding to the impedance mismatch. Afterwards, the phase-shift is calculated taking into account the index mismatch between the optical wave and the modulating MW as:

$$\Delta\phi_i = \frac{\pi n_{eff}^{op\,3} r_{33}\Gamma_i}{\lambda G}\int_0^L V\left(\tilde{x}, t(\tilde{x})\right)d\tilde{x}, \qquad (2)$$

where i designates each one of the two parallel waveguides and the values $\tilde{x}$ are a dense set of points along the electrode length. The time is chosen as: $t(\tilde{x}) = \tilde{x}\, n_{eff}^{op}/c$. Finally, the total phase-shift ($\Delta\phi$) can be calculated as the sum of the phase-shifts from both waveguides. The optical response, m, of the modulator is defined by the equation:

$$m(f_{MW}) = \left|\frac{\Delta\phi(f_{MW})}{\Delta\phi(0)}\right|, \qquad (3)$$

where f_{MW} is the microwave frequency and $\Delta\phi(0)$ is the DC phase-shift.

Modeling results

The presented calculation was applied to the structures shown in figure 1. Both structures are able to reduce the voltage-length product of the modulator by more than 50% of that of the traditional in-diffused waveguide modulators. Besides, the SCCPW gives even lower values of $V_\pi L$ than the CPW and improves velocity matching.

Waveguide separation of 9 μm was chosen as best trade-off between enhancement of electric field and optical mode separation [3].

In figure 2, the calculation of $V_\pi L$, n_{eff}^{MW} and Z is shown for the CPW on ridge and SCCPW as a function of the buffer layer thickness (t_b). One can see that the SCCPW reduces the $V_\pi L$ value by a 4%, allowing index matching with thinner buffer layer and improving impedance matching.

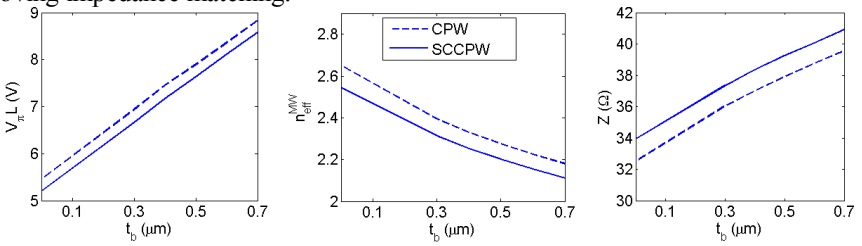


Figure 2: Calculation of the voltage-length product (left), microwave effective index (centre) and electrode characteristic impedance (right) for the CPW on ridge and the SCCPW structure.

In order to design devices with high performance, two different approaches where made. On one hand, it is important to find devices with high bandwidth and a driving voltage as reduced as possible. On the other hand, it is also interesting to find designs with lower bandwidth (say 10 GHz) but with drastically reduced driving voltage. With this aim, the calculations were focused on the SCCPW structure for two different active lengths: 25 and 50 mm, and analyzed with the buffer layer thickness as parameter. The m and $V_\pi L$ obtained parameters are shown as a function of the modulating frequency in figure 3.

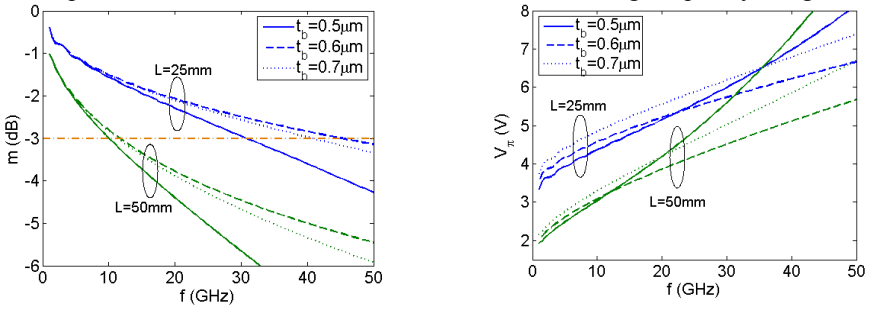


Figure 3: Calculation of frequency response (left) and driving voltage (right) for SCCPW structure as function of the modulating frequency for two active lengths. The buffer layer thickness (t_b) is used as a parameter.

In these figures, one sees how the 3dB optical bandwidth is maximum for t_b=0.6 μm, which accounts for the index matching between optical and MW signals. This is also evident in $V_\pi L$, where the value for t_b=0.6 μm is optimum for high frequencies.

Based on these results, two main designs can be proposed using the new SCCPW structure. On one hand, a broadband and low drive voltage device can be made with an

active length of 25mm using a buffer layer of 0.6 μm thickness, providing a 3dB optical bandwidth of 45 GHz, and a voltage-length product of 8.11 V·cm, which gives a driving voltage of 3.24V for DC and 6.22V for 40GHz.
On the other hand, if the active length is 50mm, using a 0.5 μm thick buffer layer, we reach a 3dB optical bandwidth of 10GHz with a voltage-length product of 7.63V·cm and a driving voltage of 1.53V for DC and 3.03V for 10GHz.
Both designs use a distance between centers of waveguides of 18μm, waveguide width of 9μm and electrode thickness of 8 μm with a characteristic loss of 0.4dB cm^{-1} $GHz^{-1/2}$.

Fabrication

The fabrication of the SCCPW modulator is a challenging issue that is currently being carried out. Wet-etching in lithium niobate and microlithography techniques are adapted and applied to the fabrication of complete ridge structure and electrodes. Micrographs of fabricated parts of the devices can be seen in figure 4.

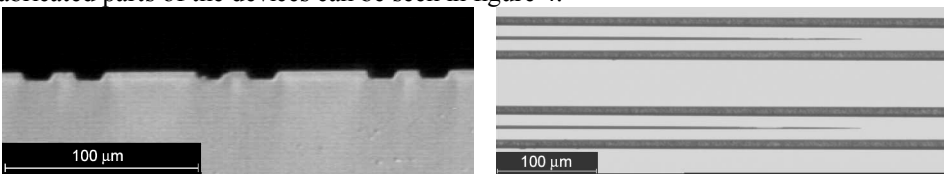


Figure 4: Fabricated end faces of the modulator ridge waveguides (left) and Y-splitters (right).

Conclusions

Two novel structures for Mach-Zehnder electrooptic modulators in $LiNbO_3$ have been analyzed in depth. These designs are based on experimental results of waveguides fabricated by wet etching technique. Two specific designs were proposed for the new SCCPW structure. One of them is able to reach a bandwidth of 45GHz with a V_π(DC) of 3.24V and length of 25mm. The other one provides 10GHz bandwidth with V_π(DC) of 1.53V and a length of 50mm. The fabrication of these devices is currently in progress.

Acknowledgements

This work was supported by the grant BES2004-4485 and project TEC2005-05541 from Spanish MEC. Special thanks to H. Herrmann, R. Ricken, V. Quiring and S. Fernández.

References

[1] A. Rahman, S. Haxha "Optimization of Microwave Properties for Ultrahigh-Speed Etched and Unetched Lithium Niobate Electrooptic Modulators". Journal of Lightwave Technology, vol. 20, 10, pp. 1856-1863, 2002.

[2] M.M. Howerton, R.P. Roeller, A.S. Greenblatt, R. Khähenbühl. "Fully Packaged Broca-Band LiNbO3 Modulator with Low Drive Voltage". IEEE Photonics Technology Letters, 12, 7, pp. 792-794, 2000.

[3] M. García-Granda, H. Hu "Design of Broadband Electrooptical Modulators Using Ti:$LiNbO_3$ Ridge Waveguides". OPTOEL'07, Bilbao, July 2007. ISBN: 978-84-95809-30-8, pp. 69-74.

[4] H. Hu, R. Ricken, W. Sohler, R.B. Wehrspohn. "Lithium niobate ridge waveguides fabricated by wet etching". IEEE Photonics Technology Letters, vol. 19, 6, pp. 417-419, 2007.

[5] E. Strake, G.P. Bava, I. Montrosset. "Guided Modes of Ti:$LiNbO_3$ Channel Waveguides: A Novel Quasi-Analytical Technique in Comparison with the Scalar Finite-Element Method". Journal of Lightwave Technology, vol. 6, 6, pp. 1126-1135, 1988.

Performance of Waveguide FPI with Si-on-$LiNbO_3$ Bragg Gratings under Temperature Gradient.

S.M. Kostritskii, A.A. Dikevich, Yu.N. Korkishko, V.A. Fedorov
Optolink Ltd, Moscow Institute of Electronic Technology, Zelenograd 124498, Moscow, Russia
skostritskii@optolink.ru

Abstract. *It was found that temperature gradient induces degradation of spectral selectivity of Fabry-Perot interferometer formed by channel $LiNbO_3$ waveguide with two Bragg gratings, because of gradient-induced grating chirp and refractive index variation along channel.*

Introduction

Grating structures, and in particular Bragg grating structures, display an effective index dependence in the wavelength of operation that has long been used to form sensing elements in integrated-optic planar devices [1]. In designing high-performance Bragg gratings, the key issue is the ability to perturb the index of the guided mode substantially, still without causing excessive radiation loss, thereby facilitating the realization of compact gratings with high reflectivity. In achieving high-reflectance gratings, a trade-off seems to exist between the process complexity and highest possible reflectivity of the grating. For instance, the high refractive index of $LiNbO_3$ potentially enables large perturbation of the mode index. However, the fabrication of high-reflectance gratings via direct etching in this crystal is an extremely difficult task. Bragg gratings in $LiNbO_3$ with drastically improved efficiencies can be achieved by integrating Si and $LiNbO_3$. Silicon overcomes the aforementioned problems associated with the processibility of corrugated waveguides in $LiNbO_3$.

Experimental

In this work, we employ the new fabrication process to make a Si-on-$LiNbO_3$ structure. A thin Si overlay was deposited by e-beam technique on z-cut $LiNbO_3$ samples, containing a set of annealed proton-exchanged (APE) channel waveguides fabricated with a mask aperture ranged from 5.6 to 9.5 μm. These waveguides were single-mode, supporting only TM_0 mode at wavelengths around 1.53μm. Si-film thickness deposited was 40, 60, 100, 120, 150, 180, 200 and 225 nm. A first order grating (Λ = 357.53 nm) pattern was then holographically defined in a photoresist film, on top of the Si overlay.

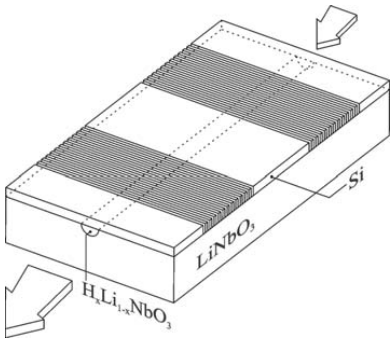


Fig.1. Sketch of waveguide Si-on-$LiNbO_3$ structure.

The delineated photoresist pattern was used as a mask to etch grating corrugations in the Si film to a depth of ≤ 125 nm, by reactive ion etching (RIE). Afterwards, a photoresist mask and wet etching were used to reduce the grating pattern length to cover the two 1.7-mm segments near the middle of the waveguide. 1.5-mm gap inserted between these segments forms waveguide Fabry-Perot interferometer (FPI), fig.1. The necessary electrode pattern was photolithographically delineated in uniform Au-Cr seed layer that was deposited over substrate.

It was found experimentally that the Si grating creates a considerably larger perturbation to the waveguide mode than conventional corrugation, profiled directly on the $LiNbO_3$ waveguide, yet without producing excessive scattering loss. We discover the existence of narrow range of Si overlay thickness from 60 to 150 nm, within which effective index of the TM_0 mode guided into an APE:$LiNbO_3$ channel can be deeply modulated by Si grating, resulting in low-loss grating, even for overlays with a larger length along channel. Outside these intervals, the mode is either absorbed due to the intrinsic loss of Si, or not perturbed by Si grating within very thin overlay. Thus, we have obtained the high grating reflectivity (as high as 0.96, see fig.2) at low-loss propagation, that provide an ideal combination of properties suitable for the fabrication of high-reflectance corrugated waveguide gratings, essential for a number of practical devices [2], in particular, waveguide FPI filters and sensors.

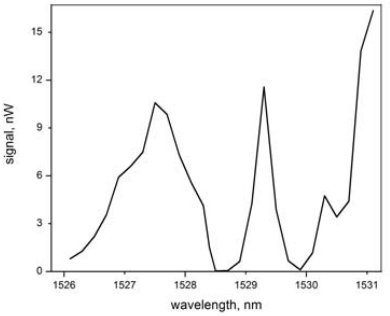


Fig. 2. Transmission spectrum of FPI, utilizing Si-on-$LiNbO_3$ structure. Attenuation of signal in wavelength range between 1526 and 1527.5 nm is caused by sharp decrease of output power of tunable light source at low limit of working range.

Experimental result and discussion

This waveguide FPI has been used by us as electro-optic sensor head in our prototype of optical voltage transducer. The reflection of Bragg gratings is highly wavelength selective, and according to coupled mode analysis it is most efficient when the period Λ satisfies the Bragg condition $\Lambda = \lambda_B/2n$, where λ_B is the free space optical wavelength at the reflectance peak, and n is the effective refractive index of the guided mode [3]. The strong dependence on wavelength for contradirectional coupling makes it possible to tune the wavelength, hence the transmittance through the waveguide FPI, by means of an applied voltage via the electrooptic effect in $LiNbO_3$. When an external voltage V is applied, it induces index changes given by $\Delta n_e = n^3_e V r_{33} \Gamma/(2g)$, where subscript e represents the extraordinary polarization of TM_0 mode, r_{33} is the relevant electrooptic coefficient, g is the separation gap between electrodes, and Γ is the overlap factor between optical and electric fields. The voltage-tuning rate of the wavelength for a

grating can then be expressed as $d\lambda_B/dV = \Lambda n_e^3 r_{33}\Gamma/g$, with Λ being the grating period. The switching voltage corresponds to half the spectral width $\Delta\lambda$ between the two transmittance minima [3]: $V_s = (\Delta\lambda/2)(d\lambda/dV)^{-1}$. The Bragg wavelength shifts linearly with voltage at a rate of 0.00316 nm/V. Using $n_e = 2.14$ and $r_{33} = 30.8$ pm/V for $LiNbO_3$, a value of 0.6 is calculated from the tuning rate equation for overlap factor, Γ.

High voltage transducers that are based on electro-optic sensor heads have several advantages when compared with their purely electrical counterparts, for example minimal field disturbance, low and high frequency operation, and immunity to electric noise and electromagnetic interference. Furthermore, when using optical fiber pigtailing they allow for both, a simple and compact design as well as excellent electromagnetic isolation. However, it has been found that it is very sensitive to surrounding temperature and, therefore, requires fine temperature stabilization. While the effect of average temperature variation can be compensated by use of a second waveguide FPI as reference, the effect of temperature gradient inside a device box is more dramatic and can't be compensated.

The resonant Bragg wavelength depends on average temperature of an integrated-optical element with waveguide FPI because of termooptic effect in lithium niobate waveguide and thermal expansion of Si film:

$$d\lambda_B/dT = 2\cdot\Lambda\cdot dn/dT + 2\cdot n\cdot d\Lambda/dT \quad (1)$$

Termooptic coefficient for extraordinary refractive index in lithium niobate [4]:

$$dn_e/dT = 3.7\cdot10^{-5}\ 1/\mathrm{K} \quad (2)$$

Change of grating period caused by thermal variation of linear dimension of Si film depends on thermal expansion coefficient of silicon [1]:

$$d\Lambda/dT = 1.41\cdot10^{-5}\cdot\Lambda_0 = 2.16\cdot10^{-2}\ \mathrm{nm/K} \quad (3)$$

Hence

$$d\lambda_B/dT = 0.048\ \mathrm{nm/K} \quad (4)$$

These relations (1-3) allow to predict with very good accuracy (<0.01 nm) the temperature dependence of peaks and deeps in transmission spectrum of our waveguide FPI. Therefore these data may be used for precision correction of average temperature effect at electric field sensing.

The measurement of transmission spectra of waveguide FPI at different values of steady-state temperature gradient show gradual degradation of spectral modulation contrast *M* (ratio between output powers at FPI peak and minimum for Bragg gratings transmittance) in transmission spectrum of waveguide FPI. For example, we have observe that $K = 10lgM = 18$ dB in absence of any marked gradient, but $K = 3.5$ dB in the field of the strong temperature gradient of 2.8 K/cm. As result, appropriate work of the electric field sensor becomes impossible.

Such a behavior of waveguide FPI can be explained by consideration of gradient-induced grating chirp $C_h(gradT)$ and gradient-induced refractive index variation along

channel. We assume that steady-state gradient induces a linear chirp of the grating period in accordance with (3):

$$\Lambda = \Lambda_0 \cdot (1 + C_h(gradT) \cdot z) \quad (5)$$

In case of a small temperature gradient, we can regard the both gratings being uniform, but having the different periods Λ_1 and Λ_2

$$\Lambda_1 - \Lambda_2 = (d\Lambda/dT) \cdot gradT \cdot L_0 \quad (6)$$

and different values extraordinary refractive index within waveguide areas covered by two Si-gratings:

$$n_1 - n_2 = (dn_e/dT) \cdot gradT \cdot L_0 \quad (7)$$

According to the theory of asymmetric FPI [2,5], the difference between resonant Bragg wavelengths of the two gratings forming FPI $\delta\lambda_B = 2n_1 \cdot \Lambda_1 - 2n_2 \cdot \Lambda_2 \approx 2\{(n_1 - n_2)\Lambda + n(\Lambda_1 - \Lambda_2)\}$ should be theoretically sufficient to induce a significant degradation of waveguide FPI performance even at $gradT \approx 0.3$ K/см. Experimental test shows that steady-state gradient 0.3 K/см, created especially by special set-up, induces decrease of maximum output power for FPI peak by factor 1.08 and broadening of FPI peak by 0.012 nm. At electric field sensing experiments, both these effects induce the marked deviation (1.4 %) of sensor response from linear law within sensor dynamic range, which is over 40 dB in absence of temperature gradient. Errors in evaluation of external voltage become more significant in case of randomly oscillating temperature gradient field. Therefore, the fine temperature stabilization, providing low temperature gradient ≤ 0.1 K/cm at our waveguide FPI surface, is required for application in an electric field sensor head.

In conclusion, a FPI intensity modulator has been fabricated and characterized in Si-on-$LiNbO_3$ structure. The Bragg reflectors are produced in an amorphous Si overlay film deposited over annealed proton-exchanged $LiNbO_3$ waveguides. The experimental results demonstrate the prospects of FPI type modulator for voltage sensing. Further improvements can be expected from optimization of the electrode design.

References

[1] T. Conese, R. Tavlykaev, C.P. Hussell and R.V. Ramaswamy, "Finite element analysis of $LiNbO_3$ waveguides with Si overlay", Journal of Lightwave Technology, vol. 16, pp. 1113-1122, 1998.

[2] Yu.O. Barmenkov, D. Zalvidea, S. Torres-Peiró, J.L. Cruz and M.V. Andrés, "Effective length of short Fabry-Perot cavity formed by uniform fiber Bragg gratings", Optics Express, vol. 14, pp. 6394-6399, 2006.

[3] D. Runde and D. Kip, "Holographic reflection filters in channel waveguides for applications as optical sensors and/drop multiplexers", OSA Trends in Optics and Photonics Series, vol. 87, pp. 615-619, 2003.

[4] Lithium Niobate properties, INRAD corp., 2004 - http://www.inrad.com/pdf/Inrad_datasheet_LNB.pdf

[5] S. Pereira and S. LaRochelle, "Field profiles and spectral properties of chirped Bragg grating Fabry-Perot interferometers", Optics Express, vol. 13, pp. 1906-1915, 2005.

Wafer Bonding and Heterogeneous Integration: III-V/Silicon Photonics

G. Roelkens, L. Liu, J. Brouckaert, J. Van Campenhout, F. Van Laere, D. Van Thourhout, and R. Baets

Ghent University/IMEC – Photonics Research group, Sint-Pietersnieuwstraat 41, B-9000 Ghent, Belgium

Gunther.Roelkens@intec.ugent.be

Abstract. *The use of bonding technology to integrate III-V opto-electronic components on top of a silicon-on-insulator (SOI) integrated waveguide circuit is presented. III-V laser diodes and photodetectors fabricated on and coupled to an underlying SOI waveguide circuit are considered.*

Introduction

Photonic integrated circuits (PICs) offer the potential of realizing low-cost and compact optical functions. Silicon-on-insulator (SOI) is an emerging material platform for this integration, due to the large omni-directional refractive index contrast that can be achieved. Moreover, the massive CMOS processing infrastructure can be used to process these optical components. The integration of light emitters, optical amplifiers and detectors operating at telecommunication wavelengths is hampered by the indirect band gap of silicon. Although several advances are being made to achieve light emission from silicon, either by changing the silicon material on a nano-scale or by exploiting its non-linear optical properties, in the foreseeable future these devices will not outperform their III-V semiconductor counterparts, supplying state-of-the-art optoelectronic components for the telecommunication market nowadays. In order to create photonic integrated circuits comprising both active and passive optical components, the heterogeneous integration of passive silicon-on-insulator waveguide circuits and active InP/InGaAsP components is proposed. To decrease the cost of the integration process, both in time and consumption of expensive III-V material, a die-to-wafer bonding process is proposed in this paper, in which unprocessed InP/InGaAsP dies are bonded, epitaxial layers down, to the processed silicon-on-insulator wafer. This reduces the material consumption, as III-V semiconductors are only bonded where they are needed, and reduces the time to perform the integration process, as limited alignment accuracy is needed due to the absence of structure on the epitaxial layers. After removal of the InP substrate, active opto-electronic components can be fabricated in the InP/InGaAsP epitaxial layers, using wafer-scale processing, while being lithographically aligned to the underlying SOI features. The fabrication process is outlined in figure 1(a). In this paper we will outline the technology we developed for integrating the InP/InGaAsP epitaxial layer structures on a silicon-on-insulator material platform using adhesive DVS-BCB die-to-wafer bonding. While there are various methods to create an InP/InGaAsP epitaxial layer structure onto the SOI waveguide wafer (hetero-epitaxial growth, molecular bonding, adhesive bonding, anodic bonding, metallic bonding), adhesive bonding offers some significant advantages over other bonding methods. The relaxed requirements on surface cleanliness, contamination and surface roughness combined with the planarizing action of the adhesive spin coating

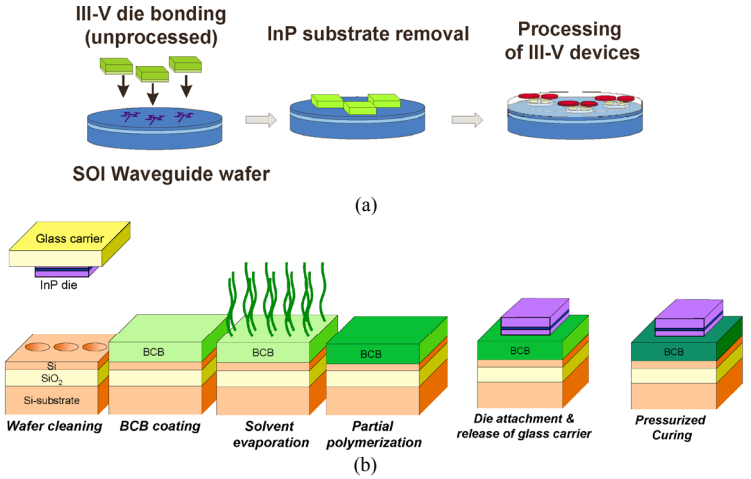
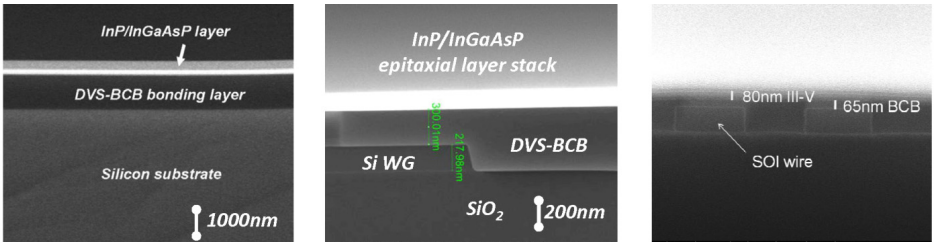


Figure 1: III-V/Silicon photonics integration (a) and the process flow for DVS-BCB bonding (b).

process, offer a significant reduction in surface preparation. Moreover, the integration process is a low temperature process, reducing the stress in the bonded stack due to the difference in thermal expansion coefficients between silicon and III-V semiconductor. The thermosetting polymer DVS-BCB (divinylsiloxane-bis-benzocyclobutene) was selected for process development due to its excellent planarizing properties, its high glass transition temperature (supplying sufficient postprocessing thermal budget), its low shrinkage and the fact that no byproducts are created upon cure. After integration of the InP/InGaAsP epitaxial layer structures, a myriad of optical components can be fabricated on the III-V/Silicon photonic integrated circuit. In this paper we report on the successful fabrication of integrated laser diodes and on the fabrication of integrated InP/InGaAsP photodetectors, both coupled to the underlying SOI waveguide circuit.

DVS-BCB die-to-wafer bonding technology

The DVS-BCB bonding process is outlined in figure 1b [1]. The cleaning of both the III-V die surface (which is temporary attached to a glass carrier) and the SOI wafer surface was optimized in order to remove pinned particles from the bonding interface. On the SOI wafer surface, a Standard Clean 1 solution ($1NH_3$:$4H_2O_2$:$20H_2O$ at 70C) is used to lift off particles. On the III-V die, the removal of a sacrificial InP/InGaAs layer pair using $3HCl$:H_2O and $1H_2SO_4$:$3H_2O_2$:$1H_2O$ respectively, resulted in particle and contamination free surfaces. The DVS-BCB layer is spin-coated afterwards onto the SOI waveguide circuit and is pre-cured in order to evaporate the solvents. After the pre-cure, the III-V die is attached to the SOI and released from the glass carrier, and the III-V/SOI stack is cured at 250C. Temporary attachment to a glass carrier allows easy handling of small III-V dies and paves the way to multiple die-to-wafer bonding, as multiple III-V dies can be attached to a single carrier, ultimately populating a full 200mm SOI wafer using a single cleaning and bonding step. After bonding, the InP growth substrate is removed using a combination of mechanical grinding and chemical etching using HCl, until an etch stop layer is reached. Three different SEM cross-sections of III-V/SOI substrates are shown in figure 2, illustrating the range of bonding layer thickness that can be achieved. This wide range of thicknesses can be achieved by diluting commercial DVS-BCB solutions using mesitylene.

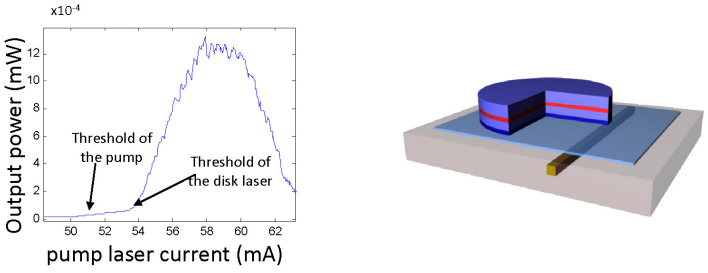


(a) (b) (c)

Figure 2: SEM cross-section of DVS-BCB bonded III-V/Silicon substrates showing a variety of bonding layer thicknesses that can be achieved: micrometer-range (a), sub-micron range (b) and 100nm range (c).

Heterogeneously integrated laser diodes on SOI waveguide circuits

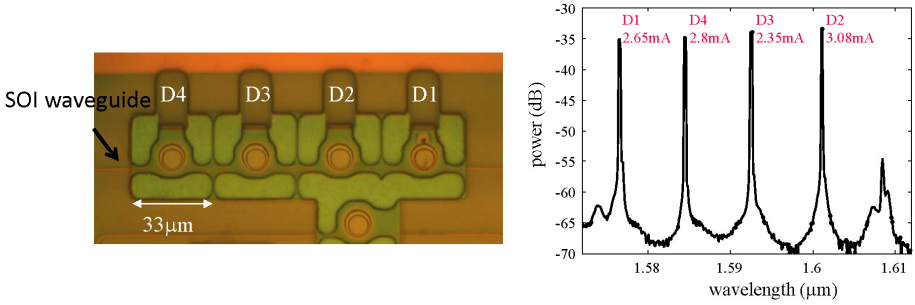
Based on this technology, laser diodes were heterogeneously integrated on the SOI waveguide circuit. We proposed the concept of using an electrically injected III-V microdisk laser to generate light on the silicon platform. Although the demonstrated electrically injected devices were based on molecular die-to-wafer bonding [2], a DVS-BCB bonded microdisk laser is also feasible. DVS-BCB bonding has the additional advantage of a better control of the bonding layer thickness (ultimately defining the coupling between the III-V laser and the SOI waveguide) compared to molecular bonding, as in the latter case the bonding layer thickness is determined by a blind CMP polishing step of the SiO_2 covering the SOI waveguide circuit. Currently, continuous wave optically pumped DVS-BCB bonded microdisk lasers coupled the underlying SOI waveguide circuit have been demonstrated, as shown in figure 3a. 1μW of optical power is coupled to the SOI waveguide, for a 260nm DVS-BCB layer. Fabrication of electrically pumped devices is ongoing. A schematic of the microdisk structure is shown in figure 3b.



(a) (b)

Figure 3: optical power coupled to an SOI bus waveguide in a continuous wave optically pumped DVS-BCB bonded microdisk laser (a) and schematic of the characterized device (b)

Besides single microdisk lasers, a multi-wavelength laser structure was fabricated as shown in figure 4a (before microdisk metallization). By slightly changing the radius of the microdisks coupled to a single SOI bus waveguide, the emission wavelength of the individual microdisks is varied. In figure 4b, the spectrum of the light coupled to the SOI bus waveguide is plotted, showing the four laser wavelengths equally distributed over the free spectral range of the disks. In order to achieve a uniform optical output power over the different channels, the drive current needs to be individually modified.

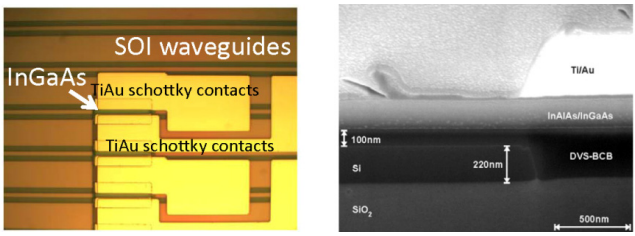


(a) (b)

Figure 4: Optical microscope image of a cascade of four rings coupled a single SOI bus waveguide (a) and the obtained optical spectrum in the SOI waveguide mode (b)

Heterogeneously integrated photodetectors on SOI waveguide circuits

Besides laser diodes, also metal-semiconductor-metal photodetector (MSM) using an InGaAs absorption layer were realized, as shown in figure 5a. The coupling between the SOI waveguide and the photodetector is achieved by vertical directional coupling between the SOI waveguide and the lossy III-V waveguide mode confined by the lateral TiAu contacts. The 3µm spacing between the coplanar Schottky contacts equals the SOI waveguide width. The dark current of the device was 3.0nA at a bias voltage of 5V (for a device length of 25µm), while the detector responsivity is 1.0A/W at 1.55µm and a bias voltage of 5V. A cross-section of the device is shown in figure 5b [3]. Currently the integration of these photodetectors on top of functional SOI waveguide circuits is ongoing and will be presented at the conference.



(a) (b)

Figure 5: Top view of the fabricated III-V metal-semiconductor-metal photodetectors integrated on an SOI waveguide platform (a) and a cross-section of the device (b).

References

[1] G. Roelkens, J. Brouckaert, D. Van Thourhout, R. Baets, R. Nötzel and M. Smit, "Adhesive bonding of InP/InGaAsP dies to processed SOI wafers using DVS-bis-BCB, " J. Electrochem. Soc. 153, G1015, 2006

[2] J. Van Campenhout, P. Rojo-Romeo, P. Regreny, C. Seassal, D. Van Thourhout, S. Verstuyft, L. Di Cioccio, J.-M. Fedeli, C. Lagahe, and R. Baets, "Electrically pumped InP-based microdisk lasers integrated with a nanophotonic silicon-on-insulator waveguide circuit," Opt. Express vol 15, pp. 6744-6749, 2007

[3] J. Brouckaert, G. Roelkens, D. Van Thourhout, and R. Baets, "Compact InAlAs/InGaAs metal-semiconductor-metal photodetectors integrated on SOI waveguides," Phot. Technol. Lett. Vol. 19, pp. 1484-1486, 2007

Long Wavelength Lasers on Silicon

Diana L. Huffaker[1,2,3]

[1] California NanoSystems Institute, University of California, Los Angeles,
570 Westwood Plaza, Los Angeles CA 90095, USA.
[2] Electrical Engineering, University of California, Los Angeles,
420 Westwood Plaza, Engineering IV Bldg., Los Angeles CA 90095, USA.
[3] Center for High Technology Materials (CHTM), University of New Mexico
1313 Goddard SE, Albuquerque NM 87106, USA.
huffaker@ee.ucla.edu

Abstract. *We demonstrate lasing at 77K of GaSb/AlGaSb quantum wells monolithically grown on a 5º miscut Si (001) substrate via a thin (50nm) AlSb layer. A 13% lattice mismatch between AlSb and Si is accommodated by using an interfacial misfit (IMF) array. The 5˚ miscut geometry enables both IMF formation and suppression of an anti phase domain.*

Introduction

Recent developments in CMOS-integrated optoelectronics make III-V lasers on Si a highly desirable and researched device. A monolithic growth of III-V materials on Si offers intriguing features such as an efficient use of the integrating platform and reduced processing complexity compared to growth on GaAs, GaSb substrates [1-4]. However, material incompatibilities such as mismatch in lattice constant, thermal expansion coefficient and process temperature hinder stable and repeatable production processes based on monolithic integration [5]. Recently, our group has demonstrated a novel growth technique involving 90˚ interfacial misfit (IMF) arrays formed during the growth of AlSb on Si (001) [6]. The IMF growth mode on Si (001) results in low defect density bulk epitaxy (~ 10^6/cm^2) that has enabled optically pumped vertical cavity surface emitting lasers (VCSELs) and super-luminescent diodes [7,8]. However, anti-phase domains (APDs) have deterred the demonstration of laser diodes on Si (001) substrates.

The APD formation in the growth of AlSb on Si (001) is an inherent issue with the growth of polar III-Vs on non-polar Si. In the absence of step-free Si(001) substrates, the established method to achieve single domain III-Vs uses miscut Si(001) substrates [9-11]. Miscut Si (2.5º to 5º) substrates, typically characterized by a double atomic-step height [12], facilitate registration of the III and V sub-lattices on the (001) plane, resulting in the suppression of APD formation. So far, high quality III-V material on Si has been produced using the APD annihilation or suppression combined with a strain-relief and defect filtering mechanism, usually a thick buffer layer [13]. These methods require a two-step growth process initiated at a rather low temperature to enable 60º and 90º dislocation formation followed by normal growth temperatures for metamorphic and bulk layer growth. Lattice-matched bulk GaAs epitaxy on miscut Ge has also been demonstrated to produce very low defect and low APD density [14].

Growth and Fabrication:

We demonstrate GaSb quantum well (QW) laser diodes monolithically grown on a 5º miscut Si (100) substrate by using the IMF growth mode. A 13% lattice mismatch at AlSb/Si interface is accommodated by an IMF array, resulting in low-defect density, single-domain III-Sb bulk material, on which the laser is grown. A schematic

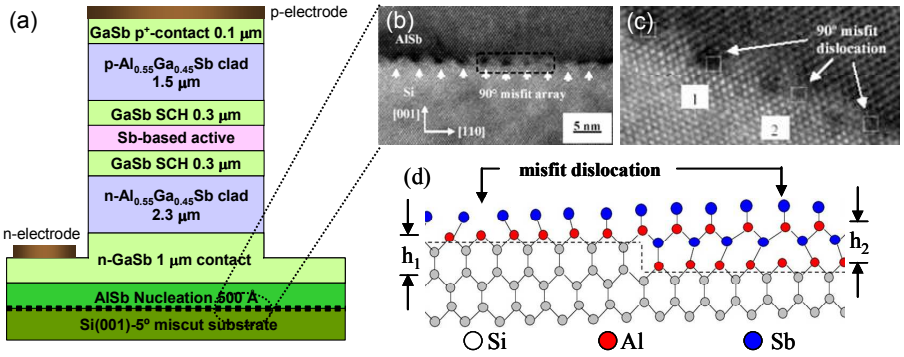


Fig. 1 (a) Schematic illustration of fabricated III-Sb based laser structures monolithically grown on 5° miscut Si (001) substrates. (b) and (c) cross-sectional transmission electron microscope images of the interface between AlSb and Si. (d) Schematic illustration of the IMF interface between AlSb and Si.

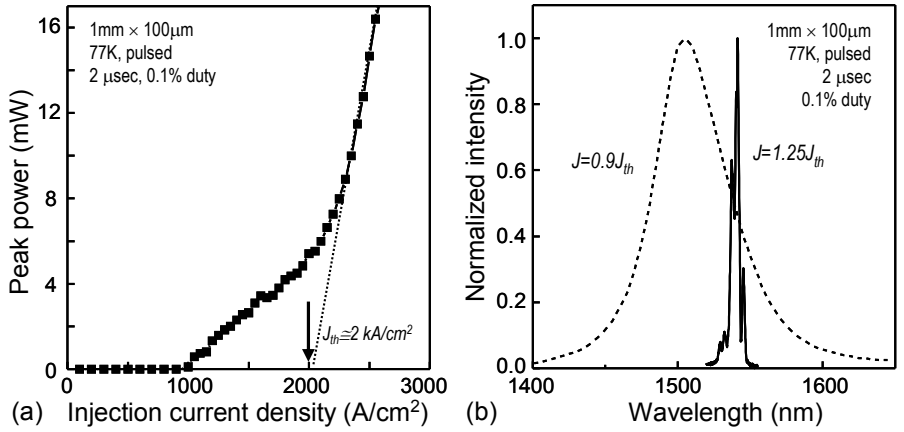


Fig. 2 (a) L-I curve of the fabricated laser devices at 77K under pulsed operation. (b) EL spectra above and below the threshold current density, Jth≅2 kA/cm^2.

illustration of the fabricated device is shown in Fig. 1(a). All the structures are grown by solid-state molecular beam epitaxy at 400°C. The growth is initiated with a 50 nm AlSb nucleation layer that is optimized for IMF formation and APD suppression on Si as shown in Figs. 1(b) and (c). It is noted that the misfit separation is ≅ 3.46 nm and corresponds to exactly 8 AlSb lattice sites grown on 9 Si lattice sites (Fig. 1(d)). The AlSb layer is followed by a 2 μm n-GaSb contact, a 2.3 μm $Al_{0.55}Ga_{0.45}Sb$ n-type clad, an active region, a 1.5 μm $Al_{0.55}Ga_{0.45}Sb$ p-type clad and a highly doped 50 nm GaSb p-type contact layer. The active region is comprised of six GaSb (10 nm) QWs separated by $Al_{0.3}Ga_{0.7}Sb$ (10 nm) barrier cladded by $Al_{0.3}Ga_{0.7}Sb$ waveguide layers. Samples are processed such that they form broad-area lasers with a stripe width of 100 μm. The process involves an inductively coupled plasma reactive ion etch into the n-GaSb contact layer, Ti/Pt/Au metal evaporations for contact to both n- and p-GaSb. The wafer is thinned to 70 μm and cleaved to bar lengths of 1 mm. It is noted that poor facet quality along with the low gain of the active region hinders the continuous wave room temperature operation of the GaSb QW lasers on Si substrate.

Device Characterization

The current-output power (L-I) curve and electroluminescence (EL) spectra are shown in Fig. 2. Lasing operation is observed at 77K is observed at a wavelength of 1.54 μm with a threshold current density (J_{th}) of 2 kA/cm^2 for a 1 mm-long device under pulsed conditions with 2 μsec pulse width and a 0.1% duty cycle. A higher J_{th} compared with the same active grown on GaAs substrates [15] is attributed to the poor quality of the cleaved facets, like observed by other groups [16]. The maximum peak output power from the device is ~ 20 mW. The current-voltage (I-V) characteristics indicate a diode turn-on of 0.7 V, which is consistent with a theoretical built-in potential of the laser diode. A very low resistance of 9.1 Ω and reverse bias leakage current density of 0.7 A/cm^2 at -5 V and 46.9 A/cm^2 at -15 V is obtained.

Conclusions

We demonstrate III-Sb based lasers monolithically grown on 5° miscut Si (100), at a emission wavelength of 1.54 μm suitable for the fiber-optic communication systems. The device operates under pulsed conditions at a temperature of 77K. We believe room-temperature lasing can be achieved by improving the facets and incorporation of indium into the active region. This IMF technique will enable the demonstration of III-Sb based VCSELs emitting at the fiber-optic communication wavelength grown on a Si platform.

References

[1] K. K. Linder, J. Phillips, O. Qasaimeh, X. F. Liu, S. Krishna, P. Bhattacharya, and J. C. Jiang: "Self-organized $In_{0.4}Ga_{0.6}As$ quantum-dot lasers grown on Si substrates", Appl. Phys. Lett., Vol. 74, 1355 (1999).

[2] D. G. Deppe, N. Holonyak Jr., K. C. Hsieh, D. W. Nam, W. E. Plano, R. J. Matyi, and H. Sichijo: "Dislocation reduction by impurity diffusion in epitaxial GaAs grown on Si", Appl. Phys. Lett., Vol. 52, pp. 1812 (1988).

[3] O. Kwon, J. J. Boeckl, M. L. Lee, A. J. Pitera, E. A. Fitzgerald, and S. A. Ringel: "Monolithic integration of AlGaInP laser diodes on SiGe/Si substrates by molecular beam epitaxy", J. Appl. Phys., Vol. 100, pp. 013103 (2006).

[4] M. E. Groenert, C. W. Leitz, A. J. Pitera, V. Yang, H. Lee, R. J. Ram, and E. A. Fitzgerald: J. Appl. Phys., 93, 362 (2004).

[5] I. Hwang, C. Lee, J.-E. Kim, and H.Y. Park: "Clustering effect and residual stress in $In_xGa_{1-x}As$/GaAs strained layer grown by metal-organic chemical-vapor deposition", Phys. Rev. B, Vol. 51, pp. 7894 (1995).

[6] G. Balakrishnan, S. Huang, L. R. Dawson, Y.-C. Xin, P. Conlin, and D. L. Huffaker: "Growth mechanisms of highly mismatched AlSb on a Si substrate", Appl. Phys. Lett., Vol. 86, pp. 034105 (2005).

[7] G. Balakrishnan, A. Jallipalli, P. Rotella, S. H. Huang, A. Khoshakhlagh, A. Amtout, S. Krishna, L. R. Dawson, D. L. Huffaker: "Room-Temperature Optically Pumped (Al)GaSb Vertical-Cavity Surface-Emitting Laser Monolithically Grown on an Si(100) Substrate", IEEE J. Sel. Top. Quant. Electron, Vol. 12, pp. 1636 (2006).

[8] G. Balakrishnan, M. Metha, M. N. Kutty, P. Patel, A. R. Albrecht, P. Rotella, S. Krishna, L.R. Dawson, D. L. Huffaker: "Monolithically integrated III-Sb CW super-luminal light emitting diodes on non-miscut Si (100) substrates", Elec. Lett., Vol. 43, pp. 244 (2006).

[9] K. Adomi, S. Strite, H. Morkoc, Y. Nakamura and N. Otsuka: "Characterization of GaAs grown on Si epitaxial layers on GaAs substrates", J. Appl. Phys., Vol. 69, pp. 220 (1991).

[10] C. L. Andre, J. A. Carlin, J. J. Boeckl, D. M. Wilt, M. A. Smith, A. J. Pitera, M. L. Lee, E.A. Fitzgerald, and S. A. Ringel: "Investigations of high performance GaAs solar cells grown on Ge-SiGe-Si substrates", IEEE Trans. on Electron Device, Vol. 52, pp. 1055 (2005).

[11] R. M. Sieg, S. A. Ringel, S. M. Ting, S. B. Samavedam, M. Currie, T. Langdo, and E.A. Fitzgerald: "Toward device-quality GaAs growth by molecular beam epitaxy on offcut Ge/Si1-xGex/Si substrates", J. Vac. Sci. Tech. B, Vol. 16, pp. 1471 (1998).
[12] L. Barbier, A. Khater, B. Salanon, and J. Lapujoulade: "Observation of the double-step–single-step transition on a vicinal surface of Si(100)", Phys. Rev. B, Vol. 43, pp. 14730 (1991).
[13] Z. Mi, J. Yang, P. Bhattacharya, and D. L. Huffaker: "Self-organised quantum dots as dislocation filters: The case of GaAs-based lasers on silicon", Electron. Lett., Vol. 42, pp. 121 (2006).
[14] H. Tanoto, S.F. Yoon, W.K. Loke, E.A. Fitzgerald, C. Dohrman, B. Narayanan and C. H. Tung: "Growth of GaAs on (100) Ge and Vicinal Ge surface by Migration Enhanced Epitaxy", Mater. Res. Soc. Symp. Proc., Vol. 891, pp. 0891-EE03-17 (2005).
[15] M. Mehta, A. Jallipalli, J. Tatebayashi, M. N. Kutty, A. Albrecht, G. Balakrishnan, L. R. Dawson, and D. L. Huffaker: "Room-Temperature Operation of Buffer-Free GaSb-AlGaSb Quantum-Well Diode Lasers Grown on a GaAs Platform Emitting at 1.65 μm", IEEE Photon. Technol. Lett. Vol. 19, pp. 1628 (2007).
[16] G. Roelkens, D. Van Thourhout, R. Baets, R. Nötzel, and M. Smit: "Laser emission and photodetection in an InP/InGaAsP layer integrated on and coupled to a Silicon-on-Insulator waveguide circuit", Opt. Exp., Vol. 14, pp. 8154 (2006).

Compact Grating Coupled MMI on DVS-BCB Bonded InP-Membrane

F. Bordas[1], F. Van Laere[2], G. Roelkens[2], E. J. Geluk[1], F. Karouta[1], P.J. van Veldhoven[1], R. Nötzel[1], D. Van Thourhout[2], R. Baets[2] and M.K. Smit[1]

[1]COBRA Research Institute, Technische Universiteit Eindhoven
P.O. Box 513, NL-5600MB Eindhoven
F.Bordas@tue.nl
[2]Photonics Research Group, Ghent University-IMEC, Ghent, Belgium

Abstract. *Compact passive components have been successfully fabricated on 200 nm thick InP membrane BCB-bonded on a GaAs wafer. The characterization reveals that 400 nm wide wires show a loss <10dB/cm, S-bends have a loss of 2dB and a very compact MMI coupler (<20μm^2) show a loss of 0.6 dB.*

Introduction

In this paper, we demonstrate compact passive devices (single-mode wires, compact bends and MMI's) in DVS-BCB bonded InP-membrane. Light is coupled into and extracted from the chip using compact grating couplers [1, 2]. The wires are completely etched through the membrane, whereas the grating couplers are shallowly etched, to avoid excessive reflection. Moreover, this shallow etch make them more tolerant to fabrication deviations from the designed gratings.

Fabrication

The layer structure consists of a 200 nm InP-membrane layer on top of 3 etch-stop layers (InGaAs-InP-InGaAs) grown on a semi-insulating InP-substrate. The first step is the pattern definition. E-beam lithography is used on a positive resist over a 50 nm SiN_x hard mask, deposited by PECVD. After development and post-bake of the resist, the hard mask is etched with a CHF_3-based RIE. The resist post-bake allows reducing the sidewall roughness, as illustrated in Fig.1-a and 1-b. Then optical lithography is performed to cover the gratings and open the remaining part of the layout. A CH_4/H_2 based ICP etching step follows, to etch the deep part through the whole InP membrane. After removal of the resist, a second etch step is performed, for the gratings to be 70 nm deep. Finally we remove the SiN_x hard mask with a HF solution. The shallow-deep transition is shown at Fig.1-c.

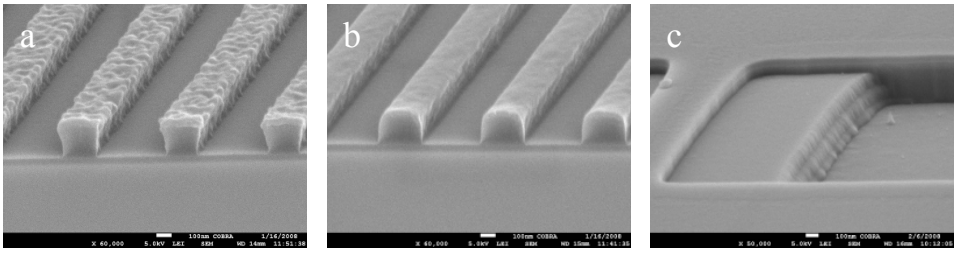


Fig 1: a – Resist pattern of a grating without post-bake;
b – Same pattern after a 150°C post-bake for 2';
c – Shallow-deep transition morphology.

After pattern definition, a BCB layer of 780 nm was spin-coated onto the InP-die, and cured for 1 hour at 250°C in a nitrogen environment. Then, the InP-sample was bonded onto a GaAs host-substrate with a 1µm thick BCB-layer [3]. This BCB-layer was also cured for 1 hour at 250°C in a nitrogen environment. The InP-substrate was removed using lapping and wet-etching in HCl until the InGaAs etch stop layer was reached. Finally, the InGaAs-InP-InGaAs etch-stop layer stack was removed using selective wet-etching.

Results and discussion

Grating couplers

The gratings are designed for an optimal coupling at 1.55µm at an angle of 10°. To avoid excessive reflections, the depth is 70nm, and two different periods are used: 730nm and 760nm for grating A and B respectively, with a filling factor of around 50%. The optimal simulated BCB thickness is 780nm + p*λ/2n, where λ is the wavelength in vacuum, p an integer, and n is the refractive index of the BCB layer. In our case p=1.

Transmission measurements are performed with a tunable laser as a source. The gratings are 10x10µm^2, and the device consists in a 50µm long 400nm wide wire and 600µm long tapers on each side. Figure 2-a shows the transmission of such a device with grating A (black) and grating B (red) as input and output couplers. The measured fiber-to-fiber loss at peak wavelength is 6.8dB for the device with grating B. For grating A, the tunable laser could not reach the peak wavelength. As the wire is very short, we assume losses only arise from the two grating couplers, which will be confirmed in the next paragraph. We can deduce a coupling efficiency of 47% at the optimal wavelength from these values, which is represented at Fig.2-b. Some measurements with a SLED as a source (not shown here) showed the same coupling efficiency for grating A at lower wavelength.

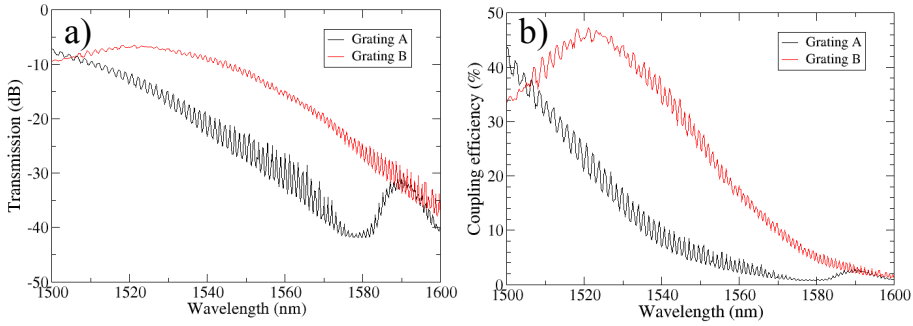


Fig. 2: a – Transmission through a 50 µm wire with two grating couplers, for two different grating;. b – Corresponding coupling efficiency.

Now the grating couplers are characterized, we can focus on the different fabricated devices, which are wires of different length, S-bends of different radii, and MMI's. For wires and MMI, the grating coupler used is grating B, whereas grating A is used for the bends.

Wires

We fabricated 400nm wide wires of four different lengths, in order to determine the losses. Fig.3 shows the transmission through 500µm (black), 300µm (red), 100µm (green) and 50µm (blue) long wires. As can be seen, it is very difficult to deduce from these measurements the loss per cm length, but we can access to a maximal value of these losses around 10dB/cm. This confirms the assumption made in the preceding paragraph. However this quite low loss value will be confirmed by fabricating wires in the mm range in the near future.

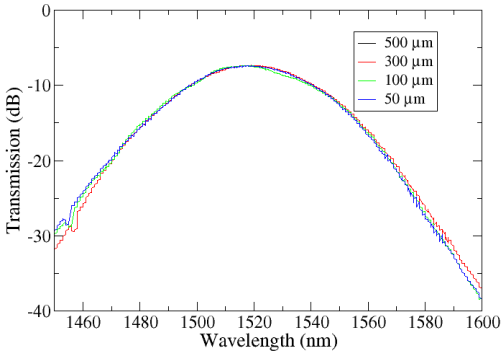


Fig. 3 : Transmission through 400nm wide wires of different lengths : 500 µm (black), 300µm (red), 100µm(green), and 50µm (blue).

Bends

The reference here is a 50µm long wire. Three different S-bends are measured, with radii of 40µm, 20µm, and 5µm. The losses are shown in Fig.4. Assuming the coupling efficiency of the gratings is the same for all devices, we can measure 2dB losses for the bends as compared to the reference, but could not measure any difference between bends of different radius.

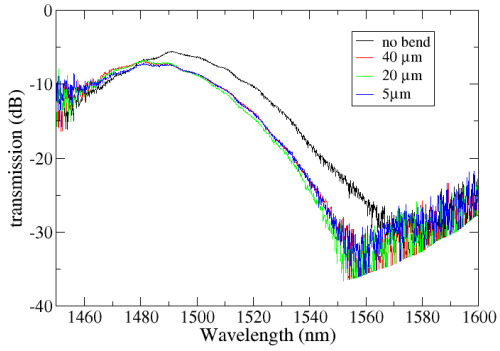


Fig.4 : Transmission through a simple wire (black) and S-bends of 40mm, 20mm, and 5mm (red, green, and blue respectively).

This suggests that very compact integrated optical circuits can be fabricated using sharp bends (5µm radius bend). Moreover the 2dB measured losses can be improved by inserting offsets between wires and bends.

MMI's

The fabricated MMI's are meant to be 1x2 couplers. Fig.5-a shows a SEM image of the resist pattern after development. The dimensions of the MMI are 6.64 x 2.75 x 0.2 μm^3. Transmission measurements on this device are shown in Fig.5-b. The reference (in black) is a 50µm long wire without MMI. Transmission through the upper and the lower branch (red and green respectively) are very comparable, and 3.6dB lower than the reference.

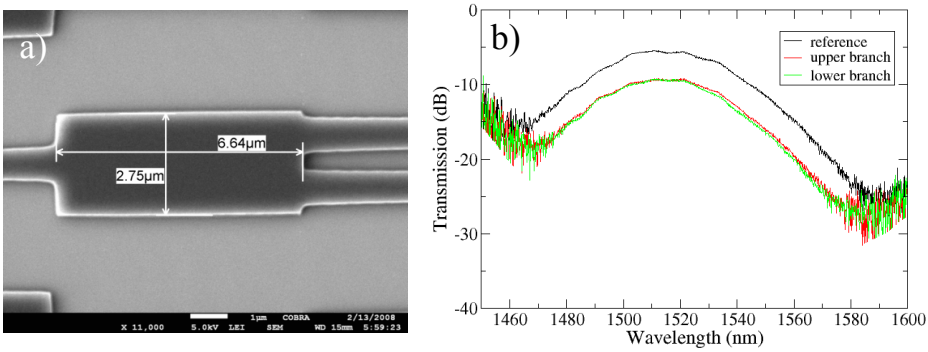


Fig.5 : a – SEM image of a fabricated MMI ;
b – transmission through both output branches, together with the reference.

Hence the fabricated MMI coupler operating as a 3dB splitter shows a loss of only 0.6dB.

Conclusion

In this paper we showed very compact and efficient devices fabricated on InP membranes bonded on GaAs with BCB. The light was coupled in and out through shallowly etched grating couplers, with an efficiency of 47%. Losses through the wires could not be accurately measured, indicating an upper limit of 10dB/cm for losses; the S-bends (radii of 5µm up to 40µm) had all 2dB losses. The most exciting result is the very compact 3dB-splitter, with a 0.6dB loss.

Acknowledgement

The authors thank the Dutch Project Smartmix-Memphis for partial financial support.

References

[1] D. Taillaert, F. Van Laere, M. Ayre, W. Bogaerts, D. Van Thourhout, P. Bienstman, and R. Baets, "Grating Couplers for Coupling between Optical Fibers and Nanophotonic Waveguides", Japanese Journal of Applied Physics, vol. 45, pp. 6071–6077, 2006.

[2] F. Van Laere, G. Roelkens, M. Ayre, J. Schrauwen, D. Taillaert, D. Van Thourhout, T. F. Krauss, and R. Baets, "Compact and Highly Efficient Grating Couplers Between Optical Fiber and Nanophotonic Waveguides", Journal of Lightwave Technology, vol. 25, pp. 151-156, 2007.

[3] G. Roelkens, J. Brouckaert, D. Van Thourhout, R. Baets, R. Nötzel, and M. Smit, " Adhesive Bonding of InP/InGaAsP Dies to Processed Silicon-On-Insulator Wafers using DVS-bis-Benzocyclobutene", Journal of The Electrochemical Society, vol. 153, pp. G1015–G1019, 2006.

Monolithic Directly-Modulated Multi-Wavelength-Channel GaInAsP/InP Micro-Ring Laser Array

A. Bennecer[1], R.V. Penty[1], I.H. White[1], K.A. Williams[2], M. Hamacher[3] and H. Heidrich[3]

[1]Cambridge University Engineering Department, Cambridge, UK
ab598@cam.ac.uk
[2]TU Eindhoven, Eindhoven, the Netherlands
[3]Fraunhofer Institute for Telecommunications, Heinrich-Hertz Institut, Berlin, Germany

Abstract. *Two directly-modulated GaInAsP/InP micro-rings with different radii vertically-coupled on a common bus are assessed for both independent and simultaneous operation. A device area <0.12mm^2 per microring allows the generation of 2λx1Gb/s WDM signals with 6nm wavelength separation. These show successful transmission over 25km of single-mode-fibre with < 0.2dB power penalty.*

Introduction

There is an increasing need for ultracompact direct modulated wavelength multiplexed sources in power efficient data transceivers. Microring laser arrays, vertically coupled to a single passive waveguide bus offer a highly scalable route to integration with a minimum of photonic components and chip footprint. The vertical coupling approach further allows an independent optimisation of epitaxy and waveguide fabrication for close proximity active and passive photonic devices.

Ring resonator lasers have been considered for some time as highly attractive sources in integrated photonics [1]. The coupling of ring lasers has been explored to enhance output power to 6.5mW and spectral purity with high side mode suppression ratio of >40 dB. Multiple coupled cavities have also enabled digital wavelength tuning [2]. Progress in reducing the dimensions for microring lasers has more recently enabled array scaling of active microrings for multiwavelength sources [3] and modulator based demultiplexer arrays [4]. The direct modulation bandwidth of vertically coupled microring laser array has further been demonstrated for 7Gb/s data modulation [5].

In this work we present a directly modulated monolithic microring laser array. The performance of individual channel operation is compared directly with wavelength multiplexed performance at a data rate of 1Gb/s. Transmission over 25km is further shown in system level assessments.

Fabrication

Figure 1(a) shows a schematic of the device structure. A conventional multiple quantum well ridge waveguide laser structure designed to target an emission wavelength of 1.55μm is grown on top of a passive bus waveguide on a 2" InP substrate in a single epitaxial step. The lasers are fabricated first and the p-metalisation is performed. The passive bus is defined between the substrate and the laser epitaxy. The wafer is subsequently transferred epitaxial side down onto a GaAs carrier wafer to which it is bonded by means of a BCB intermediate layer for mechanical support. The substrate and buffer layers are then removed in order to allow the subsequent definition of the bus waveguide. The bus waveguide layer also serves as an etch-stop layer for the wafer

thinning. The p-contact is accessed at the ring using a via hole whilst the outside-lying n-contact is split into two parts to avoid additional metal induced losses in the passive bus waveguide. Both parts are connected with an air bridge to allow a homogeneous current injection to the ring resonator.

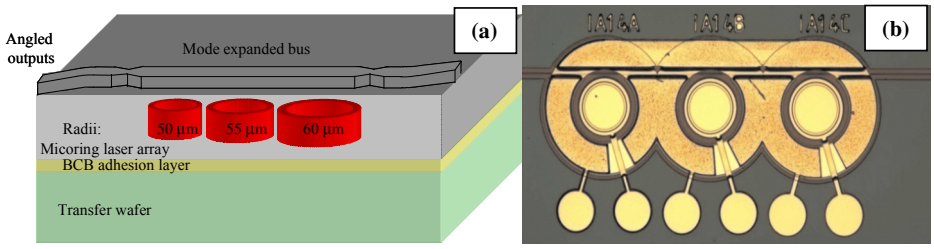


Fig. 1. (a) Schematic diagram for the bus coupled microring laser array showing micro-rings with three distinct radii and the mode expanded bus design. The 60µm and 55µm radius rings emit at 1561nm and 1567nm respectively (b) Photograph of the microring laser array

The ring waveguide width is 1.8µm. The passive bus is 2.5µm where the ring and bus waveguides are in close proximity to relax alignment tolerance. Microring radii of 60, 55 and 50µm are defined for the three bus coupled lasers. Away from the microring, the bus tapers to 1.8µm width over a length of 50µm for mode filtering before rebroadening back to 2.5µm [6]. Waveguides are angled at 7º towards the outputs to reduce reflections from the uncoated cleaved facets. Figure 1(b) shows a photograph of the completed photonic integrated circuit (PIC).

Device Characterisation and Fibre Transmission

In the experiment, the two larger radius lasers are directly probed with broadband coplanar probes contacting the n and p bond pads. The schematic of the experimental setup is shown in Fig. 2.

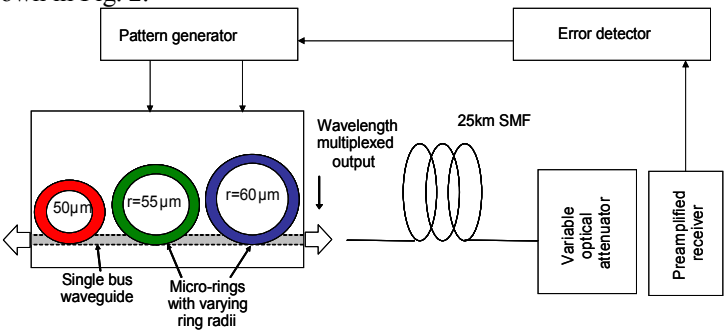


Fig. 2. Experimental arrangement for the assessment of the array of micro-ring lasers

DC measurements indicate threshold currents of 20mA and 22mA and series resistances of 28 and 24Ω for the 60µm and 55µm micro-ring radii respectively. The light is collected from both facets using lensed fibre. Under modulation with a 350mV peak to peak voltage at a 1Gb/s data rate, the optical spectrum is near identical for emission from both facets and comparable side mode suppression ratios of -28.1dB for the 1561nm channel and -25.4dB for the 1567nm channel are observed at applied DC

currents of 42.2mA and 37mA, respectively. The submount is held at a temperature of 20°C.

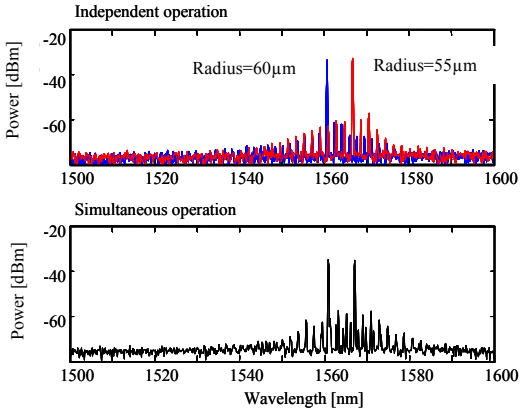


Fig. 3. Spectral characteristics for the directly modulated microring lasers for independent operation (top – overlaid spectra) and simultaneous operation (bottom)

Fig. 3. shows the spectra for both the independent and simultaneous operation of the microring lasers under data modulation. For the case of independent operation, the spectra are overlaid. A comparison of the modal structure indicates very similar spectral performance both as individual data transmitters and as wavelength multiplexed transmitters, indicating consistent behaviour and good immunity to electrical and thermal cross talk between the to lasers.

Transmission tests over 25km of single mode fibre have been carried out. After transmission, a mean received power of over 10µW is injected into an Erbium doped preamplifier at the receiver. Channels are selected with a 1nm bandwidth optical filter. A 933MHz low pass electrical filter is implemented after the photo-receiver. The optically preamplified receiver exhibits a -26dBm sensitivity.

As the longer wavelength channel is outside the gain bandwidth of the receiver, the signal to noise ratio for that channel is severely degraded. Received powers after the Erbium preamplifier are measured to be -1dBm and -18.6dBm for the two channels due to the wavelength dependent amplifier gain. Due to this relatively low received power from the 1567nm channel, BER measurements are carried out only on the 1561nm channel at the output of the bus waveguide. This is used as a reference for power penalty measurements and data are denoted by open square symbols in Fig. 4. In addition, BER measurements after the 25km transmission, where data are denoted by solid square symbols in Fig. 4, exhibit a negligible power penalty of 0.2dB. It should be noted that the modulation performance is sensitive to the bias conditions. At bias points near to a mode hops, closed eyes are found under modulation, even if the stationary starting point showed good single mode operation. However, for the correct bias points, good quality eyes are observed as shown in the inset of fig. 4.

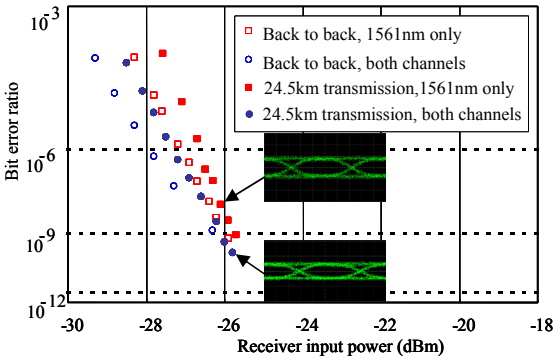


Fig. 4. Bit error rate performance for individual and wavelength multiplexed operation for 0km (back to back: open symbols) and 25km fibre transmission (filled symbols). Single wavelength operation is denoted by squares and wavelength multiplexed operation by circles. Insets show eye diagrams over 25km for independent and simultaneous operations.

The addition of the 1567nm channel is observed to only slightly affect the error rate performance of the 1561nm channel under wavelength multiplexed operation. For back to back multiplexed operation, a slight improvement is even observed and the transmission penalty is low. The observed low power penalties are indicative that the two lasers do not appear to influence each other greatly.

Conclusion

Simultaneous data modulation of monolithically integrated microring laser arrays vertically coupled to a single passive bus waveguide is demonstrated. 2λx1Gb/s WDM transmission assessment over 25km of single-mode-fibre is demonstrated with low 0.2dB multiplexed power penalty. The comparable performance of individual and multiplexed operation is indicative of low interference between the laser channels, suggesting a potential solution for small size integrated wavelength multiplexed laser arrays. Further resonator integration may extend the number of WDM sources as well as the aggregate data rate.

References

[1] A.S.-H. Liao and S. Wang, "Semiconductor injection lasers with a circular resonator", Applied Physics Letters, Vol. 36, No. 10, pp. 801-803, 1980.

[2] S. J. Choi, Z. Peng, Q. Yang, E. H. Hwang, P. D. Dapkus. “A semiconductor tunable laser using a wavelength selective reflector based on ring resonators”. Proc. OFC/NFOEC, 2005,

[3] S.J. Choi, Z. Peng, Q. Yang, S.J. Choi and P.D. Dapkus, "An eight-channel demultiplexing switch array using vertically coupled active semiconductor microdisk resonators", IEEE Photonics Technology Letters, 16, 11, pp. 2517-2519, 2004

[4] S.J. Choi, Z. Peng, Q. Yang, S.J. Choi and P.D. Dapkus, "Eight-channel microdisk CW laser arrays vertically coupled to common output bus waveguides", IEEE Photonics Technology Letters, 16, 2, pp. 356-358, 2004

[5] A. Kapsalis, U. Troppenz, M. Hamacher, H. Heidrich, D. Syvridis, "7 Gb/s direct modulation of vertically coupled microring lasers", Proc. OFC/NFOEC 2008

[6] C.W. Tee, K.A. Williams, R.V. Penty, I.H. White, "Fabrication-tolerant active-passive integration scheme for vertically coupled microring resonator," IEEE Journal of Selected Topics in Quantum Electronics, 12, 1, pp. 108-116, 2006

Sensors and photonic integration

M.J. van der Hoek

VanderHoekPhotonics, Vlaardingen, the Netherlands
mj@vanderhoekphotonics.com

Abstract. *Photonic integration will become more and more a dominant factor for successful economic deployment of optical sensors, enabling a fast growing number of applications. Because the present sensors employ many discrete photonic and opto-electronic components, development of sensor-dedicated devices and photonic integrated circuits is now the required next step to fuel many new applications.*

Photonic integration for sensors: benefiting from telecom achievements

In analogy to the application of Photonic Integrated Circuits (PICs) for ultra-high capacity telecommunications networks, the role of photonic integration becomes more and more a decisive factor for the economic implementation of sensors. The telecom-drive for cost-effective realization of complex photonic and opto-electronic circuits is now even more urgently required to spur the development of photonic sensors. At the same time, specific requirements for sensors can initiate PIC-oriented research that will enable realization of novel telecom devices and complex circuits as well.

Challenges and opportunities for photonic integration

Photonic integration will benefit a great number of applications in the field of photonics-based sensing [1]. Figure 1 indicates only two out of many basic sensor configurations and lists some specific features of sensor-oriented PICs.

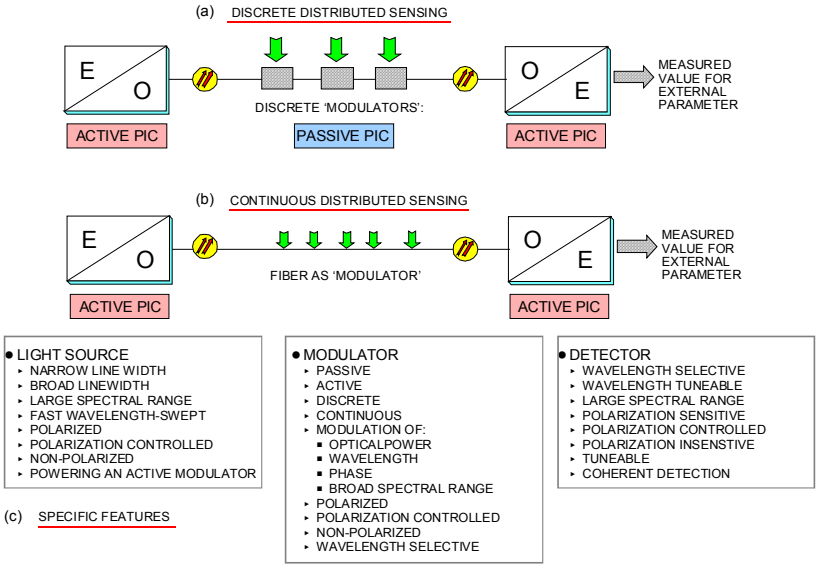


Fig. 1: Sensor configurations employing: (a) passive- and (b) active PICs, (c) some specific features for sensor-oriented PICs

Dedicated functionality in (low-cost) photonic integrated circuits will enable many novel applications for sensors, similar to the way micro-electronics has changed society in many ways. Worldwide, novel sensor concepts are designed, being the response to measure an ever increasing number of phenomena on a more and more accurate scale. Applications range from e.g. structural integrity monitoring to security to process control to medical biophotonics. Frequently these novel sensor concepts require advanced photonic excitation – and analysis techniques to resolve the parameters of interest. Also, ongoing developments in the field of e.g. micro structured fibers and photonic crystals offering advanced photonic effects for sensing will require precise excitation and complex read-out techniques. Presently, one is usually pressed to realize such complex functionalities using many separate photonic- and opto-electronic components. PICs offering equivalent or better performance at attractive costs will therefore serve as an *enabling technology* for novel sensors. Small volume, low mass, vibration-immunity, increased performance and high-reliability are key factors for high-tech applications in e.g. aerospace and automotive industry. Active PICs can be used as advanced light sources and detectors connected to e.g. passive 'modulators' (being PIC-based or otherwise) or as 'active' sensing platforms. Optically powered sensors shown in Figure 2 will expand their applications by PIC-based ultra low power lasers and sensing circuits.

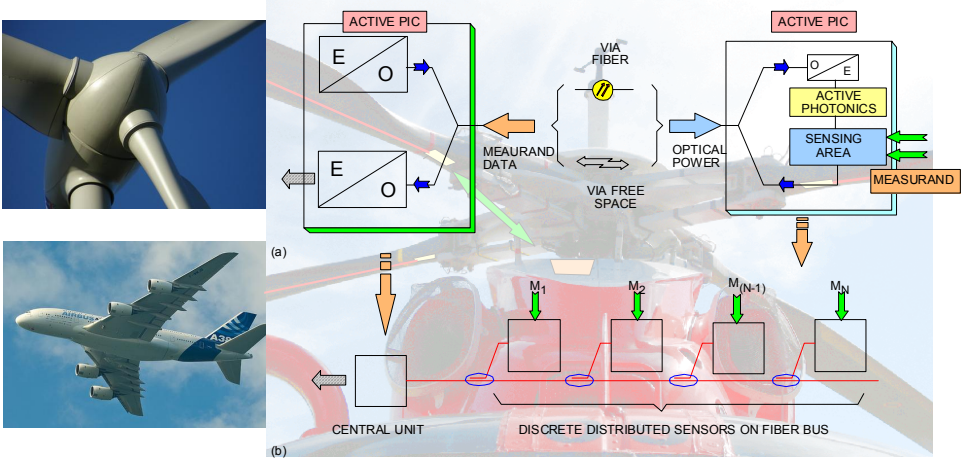


Fig.2: PIC-based opto-powered sensing: (a) basic configuration, (b) bus structure. Background: application of free-space sensors for helicopter rotor blade monitoring

Depending on sensing area design, an active PIC can responds to (multiple) physical and chemical parameters, transmitting encoded measurand-data back to the opto-powering unit. For example, an active PIC employing an interferometer with a chemo-optical transduction layer on top of its sensing-waveguide responds to a specific chemical parameter, while electro-optic effects in the waveguide will respond to electrical parameters. The sensing-PIC can be powered via fiber or free space, the latter enabling applications requiring wireless operation of the sensing-PIC, as in wind turbines, airplane propellers or rotor blades of helicopters. Such applications require however receivers and transmitters being optimized for free-space optical communication. A challenge will be to keep their related power consumption within requirements.

Application: Continuous distributed sensing of strain and temperature

Distributed sensing of strain and temperature becomes increasingly important for e.g. structural health monitoring and economic optimization of e.g. bridges, quay walls, wind turbine blades, large-area roofs and high-power (intercontinental) electrical power cables. Such applications require large objects to be monitored at multiple spots, urging low costs for sensors, cabling and installation. Presently, distributed strain and temperature are mostly monitored using a telecom optical fiber as sensor, being reinforced and embedded into the object or attached to its outside. Spatial-resolved monitoring of strain is based on analysis of the Brillouin shift of a backscattered light pulse while traveling along the fiber, as shown in Figure 3.

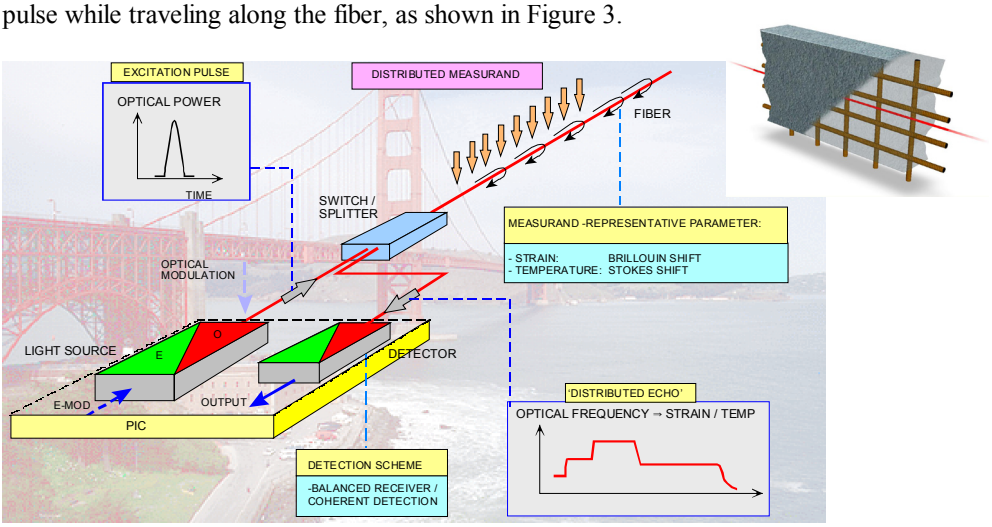


Fig. 3: Distributed sensing of strain and temperature using an optical fiber as sensor

Temperature measurement is based on analysis of time-resolved Raman scattering. A strain of 1% in a telecom grade fiber introduces a frequency shift of about 497 MHz. Resolving a much-wanted strain detection limit of 1 microstrain requires to detect a frequency change of 49.7 kHz at a power level that is about 10^5 times lower than that of the excitation pulse. In addition, a spatial resolution of e.g. 0.2 m requires the strain-induced frequency deviations to be measured within 1 ns. Commercial systems for distributed strain are specified at 20 microstrain detection and 0.4 m spatial resolution for a price of about k€100. PIC-based instruments are targeted at 10-15 % of this price

Application: A Neutrino telescope using discrete distributed sensors

The KM3NeT ('Cubic Kilometer Neutrino Telescope') [2] as under design by Nikhef and an international collaboration of scientific institutes, is deep-water neutrino detector to be operating at a seabed at 3-5 km depth (Fig. 4). High-energy astrophysical neutrinos are elementary particles with zero charge and very low mass. After traveling through the Earth they can interact with sea water, creating a muon traveling at a speed higher than the speed of light in the sea water. Under this condition, the slowing-down muon emits the characteristic blue-colored Cherenkov radiation along its track. KM3NeT will detect this radiation using some 10.000 Optical Modules, being glass spheres of 400 mm

diameter, each containing up to 32 photomultiplier tubes (PMTs). Digital PMT-data must be real-time transmitted to the shore station for Cherenkov-track reconstruction, requiring a 1ns on-shore timing accuracy of a photon hit. Data will be transmitted over up to 100 km via submarine electro-optical cable containing up to 100 fibers each carrying 100 DWDM channels at 0.4 nm spacing. Total data rate to the shore station will be 10.000 x 10 Gb/s, or 100 Tbit/s. Specific PICs for KM3NeT, and distributed sensor networks in general, are multi-wavelength laser arrays, E/O data interfaces, all-optical serializing/de-serializing and data processing in the photonic domain.

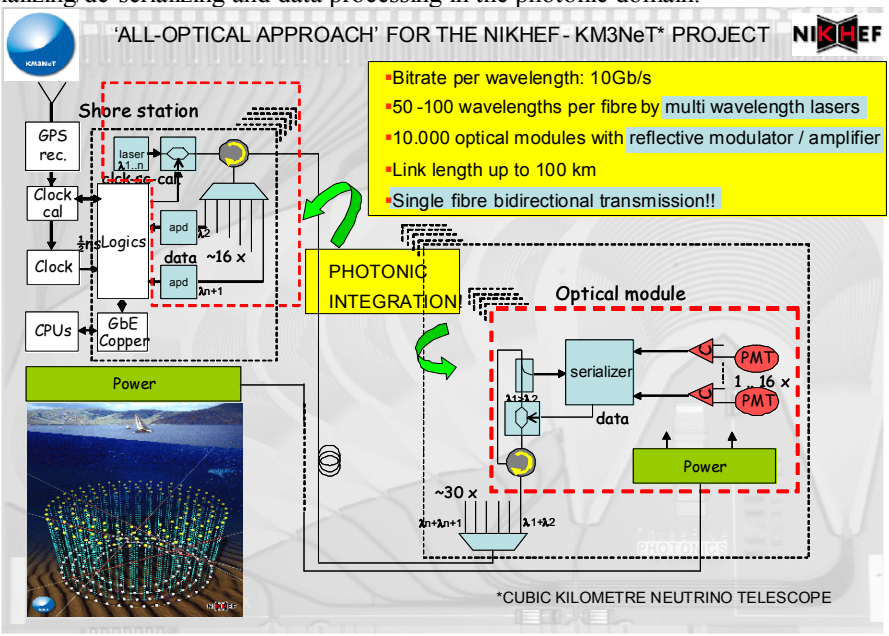


Fig. 4: Photonics for KM3NeT: a cubic kilometer volume deep-sea Neutrino telescope

Closing remarks

Apart from applications in telecom, passive and active PICs will, more than ever, enable to expand the number of applications of photonic sensors. PICs will spur development of novel sensors and advanced photonic techniques for sensor excitation and readout. Also, the synthesis between complex functionalities offered by PICs and photonic effects in e.g. micro structured fibers and photonic crystals will enable sensors being capable to measure multi-parameter phenomena simultaneously. Dedicated PICs will also contribute decisively to the success of scientific programs in the field of fundamental research, where massive collection of vast amounts of data from thousands of distributed signal sources is crucial for progress in e.g. fundamental sciences. Governmental rules on safety, liability and insurance regulations will act as a very efficient catalyst to accelerate the development and expansion of novel types of photonic sensors.

References

[1] J.M. López-Higuera, Handbook of Optical Fibre Sensing Technology, John Wiley and Sons, LTD, 2002, ISBN 0-471 82053 9.

[2] KM3NeT Neutrino Telescope: www.km3net.org , www.nikhef.nl.

Fluorescence sensing with femtosecond laser written waveguides in a capillary electrophoresis chip for monitoring molecular separation

C. Dongre[1], R. Dekker[1], H.J.W.M. Hoekstra[1], D. Nolli[2], R. Martinez-Vazquez[2], R. Osellame[2], G. Cerullo[2], G. A. J. Besselink[3] and M. Pollnau[1]

[1] Integrated Optical MicroSystems (IOMS), MESA+ Institute for Nanotechnology, University of Twente, PO Box 217, 7500 AE Enschede, The Netherlands
[2] Dipartimento di fisica and Istituto di fotonica e nanotecnologie del CNR, Politecnico di Milano, Piazza Leonardo da Vinci 32, 20133 Milan, Italy
[3]Capilix BV, PO Box 455, 7500 AL Enschede, The Netherlands
E-mail: C.Dongre@ewi.utwente.nl

Abstract: *Fluorescence detection is one of the most sensitive among different optical sensing techniques. This work focuses on integrated optical excitation/detection of fluorescence originating from dye molecules during on-chip capillary electrophoresis. Excitation occurs via femtosecond laser written waveguides intersecting the microfluidic channels both integrated in a commercial capillary electrophoresis chip.*

Introduction

Recent advances in microchip fabrication technology and microfluidics have enabled the implementation of a large number of biochemical processes in miniaturized lab-on-chip systems. Many of these systems largely depend on conventional bench-top measurement instrumentation for monitoring. On-chip integration of biochemical sensors therefore continues to be a challenging field of research, empowering the existing lab-on-chip systems with ever more functionalities while also making them a more cost-effective option. In particular, integrated optical detection has emerged as an attractive tool to fulfill the requirements of such an on-chip *in-situ* probing strategy [1]. Current detection schemes mostly depend on the hybrid integration of an existing microfluidic system with external detection optics. The work presented in this paper focuses on integrating both functionalities in a single substrate viz. glass. Parallel to the progress in glass-based on-chip microfluidics, femtosecond (fs) laser writing has emerged as an interesting technique to inscribe optical WGs in bulk glass substrates [2]. The combination of these two developments to integrate a detection system of fs laser written WGs in a glass microfluidic chip is a novel approach, forming the key focus of this work [3]. In this paper we describe the experimental progress in integration of optics and microfluidics in a capillary electrophoresis (CE) chip, the concept of on-chip CE, the integrated detection scheme to monitor the same, and concluding with an experimental demonstration.

Waveguide fabrication and characterization

Fs laser irradiation of glass leads to localized melting in the focal volume of the beam followed by re-solidification upon removal of the beam. The corresponding localized densification leads to a refractive index variation. WGs are written by a continuous transverse movement of the substrate with respect to the writing beam. In principle a suitable movement of the substrate during writing could create any desired 3D waveguiding structure hence making this technique extremely attractive [2]. The WGs under investigation were fabricated by means of a Ti:sapphire laser at a repetition rate of 1 kHz, with typical pulse energies of 1 μJ, pulse durations up to 200 fs, and writing speeds of 100 μm/s, in a commercial fused silica microfluidic chip aimed at on-chip CE applications. The WGs were in turn thoroughly characterized [4]. The writing

process was optimized to obtain single-mode WGs with a circular cross-section (diameter: 10 μm) to ensure low fiber-chip coupling losses (~4 dB/end-facet). Propagation losses were found to be as low as 0.5 dB/cm. Cross-sectional refractive index profiles were evaluated and the maximum refractive index change was measured to be 1×10^{-3}.

Micro-opto-fluidic integration

A fused silica CE chip (commercially available from LioniX BV) was empowered with fs laser written WGs. Such a chip layout can be seen in figure 1.



Fig. 1 Left: CE chip with integrated WGs crossing the microfluidic channels
Right: Side view image of WG array – microfluidic channel intersection

The chip consists of 4 fluidic reservoirs (volume ~ 400 nl, each of them numbered and denoted by circles in Fig. 1) connected to each other by means of mf channels (cross section dimensions: 50 μm × 12 μm). The vertical lines along the breadth of the chip denote WGs crossing the mf channels in their plane. As a preliminary test of the quality of integration, the entire mf channel network in such a chip was suction-filled with Rhodamine-B which is a strongly fluorescent dye. Light from a green He-Ne laser (λ = 543.5 nm) was coupled into the WGs by means of an in-house-assembled fiber array unit glued to the chip end-facet. An on-off switchable Hg arc lamp served as background illumination for monitoring the entire chip. Detection was performed with an inverted microscope (Olympus IX-71). A combination (from Chroma Technology Inc.) of band-pass filters and a dichroic mirror was used to pass only the fluorescence signal while cutting off all other wavelengths including the scattered laser light and background illumination. A sharp fluorescent segment (breadth ~ 13 μm) was then observed at the WG - mf channel intersection, with and without a background illumination, as shown in figure 2. This result demonstrates that the desired quality of micro-opto-fluidic integration has been achieved.

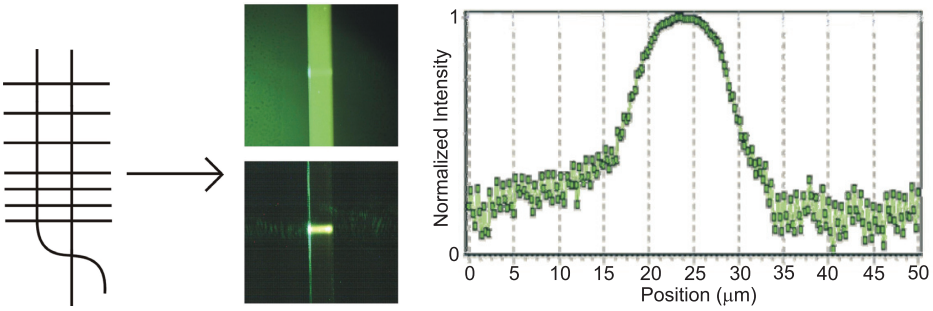


Fig. 2 WG excitation of Rhodamine-B at 543.5 nm and corresponding distribution of fluorescence intensity along the microfluidic channel

Fluorescence imaging of microchip capillary electrophoresis (MCE)

MCE corresponds to the separation of species with different charge density and mobility as they flow along an electric field applied at the ends of a microcapillary (in this case at the mf reservoirs at the ends of the mf channels). In order to perform this experiment the entire mf channel network was suction-filled with MES/His buffer (pH: 6.2). A mixture of species to be separated was added to reservoir 1, which in this proof of principle consisted of strongly fluorescent dyes Fluorescein and Rhodamine-B. In a practical application, the mixture would typically consist of biologically relevant species pre-labeled with fluorescent dye molecules. The mixture is transported to reservoir 3 via the injection channel by means of electro-osmotic flow on application of optimized, strong electric potentials (in the order of 10^3 V) at the reservoirs using integrated platinum electrodes. A continuous influx of the fluorescent mixture into reservoir 1 ensures that the injection channel (volume ~ 40 nl) connecting reservoir 1 and 3 is always filled with the mixture. Pinching potentials applied at reservoirs 2 and 4 prevent the mixture from leaking into the separation channel connecting reservoirs 2 and 4, resulting in the formation of a well-defined plug (volume: 30 pl) at the channel junction. Next, by suitably switching the potentials the plug is launched into the separation channel resulting in separation of the individual species. This series of events is captured and depicted in figure 3.

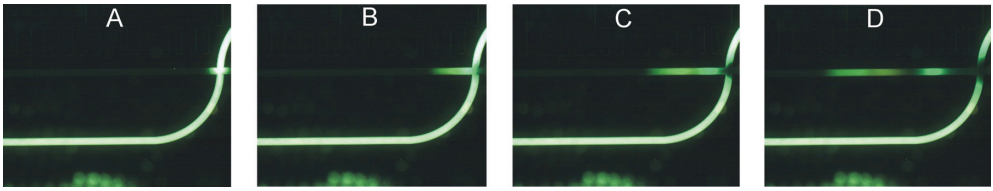


Fig 3. a) Formation, b) launching and c-d) MCE separation of a 30 pl plug consisting of Fluorescein and Rhodamine-B along a microfluidic channel

On-chip integrated dynamic fluorescence monitoring

The approaches described in the previous two sections have further been combined to demonstrate the monitoring of MCE using integrated WGs. As described earlier, a plug consisting of Fluorescein and Rhodamine-B was ejected into the separation channel. Light from a green He-Ne laser (λ = 543.5 nm) was coupled into a WG crossing the separation channel 3 mm away from the mf channel junction. Movement of the separated plugs was followed with Hg lamp background illumination. It was observed that only the Rhodamine-B plug showed a sharp increase in fluorescence intensity as it flowed across the excitation WG owing to the additional excitation signal. Wavelength selectivity is therefore demonstrated by the observation that the Fluorescein plug showed no response to WG excitation, owing to the absence (in the present experiment) of a light source corresponding to the absorption spectrum of Fluorescein, which extends up to λ = 525 nm. The observed series of events is depicted in figures 4 and 5. Rhodamine-B plug leads the flow while the Fluorescein plug follows. With the first and the last images in fig. 5 corresponding to the lowest Fluorescein concentration in the channel, it is still possible to detect along the WG a negligible localized fluorescence originating from residual Rhodamine-B particles sticking to the channel walls from inside, .

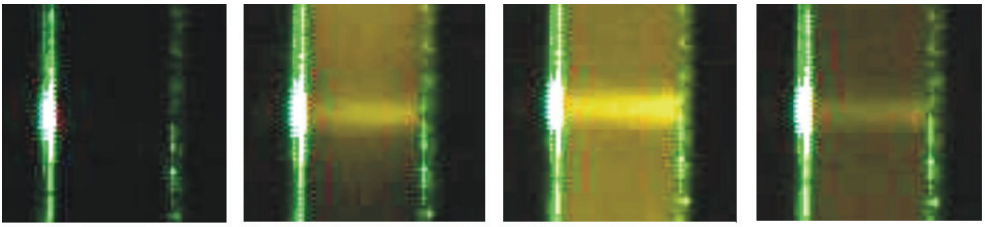


Fig. 4 Flow of Rhodamine-B (leading) plug across the excitation WG after CE separation

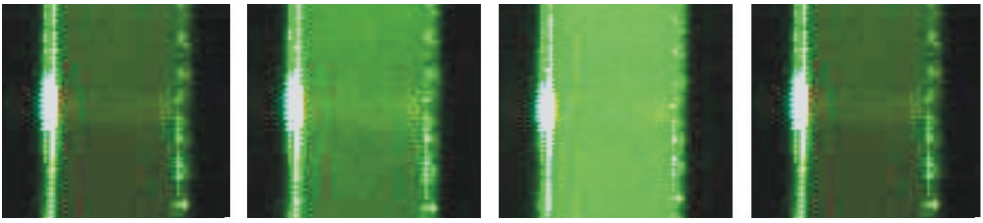


Fig. 5 Flow of Fluorescein (lagging) plug across the excitation WG after CE separation

Concluding Remarks

The paper presents recent progress in the field of monitoring on-chip capillary electrophoresis, using fluorescent molecules excited via integrated femtosecond laser written optical waveguides. It has been demonstrated that Fluorescein and Rhodamine-B molecules, separated by capillary electrophoresis, can be detected with the described set-up in a wavelength selective manner. Experiments are in progress to demonstrate integrated optical sensing for monitoring CE separation of fluorescence-labelled DNA fragments which would be an important diagnostic application of the presented work.

Acknowledgements

This work is supported by the European Union, contract IST-2005-034562 (Hybrid Integrated BIophotonic Sensors Created by Ultrafast laser Systems - HIBISCUS).

References

[1] P.V. Lambeck, "Integrated optical sensors for the chemical domain", Meas. Sci. Technol. 17 (8), pp. 93-116, 2006

[2] S. Nolte, M. Will, J. Burghoff, and A. Tünnermann, "Femtosecond waveguide writing: a new avenue to three-dimensional integrated optics", Appl. Phys. A 77 (1), pp. 109-111, 2003

[3] R. Osellame, V. Maselli, R. Martinez-Vazquez, R. Ramponi, and G. Cerullo, "Integration of optical waveguides and microfluidic channels both fabricated by femtosecond laser irradiation", Appl. Phys. Lett. 90, 231118, 2007

[4] C. Dongre, R. Dekker, H. J. W. M. Hoekstra, D. Nolli, R. Martinez-Vazquez, R. Osellame, P. Laporta, G. Cerullo, M. Pollnau, "Characterization of femtosecond laser written waveguides for integrated biochemical sensing", Proc. IEEE / LEOS Benelux Annual Symposium 2007, Brussels, pp. 27-30.

Grated Waveguide Optical Cavity as a Compact Sensor for Sub-nanometre Cantilever Deflections

L.J. Kauppinen, H.J.W.M. Hoekstra, M. Dijkstra, R.M. de Ridder and G.J.M. Krijnen

MESA$^+$ Research Institute for Nanotechnology, University of Twente,
7500 AE Enschede, The Netherlands

L.J.Kauppinen@utwente.nl

Abstract. **We propose a novel and highly sensitive integrated read-out scheme, capable of detecting sub-nanometre deflections of a cantilever in close proximity to a grated waveguide structure. We discuss modelling results for an SiO_2 cantilever to be integrated with an optical cavity defined by a grated Si_3N_4 waveguide.**

1. Introduction

Microcantilever-based sensors can be used to detect molecular adsorption, which causes changes in the surface stress [1], leading to deflection of the cantilever. Often, an optical beam deflection method is used to measure the cantilever deflection [2]. Although the method is simple and accurate, it is bulky, and therefore dense and compact integration of cantilever sensors is not possible with this method.

Different designs for integrated optical read-out of microcantilever deflection have been proposed and demonstrated e.g. [3] and [4]. Based on our simulations we propose a compact, novel and highly sensitive integrated read-out scheme to detect small deflections of a cantilever in close proximity to a grated waveguide (GWG) structure.

2. Device structure and principle of operation

We consider a grating defined in a shallow ridge silicon nitride (Si_3N_4) waveguide (WG), as shown in the inset of Fig. 1. The grating can be realized e.g. with laser interference lithography [5]. A very compact and stable sensor element can be realized by monolithically integrating a microcantilever structure with the GWG, using conventional layer deposition and sacrificial layer etching techniques. The cantilever core material can be silicon dioxide (SiO_2) or Si_3N_4.

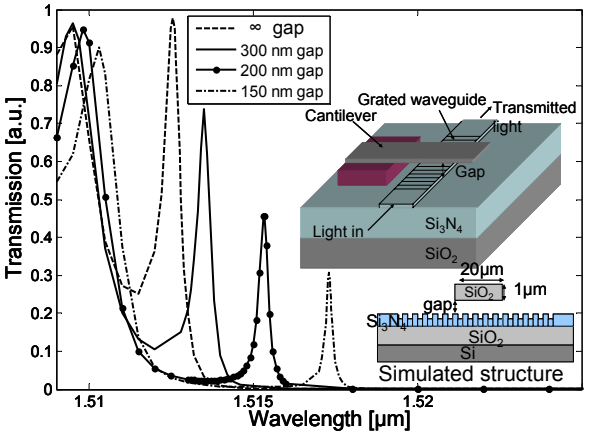


Fig. 1. Simulated transmission spectra of a 200-period grating, with the cantilever position as parameter, using a 2D bidirectional eigenmode propagation method [8]. Insets: device structure and its 2D model.

The device can be functionalized by depositing a sensitive layer on top of the cantilever, e.g. palladium (Pd) for hydrogen (H_2) sensing. Absorption of H_2 into Pd will cause the cantilever to bend [6]. This bending of the cantilever can then be optically detected

by exploiting the properties of the GWG.
The presence of a dielectric object, in this case a cantilever, in the evanescent-field region of the GWG may lead to the occurrence of propagating modes for wavelengths inside the stop band of the grating, and so to resonances (defect modes) inside the stop band, as shown in Fig. 1. As the cantilever approaches the grating, the first near band-edge resonance peak is pulled inside the stop band and its spectral width decreases. This effect can be used for the detection of cantilever displacements.

3. One-dimensional modelling

The optical deflection sensitivity (*dT/dgap*) depends strongly on the maximum slope of the transmission peak of the mode that the cantilever pulls into the stop band. Because of noise considerations, the sensitivity depends on the peak amplitude as well. Sensitivity is dependent on width, thickness and initial gap of the cantilever. To analyze the effect of cantilever width on the slope of the transmission peak, 1D calculations were performed applying the transfer matrix method to the cantilever-loaded grating structure. The cantilever-induced effective-index change was calculated with a 2D mode solver, and the obtained values were used in the 1D calculations. The modelled 1D grating is composed of layers arranged as HLHL…H'L'H'L'…HLHL, where H and L represent high- and low-index layers, respectively, and H' and L' are the corresponding indices in the cantilever induced defect region. The period of the modelled grating is 490 nm and the refractive indices of the layers H and L are 1.5928 and 1.53211, respectively. The proximity of the cantilever increases the indices below it by ~0.5%. A cantilever induced defect region width of 20 to 30 periods in a 100-period grating produces the steepest slope, as shown in Fig. 2. The slope also depends strongly on the grating length. Using the same method as above, the slope was calculated as a function of grating length. Two cases were studied: (a) the cantilever width is fixed at 20 periods, and (b) the relative cantilever width is constant, in this case at 20% of the total grating length. Doubling the grating length provides more than one order of magnitude slope improvement, as shown in Fig. 3. A large spectral slope means a high quality factor *Q* of the defect mode. However, the 1D method does not account for scattering loss that is often high for a high Q resonance [7].

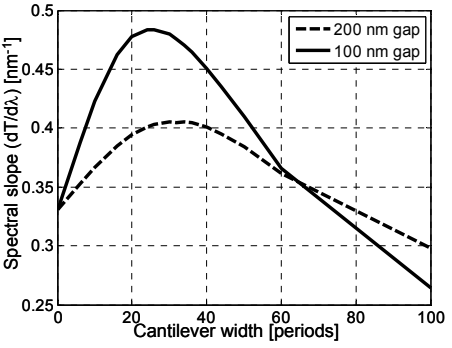


Fig. 2. Spectral slope of defect-mode transmission peak in a 100-period grating versus of cantilever width.

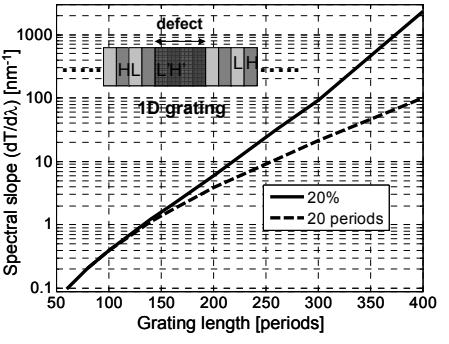


Fig. 3. Spectral slope versus grating length. Dashed line: constant 20 periods defect length; solid line: constant relative defect length (20%). Inset: simulated 1D structure with induced defect region.

4. Two-dimensional modelling

A 2D bidirectional eigenmode propagation (BEP) method [8] was applied to the model shown in Fig. 4, to analyze the effect of cantilever thickness on the deflection sensitivity. The defect-mode spectra corresponding to various cantilever thicknesses are shown in Fig. 5. Thinner cantilevers induce defect modes closer to the stop band edge and with higher transmittance than thicker ones. The difference in slope is small and thus the difference in deflection sensitivity comes mainly from the spectral shift. Since the defect modes of the thicker cantilevers are deeper in the stop band, they experience a larger spectral shift when the gap decreases from infinity to 200 nm. This suggests that the optical sensitivity is higher for the thicker cantilevers at this gap range (∞ to 200 nm).

The optical deflection sensitivity of the grating was calculated with two different cantilever thicknesses, 200 nm and 1 μm. Figure 6 shows the transmitted power versus the cantilever deflection for 2 different initial gaps, 200 nm and 300 nm. The wavelength is fixed at the resonance peak of the corresponding defect mode at each initial gap. Figure 6 shows that the sensitivity at an initial 300 nm gap is higher for the thick cantilever, although the difference is not large. However, at 200 nm gap the thin cantilever is preferred due to a higher transmission power and a slightly higher sensitivity.

The theoretical deflection sensitivity can be estimated from the graphs in Fig. 6. The sensitivity slope of the 200 nm thick cantilever at 200 nm initial gap is 0.058/nm. By assuming that the noise level allows power detection at an accuracy of 10^{-2} (e.g. transmission unit is in μW and noise level is <10 nW), the deflection can be detected with a resolution of 0.17 nm. Higher sensitivity is possible, e.g. with a longer grating, provided that the losses remain low.

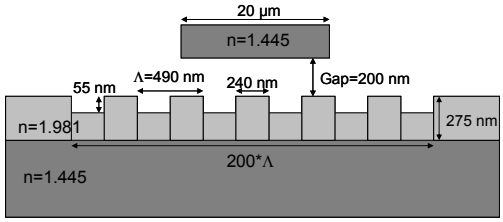


Fig. 4. 2D cross-sectional model of the device used in simulations.

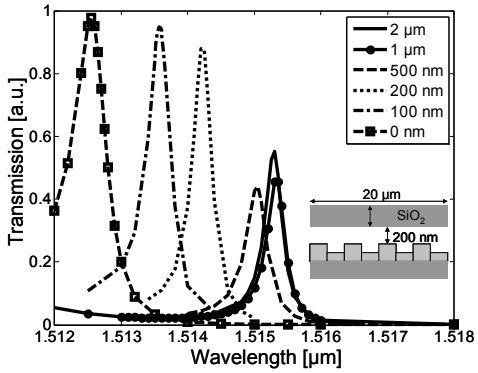


Fig. 5. Defect mode positions obtained with different cantilever thicknesses. Thinner cantilevers induce defect modes that are closer to the stop band edge.

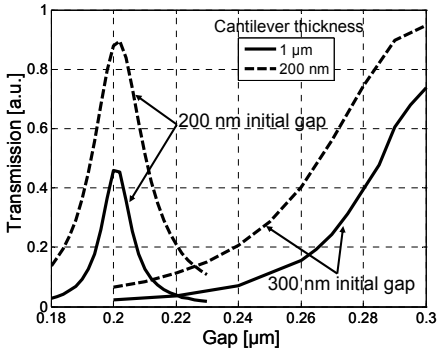


Fig. 6. Simulated transmitted power versus cantilever deflection, calculated for 2 cantilever thicknesses and 2 fixed wavelengths corresponding to resonances at 200 and 300 nm initial gap values.

The choice of cantilever thickness should be carefully considered to obtain maximum sensitivity and stable operation. Thinner cantilevers are more sensitive to mechanical bending that arises from differential surface stress, as follows from Stoney's model [2], $\Delta z = 3\,\Delta\sigma\, L^2(1-\nu)/(Et^2)$, where Δz is the tip displacement of a cantilever having length L, thickness t, Poisson's ratio ν and Young's modulus E, and $\Delta\sigma$ is the differential surface stress. However, the thermal and mechanical stability of thin cantilevers is low due to this high sensitivity. Also, if a thin cantilever is coated with a metal layer, the evanescent field of the WG may reach the metal layer through the thin silicon dioxide layer, increasing optical loss. Partial metal coating can be used to avoid such a loss, but at the expense of smaller sensitive area and therefore smaller surface stress.
From the fabrication point of view, it is convenient to have the initial gap between the WG and the cantilever as large as possible. For the considered WG design, the maximum gap for getting an optical response on downward deflection is around 400 nm. For this initial gap there is not a large difference in optical sensitivity between thin (200 nm) and thick (1 μm) cantilevers.
For maximum sensitivity, a thin cantilever with a small initial gap should be selected, whereas a safer design calls for a thick cantilever with a large initial gap.

6. Conclusions

Based on our simulations we have shown that GWG can be used to sense deflections of micromechanical cantilevers at sub-nanometre resolution. The presented read-out scheme is a good candidate to enable dense integration of cantilever sensors, providing an accurate and stable optical position detection.

Acknowledgement

This research is supported by the Dutch Technology Foundation STW, applied science division of NWO and the Technology Program of the Ministry of Economic Affairs.

References

[1] C. Ziegler, "Cantilever-based biosensors", Anal. Bioanal. Chem., vol. 379, pp. 946–959, 2004.

[2] N.V. Lavrik, M.J. Sepaniak and P.G. Datskos, "Cantilever transducers as a platform for chemical and biological sensors", Rev. Sci. Instrum., vol. 75, pp. 2229-2253, 2004.

[3] C.A. Barrios, "Ultrasensitive nanomechanical photonic sensor based on horizontal slot-waveguide resonator", IEEE Photonics Technol. Lett., vol. 18, pp. 2419-2421, 2006.

[4] M. Nordström, D.A. Zauner, M. Calleja, J. Hübner and A. Boisen, "Integrated optical readout for miniaturization of cantilever-based sensor system", Appl. Phys. Lett., vol. 91, p. 103512, 2007.

[5] W.C.L. Hopman, R. Dekker, D. Yudistira, W.F.A. Engbers, H.J.W.M. Hoekstra, and R.M. de Ridder, Fabrication and characterization of high-quality uniform and apodized Si_3N_4 waveguide gratings using laser interference lithography", IEEE Photon. Technol. Lett., vol. 18, pp. 1855-1857, 2006.

[6] Y.I. Chou, H.C. Chiang and C.C. Wang, "Study on Pd functionalization of microcantilever for hydrogen detection promotion", Sens. Actuators B, vol. 129, pp. 72–78, 2008.

[7] W.C.L. Hopman, H.J.W.M. Hoekstra, R. Dekker, L. Zhuang, R.M. de Ridder, "Far-field scattering microscopy applied to analysis of slow light, power enhancement, and delay times in uniform Bragg waveguide gratings", Opt. Express, vol. 15, pp. 1851-1870, 2007.

[8] OlympIOs Integrated Optics Software. C2V, P.O. Box 318, 7500 AH Enschede, The Netherlands,(http://www.c2v.nl/software/)

Multiaperture Fourier transform arrayed waveguide spectrometer

M. Florjańczyk[1,2], P. Cheben[2], S. Janz[2], A. Scott[3], B. Solheim[1], and D.-X. Xu[2]

[1]CRESS Space Instrumentation Laboratory, York University, Toronto, Ontario, Canada
[2]Institute for Microstructural Sciences, National Research Council Canada, Ottawa, Ontario, Canada
[3]COM DEV Ltd., Kanata, Ontario, Canada
m.florjanczyk@osa.org, pavel.cheben@nrc-cnrc.gc.ca

Abstract. *We present a new Fourier transform waveguide spectrometer concept based on Mach-Zehnder interferometer arrays. Multiaperture input provides a markedly increased optical throughput. Unlike conventional FT spectrometers, the device has no moving parts. Phase and amplitude errors can be readily measured in this device and numerically corrected with no need for costly modifications of the waveguide physical properties. An example of the spectrometer designed for the silicon-on-insulator platform with sub-nanometer resolution is discussed.*

Introduction

Waveguide spectrometers such as waveguide echelle gratings and arrayed waveguide gratings (AWGs) [1] are key devices in optical telecommunication networks. New applications are emerging, including spectroscopy, environmental sensing, and health diagnostics. In spectroscopic applications, a common figure of merit to be maximized is the optical throughput, or *étendue*. Large *étendue*, also referred to as the Jacquinot advantage [2], is an intrinsic property of a Michelson interferometer. This is also one of the main reasons why Fourier transform (FT) Michelson interferometers are currently dominating the field of infrared spectroscopy.

In order to exploit the *étendue* benefit of the Michelson interferometer, we proposed the first Fourier-transform Michelson-type arrayed waveguide grating (AWG) spectrometer [3]. This device further develops the concept by Harlander et al. who proposed replacing the mirrors in a Michelson interferometer by bulk optics diffraction gratings, which results in an obvious *étendue* benefit [4, 5]. Compared to a conventional AWG which is a generalized multi-path Mach-Zehnder interferometer, an FT AWG, as a Michelson-type device, allows for a larger *étendue*. Furthermore, unlike the conventional Fourier-transform Michelson spectrometer which requires moving parts (a scanning mirror), the FT AWG is a static device obviating the need for scanning elements.

To further increase the spectrometer light throughput, we have recently extended the FT AWG concept into configurations with multiple input apertures [6, 7]. In this paper, we present a multiaperture spectrometer based on an array of Mach-Zehnder interferometers. We discuss device fundamentals and also include an example of spectral retrieval for the application in spatial heterodyne observations of water (SHOW) experiment.

Multi-aperture FT Mach-Zehnder interferometer array

The Mach-Zehnder interferometer is an established device both in bulk optics and waveguide implementations. It has periodic transmission characteristics which is a function of the optical path difference between the two interferometer arms. We use

this fundamental property of periodic MZI transmission to form a new type of spectrometer. The spectrometer comprises an array of independent MZIs with different phase delays, as shown schematically in Fig. 1 (left panel). It has a multiaperture input formed by N waveguides each feeding into an individual MZI. An obvious advantage of this device is that the optical throughput is significantly increased by using multiple inputs simultaneously.

The operating principle of the device is as follows. The path difference ΔL_i in the MZI array changes by a constant increment across the array. For a given monochromatic input, different transmission characteristics of each MZI results in a different power value at its output. A monochromatic input results in a periodic (sinusoidal) spatial distribution of power across the different output ports $P^{out}(x_i)$, which is the Fourier-transform of the monochromatic input spectrum. Since the spatial power distribution $P^{out}(x_i)$ and the input spectrum are a Fourier transform pair, a polychromatic input produces a power distribution from which the input spectrum can be calculated using Fourier transformation.

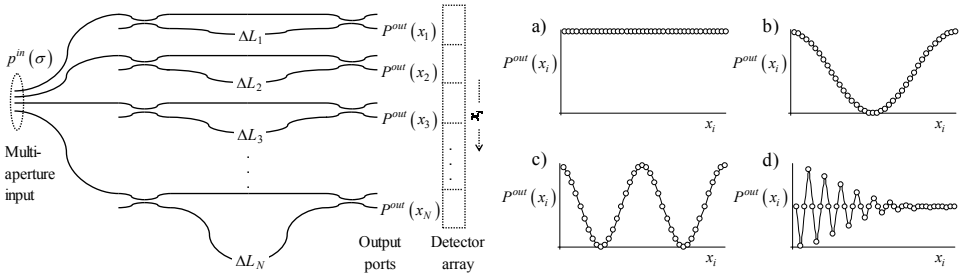


Fig. 1. Left: The schematics of the waveguide spectrometer formed by arrayed Mach-Zehnder interferometers. Right: Spatial fringe formation at the arrayed MZI outputs corresponding to monochromatic inputs at a) the Littrow wavenumber σ_L, b) $\sigma_L+\delta\sigma$, c) $\sigma_L+2\delta\sigma$, and d) superposition of monochromatic inputs.

The MZI array can be designed such that for a particular monochromatic input of a wavenumber $\sigma_L=1/\lambda_L$, a constant spatial power distribution $P^{out}(x_i)$ is obtained at the output, as shown in Fig. 1a. This we denote as the Littrow condition, with the zero spatial frequency corresponding to the Littrow wavenumber σ_L. For $\sigma = \sigma_L$, the phase delays in different MZIs are integer multiples of 2π resulting in constant output spatial power distribution. As the wavenumber of the monochromatic input σ changes from the Littrow value, the output power distribution becomes periodic with the spatial frequency, increasing with $|\sigma-\sigma_L|$. Changing the wavenumber from the Littrow condition to $\sigma_L+\delta\sigma$, where $\delta\sigma$ is the instrument resolution, results in one spatial fringe along the output ports as shown in Fig. 1b. The number of fringes further increases with the increasing wavenumber (Fig. 1c). For a polychromatic signal, a corresponding interferogram is formed by superposition of the respective periodic fringes, as illustrated in Fig. 1d. The input power spectrum can be calculated from the measured interferogram using the discrete Fourier cosine transform [6]:

$$p^{in}\left(\bar{\sigma}\right) = \frac{\Delta x}{N} P^{in} + 2\frac{\Delta x}{N}\sum_{i=1}^{N} F(x_i)\cos 2\pi\bar{\sigma}x_i \qquad (1)$$

where $F(x_i)$ is the measured interferogram, discretized at N equally spaced values of the spatial coordinate x_i corresponding to the outputs of different MZIs, P^{in} is the total input power, and $\bar{\sigma} = \sigma - \sigma_L$ is the normalized wavenumber shifted with respect to the Littrow wavenumber σ_L.

It can be shown [6] that the wavenumber resolution $\delta\sigma$ of the spectrometer is determined by the maximum interferometric delay ΔL_{max}, that is, the delay corresponding to the most unbalanced MZI in the array. A useful expression for ΔL_{max} can be obtained in terms of the resolving power $R = \lambda_0/\delta\lambda$:

$$\Delta L_{max} = \frac{1}{\delta\sigma n_{eff}} = R\frac{\lambda_0}{n_{eff}} \tag{2}$$

where λ_0 is the spectrometer central wavelength and n_{eff} is the waveguide mode effective index. The minimum number of discrete points N in the interferogram, that is the number of MZIs in the array, can be found from the Fourier sampling theorem:

$$N_{min} = 2\Delta x \Delta\sigma = 2\frac{\Delta\sigma}{\delta\sigma} = 2\frac{\Delta\lambda}{\delta\lambda} \tag{3}$$

where $\Delta\lambda$ (or $\Delta\sigma$) is the is the spectrometer operational spectral range. For example, an arrayed MZI spectrometer operating over the 2.5 nm wavelength range at 0.1 nm resolution requires 50 MZIs. Since each MZI couples to a separate input waveguide, in this example the optical throughput is obviously increased by a factor of 50 compared to a single input device.

In addition to the *étendue* benefit, an important advantage of this device is that deviations from the ideal design appear as systematic errors in the interferograms. Once the waveguide device has been fabricated and characterized, the errors can simply be corrected by a software calibration. This calibration ability is an important advantage of our device compared to an AWG. In the AWGs there is no direct physical access to the arrayed waveguide output aperture, which makes measuring and correcting phase errors of an AWG a formidable task. Unlike in an AWG, our device provides physical access to each of the arrayed interferometer outputs where both phase and amplitude errors can be readily measured as part of the spectrometer calibration procedure.

The arrayed MZI spectrometer was simulated for the silicon-on-insulator (SOI) waveguide platform for the application in spatial heterodyne observations of water (SHOW). The SHOW experiment includes detection of water absorption bands on the solar irradiance background in the 2.5 nm wavelength range centered at 1364.5 nm, with spectral resolution 0.1 nm. We choose an SOI with a comparatively thick Si layer (4 μm) to maximize the aperture size of the individual waveguides. According to vectorial mode solver calculations, the etch depth of 2.3 μm and the ridge width of 2.6 μm give a singlemode waveguide with the effective index n_{eff} = 3.4977, where the TE- and TM-like polarization modes are degenerate, as required for polarization insensitive operation. According to Eqs. 2 and 3, for the wavelength resolution of $\delta\lambda$ = 0.1 nm, an array comprising 50 MZIs with the maximum delay ΔL_{max} = 5.32 mm is required. By comparing the ideal water absorption spectrum (Fig. 2, curve a) and the retrieved spectrum (Fig. 2, curve b), it is observed that spectral features finer than the Rayleigh resolution limit (0.1 nm) are not yet resolved. These spectral features can be retrieved by improving the spectrometer resolution from 0.1 nm to 0.025 nm. This is done by increasing the maximum delay from 5.32 mm to 21 mm and using 200 MZI structures

instead of 50. The spectrum retrieved by such a device is shown in Fig. 2, curve e. It is also noticed that the optical throughput of such device is increased by a factor of 200 compared to a single aperture device.

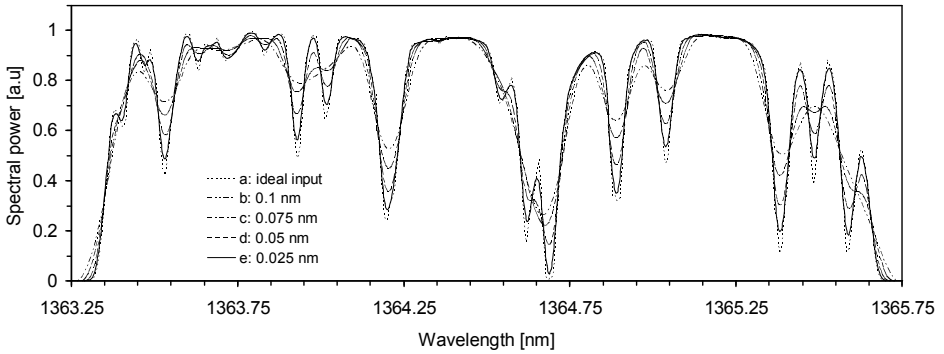


Fig. 2. Ideal input (curve a) and calculated spectra for the arrayed MZI spectrometer with the wavelength resolution of 0.1 nm (b), 0.075 nm (c), 0.05 nm (d), and 0.025 nm (e).

Conclusions

We have discussed a new waveguide spectrometer concept, namely multiaperture Mach-Zehnder interferometer array. Its advantages include a large optical throughput and a static (no moving parts) design. These are important benefits in applications where size and weight are critical. Fabrication robustness is another obvious advantage of this device. Phase and amplitude errors can be readily measured and corrected by calibration software with no need for costly modification of the waveguide physical properties by microfabrication tools.

References

[1] P. Cheben, "Wavelength dispersive planar waveguide devices: Echelle gratings and arrayed waveguide gratings," in Optical Waveguides: From Theory to Applied Technologies, M. L. Calvo and V. Laksminarayanan, Eds., London: CRC Press, 2007, pp. 173-230.

[2] P. Jacquinot, "The luminosity of spectrometers with prisms, gratings, or Fabry-Perot etalons," J. Opt. Soc. Am., vol. 44, pp. 761-765, 1954.

[3] P. Cheben, I. Powell, S. Janz, and D.-X. Xu, "Wavelength-dispersive device based on a Fourier-transform Michelson-type arrayed waveguide grating," Opt. Lett., vol. 30, pp. 1824-1826, 2005.

[4] J. Harlander, R. J. Reynolds, and F. L. Roesler, "Spatial heterodyne spectroscopy for the exploration of diffuse interstellar emission lines at far-ultraviolet wavelengths," Astrophys. J., vol. 396, pp. 730-740, 1992.

[5] I. Powell and P. Cheben, "Modeling of the generic spatial heterodyne spectrometer and comparison with conventional spectrometer," Appl. Opt., vol. 45, pp. 9079-9086, 2006.

[6] M. Florjańczyk, P. Cheben, S. Janz, A. Scott, B. Solheim, and D.-X. Xu, "Multiaperture planar waveguide spectrometer formed by arrayed Mach-Zehnder interferometers," Opt. Express, vol. 15, pp. 18176-18189, 2007.

[7] J. A. Rodrigo, P. Cheben, T. Alieva, M. L. Calvo, M. Florjańczyk, S. Janz, A. Scott , B. Solheim, D.-X. Xu, and A. Delâge, "Fresnel diffraction effects in Fourier-transform arrayed waveguide grating spectrometer," Opt. Express vol. 15, pp. 16431-16441, 2007.

Multi-Waveguide Based Collector for the Detection of Backscattered Light from Highly Scattering Media

N. Ismail, E. J. Klein, G. Sengo and A. Driessen

Integrated Optical Micro Systems Group, MESA+ Research Institute
University of Twente P.O.Box 217, 7500 AE Enschede, the Netherlands
n.ismail@ewi.utwente.nl

Abstract. *A novel technique to collect backscattered light from the surface of highly scattering media is presented. The design parameters for the proposed structure have been determined by simulating light transport in the target medium with a Monte Carlo approach. We also present a comparison of the simulation results with measurements.*

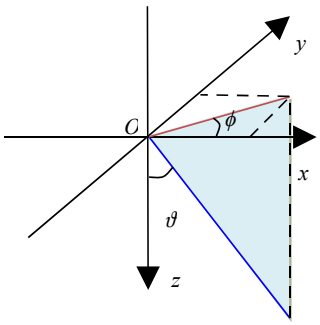
Introduction

The proposed structure is entirely based on integrated optics and is composed of a source waveguide and a number of collector waveguides disposed at increasing distances from the source and in direct contact with the target's surface. These distances, as will be discussed in the next section, are strongly related to the depth at which the detected scattering events occur. For the correct design of the structure we used a Monte Carlo approach to simulate light transport through the scattering medium and to gather information on the backscattered light, such as the positions and angles at which each output photon is leaving the surface. Different layouts have been fabricated and tested. In each of them the relative positions of the detector waveguides with respect to the source have been changed together with other relevant parameters. The devices have been fabricated in the MESA+ cleanroom using silicon oxynitride (SiON) waveguide fabrication technology[1].

Monte Carlo simulation

Light from a laser source is coupled into a rectangular SiON waveguide. The source waveguide and the detector waveguides end directly in contact with the surface of the sample to be measured. The photons which are not reflected by the surface will interact with the target material being absorbed or scattered. Our main interest is aimed towards the backscattered photons that get directed out of the medium after one or more scattering events. The distribution of the backscattered photons on the surface is of great importance together with their propagation direction and the position inside the medium of the last scattering event. This information allows us to design an efficient coupling mechanism between a hypothetical device and the sample.

The waveguides are SiON channel waveguides with core index of n_c=1.529 and cladding (SiO_2) index of n_{cl}=1.457 designed within the ePIXnet Joint Research Activity on sensors. The spatial distribution of the incident photons is obtained from the mode profile of the input waveguide. For each generated photon we associate an initial direction of propagation that in a polar coordinate system forms an angle ϑ with the z axis and an angle ϕ with the x axis as shown in Fig. 1.a. The origin of the x and y axes is chosen to be in the center of the source waveguide's facet, while the z axis origin is on the sample's surface.



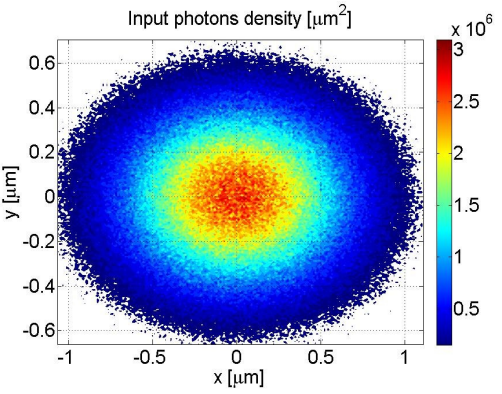


Fig. 1-a) Direction of propagation in polar coordinates.

b) Distribution of incident photons in case of 2 million total photons.

The angle ϕ is uniformly distributed between 0 and 360°, while ϑ is initially distributed between 0 and *arcsin(NA)*, with NA the numerical aperture of the waveguide. Since the waveguide is rectangular we consider two equivalent slab waveguides [2], assuming two different numerical apertures in x and y directions. Each of the randomly generated photons is tracked until it is absorbed or scattered/reflected out of the medium. All the photons that propagate outwards from the surface are considered as output photons: backscattered photons as well as photons that have been reflected from the surface. The two kinds of outputs can be easily distinguished by the program and each output photon is saved into an array that holds the position, the propagation angle relative to the z axis, the optical depth and the penetration depth inside the target as well as the path length of the photon.

Test structure design and fabrication

The devices have been fabricated in the MESA+ cleanroom using our metal-free waveguide fabrication technology [3]. After standard cleaning a PECVD SiON layer of 850nm with a refractive index of 1.53 was deposited on a wafer of 8μm thermal oxide. After resist deposition and development, the wafers were dry etched in a CHF_3/O_2 plasma. A thin layer of LPCVD Si_3N_4 of 20nm was grown to serve as etch stop for the wet etching in case sensing windows have to be defined on the device. On top of the nitride layer, a PECVD cladding layer of 3.5μm SiO_2 with a refractive index of 1.47 was grown. Finally, the wafers were annealed to remove the hydrogen. The final waveguide structure is shown in Fig. 2.a. The architecture, as can be seen in Fig. 2.b, is based on a single source waveguide and multiple detector waveguides disposed in direct contact with the sample (dark region in Fig. 2.b). The container for the liquid sample has been integrated on a chip by wet etching a rectangular area in contact with the collector array and the source waveguides (etching through the Si_3N_4 layer and 5μm in the thermal oxide). Different layouts have been fabricated and tested. In each of them the relative positions of the detector waveguides with respect to the source have been changed together with other relevant parameters such as waveguide width, and distance between the waveguides of the collector.

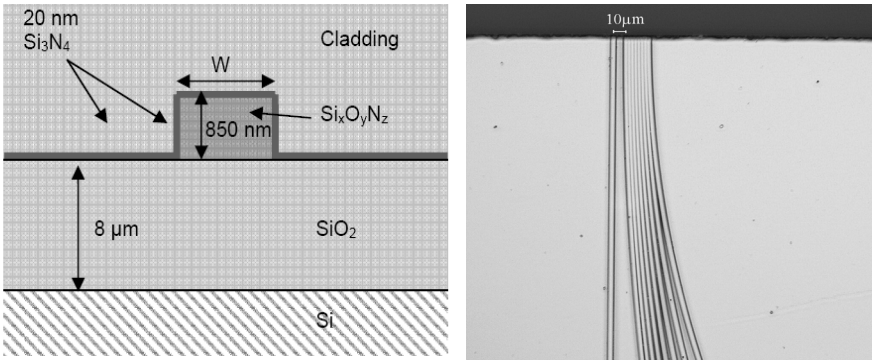


Fig. 2.a) The ePIxnet's JRA Sensors SiON waveguide used in the fabrication of the devices. **b)** Optical microscope picture of a test device.

Comparison of measurements with simulation results

In the Monte Carlo simulation and in experiments we have used commercial milk as the scattering medium. The optical parameters of milk used in the simulation are μ_s'=40cm^{-1}, μ_a=0.01cm^{-1} and g=0.72, where μ_s' is the reduced scattering coefficient, μ_a is the absorption coefficient and g is the anisotropy factor. These values have been found in literature[4] for a concentration of 100% milk at a wavelength of 660nm. As source radiation a He-Ne laser (633nm) was used assuming that the scattering coefficient of milk would not significantly change at this wavelength. This is due to the fact that scattering in milk follows Mie scattering in this range of light frequencies and so it is little affected by wavelength. The simulation results are shown in Fig. 3.

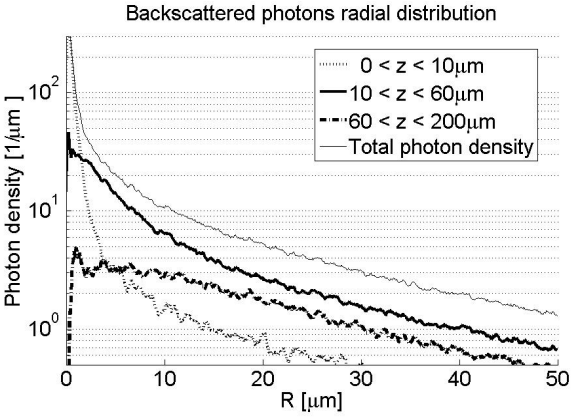


Fig. 3) Density of photons that are scattered to the surface from different depths inside the target medium.

In the experiments two different devices have been measured: the first device has a CSD (collector to source distance) of 25µm, waveguide width of 1.3µm, and waveguide spacing of 1.25µm; while the second device has CSD=10µm, w=1.6µm, and waveguide spacing of 0.95µm. The backscattered light intensity from the 8 output waveguides of the collector has been measured with a photomultiplier. The results of the measurement are shown in Fig. 4, in which the intensity of the detected light is given in function of the distance from the source waveguide for the two devices.

The measured points have been scaled to the simulation by applying a multiplication factor. It is clear that by simply changing the distance of the detector waveguides to the source it is possible to increase the sensing sensitivity only to those photons scattered from a given layer under the surface of the sample as can be seen in . This can be of great interest in spectroscopic applications in which it is mandatory to consider only certain layers of the medium under study.

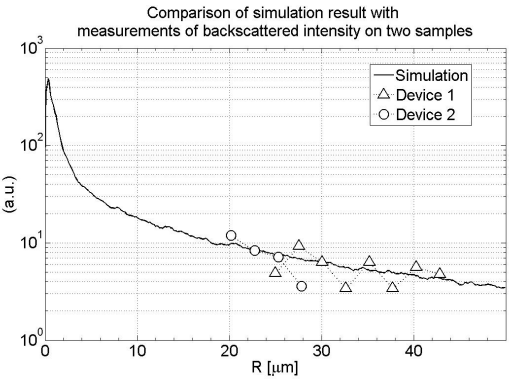


Fig. 4) Comparison of simulated and experimental backscattered intensity measured at the collector waveguides for two different devices. The intensity of the three sets of data is scaled linearly to obtain an optimum overlap.

Conclusions

This study provides a first step towards the design of integrated optics micro devices and sensors which can be directly coupled to the measurand, e.g. biological tissues, without means of lens systems. We have presented a collector system based on multiple waveguides for the detection of backscattered light in highly scattering media. From simulation results it can be seen that it is possible to detect photons backscattered from different depths inside the target by simple changing the CSD parameter.

Acknowledgments: We gratefully acknowledge financial support from the European Network of Excellence ePIXnet and especially from the IOP Photonic Devices supported by Senter and STW.

References

[1] Wörhoff, K., L.T.H. Hilderink, A. Driessen, P.V. Lambeck, Silicon oxynitride: a versatile material for integrated optics application, Journal of the Electrochemical Society, 149, 85-91, 2002.

[2] Michael Munowitz and David J. Vezzetti – Numerical Procedures for Constructing Equivalent Slab Waveguides. An Alternative Approach to Effective-Index Theory – J. of Lightwave Tech. Vol.9, No. 9, September 1991.

[3] Sengo, G. and van Wolferen, H.A.G.M. and Wörhoff, K. and Driessen, A. Optimized Deep UV hardbake process for metal-free dry-etching of integrated optical devices, Proceedings ECIO 2007, 25-27 April 2007, Copenhagen, Denmark. ThG 05-THG 05/1. Technical University Denmark.

[4] J. Taniguchi, H. Murata, and Y. Okamura, Determination of particle size and number of opaque colloidal mixtures using diffuse photon density waves and two-wavelength light sources, Japanese Journal of Applied Physics, vol. 46, No. 5A, 2007, pp. 2953-2961.

[5] Z. Zhao, and R. Myllylä, The effects of optical scattering on pulsed photoacustic measurement in weakly absorbing liquids, Meas. Sci. Technol. 12 (2001), 2172-2177.

InP-Based Photonics Integration

R. Nagarajan, M. Kato, S. Corzine, P. Evans, A. Dentai, C. Joyner, R. Schneider, S. Grubb, F. Kish and D. Welch

Infinera, 169 Java Drive, Sunnyvale, CA 94089
rnagarajan@infinera.com

Abstract. *Monolithic integration on InP has reached complexity levels extending to over 200 discrete functions on a single substrate, including optical signal amplification, and demonstration of multi channel devices capable of aggregate data rates in excess of 1Tb/s. In this presentation we will review the progress in this field.*

Introduction

Monolithic photonic integration has a very long history dating back to the late 1960's, and it is interesting to note that the first proposal for a photonic integrated circuit (PIC) predates the first demonstration of a CW semiconductor laser [1]. Historically InP has been the substrate of choice for monolithic integration with light emitting and passive optical components. Although a lot of progress was made in the last thirty years and integrated components with two to four elements were being manufactured, it was not until four years ago that the first large scale (with component counts higher than 50) PIC (LSPIC) was successfully deployed in long haul telecommunication networks carrying commercial traffic [2].

LSPIC's have been shown to be highly manufacturable and reliable to meet the stringent requirements of carrier grade equipment. At this point, 100Gbit/s (10channels x 10Gbit/s) version of the Infinera PIC, in field deployment carrying live traffic, has passed the 50 million hour mark of operation without any failures.

Scaling of Photonic Integrated Devices

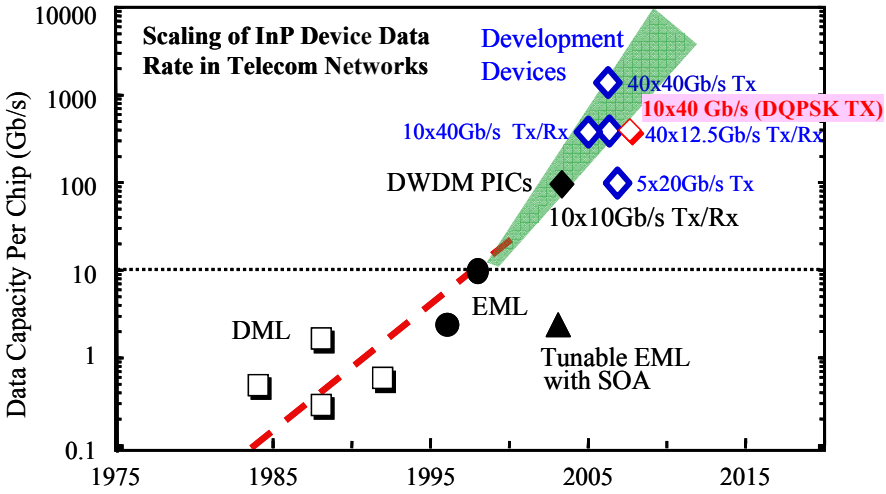


Fig. 1 Scaling of InP device data rate in Telecom transmission networks

Fig. 1 shows the historical data rate scaling in photonic integrated circuits [2,3,4] deployed in commercial transport networks (the devices under development at Infinera are shown in blue for comparison). From mid 1990's to until the introduction of the 100Gbit/s LSPIC four years ago, the data rate for an optical integrated device was largely flat at 10Gbit/s. We have since then demonstrated 40 channel transmitters with per channel data rates up to 40Gbit/s with the NRZ modulation format. The total aggregate data rate from such an integrated device is in excess of 1Tb/s. More recently we have developed 10 channel, 40Gbit/s per channel, DQPSK PIC's [4] which enables us to deploy transport systems with higher spectral efficiency in the fiber. The DQPSK PIC's have integrated Mach Zehnder (MZ) modulators whilst the current generation PIC's have integrated electro absorption modulators (EAM).

We have also demonstrated high functional count devices (transmitters and receivers with up to 40 channels) integrated with semiconductor optical amplifiers (SOA) [5,6]. The requirement for polarization independent, multi channel operation makes integrating the SOA's in a receiver PIC especially challenging. We have demonstrated (see Fig. 2) 10 channel, receiver PIC's with wide optical bandwidth SOA with median gain in excess of 22dB, and worst case polarization dependent gain (PDG) of less 0.8dB in manufacturing [5]. The intrinsic noise figure of the SOA (not including fiber coupling) is a little under 4dB.

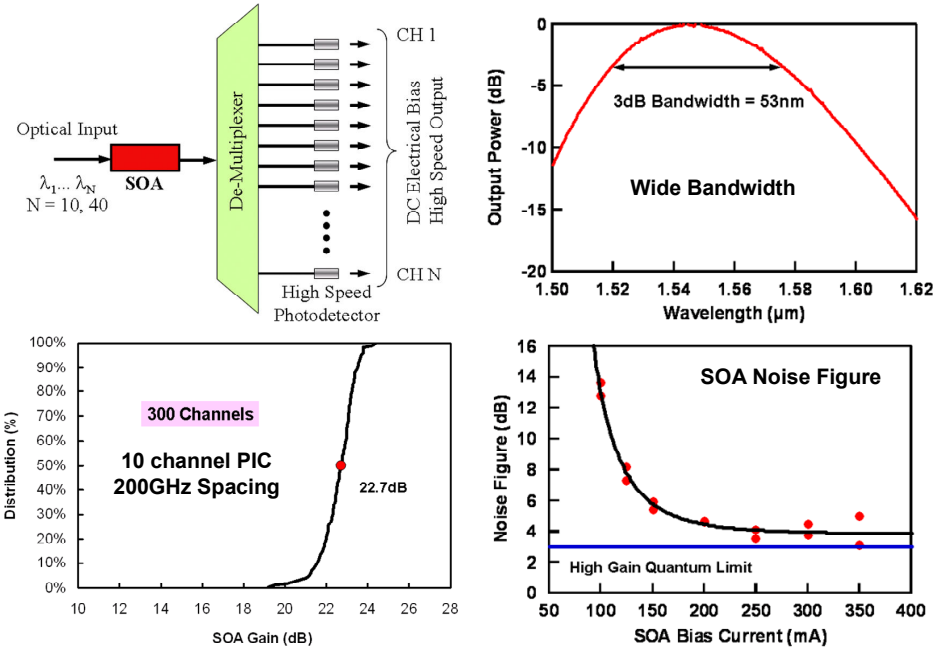


Fig. 2 Characteristics of SOA integrated multi channel receiver PIC.

In the talk we will review these results and give a historical perspective on the progress in the field if InP based photonic integration.

Acknowledgment

The work at Infinera would not have been possible without the collaboration of a special group of very talented engineers. We would like to acknowledge their contributions to the field of photonic integration.

References

[1] R. Nagarajan, and M. Smit, "Photonic Integration", IEEE LEOS Newsletter, pp. 4-10, June 2007.

[2] R. Nagarajan, et al., "Large-Scale Photonic Integrated Circuits", IEEE J. Selected Topics Quantum Electron., vol. 11, pp. 50-65, 2005.

[3] R. Nagarajan, et al., "Single-Chip 40-Channel InP Transmitter Photonic Integrated Circuit capable of Aggregate Data Rate of 1.6 Tbit/s", Electron. Lett., vol. 42, pp. 771-773, 2006.

[4] S. Corzine, et al., "10-Channel x 40Gb/s per channel DQPSK Monolithically Integrated InP-based Transmitter PIC", OFC/NFOEC 2008, paper PDP18.

[5] R. Nagarajan, et al., "Multi-Channel Operation of a Receiver Photonic Integrated Circuit with an Integrated Semiconductor Optical Amplifier", ECOC 2007, paper 05.5.5.

[6] S. Murthy, et al., "Large-Scale Photonic Integrated Circuit Transmitters with Monolithically Integrated Semiconductor Optical Amplifiers," OFC/NFOEC 2008, paper OTuN1.

Active plasmonic materials and divices

H. Atwater
CalTech, United States of America

Integrated InP Devices for Advanced Optical Modulation Formats

R. A. Griffin

Bookham, Inc, Caswell, Towcester, UK, NN12 8EQ
Tel. +44 (0)1327 356678 Email robert.griffin@bookham.com

Abstract. *Approaches towards integration with InP technology are discussed for the development of complex optical modulator and demodulator structures for 40Gb/s and 100Gb/s transmission.*

I. Introduction

Both the current adoption of 40 Gb/s transmission occurring in core networks, and demonstrations of 100G Ethernet transport utilise advanced modulation formats rather than simply scaling on-off key modulation from 10 Gb/s. The requirements for advanced modulation formats have provided great impetus for the development of InP-based transmitter and receiver elements, since small size and integrated functionality are increasingly valued. In the following sections, the architecture for two key modulation approaches are outlined, and the design of integrated InP devices which can enable their realisation are described.

II. Applications Requiring Integrated Devices

A. 40 Gb/s DQPSK

While there has been much debate over many years around the preferred modulation format for 40 Gb/s transmission, there is growing consensus that differential quadrature phase-shift key (DQPSK) [1] is the best choice for many applications. As shown in Fig. 1, DQPSK transmits 2 bits per symbol at half the clock rate of binary approaches using dual-parallel Mach-Zehnder modulators (MZMs). Both upper and lower MZMs are configured as binary phase modulators, biased at minimum optical output and driven with pre-coded NRZ data. A relative phase shift of $\pi/2$ between upper and lower branches provides quadrature addition of the 2 fields. At the receive side, a delay-and-add decoder together with a pair of balanced receivers provides binary outputs without requiring additional processing.

Key advantages of DQPSK are resilience to chromatic and polarization-mode dispersion, and reduced spectral width for compatibility with 50GHz DWDM spacing and the use of reconfigurable optical add-drop multiplexers (ROADMs). DQPSK is also advantageous compared to OOK and duobinary in terms of OSNR performance. The use of RZ pulse shaping combined with DQPSK improves the nonlinear resilience of DQPSK for long-haul transmission, and provides almost equivalent OSNR performance to binary DPSK.

Currently the main obstacle to wider deployment of 40 Gb/s DQPSK is cost. The greater complexity of DQPSK requires a larger number of components – which presently are designed to meet the demanding requirements of binary 40Gb/s DPSK – leading to high cost. However, the cost of DQPSK subsystems is soon likely to decrease below that of binary 40 Gb/s approaches. The bandwidth requirements of binary

40 Gb/s dictates the use of expensive connectorised modules for MUX, DEMUX, electrical drivers, optical transmitter and optical receivers, together with RF 'plumbing' with cable interconnects. Since DQPSK requires only bandwidths commensurate with 20 Gb/s transmission, surface-mount packaging on PCB assemblies is viable, offering significant savings over binary approaches at the full 40 GHz clock rate. A key step to realisation of this cost saving, however, is the greater integration of optoelectronic functionality discussed in following sections.

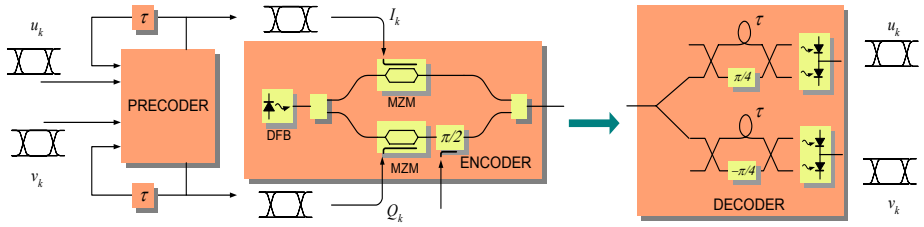


Fig. 1: Schematic illustration of optical DQPSK link.

B. 100 Gb/s PDM-QPSK

Whereas a number of alternative approaches have been considered viable for 40 Gb/s transmission, the demands of 100 Gb/s operation has meant greater focus on a more limited number of approaches. In particular, coherent QPSK transmission employing polarization-division multiplexing (PDM) has attracted much interest. The application of post-receiver digital signal processing (DSP) has been shown to overcome many of the traditional challenges of coherent detection associated with LO stabilization and polarization management [2,3]. Since information from the transmitted optical field can be fully recovered from coherent detection with polarization diversity, post-detection DSP also allows the mitigation of chromatic dispersion accumulated over the transmission span.

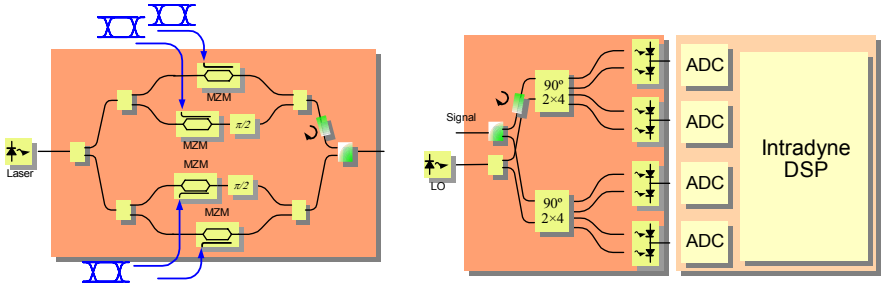


Fig. 2: Schematic illustration of PDM-QPSK link.

As shown in Fig. 2, PDM-QPSK provides 100 Gb/s capacity for a single optical carrier while operating at a 25 GHz clock rate. The 4×25 Gb/s architecture is compatible with low-cost electronic packaging, but – even more so than for DQPSK – is dependent on integration of optoelectronic functionality in order to minimize cost, footprint and assembly complexity.

III. InP MZMs

Efficient electro-optic modulation and tight waveguide confinement allow realisation of InP dual-parallel MZ structures for QPSK modulation with very compact footprint. Figure 3 shows an RZ-QPSK layout (using a third serial MZ for RZ pulse-carving) with a chip size of 7×1 mm^2. The design uses proven 10 Gb/s NRZ technology, based on p-i-n epitaxy on an n+ InP substrate. The multiple quantum well (MQW) modulator core consists of InGaAsP quantum wells and Q=1.1μm InGaAsP barriers, with the guided mode highly confined to the MQW core by deep ridge etching. The RF electrodes of each MZ are independent microstrip elements, with the base of the chip grounded.

By suitably engineering the core thickness and ridge width, a lumped-element design suitable for 10 Gb/s has been modified to a travelling-wave design with impedance well-matched to 50Ω. Results in Fig. 4 for probed chip measurements illustrate S_{11} < 10dB and electro-optic bandwidth exceeding 20GHz, commensurate with 40 Gb/s DQPSK and 100 Gb/s PDM-QPSK operation. V_π for InP MZMs is not a constant, but depends on the *dc* bias and operating wavelength – deeper bias reduces V_π at the expense of additional absorption optical loss. Our design achieves < 3.5V V_π with < 0.5dB voltage-induced absorption over C-band operation. A low value for V_π enables full $2V_\pi$ modulation to maximise optical power and signal quality.

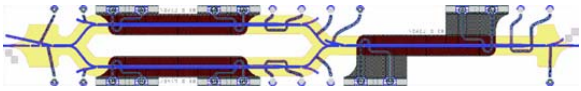


Fig. 3: Layout for integrated InP RZ-QPSK encoder chip.

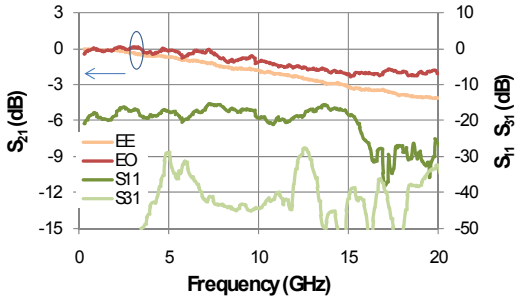


Fig. 4: Measured performance for one MZ element of a QPSK encoder chip.

The separation between upper and lower MZMs shown in Fig. 3 is a compromise between reducing RF crosstalk and minimising optical waveguide bend loss. Differential drive for each MZ is advantageous in reducing crosstalk between the multiple modulators; as shown in Fig. 4, crosstalk between MZs is < -28dB. Multiple InGaAs photodiodes are incorporated monolithically with the modulator structure, allowing monitoring of the critical optical phase shifts in individual and parallel MZMs. In conjunction with short control electrodes, monitor photodiodes enable realisation of a complete control shell for stable operation of the RZ-QPSK transmitter.

Extension of the QPSK encoder to a PDM-QPSK structure like that in Fig. 2 requires replication of the dual-parallel MZMs together with an additional input splitter. While the addition elements for polarisation rotation and multiplexing have previously been

demonstrated in InP, these would require additional process development for our modulator platform. An alternative approach is to perform the polarisation manipulation functions with micro-optics. The small size of InP MZMs makes them well suited to co-packaging with the source laser, with advantages in reduced footprint, greater functionality, and eased assembly. Since our co-packaging approach already utilises micro-optics for modulator-to-fibre coupling, adding additional polarisation elements can be achieved without excessive complexity.

IV. Integrated InP Receivers

While a number of technologies – micro-optic, fibre and PLC – have been demonstrated as viable to perform the delay-and-add functionality for DPSK systems, to date commercial products use a fibre-coupled output in conjunction with fibre-coupled receiver modules. An attractive approach to reduce size, footprint and cost is to integrate all functionality on a single InP chip, combining split, delay and 90° hybrid coupler together with waveguide photodiodes. All the individual elements required have previously been demonstrated on InP. Realisation of a 3dB MMI combiner with integrated balanced detectors was achieved more than a decade ago [4]; more recently an integrated DQPSK decoder incorporating split and delay was demonstrated [5].

Whereas some functionality – hybrid coupler with waveguide photodetection – is similar for both 40 Gb/s DQPSK and 100 Gb/s PDM-QPSK, polarisation management is different for the two approaches. For DQPSK, a key challenge is to control birefringence in order to minimize polarisation-dependent frequency shift (PDF) of the decoder free-spectral range (FSR). For PDM-QPSK, additional polarisation split and rotation elements are required, but design of 90° hybrids and photodiodes is eased, since these may operate with only TE inputs. One attractive option is to adopt micro-optics to perform the delay and polarization-management elements using co-packaging as discussed previously for PDM-QPSK transmitter.

V. References

[1] R. A. Griffin and A. C. Carter, “Optical differential quadrature phase-shift key (oDQPSK) for high capacity optical transmission”, OFC’02, WX 6 (2002).

[2] M. G. Taylor, “Coherent detection method using DSP for demodulation of signal and subsequent equalization of propagation impairments”, IEEE Photon. Technol. Lett. 16, pp. 674 – 676, 2004.

[3] C. Laperle et al, “Wavelength Division Multiplexing (WDM) and Polarization Mode Dispersion (PMD) Performance of a Coherent 40Gbit/s Dual-Polarization Quadrature Phase Shift Keying (DP-QPSK) Transceiver”, PDP16, Proc. OFC/NFOEC 2007.

[4] R. J. Deri et al, “Ultracompact monolithic integration of balanced, polarization diversity photodetectors for coherent lightwave receivers”, IEEE Photon. Technol. Lett. 4, pp. 1238-1240, 1992.

[5] C. R. Doerr, “Monolithic DQPSK Receiver in InP With Low Polarization Sensitivity”, IEEE Photon. Technol. Lett. 19, pp. 1765-1767, 2007.

High bandwidth waveguide photodetector based on an amplifier layer stack on an active-passive semi-insulating InP at 1.55 μm

M. Nikoufard, L. Xu, X.J.M Leijtens, T. de Vries, E. Smalbrugge, R. Nötzel, Y.S. Oei, M.K. Smit

COBRA Research Institute, Technische Universiteit Eindhoven
Postbus 513, 5600 MB Eindhoven, The Netherlands

A waveguide photodetector based on semi-insulating indium phosphide (InP) was designed and fabricated. The layer stack for this photodetector was optimized for use as an optical amplifier or laser. By reversely biasing the structure, an efficient, high-speed photodetector was made, which allows for easy integration of source, detector and passive optical components on a single chip. Based on the simulation results, we designed a $30\,\mu m \times 1.5\,\mu m$ *waveguide photodetector integrated with a passive access waveguide, which has achieved a 3 dB bandwidth of 35 GHz and 0.25 A/W external reponsivity at 1.55* μ*m wavelength at* -4 *V bias voltage.*

Introduction

The photodetector is a key component in the optical communication system[1]. One of the requirements on photodetectors is a high bandwidth-efficiency product. Compared to the top-illuminated photodetector, the waveguide photodetector has the advantage of almost independent relationship between the bandwidth and the efficiency[2]. Although it has a disadvantage in the fiber-chip coupling efficiency, it is easier to be integrated with laser/preamplifier, AWGs, and other passive components. By optimizing the waveguide geometry and absorption layer thickness of the waveguide photodetector, high bandwidth-efficiency product of 55 GHz has been reported[3]. However, the layer stacks of these reported devices are not suitable for the realisation of semiconductor optical amplifiers (SOA) or lasers, which would limit the flexibility in the monolithic integration of the source and the detector. In[1], the laser is based on quantum wells while the photodetector is based on bulk material, and 12.5 Gbit/s per channel is achieved. To ease the technology for such an active-passive integration, we investigate RF bandwidth of the photodetector by using the same layer stack as SOA/laser. For proper RF performance, we use a semi-insulating InP substrate and coplanar waveguide design. The measurement results show that a 30 μm (80 μm) long photodetector can operate up to 35 GHz (28 GHz) with external responsivity up to 0.25 A/W (0.35 A/W) at a wavelength of 1.55 μm.

Design and Fabrication

The layer stack shown in figure 1 which was previously used for fabricating lasers and optical amplifiers[4], is now being used for the realization of high-speed photodetectors. Due to n.i.d. doping in the film layer, this film layer will be completely depleted even under a small reverse bias voltage. Therefore, in the following calculation, the depletion

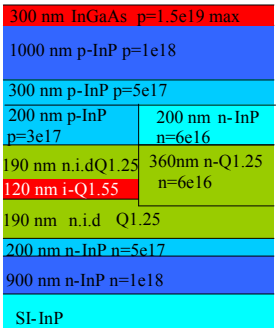


Figure 1: Active-passive butt-joint layer-stack with specifications based on a semi-insulating substrate .

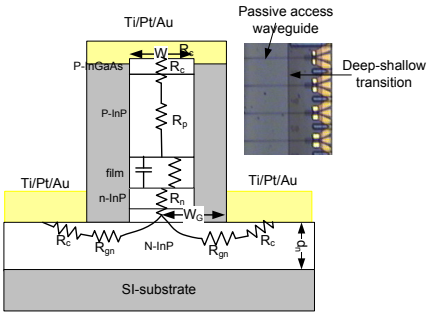


Figure 2: Schematic of the crosssection and a photograph of finished devices.

layer thickness was taken as 500 nm, the same as the thickness of the film, corresponding to a 44 GHz transit time bandwidth[5, 6]. To achieve the best performance, the waveguide photodetector was designed 1.5 μm wide and deeply etched through the film layer to minimize the capacitance. The calculated series resistances[7] are 105 Ω (40 Ω) respectively for 30 μm (80 μm) long photodetector. By assuming the parasitic capacitance of the bond-pad to be 12 fF[7], the calculated RC bandwidth is about 72 GHz (52 GHz). Therefore, the total bandwidth is about 38 GHz (32 GHz) for 30 μm (80 μm) long photodetector, mainly limited by the transit time bandwidth.

The active-passive epitaxial material was grown on a semi-insulating InP substrate by a three-step low pressure metal-organic-vapor-phase epitaxy (MOVPE)[8]. In the active part, a 120 nm thick absorption/active InGaAsP layer (Q1.55, $\lambda_{gap} = 1.55\,\mu$m), embedded between two 190 nm quaternary confinement layers (Q1.25), covered by a 200 nm thick p-InP layer. In the passive part, the film layer (Q1.25) thickness is 500 nm, and n-doped ($N_d = 6 \times 10^{16}\text{cm}^{-3}$), covered by 200 nm thick n-InP layer with same doping level. The common layers for both active and passive part is 1300 nm gradually p-doped InP and 300 nm highly p-doped contact layer InGaAs. All the waveguides were fabricated by RIE. The access waveguide was shallowly etched to minimize the optical transmission loss, and the photodetector was deeply etched and stopped at $1 \times 10^{18}\,\text{cm}^{-3}$ n-InP layer below the film. The etching depth of the photodetector is about 3 μm. Polyimide was spun for passivation and planarization. Before metallisation, firstly we etched back the polyimide in the barrel etcher to expose p-InGaAs. Afterwards, we used the photoresist as a mask to protect the exposed p-contact, and etching the polyimide directionally to open n-InP contact layer. To form the metal contact, Ti/Pt/Au were evaporated on the top p-InGaAs and the lateral grounds (n-InP) through lift-off. Due to the limitation in the lift-off, the gap distance between the p- and n-contact was designed 10 μm. To minimize the RF transmission loss, the fabrication proceeded with the electroplating until the thickness of the gold is about 1.5 μm, which is three times larger than the skin depth[4]. The crosssection and the top view of the finished device are shown in figure 2. The photograph shows the photodetector with its coplanar waveguide transmission line, which are tapered

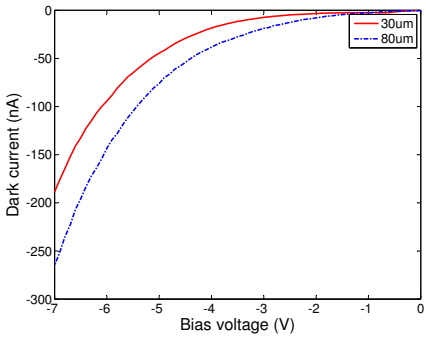


Figure 3: Measured dark current for 1.4 μm wide deeply etched 30 μm long (solid) and 80 μm long (dash) photodetectors.

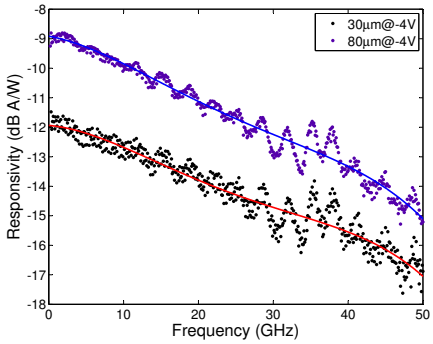


Figure 4: Frequency response of a 30 μm long photodetector (below) and an 80 μm long photodetector. The dot line is the measured data, and the the solid line is the fitting.

from the photodetector to the probepad which has a 100 μm pitch. The central metal is 70 μm wide, and the gap width is 30 μm.

Experimental results

The optical signal is coupled into the waveguide via the cleaved facet of the chip. All measurements were performed using on-wafer probing technique. The photodetectors exhibit low dark current, less than 50 nA dark currents at -4 V bias voltage for the photodetectors up to 80 μm long, figure 3.

On-wafer S-parameter measurements are performed in the range of 10 MHz to 67 GHz with a lightwave component analyzer and a 50 GHz RF-probe. The photodetector was biased at -4 V through a 67 GHz bias tee, and the injected wavelength from the lightwave analyzer is 1.55 μm with -1 dBm optical power. The measured small signal frequency response is given in figure 4. The 30 μm long photodetector achieved 35 GHz 3-dB bandwidth, while the 80 μm long photodetector obtained 28 GHz bandwidth. The measured external reponsivity in the left axis showed that the external responsivity is 0.25 A/W and 0.35 A/W for 30 μm and 80 μm long photodetector, respectively. The measured RC bandwidth from S_{22} is in agreement with the calculated RC bandwidth. The measured total bandwidths are slightly smaller than the calculated bandwidth mainly because the depletion layer thickness is actually thicker than 500 nm under -4 V reverse bias voltage, which further decreased the transit time bandwidth. Furthermore, the actual series resistance extracted from S_{22} is about 125 Ω (60 Ω) for 30 μm (80 μm) long photodetector, higher than the calculated value, which is due to the fabrication and the series resistance of the transmission line and the bondpad.

Conclusions

We demonstrated high-frequency waveguide photodetectors in an amplifier layer stack operating up to 35 GHz with 0.25 A/W external responsivity. This result enables the monolithic integration of source and high performance photodetector based on flexible butt-joint active-passive material without the need for a dedicated detector layer stack.

This work is partly funded by the Dutch National Broadband Photonics Access project and the Dutch National Smartmix project Memphis.

References

[1] M. Kato, R. Nagarajan, J. Pleumeekers, P. Evans, A. Chen, A. Mathur, A. Dentai, S. Hurtt, D. Lambert, P. Chavarkar, M. Missey, J. Bäck, R. Muthiah, S. Murthy, R. Salvatore, C. Joyner, J. Rossi, R. Schneider, M. Ziari, F. Kish, and D. Welch, "40-channel transmitter and receiver photonic integrated circuits operating at per channel data rate 12.5 Gbit/s," *Electron. Lett.*, vol. 43, no. 8, Apr. 2007.

[2] K. Kato, "Ultrawide-band/high-frequency photodetectors," *IEEE Transactions on Microwave Theory and Techniques*, vol. 47, no. 7, pp. 1265–1281, July 1999.

[3] K. Kato, A. Kozen, Y. Muramoto, Y. Itaya, T. Nagatsuma, and M. Yaita, "110-GHz, 50%-efficiency mushroom-mesa waveguide p-i-n photodiode for 1.55-μm wavelength," *IEEE Photon. Technol. Lett.*, vol. 6, no. 6, pp. 719–721, June 1994.

[4] J. den Besten, "Integration of multiwavelength lasers with fast electro-optical modulators," Ph.D. dissertation, Technische Universiteit Eindhoven, Eindhoven, The Netherlands, 2004, ISBN 90-386-1643-0.

[5] R. Sabella and S. Merli, "Analysis of InGaAs P-I-N photodiode frequency response," *IEEE J. Quantum Electron.*, vol. 29, no. 3, pp. 906–916, Mar. 1993.

[6] K. Kato, S. Hata, K. Kawano, and A. Kozen, "Design of ultrawide-band, high-sensitivity p-i-n photodetectors," *IEICE Trans. Electron.*, no. 2, pp. 214–221, Feb. 1993.

[7] Y.-G. Wey, K. Giboney, J. Bowers, M. Rodwell, P. Silvestre, P. Thiagarajan, and G. Robinson, "110-GHz GaInAs/InP double heterostructure p-i-n photodetectors," *J. Lightwave Technol.*, vol. 13, no. 7, pp. 1490–1499, July 1995.

[8] Y. Barbarin, E. Bente, C. Marquet, E. Leclère, T. de Vries, P. van Veldhoven, Y. Oei, R. Nötzel, M. Smit, and J. Binsma, "Butt-joint reflectivity and loss in InGaAsP/InP waveguides," in *Proc. 12th Eur. Conf. on Int. Opt. (ECIO '05)*. Grenoble, France, April 6–8 2005, pp. 406–409.

All Optical Wavelength Conversion Based on Injection Locking in InP Ring Laser

O.Raz, Y.S. Oei, H. J. S. Dorren

Eindhoven University of Technology, PO. Box 512, 5600MB – Eindhoven, The Netherlands
tel:+31 (0) 40 247 3521 fax:+31 (0) 40 245 5197
o.raz@tue.nl

Abstract. *A wavelength converter based on an InP ring laser is demonstrated which requires no external probe signal. Conversion at 100Mb/s results in a wide open eye with a speed limit arising from the recovery time of the natural lasing mode of the long ring cavity (2mm)*

Introduction

All Optical Wavelength Conversion (AOWC) is a key technology for future optical packet switching networks [1]. Popular among AOWC schemes are those based on non-linear effects in Semi-conductor Optical Amplifiers (SOAs) [2] as those can be monolithically integrated. In many of the suggested implementations for AOWC the interaction of two laser signals, pump and probe, is required for the transfer of information from one signal to another. Other methods relying on modulation of a laser cavity by an external laser source such as a semiconductor fiber ring laser are based on Four-Wave-Mixing effects which require both high biasing current of the SOA and high optical power of pump signal[3]. Integrated solutions such as those based on Fabry-Perot Lasers and injection locking [4] require mirrors as part of the laser cavity limiting the placement of such WC in most integrated designs (usually to the end cleaved facet of the chip for simplicity). Recently published work [5], has suggested the use of ring lasers under unidirectional operation for wavelength conversion, but this operation mode of the ring lasers requires relatively high pumping current for sustainable uni-directionality [6].

In this paper we report on the operation of a wavelength conversion scheme which is utilizing a monolithically integrated semiconductor ring laser. The suggested structure is a very compact one and can be made potentially two orders of magnitude smaller if disc lasers are employed[5]. A data signal modulated onto an external optical field and injected into this laser structure via one of the laser's two output waveguides will lock the ring laser to its wavelength, thus completely suppressing the natural lasing mode. An inverted optical signal at the wavelength of the ring laser is thus obtained.

Experimental Set-up and Results

The experimental set-up used is shown in Figure 1. The InP ring laser was placed in a probe station and powered using two different current sources to provide maximal flexibility in optimizing single mode operation. Since the ring laser was fabricated on an all active Q1.25 InP chip, both the ring and the waveguide to which the laser light was coupled had to be electrically pumped. Pumping currents of 320mA and 350mA for the ring and waveguide respectively insured a single mode lasing fiber coupled output power of -8dBm with side mode suppression of approx 18dB (see Fig. 2). The device was cooled to a temperature of 10^{o}C which resulted in lasing at a wavelength of

1548.1nm. The tunable laser's output was set to 1550.05nm & 5dBm, to co-inside with a longitudal mode of the ring laser so that injection locking will occur.

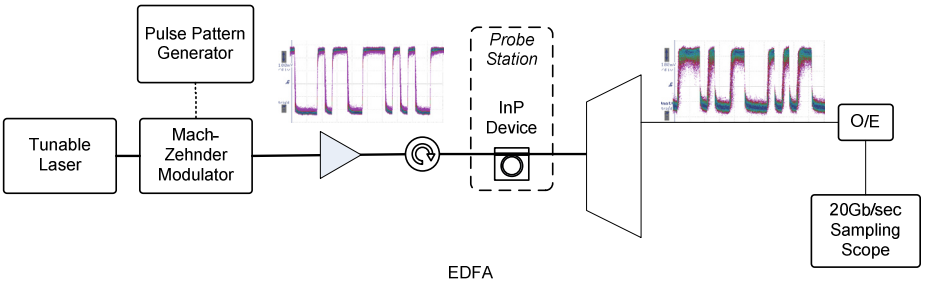


Figure 1 - Experimental Set-up

The laser's output was modulated with a PRBS of 2^7-1 at a speed of 100Mbit/s using a Mach-Zehnder modulator and then amplified using an EDFA with an output power of 8dBm, and a gain of 20dB. The coupling losses into the chip are expected to be 6-10dB, so that actual power coupled to the laser ring structure is around 0dBm. The wavelength converted signal, coming out of the other side of the chip was picked up along with the original signal, filtered with a 100GHz DWDM demultiplexer and then converted to an electrical signal using an APD receiver with a 2.5Gb/s bandwidth.

In Fig. 2, the spectra of the ring laser with and without injection of a modulated signal are shown. The solid line shows the lasing spectrum for the free running laser which is single mode with a suppression of 18dB for the next strongest lasing mode. Under modulated injection the natural lasing mode is shown to drop by 4dB (compared to an expected 3dB for a 50% on-off modulation). This extra 1dB power loss is due to slow recovery time of the natural lasing mode. Also visible in Fig. 2 is the co-incidence of the injected laser with a longitudal mode of the ring cavity.

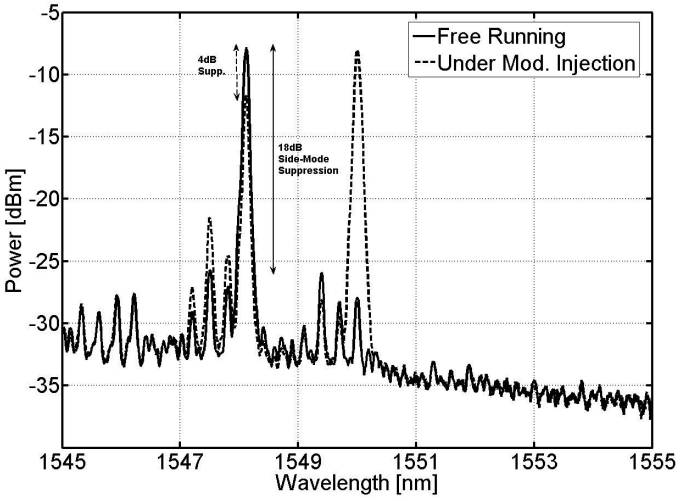


Figure 2 - Lasing Spectra

Finally in Fig. 3 eye patterns for input and output signals are given showing the fast suppression under injection (fast fall time) and slower recovery of the natural lasing mode (slow rise time).

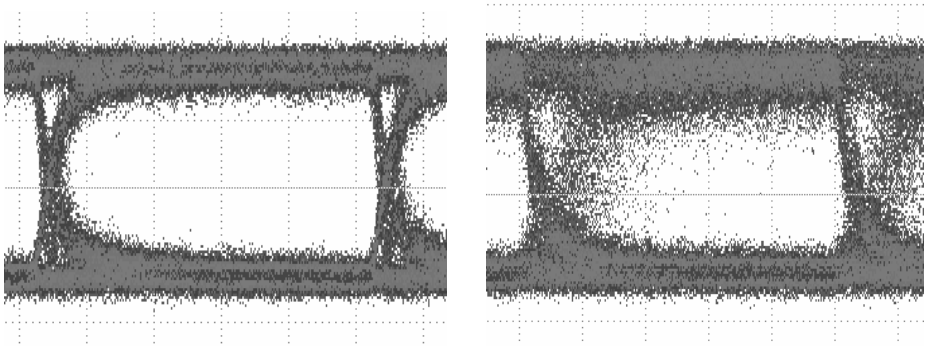


Figure 3 - Input (left) and output eye patterns at 100Mb/s

Discussion and Conclusions

A novel wavelength converter based on injection locking of a semiconductor ring laser is introduced. High extinction ration due to complete suppression of the ring's free running lasing mode is a key advantage while the relatively slow recovery time, of the same lasing mode, limits operation speed. By reducing the ring's size to a few microns in diameters, as was already demonstrated, the same scheme could be used for wavelength conversion at 10Gb/s and perhaps 40Gb/s.

References

[1] S.J. Ben Yoo, "Optical packet and burst switching technologies for the future photonic internet", *J. Lightwave Technol.*, 2006, 24 (12), p. 4468

[2] A.E. Kelly, "Ultra high-speed wavelength conversion and regeneration using semiconductor optical amplifiers", *proceedings of the OFC*, 2001, Mon B1-1

[3] K.K. Chow *et al*, "Widely tunable all-optical wavelength converter using a fiber ring cavity incorporating a semiconductor optical amplifier", *Optics Comm*., 2002, 203, p. 101

[4] Gong-Ru Lin *et al*, "All-optical data format conversion in synchronously modulated single-mode fabry–pérot laser diode using external injection-locking-induced nonlinear threshold reduction effect", *Photonics Technology Let.*, 2005, 17, p. 1307

[5] U. Troppenz et al, "Optical switching of clockwise/anti-clockwise lasing in bus coupled microrings", proceedings of the *IPRM*, 2005, p.307

[6] C.J. Born et al, "Controllable and stable mode selection in a semiconductor ring laser by injection locking", proceedings of the CLEO, 2003, p. CWK4

Experimental investigation of bistable operation of semiconductor ring lasers under optical injection

N. Calabretta[1], S. Beri[1,2], L. Gelens[2], R. Nötzel[1], E.A.J.M. Bente[1], J. Danckaert[2], M.K. Smit[1], and H.J.S. Dorren[1]
[1]Eindhoven University of Technology, PO. Box 512 – Eindhoven, The Netherlands
n.calabretta@tue.nl
[2]Dept. of Applied Physics and Photonics, Vrije Universiteit Brussel, B-1050 Brussels, Belgium

Abstract. *We present detailed characterizations of the bistable operation of a semiconductor ring-laser with emphasis on the response to optical injection. Details revealed that the switching between the two bistable states occurs independently either on the direction and the wavelength of the injected set/reset-signals, while wavelength-detuning of two states was observed.*

Introduction

All-optical bistable memory is one of the crucial components required to realize an ultra-fast packet switched cross-connect node [1]. Monolithic semiconductor ring lasers (SRL) are good candidates to realize an all-optical bistable element due to the nonlinear coupling mechanisms between the clockwise (CW) and counter-clockwise (CCW) propagating modes. Exploiting the nonlinear dynamics, optical memories were demonstrated [2-6]. In [2], two coupled ring lasers where employed to obtain a bistable device which can be externally triggered. Bistability in a single SRL has been demonstrated in [3, 4] by using an external electrical control. The capability to control the SRL by an external optical signal is more attractive than the electronic control because it allows the processing of the signal in all-optical manner without optical-to-electrical conversion stage. A first interesting experimental evidence of directional bistability in a single SRL induced by external optical signal was shown in [5, 6]. For the set (reset) bistable operation, the SRL required an optical control signal injected in the direction opposite to the lasing direction. However, besides those works important details on set/reset switching dynamics and optical spectral analyses of the two unidirectional bistable modes have not been presented yet.
In this paper, we present a detailed characterization of bistability operation in SRL with special emphasis on the response to optical injection. We analyze in detail the effects of the optical power, the direction and the wavelength of the injected set/reset signals on the operation of the optical memory, and we report time domain analyses on the switching between the two states. In contrast with [6], we found out that the directional switching occurs independently of the direction and of the wavelength (at the SRL resonance) of the injected set/reset signals. Those effects have a practical impact in the realization of an optical memory and can be useful to obtain a refined SRL model.

Experimental characterization of the bistable memory

The experimental set-up and the micrograph of the layout of the SRL employed for the investigation of the SRL based optical memory is depicted in Figure 1. The SRL was grown on n-type InP (100) substrates by metal-organic vapor-phase epitaxy (MOVPE). The active region, is a 120 nm thick lattice-matched $\lambda = 1.55$ µm bulk InGaAsP layer placed in the center of a 500 nm thick $\lambda = 1.25$ µm InGaAsP waveguide core. Bottom

and top claddings of the laser structure are 500 nm n-InP buffer and 1.5 μm p-InP with gradual doping levels completed by a 50 nm p-InGaAs contact layer. The ridge waveguides are 2 μm wide. The ring is 2.0 mm long and thus a free-spectral-range (FSR) of 40 GHz. In order to minimize reflections, the bends have a radius of curvature which decreases adiabatically down to 100 μm in order to avoid offsets between straight and curved waveguides. The directional coupler is 200 μm long and the gap is 0.9 μm in width. The reflectivity of the cleaved facets of the output waveguides is reduced by the 7^o angle and anti-reflection coating. The laser has three separate electrical contacts as illustrated in figure 1. The larger contact is used to bias the ring and the directional coupler and it was set to 288 mA. The output waveguide current was set to 30 mA. The temperature of the chip was set to 6.5 degree Celsius. Under those conditions the SRL operates in unidirectional single mode with directional bistability, which allows bistable operation under optical external signals. The CW propagating mode and CCW propagating mode represent state 1 and state 2 of the memory, respectively. In figure 2a the optical spectra recorded with a high resolution (0.18 pm) OSA of the CW and CCW modes is reported when the optical memory is in the initial condition set in state 1. The directional extinction ration (DER) was higher than 35 dB.

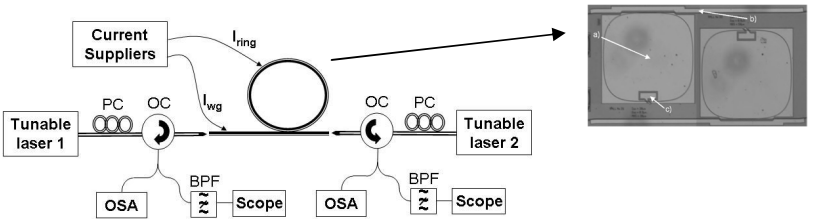


Fig 1. Experimental set-up for SRL characterization. Chip top-view and ohmic contacts are also reported.

First, we investigate the response of the bistable device with respect to the direction of injection of the set/reset signals. The wavelengths of the set and reset signals were 1561 nm and 1561.28 nm, respectively. Starting from the memory set in state 1 as shown in figure 2a, we injected the optical set signal counter-propagating to the CW lasing mode. As a result, the memory commutes to state 2, as reported in figure 2b. The measured DER was higher that 35 dB. We inject the reset signal counter-propagating to the CCW lasing mode to commute the optical memory back to state 1. The optical spectra are shown in figure 2c. Note that between 'state 1' and 'state 2' there is a wavelength difference of 0.037 nm (4.625 GHz). It is worth to mention that if a reset signal at 1561 nm (the wavelength of mode representing state 1) is injected, no switch occurred. The choice of the correct wavelengths for set and reset signals is crucial in the operation of the optical memory. The reason is that the cavity's resonances are slightly different when the SRL operates in CW mode or in CCW mode. Therefore, if the injected signal does not match the cavity resonance no power is coupled in the ring and then no switch occurs. As the cavity resonance depends on the length of the ring and the refractive index, the former is fixed at the fabrication stage and the latter depends on the carrier density of the active material, we ascribe the resonance change to a refractive index change due to a different carrier density resulting by a difference of optical power for the CW and CCW propagation modes. Indeed, around 10 dB of optical power difference between the CW and CCW propagation modes can be observed from figure 2a and 2b.

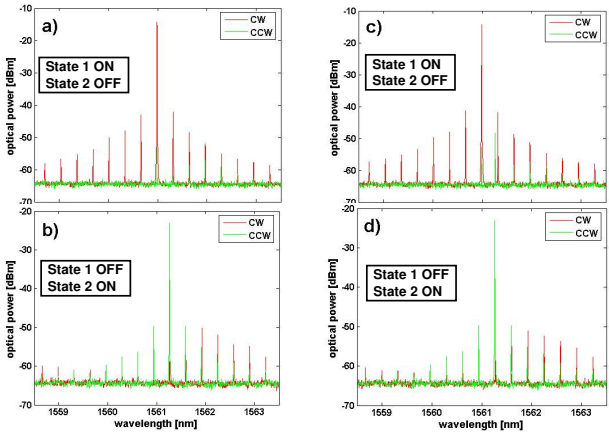


Figure 2. Optical spectra of the CW and CCW modes at different memory states.

Bistable switching has been performed by injecting the set/reset signals in the counter-propagation direction with respect to the lasing mode. To show that the switching can occur independently of the injection direction, we performed the switching by injecting the set/reset signal in co-propagating direction with respect to the lasing mode. Figure 2d shows the performed switch from 'state 1' to 'state 2' by injecting the set signal co-propagating to the CW lasing mode. Then we applied a reset signal co-propagating to the CCW lasing mode to set back to state 1 (shown in figure 2a). Thus, the results obtained in figure 2 demonstrate that the switching between different states is independent of the injection direction, but it is very important the choice of the wavelength of the set and reset signals. Indeed, by using the correct wavelength for the set and reset signal, directional switching between the two bistable modes occurs independently of the injection direction. However, since those two wavelength differ, no switch occurs if the same wavelength is used for both set and reset operation.

We also investigated the switching operation of the memory with respect to the wavelength of the injecting set/reset signals. We observed that switching from state 1 (figure 3a) to state 2 (figure 3b) can be obtained by injecting a set signal at 1559 nm, while a reverse operation (figure 3c) was obtained by injecting a reset signal at 1563.25 nm. In figure 3d shows the optical spectra after injecting a set signal at 1563.28 nm. Those results thus confirm that the switching can be performed by injecting the set/reset signals at the wavelength matching any of the resonance modes of the SRL, as soon as the wavelength is within the SRL gain bandwidth and at one of the ring resonance.

We also reported measurement of the switching time between the two bistable states. Figure 3e shows the time domain traces of the switching of the memory between the CW and CCW propagating modes. The measurements were recorded using the static set-up shown in figure 1 setting the trigger of the real-time oscilloscope on positive and negative slope events. The measured switching speed was 1.5 ns. Faster operation can be obtained by reducing the dimension of the laser [2]. Moreover, the figure 3e confirms the optical power difference between the CW and CCW propagating modes.

In figure 3f the optical transfer function of the state 1 (state 2) is reported as function of the optical input power of the set (reset) signal. The optical power is to be considered at the chip input after the tapered fiber employed to couple the light into the SRL.

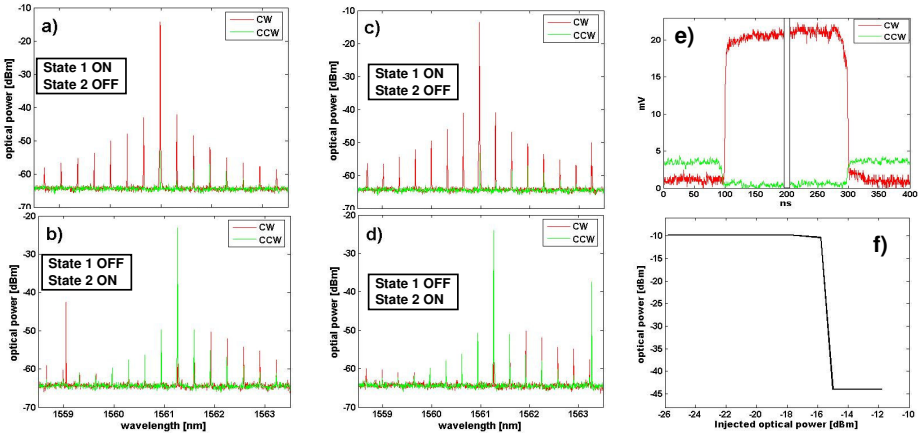


Figure 3. a-d) Optical spectra of the CW and CCW modes for injected signal at different wavelengths. e) Time domain traces showing the switching between bistable states. f) Optical transfer function of state 1 (state 2) as function of the optical input power of the set (reset) signal.

Once reached the threshold (-15.7 dBm), the optical memory abruptly switches to the other state. It is worth to note the extremely low power operation required for switching. This is very important in case of cascading several devices in more complex configuration, such as buffers. Indeed, to drive the next cascaded SRL memory, the output power of the memory should be higher than the required switching power.

Conclusions

We presented a detailed characterization of bistability operation in SRL with special emphasis on the response to optical injection. We analyze in detail the effects of the optical power, the direction and the wavelength of the injected set/reset signals on the operation of the optical memory, and we report time domain analyses on the switching between the two states. We found out that the directional switching occurs independently of the direction and of the wavelength (at the SRL resonance) of the injected set/reset signals. Details also reveal a wavelength detuning between the two bistable modes that in practice implies the use of detuned wavelengths for the set and reset signal. Those results have a practical impact in the realization of an optical memory and can be useful to obtain a refined SRL model.

References

[1] D.J. Blumenthal et al, "All-optical label swapping networks and technologies", *Journal of Lightwave Technology,* vol. 18, 2058-, 2000.

[2] M.T. Hill et al, "A fast low-power optical memory based on coupled micro-ring lasers"**,** Nature, vol. 432, pp. 206-208, 2004.

[3] M.F. Booth, A. Schremer, and J.M. Ballantyne, "Spatial beam switching and bistability in a diode ring laser," Applied Physics Letters, vol. 76, pp. 1095-1097, 2000.

[4] C. Born, M. Sorel, and S. Yu, "Linear and nonlinear mode interactions in a semiconductor ring laser", Journal of Quantum Electronics, vol. 41, pp. 261–271, 2005.

[5] M. Hamacher, U. Troppenz, H. Heidrich, and D. Rabus, "Active ring resonators based on GaInAsP/InP," Proceedings of SPIE, vol. 4947, pp. 212-222, 2003.

[6] S. Yu et al, "Optically triggered monostable and bistable flip-flop operation of a monolithic semiconductor ring laser", Photonics in Switching, WA2.5, San Francisco, USA, 2007.

Method for polarization effect suppression in semiconductor optical amplifiers

L.M. Augustin, J.J.G.M. van der Tol, E.J. Geluk, Y.S Oei, M.K. Smit

COBRA research institute
TU Eindhoven, Eindhoven, the Netherlands
l.m.augustin@tue.nl

Abstract *- In this paper a new method is demonstrated for the suppression of polarization dependent operation of a semiconductor optical amplifier (SOA). This scheme averages out the polarization dependency by integrating a polarization converter in between two half SOAs. The concept is investigated with simulations and the operation is experimentally demonstrated.*

Introduction

In SOAs the polarization dependent behaviour can be problematic, leading to different propagation, amplification and non-linear phase shifts for the two orthogonal polarizations. To overcome this problem, different approaches can be applied. One approach is to remove polarization dependency by changing the properties of the material [1] or the geometry of the waveguides [2]. This can be very hard and even impossible, and furthermore will always be compromising with respect to optimal performance for one of the polarization states. These strategies are all focussed on equalizing the gain between the two polarizations. The refractive index, and hence the phase transfer, is not equal in these cases.
An obvious solution is polarization diversity: the input polarization is split and subcircuits are created for each of the two polarization states. This is a bulky solution.
In this paper an alternative solution is presented, based on on-chip polarization handling: the polarization is changed halfway the SOA and hence the polarization properties are averaged out. In this way, components optimized for one certain state of polarization and the overal performance of the device is polarization independent.

Principle

In a PESSOA (Polarization Effect Suppression in Semiconductor Optical Amplifiers) device, on-chip polarization manipulation is employed to avoid polarization dependency. The principle is depicted in Fig. 1. A polarization converter (PC) is placed halfway in an SOA, causing any arbitrarily polarized signal at the input to experience TE-amplification and TE-phase shift in one half of the device, but TM-amplification and TM-phase shift in the other half. The net effect is in principle polarization independent, both for amplification and phase shift.

Simulations

VPI transmission maker is used to investigate the performance of the PESSOA structure and compare it to a standard SOA. The SOA model is a simple rate equation model. The SOA is polarization independent, but a polarization dependent gain (PDG) is obtained

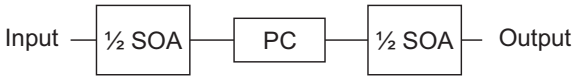
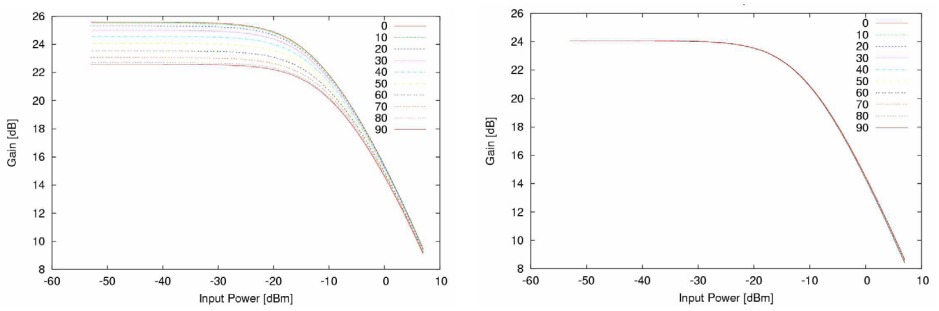


Figure 1: Schematic of PESSOA (Polarization Effect Suppression in Semiconductor Optical Amplifiers).

by placing a polarization dependent attenuator, having 3 dB difference in attenuation, in front of the SOA. The polarization converters are ideal components.
In this article only the dependence of the gain is considered. In Fig. 2, the gain as a function of input power is plotted for the two cases: the standard SOA and the PESSOA. From the plots it is clear that in the linear regime of the SOA complete compensation



(a) Standard SOA (b) Cascade PESSOA

Figure 2: Simulated gain in SOA and PESSOA.

can be achieved for PESSOA. As the device saturates, the PESSOA averages the transfer and still full compensation is obtained. This is advantageous over a polarization diversity solution in which polarization dependency is present in saturation, because the SOAs do not receive the same power at their inputs and hence their saturation is not equal. It is anticipated that the phase transfer, specially for non-linear operation of the SOAs is also polarization independent in the PESSOA case.

Design and fabrication

The PESSOA devices are designed to be integrated in an active-passive butt-joint integration scheme [3] extended with polarization handling capability. The extended generic platform is obtained by adding polarization converters, based on the design in [4].
The active layerstack used for the SOAs contains 8 unstrained InGaAs quantum wells and 9 strained InGaAs barriers centered in a 500 nm thick Q1.25 waveguide layer. The passive waveguide is a 500 nm thick Q1.25 layer. The layers are grown on an N-InP substrate. The topcladding consists of a 1.5 µm thick P-InP layer. The top contact is made on a 100 nm InGaAs layer, this layer is selective removed on the passive waveguides.
All the waveguides used in the PESSOA devices are 3 µm wide. The SOAs are 2 µm wide, both are shallowly etched, 100 nm into the waveguide layer. The SOAs and the passive waveguides are connected using 150 µm long tapers. The waveguides enter the active region at an angle of 10° to avoid reflections from the butt-joint interfaces. Furthermore

the waveguides are placed at an angle of 7° with respect to the facets of the chip, again to avoid reflections from the facets without the need for anti-reflection coating.
The SOAs fabricated in this way are very polarization dependent for low injection currents.
The fabrication is similar to the fabrication described in [4], all waveguides but the polarization converters are defined using optical lithography, the converters are defined using Electron Beam lithography (EBL). The EBL written patterns are aligned to optically defined alignement marks. The fabrication is extended with a process for the active components. To this end, as a first step, the contactlayer is removed everywhere but on the active region. After the process as described earlier, the chip is planarized and passivated by multiple layers of polyimide. A top P-contact and a backside N-contact consisting of Ti, Pt and Au are deposited. The P-contact is made approximately 1 μm thicker by means of electro-plating. A microscope photograph of the finished chip is shown in Fig. 3.

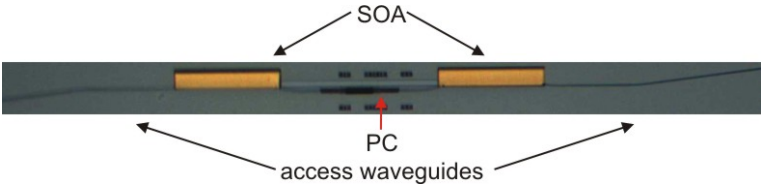


Figure 3: Photographs of the fabricated PESSOA devices.

Measurements

The PDG of the PESSOA is measured with a transmission measurement and compared to a normal SOA processed on the same chip. The PESSOA consists of 2 SOAs with a length of 800 μm each. The standard SOA is 1500 μm long.
A tuneable laser with a polarization maintaining fiber output is used. The light is fed to the input of the devices by using a polarization maintaining lensed fiber. The laser is modulated at a frequency of 1 kHz to be able to detect the light using a lock-in amplifier and to isolate the light from the ASE coming from the SOA.
The power input in the SOA is -15 dBm and hence the small-signal gain is studied. The gain as a function of wavelength is recorded for both TE and TM polarized light. The PDG for both the PESSOA and the standard SOA are plotted in Fig. 4. The measurements demonstrate the principle of PESSOA. A clear improvement is indicated. For a wavelength of 1515 nm a maximum compensation of the PDG of 12 dB is obtained. The compensation works well over a large wavelength range.
Some problems in the realization have to be overcome. The polarization converter has an efficiency of approximately 80% and thus a complete compensation is not possible. The PESSOA has larger losses and hence a lower absolute gain as compared to a regular SOA. The low compensation for wavelengths longer than 1525 nm has to be investigated further.

Conclusions

The PESSOA concept is introduced to improve the polarization independent behaviour of SOAs. It is an averaging solution, in which a polarization converter is placed halfway an

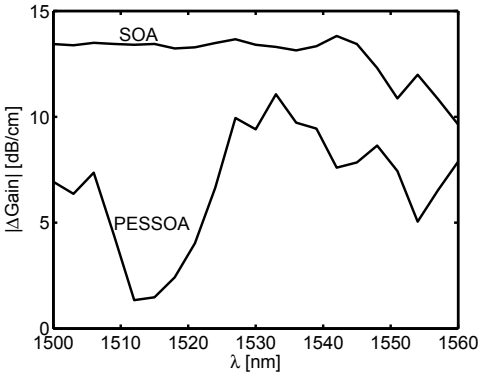


Figure 4: Comparison of the polarization dependent gain as a function of wavelength for PESSOA and a regular SOA.

SOA.
The device is simulated and compared to a standard SOA. The PDG is fully compensated both in the linear and in the saturated regime.
PESSOA devices are fabricated in a generic active-passive integration scheme. The performance of the concept is experimentally demonstrated: the polarization dependent small signal gain is reduced for 12 dB.
Some improvements are required in the process to achieve full compensation and lower losses. The feasibility of a true polarization independent SOA without the need for large circuitry is demonstrated.

Acknowledgements

This work is supported by the European Commission in the IST-MUFINS project, and by the NRC Photonics funded by the Netherlands Foundation for Scientific Research (NWO).
The Centre for Integrated Photonics in Ipswich, UK is kindly acknowledged for supplying the wafer for this experiment.

References

[1] J.-Y. Emery, T. Ducelier, M. Bachmann, P. Doussière, F. Pommereau, R. Ngo, F.Gaborit, L. Goldstein, G. Laube, and J. Barrau. High performance 1.55 μm polarization-insensitive semiconductor optical amplifier based on low-tensile-strained bulk GaInAsP. *Electron. Lett.*, 33(12):1083–1084, June 1997.

[2] P. Doussiere, P. Garabedian, C. Graver, D. Bonnevie, T. Fillion, E. Derouin, M. Monnot, J.G. Provost, D. Leclerc, and M. Klenk. 1.55 μm polarization independent semiconductor optical amplifier with 25 dB fiber to fiber gain. *IEEE Photon. Technol. Lett.*, 6(2):170–172, February 1994.

[3] J.J.M. Binsma, R.G. Broeke, and J.H. den Besten. InP-based photonic integration technology. In *Technical Digest Integr. Photon. Res. (IPR '04)*, page IFB1. San Francisco, USA, Jun. 30–Jul. 2 2004. Invited paper.

[4] L.M. Augustin, J.J.G.M. van der Tol, E.J. Geluk, and M.K. Smit. Short polarization converter optimized for active-passive integration in InGaAsP/InP. *IEEE Photon. Technol. Lett.*, 19(20):1673–1675, October 2007.

Advances in quantum communication using integrated optics

S. Tanzilli, S. Tascu, P. Aboussouan,
O. Alibart, M.P. De Micheli, D.B. Ostrowsky, and P. Baldi

Laboratoire de Physique de la Matière Condensée, University of Nice Sophia-Antipolis,
CNRS UMR 6622, 06108 Nice Cedex 2, France
sebastien.tanzilli@unice.fr

Abstract *- In this paper, we investigate the possibility of increasing the maximal achievable transmission distance of a one-way quantum key distribution link using integrated optical technology on $LiNbO_3$. Based on our experience on guided-wave quantum communication, we studied numerically and fabricated a telecom oriented chip that merges all the necessary optical functions at the heart of a quantum relay based on the quantum teleportation scheme. We report here on experimental characterizations in both classical and single photon counting regimes of this first "quantum relay chip" that allow predicting an improvement of the maximal achievable distance by a factor of 1.8.*

Introduction on quantum communication

In our everyday world, almost all the information exchanged, stored, and processed is encoded using elementary entities called bits, conventionally represented by the discrete values 0 or 1. In today's fiber-based telecommunications systems, these classical bits are carried by light pulses, corresponding to macroscopic packets of photons, allowing a classical description of their behaviour and propagation. To draw a simple picture, each light pulse consists of at least hundreds of photons to encode the bit value 1, or of no photons to encode the bit value 0.

In the past twenty years, physicists have realized that individual quantum objects, for instance photons, could also be employed to deal with another kind of information. Here information is no longer encoded on the number of involved photons, but individual photons merely serve as carriers and quantum information is encoded on their quantum properties, like polarization or time-bins of arrival [1]. Indeed, by selecting two orthogonal states spanning the Hilbert space, $|0\rangle$ and $|1\rangle$ now encode the 0 and 1 values of the quantum bit (qubit), and quantum superposition makes it possible to create states of the form $|\psi\rangle = \alpha|0\rangle + e^{i\phi}\beta|1\rangle$, provided α and β follow the normalization rule $|\alpha|^2 + |\beta|^2 = 1$.

A profound way in which quantum information differs from classical information lies in the properties, implications, and uses of quantum entanglement when two or more particles are involved in the considered quantum system. Here, the information contained in such a system is stored in the form of quantum correlations between the subsystems and have no classical analog. Entanglement is a generalization of the superposition principle to multi-particle systems but in this case the entangled state describing the whole system cannot be factorized, i.e. written as a tensor product of the properties associated with each subsystem. For instance, entangled pairs of qubits implying two particles can be described by a state of the form $|\Phi\rangle_{A,B} = \alpha|0\rangle_A|0\rangle_B + e^{i\phi}\beta|1\rangle_A|1\rangle_B$, with $|\alpha|^2 + |\beta|^2 = 1$, where indices *A* and *B* label the two qubits. Then, measuring for instance qubit A provides a random result, but if we find it to be $|0\rangle$ (with probability $|\alpha|^2$), we learn from the

entangled state that qubit B will be found in the same state for a similar measurement, and conversely for $|1\rangle$. These are the correlations exploited in quantum communication. Let us emphasize that $\{|0\rangle, |1\rangle\}$ can represent any observable related to the considered quantum system. Moreover, from an abstract point of view, the nature of the carrier is irrelevant because only amplitudes and relative phases are exploited in the above states to encode the qubits. It is clear however that photons are the natural "flying qubit carriers" for quantum communication, and the existence of telecommunication optical fibres makes the wavelengths of 1310 and 1550 nm particularly suitable for distribution over long distances.

Quantum communication protocols, such as quantum key distribution (QKD), quantum teleportation [3] and entanglement swapping [4], mainly deal with single qubit and entangled qubit resources. Particularly, QKD offers a provably secure way to establish a confidential key between distant partners commonly called Alice and Bob [2] and is already commercially available [2]. In spite of progress in photonics and telecommunications technologies, losses in optical fibres, and especially dark-counts in the detectors, limit the maximum achievable distance for QKD to about $\sim 100\,km$. A quantum relay, based on quantum teleportation, allows increasing the communication signal-to-noise ratio (SNR) and thus extending this maximum achievable distance [4].

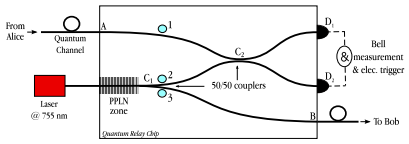
In this context, we show that integrated optics offers the possibility of compact and stable components suitable for enabling quantum communication experiments. More specifically, we will describe in the following preliminary results obtained with a "relay-chip" for fiber-based quantum communication systems.

A quantum relay chip based on the teleportation scheme

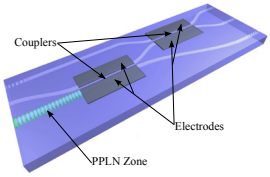
As already mentioned, the channel SNR severely limit the quantum communication distance. Basically, for increasing the maximal achievable distance of a quantum communication channel, one could think that photon amplifiers like those used for telecommunications could be useful. However in quantum communication, only states matter and the no-cloning theorem forbids replicating unknown quantum states with a perfect fidelity [5].

A viable possibility for extending the distance is based on the quantum relay. Here we take advantage of another quantum communication protocol, quantum teleportation. In this scheme, the qubits encoded on photons by Alice are teleported onto other photons at some points along their propagation, for instance in the middle of the channel, without destroying their quantum properties. At the same time, when teleportation succeeds, the final user, here Bob, receives the relayed qubit-photon together with an electrical signal which makes it possible to synchronize his detectors and to increase the SNR of the communication channel and therefore the maximum achievable distance [4, 6]. In the case of long-distance quantum communication, integrated optics on lithium niobate permits realizing a telecom-like quantum relay chip that could provide the relay function, in a compact, stable, efficient, and user-friendly fashion. Figure 1(a) presents the structure's description where all the necessary optical functions are merged on the same chip. We will now discuss how this chip works.

Let's suppose there's an unknown qubit 1, encoded on a photon at $1550\,nm$ and travelling along a fiber quantum channel connected at port A to the relay chip. At the same time, a photon from a laser pulse at $775\,nm$, synchronized with the arrival time of qubit 1, enters



(a)



(b)

Figure 1: (a) – Quantum relay chip, see description in the text. (b) – 3D representation of the quantum relay chip with its two electro-optically controllable couplers C_1 et C_2.

a non-linear zone of the chip which consists of a waveguide integrated on periodically poled lithium niobate (*PPLN*). Thanks to the appropriate choice of the periodic poling grating period (here around $16\,\mu m$), this pump photon can be converted by spontaneous parametric downconversion (SPDC) into an entangled pair of photons (2 and 3) whose wavelengths are also centred at $1550\,nm$ [7]. Then, the first 50/50 directional coupler (C_1) is used to separate the created entangled photons in such a way that photons 1 (sent by Alice) and 2 arrive at the same time at the second 50/50 coupler (C_2). If conditions on the polarization states, central wavelengths, and coherence times are met, photons 1 and 2 can be projected onto one of the four entangled "Bell states". The resulting state is identified by detectors D_1 and D_2 placed at the output of the chip. This measurement signals that the qubit initially carried by photon 1 has been teleported to photon 3 that exits the chip at port B, in theory without any loss in its quantum properties. This has been possible since photon 3 was initially entangled with photon 2 providing quantum correlations that cannot be described classically. In other words, entanglement has to be seen as a quantum resource that is consumed during the teleportation process. Note that the initial quantum state has not been cloned since photon 1, together with photon 2, have disappeared in the measurement. As a consequence the resulting electrical trigger is not only the signature of the presence of the initial carrier photon at the relay chip location but also of the departure of a new carrier photon encoded with the same qubit state, which remains unknown.

From a practical point of view, when this teleportation process is repeated on all the qubits travelling along the quantum channel, we obtain, at the output of the chip, qubits still encoded on photons at $1550\,nm$ but now synchronized with an electrical signal given by the Bell state measurement at detectors D_1 and D_2. This allows triggering Bob's detectors only when the initial qubits have traveled half the distance, leading to an increase of both the SNR and the communication distance. Of course, the price to pay is a reduction of the quantum bit rate since such a chip introduces propagation and interconnection losses. From a technological point of view (see figure 1(b)), the chip features a photon-pair creation zone, two $50/50$ couplers, and tapered waveguides at all input/output ports to maximize the mode overlap between the fibers and the waveguides at the particular wavelength of $1550\,nm$. PPLN waveguide-based photon-pair sources have already been developed in our group [7]. As usual, the SPDC non-linear interaction is ruled by the energy and momentum conservation laws. In this waveguide configuration, the latter is achieved using the so-called quasi-phase matching technique which compensates periodically for the dispersion between the three interacting photons (pump, 2 and 3). This technique allows phase-matching any desired wavelengths. Moreover, the waveguiding structures, ob-

tained by soft proton exchange, enables light propagation with low losses ($\simeq 0.3\,dB/cm$) and very high conversion efficiencies thanks to strong light confinement over long distances ($\delta n \simeq 2.2 \cdot 10^{-2}$). The directional couplers C_1 and C_2 consist of two waveguides integrated close to each other over a certain distance. If the spacing is sufficiently small, energy is exchanged between the two guides. An electro-optical control of the coupling ratio can be made using deposited electrodes. To correctly separate photons 2 and 3 and entangle 1 and 2, we have worked with 50/50 couplers, for both C_1 and C_2.

Experimental characterizations

We therefore studied numerically, and then fabricated, a 4.9 *cm* long quantum relay chip merging all the necessary functions. To implement an actual quantum relay based on such a chip, as depicted in figure 1, we first test separately all the optical functions in the classical regime, i.e. using standard lasers.
The photon-pair source is designed to ensure the conversion of 775 *nm* pump photons into two photons at 1550 *nm*. This can be achieved thanks to lithium niobate periodic polings between 16.4 μm and 16.7 μm. In previous work we have already shown that photon-pair sources based on PPLN waveguides lead to the highest conversion efficiency reported to date and to very high quality of entanglement [7]. Here, the PPLN zone used in our new chip is 10 *mm* long. The SPDC response of this non-linear waveguide zone when pumped by a CW laser at 765 *nm* is represented in figure 2(a).

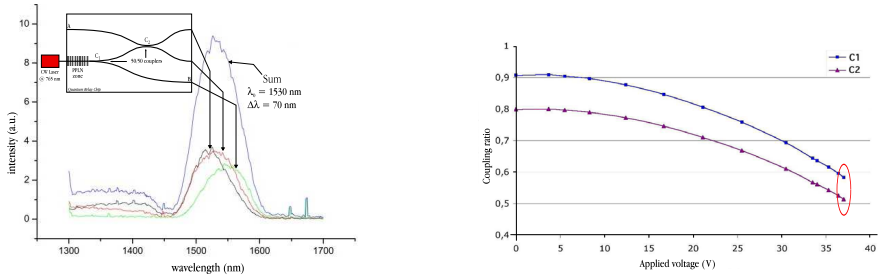


Figure 2: (a) – SPDC from the non-linear waveguide zone, see the text for explanations. (b) – Characterization of the coupling ratios obtained with couplers C_1 and C_2 in both classical (lines) and single photon counting (dots) regimes.

We see in this figure that the SPDC signal is distributed at the three output ports of the chip due to the presence of the two couplers. To characterize significantly the response of the non-linear zone, the sum of these three contributions have been added in figure 2(a). We get here a degenerate signal around 1530 *nm* for a poling period of 16.6 μm and at a temperature of 80°*C*. Both the spectral width and SPDC efficiency are in excellent agreement with theoretical calculations and with previously obtained results for the same poling period (see [7] for more details).
Regarding the couplers, numerical simulations have been carried out using the beam propagation method in order to choose and optimize their size parameters so as to get the 50/50 required ratios. Here the radius of the bends have to be carefully chosen since too small radii would introduce important losses while the opposite would lead to too long a chip. We selected 10 *mm* long bends, corresponding to losses lower than 1 *dB*

for the propagation over the entire component. Note that the waveguides input/output spacing was imposed by external consideration since standard V-Grooves with 250 μm separated fibers were used at both end facets to couple photons into and out of the chip. The interaction length required to transfer half of the energy to the opposite arm is of a few *mm*, and strongly depends on the separation between the two waveguides forming the couplers. Taking into account all these constraints we selected couplers made with 6 μm width waveguides and having a set of parameters going from 5.0 to 5.3 μm for the waveguides separation.
Figure 2(b) presents the characterization of the two couplers in both classical and single photon counting regimes at 1550 *nm*. To carry out the measurements, we launched successively a standard laser and single photons coming from a source previously built in our lab [8]. The results reported here are in good agreement with theoretical calculations. We see moreover that the electro-optical control permits obtaining our necessary 50/50 coupling ratios for a voltage of around 40 V. This is higher than expected but still shows we can correct the coupling length despite fabrication errors. These results show that we obtained couplers fulfilling the requirements for a quantum relay chip. Note that the repeatability of the fabrication was demonstrated to be good since couplers coming from different runs showed the same coupling lengths within a few percent.
Moreover, loss measurements at 1550 *nm* over the entire chip have been performed and shown to be 5.5 *dB* between any couple of input/output ports. This has been made possible using tapered-waveguides at all the input and output ports [9]. This result is in good agreement with the simulations when coupling, propagation as well as separation losses at the couplers are taken into account.

Conclusion and outlook

We have seen that all the elements of the integrated quantum relay have been tested separately: the photon-pair source, the taper-waveguides and the couplers. Taking into account all the above mentioned characterization results, we expect an increase of the maximum achievable distance for a one-way QKD link by a factor of 1.8. Current work now consists of testing this quantum relay chip in the quantum regime, i.e. when actual qubits are first encoded and then teleported through the chip. We believe this is a significant demonstration of the applicability of integrated optical technology to photonic quantum information treatment.

References

[1] G. Weihs and W. Tittel, Quant. Inf. Comp. **1**, pp. 3-56 (2001).
[2] N. Gisin *et al*, J. Mod. Phys. **74**, pp. 145-195 (2002), and references therein, see also `www.idquantique.com` and `www.magiqtech.com`.
[3] I. Marcikic *et al*, Nature **421**, pp. 509-513 (2003).
[4] H. De Riedmatten *et al*, Phys. Rev. Lett. **92**, 047904 (2004), and references therein.
[5] W.K. Wootters and W.H. Zurek, Nature **299**, pp. 802-803 (1982).
[6] D. Collins *et al*, J. Mod. Opt. **52**, pp. 735-753 (2005).
[7] S. Tanzilli *et al*, Eur. Phys J. D **18**, pp. 155-160 (2002).
[8] O. Alibart *et al*, Opt. Lett. **30**, pp. 1539-1541 (2005).
[9] D. Castaldini *et al*, J. of Light. Tech. **25**, pp. 1588-1593 (2007).

Quantum Mechanics with Curved Photonic Structures

Stefano Longhi[1]

[1] Dipartimento di Fisica and Istituto di Fotonica e Nanotecnologie del CNR, Politecnico di Milano, Piazza L. da Vinci 32, I-20133 Milan, Italy
longhi@fisi.polimi.it

Abstract *- Curved waveguide structures provide an accessible laboratory tool to investigate the optical analogues of many quantum phenomena encountered in atomic, molecular, and condensed-matter physics. In this contribution the most relevant quantum-optical analogies will be reviewed, including coherent destruction of tunneling, Bloch oscillations, coherent population transfer, and quantum Zeno effect.*

Introduction

Similarities between quantum and classical phenomena are not uncommon in physics albeit quantum and classical physics are grounded on different paradigms. Such analogies have been fruitfully exploited in emerging research areas such as photonic crystals, quantum computing, nano-devices and new forms of light (see [1] and references therein). Quantum-classical analogies in apparently unrelated fields have been also successfully exploited to mimic at a macroscopic level many quantum phenomena which are currently not of easy access in microscopic quantum systems. In particular, in the past recent years specially-designed waveguide-based photonic structures have proven to be a useful laboratory tool to investigate the optical analogues of a wide variety of coherent quantum effects encountered in different physical contexts, ranging from atomic, molecular, condensed-matter and matter-wave physics. Among others, we mention here the optical analogues of electronic Bloch oscillations and Zener tunneling [2, 3, 4, 6, 5, 7, 8], dynamic localization [9, 10], coherent enhancement and destruction of tunneling [11, 12], adiabatic stabilization of atoms in strong laser fields [13], Anderson localization [14, 15], and coherent population transfer [17, 18, 19]. In particular, the use of coupled waveguides with a curved optical axis introduces a kind of "non-inertial forces" for light waves which are capable of mimicking the effects of electric and magnetic fields on the coherent quantum dynamics of a charged particle [16, 20].
It is the aim of the present contribution to review some of the most relevant quantum-optical analogies, including: coherent destruction of tunneling in driven bistable systems; electronic Bloch oscillations and related effects in crystalline potentials; coherent population transfer and adiabatic passage in laser-driven multilevel atomic or molecular systems; ionization suppression and adiabatic stabilization of atoms in ultra-strong laser fields; quantum decay control and Zeno effect in unstable quantum systems. Besides of general interest, the proposed analogies highlight new and unexpected ways to control light transfer and photon tunneling in integrated photonic structures.

Analogies with solid-state physics

The first broad category of quantum-optical analogies is that between light propagation in curved waveguide arrays and coherent electronic dynamics in crystalline potentials subjected to an applied dc or ac electric field. In this case, spatial light propagation along

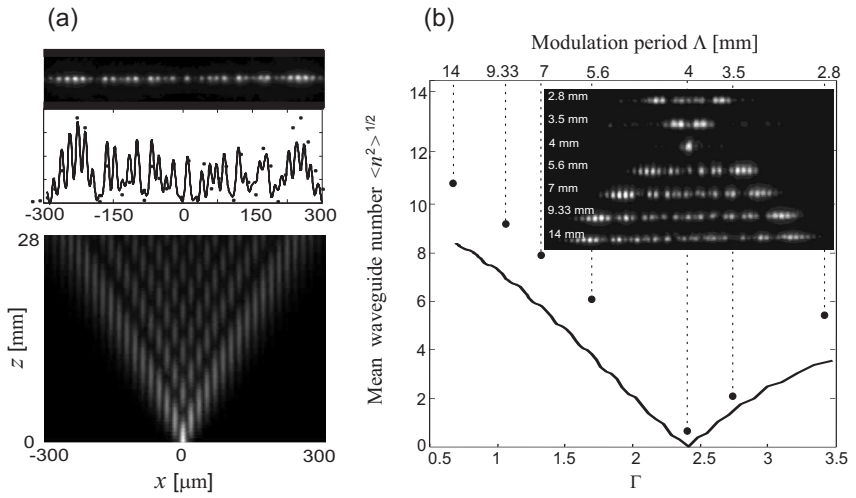


Figure 1: Optical analogue of electronic dynamic localization in an array of sinusoidally-curved waveguides (Ref.[9]). By varying the period Λ of waveguide bending, discrete diffraction in the array [in panel (a)] can be suppressed [see panel (b)].

the curved waveguide array mimics the temporal evolution of an electronic wave packet in the lattice driven by the applied electric field. The use of circularly-curved waveguide arrays mimics the effect of a dc electric field and results in the optical analogue of electronic Bloch oscillations and, at large curvatures, Zener tunneling [2, 3, 4, 6, 7, 8]. In periodically-curved arrays, an ac electric field is instead simulated, which enabled to demonstrate in the optical realm the analogue of dynamic localization [9] of electrons is solids (see Fig.1). Such effects have been observed by mapping the flow of light, visualized from the top of the waveguiding structure, using fluorescence imaging or near-field scanning optical microscopy (SNOM). The introduction of disorder in waveguide arrays have been also proposed and demonstrated to allow for the observation of the optical analogues of Anderson localization and metal-insulator transitions [14, 15]. Additionally, introduction of waveguide twist enables to mimic the dynamics of a Bloch particle in a magnetic field [20].

Analogies with atomic and molecular physics

The second broad category of quantum-optical analogies is that between light propagation in curved coupled waveguides and electronic dynamics and coherent population transfer induced by laser fields in atomic or molecular systems. A single waveguide possessing one (or more) guiding mode and the continuous spectrum of radiation modes behaves like an isolated atom. Introduction of a periodic curvature of the waveguide axis mimics the action of a laser field which can induce optical transitions between bound states of the atom or between a bound state and the continuum (ionization). In the optical system the temporal evolution of the electronic state is mapped into the spatial propagation of the light waves, and can be thus visualized in an experiment by fluorescence or SNOM imaging as briefly mentioned above. In this way, one can observe in the optical realm some unusual and still unexplored effects of atomic physics, such as suppression of ion-

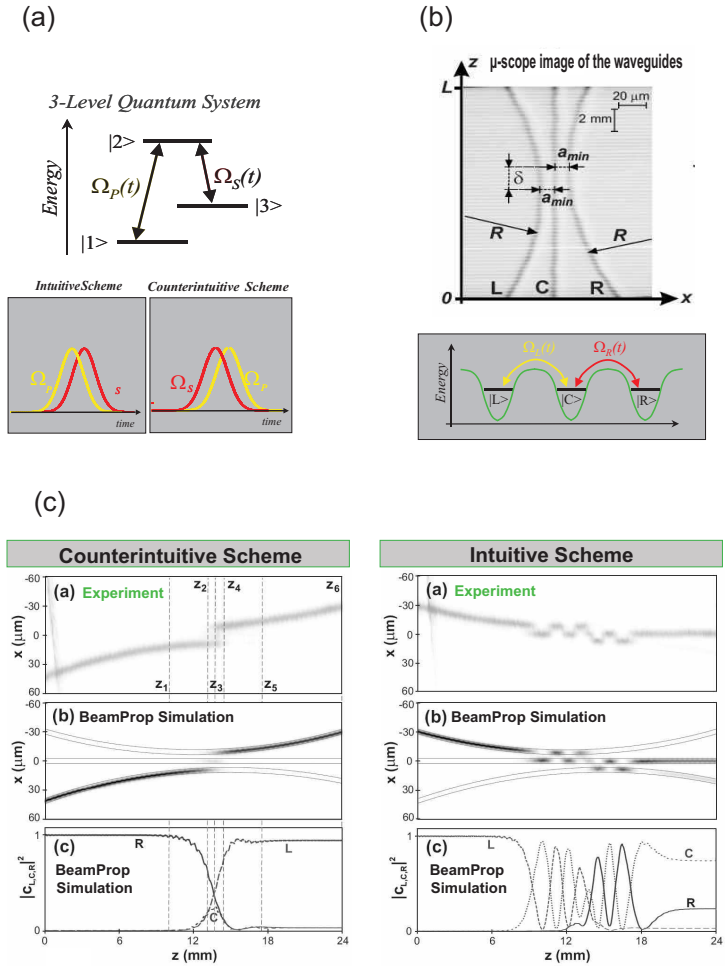


Figure 2: Adiabatic transfer of light in a triple waveguide system which mimics stimulated Raman adiabatic passage (STIRAP). (a) Schematic of coherent population transfer in a three-level atom driven by two delayed optical pulses in the intuitive and counterintuitive schemes. (b) Optical tunneling in a triple waveguide system and quantum-optical correspondence. (c) Light transfer dynamics (theory and experiment) corresponding to an intuitive and counterintuitive (STIRAP) pulse sequence (Ref.[17]).

ization and adiabatic stabilization of atoms in ultrastrong and high-frequency laser fields [13]. Other methods of coherent population transfer in atoms or molecules driven by laser pulses can be also exploited to transfer light among evanescently coupled optical waveguides in a counterintuitive way. For instance, the photonic analogue of stimulated Raman adiabatic passage enables to transfer light between two outer waveguides of an array with negligible excitation of all intermediate waveguides [17, 19](see Fig.2).

Analogies with quantum physics

The third category of quantum-optical analogies can be related to some rather general phenomena encountered in quantum physics. We just mention here coherent control of tunneling in driven bistable potentials and its enhancement [11] or suppression [12], the optical analogues of quantum collapses and revivals [21, 22], the control of quantum decay in unstable systems and the quantum Zeno effect [23, 24].

References

[1] D. Dragoman and M. Dragoman, *Quantum-Classical Analogies* (Springer, Berlin, 2004).
[2] R. Morandotti, U. Peschel, J.S. Aitchison, H.S. Eisenberg, Y. Silberberg, Phys. Rev. Lett. **83**, 4756 (1999).
[3] T. Pertsch, P. Dannberg, W. Elflein, A. Bräuer, F. Lederer, Phys. Rev. Lett. **83**, 4752 (1999).
[4] G. Lenz, I. Talanina, and M.C. de Sterke, Phys. Rev. Lett. **83**, 963 (1999).
[5] D. N. Christodoulides, F. Lederer, and Y. Silberberg, Nature **424**, 817 (2003).
[6] N. Chiodo, G. Della Valle, R. Osellame, S. Longhi, G. Cerullo, R. Ramponi, P. Laporta, and U. Morgner, Opt. Lett. **31**, 1651 (2006).
[7] H. Trompeter, T. Pertsch, F. Lederer, D. Michaelis, U. Streppel, A. Bräuer, and U. Peschel, Phys. Rev. Lett. **96**, 023901 (2006).
[8] H. Trompeter, W. Krolikowski, D. N. Neshev, A. S. Desyatnikov, A. A. Sukhorukov, Yu. S. Kivshar, T. Pertsch, U. Peschel, and F. Lederer, Phys. Rev. Lett. **96**, 053903 (2006).
[9] S. Longhi, M. Marangoni, M. Lobino, R. Ramponi, P. Laporta, E. Cianci, and V. Foglietti, Phys. Rev. Lett. **96**, 243901 (2006).
[10] R. Iyer, J. S. Aitchison, J. Wan, M. M. Dignam, and C.M. de Sterke, Opt. Express **15**, 3212 (2007).
[11] I. Vorobeichik, E. Narevicius, G. Rosenblum, M. Orenstein, and N. Moiseyev, Phys. Rev. Lett. 90, 176806 (2003).
[12] G. Della Valle, M. Ornigotti, E. Cianci, V. Foglietti, P. Laporta, and S. Longhi, Phys. Rev. Lett. **98**, 263601 (2007).
[13] S. Longhi, M. Marangoni, D. Janner, R. Ramponi, P. Laporta, E. Cianci, and V. Foglietti, Phys. Rev. Lett. **94**, 073002 (2005).
[14] T. Schwartz, G. Bartal, S. Fishman, and M. Segev, Nature **446**, 55 (2007).
[15] Y. Lahini, A. Avidan, F. Pozzi, M. Sorel, R. Morandotti, D. N. Christodoulides, and Y. Silberberg, Phys. Rev. Lett. **100**, 013906 (2008).
[16] S. Longhi, D. Janner, M. Marano, and P. Laporta, Phys. Rev. E **67**, 036601 (2003).
[17] S. Longhi, G. Della Valle, M. Ornigotti, and P. Laporta, Phys. Rev. B **76**, 201101 (2007).
[18] Y.V. Kartashov, V.A. Vysloukh, and L. Torner, Phys. Rev. Lett. **99**, 233903 (2007).
[19] G. Della Valle, M. Ornigotti, T. Toney Fernandez, P. Laporta, S. Longhi, A. Coppa, and V. Foglietti, Appl. Phys. Lett. **92**, 011106 (2008).
[20] S. Longhi, Phys. Rev. B **76**, 195119 (2007).
[21] M. Berry, I. Marzoli, and W. Schleich, Phys. World **14**, 39 (2001).
[22] S. Longhi, Phys. Rev. A (in press, 2008).
[23] S. Longhi, Phys. Rev. Lett. **97**, 110402 (2006).
[24] S. Longhi, Opt. Lett. **32**, 557 (2007).

Light localization at surfaces of modulated photonic lattices

Ivan L. Garanovich[1,*], Alexander Szameit[2], Andrey A. Sukhorukov[1], Matthias Heinrich[2], Felix Dreisow[2], Thomas Pertsch[2], Stefan Nolte[2], Andreas Tünnermann[2], and Yuri S. Kivshar[1]

[1] Nonlinear Physics Centre and Centre for Ultra-high bandwidth Devices for Optical Systems (CUDOS), Research School of Physical Sciences and Engineering, Australian National University, Canberra, ACT 0200, Australia
*ilg124@rsphysse.anu.edu.au
[2] Institute of Applied Physics, Friedrich-Schiller-University Jena, Max-Wien-Platz 1, 07743 Jena, Germany

Abstract *- We predict that truncated but otherwise perfect modulated photonic lattices can support a novel type of generic surface states, which are fundamentally different from the previously studied Tamm or Shockley type surface waves, and present the first experimental observation of such defect-free surface waves in laser-written waveguide arrays.*

Interfaces separating different physical media can support a special class of transversally localized waves known as surface waves. Linear surface waves have been studied extensively in many branches of physics [1]. Electro-magnetic waves localized at the boundaries of periodic photonic structures, such as optical waveguide arrays or photonic crystals, have been extensively analyzed theoretically and experimentally [2]. The appearance of localized surface waves in photonic structures is commonly explained as the manifestation of either Tamm or Shockley type localization mechanisms [3]. In particular, it was found that surface waves can exists at the edge of an array of optical waveguides when the effective refractive index of the boundary waveguide is modified [4], whereas surface localization was shown to be impossible when all waveguides are exactly identical, as sketched in Fig. 1(a). In the latter case, the beam launched into array delocalizes due to diffraction [Fig. 1(b)], and it is also strongly reflected from the boundary as illustrated in Fig. 1(c).

We predict, for the first time to our knowledge and contrary to the accepted notion, that *novel type of generic defect-free surface waves* can exist at the boundary of a periodic array of identical optical waveguides, which axes are periodically curved along the propagation direction as schematically shown in Fig. 1(d). We note that the periodic bending of waveguide axes was shown to result in the modification of diffraction [5, 6], which strength nontrivially depends on the bending amplitude and optical wavelength. An interesting feature is that the diffraction can be completely suppressed for particular values of the bending amplitude, and this effect is known as dynamic localization or beam self-collimation. Under such very special conditions, the beam remains localized at its input location, either inside the array [Fig. 1(e)] or at its boundary [Fig. 1(f)]. However, our most nontrivial finding is that *surface localization is possible for an extended range of structural parameters even when diffraction is non-vanishing*.

We perform direct numerical calculations of the full mode spectrum, and present the dependence of the mode wavenumbers on the bending amplitude in Fig. 2(a). One can see

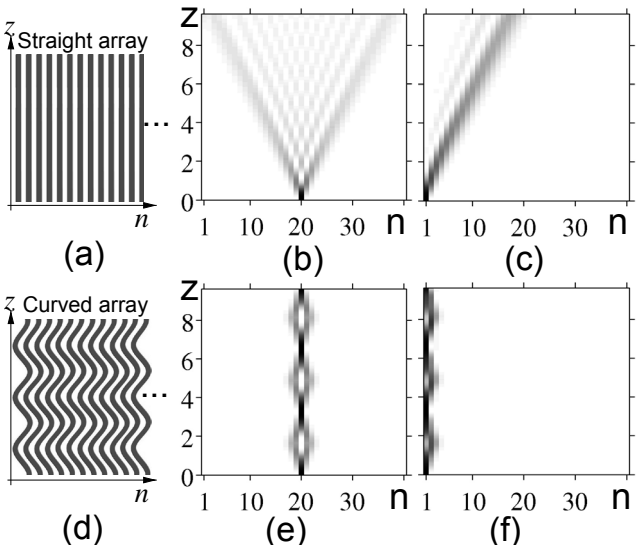


Figure 1: Beam propagation in (a-c) straight and (d-f) periodically curved waveguide arrays. (a),(d) Sketches of waveguide arrays. (b) Beam diffraction in the middle of straight waveguide array. (c) Beam reflection from the boundary and subsequent diffraction in a straight waveguide array. (e),(f) Dynamic localization inside and at the boundary of curved waveguide array, for a specific value of the bending amplitude corresponding to the regime of diffraction cancelation.

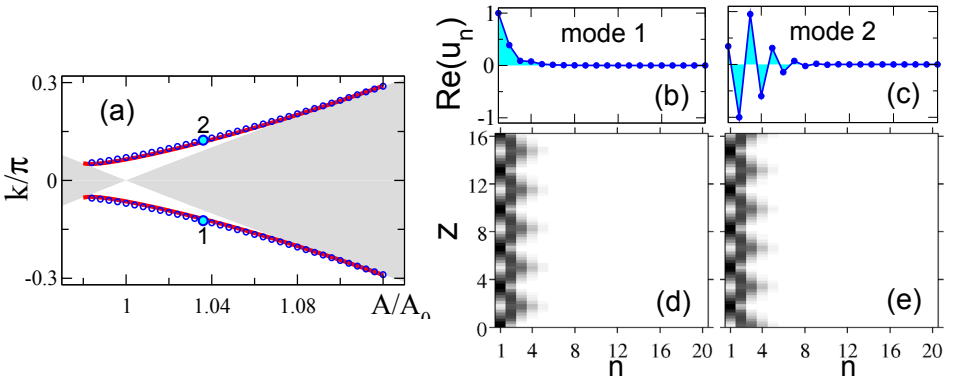


Figure 2: (a) Dispersion of defect-free surface modes vs. the bending amplitude. Circles and solid lines show modes Bloch wave numbers k calculated numerically and using asymptotic analytical expansion, respectively. Shading marks transmission band of the lattice. (b-c) Numerically calculated modes profiles at $z = 0$ and (d-e) their dynamical reshaping are shown for the points marked 1 and 2 in (a), respectively.

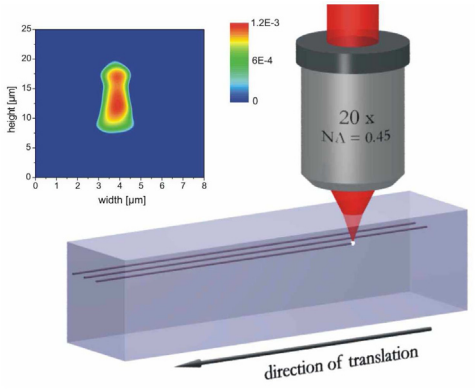


Figure 3: Schematic of the direct femtosecond laser-writing method of waveguides in a glass sample.

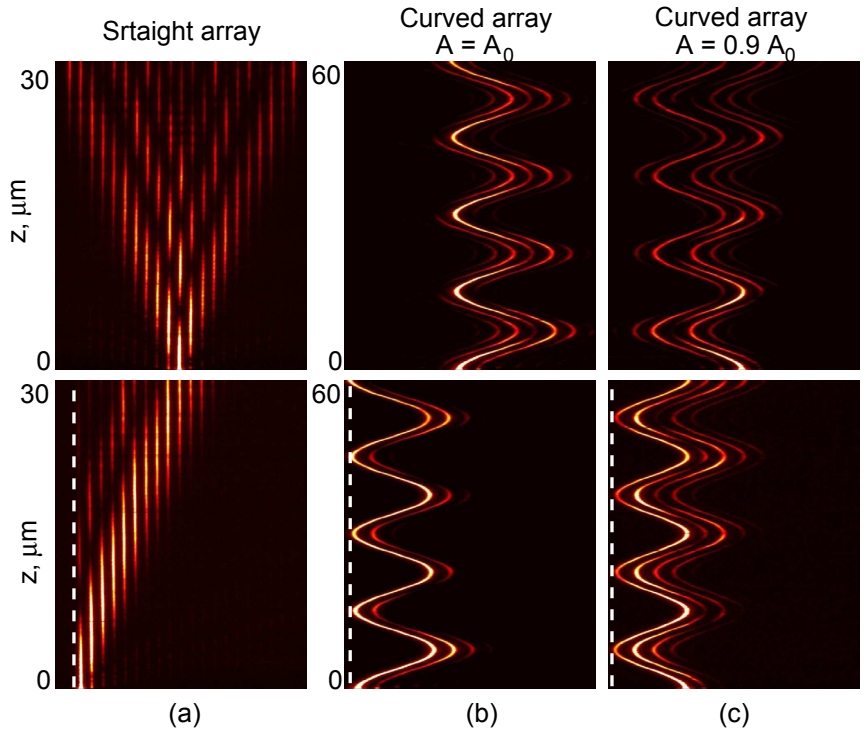


Figure 4: Observed experimentally fluorescent images of light propagation in femtosecond laser-written waveguide arrays. Top row: input beam position is away from the surface. Bottom row: beam is coupled at the edge waveguide [the surface position is marked with dashed lines]. (a) Diffraction in a straight waveguide array (top), combined with strong reflection from the boundary (bottom). (b) Diffraction cancelation in curved waveguide array, enabling beam self-collimation at arbitrary positions. (c) Reduced, but non-vanishing, diffraction in curved array (top), and mode localization at the surface in the same structure (bottom). Waveguides bending amplitude is $A_0 = 28.5$ μm.

that for modulation amplitudes around the self-collimation value there indeed appears a pair of surface modes, which existence is defined by the condition that the wavenumbers are outside the lattice transmission band indicated with grey shading. One mode has unstaggered input profile [Fig. 2(b)], while the other one exhibits staggered structure [Fig. 2(c)]. We have observed numerically stable propagation of these surface modes over distances of several thousands of bending periods, examples of their propagation dynamics are shown in Figs. 2(d) and (e).

To study these effects experimentally, we fabricated waveguide arrays in fused silica using the femtosecond laser writing technique, which was performed using a Mira/RegA (Coherent) system [7], see a schematic of the writing setup in Fig. 3. Our arrays consisted of 21 waveguides, with separation of 14 μm, the sample length of 70 mm, and the wavelength was $\lambda = 633$ nm. Most importantly, we were able to *monitor directly the beam evolution inside the glass sample*, by observing the fluorescence form excited oxygen centers. In straight waveguide array, we observe beam diffraction and repulsion from the surface [Fig. 4(a)], in agreement with theoretical prediction [Fig. 1(b,c)]. In curved waveguide arrays, when the modulation amplitude corresponds to the self-collimation condition, the beam remains localized at arbitrary locations [Fig. 4(a), c.f. Fig. 1(e,f)]. Most remarkably, when the modulation amplitude is tuned away from the self-collimation condition, the surface mode remains localized [Fig. 4(c), bottom], despite the significant beam diffraction away from the boundary [Fig. 4(c), top]. This illustrates the fundamental difference between the dynamical localization in infinite waveguide arrays [6] and formation of the defect-free surface modes. While dynamical localization is a purely resonant effect which takes place just for a specific value of the modulation amplitude $A = A_0$ [see Fig. 4(b)], the defect-free modes form families which always exist in a finite region of the modulation amplitudes.

Since the normalized modulation amplitude is proportional to the optical wavelength, our results suggest *new possibilities for the manipulation of polychromatic surface waves* in photonic lattices [8]. We note that the defect-free surface states introduced here for modulated photonic lattices may also appear in other physical systems. In particular, by introducing special periodic shift of lattice potential it may be possible to observe peculiar surface localization in Bose-Einstein condensates. On the other hand, our results indicate the possibility for novel mechanism of surface localization of charged particles in complex time-varying driving electric fields.

References

[1] S. G. Davidson and M. Steslicka, *Basic theory of surface states* (Oxford Science Publications, New York, 1996).

[2] P. Yeh, A. Yariv, and A. Y. Cho, Appl. Phys. Lett. **32**, 104 (1978).

[3] N. Malkova and C. Z. Ning, Phys. Rev. B **76**, 045305 (2007).

[4] S. Suntsov *et al.*, Phys. Rev. Lett. **96**, 063901 (2006).

[5] H. S. Eisenberg *et al.*, Phys. Rev. Lett. **85**, 1863 (2000).

[6] S. Longhi *et al.*, Phys. Rev. Lett. **96**, 243901 (2006).

[7] A. Szameit *et al.*, Opt. Express **15**, 1579 (2007).

[8] A. A. Sukhorukov, D. N. Neshev, and Yu. S. Kivshar, Opt. Express **15**, 13058 (2007).

Probing the dispersion properties of 1D nanophotonic waveguides with far-field Fourier optics

N. Le Thomas[1], J. Jágerská[1],R. Houdré[1], M. V. Kotlyar[2], L. O'Faolain[2], D. M. Beggs[2], D. O'Brien[2], T. F. Krauss[2], J. Bolten[3], C. Moormann[3], T. Wahlbrink[3], J. Čyroký[4], M. Waldow[5], M. Först[5], L. H. Frandsen[6], J. Fage-Pedersen[6], A. V. Lavrinenko[6], and P. I. Borel[6]

[1]Institut de Photonique et d'Électronique Quantique, Faculté des Sciences de Base, École Polytechnique Fédérale de Lausanne, CH-1015 Lausanne, Switzerland
nicolas.lethomas@epfl.ch
[2]SUPA, School of Physics and Astronomy, University of St. Andrews, St. Andrews Fife, KY16 9SS, United Kingdom
[3]Advanced Microelectronic Center Aachen, AMO GmbH, D-52074 Aachen, Germany
[4]Institute of Photonics and Electronics ASCR, v.v.i., Chaberská 57, 182 51 Prague 8, Czech
[5]Institut für Halbleitertechnik, RWTH Aachen University,D-52074 Aachen, Germany
[6] DTU Fotonik, Department of Photonics Engineering, Nano.DTU, Technical University of Denmark, DK-2800 KGS. Lyngby, Denmark

Abstract. *We present an advanced Fourier space imaging technique to probe guided light in nanophotonic structures with an effective numerical aperture of 2.5. This superresolution technique allows us to successfully investigate the dispersive properties of 1D nanowaveguides such as photonic crystal W1 waveguides, photonic wire, slot waveguides, and couplers.*

Introduction

The propagation of light in photonic structures is governed by the dispersion curve $\omega(k)$ relating the frequency ω to the spatial wave vector k. Engineering the slope of $\omega(k)$ allows the implementation of innovative concepts such as slow light in photonic crystal (PhC) waveguides [1] and ultra-fast wavelength conversion in silicon waveguide [2] where the achievement of the phase matching condition between pump and Stokes beams is crucial. Therefore, the experimental investigation of $\omega(k)$ is very important to understand the properties of propagation in such integrated photonic devices.

Some important regions of the dispersion curves lie outside of the light cone, implying that the associated modes do not radiate into free space and as a result propagate with minimal optical losses. Far-field optical techniques are at first view relevant only for the characterization of radiating modes, i.e. inside the light cone, and scanning near-field optical microscopy (SNOM) is currently used to characterize such nanophotonic structures. To retrieve $\omega(k)$, the required phase is determined via heterodyne techniques, which complicate the already cumbersome SNOM technique.

In this paper, we show that far-field optical experiments can be used to accurately extract the dispersion curve of modes propagating below the light cone.

Description of the Fourier space imaging technique

We have combined an end-fire set-up working in the 1.5μm range, generally used to measure the transmission through the waveguide, with a high numerical aperture Fourier space imaging set-up [3]. A single point in the Fourier space that is located in the back

focal plane of the collecting lens corresponds to an unique direction of the light scattered from the sample. The continuity of the parallel component of the mode wave-vector at the sample surface implies that a unique in-plane wave-vector of the propagating field is associated with a single measured point in the Fourier space. Therefore, the measurement of the scattered field in the Fourier space for different excitation wavelengths permits, in principle, the retrieval of the dispersion curve of a mode propagating in a photonic waveguide. As the far field characterization of infinite photonic structures cannot record information carried by modes whose wave vector lies below the light line, we used an integrated linear probe grating (LPG) to fold the dispersion curve of truly guided mode into the light cone [4] as shown in Fig.1. Such a LPG acts as a local probe that scatters the transverse evanescent tail of the propagating mode with minimal disturbance if the LPG is far enough from the waveguide. In the present case the chosen lattice constant Λ of the LPG allows us to collect 2 scattered orders, which appears as straight lines in the pupil of the collecting objective (the red circle in Fig.1-center). The variation of the position of the observed lines in the Fourier space versus the different excitation wavelengths mimics the dispersion of the guided mode and can be unfolded back with the knowledge of Λ.

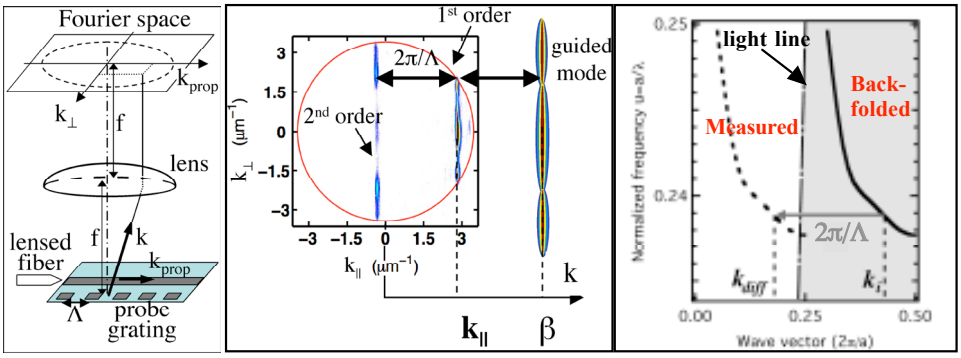


Fig. 1 Left: Schematic of the Fourier-space imaging principle. Center: Optical Fourier space images of a photonic waveguide. The wave vector of the guided mode lies far below the light cone. The first and second orders scattered at the linear probe gratings are however collected in the pupil of the imaging lens (red circle). Right: Illustration of the folding of a theoretical dispersion curve (dark line) into the light cone (dash line). Gray region: region below the light cone.

Dispersion curve of photonic wires and slot waveguides

We investigated rectangular silicon-on-insulator (SOI) waveguides of 300 and 400-nm-width (labelled as R300 and R400, respectively), as well as two different slot waveguides [5]. Waveguide patterns were defined by electron-beam lithography (EBL) using hydrogen silsesquioxane as a resist and transferred to the silicon layer by reactive-ion etching. The lateral profiles of the slot waveguides, S70 and S130, consist of two 180-nm-wide silicon sections spaced by an air trench of 70 and 130 nm, respectively. As shown in Fig.2-left, LPGs have been etched on both sides of the waveguides at the separation distance of Y=1μm or Y=3μm. The comparison of the experimental dispersion curves with simulations (empty circles) based on the Film Mode Matching method reveals a very good agreement. In Fig.2-right, the first order dispersion

coefficients are deduced from the experimental dispersion data obtained in Fig.2-center. The observed anomalous first order dispersion results from the effect of the sub-wavelength waveguide geometry that dominates the material dispersion. These data confirm that not only properly designed rectangular wire waveguides but also slot waveguides allow wavelength separated laser beams to be phase-matched around 1.55 μm for nonlinear interactions. Based on the intrinsic fine spectral analysis of this technique we also succeeded to determine the coupling length of SOI wire couplers for different wire widths and relative waveguide separation distances [6].

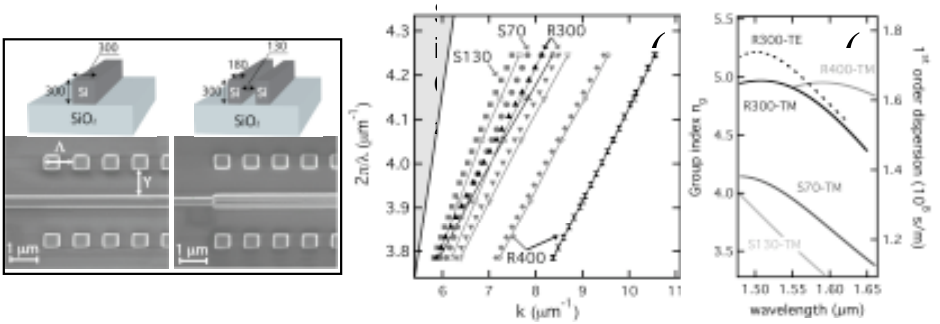


Fig. 2 Left: Perspective layout and top-view SEM images of rectangular R300 (left) and slot S130 (right) wire waveguides. The dimensions are given in nm. Center: Experimental (dots) and theoretical (dots and line) dispersion curves of the TE (dark) and TM (grey) modes propagating in the rectangular and slot nanowires. Right: Experimental group index dispersion curves.

Investigation of slow light modes in PhC waveguides

Figure 3 shows the dispersion curve of a specially designed W1 photonic crystal waveguide (SW1) as well as a standard W1 waveguides. The SW1 waveguide was engineered to operate in a slow-light regime over a large frequency bandwidth, by changing the diameter of the first and second row of holes near the line defect [1]. Two LPGs were etched outside of the PhC pattern in order to probe the dispersion properties of the W1 waveguide. The Fourier space image of the emitted light from the gratings exhibits sharp lines, labeled D1, D2 and Dr1 corresponding to the forward first-order, the forward second-order, and the backward-scattered first-order waves, respectively. The spacing between D1 and D2 is exactly equal to the modulus of the LPG reciprocal wave vector. Note that the phase wave vector of each component of the Bloch wave is unambiguously determined in the Fourier imaging space, which is not the case for a numerical Fourier transform of the real space image. The k_x-position of these lines varies according to the wavelength as plotted in Fig.3-left. This variation accelerates when the excitation wavelength enters the slow-light regime, i.e. for wavelengths λ longer than ~1.53μm. A 3D plane wave expansion calculation of the SW1 band structure is in very good agreement with the unfolded experimental data. In addition to the dispersion curves, the linewidths of the far-field spectra, which are not limited by the set-up resolution, provide a direct access to the modal losses. Note that wave vectors corresponding to group index higher than 150 could not be measured due to the disorder and the impedance mismatch at the input coupling between the PhC waveguide and the access ridge waveguide. This explains in particular why the

dispersion curve of the W1 reference waveguide stops at k=0.39 (2π/a) whereas in the case of the SW1 even mode the limit is at k=0.45 (2π/a).

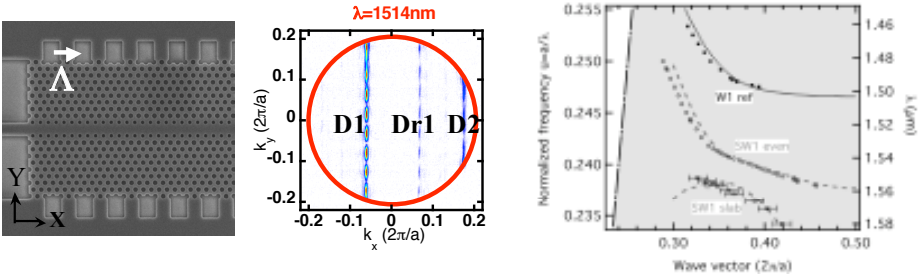


Fig. 3 Left: an electron microscopy image of a SW1 waveguide with the linear probe gratings at the waveguide boundaries (lattice constant *a*=370nm and Λ=4a). Center: a Fourier space far-field image of the Bloch wave mode propagating in the SW1 waveguide and scattered at the linear probe gratings. Right: experimental (dots) and theoretical (lines) dispersion curves.

Conclusion

An advanced Fourier space imaging technique has been successfully applied to retrieve important information about the optical properties of SOI nanophotonic waveguides. The ability to probe the wave vectors below the light cone, i.e. wave vectors of evanescent modes, has to be linked with the issue of the resolution of optical microscope. Here the largest wave vectors measured correspond to an effective numerical aperture of 2.5. In the present study the integrated optics and the optical microscopy fields merge naturally and both benefit from each other.

Acknowledgement

The authors would like to acknowledge support from the European projects ePIXnet (IST-004525), Funfox (IST-004582), the COST P11 action and the Swiss NCCR-Quantum Photonics. We would particularly like to stress that such a study strongly relied on the role played by the European network of excellence ePIXnet as a catalyst of advanced integrated European research.

References

[1] L.H. Frandsen, A.V. Lavrinenko, J. Fage-Pedersen, P.I. Borel, "Photonic crystal waveguides with semi-slow light and tailored dispersion properties", Opt. Express **14**, pp. 4357-4362, 2006.

[2] R. Dekker, A. Driessen, T. Wahlbrink, C. Moormann, J. Niehusmann, and M. Först, "Ultrafast Kerr-induced all-optical wavelength conversion in silicon waveguides using 1.55 μm femtosecond pulses", Opt. Express **14**, pp. 8336-8346, 2006.

[3] N. Le Thomas, R. Houdré, L. H. Frandsen, J. Fage-Pedersen, A. V. Lavrinenko, and P. I. Borel, "Grating assisted super-resolution of slow waves in the Fourier space", Phys. Rev. B **76**, 035103 2007.

[4] N. Le Thomas, R. Houdré, M. V. Kotlyar, D. O'Brien, T. F. Krauss, "Exploring light propagating in photonic crystals with Fourier optics", J. Opt. Soc. Am. B **24**, pp. 2964-2971, 2007.

[5] J. Jágerská, N. Le Thomas, R. Houdré, J. Bolten, C. Moormann, T. Wahlbrink, J. Čyroký, M. Waldow, M. Först, "Dispersion properties of silicon nanophotonic waveguides investigated with Fourier optics", Opt. Lett. **32**, pp. 2723-2725, 2007.

[6] J. Jágerská, N. Le Thomas, R. Houdré, D. M. Beggs, D. O'Brien, T. F. Krauss, "Coupling length of SOI couplers probed by Fourier-space imaging", submitted.

CW laser oscillation in Nd:YAG ceramic waveguides fabricated by femtosecond laser writing

E. Cantelar[1], A. Rodenas[1], A. Benayas[1], G.A. Torchia[2,3], L. Roso[2] and D. Jaque[1]

[1]Departamento de Física de Materiales, C-IV. Facultad de Ciencias, Universidad Autónoma de Madrid, 28049 – Madrid (SPAIN)
eugenio.cantelar@uam.es
[2]Grupo de Óptica, Dpto. Física Aplicada, Facultad de Ciencias Físicas, Universidad de Salamanca, 37008 – Salamanca (SPAIN)
[3]Centro de Investigaciones Ópticas CIC-Conicet CC124, 1900 La Plata (ARGENTINA).

Abstract. *In this work, the laser oscillation at 1.06 μm in Nd:YAG ceramic channel waveguides fabricated by femtosecond direct laser writing is reported. Stable laser oscillation has been achieved by using the natural Fresnel reflection for optical feed-back. Output laser power in excess of 80 mW and a laser slope efficiency of 60 % have been demonstrated.*

Introduction

Nowadays the use of ultrafast lasers to write lightwave circuits has been revealed as a promising technique to define microstructures in dielectric materials. In particular, femtosecond (fs) direct laser writing (DLW) offers the possibility of three dimensionally modifying the optical properties of the irradiated media. When fs pulses are focused inside a dielectric material a local and permanent refractive index change is produced, in such a way that channel waveguides could be generated. This possibility has been already demonstrated in a great variety of glasses and crystals [1-3]. On the other hand, ligthwave circuits can be performed by using DLW without the expensive clean-room envioronment, in contrast to most waveguide fabrication approaches in which different photolithographic steps are needed to define the channels.

Neodymium doped YAG transparent ceramics are attracting materials because of its advantages over the traditionally used Nd:YAG crystals. These advantages are the lower manufacturing costs, the possibility of high Neodymium contents without any decrease in the optical quality of the gain medium and also the possibility of direct composite fabrication [4]. As a matter of fact, the laser performance of Nd:YAG ceramics has been found to be equal or even superior to that corresponding to Nd:YAG crystals [5]. Recently, authors reported on the fabrication of near surface channel waveguides in Nd:YAG ceramics by taking advantage of the permanent induced modifications created around the focal volume after fs ablation [6]. Nevertheless, up to date no attempt has been made, to the best of our knowledge, for the fabrication of buried channel waveguides in Nd:YAG ceramics by fs DLW. The possible application of such waveguides as reliable and integrated laser sources is, therefore, still unexplored.

In this work, the fabrication of buried channel waveguide lasers in Nd:YAG ceramics by using a two line confinement approach is reported. Light confinement has been achieved between two parallel tracks due to filamentation of the fs laser pulses. The spectroscopic properties of Nd^{3+} ions within the guiding region have been

investigated by Time-resolved Confocal Microscopy. The quality of the channel waveguides has allowed to obtain highly efficient and stable laser oscillation under continuous wave conditions.

Waveguide fabrication

The Nd:YAG ceramic sample used in this work was provided by Baikowski Ltd. (Japan). The sample was a 5x5x5 mm^3 cube with all its faces polished up to optical quality ($\lambda/4$). The nominal Nd^{3+} concentration was 2 at.%. The waveguide laser was fabricated by using a CPA Ti:Shappire laser system providing 120 fs pulses at 796 nm and 1 kHz of repetition rate. The laser beam was focused with a 10x microscope objective (NA=0.3).

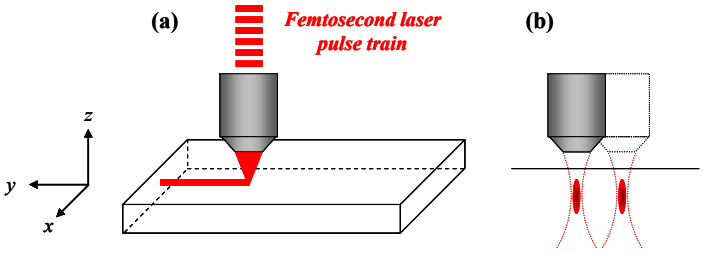


Fig. 1: (a) Diagram showing the direct laser writing of waveguides by using a femtosecond laser. (b) Two parallel lines, separated 20 μm, were written by translating the sample in the x-direction.

The waveguide was written by translating the sample with an XYZ motorized stage with a spatial resolution of 0.8 μm, the situation is sketched in Fig. 1(a). With the linear focus of the objective located 500 μm below surface, 29 μm long filaments were written with a pulse energy of 11 μJ, which corresponds to a laser power of 85 MW, well above the YAG threshold power for self-focusing (≈1 MW) which has been estimated by $\lambda^2/2\pi n_0 n_2$ where n_0=1.8 and n_2 = 6.22x10^{-16} cm^2/W are the linear and nonlinear refractive indexes of YAG. Two parallel lines were written separated 20 μm by translating the sample with a speed of 50 μm/s, see Fig. 1(b).

Experimental results and discussion

The ability of the written structure as an optical waveguide was firstly investigated by end-coupling a He-Ne laser (632.8 nm). Light confinement between the two inscribed channels was observed for both TM and TE polarizations, electric field parallel and perpendicular to the filaments, respectively. Fig 2 (a) shows an optical transmission image of the end face.

The spectroscopic properties of Nd^{3+} ions in the guiding region have been checked, and compared with the bulk. For that purpose an Olympus BX41 Confocal Microscope was used to perform time-resolved micro-photoluminescence (μPL) experiments. Fig. 2(b) shows the room temperature $^4F_{3/2} \rightarrow {}^4I_{11/2}$ μPL spectra measured at the waveguide region and that at the bulk, points A and B in Fig. 2(a), respectively, after excitation at 808 nm by using fiber coupled pulsed diode.

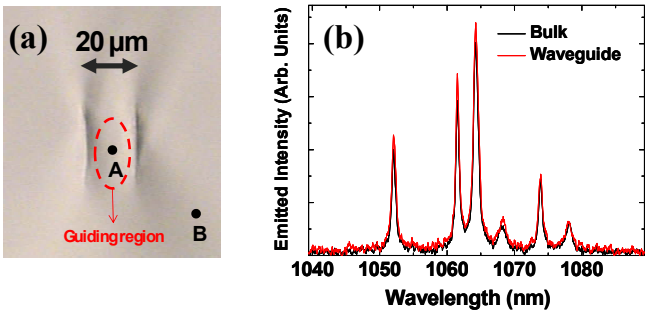


Fig. 2: (a) Optical transmission image of the end face, the guiding region has been indicated. (b) $^4F_{3/2} \rightarrow {}^4I_{11/2}$ Nd^{3+} emission band measured at the waveguide and at the bulk, points A and B in Fig. 2(a), respectively.

As it can be observed, the emission spectra were coincident and only slight differences in the peak intensities were detected. The fluorescence lifetime of the $^4F_{3/2}$ metastable state inside the waveguide was also measured. A fluorescence lifetime of 141 µs was found, in good agreement with that obtained at position B (140 µs). The invariance of both spectral shape and lifetime indicates that the spectroscopic properties of Nd^{3+} are basically preserved by this waveguide fabrication technique.

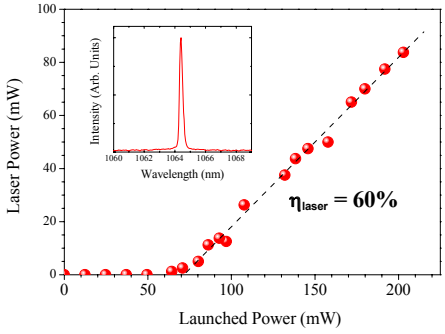


Fig. 3: Experimental output efficiency curve. The inset shows the laser line, obtained for TM excitation at 748 nm.

The laser oscillation, under continuous wave conditions, was investigated by forming a single pass laser cavity. For that purpose a plane dielectric mirror was attached to the entrance end face ($T > 80\%$ @ $\lambda = 748$ nm and $T > 99$ % for 1020 nm $< \lambda <$ 1100 nm). The optical feedback, at the exit end face, was provided by Fresnel reflection. In this case, Nd^{3+} ions were excited at 748 nm, $^4I_{9/2} \rightarrow {}^4F_{7/2}$ absorption band, by end coupling the beam from a Ti:Sapphire laser. The geometry of the experiment was adopted to couple the pump beam into the channel waveguide as a quasi-$TM_{0,0}$ propagating mode.

Fig. 3 shows the 1.06 µm laser power as a function of the launched pump power. For all the pump powers explored in this work laser oscillation was found to be quasi-$TM_{0,0}$ polarized and single-line, inset in Fig. 3. A best fit to the experimental points gives a laser slope efficiency with respect to launched power as high as 60 %, and a laser threshold of 68 mW. This laser slope efficiency is, up to the best of our

knowledge, the highest ever reported in a Nd:YAG based waveguide laser. As a matter of fact, it is close to 6 times the laser slope efficiency previously reported for a fs written waveguide laser fabricated in a Nd:YAG crystal, and 1.5 times larger than the laser slope efficiency achieved with an epitaxially grown Nd:YAG waveguide laser [7,8]. The high laser slope efficiency here reported is achieved due to the absence of any output coupler. Assuming a complete absorption of the launched pump power and a 100% pumping efficiency, the laser slope efficiency, η_{laser}, can be approximately written as [9]:

$$\eta_{laser} = \frac{\lambda_{pump}}{\lambda_{laser}} \frac{Ln\left(\frac{1}{R}\right)}{2\alpha l + Ln\left(\frac{1}{R}\right)} \frac{dS}{dF} \qquad (1)$$

where λ_{pump} = 748 nm is the pumping wavelength, λ_{laser} = 1064 nm is the laser wavelength, $R \approx 0.08$ is the output reflectance (given, in our case, by the Fresnel reflection), α is the loss coefficient, $l = 5$ mm is the waveguide length and ds / dF is the mode-overlap factor defined in [9]. Considering negligible population in the terminal laser level, due to the four level scheme, and pump beam waist smaller than laser beam waist, it can be assumed that $ds / dF \approx 1$ [9]. By substituting the experimental value found for the laser slope efficiency in expression (1), a value of α = 0.4 cm^{-1} (1.7 dB/cm) was found for the loss coefficient. According to expression (1) the laser slope efficiency the waveguide laser can be even improved by using longer pump wavelengths, since they would lead to a significant reduction in the quantum defect between pump and laser photons which, in turn, will be accompanied by a reduction in the pump induced thermal loading and, therefore, in the undesirable thermal effects [10].

Acknowledgements

This work has been supported by the Ministerio de Educación y Ciencia (MAT2004- 03347, TEC2004-05260-C02-02 and MAT2005-05950) by FEDER founds (FIS2005-01351), by the Universidad Autónoma de Madrid and Comunidad Autonoma de Madrid (projects MICROSERES-CM and CCG06-UAM/MAT-0347) and by the Junta de Castilla y León (Grant No. SA026A05).

References

[1] M. Hughes, W. Yang and D. Hewak. Appl. Phys. Lett. vol. 90, 131113, 2007.
[2] G. Della Valle, R. Osellame, N. Chiodo, S. Taccheo, G. Cerullo, P. Laporta, A. Killi, U. Morgner, M. Lederer, and D. Kopf, Opt. Express vol. 13, 5976, 2005.
[3] A. Nejadmalayeri and P. Herman. Opt. Express vol 15, 10842, 2007.
[4] Y. Sato, A. Ikesue and T.Taira. IEEE J. Select. Top. Quantum Electron. vol. 13, 838, 2007.
[5] J. Lu, M. Prabhu, J. Xu, K. Ueda, H. Yagi, T. Yanagitani and A.A. Kaminskii. Appl. Phys. Lett. vol. 4, 3707, 2000.
[6] G.A. Torchia, P. Meilan, A. Rodenas, D. Jaque, C. Mendez and L. Roso. Opt. Exp. vol. 15, 13266, 2007.
[7] A.G. Okhrimchuk, A.V. Shestakov, I. Khrushchev and J. Mitchell. Opt. Lett. vol. 30, 2248, 2005.
[8] I. Chartier, B. Ferrand, D. Pelenc, S.J. Field, D.C. Hanna, A.C. Lage, D.P. Sheperd and A.C. Tropper. Opt. Lett. vol. 17, 810, 1992.
[9] W.P. Risk. J. Opt. Soc. Am. B. vol. 5, 1412, 1988.
[10] Z.D. Luo, Y.D. Huang, M. Montes and D.Jaque. Appl. Phys. Lett. vol. 85, 715, 2004.

Design of an Integrated Electro-optically Tunable Filter for Tunable Laser purposes

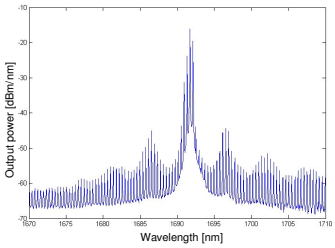
B.W. Tilma, E.A.J.M. Bente, X.J.M. Leijtens, R. Nötzel and M.K. Smit

TU Eindhoven, Eindhoven, the Netherlands
b.w.tilma@tue.nl

Abstract. *We present the design of a monolithic integrated electro-optically tunable filter based on two cascaded tunable arrayed waveguide gratings. The filter is designed to be used in a fully integrated single mode InAs/InGaAsP/InP quantum dot tunable ring-laser with a tuning range of 100nm to 200nm and a linewidth under 0.07nm.*

Introduction

Lasers that can make wavelength scans over wide ranges are useful tools for e.g. spectroscopy, gas detection and frequency domain optical coherence tomography (FD-OCT) [1]. Such laser systems are typically bulk solid-state laser systems that are scanned opto-mechanically or opto-acoustically. These systems are however limited in scanning speed due to their size. Besides that they are bulky and costly to operate. In this project we are developing monolithically integrated InAs/InGaAsP/InP (100) quantum dot semiconductor laser systems that can make continuous sweeps of 100nm up to 200nm in the 1600 to 1800nm wavelength range, at repetition rates of 20 kHz to 50 kHz and a linewidth better than 0.07nm. Such properties are desirable for the applications listed above and surpass the capabilities of available tunable semiconductor lasers [2]. To realize a laser for these applications we want to make a monolithically integrated ring-laser with a continuously scanning intra-cavity tunable filter based on electro-optically tunable arrayed waveguide gratings (AWGs). Combinations of tunable AWGs that have the 100 to 200nm scanning range can be realised in our active-passive integration technique and thus be used in a fully integrated tunable laser. Significant advantages of such filters are: full configurability through control voltages; continuous scan capability over the full range; no heating effects in the filter (only tens of nA current flow through the modulators, in contrast to injection current controlled gratings).



The laser gain medium will be InAs/InGaAsP/InP (100) quantum dots layers [3]. This medium can provide gain in the 1600-1800nm wavelength range. The output spectrum of a monolithic ring laser operating around 1700nm is presented in figure 1.

Figure 1: *Laser output spectrum of a monolithic quantum dot ringlaser with a 4mm long cavity.*

In this paper we present the design of a monolithic integrated electro-optically tunable filter based on tunable AWGs. First of all, we will discuss the requirements on the tunable filter and secondly we will present the design of the filter.

Filter specifications

Assuming a ring-laser configuration with an intra-cavity tunable AWG, we expect that the total length of the cavity will be approximately 15mm. The mode spacing of such a

laser in this case will be 0.05nm. This means that the ring-laser must be near single mode to achieve a linewidth of 0.07nm. To scan the laser over 100nm in 1000 steps and with a scanning frequency of 20kHz the filter must be able to change in 50ns from 1 wavelength to the next wavelength. To determine the requirements on the filter characteristics we have simulated the ring-laser structure with a simple time dependent multimode laser model. The parameters in the model are typical for a bulk amplifier structure. The losses for the different modes are the calculated values for the tunable AWG. The dynamical and CW behavior of the laser can then be simulated for various filter properties. From the CW state simulations one can find a set of minimum required loss values for the unwanted laser modes. When the filter is scanned the situation becomes more involved. As the filter will be scanned the laser must change from one mode to the next. To study the speed at which the laser mode intensities can follow the filter tuning one also has to consider the relative losses of the modes, the cavity length, the laser pump level, overall cavity losses and the spontaneous emission intensity. The multimode dynamics in the laser and the SOA and the limits on the switching speed are still under investigation. Two results from simulations are given in figure 2. On the left hand side the evaluation of the output power is shown when the laser starts up and reaches the CW state. All modes are building up, but the mode with the smallest loss in the filter (wl3) will win the competition and suppress the other modes. On the right hand side the evaluation of the output power is depicted when the laser is already on and the filter is switched from wl3 to wl2. In this case wl3 will decrease and wl2 will increase. In these figures we immediately see that the laser can switch from one wavelength to another within 50ns. In our first design we have chosen to make a tunable filter with a loss difference of at least 0.06dB at 0.05nm (the modespacing) from the center wavelength. This choice is based on the modeling results.

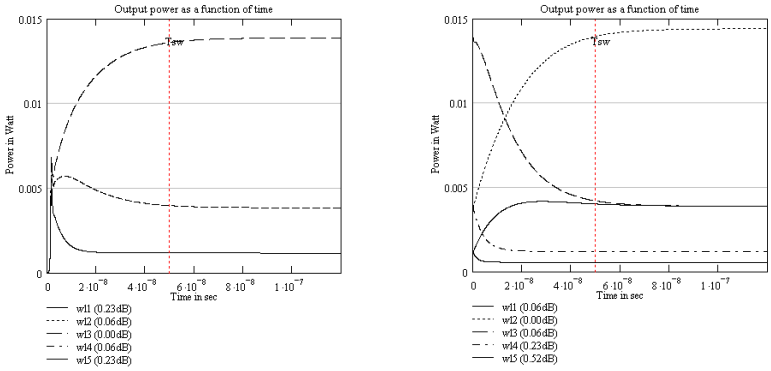


Figure 2: *Simulated output power levels for the different laser modes. In the figure on the left, the laser starts up with the filter at its center wavelength at wl3. The figure on the right depicts the evolution of the modes when the filter switches from wl3 to wl2 at t=0. The legend gives the relative loss values for the different modes. The vertical line marks the 50ns switching time.*

Filter design

The filter we will use is based on the interference principle in an arrayed waveguide grating (AWG) [4]. Including electro-optical phase shifters in the arms of the AWG makes it possible to tune the AWG [5]. An AWG without phase shifters is designed to have a linear length difference between the arms of the waveguide array. This length

difference in the waveguide array acts as a dispersive element. Waves at different wavelengths will have a differently oriented phase front at the end of the waveguide array and will focus on separate positions on the image plane of the output free propagation region (FPR). The central wavelength will have his focal point exactly in the middle of the image plane where the output waveguide is located. Adding phase shifters in the arms of the waveguide array will allow electro-optic tuning of the AWG. By applying a combination of voltages on the phase shifters, the orientation of the phase front at the end of the waveguide array can be changed. The focal point of the central wavelength of the AWG can thus be tilted away from the output waveguide and another wavelength will be focused on the output waveguide. The refractive index change in the phase shifters is due to field induced electro-optical effects and free carrier depletion based electro-optical effects [6].

The filter also must be tunable over at least 100nm. In theory it is possible to design a filter with one AWG which fulfils these requirements. However this would become a large AWG with more than 200 arms and phase shifters, which is impractical. In our design we have cascaded two different AWGs, the first one is a high resolution AWG with 28 arms that selects a single laser cavity mode and suppresses the other modes with at least 0.06dB (figure 3B). Since this filter needs to have a sufficiently narrow bandwidth to suppress the neighboring laser modes, it will also have a free spectral range (FSR) of approximately 10nm. The second AWG with 11 arms selects a single peak of the high resolution AWG transmission and suppresses the other peaks with at least 1dB (figure 3A). The combination is optimized to be tuned over 200nm between 1600nm and 1800nm.

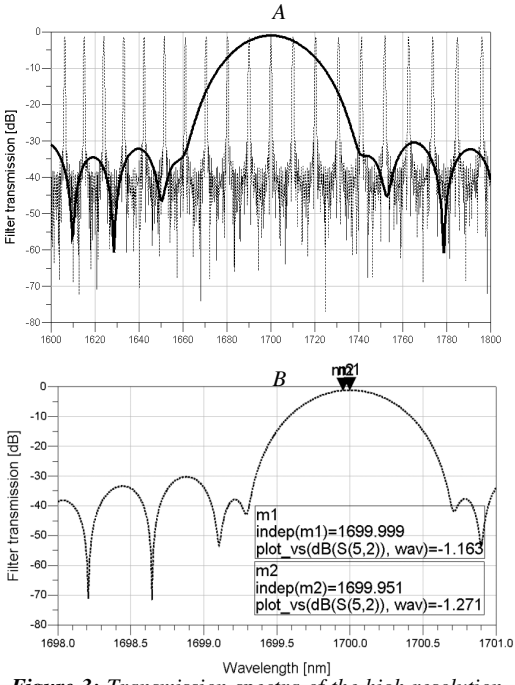


Figure 3: *Transmission spectra of the high resolution AWG (dot) and the low resolution AWG (solid). Figure B is a zoom in on the high resolution AWG at 1700nm and has two markers on laser mode positions.*

Figure 4 depicts the mask layout of the tunable filter and some test structures. It contains a high resolution tunable AWG filter with 28 phase shifters in the arms and a low resolution tunable AWG filter with 11 phase shifters in the arms. These filters can be measured separately but also in sequence. Furthermore it contains a low resolution tunable MMI filter which possibly can replace the low resolution AWG filter. To measure only the passive waveguide characteristics and the passive filter characteristics we included some passive AWGs and other test structures. Both AWGs designs are standard orthogonal AWG designs that are modified to have equal spacings between the phase modulators in the arms. This has been done in order to increase the reliability of

the fabrication of the electrical contacts. In the low order AWG the path length difference between the arms need to be only eight wavelengths. This was achieved by designing this AWG in an S-shape to cancel out all path length differences and changed one side to include the small path length differences.

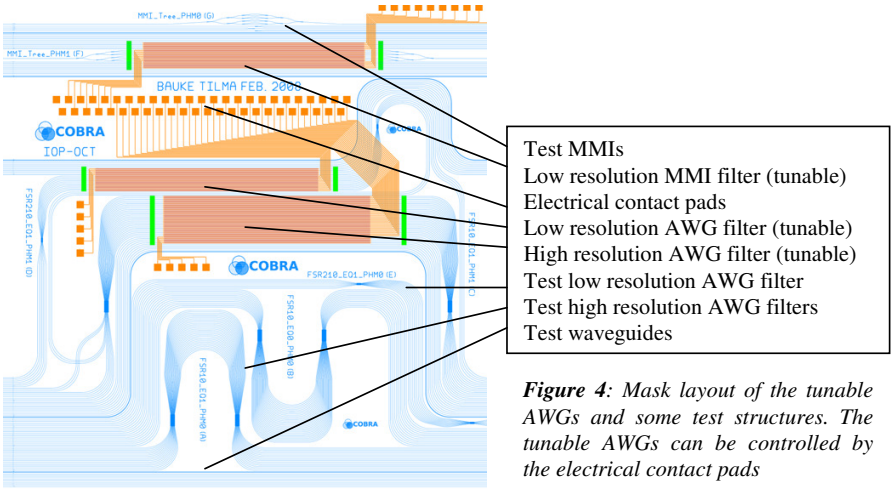


***Figure 4**: Mask layout of the tunable AWGs and some test structures. The tunable AWGs can be controlled by the electrical contact pads*

Conclusion

We present the design of a monolithic integrated electro-optically tunable filter based on two cascaded AWGs with phase shifters as tuning mechanism. The first AWG is a high resolution filter with a suppression of 0.06dB at 0.05nm from its center wavelength and the second AWG is a low resolution filter with a suppression of 1dB at 10nm from its center wavelength to select one peak from the first AWG. The filter is designed to make a fully integrated single mode tunable ring-laser with a tuning range over 100nm and a linewidth beneath 0.07nm.

Acknowledgement
This work is supported by the IOP Photonic Devices program managed by the Technology Foundations STW and SenterNovem.

References

[1] A.F. Fercher, C.K. Hitzenberger, G.Kamp and S.Y. El-Zaiat, "Measurement of intraocular distances by backscattering spectral interferometry," *Opt. Com.*, vol. 117, pp. 43-48, 1995.

[2] J. Buus, M.C. Amman, D.J. Blumenthal, "*Tunable Laser Diodes and Related Optical Sources*", Wiley-IEEE Press; 2nd edition, 2005, ISBN 978-0471208167

[3] R. Nötzel et al., "Self assembled InAs/InP quantum dots for telecom applications in the 1.55 µm wavelength region: wavelength tuning, stacking, polarization control and lasing.", Review paper in *Japanese Journal of Applied Physics*, Vol. 45, No. 8B, 2006, pp. 6544-6549.

[4] M.K. Smit and C. van Dam, "PHASAR-based WDM-devices: principles, design and applications," *J. of Sel. Topics in Quantum Electron.*, vol. 2, no. 2, pp. 236-250, June 1996.

[5] A. Alonso, J. Stulemeijer, F. Soares, X. Leijtens, and M. Smit, ``Electro-optical and temperature tunable WDM filter," in *Proc. IEEE/LEOS Symposium (Benelux Chapter)*. Nov. 2003, pp. 51-54, Enschede, The Netherlands.

[6] D.H.P. Maat, *InP-based integrated MZI switches for optical communications*, Ph.D. thesis, Delft University of Technology, Delft, The Netherlands, 2001, ISBN 90-9014700-4.

Electro-optic Modulation of InAs Quantum Dot Waveguides

I. B. Akca[1], A. Dâna[1], A. Aydinli[1], M. Rossetti[2], L. Li[2], A. Fiore[2] and N. Dagli[3]

[1]Materials Science and Nanotechnology Program, Physics Department, Bilkent University, Ankara, Turkey
imran@bilkent.edu.tr
[2]Institute of Quantum Electronics and Photonics, Ecole Polytechnique Fédérale de Lausanne EPFL, Lausanne, Switzerland
[3]ECE Department, University of California at Santa Barbara, USA

Abstract. *The linear electro-optic properties in waveguides containing self-organized InAs quantum dots were studied experimentally. Fabry-Perot measurements at 1515 nm on InAs/GaAs quantum dot structures yield a significantly enhanced linear electro-optic efficiency compared to bulk GaAs.*

Introduction

Semiconductor-based nonlinear optical and electro-optic materials would be useful for switching and modulation devices in photonic integrated circuits. Electro-optic (EO) modulators are candidates for use in external modulation links in telecommunications. These modulators can be realized using either bulk semiconductor materials [1] or materials with multiple quantum dots or wells [2]. Due to the modification in the density of states, quantum dots and quantum wells are expected to exhibit enhanced optical nonlinearities and enhanced electro-optic effects [3]. Since EO modulators require small size and low modulation voltages, possibility of obtaining quantum dots with enhanced electro-optic and/or electro-absorption coefficients makes them attractive for such applications.

In the literature there is limited data on EO effects in quantum dots. Furthermore, little has been reported on the voltage dependent modulation of quantum dot embedded waveguides [4-5-6-7]. In this article, we report on the measurements of EO properties of multilayer InAs/GaAs self-organized quantum dots. We use the transmission through Fabry-Perot resonators formed by two cleaved facets in waveguides at 1500 nm to determine the electro-optical properties of quantum dots.

Samples

The waveguide structures containing three layers of quantum dots (3QDs) were measured. Their lengths are in the range of 1-1.6 mm. These structures were grown by molecular beam epitaxy to be used as quantum dot lasers. The active region is formed by three layers of self-assembled InAs QDs, which are covered by a 5-nm $In_{0.15}Ga_{0.85}As$ QW and separated from each other by a 40-nm GaAs spacer layer. The areal dot density

of the lens-shaped QDs is $3x10^{10}$ cm^{-2}. The devices are single mode ridge waveguide structures with varying widths between 2-5 μm. Both facets are as cleaved. For each sample lasing is peaked at nearly 1285 nm [8]. Detailed structure is given in **Figure 1**.

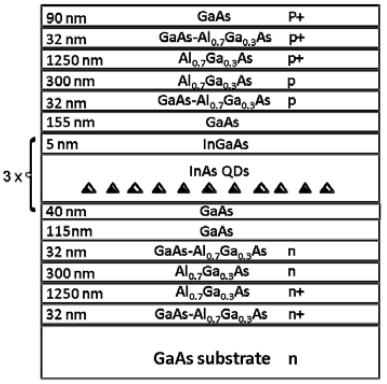


FIG. 1. Detailed structure of the samples used in the measurements**.** $Al_{0.7}Ga_{0.3}As$ layers at the GaAs interfaces are graded.

Measurements and results

The electro-optic coefficients were measured at 1515 nm by coupling a TE polarized light from a tunable laser (Santec Tunable LD Light Source TSL-520) onto one end of the waveguide with a lens shaped fiber. A DC voltage source was used to apply 0 to 20 Volt reverse bias to the samples. The detailed measurement set-up is shown in **Figure 2**. At each voltage level, the transmission through the device was recorded as a function of wavelength and voltage. Experimental results are given in **Figure 3**. Fabry-Perot resonances with large contrast were obtained and experimental data fitted well with the theoretical formula. The well known Fabry-Perot transmission equation is used in fitting to the measured data and the fitting parameters were mode effective index, loss coefficients and a voltage independent phase factor. The effective mode index was then calculated based on this curve fitting.

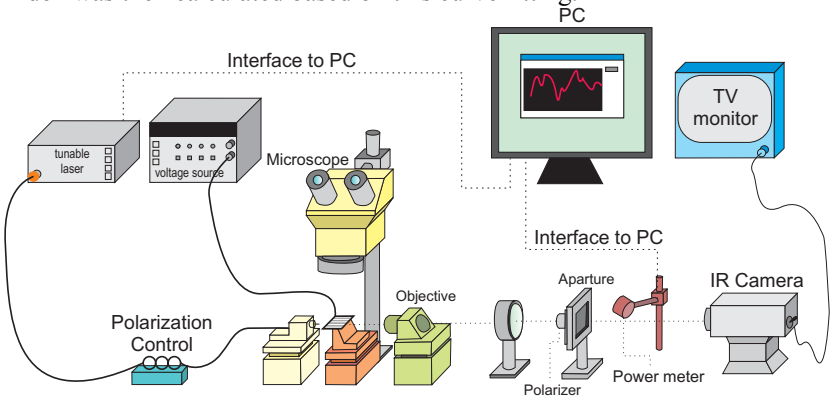


FIG. 2. The experimental set-up for measuring the Fabry-Perot resonances of quantum dot waveguides.

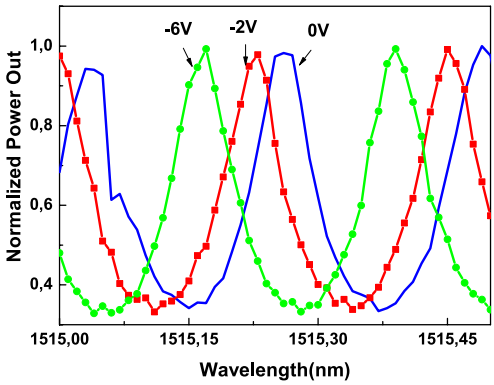


FIG.3. Voltage dependent shift of Fabry-Perot resonances. Significant tuning is observed with relatively low voltages.

The linear electro-optic coefficients are obtained by fitting the measured data to the equation of transmission through a Fabry Perot modulator [3] and calculating the refractive index difference between two specific voltages. The change in refractive index due to applied voltage is $\Delta n(V)$ is given as [3]:

$$\Delta n(V) = \frac{1}{2} n_e^3 r_{41} \frac{V}{t} \Gamma \tag{1}$$

where r_{41} is the electro-optic coefficient, t is the thickness of the epilayer, n_e is the effective index, V is the voltage difference between two curves and confinement factor Γ is the overlap of the vertical electric field component with the optical mode. To obtain r_{41}, Γ needs to be known precisely. The overlap factor of InAs quantum dot layers is calculated using finite difference beam propagation method simulations and is approximately 0.015 for all samples. Using this confinement factor the electro-optic coefficient of the InAs quantum dot structures are obtained as 9×10^{-11} which is significantly enhanced linear electro-optic efficiency compared to bulk GaAs. Figure 4 shows the Beamprop simulation results.

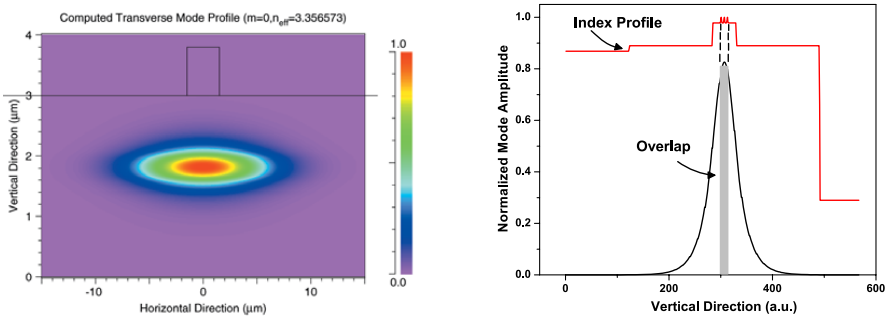


FIG.4. (a) Fundamental mode profile of the quantum dot waveguide structure. The effective index of the structure is obtained as 3.356. Note that the field is confined to the core region

where the quantum dots are placed. **(b)** The graphical representation of the calculation of overlap factor. The locations of the InAs layers are determined using the index profile, and these points are mapped onto the vertical mode profile. The confinement factor is calculated from this overlap region by simply integrating the shaded area.

As a matter of fact examination of **Fig. 1a** reveals that full on/off modulation is possible for 1.6 mm long 3 QD sample using 6 V. This corresponds to less than 1 V-cm modulation efficiency. In other words using this modulator as the arms of a push pull driven Mach-Zehnder modulator, less than 1 V drive voltage would result for 1 cm long arms

Conclusions

In conclusion, the low voltage modulation in InAs quantum dot waveguides was observed. The linear electro-optic coefficients of multilayer InAs quantum dot structures far away from the lasing wavelength were measured and is found to be significantly larger than that of GaAs bulk material. This result is promising for QD-based electro-optic modulators.

Acknowledgement: This project is supported by Turkish Scientific and Technical Research Council (TUBITAK); Grant No: 103T115.

References

[1] R. B. Welstand, S. A. Pappert, C. K. Sun, J. T. Zhu, Y. Z. Liu, and P. K. L. Yu, "Dual-function electroabsorption waveguide modulator/detector for optoelectronic transceiver applications," IEEE Photon. Technol. Lett. vol. 8, pp. 1540–1542, 1996.

[2] L. Lembo, F. Alvares, D. Lo, C. Tu, P. Wisseman, C. Zmudzinski, and J. Brock, "Optical electroabsorption modulators for wideband, linear, low-insertion loss photonic links," Proc. SPIE Photon. Device Eng.Dual-Use Appl. vol. 2481, pp. 185–196, 1995.

[3] L. Davis, K. K. Ko, W.-Q. Li, H. C. Sun, Y. Lam, T. Brock, S. W. Pang, and P. Bhattacharya, "Photoluminescence and electro-optic properties of small (25–35 nm diameter) quantum boxes," Appl. Phys. Lett. vol. 62, pp. 2766, 1993.

[4] O. Qasaimeh, K. Kamath, P. Bhattacharya, and J. Phillips, "Linear and quadratic electro-optic coefficients of self-organized $In_{0.4}Ga_{0.6}As/GaAs$ quantum dots," Appl. Phys. Lett. vol. 72, pp. 1275, 1998.

[5] S. Ghosh, A.S Lenihan, M.V.G Dutt, O Qasaimeh, D.G Steel and P. Bhattacharya, " Nonlinear optical and electro-optic properties of InAs/GaAs self-organized quantum dots," J. Vac. Sci. Technol. B vol. 19, pp. 1455–1458, 2001.

[6] J. Tatebayashi, R.B. Laghumavarapu, N. Nuntawong and D.L. Huffaker, " Measurement of electro-optic coefficients of 1.3 μm self-assembled InAs/GaAs quantum dots," Electronics Letters, vol. 43, pp. 410-412, 2007.

[7] G. Moreau, A. Martinez, D.Y. Cong, K. Merghem, A. Miard, A. Lemaître, P. Voisin, A. Ramdane I. Krestnikov, A. R. Kovsh M. Fischer and J. Koeth, "Enhanced In(Ga)As/GaAs quantum dot based electro-optic modulation at 1.55 μm," Appl. Phys. Lett. vol. 91, pp. 91118, 2007.

[8] A. Markus, J. X. Chen, C. Paranthoen, A. Fiore, C. Platz, and O. Gauthier-Lafaye, "Simultaneous two-state lasing in quantum-dot lasers," Appl. Phys. Lett. vol. 82, pp. 1818, 2003.

[9] S. Nishimura, H. Inoue, H. Sano, and K. Ishida, "Electrooptic Effects in an InGaAs/InAlAs Multiquantum Well Structure," IEEE Photonics Tech. Lett. vol. 4, pp. 10, 1992.

Local Reconstruction of Birefringence in Bent Waveguides by Polarization-Sensitive Optical Low-Coherence Reflectometry

M. Ferrario[1], R. Bratovich[1], F. Morichetti[1] and A. Melloni[1,2]

[1] CoreCom, Via G. Colombo 81, 20133 Milano, Italy
ferrario@corecom.it
[2] Politecnico di Milano, Dipartimento di Elettronica e Informazione, Via G. Ponzio 34/5, 20133 Milano

Abstract. *Polarization-sensitive optical low-coherence reflectometry (PS-OLCR) is advantageously exploited to recover local birefringence evolution inside planar waveguides, with a micrometer spatial resolution. In particular, PS-OLCR characterizations on bent waveguides have experimentally highlighted a bend-induced birefringence dependence on the square of the radius of curvature.*

Introduction

Waveguide birefringence and related polarization dependent effects are an important and still open issue in integrated optical systems, particularly in silica-on-silicon planar waveguide technology, which can adversely affect device transfer function performances. Waveguide birefringence is defined as the difference between effective indexes of the two orthogonally polarized waveguide modes, that is, $\Delta n_{eff} = n_{eff}^{TM} - n_{eff}^{TE}$.

Birefringence results from geometrical and stress-induced birefringence [1,2]. Yet, bent waveguide sections have been theoretically demonstrated to introduce a bend-induced birefringence [3,4] as a further contribution to the overall waveguide birefringence.

For a more comprehensive understanding of birefringence dependence on material and structural parameters, and for a more efficient waveguide design, measurement techniques providing a feedback of the actual birefringence are required. To this purpose, several methods have been introduces by previous art, yet, they are mainly limited by the fact that they provide only spatially averaged birefringence values, as they rely on an integral measurement along the waveguide length [5]. Thus, they do not allow to investigate the existence of local variation of birefringence inside the waveguide caused by defects of the manufacturing process, or induced on purpose. Moreover, if planar waveguides, including bent sections, have to be analyzed, these techniques can not cut out and estimate the contribution to birefringence due to curvature.

In the present work we have proved how polarization-sensitive optical low coherence reflectometry (PS-OLCR) [6] can be advantageously exploited to recover local birefringence evolution inside waveguides, with a micrometer spatial resolution, from the analysis of the state of polarization (SOP) of the backscattered light. In this way the PS-OLCR technique provides information on phase birefringence without suffering of the 2π-phase ambiguity. The peculiar features and potentialities of PS-OLCR have been demonstrated by characterizations carried out on bent waveguides which provided a first experimental evidence of a bend-induced birefringence dependence on the square of the waveguide radius of curvature.

The PS-OLCR experimental setup

Fig.1 shows a schematic of the PS-OLCR system realized in this work. It is basically a Michelson interferometer which detects the interference of a reference signal with the backscattered light from the waveguide under test. In order to analyze the birefringence-induced SOP evolution of the backscattered signal along the waveguide sample, the polarimetric scheme described in [6] has been conceived. In particular, in the detection arm the light is split into its horizontal and vertical components, with complex amplitudes A_H and A_V, by a polarization beam splitter (PBS) and focused onto two photodiodes to detect each single polarization. Since light from the reference arm, linearly polarized at 45° through the double passage through the λ/4 waveplate, is split equally into the horizontal and vertical polarization states, A_H and A_V result proportional to the light amplitude fields backscattered from the waveguide sample

$$A_H = \sqrt{R(z)}\, sin\left(k_0 z \Delta n_{eff}\right) e^{\left(\Delta z / l_c\right)^2} cos\left(2k_0 \Delta z + 2\phi\right)$$

$$A_V = \sqrt{R(z)}\, cos\left(k_0 z \Delta n_{eff}\right) e^{\left(\Delta z / l_c\right)^2} cos\left(2k_0 \Delta z\right) \quad (1)$$

where $k_0 = 2\pi/\lambda$, Δn_{eff} is the phase birefringence and ϕ the orientation of the birefringence axes. *R(z)* describes the reflectivity of the sample at depth z and the attenuation accumulated up to *z*, Δz is the optical path difference between the sample and reference arm of the interferometer and $l_c = \lambda^2/\Delta\lambda$ is the spatial coherence length of the light. In particular, the use of a broadband optical source ($\Delta\lambda \approx 30$nm, at $\lambda = 1.55$μm), provides short coherence interference and results in a spatial resolution of $l_c/2n = 26$μm, where *n* is the waveguide refractive index (n=1.5). The input signal is coupled to the waveguide under test by means of a 30x objective followed by a 15cm-long small-core fiber, with a 2μm core diameter. A piezoelectric transducer, attached to the small-core fiber, modulates the sample arm length by $\Delta z = \pm 1\,\mu m$ at a carrier frequency $f_c = 4kHz$, thus generating a frequency up- shifted interference signal whose components A_H and

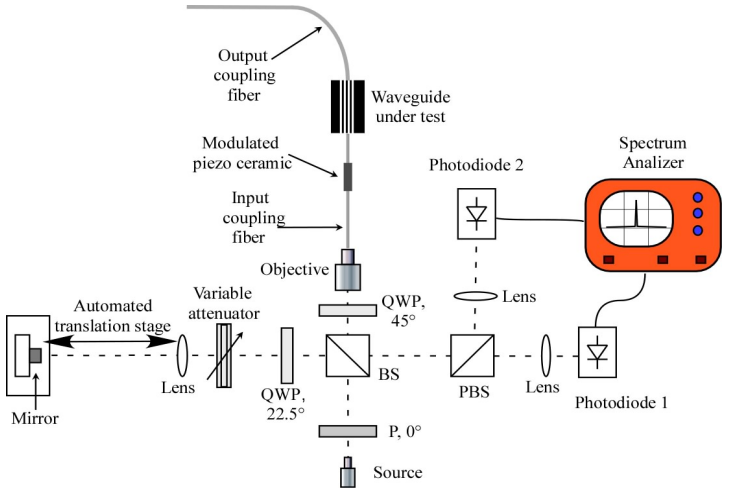


Fig. 1. PS-OLCR experimental set-up. BS=beam splitter; P=polarizer; QWP=λ/4 waveplate.

A_V are analyzed with a HP3585A electrical spectrum analyzer with a -63dBm sensitivity. According to [7], in order to improve the signal to noise ratio a variable attenuator was positioned in the reference arm to search for optimum attenuation of the reference power, which lead to a noise floor level of -55dBm. The power coupled to the waveguide was about 400μW, resulting in an averaged interference signal level of -40dBm, as detected by the photodiodes, that is, about 15dB above the noise floor. From the measurement of A_H and A_V at each backscattering point inside the sample, the evolution of the birefringence-induced phase retardation δ between the two-orthogonal polarization components could be retrieved by the following expression, simply derivable from (1)

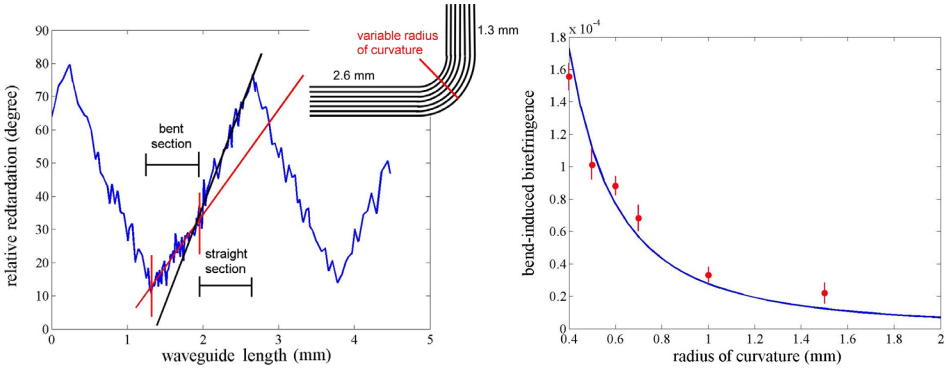
$$\delta(z) = \frac{2\pi}{\lambda} z\left|\Delta n_{eff}\right| = tan^{-1}\sqrt{I_H(z)/I_V(z)} \qquad (2)$$

where $I_H = |A_H|^2$ and $I_V = |A_V|^2$ are the intensities of the two backscattered components. According to (2) phase retardation δ goes from 0° to 90° and from the slope of the retardation profile the local birefringence $\left|\Delta n_{eff}\right|$ inside the waveguide can be retrieved.

Experimental recovery of bend-induced birefringence

The feasibility and reliability of the PS-OLCR technique in waveguide birefringence recovery has been first verified by characterizing straight silica-on-silicon waveguides with different core widths. The measured birefringence values as a function of the core shape proved in good agreement with theoretical predictions [2]. Yet, to put into evidence the peculiarity of this technique with respect to other methods, which recover spatially averaged birefringence values, we have exploited the PS-OLCR set-up to characterize planar waveguide devices including bent sections. In particular we have analyzed a series of waveguides, as those shown in the inset of Fig.2(a), with the bent waveguides having radius of curvature R ranging from R=1.5mm to R=200μm. The waveguides featured a $2.2\times2.2\mu m^2$ SiON core and a SiO_2 cladding, with a contrast index Δn=4.4%. Fig.2(a) shows an example of birefringence-induced phase retardation profile reconstructed, by means of (2), along the waveguide length. Retardation profiles, as the one in Fig.2(a), were measured with backward steps of the reference arm of few tens of μm. Let's notice that, according to (2), retardation curves should range from 0° to 90°. The lower visibility in Fig.2(a) is mainly ascribable to the maximum achievable extinction ratio between the two polarization components of the backscattered signal, which in turn depends on the level of the backscattered signal with respect to the noise floor, that is, to the minimum detectable backscattered signal.

In Fig.2(a) the fitting lines indicate the slope of the birefringence-induced retardation profile in the bent section and in the subsequent straight waveguide section. It can be noticed that the effect of the curvature is to give rise to a bend-induced contribution that changes the overall waveguide birefringence, the effect having been measured to be more evident for smaller radii. A quantitative estimate of the bend-induced birefringence has been achieved by fitting measured data and comparing the slope of the retardation profile in bent and straight sections. Repeated measurements carried out on each waveguide, resulted in a standard deviation of ±1° in recovered slopes, thus proving the accuracy and reproducibility of retrieved birefringence values.



(a) (b)

Fig. 2. (a) Measured spatial behaviour of birefringence-induced phase retardation in a waveguide with a bent section of radius $R=400\mu m$. (b) Bend-induced birefringence as a function of the radius of curvature.

Results of bend-induced birefringence as recovered from characterizations of the above mentioned waveguides with different radius of curvature are reported in Fig.2(b). The fitting curve has a dependence on R^{-2}. Vertical bars represent the measurement uncertainties obtained from repeated phase retardation measurements. Thus, characterizations performed on bent waveguides with the PS-OLCR set-up fairly confirm theoretical predictions advanced in [3,4] which foresee a bend-induced birefringence proportional to the square of the waveguide radius of curvature.

Conclusions

It has been proven how PS-OLCR can be advantageously exploited to recover local birefringence evolution inside planar waveguides, with a micrometer spatial resolution. PS-OLCR may thus become a useful tool to investigate the existence of local variations, spurious or induced on purpose, of birefringence inside waveguides. The PS-OLCR peculiarity has been demonstrated by characterizations of waveguides including bent sections, as the contribution to birefringence due to curvature could be separated and put into evidence from the contributions of the straight waveguide sections. In particular, results have provided a first experimental confirmation of bend-induced birefringence dependence on the square of the waveguide radius of curvature.

References

[1] M. Huang, "Analytical solutions for thermal stresses in buried channel waveguides," *IEEE J. Quantum Electron.,* vol. 40, pp. 1562-1568, 2004.

[2] K. Okamoto, *Fundamentals of Optical Waveguides*. New York: Academic, 2000.

[3] F. Morichetti, A. Melloni, M. Martinelli, "Effects of polarization rotation in optical ring-resonator-based device," *IEEE J. Ligthwave Technol.*, vol. 24, pp. 573-585, 2006.

[4] A. Melloni, F. Carniel, R. Costa, M. Martinelli, "Determination of bend mode characteristic in dielectric waveguides," *IEEE J. Ligthwave Technol.*, vol. 19, pp. 571-577, 2001.

[5] S.Y. Cheng, K.S. Chiang, H.P. Chan, "Birefringence in Benzocyclobutene strip optical waveguides," *IEEE J. Photon Technol.*, vol. 15, pp. 700-702, 2003.

[6] J.-T. Oh, S.-W. Kim, "Polarization-sensitive optical coherence tomography for photoelasticity testing of glass/epoxy composites," *Opt. Express*, vol. 11, pp. 1669-1676, 2003.

[7] W.V. Sorin, D.M. Baney, "A simple intensity noise reduction technique for optical low-coherence reflectometry," *IEEE J. Photon. Technol.*, vol. 4, pp. 1404-1406, 1992.

Resonance characteristics of rib-type slot waveguides

P. Muellner[1], N. Finger[2], and R. Hainberger[1]

[1] Nano System Technologies and
[2] Smart Systems,
Austrian Research Centers GmbH - ARC, Donau-City-Str. 1, 1220 Vienna, Austria
rainer.hainberger@arcs.ac.at

Abstract - *We numerically investigate the lateral leakage behavior of horizontal rib-type slot waveguides at $\lambda = 1.55\mu m$. We focus on resonance effects, which can be exploited to achieve waveguide structures ensuring high power confinement in the slot and low loss operation at the same time.*

Introduction

While the horizontal wire-type slot waveguide structure [1, 2] offers several important advantages over the vertical structure [3] such as better layer thickness control, smoother interfaces and larger waveguide width-to-height ratios, it lacks the possibilities of electric wiring and self-suspension. Horizontal rib-type slot waveguides (see Fig. 1 (a)) offer these features but can suffer from lateral leakage loss due to TM-TE mode conversion [4, 5, 6]. This lateral leakage can be effectively suppressed by taking advantage of resonance effects occurring for certain rib widths. The wire/slab-type slot waveguide shown in Fig. 1 (b) is another interesting structure. It could offer better lateral confinement compared to the rib type and therefore would be particularly attractive for waveguide sections in active photonic devices where no direct electrical wiring is necessary. However, also for this structure lateral leakage is a critical issue. In this study, we investigate the resonance characteristics of rib-type and wire/slab-type slot waveguides in detail employing the variable mode-matching (VMM) method [7].

The lateral leakage & resonance effect

Lateral leakage in rib-type structures occurs due to coupling of the minor TE field components of a TM-like rib mode to a TE slab mode outside the rib that has a higher effective index than the TM-like rib mode [4, 5]. In principle, the slot waveguide structure supports two first order modes for each polarization, an even and an odd one [8]. The highly

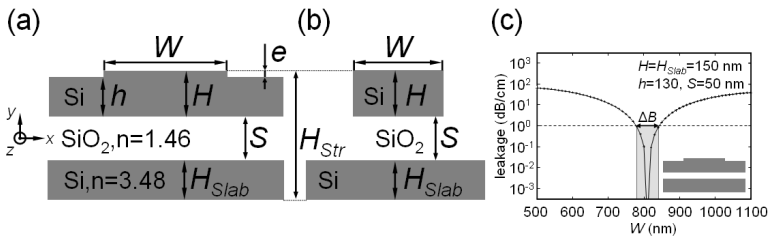


Figure 1: Cross sections of (a) rib-type and (b) wire/slab-type slot waveguide structures. (c) Typical width dependent resonance behavior of a rib-type slot waveguide; ΔB defines the range of width within which lateral leakage losses are below 1 dB/cm.

confined slot mode corresponds to the TM-polarized even mode.
Except for vertical fully symmetric systems, coupling to both the even and odd TE slab mode takes place [6]. The coupling to the even TE slab mode is always more critical because it has a higher effective index than the odd TE slab mode. For all rib-type slot waveguide structures this coupling can be avoided by decreasing the effective index of both TE slab modes below that of the TM rib mode, which is achieved by choosing a geometry with $H \gg H_{\mathrm{Slab}}$. Unfortunately, this measure leads to a severe reduction of the maximum power confined in the slot to well below 20% [9].
By exploiting resonance effects for otherwise leaky geometries, low loss operation becomes possible without sacrificing optical power confinement in the slot. These resonance effects are related to TE waves generated through mode-conversion of the TM rib mode at the rib side walls. While one part of these TE waves propagates into the slab region the other part is reflected at the side wall and traverses inside the rib to the other side wall, where it interferes with newly generated TE waves. For certain rib widths (see Fig. 1 (c)) this results in a cancellation of TE waves leaking into the slab region thus suppressing the leakage loss.

Influence of imperfections

With respect to deviations of the geometry caused by fabrication processes the rib width is the most critical parameter. Thus, the width range for which leakage losses are small has to be maximized to ensure low loss operation for waveguides with slightly fluctuating width. For this purpose, we define ΔB as the width range for which losses are below 1 dB/cm (see Fig. 1 (c)) and study this parameter in dependence of the geometry parameters. The etch depth e has a major impact on ΔB as Fig. 2 (a) shows. For shallow etch depths, ΔB significantly increases and the influence of the slot thickness is small. However, for rib-type slot waveguides the applicable range of S is limited by the effective index of the odd TE slab mode outside of the rib [8]. If the effective index of the odd TE slab mode becomes higher than that of the TM-like slot mode leakage occurs again because the resonance condition can only be fulfilled for one of the two TE slab modes at the same time. In the example shown in Fig. 2 (a) this situation occurs for $e = 0.07 H_{\mathrm{Str}}$ at $S \approx 70$ nm. With increasing etch depth this effect diminishes and for the slab/wire-type,

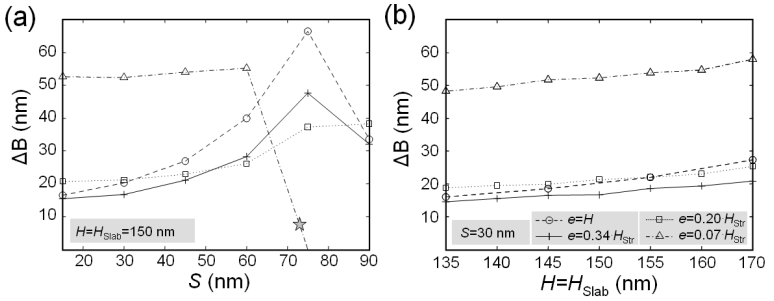


Figure 2: Dependence of ΔB on (a) the slot thickness S and on (b) the waveguide thicknesses $H = H_{\mathrm{Slab}}$ for different etch depths e. The star indicates the slot thickness where coupling to the odd TE slab mode occurs.

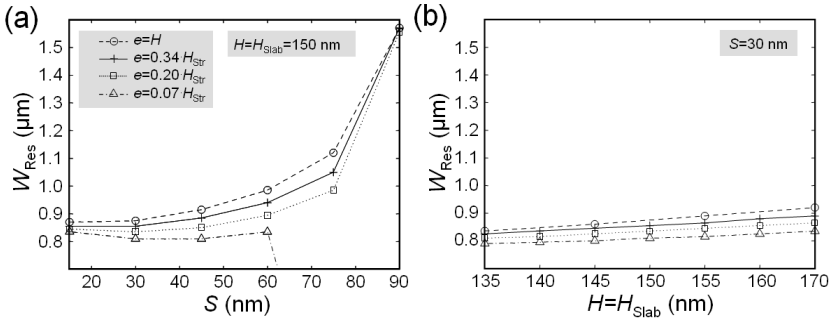


Figure 3: Width W_{Res} for which the resonance occurs as a function of (a) the slot thickness S and (b) the waveguide thickness $H = H_{\mathrm{Slab}}$ for different etch depths e.

i.e., for $e = H$ the effective index of the even and odd TE slab mode outside the rib become identical. Deeply etched structures, on the other hand, show a strong dependence of ΔB on the slot thickness. For $e = H$ the width range ΔB reaches its maximum at $S \approx 75$ nm. In contrast, the dependence of ΔB on the thicknesses H and H_{Slab} is almost negligible (see Fig. 2 (b)) while the etch depth again has a strong influence. Asymmetries in the amount of $H_{Slab} = H \pm 15$ nm do not affect the ΔB as well.

Apart from the width range ΔB also the shift of the rib width W_{Res} at which the resonance occurs is of high importance. Figure 3 (a) and (b) reveal that the slot thickness has a major impact on W_{Res} for $S > 70$ nm, whereas the influence of the waveguide thickness $H = H_{\mathrm{Slab}}$ is small.

Not only the deviating width also the variations of the other geometry parameters due to fabrication processes have to be taken into account. In order to study this influence we varied all geometry parameters, *i.e.*, H, H_{Slab}, e and S by ± 5 nm resulting in sixteen different geometries. As an example, Fig. 4 (a) shows the leakage losses of all these geometries for a structure centered at $H = H_{\mathrm{Slab}} = 135$ nm, $e = 0.081 H_{\mathrm{Str}}$ and $S = 50$ nm. The envelope of these curves (solid line) represents the maximum losses that can occur considering all possible variations. This envelope is a result of the shift of the resonant minimum W_{Res} for each geometry which leads to a reduction of the width range ΔB compared to 50 nm for a perfect system.

Next, we studied the envelope characteristic for rib-type slot waveguides with different $H = H_{\mathrm{Slab}}$, e and S (Fig. 4). As for the perfect system, also for the rib-type slot waveguides with variations the etch depth e and the slot thickness S have a major impact on the lateral leakage losses. Interestingly, smaller waveguide thicknesses H and H_{Slab} result in lower losses. For a rib-type slot waveguide with $H = H_{\mathrm{Slab}} = 135$ nm, $e = 0.081 H_{\mathrm{Str}}$ and $S = 30$ nm the width range of operation is larger than 20 nm.

Taken together, the results show that small slot thicknesses of $S < 50$ nm, shallow etch depths and thin waveguides are beneficial for maximizing ΔB. For a wire/slab system these optimizations are not sufficient and accordingly no low loss width range for geometries with variations of ± 5 nm can be obtained.

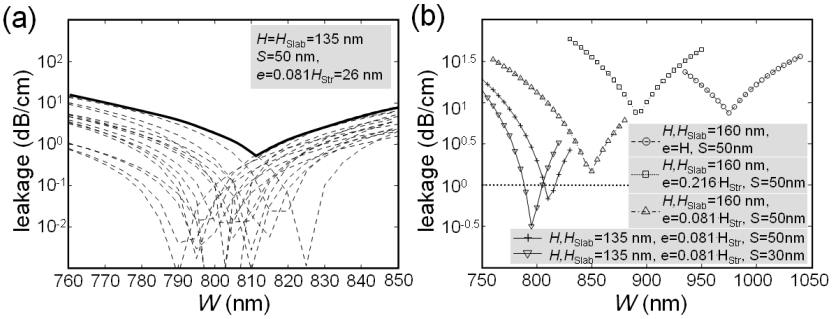


Figure 4: (a) Lateral leakage losses of a typical rib-type slot waveguide structure taking into account the variations of all geometry parameters by ± 5 nm. The envelope of these loss curves (solid line) indicates the maximum losses that can occur; (b) dependence of the maximum losses on the etch depth, waveguide thicknesses and slot thickness.

Conclusion

As our studies reveal, geometry parameters for rib-type slot waveguides can be found which ensure both low loss operation and high optical power confinement in the slot. Moreover, the results show that they can be designed to be sufficiently tolerant against variations of all geometry parameters. Therefore, rib-type slot waveguides have the potential to be utilized for applications were electric wiring or self-suspension are required without foregoing the inherent advantages of the horizontal configuration.

References

[1] C. A. Barrios and M. Lipson, "Electrically driven silicon resonant light emitting device based on slot-waveguide," Opt. Express **13,** 10092–10101, 2005.

[2] P. Muellner and R. Hainberger, "Structural optimization of Silicon-On-Insulator Slot waveguides," IEEE Photon. Technol. Lett. **18,** 2557–2559, 2006.

[3] V. R. Almeida, Q. Xu, C. A. Barrios, and M. Lipson, "Guiding and confining light in void nanostructure," Opt. Lett. **29,** 1209–1211, 2004.

[4] A. A. Oliner, S.-T. Peng, T.-I. Hsu, and A. Sanchez, "Guidance and leakage properties of a class of open dielectric waveguides. II - New physical effects," IEEE Trans. Microwave Theory Tech. **29,** 855–869, 1981.

[5] M. A. Webster, R. M. Pafchek, A. Mitchell, and A. Koch, "Width dependence of inherent TM-mode lateral leakage loss in Silicon-On-Insulator ridge waveguides," IEEE Photon. Technol. Lett. **19,** 429–431, 2007.

[6] P. Muellner, N. Finger and R. Hainberger, "Lateral leakage in symmetric SOI rib-type slot waveguides," Opt. Express **16,** 287–294, 2008.

[7] N. Finger, C. Pacher, and W. Boxleitner, "Simulation of guided-wave photonic devices with variational mode-matching," *AIP Conference Proceedings*, 893, pp. 1493–1494, 2007.

[8] R. Hainberger and P. Muellner, "Modal behavior of SOI slot waveguides," *Proceedings of the Symposium on Photonics Technologies for 7th Framework Program*, pp. 282–285, Wroclaw, 2006.

[9] P. Muellner, N. Finger and R. Hainberger, "Leakage studies on SOI slot waveguide structures," *Proceedings of SPIE*, 6898, San Jose, 2008.

Liquid crystal-infiltrated nanocavity and waveguide in deeply etched InP-based photonic crystals

I. Barbu[1], H.H.J.E. Kicken[1], P.A.M. Nouwens[1], R.W. van der Heijden[1], F. Karouta[1], R. Nötzel[1], and H.W.M. Salemink[1,2]

[1]COBRA Inter-University Research Institute and Centre for NanoMaterials, Eindhoven University of Technology, POBox 513, NL 5600MB Eindhoven, The Netherlands
i.barbu@student.tue.nl
[2]Kavli Institute of Nanoscience, Delft University of Technology, POBox 5053, NL 2600 GB Delft, The Netherlands

Abstract. *Deeply etched InP-based planar photonic crystals incorporating point and line defect structures were fabricated and experimentally investigated. Tuning of the H1 cavity mode and the W3 waveguide mini-stopband by infiltration with the liquid crystal K15 is experimentally demonstrated.*

Introduction

Much research effort has been devoted to the study of photonic crystals (PC) [1] due to their unique optical properties. A practical realization of 2D planar PCs consists of a periodic arrangement of air cylinders deeply etched in a semiconductor heterostructure slab waveguide of the type InP-InGaAsP-InP [2,3], which is an important system for photonic integrated circuits, operating at telecom wavelengths. PCs incorporating defects can then serve as building blocks for circuit components.

In this contribution we report the smallest possible cavity in this 2D PC, created by omitting the etching of a single hole, known as H1 cavity. Small cavities are of interest for components as a low-threshold laser [4,5] or drop filter [6]. Also the W3 waveguide, consisting of a line defect with three missing rows of holes is investigated. It displays a Mini Stopband (MSB), which can be employed as a wavelength division demultiplexer [7]. Both devices were studied in combination with infiltration of the air holes with Liquid Crystal (LC) [8,9] to create the possibility of tuning or trimming the PC-based devices.

Experimental details

2D PCs consisting of a triangular array of air holes were deeply etched in an InP/InGaAsP/InP slab waveguide with the lattice constant a varying from 309 to 522 nm (Δa = 20 nm) ("lithographic tuning") and hole radii r designed to be r/a~0.3. The structures were defined by 30 keV electron-beam lithography and etched using Cl_2-based Inductively Coupled Plasma (ICP) etching [3]. The etched holes show almost vertical sidewalls in their upper part [3]. The 500 nm-thick quaternary layer was sandwiched between an upper 500-nm thick InP cladding layer and a bottom InP buffer layer. Transmission measurements based on the end-fire approach used as light source a tunable external cavity diode laser (1470-1570 nm tunable range). Tapered ridge waveguides were used to couple the light into and out of the PC waveguide or cavity. The nematic liquid crystal K15 (5CB) used for infiltration has a crystalline to nematic phase transition temperature T_{cn} = 23°C and a nematic to isotropic transition temperature (clearing temperature) T_{ni} = 35.4°C [9]. In the nematic state the LC-K15 is a birefringent material with n_o = 1.516 and n_e = 1.682 as the ordinary and extraordinary

refractive indices, respectively at a wavelength of 1.5 μm. In the isotropic state the refractive index at $T = 40^oC$ is $n_i = 1.575$.

Experimental results and discussion

In order to assess the LC infiltration efficiency of our InP-based PCs, transmission measurements were first performed at room temperature (RT) (approximately 23°C). A comparison between the RT transmission spectra in the frequency region near the H1-cavity resonance peak is shown in Fig. 1(a) both for the LC-K15 infiltrated and uninfiltrated sample. The cavity is shown in the inset to Fig. 1(a) and has 4 PC rows between its center and the access waveguides. All data are disturbed by strong modulations, resulting from Fabry Perot interferences in the cavities formed by the entrance and exit access ridge waveguides. Both waveguides are approximately one mm long, and are terminated by the highly reflective cleaved facet at one side and the photonic crystal mirror at the other side. Mostly, a data sampling period of typically $d\lambda$ = 1 nm is chosen that does not resolve the FP-fringes, so that the data as in Fig. 1(a) appear noisy. For accurate measurements, or quantitative estimates, the sampling period is decreased to $d\lambda$ = 10 pm, which fully resolves the FP fringes as in Fig. 1(b). The two access ridge waveguides have slightly different lengths l_1 and l_2, leading to a low-frequency beat in the FP-modulation, which is also clearly present in Fig. 1(b). From the convolution of the high-frequency FP fringes in Fig.1(b) the cavity quality factor Q can be reliably estimated as Q ≈ 63. This Q-factor value compares favorably to that typically reported for the much larger FP-type cavity in similar InP-based PC's, which are in the order 20 to 30 [2]. Optimized chemically assisted ion beam etching (CAIBE) processes, however, have yielded single row Fabry-Perot cavities with Q up to ~300 [10].

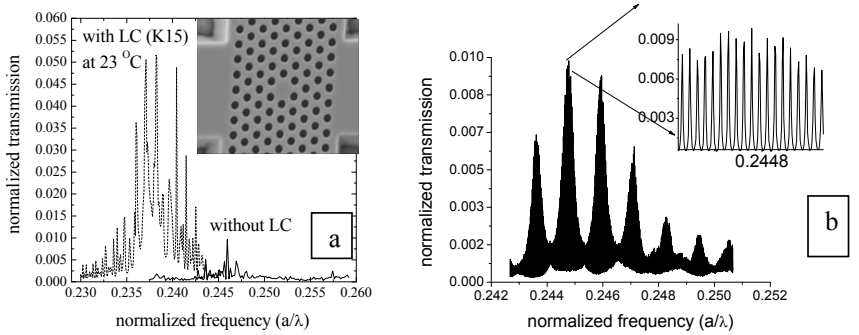


Figure 1: (a) H1-cavity resonance peak with (dashed line) and without (solid line) LC-K15 infiltration. The peak energy position redshifts, clearly indicating an increase in the average refractive index of the holes n_{hole}. A top-view scanning electron microscopy image (SEM) illustrating the H1 cavity is given in the inset. (b) High resolution measurement of the H1 cavity resonance for the uninfiltrated case. Both the low and the high frequency modulation (inset) are illustrated. The inset is a zoom-in on the peak centered at a/λ = 0.2448.

Infiltration has a strong effect on the H1 cavity resonance as shown in Fig 1(a). The cavity peak redshifts by approximately $\Delta(a/\lambda)=0.8\times10^{-2}$. The redshift corresponds to an increase in the average refractive index n_{hole} of the holes, as expected. Martz *et al.* [9] have observed the redshift of a ~1-row FP cavity resonance upon infiltration with the same LC of $\Delta(a/\lambda)=1.38\times10^{-2}$. Simulations suggest that our lower value for the H1

cavity results from a lower effective index of the holes, or incomplete infiltration. Although the H1 cavity mode peak transmission T_{peak} is enhanced by 5 times after infiltration, its quality factor decreases to only Q~36. Both the transmission enhancement and peak broadening were also observed for the FP-cavity with an empty-hole Q-factor of ~300 [9]. This behavior may be explained by a modification of the PC mirror optical properties and the H1 intracavity losses [9] which are likely to influence both the cavity mode excitation efficiency and the mode profile. It is believed that higher excitation efficiency might account for larger T_{peak} whereas weaker confinement of the mode inside the cavity (greater penetration into the PC mirrors) could result into lower cavity quality factors. However, further experimental and theoretical investigations should be performed in order to verify these assumptions.

The second defect structure whose spectral properties were investigated was the PC W3 waveguide. It is now a well-known fact [7,11] that in such a 2D PC multimode channel waveguide an anticrossing phenomenon takes place when the guided fundamental mode (FM) couples to a counterpropagating higher order mode (HOM). Then part of the FM energy is transferred to the HOM and thus a dip T_{min} called a "mini-stopband" (MSB) [11] appears in the transmission spectrum. The HOM corresponds to light bouncing between the PC boundaries, thus slowly propagating and resembling the FP resonator.

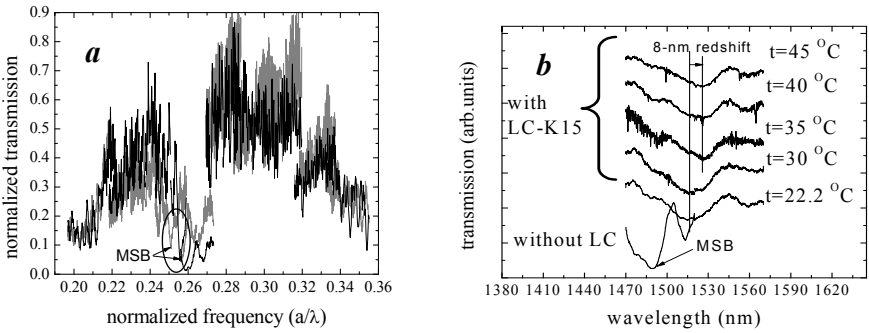


Figure 2: (a) wide frequency, low resolution transmission spectrum versus a/λ ("lithotuned") before (black) and after infiltration (grey) (b) transmission versus wavelength scan for a single PC for the sharp MSB dip before and after infiltration and in the latter case at several temperatures. All spectra are vertically shifted for clarity.

We observe the MSB in a W3 waveguide easily and consistently in several W3 guides investigated, as shown in the wide frequency scan in Fig. 2(a) for a 10 μm long guide. This wide scan, which is necessarily obtained from several PCs with different lattice constants (lithotuning) and low resolution, is not necessarily continuous as the properties may differ somewhat from crystal to crystal. For accurate measurements, one particular PC is picked that contains a sharp dip due to the MSB. The MSB is shown in Fig. 2(b) for the crystal with interhole spacing a = 381 nm before and after the infiltration. Data are taken in high resolution, but Fabry-Perot fringes are numerically averaged out. Near the dip, the FP fringe amplitude decreases strongly as the W3 waveguide becomes lossy. RT transmission measurements (22.2±0.2°C) of the infiltrated sample revealed a redshift of 30.3 nm from 1487 nm to 1517.3 nm of the MSB wavelength location. When the temperature was raised up to 30±0.2°C with the LC still deep in the nematic state, no measurable shift of the MSB was noticed. Only

when the PC device reached the LC K15 clearing temperature of 35 ^{0}C, an additional redshift of 8 nm of T_{min} was noticed. A similar redshift upon temperature tuning was observed for the FP resonance peak [12]. The LC is now in the isotropic state and in this regime the refractive index is constant n_i = 1.575. Therefore, a variation of the MSB position is not expected when the temperature is increased above T_{ni}. The spectra in Fig. 2 corresponding to 35, 40 and 45^{o}C illustrate the expected zero shift of the MSB.

Conclusions

We have demonstrated the possibility of tuning the spectral properties of a H1 cavity mode formed in a deeply etched InP-based 2D PC by infiltration with the liquid crystal K15. A redshift of the H1 cavity resonance was observed simultaneously with enhanced peak transmission and decreased cavity quality factor. Furthermore, a similar PC containing a W3 waveguide was filled with the same LC. We successfully demonstrated the temperature tuning of the waveguide MSB by thermally modifying the LC refractive index.

We like to thank C.W.M. Bastiaansen and D.J. Broer for help and advice on the liquid crystals. This work is supported by FOM and NanoNed.

References

[1] J.D.Joannopoulos, R.D. Meade, and J.N. Winn, *Photonic crystals: Molding the flow of light*, Princeton, NJ: Princeton Univ. Press, 1995

[2] R. Ferrini, D. Leuenberger, M. Mulot, M. Qiu, J. Moosburger, M. Kamp, A. Forchel, S. Anand, and R. Houdre, "Optical study of two-dimensional InP-based photonic crystals by internal light source technique", *IEEE J. Quantum. Electron.*, vol. 38, pp.786-799, 2002

[3] C. F. Carlström, R. van der Heijden, F. Karouta, R.W. van der Heijden, H.W.M. Salemink, and E. van der Drift, "Cl_2/O_2-inductively coupled plasma etching of deep hole-type photonic crystals in InP", *J. Vac. Sci. Technol. B*, vol. 24, pp. L6-L9, 2006

[4] O. Painter, R.K. Lee, et al., "Two-dimensional photonic band-gap defect mode laser", *Science*, vol. 284, pp. 1819-1821, 1999

[5] C. Monat, C. Seassal, X. Letartre, P. Viktorovitch, et al., "InP 2D photonic crystal microlasers on silicon wafer: room temperature operation at 1.55 μm", *Electron. Lett.*, vol.37, pp. 764-765, 2001

[6] H. Takano, Y. Akahane, T. Asano, S. Noda, "In-plane-type channel drop filter in a two-dimensional photonic crystal slab", *Appl. Phys. Lett.*, vol. 84, pp. 2226-2228, 2004

[7] L. Martinelli, H. Benisty, O. Khayam, G.-H. Duan, H. Heidrich, and K. Janiak, "Analysis and optimization of compact demultiplexer monitor based on photonic-crystal waveguide", *J. Lightwave Technol.*, vol. 25, pp. 2385-2394, 2007

[8] K. Busch and S. John, "Liquid-crystal photonic-band-gap materials: the tunable electromagnetic vacuum", *Phys. Rev. Lett.*, vol. 83, pp. 967-970, 1999

[9] J. Martz, R. Ferrini, F. Nüesch, L. Zuppiroli, B. Wild, L.A. Dunbar, R. Houdré, M. Mulot, and S. Anand, "Liquid crystal infiltration of InP-based planar photonic crystals", *J. Appl. Phys.*, vol. 99, pp. 103105 1-4, 2006

[10] A. Berrier, M.Mulot, S. Anand, A. Talneau, R. Ferrini, and R. Houdré, "Characterization of the feature-size dependence in Ar/Cl_2 chemically assisted ion beam etching of InP-based photonic crystal devices", J. Vac. Sci. Technol. B, vol. 25, pp 1-10, 2007

[11] S. Olivier, M. Rattier, H. Benisty, C. Weisbuch, C.J.M. Smith, R.M. de la Rue, T.F. Krauss, U. Oesterle, R. Houdré, "Mini-stopbands of a one-dimensional system: the channel waveguide in a two-dimensional photonic crystal", *Phys. Rev. B.,* vol.63, pp. 113311 1-4, 2001

[12] R. Ferrini, J. Martz, L. Zuppiroli, B. Wild, V. Zabelin, L.A. Dunbar, R. Houdré, M. Mulot and S. Anand, "Planar photonic crystals infiltrated with liquid crystals: optical characterization of molecule orientation", Opt. Lett., vol. 31, pp 1238-1240, 2006

Efficiency enhancement of grating couplers for single mode polymer waveguides through high index coatings

Roman Bruck and Rainer Hainberger

Austrian Research Centers GmbH - ARC, Nano-System-Technologies
Donau-City-Str. 1, 1220 Vienna, Austria
rainer.hainberger@arcs.ac.at

Abstract - *High-index coatings on top of surface gratings strongly enhance the grating coupling strength in low-index contrast waveguide systems. This opens up new fields of applications for grating couplers such as coupling into single-mode polymer waveguides.*

Introduction

Polymers are an attractive material system for the realization of planar integrated optical waveguide devices in a wide range of applications [1]. Their fast and easy processing allows for cost-effective mass production using injection molding or hot embossing, while their tunable properties provide high flexibility in design. Beside data and telecom applications sensing is an important emerging market segment for polymer waveguide devices. Single mode behavior of waveguides is essential for sensing and for high performance telecom devices. Coupling into thin waveguides is a challenging task where grating couplers showed promising results for different material systems (gratings in polymers [2], silicon nitride (SiN) [3] or silicon (Si) [4]).

The coupling strength α of a grating for coupling out of a waveguide expresses the rate of leakage of the guided mode into the adjacent media [5]. In the case of input couplers, which are the focus of this paper, it determines the optimum spot size for an incident Gaussian beam at which maximum coupling efficiency is achieved. In high-index contrast waveguides systems such as silicon-on-insulator (SOI) α can be in the order of 0.05 μm^{-1} allowing for spot sizes as small as 10 μm [6, 7] without sacrificing coupling efficiency. In polymer waveguide systems, on the other hand, α only amounts to 0.0013 μm^{-1} even for a comparatively high index difference (n=1.46/1.65/1.52 for substrate/waveguide/cladding) leading to an optimum spot size of several hundred microns as illustrated in Fig. 1b). Behind gratings, lateral tapers are needed for coupling into single mode waveguides. The

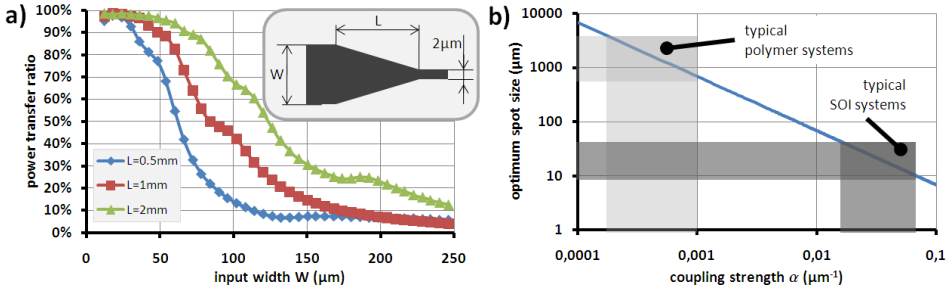


Figure 1: a) PTR of lateral polymer waveguide tapers. b) Optimum spot size of an incident Gaussian beam as a function of the coupling strength of a uniform grating.

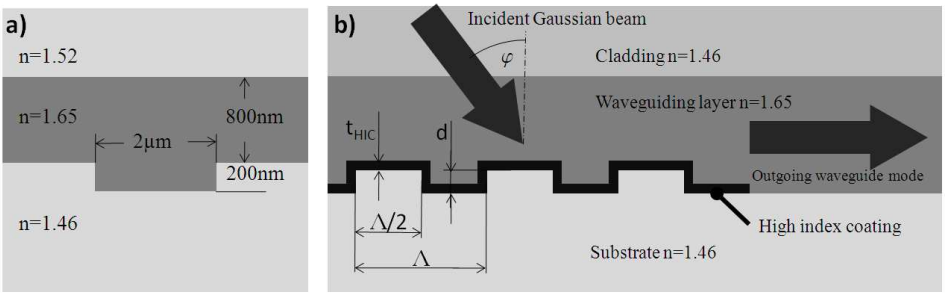


Figure 2: a) Cross section of single mode polymer waveguides and b) schematic view of the grating structures with high index coating investigated in this study.

power transfer ratio (PTR) of lateral tapers is a highly nonlinear function of the input width. Fig. 1a) shows the results of 2D beam propagation method simulations for the polymer system depicted in Fig. 2a). In the given example, tapering with a 1-mm long taper is possible for input widths up to 50 μm (PTR $>$ 90%). Thus, a spot size sufficiently small for low-loss lateral tapering results in a strongly reduced coupling efficiency of the grating and vice versa. In this paper, we show that this conflict can be solved by depositing a thin high-index coating (HIC) on the grating. Due to the strong dependence of α on the index difference [8] the higher index difference leads to a reduction of the optimum spot size for the grating, thus enabling efficient coupling via lateral tapers into single mode waveguides. In the following, simulations and experimental results illustrating the effect of an HIC on a polymer waveguide system is presented.

Simulation results

The numerical model of the simulation tool used for the calculation of grating input couplers employs a rigorous Floquet-Bloch (FB) approach [9, 10, 11]. For the computation of the 1D grating layer eigenmodes [10] an efficient and numerically extremely stable high-order finite-element approach is applied. The polymer waveguide system studied in this paper is assumed to consist of a polymethylpeptene (PMP) substrate (n=1.46), a polyimide (PI) waveguide core layer (n=1.65) and an Ormoclad (OC) cladding (n=1.52). The surface grating at the substrate/waveguide core interface (see Fig. 2b)) comprises hundred periods of Λ=1.75 μm, *i.e.*, the coupling condition is fulfilled for an angle of incidence φ of about 45deg in air at λ=1.55 μm. The grating has a duty cycle of 0.5 and the diameter of the incident TE-polarized Gaussian beam is 30 μm. Fig. 3 shows the calculated PTR of input gratings with a 1 μm thick polymer waveguide layer as a function of the etch depth *d* for a SiN (n=2) and an amorphous Si (n=3.48) HICs with different thicknesses. The PTR increases with the HIC thickness. The termination condition of the simulation was the excess of the effective index of the waveguide mode over the refractive index of the waveguide core layer. The simulations were verified with 2D-FDTD simulations. These FDTD-simulations indicated that a further increase of the HIC thickness has a negative effect on the PTR.

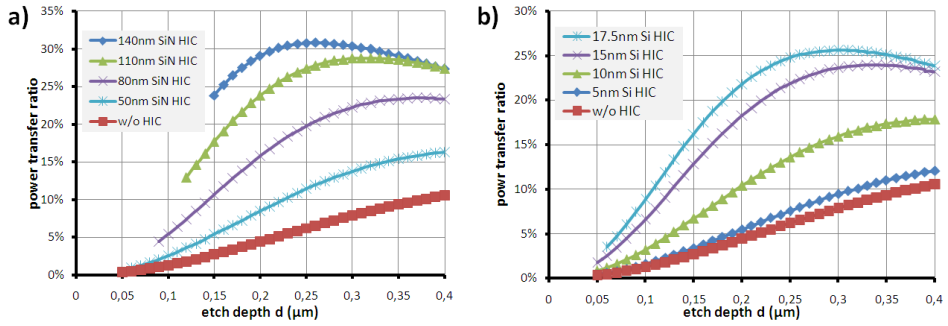


Figure 3: Calculated PTR of a 1 μm thick polymer waveguide as function of the etch depth d for a) a SiN (n=2) and b) amorphous Si (n=3.48) HICs.

Fabrication and experimental results

In order to experimentally verify the positive effect of a HIC on grating couplers in low index contrast waveguides samples were prepared on silicon wafers. Instead of PMP, SiO_2 was used as lower cladding, which matches the refractive index of PMP in the near infrared. A 210nm SiN anti-reflection layer and a 3 μm thick SiO_2 layer were deposited on a silicon wafer via PECVD. The gratings and the inverse rib waveguides were patterned using standard photolithography and etched into the SiO_2 layer with an SF_6 RIE process. The etch depth varied slightly between 200 nm and 250 nm over the sample due to variations in the RIE process. The SiN HIC was deposited using PECVD and selectively removed outside the grating area employing a RIE etch step. A 1-μm thick layer of a spin-coatable PI from HD Microsystems was used as waveguide core layer material. After spin-coating of Ormoclad as cladding the samples were cleaved to enable fiber butt coupling for the output waveguides.

Four series of samples were prepared with different thicknesses of the SiN HIC. For each series eleven gratings with and eleven without HIC were measured. The enhancement of the input coupling efficiency induced by the HIC could be confirmed. Despite

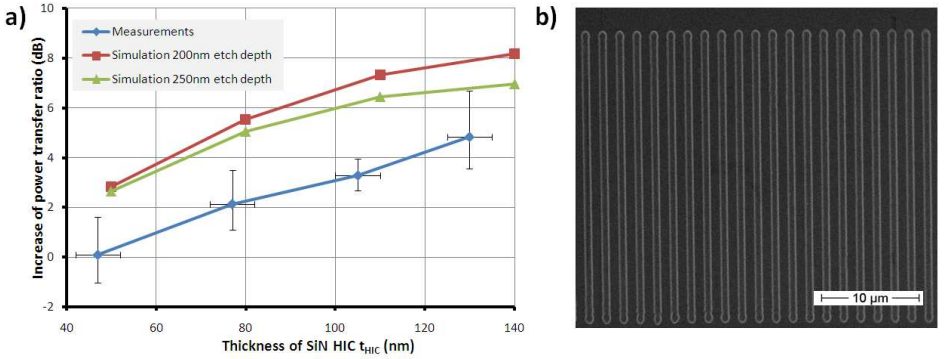


Figure 4: a) Calculated and measured PTR increase as a function of the SiN HIC thickness and b) SEM picture of a 30 μm width grating with 140-nm HIC.

a nearly 5-dB increase in the coupling efficiency with a 135-nm SiN HIC, the measured enhancement is not as high as in the simulation. This mismatch and the comparatively large variations between gratings of the same HIC thickness can be most likely attributed to imperfections of the fabricated grating structures such as non-vertical side walls, and variations of the duty cycle and the thickness of the waveguide core layer.

Conclusion

The coupling strength of polymer waveguide grating couplers can be significantly increased by applying a HIC. This technique allows for compact grating couplers with optimum spot sizes of several tens of microns, which facilitate the coupling to single mode waveguides using adiabatic tapers in low index difference material systems. A wide range of materials is suitable to act as HIC. Since the HIC is only present in the comparatively small grating area the optical quality and absorption losses of the HIC have only minor influence on the PTR. Therefore, low-temperature thin film deposition techniques usually not used for optical waveguide fabrication because of lower optical layer quality such as sputtering could be employed for the HIC deposition on polymers waveguides.

Acknowledgment

This research was supported through the grant PLATON PolyWaG (project no. 1152) funded by the Austrian NANO Initiative. The authors thank Norman Finger for his work on the simulation tools and his support.

References

[1] KK. Tung, W.H. Wong and E.Y.B. Pun, "Polymeric optical waveguides using direct ultraviolet photolithography process", *Appl. Phys. A* , vol. 80, pp. 621-625, 2005.

[2] R. Waldhäusl, B. Schnabel, P. Dannberg, E.-B. Kley, A. Bräuer and W. Karthe, "Efficient coupling into polymer waveguides by gratings", *Appl. Opt.* , vol. 36, pp. 9383-9390, 1997.

[3] G. Voirin, D. Gehringer, O.M. Parriaux and B. Usievich, "Si3N4/SiO2/Si waveguide grating for fluorescent biosensors", *Proceeding of SPIE* , pp. 1009-116, 1999.

[4] R. Orobtchouk, A. Layadi, H. Gualous, D. Pascal, A. Koster and S. Laval, "High-efficiency light coupling in a submicrometric silicon-on-insulator waveguide", *Appl. Opt.* , vol. 39, pp. 5773-5777, 2000.

[5] N. Destouches, D. Blanc, J. Franc, S. Tonchev, N. Hendrickx, P. Van Daele and O- Parriaux, "Efficient and tolerant resonant grating coupler for multimode optical interconnetions", *Opt. Express* , vol. 25, pp. 16870-16879, 2007.

[6] D. Taillaert, P. Bienstman and R. Baets, "Compact efficient broadband grating coupler for silicon-on-insulator waveguides", *Opt. Lett.* , vol. 29, pp. 2749-2751, 2004.

[7] G. Roelkens, D. Van Thourhout and R. Baets, "High efficiency grating coupler between silicon-on-insulator waveguides and perfectly vertical optical fibers", *Opt. Lett.* , vol. 32, pp. 1495-1497, 2007.

[8] T. Tamir and S.T. Peng, "Analysis and Design of Grating Couplers", *Appl. Phys.* , vol. 14, pp. 235-254, 1977.

[9] N. Finger and E. Gornik, "Analysis of metallized-grating coupled twin-waveguide structures", *IEEE J. Quantum Electron.* , vol. 35, No. 5, pp. 832-843, 1999.

[10] R. J. Noll and S. H. Macomber, "Analysis of grating surface emitting lasers", *IEEE J. Quantum Electron.* vol. 26, pp. 456, 1990.

[11] G. Hadjicostas, J. K. Butler, G. A. Evans, N. W. Carlson, R. Amantea, "A numerical investigation of wave interactions in dielectric waveguides with periodic surface corrugations", *IEEE J. Quantum Electron.* , vol. 26, pp. 893, 1990.

Design on tolerances in integrated optics

A. Melloni[1], G. Cusmai[1] and F. Morichetti[1,2]

[1]*Dipartimento di Elettronica e Informazione – Politecnico di Milano - Italy*
melloni@elet.polimi.it
[2]*Corecom, Milano, Italy*

Abstract. *The aim of the "design on tolerances" technique is to design a circuit that is robust against statistical variations of the parameters due to technological processes and aging, maximize the yield and locate the most critical parameters of the circuit. Preliminary numerical examples concerning integrated optical filters are discussed.*

Introduction

The scenario of optical interconnects, optical networks and wideband connections will shortly require large and complex optical circuits, probably based on integrated planar technologies, but exploiting hybrid integration to combine a large number of functions towards a VLSI level (Very Large Scale of Integration, a well known concept in electronics). It will be then of major importance the availability of software platforms able to simulate and design complex and large circuits, in order to reduce design, production and packaging costs and increase the yield and the reliability of the devices.
The design of a circuit is typically carried out by searching the circuit parameters values that satisfy a given spectral transfer function or a time response in very well specified conditions. The designer operates by using synthesis techniques, optimization procedures and his own experience. However, the set of nominal values corresponds to a single point in the multi-dimensional space of the circuit variables, moving within a domain whose boundaries are fixed by technological tolerances, the uncertainty of the parameters and the drift due to aging or other phenomena. For these reasons, an even more important aspect in the design procedure is the possibility to access more sophisticated calculations such as optimizations, sensitivity analysis, yield estimation, risk analysis and concepts as 'statistical design' or 'design on tolerances'.
In this contribution it is not possible to be exhaustive on this subject but an initial investigation is carried out. The idea, quite well known in many other fields such as electronics and microwave, is to modify the parameters of the circuits obtained with classical 'deterministic' design techniques to get a more robust or 'optimal' set of parameters of the circuit. The technique is briefly described and some results concerning the yield and the sensitivity obtained on two filters with different architectures and similar spectral responses are discussed.

Yield and sensitivity

Let's define a measure of the characteristics or performances of a circuit, called "circuit performance space" and a space defined by all the variables and parameters that have some role in determining the circuit behavior. The circuit requirements requested in the circuit performance space define an acceptability region R_A in the space of variables, in which the values assumed by the circuit variables satisfy such specifications. If the region R_T in the variable space identified by processes tolerances (for example) around the nominal values of the variables is not completely included in the acceptability region, some circuits will not satisfy the requirements defined in the performance space.

This typically happens in mass production processes. The yield is related to such overlap, that is as the ratio between the number of circuits satisfying specifications and the total number of produced circuits [1, 2] or, equivalently, as the probability to generate a circuit satisfying the specifications. Said $f(\phi)$ the joint probability density distribution of the circuit variables, the yield is given by [2]

$$Y = \int_{R_A} f(\phi)d\phi = \int_{-\infty}^{+\infty} I_A(\phi) f(\phi)d\phi = E\{I_A(\phi)\} \quad (1)$$

where I_A defines the acceptability region R_A. The yield is therefore the average value of the acceptability function in the whole variables space. The integral in (1) can be estimated with the Monte-Carlo method, by generating N circuit parameters sets ϕ_k, ($k=1...N$) according to $f(\phi)$ and estimating the integral (1).

The variance of the estimated yield decreases only as the square root of N and in order to reduce the Monte-Carlo estimator variance, we have chosen to modify the algorithm by introducing the correlation between successive estimations (correlated sampling). The information on the yield can be exploited to adjust the nominal design of the circuit variables by using a standard optimizer routine, or a more efficient algorithm for the specific yield optimization problem, such as the "gravity centers" algorithm [3,4] to find the "best" set of circuit parameters.

Fig. 1 shows schematically the concept for a simple case with only two parameters, P_1 and P_2. In a) the nominal design D_N ensure the 'best' circuit performance but the uncertainty on the parameters defines a space R_T with a poor overlap with the acceptability region, that is a low yield. In b) the parameters of the circuit have been moved to D_F with an evident increase of the yield.

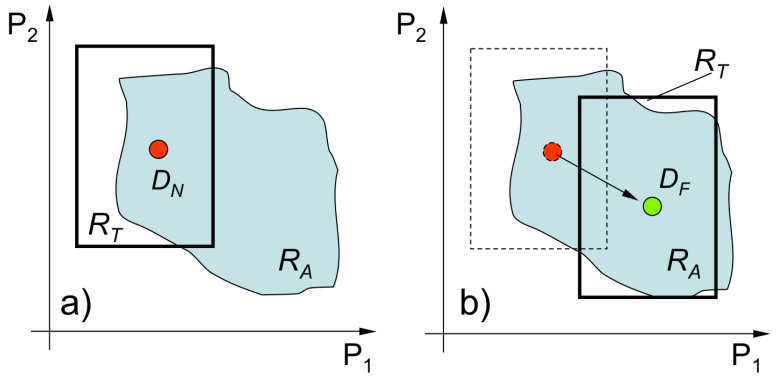


Fig. 1 – Yield maximization and design centering by using information on parameters tolerances.

The sensitivity parameter *M*

This analysis brings naturally to the definition of the parameter M, connected to the sensitivity of the yield with respect to each parameter of the circuit. The parameter M is based on the concept of statistic independence: for a variable x we call $p(x)$ the relative density of probability, $p_P(x)$ the conditioned probability to pass the specifications and $p_F(x)$ the conditioned probability to fail the specifications. The overlap degree of the two probability densities $p_P(x)$ and $p_F(x)$ is a direct measure of the weight of the variable on the yield of the circuit. M is evaluated by using a Monte-Carlo approach [5] as

$$M = \int_{-\infty}^{+\infty} |p_P(x) - p_F(x)| dx . \quad (2)$$

The parameter (component) of the circuit with the smaller degree of overlap, that is with the largest *M,* is the greatest responsible for the deterioration of the yield. The parameter *M* can assume a value between 0, in case of no influence, and 2 in case of total mismatch between $p_P(x)$ and $p_F(x)$.

Optical Filter Comparison

In this section, as an example of "design on tolerances", a 7-cascaded Mach-Zehnder filter and a 4 coupled-ring-resonator filter are considered. The two different filter architectures are designed with classical techniques in order to respect the same spectral specifications. The number of stages has been found by maximizing the yield with respect to the number of stage in case of tolerances both on the coupling coefficients *K* of the directional couplers and on the effective refractive index n_{eff} of the waveguides. The FSR of the filters is 100GHz, the bandwidth is 20GHz and the minimum requirements in both passband and stopband are clearly marked in Fig. 2. The minimum off-band rejection is 18 dB and the in-band return loss is 15 dB.

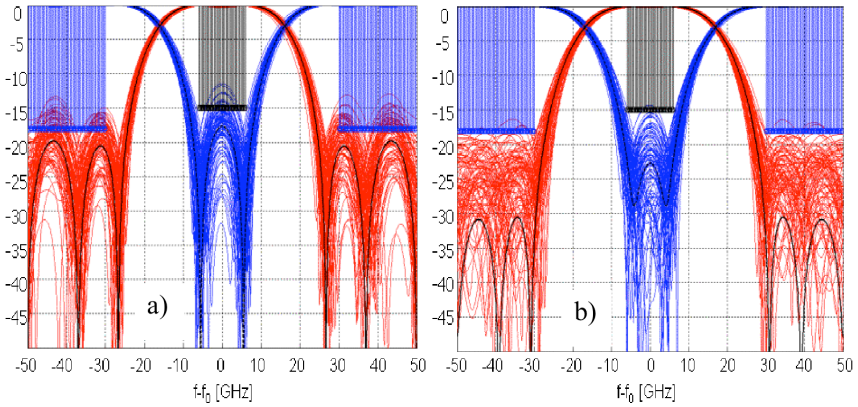


Fig. 2 - *Impact of the tolerances on a 7-cascaded Mach-Zehnder before a) and after b) yield optimization.*

Fig. 2a) shows the impact of the tolerances of the eight coupling coefficients {98.41; 0.76; 5.13; 41.99}% of the cascaded Mach-Zehnder symmetrical filter. In these conditions only the 24.5% of the realized circuits satisfy both in-band and off-band requirements. The probability distribution of the *K* coefficients has been assumed Gaussian with a standard deviation of the field coupling κL equal to 1 degree. A Gaussian statistic of the local effective refractive index with a standard deviation equal to $\sigma_{neff} = 5 \cdot 10^{-6}$ has been assumed. By means of an optimization technique, the new coupling coefficients {99.36; 0.87; 4.15; 43.20}% are calculated. Fig. 2b) shows the transfer function of 100 realizations on the optimized filter design and the yield now is greater than 90%. It is interesting to note that such a design is more critical compared with the nominal one as can be seen by the wider spread of the spectral responses but the final yield is much higher. In general it is difficult to say 'a priori' which is the 'best' design and a 'yield optimizer' is the only tool to perform such a process.

Similar results are found for the cascaded coupled-ring architecture, not shown for brevity. In this case the yield increases from 89.3% to 92.4% and the coupling coefficients move from D_N={83.09; 34.92; 20.97; 34.92; 83.09}% to D_F={83.29; 34.7; 21.26; 34.7; 83.29}%. Note that despite the very high yield of the nominal design, a small improvement in the yield is found as well with a very small adjustments of the parameters. This does not means that the coupling coefficient should be realized with such a precision but that the design must centered in D_F, a substantial difference.
An even more important information derives from the sensitivity analysis of the various parameters of the circuits. Fig. 3 shows the parameter *M* relative to the parameters of the coupled-ring filter. In the figure it is clearly visible that the parameter *M* of the couplers decreases with the standard deviation of the n_{eff}. This means that if the control on the refractive index is very tight, the couplers, and especially the central couplers, are the most critical components of the circuit. The parameters *M* related to the refractive index of the rings, instead, increase with respect to σ_{neff}. Note that the refractive index of the first rings is almost non-influent. The curves cross near the standard deviation σ_{neff}=5e-6. Before this value the most critical components are the directional couplers, while for higher values it is the refractive index that is responsible of a decrease of the yield.

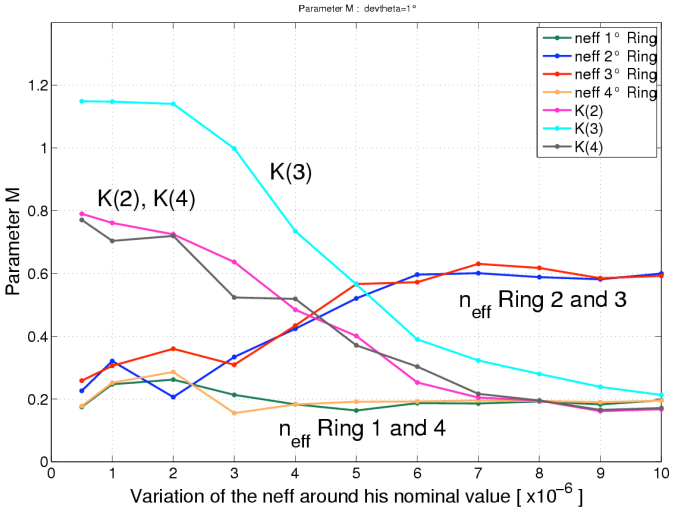


Fig. 3 – 4-cascaded ring filter. Parameter M of the central couplers and of the refractive index of the rings versus the standard deviation of the refractive index.

References

[1] R.Spence and R.S. Soin, *Tolerance Design of Electronic Circuits*, World Scientific Publishing Company, 1997.

[2] K.J. Antreich and H.E. Graeb and C.U. Wieser, "Circuit analysis and optimization driven by worst-case distances", IEEE Trans. on CAD design of integrated circuits and systems, Vol. 13, No. 1, 1994

[3] M. Keramat and R. Kielbasa, "Optimality aspects of Centers of Gravity algorithm for statistical circuit design", IEEE 1997.

[4] S.W. Director and G.D.Hatchel, "The simplicial approximation approach to design centering", IEEE Trans. on circuits and systems, 24, July1997.

[5] G.S. Fishman, "Monte Carlo concepts, algorithms and applications", Springer, 1996.

Deep-Subwavelength Optical Waveguides Based on Near-Resonant Surface Plasmon Polariton

Min Yan[1], Lars Thylén[1], Min Qiu[1], Devang Parekh[2]

[1] Department of Microelectronics and Applied Physics, Royal Institute of Technology, and Kista Photonics Research Center, Electrum 229, 16440 Kista, Sweden
min@kth.se
[2] Department of Electrical Engineering and Computer Sciences, University of California, Berkeley, Berkeley, CA94720

Abstract *- We discuss the feasibility of deploying two materials with close but opposite epsilon values for achieving deep-subwavelength surface plasmon polariton waveguides. In particular, waveguiding properties of a silver-silicon waveguide with a 25nm core size at 600nm wavelength are examined. Such waveguides potentially allows for ultrahigh-density optical integration.*

Introduction

Surface plasmon polaritons (SPPs) have recently attracted a great amount of attention in achieving subwavelength optical waveguiding. Unlike in convetional dielectric waveguides, light guided by SPP waveguides does not experience a diffraction limit. Therefore mode field of such a SPP waveguide can be squeezed into an arbitrarily small size. However, it should be noticed that not all SPP waveguides reported so far have subwavelength mode field size (MFS). For example, most long-range SPP waveguides achieve relatively low propagation loss because their modal energy is largely distributed in the low-loss dielectric material. Such waveguides usually have a very large MFS. In order to deploy SPP waveguides as integrated optical circuits, one has to design true subwavelength waveguides.

To date, there are several types of SPP waveguides known for their capability in achieving subwavelength guidance, such as the gap SPP waveguide [1], and metal corner SPP waveguide [2], etc. These subwavelength SPP waveguides are however all based on geometrical tailoring. In fact, the peculiar guidance principle of SPP waveguides allows their mode field to be confined in a subwavelength fashion without resorting to geometrical tailoring. For a 1D metal-dielectric interface, the guided SPP mode has its n_{eff} value defined as

$$n_{\text{eff}} = \sqrt{\frac{\varepsilon_+ \varepsilon_-}{\varepsilon_+ + \varepsilon_-}}, \tag{1}$$

where ε_+ and ε_- ($|\varepsilon_-| > \varepsilon_+$) are permitivities of the dielectric material and metal, respectively. From Eq. 1, it is noticed that n_{eff} can be arbitrarily large, depending on how close $(\varepsilon_+ + \varepsilon_-)$ is to zero. It follows that the transverse field decay constant in the cladding, $k_t = k_0\sqrt{n_{\text{eff}}^2 - \varepsilon_{\text{clad}}}$ ($\varepsilon_{\text{clad}}$ is either ε_+ or ε_-), can also be made arbitrarily large. This gives rise to the possibility of tightly confined field at the interface. A section of the interface can potentially confine light in nanodimensions in the 2D transverse domain. Such a subwavelength waveguide has the obvious advantage of being structurally very simple. A primiary reason for lack of proper study on such waveguide probably is that,

in addition to the divergent propagation constant, the propagation loss will also tend to infinity as the operation is near to the $\varepsilon_+ = -\varepsilon_-$ resonance condition. In fact, the contradictory relationship between confinement and loss for SPP waveguides has been observed for a wide varieties of guiding structures (e.g. [2, 3]). In view of many published results on SPP waveguides, it has generally been accepted that some novel loss reduction technique (rather than merely geometric optimization) has to be deployed in order to make functioning integrated optical circuits based on SPP. Decreasing environment temperature [4] and using quantum-dot-based metamaterials [5] could be two viable ways to achieving the goal. Considering this factor, SPP waveguides based on a single near-resonant interface deserve as much attention as other types of SPP waveguides do in realizing subwavelength light channeling. Effectively, such a near-resonant SPP waveguide relies on material engineering, other than geometrical tailoring. In the following, from the perspective of integrated photonic circuit, we will look into a realistic waveguide design based on a finite section of near-resonant metal-dielectric interface. Our preliminary analysis is based on materials available in nature. The modal properties of the waveguide, especially its attenuation loss, will be examined. The potentials and challenges of such waveguides will be discussed.

Realistic waveguide design

Two materials with close but opposite epsilon values (in their real part ε') at certain wavelengths do exist in nature, but not without loss. One example is silver (Ag) and silicon (Si). An examination of their dispersion curves tells that their epsilon values meet our requirement around the free-space wavelength of 600nm, at which $\varepsilon_{\mathrm{Ag}} = -16.08 + 0.4434i$ [6] and $\varepsilon_{\mathrm{Si}} = 15.58 + 0.2004i$ [7]. However, these two materials are highly lossy at this particular wavelength, which is manifested by the relatively large imaginary parts of the epsilon values (denoted as ε"). A single surface mode formed by the two materials at $\lambda = 600$nm has a loss value as large as 690.7dB/μm, rendering almost any waveguide built upon such a surface impractical. One of our objectives is to investigate how small the imaginary epsilon values (ε") of Ag and Si should be for practical applications.

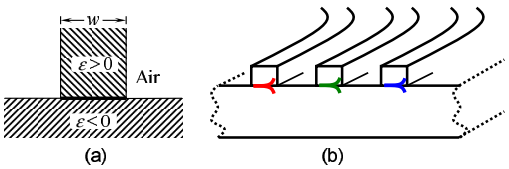


Figure 1: (a) Schematic diagram of the SPP waveguide. (b) Possible integration of the near-resonant SPP waveguides.

Figure 1(a) shows a schematic cross-section diagram of one possible waveguiding structure. The waveguiding interface has finite lateral size (w). The structure can be used to achieve high-density photonic integration in two dimensions on a planar substrate. Such an example is illustrated in Fig. 1(b). It should be noticed that several SPP waveguides which are similar to that sketched in Fig. 1(a) have been reported (e.g. [4]). However few of the studies have paid particular attention to achieving subwavelength guidance. First, to make sure the waveguide is single-mode, we calculate the geometric dispersion as a

function of the core width w at $\lambda = 600$nm (Fig. 2, left panel). Mode derivation is done in COMSOL with an electric-field- and edge-element-based finite element method. The blue curves (with dots) are the first two modes derived with $\varepsilon'' = 0$ for both Si and Ag materials. The red dots are calculated with ε'' values reduced to 1% (compared to their natural values). The mode index changes little when the ε'' values change from 0 to 1%. We will show later that when losses are higher, the waveguide is too lossy to be useful. From Fig. 2, it is seen that the waveguide is single-mode when $w < 27$nm. We hence take $w = 25$nm in our following analyses. The n_{eff} value is $\sim$15.6 at $w = 25$nm, which ensures the mode field is highly evanescent in the cladding regions.

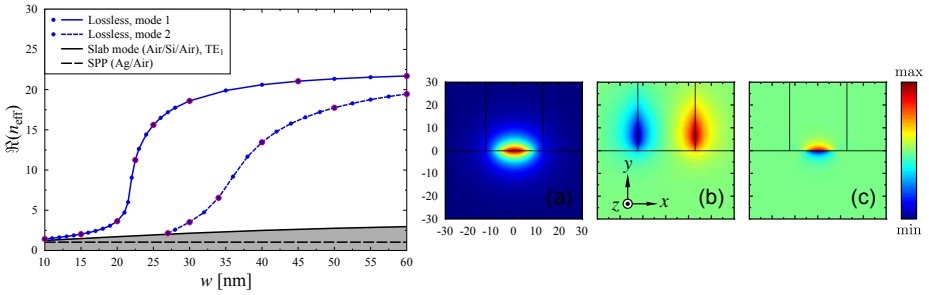


Figure 2: Left panel: Geometric dispersions of first two modes of the waveguide with respect to w. Loss is assumed to be zero. Red dots: the n_{eff} values when ε'' values of both Ag and Si are reduced to their 1%. Right three panels are field plots of the waveguide with a 25nm-sized core: (a) H_x field (min:0, max:1.27); (b) H_y field (min:-5.02e-2, max:5.02e-2); and (c) z-component Poynting vector S_z (min:-6.0e2, max:6.2e2). Axis unit: nm.

Mode supported by the waveguide is depicted in Fig. 2(a)-(c). The field does not change appreciably when the material losses vary from 0 to 0.1 (in fractions of their natural values). In the cladding regions, the mode field decreases to its $1/e$ over a $\sim$6nm distance. Therefore its MFS is approximated to be 37×12nm^2. The mode field has a major polarization along y direction. The z-component of the Poynting vector (S_z) shown in Fig. 2(c) confirms the highly confined energy flow in the waveguide. Notice that, although S_z in Ag region is negative, the net energy flow is positive.

The loss of the waveguide with $w = 25$nm is then computed as ε'' values of both Ag and Si are varied. The result is shown in a contour map in Fig. 3. ε'' values of both materials are varied from 10^{-6} to 10^{-1}, in fractions of their natural values. It is observed that the waveguide loss is almost equally sensitive to variations in each of the two ε'' values. In practice, the requirement of propagation length depends on the application. Here, given such a tiny circuit cross-section, a loss level of 1dB/μm (corresponding to a propagation length of a few micrometers) could be suitable for a wide range of purposes. A circuit with over 100 length-to-crosssection aspect ratio permits necessary waveguide bends for forming basic components (coupler, interferometer etc) and inter-connecting various ports in a high-density fashion. From Fig. 3, it is shown that both ε'' values (or equivalently, conductivities of the two materials) have to be decreased by $\sim$1000 times in order to have 1dB/μm propagation loss. It should be noted that keeping the desired negative ε' and decreasing ε'' will, as dictated by the Kramers-Krönig relations, require either other (meta)materials than the materials employed here, or possibly low temperature operation.

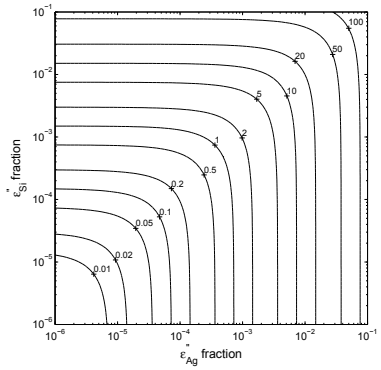


Figure 3: Contour plot of the loss values in dB/μm when the ε" values of both Ag and Si are varied in fractions of their natural values at room temperature.

Conclusion

In conclusion, we have shown that apart from solely relying on geometrical tailoring, choosing appropriate materials can be an equally compelling approach for achieving deep subwavelength mode field size for an SPP waveguide. From practical point of view, the main concern of such near-resonant waveguides is their relatively high propagation loss. However, we foresee that once the low-loss metamaterial or loss compensation technology matures, such SPP waveguides can be potentially useful for constructing exotic miniature optical devices.

Acknowledgement: This work is supported by the Swedish Foundation for Strategic Research (SSF) through the INGVAR program, the SSF Strategic Research Center in Photonics, and the Swedish Research Council (VR).

References

[1] D. F. P. Pile, T. Ogawa, D. K. Gramotnev, Y. Matsuzaki, K. C. Vernon, K. Yamaguchi, T. OKamoto, M. Haraguchi, and M. Fukui, "Two-dimensionally localized modes of a nanoscale gap plasmon waveguide," Appl. Phy. Lett. **87**, 261,114 (2005).

[2] M. Yan and M. Qiu, "Guided plasmon polariton at 2D metal corners," J. Opt. Soc. Am. B **24**, 2333–2342 (2007).

[3] G. Veronis and S. Fan, "Guided subwavelength plasmonic mode supported by a slot in a thin metal film," Opt. Lett. **30**, 3359–3361 (2005).

[4] A. Karalis, E. Lidorikis, M. Ibanescu, J. D. Joannopoulos, and M. Soljacic, "Surface-plasmon-assisted guiding of broadband slow and subwavelength light in air," Phys. Rev. Lett. **95**, 063,901 (2005).

[5] D. Parekh, L. Thylén, and C. Chang-Hasnain, "Metal nanoparticle metamaterials for engineering dielectric constants and their applications to near resonant surface plasmon waveguides," in *Frontiers in Optics, OSA Technical Digest Series*, p. FThF6 (Optical Society of America, 2007).

[6] P. B. Johnson and R. W. Christy, "Optical constants of the noble metals," Phys. Rev. B **6**, 4370–4379 (1972).

[7] E. D. Palik, *Handbook of Optical Constants of Solids*, (Academic Press, 1985).

Phase velocity estimation of a modulation wave in a quasi-velocity-matched electro-optic phase modulator using electro-optic sampling system

S. Hisatake[1], Y. Takemoto[1], K. Tada[1], T. Nagatsuma[1], and T. Kobayashi[2]

[1] Graduate School of Engineering Science, Osaka University, Japan
hisatake@ee.es.osaka-u.ac.jp
[2] Center for Advanced Science and Innovation, Osaka University, Japan

Abstract *- Direct observation of an electric field distribution on a resonant microstrip line (width:0.5 mm, height:0.5 mm, substrate: stoichiometric $LiTaO_3$) has been carried out using electro-optic sampling system. The phase velocity of* $5.4 \pm 0.25 \times 10^7$ *m/s has been estimated from a resonance frequency and an observed wavelength of a standing wave.*

Introduction

Wide expansion of an optical spectrum by deep phase modulation at a high modulation frequency is essential technique for many electro-optic (EO) light controlling fields, such as ultrashort pule generation[1], comb generation [2], time-to-space mapping of an optical signal[3] and so on. At a high modulation frequency region, traveling-wave EO modulator (EOM) has been widely used because of a long interaction length between an optical wave and a modulation wave. However, since there is so-called velocity mismatching between the optical wave and the modulation wave in the EO crystal, when the modulation frequency is as high as over ten gigahertz, the modulation index varies periodically as the interaction length increases.

To achieve deep modulation at high frequency, quasi-velocity-matching (QVM)[4] with periodic domain inversion of a ferroelectric crystal is effective technique. In the QVM technique, phase velocity of the modulation wave should be known so that the period of the periodic domain inversion can be determined. We calculated the modulation phase velocity through the empirical formula using relative permittivity [5, 6] which is measured for other $LiTaO_3$ samples at other modulation frequency so far. The modulation phase velocity can also be estimated from the $|S_{11}|$ spectrum of the resonant microstrip line, however the estimation is largely influenced by the electrode implementation (for example, the electrical contact between the microstrip line and the connector) and is inaccurate.

In this paper, we estimate the phase velocity of the modulation microwave of 16 GHz on the basis of the direct observation of the electric field distribution in the resonant microstrip line using EO sampling system[7]. Based on the EO sampling system, we can measure the wavelength of the standing wave precisely. The phase velocity v_m is calculated from measured wavelength of the standing wave λ_m and resonance frequency f_m as $v_m = \lambda_m f_m$.

Quasi-velocity-matching

Figure 2 (a) and (b) shows the schematic of the traveling-wave EOM and QVM-EOM, respectively. To avoid unnecessary complexities, we employ a one-dimensional analysis

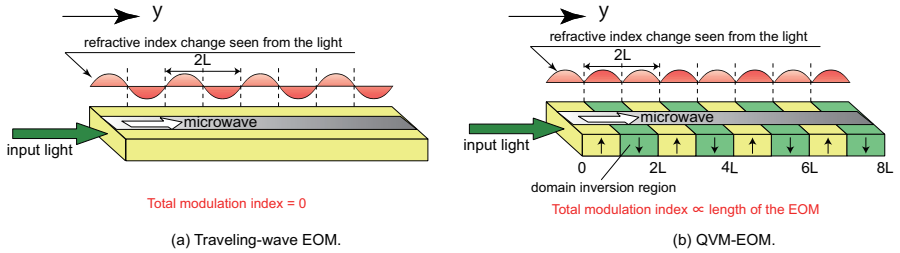


Figure 1: (a) Traveling-wave EOM, (b) QVM-EOM with periodic domain inversion.

for our devices. For a traveling-wave EOM, if the y axis is the direction in which the optical and modulation wave propagate in a virgin (single domain) EO crystal, the variation of the refractive index induced by an electric field $E_m \cos(\omega_m t)$ is obtained at y as

$$\Delta n(y,t_0) = n_m \cos(\omega_m t_0 - \frac{\pi}{L} y), \tag{1}$$

where $n_m = \frac{1}{2} n_e^3 \gamma_{33} E_m$ is the amplitude of index changes, n_e is the extraordinary refractive index of the crystal, γ_{33} is the EO coefficient of the crystal, and $\omega_m = 2\pi f_m$. L is a half-period of the domain inversion for QVM given by $L = [2f_m(v_m^{-1} - v_o^{-1})]^{-1}$, where v_m is the phase velocity of the modulation wave, and v_o is the group velocity of the optical wave. Here, we assume that the optical wave arrives at point $y = 0$ at time $t = t_0$.
For $v_o > v_m$, the phase shift of light at the position y is expressed as

$$\theta = \frac{2\pi}{\lambda} \int_0^y \Delta n(y,t_0) dy = \Delta\theta \cos(\omega_m t_o - \frac{\pi}{2L} y), \tag{2}$$

where,

$$\Delta\theta = \frac{4L}{\lambda} n_m \sin(\frac{\pi}{2L} y). \tag{3}$$

Since the traveling-wave EOM has so-called velocity mismatching between modulation wave and optical wave, the modulation index $|\Delta\theta|$ becomes a periodical function of y with period $2L$.
When a traveling-wave EOM has a suitable domain-inverted half-period of L, QVM occurs and accordingly a large modulation index is achieved. In such a situation, phase retardation $\Delta\phi(x,t_0)_M$ given to the light passing through the length of $2ML$ in a periodically domain-inverted crystal as shown in Fig. 2(b) is expressed as

$$\Delta\phi(x,t_0)_M = \frac{2M\pi}{\lambda} \int_0^{2L} g(x,y) \Delta n(y,t_0) dy, \tag{4}$$

where λ is the vacuum wavelength of the light, $g(x,y)$ is -1 and 1 for domain-inverted regions and non-domain-inverted regions, respectively.
Figure 2 shows modulation indices of EOM with (a) QVM-EOM, and (b) traveling-wave EOM (velocity mismatching). The QVM modulation index is almost proportional to the interaction length though it is lower than perfect velocity-matched condition by a factor of $2/\pi$.

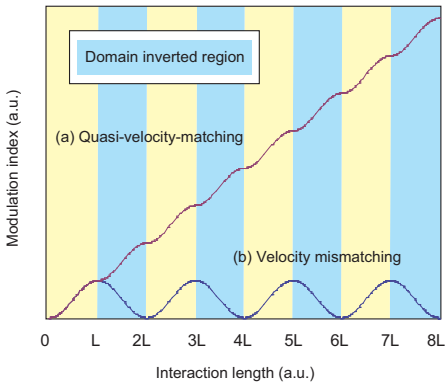


Figure 2: Modulation indices of EOM. (a) QVM-EOM with periodic domain inversion, and (b) traveling-wave EOM (velocity mismatching).

Estimation of the phase velocity of the modulation wave

The half-period of the domain inversion for the QVM is calculated as

$$L = \frac{1}{2f_m(\frac{1}{v_m} - \frac{1}{v_o})}, \tag{5}$$

and it is obvious that the modulation efficiency is directly influenced by the estimation accuracy of the phase velocity of the modulation wave, v_m, and the group velocity of the optical wave, v_o. Optical group velocity can be measured in relatively high accuracy. It is important to estimate the phase velocity of the modulation wave precisely to optimize the operation of the QVM-EOM.

Figure 3(a) shows experimental setup. We fabricated the resonant EOM with stoichiometric $LiTaO_3$ substrate. The height of the $LiTaO_3$ crystal was 0.5 mm. A silver microstrip line of 0.5 mm width was evaporated on the crystal. The resonant frequency was 15.91 GHz. The pulsed fiber laser (repetition rate: 40 MHz) was used for probe pulses. The beam spot size was about 80 μm. The CdTe crystal was used for the EO sensor. We scanned the probe beam in the y direction and measured electric field profile of the resonant standing wave.

Figure 3(b) shows a typical experimental result. From the amplitude distribution of the standing wave, the resonant half- wavelength was determined as $\lambda_m/2 = 1.7$ mm. Consequently, the phase velocity can be calculated as $v_m = 5.4 \times 10^7$ m/s. By measuring λ_m for four times at different position of the microstrip line, we estimated the phase velocity as $v_m = 5.4 \pm 0.25 \times 10^7$ m/s. The half-period of domain inversion of $L = 2.95$ mm can be derived from the phase velocity of $v_m = 5.4 \times 10^7$ m/s. If the $v_m = 5.4 \times 10^7$ m/s is correct value rather than the $v_m = 5.3 \times 10^7$ m/s, which is used in our former experiment, improvement of about 10% of the modulation index can be expected.

Conclusion

We have estimated the modulation phase velocity in the QVM-EOM by direct observation of the electric field of the resonant standing wave using EO sampling system. The phase velocity of $v_m = 5.4 \pm 0.25 \times 10^7$ m/s has been estimated.

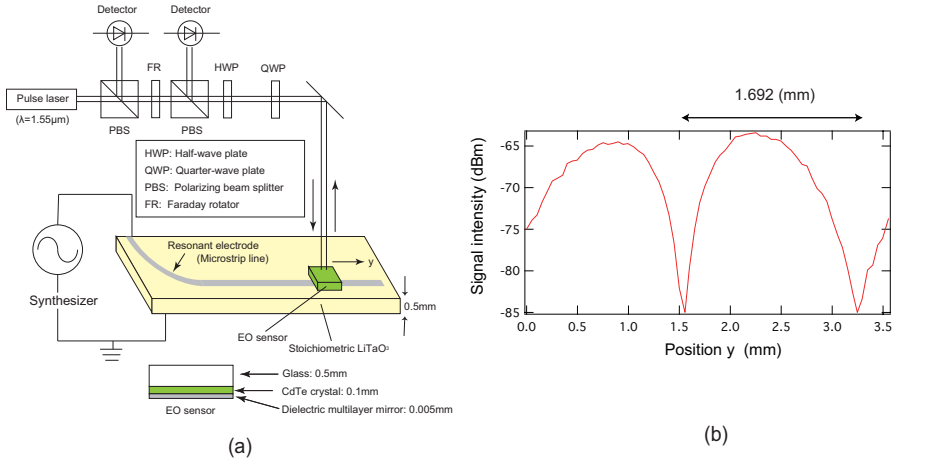


Figure 3: (a)Experimental setup. (b) Measured electric field for modulation frequency of 15.91 GHz.

Acknowledgment

This research was partially supported by a grant from the Global COE Program, "Center for Electronic Devices Innovation," from the Ministry of Education, Culture, Sports, Science and Technology of Japan, Grant-in-Aid for Scientific Research on Priority Areas, 19023006, 2007 and Young Scientists (B), 18760040, 2007.

References

[1] K. Shibuya, S. Hisatake, and T. Kobayashi, "Sub-picosecond optical pulse generation with repetition rate of several tens of gigahertz using electrooptic standing-wave phase grating with periodic domain inversion," *Jpn. J. Appl. Phys*, vol. 44, pp.6558-6563 (2005).

[2] S. Hisatake, Y. Nakase, K. Shibuya, and T. Kobayashi, "Generation of flat power-envelope terahertz-wide modulation sidebands from a continuous wave laser based on an external electrooptic phase modulator," *Opt. Lett.*, vol. 30, No. 7, pp.777-779 (2005).

[3] S. Hisatake and T. Kobayashi, "Time-to-space mapping of a continuous light wave with picosecond time resolution based on an electrooptic beam deflection," *Optics Express*, vol. 14, Issue 26, pp. 12704-12711 (2006).

[4] A. Motimoto, M. Tamaru, Y. Matsuda, M. Arisawa, and T. Kobayashi, in Pacific Rim Conference on Lasers and Electro-Optics (Institute of Electrical and Electronics Engineers, Piscataway, N.J., 1995), p. 234.

[5] M. V. Jacob, J. G. Hartnett, J. Mazierska, J. Krupka, and M. E. Tobar, "Lithium tantalate - A high permittivity dielectric material for microwave communication systems," *Proceedings of IEEE Region 10 Conference on Convergent Technologies For The Asia-Pacific*, pp. 1362-1366, (2003).

[6] M. V. Jacob, J. G. Hartnett, J. Mazierska, V. Giordano, J. Krupka, and M. E. Tobar, "Temperature dependence of permittivity and loss tangent of lithium tantalate at microwave frequencies," *IEEE transactions on microwave theory and techniques*, vol. 52, (2004).

[7] J. A. Valdmanis, G. Mourou, and C. W. Gabel, "Picosecond electro-optic sampling system," *Appl. Phys. Lett.*, vol. 41, pp. 211- 212 (1982).

Confocal optical techniques to study channel waveguides in $LiNbO_3$

E. Martín Rodríguez[1], M. Quintanilla[1], D. Jaque[1], E. Cantelar[1], G. Lifante[1], F. Cussó[1], A.C. Busacca[2], A.C. Cino[2,3] and S. Riva Sanseverino[2,3]

[1]Departamento de Física de Materiales, C-IV. Universidad Autónoma de Madrid, 28049 Madrid, Spain
marta.quintanilla@uam.es
[2]DIEET, Università degli Studi di Palermo, v.le delle Scienze, 90128 Palermo, Italy
[3]Centro per la Recerca Elettronica in Sicilia (CRES), Via Regione Siciliana 49, 90046 Monreale, Italy

Abstract. *Optical properties of rare-earth ions incorporated into channel waveguides can be used as optical probes to investigate the characteristics of the waveguides by using sub-micrometric resolved confocal fluorescence imaging. In this work, luminescence together with Raman spectroscopy, have been used to evaluate waveguides fabricated by different procedures in $LiNbO_3$ crystals.*

Introduction

$LiNbO_3$ is a well established material for integrated optics applications [1] due to its electro-optical, acousto-optical and nonlinear properties and to the availability of well developed techniques to fabricate low-loss channel waveguides. The incorporation of active ions, frequently rare-earth ions (RE), allows the fabrication of photonic devices such as integrated lasers and amplifiers [2,3]. For those applications, the channel waveguide characteristics and the modifications that the fabrication procedures induce in the $LiNbO_3$ lattice are of great relevance. This has motivated a wide activity in that field throughout the last years, although the details of the lattice changes induced by the different procedures used for waveguide fabrication are not completely understood yet. Along this line, it has been recently demonstrated that confocal micro-luminescence can provide direct and precise information on the local properties of the material [4-6].
In this work, different optical techniques (continuous wave, time resolved luminescence, as well as Raman spectroscopy) have been used in a confocal configuration, in order to characterize the diverse micro-structural modifications induced by the different waveguide fabrication procedures. As optical probes, Tm^{3+} and Nd^{3+} ions have been selected because of their intrinsic interest as active photonic ions with applications in fields such as surgery, optical communications or remote sensing, as well as due to the availability of suitable optical transitions highly sensitive to the host surroundings.

Experimental

Z-cut samples of $LiNbO_3$ doped with rare-earth ions (Tm^{3+} or Nd^{3+}) have been used in this work as substrates to create channel waveguides. Different channel widths (w) are defined by a previous standard ultraviolet lithography, using a suitable silica mask.
Two fabrication procedures have been used: reverse proton exchange (RPE) and Zn-indiffusion. The RPE waveguides are obtained by a proton exchange process in benzoic acid at 300 ºC during 14.5 hours in a sealed ampoule, followed by a reverse ionic exchange, in which the sample was immersed in a mixture of Li/Na/K nitrides at 350 ºC during 38.5 hours. This procedure creates two different waveguides, each one confining a different propagating mode: an ordinary waveguide (TE propagating mode) close to the

surface and an extraordinary waveguide (TM propagating mode) buried below the ordinary one, in the region where protons remain after the whole process.
In the Zn-diffusion technique the substrate is heated to 500 ºC during 2 hours in a metallic Zn atmosphere, creating a rich-Zn layer on the sample surface. Then the sample is heated to 850 ºC for 4 hours. This facilitates the diffusion of Zn^{2+} ions from the surface to the bulk creating a waveguide that confines both, extraordinary and ordinary, polarization modes.
To investigate the changes that the index modifiers, namely protons or Zn^{2+} ions, are causing to the $LiNbO_3$ substrate, confocal micro-luminescence experiments were performed using an Olympus BX41 fiber coupled confocal microscope. Excitation of the dopant ions is performed using either a continuous argon laser or an 808 nm diode laser (LIMO GmbH). The excitation beam was focused on the sample surface by means of an x100 achromatic microscope objective (NA 0.9) down to a ≈0.6 and ≈ 0.8 μm spot size for the case of Argon and diode pumping, respectively (Figure 1). To separate the excitation beam and the sample luminescence, a Notch filter was used. The fluorescence was focused into a fiber-coupled high resolution spectrometer (SPEX 500M).
The reference system used all along this work is sketched in Figure 1. The *x*-axis stands for the direction parallel to the sample surface, while the *y*-axis stands for the depth, being the origin of the coordinates located on the $LiNbO_3$ surface, in the middle of the mask opening. To control the samples position, they were situated onto an XY motorized with 0.1 μm spatial resolution stage that allows the possibility of mapping fluorescence properties such as intensity, spectral position and bandwidth of the emission bands.
For lifetime measurements, the collection fiber was connected to a photomultiplier tube and the generated signal was averaged and recorded by a 500MHz Lecroy digital oscilloscope.

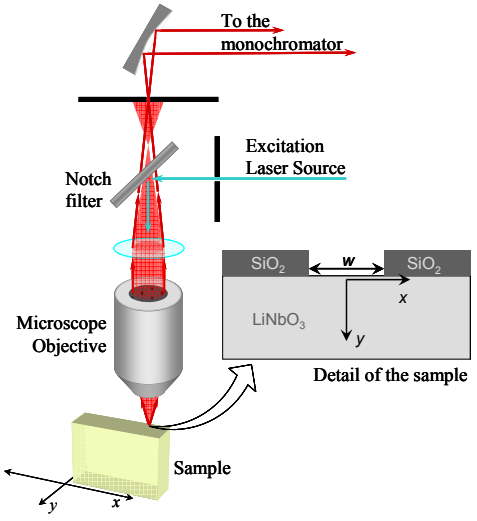


Fig. 1: Confocal microscope schematically represented showing the experimental setup and a cross section view of the sample with the silica mask channel opening. The reference axes used in this work, *x* and *y*, are represented.

Results

Figure 2 shows the micro-fluorescence spectra of the Tm^{3+}:$^3H_4$ → $^3H_6$ and the Nd^{3+}:$^4F_{3/2}$ → $^4I_{9/2}$ transitions. Those transitions have been selected as probes to characterize the

possible local lattice changes of the sample, produced during the waveguide fabrication, due to their high intensity and high sensibility to the host surroundings.

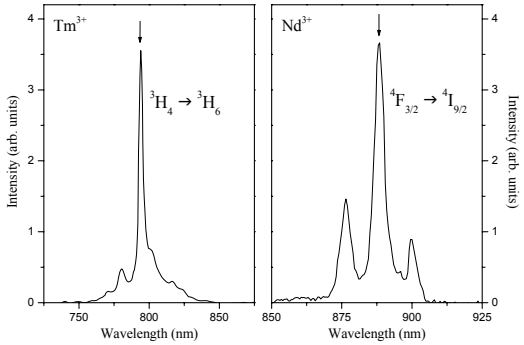


Fig. 2: Micro-fluorescence spectra of the Tm^{3+}: $^3H_4 \rightarrow {}^3H_6$ and the Nd^{3+}:$^4F_{3/2} \rightarrow {}^4I_{9/2}$ transitions. The arrows point to the peaks selected to be used as probes for the local changes induced in the material.

Reverse proton exchange waveguides:

Previous works ensure that proton exchange waveguides show a noticeable change in the luminescence lifetime of the dopant levels, being the de-excitation faster in the waveguide than in the bulk [7]. Confocal experiments in Nd^{3+}-doped $LiNbO_3$ RPE waveguides confirm those results (Figure 3a), and add the possibility of monitoring the lifetime value at any position within the waveguide and its surroundings, which could bring a further understanding of such lifetime reduction. A scanning through the sample edge confirms the correlation between lifetime reduction and the density of protons in the waveguide. The buried waveguide defines a minimum lifetime, located 6 μm below the surface and a Gaussian-shaped distribution along the *x*-axis as depicted in Figure 3b (full circles).

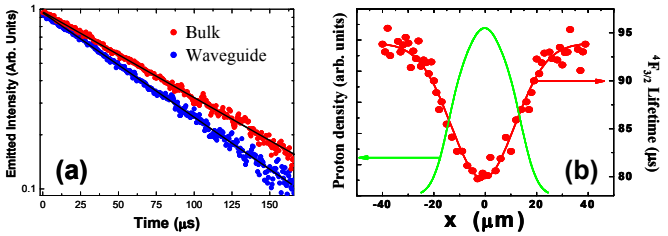


Fig. 3: (a) Lifetime value of the $^4F_{3/2}$ energy level of Nd^{3+} ions inside and outside the RPE waveguide (w = 17 μm). (b) $^4F_{3/2}$ lifetime as function of x position (full circles) and calculated proton density in the same positions.

This mapping and modifications can also be tracked by following the luminescence associated to the $^4F_{3/2} \rightarrow {}^4I_{9/2}$ transition where protons induce a blue-shift of the main peak energy position (about $\Delta E \approx 0.8$ cm^{-1} [5]). Both spectral shift and lifetime reduction are in complete agreement with proton distribution.

Zn-diffusion waveguides:

The energy shift of RE luminescence transitions have been also detected following the luminescence of Nd^{3+} and Tm^{3+}-doped $LiNbO_3$. In this case it has been observed that the luminescence peak is shifted to higher or lower energies depending on the depth (y distance). Figure 4 shows the results obtained for a waveguide (w = 10 μm) in Tm^{3+}:$LiNbO_3$, measured along x-axis and y-axis directions, and quantifying different

spectroscopic characteristics. It can be seen how the luminescence intensity (a), the energy position of the peak (b) and its width (c) have a noticeable spatial dependence in the waveguide region. The energy position of the luminescence peak (Figure 4b) is blue shifted in a buried region (around 3 μm depth) surrounding a central section in which the shift is in the opposite direction. According to previous works [4], this can be understood in relation with the lattice modification of the substrate, indicating a contraction of the lattice in the waveguide surface, surrounded by a lattice-dilatation zone in the deeper regions. In Figure 4c, the width of the main luminescence peak is mapped, showing that in the red-shifted region there is also a broadening of the peak, indicating a higher disorder in that region.

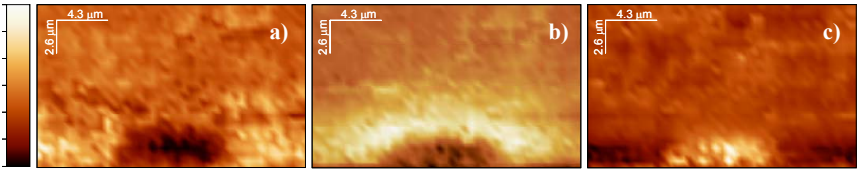


Fig. 4: Tm^{3+} luminescence dependence on position of: a) the luminescence intensity at 795 nm, b) energy position of the peak and c) peak width.

Those lattice modifications can be also detected by means of Raman spectroscopy, using the same confocal geometry. In particular, the 504 nm $LiNbO_3$ Raman peak, measured under ZZ polarization, has been used for that purpose.

Acknowledgements

This work has been partially supported by the Ministerio de Educación y Ciencia, under project MOISES (MAT2005-05950), Comunidad de Madrid under project MICROSERES-CM (S-0505/TIC/0191) and UAM-Grupo Santander under project MINAS-2007. E. Martín Rodríguez and M. Quintanilla are supported by FPU program from Ministerio de Educación y Ciencia (AP2006-02795 and AP2005-0763).

References

[1] V. Pruneri, "Integrated electro-optic modulators in micro-structured $LiNbO_3$", Invited Talk ECIO`08.

[2] E. Lallier, J. P. Pocholle, M. Papuchon, C. Grezes-Besset, E. Pelletier, M. De Micheli, M. J. Li, Q. He and D. B. Ostrowsky, "Laser oscillation of single-mode channel waveguide in Nd-MgO-$LiNbO_3$", Electron. Lett., 25, pp. 1491-1492, 1989

[3] B.K. Das, H. Suche and W. Sohler, "Single-frequency Ti : Er : $LiNbO_3$ distributed Bragg reflector waveguide laser with thermally fixed photorefractive cavity", Appl. Phys. B, 73, pp. 439-442, 2001

[4] V. Dierolf and C. Sandmann, "Confocal two photon emission microscopy: a new approach to waveguide imaging", J. Lumin., 102-103, pp. 201-205, 2003.

[5] D. Jaque, E. Cantelar and G. Lifante, "Lattice micro-modifications induced by Zn diffusion in Nd:$LiNbO_3$ channel waveguides probed by Nd^{3+} confocal micro-luminescence", App. Phys. B, 88, pp. 201-204, 2007

[6] E. Martín-Rodríguez, D. Jaque, E. Cantelar, F. Cussó, G. Lifante, A.C. Busacca, A.C. Cino and S. Riva Sanseverino, "Time resolved confocal luminescence investigations on reverse proton exchange Nd:$LiNbO_3$ channel waveguides", Opt. Express, 15, pp. 8805-8811, 2007

[7] F. Cussó, G. Lifante, J.A. Muñoz, E. Cantelar, R. Nevado, A.Cino, M.P. de Micheli and W. Sohler, "Spectroscopic investigation of proton exchanged Er-doped $LiNbO_3$ waveguides", Rad. Eff. & Defects in Solids, 155, pp. 217-221, 2001

Carrier Transport Effects in Multi Layer Quantum Dot Lasers and SLDs

M. Rossetti[1], P. Bardella[1], M. Gioannini[1] and I. Montrosset[1]

[1] Dipartimento di Elettronica, Politecnico di Torino, Turin, Italy
mattia.rossetti@polito.it

Abstract. *Influence of carrier diffusion in the separate confinement heterostructure (SCH) region and carrier capture by each quantum dots layer (QDL) in quantum dot lasers and SLDs is studied with a modified rate equations model. We perform the static analysis of several Dots-in-a-Well lasers and SLDs with different numbers of QDLs.*

Introduction

In the last years, semiconductor Quantum Dots (QD) lasers and SLD have shown improved performances as compared with Quantum Well (QW) devices i.e. lower threshold currents and reduced temperature sensitivity.
Carrier transport effects in Multi-Quantum-Well (MQW) lasers have been widely studied in the past decade. The effect of transport and capture times on threshold current, quantum efficiency [1-2], modulation bandwidth [2-3] and large-signal responses [2] have been clearly demonstrated both experimentally and from simulations.
In QD based devices these effects are expected to be considerably greater. The presence of deeper localized QD states considerably reduces the escape rates from the confined states to the SCH bulk states, increasing therefore the non-uniformity between the carriers concentrations in each QDL. Inhomogeneous carrier distribution in the QDLs is expected to limit the performances of structures with a large number of QDLs.
We developed a time-domain rate-equation-model able to resolve carriers concentrations in each QDL and in the SCH region. The model considers carrier diffusion across SCH region, carriers relaxation in the confined states and thermionic emission from confined states. Three confined QD states (GS, ES1, ES2) are included.
In the following, a brief description of the model is given and then its application to the analysis of static properties of DWELL lasers with different number of QDLs is shown. Performances of multi layer SLDs when the number of QDL is changed are presented.

Description of the model

Carrier transport in QD lasers and SLD with an arbitrary number of QDLs is described via a rate equations based model, shown in figure 1.
In order to resolve carrier and photon densities variations along the waveguide in SLD structures, the cavity is divided in many slices in the propagation direction (z axis in figure 1) and a travelling wave (TW) method is applied.
Three populations of photons associated to GS, ES1 and ES2 transitions are considered. Each population is then subdivided in forward and backward propagating waves.
The spatial and temporal evolution of the photon number inside the cavity is therefore obtained as $S_k^{\pm}(z \pm \Delta z) = S_k^{\pm}(z) e^{\left(\sum_l \Gamma_{xy}^l g_k(\rho_k^l(z)) - \alpha_i - \alpha_{plasma}(z) \right) \Delta z} + S_{esp,k}(z)$, where subscript k represents GS, ES1 and ES2 photon populations; subscript l goes from 1 to the total

number of QDLs; S_k^+ and S_k^+ are forward and backward propagating photons associated to the k^{th} population; g_k is the material gain for the k^{th} population calculated via the carrier occupation probability in the k^{th} QD state, ρ_k; Γ_{xy}^l is the confinement factor in the l^{th} QDL; α_i and α_{plasma} are respectively internal and plasma losses; and $S_{esp,k}$ is the spontaneous emission rate in section z. Slice width Δz is related to the simulation time step Δt via the photons group velocity; Δt is chosen to be much smaller than the transition times involved in carrier rate equations in order to ensure a proper simulation accuracy.

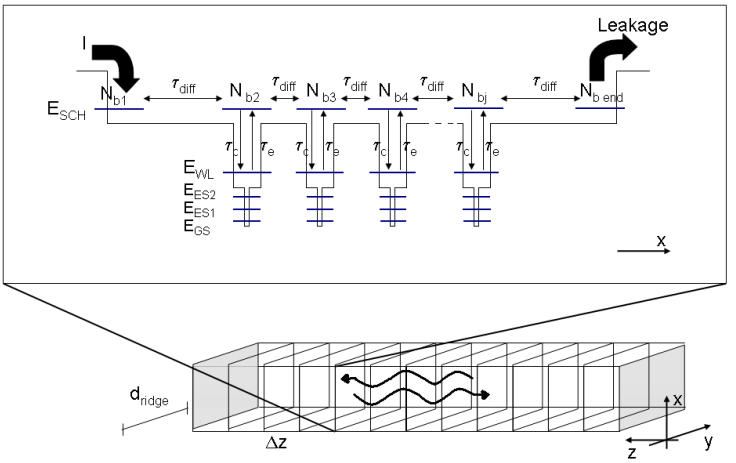


Figure 1 Schematic of the TW rate equation model: a 3D view of the optical cavity with forward and backward propagating waves is shown. The upper inset shows the energy level scheme in the direction perpendicular to the heterostructure (x axis) used to model carrier diffusion across the SCH [3]. Capture and escape times are reported. Wetting layer (WL) and QD states energies are shown. Intra-band transitions times between QD energy states, radiative and non-radiative recombination times are here omitted.

Carrier dynamics is described with a complex set of rate equations. Charge neutrality in each QDL layer is assumed. We suppose the dynamics to be dominated by holes, having an effective mass much bigger than the electron one. This simplification allows us to considerably increase the computational efficiency of the model.

In order to model carrier diffusion across the SCH, we define a set of fictitious gateway states spatially distributed across the SCH [3] as shown in figure 1. Carrier diffusion between two adjacent gateways is modelled via an effective diffusion time $\tau_{diff} = \Delta x^2 / 2D_a$ where Δx is the barrier width and D_a is the diffusion coefficient. The diffusion rate between the i$^{\text{th}}$ and j$^{\text{th}}$ SCH state is calculated as $R_D^{ij} = \left(N_{bj} - N_{bi}\right) / \tau_{diff}^{ij}$.

Carrier relaxation in the two dimensional WL states is modelled via an effective capture time τ_c. The escape time τ_e is calculated from the capture time assuming no net transition rate at thermodynamic equilibrium.

Carrier dynamics in confined QD states in each QDL is described using a set of 4 rate equations (one for each confined state) for each QDL. This allows to resolve carrier distribution in each QDL. Intraband relaxation rates, non-radiative and Auger recombination as well as radiative recombinations are considered in each equation.

P-I characteristics of multi layer QD lasers

We apply the model to the P-I characteristic analysis of Dots-in-a-Well (DWELL) lasers with large SCH regions (about 1250 nm) and various number of QDLs. Figure 2a shows P-I curves obtained for structures with 6, 12 and 15 QDLs. An abrupt jump in the P-I characteristic of the 15 QDL structure appears just above threshold. This behaviour has been experimentally measured in many QD lasers with similar structure.

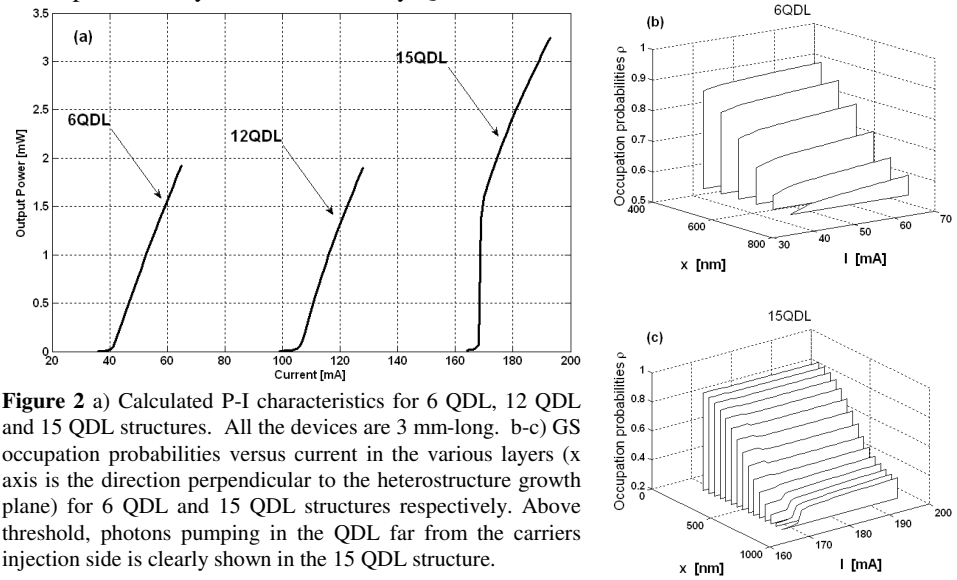


Figure 2 a) Calculated P-I characteristics for 6 QDL, 12 QDL and 15 QDL structures. All the devices are 3 mm-long. b-c) GS occupation probabilities versus current in the various layers (x axis is the direction perpendicular to the heterostructure growth plane) for 6 QDL and 15 QDL structures respectively. Above threshold, photons pumping in the QDL far from the carriers injection side is clearly shown in the 15 QDL structure.

The explanation of this effect can be obtained representing the occupation probabilities in the various QDL for the GS and the ESs. Figure 2b shows the GS occupation probability versus current in each QDL for the 6 QDL structure. The occupation increases in all the layers up to the threshold current (41 mA) and is significantly greater in the layers closer to the carrier injection side (p-side). These layers are almost saturated for the GS, while the last ones are just above transparency. Above threshold only a small change in the occupation probability takes place due to photons absorption in the last layers. In the case of the 15 QDL structure (figure 1c) the carrier density grows up to the threshold (around 168 mA) but strong carrier redistribution takes place among the layers just above threshold. In the layers far from the injection side, the GS is initially below transparency. However when the laser turns on, the photons generated by the more populated layers can pump the carriers of the last layers (photon pumping) which can reach the transparency. This behavior determines the slope discontinuity in the P-I characteristic.

Multi layer QD SLD

Multi layer QD SLDs with output power of several mW and about 100 nm optical bandwidth have been recently realized. In QD SLDs maximum modal gain is generally lower than in QW lasers, due to strong Pauli blocking effect in the QD states. In order to get considerable output powers, structures with a high number of QDLs must therefore be considered. It has been showed that increasing the number of QDLs up to 10, output powers can be considerably increased. In SLD structures with 10 QDLs, output power about 10 times greater than in an equivalent 5 QDLs structure has been obtained [4].

However carrier transport effects can represent a limit in the maximum number of QDLs useful to optimize SLD performances. Here we present a comparison between three 4.5 mm-long QD SLDs with 6, 12 and 15 QDLs respectively.

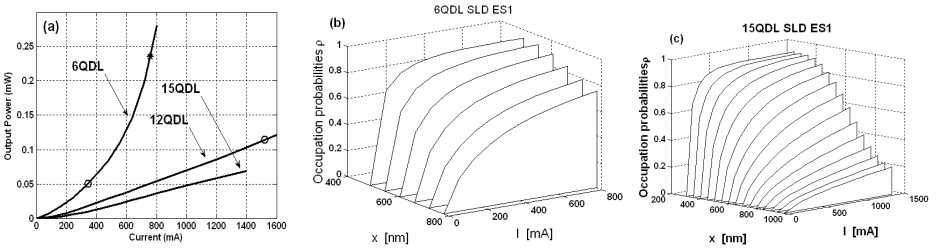


Figure 3 a) P-I characteristics for 4.5-mm-long SLDs with 6, 12 and 15 QDLs. b-c) ES1 occupation probabilities versus current in the various layers for 6 QDL and 15 QDL structures respectively.

Figure 3a shows the P-I characteristic of each structure. Circle and asterisk in the 6QDL SLD curve represent $P_{GS} = P_{ES1}$ and $P_{ES1} = P_{ES2}$ regimes.
In structures with 12 and 15 QDLs, the output power is considerably lower and a strong shift of the $P_{GS} = P_{ES1}$ regime occurs so that GS power is the main contribution to the total power for a wide range of currents. Figures 3b and 3c show ES1 occupation probabilities vs current in each layer for the 6 and 15 QDL SLDs. In the 15 QDL structure a strong non-uniformity between the ES1 occupation probabilities in the different layers occurs. Even if QDLs closer to the injection side are almost saturated, ES modal gain is quenched to very low values, considerably limiting the SLD output power.

Conclusions

Carrier transport effects in multi layer QD lasers and SLDs can be modeled with a travelling wave rate equation model; using this model static behavior of lasers and SLDs with different number of QDLs can be analyzed and performance limitations due to carrier transport effects can be underlined. Lasers with a high number of QDL (15) show abrupt jumps in the P-I characteristics at threshold and the differential efficiency is not considerably increased compared with 6 QDL lasers. Increasing the number of layers up to 15 in SLD structures the output power is considerably reduced due to the strong non-uniformity of carrier concentrations in each QDL.

This project was supported by the IST NanoUBSources European Project

References

[1] H. Hirayama, J. Yoshida, Y. Miyake and M. Asada, "Carrier capture time and its effect on the efficiency of quantum- well lasers", IEEE J. Quantum Electron., vol. 30, pp. 54-62, 1994.

[2] L.V.T. Nguyen, A.J. Lowery, P.C.R. Gurney and D. Novak, "A time-domain model for high-speed quantum-well lasers including carrier transport effects", IEEE J. Sel. Topics Quantum Electron., vol. 2, pp. 494-504, 1995.

[3] G. Rossi, R. Paoletti and M. Meliga, "SPICE simulations for analysis and design of fast 1.55 μm MQW laser diodes", J. Lightwave Technol., vol.16, pp. 1509-1516, 1998.

[4] M. Rossetti, L. Li, A. Markus, A. Fiore, L. Occhi, C. Vélez, S. Mikhrin, I. Krestnikov and A. Kovsh, "Characterization and modeling of broad spectrum InAs-GaAs quantum-dot superluminescent diodes emitting at 1.2-1.3 μm", IEEE J. Quantum Electron., vol. 43, pp. 676-686, 2007.

Design of nonlinear SOI slot waveguides

V. M. N. Passaro [1], M. Lagioia [1] and F. De Leonardis [2]

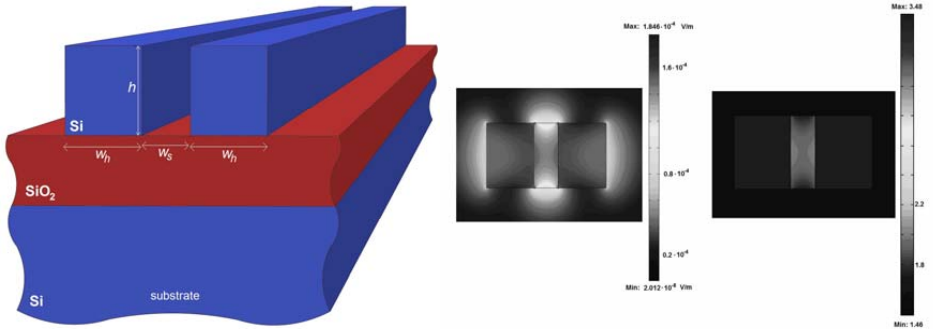
[1]Photonics Research Group, Dipartimento di Elettrotecnica ed Elettronica, Politecnico di Bari, Italy
passaro@deemail.poliba.it
[2]Photonics Research Group, Dipartimento di Ingegneria dell'Ambiente e per lo Sviluppo Sostenibile, Politecnico di Bari, Italy

Abstract. *An investigation and optimization of silicon-on-insulator nanometer slot waveguides for nonlinear applications is proposed by using a novel iterative calculation method.*

Introduction

The actual use of existing CMOS-compatible technologies enables Silicon Photonics to exhibit many advantages with respect to III-V semiconductors in terms of high-density integration of photonic devices [1]. At the same time, some kinds of nonlinear optical effects have been observed in silicon waveguides, leading to focus significant attention on device applications using third order optical nonlinearity [2]. Recently, the possibility of guiding light in a low refractive index medium of a waveguide by total internal reflection has been proposed and demonstrated [3] due to an innovative structure, well known as a Silicon-on-Insulator (SOI) slot waveguide, as in Fig. 1(a). It is constituted by two silicon wires spaced by a nanometer low index region (called either slot or gap region), and confined by a silicon oxide layer (SOI substrate). The discontinuity of the electric field on the high index contrast interface between slot and wires causes a high confinement factor in the slot region for quasi-TE mode, whose E_x component is orthogonal to the interface. Using slot waveguides, a great variety of optical devices has been recently proposed and fabricated, including sensors [4]. In such an ultrasmall waveguide, the light intensity is considerably larger than that of conventional optical waveguides, giving a dramatic enhancement of nonlinear optical effects. A stationary modal analysis of nonlinear slot waveguides is presented in this work by a full-vectorial 2D finite element method (FEM) [5], using at least 100,000 triangular mesh elements.

To calculate the nonlinear effective index of quasi-TE mode, an iterative method based on FEM has been implemented and compared with a different approach in literature [6].



(a) (b) (c)

Fig. 1.(a) SOI slot waveguide scheme; (b) quasi-TE electric field and (c) nonlinear index.

Our method consists of solving the full vectorial e.m. wave equation and, then, deriving the refractive index in each region as:

$$n = n_0 \left(1 + \frac{n_2 |\mathbf{E}|^2}{Z_0} \right)^{1/2} \quad (1)$$

where Z_0 is the free-space impedance, and n_0 and n_2 are the linear and non linear refractive indices for each region, respectively. Then, new values of effective index and field distributions are calculated and new refractive index evaluated again by Eq. (1). This iteration is repeated until a fixed effective index tolerance has been reached. The correctness and applicability of the described method has been verified and proved by comparing with other results [6] in terms of nonlinear effective index. The guiding structure used for comparison is a SOI slot waveguide with silicon wires and SiO_2 cover, while the slot (gap) region is filled with silicon nanocrystals (Si:nc), which allow a larger value of n_2 than SiO_2 to be obtained. The physical and geometrical parameters include silicon wire index 3.48, cover and buried oxide index 1.46, slot region index 1.46, slot width 100nm, wire width 200 nm, waveguide height 250 nm, nonlinear index of silicon nanocrystals in slot region 10^{-16} m^2/W, operative wavelength 1550 nm. The nonlinear index has been considered only in the slot region, while all the other materials are assumed as linear, as in [6]. Moreover, the tolerance on successive iterative steps was assumed as 10^{-4}, in order to ensure a sufficient accuracy for the effective index convergence without excessive time consuming. After setting the simulation parameters, modal analyses for estimating the quasi-TE effective index versus input power have been performed.

Numerical results

As an example, the graphs in Fig. 1(b-c) show the field distribution module $|\mathbf{E}'|$ for a linear waveguide (i.e. $n_2 = 0$), and the nonlinear refractive index in gap region, as given by Eq. (1), respectively. A linear effective index of 1.728703, in very good agreement with 1.729706 given in [6], has been evaluated. Calculation of quasi-TM mode shows an effective index of 1.755593, very similar to 1.755922 [6]. In Fig. 2 the convergence of iteration method is sketched. Clearly the number of iterative cycles, required to reach the fixed tolerance, depends on the input power P. In fact, six cycles are needed for $n_2^{nc}P = 0.01$ μm^2, while the cycles are up to 23 for $n_2^{nc}P = 0.04$ μm^2. After the final nonlinear effective index n_{eff}^{NL} is found, the nonlinear phase shift per unit length is calculated as:

$$\Delta\phi_{slot} = \frac{2\pi}{\lambda_0}\left(n_{eff}^{NL} - n_{eff}^{L} \right) \quad (2)$$

where n_{eff}^{L} is the linear effective index and $\Delta\phi_{slot}$ stands for a phase change depending on nonlinear material in the slot region. Then, $\Delta\phi_{slot}$ versus product $n_2^{nc}P$ has been compared with results in [6], as illustrated in Fig. 2(b). It can be noted a remarkable agreement at low input powers. In fact, the graphs are substantially identical for $n_2^{nc}P \le 0.02$ μm^2, but the other method tends to overestimate $\Delta\phi_{slot}$ when $n_2^{nc}P > 0.02$ μm^2. In fact, our phase difference is 13% smaller than in [6] for $n_2^{nc}P = 0.04$ μm^2. This result is satisfactory, because larger input powers are unlikely due to possible optical

damage and necessity of high quality light sources with large intensity.

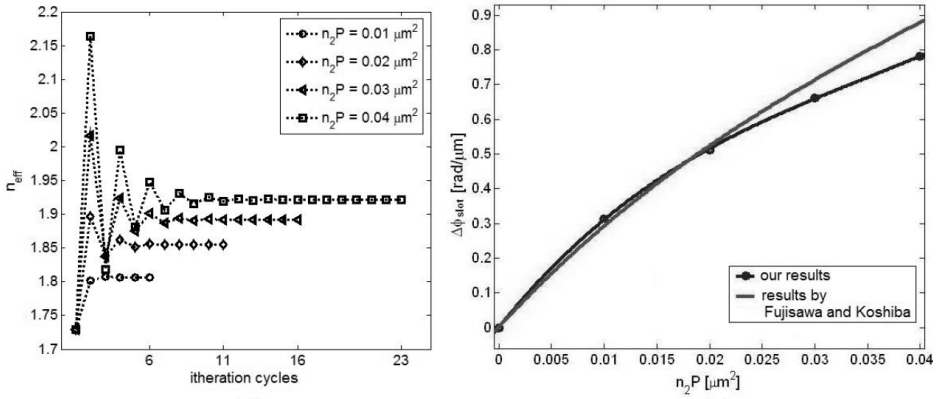


Fig. 2.(a) Quasi-TE effective index versus iteration cycles for various $n_2^{nc}P$ (tolerance 10^{-4}); (b) nonlinear phase difference per unit length versus $n_2^{nc}P$: by our method and as in [6].

The above results are relevant to a medium nonlinearity only in the slot region, i.e. where the transversal electric field of quasi-TE mode is at least one order of magnitude larger than in the other regions. Although only a slight influence on the guided field is expected, nonlinearities are to be considered in the whole domain, allowing a more accurate analysis of nonlinear phase change $\Delta\phi_{glob}$ to be carried out, closer to real case. For instance, $\Delta\phi_{glob}$ is defined as in Eq.(2) including nonlinearities in each material and Si:nc nonlinear index $3\cdot10^{-17}$ m^2/W [7]. Then, the results show a linear increase of $\Delta\phi_{glob}$ with increasing the input power, the slope varying with geometrical parameters (slot width, wire width and height). However, the trend of $\Delta\phi_{glob}$ as a function of waveguide height h and wire width w_h is surprisingly different from that expected. Results can be seen in Fig. 3(a-b) in terms of nonlinear phase shift and effective area (A_{eff}) versus h and w_h, being A_{eff} defined as [8]:

$$A_{eff} = \frac{\left(\iint_{\mathbb{R}^2} \left|\mathbf{E}(x,y)\right|^2 dx\, dy \right)^2}{\iint_{slot} \left|\mathbf{E}(x,y)\right|^4 dx\, dy} \tag{3}$$

It can be observed the different trend of linear effective area and nonlinear phase shift versus both width and height of silicon wires. In fact, w_h values giving maxima of $\Delta\phi_{glob}$ do not correspond to those for A_{eff} minima. For example, for h=300 nm minimum A_{eff} occurs for w_h = 210nm but, for the same value of h, the maximum of $\Delta\phi_{glob}$ is obtained for w_h = 190nm. Furthermore, while the effective area decreases with h, nonlinear phase shift shows a maximum in correspondence of wire height h = 300nm. Thus, it can be deduced that $\Delta\phi_{glob}$ is only partially influenced by the optical field confinement in the gap region. These simulation results can be fitted by a third order polynomial function. Our results demonstrate that an effective area minimization is not

a correct criterium for nonlinear applications, although usually used for linear devices.

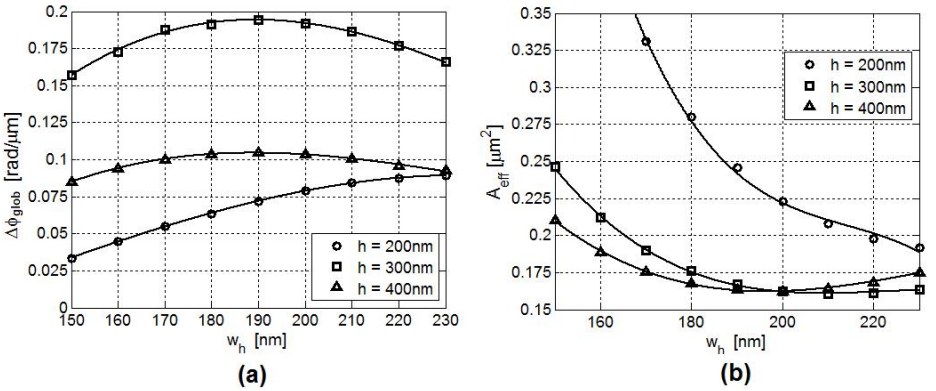


Fig. 3. (a) Quasi-TE mode nonlinear phase shift and (b) effective area as a function of silicon wire height and width (w_s = 100 nm).

Finally, the largest nonlinear response of a SOI slot waveguide, approaching 0.2 rad/μm, can be achieved with w_h = 190 nm and h = 300 nm, assuming a technological limitation on the slot width as w_s = 100 nm.

Conclusion

An optimization of nonlinear behavior of silicon nanometer slot guiding structures is presented in this work. A different behavior between effective area and nonlinear phase shift versus waveguide sizes has been demonstrated for quasi-TE mode when silicon nanocrystals are used as nonlinear material. Finally, taking into account the technological limitation on slot width, the slot geometrical parameters have been optimized to achieve the maximum nonlinear shift.

References

[1] B. Jalali, M. Paniccia, and G. Reed, "Silicon photonics", IEEE Microwave Mag., vol. 7, pp. 58-68 2006.

[2] Q. Lin, O. J. Painter, and G. P. Agrawal, "Nonlinear optical phenomena in silicon waveguides: Modeling and applications", Opt. Express, vol. 15, pp. 16604-16644, 2007.

[3] V. R. Almeida, Q. Xu, C. A. Barrios, and M. Lipson "Guiding and confining light in void nanostructure", Opt. Lett., vol. 29, pp. 1209-1211, 2004.

[4] F. Dell'Olio and V. M. N. Passaro, "Optical sensing by optimized silicon slot waveguides", Opt. Express, vol. 15, pp. 4977-4993, 2007.

[5] Comsol Multiphysics by COMSOL ©, ver. 3.2, single license, 2005.

[6] T. Fujisawa and M. Koshiba, "Guided modes of nonlinear slot waveguides", IEEE Photon. Tech. Lett., vol. 18, pp. 1530-1532, 2006.

[7] R. Spano, M. Cazzanelli, N. Daldosso, Z. Gaburro, L. Ferraioli, L. Tartara, J. Yu, V. Degiorgio, S. Hernandez, Y. Lebour, P. Pellegrino, B. Garrido, E. Jordana, J. Fedeli, and L. Pavesi, "Nonlinear optical properties of Si nanocrystals", Mat. Research Society Symp. Proc., vol. 958, L08-06, 2007.

[8] P. Sanchis, J. Blasco, A. Martínez, and J. Martí, "Design of silicon-based slot waveguide configurations for optimum nonlinear performance", J. Lightwave Technol., vol. 25, pp. 1298-1305, 2007.

Passive polarization rotator in anisotropic $LiNbO_3$ graded-index waveguide

A.V. Tsarev

Institute of Semiconductor Physics, Siberian Branch of Russian Academy of Sciences
Prospect Lavrenteva, 13, Novosibirsk, 630090, Russia
tsarev@.isp.nsc.ru

Abstract: *The new passive polarization rotator in the near-Z-axis anisotropic graded index Ti:$LiNbO_3$ channel waveguide has been investigated by 3D beam propagation method (BPM). The polarization conversion from quasi-TE to quasi-TM guided modes (and backwards) along the 8 mm long waveguide with an index contrast 0.015 has been numerically demonstrated.*

1. Introduction

A great number of investigations are devoted for studying the anisotropic graded index waveguides in lithium niobate ($LiNbO_3$.). It was shown that optical guided modes are strongly hybrid [1]. By means of artificial anisotropy induced by external electric-field the polarization conversion had been demonstrated in ***Z***-axis directed channel waveguides [2]. It was shown that at near-***Z***-axis propagation direction the hybrid quasi-TE and quasi-TM guided modes could have a circular polarization [3-6] with opposite directions of rotation. Nevertheless it is very interesting to construct the polarization rotator also in passive $LiNbO_3$ structures. It is possible [5, 6] as the input linear polarization could be rotated during the light propagation along the anisotropic channel waveguide by means of two hybrid modes that have different effective indexes and opposite directions of rotation for their circular polarizations. This effect of polarization conversion/rotation in anisotropic graded index channel waveguides has been studied in this paper for the first time by full-vectorial 3D beam propagation method (BPM) [7].

2. Simulated results and discussion

The polarization rotation has been examined for different input linear polarizations and directions θ of the channel waveguide related to the crystallographic ***Z***-axis on ***Y***-cut $LiNbO_3$. The waveguide width is $w = 13$ μm, waveguide height is $h = 2.4$ μm, maximum refractive index contrast in the diffused waveguide is $\Delta n = 0.015$, substrate main refractive indices are $N_e = 2.138$ and $N_o = 2.212$. All these parameters are relevant to a Ti-diffused $LiNbO_3$ waveguide simulated example [7] at the optical wavelength 1.55 μm. However, for simplicity we use the same value Δn for both extraordinary and ordinary increases of refractive indices.

In order to study the effect of polarization rotation in the near-***Z***-axis channel anisotropic waveguides *($\theta \neq 0$)*, we use the optical fields of quasi-TE or quasi-TM polarizations as input, then examining by BPM the optical wave propagation through the anisotropic waveguide by determination of the overlap integral of the resulted field with the distribution of quasi-TE and quasi-TM modes determined for $\theta = 0$.

Typical behaviour of optical waves propagated along the diffused channel waveguides directed at angle 5.27° is shown in Fig. 1 for the case of incidence of quasi-TE

fundamental mode. The left part of Fig. 1 shows propagation of quasi-TE mode along the waveguide. The right part of the Fig. 1 presents power amplitudes of the both quasi-TE and quasi-TM guided modes.

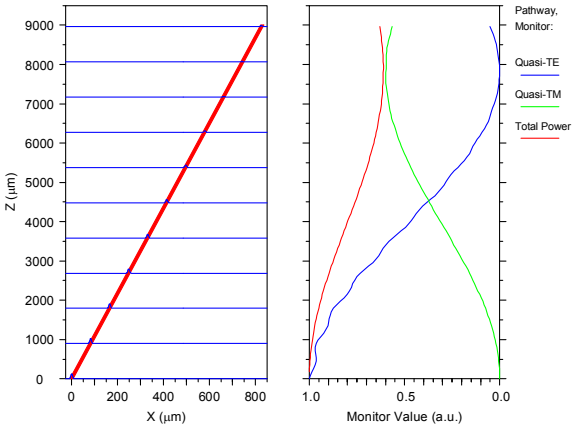
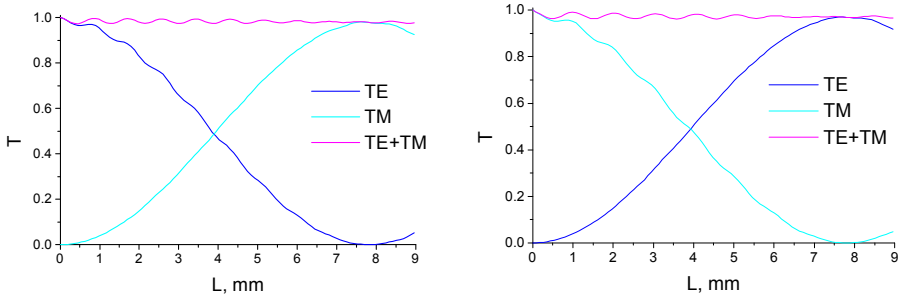


Fig. 1. 3D BPM simulation of polarization conversion in the near-***Z***-axis anisotropic channel waveguide directed at angle θ = 5.27°. Input polarizations: quasi-TE.

One can see that the incident quasi-TE fundamental mode has to change the polarization to quasi-TM mode, while propagating along the waveguide. This effect of polarization rotation/conversion in an anisotropic channel waveguide could be explained in the following way [5, 6]. The incident optical beam excites two hybrid guided modes of circular polarization. Because of the phase delay due to the difference of effective refractive index of these modes, their superposition produces different polarization of the resulting field at the waveguide end, depending on the propagation length L.

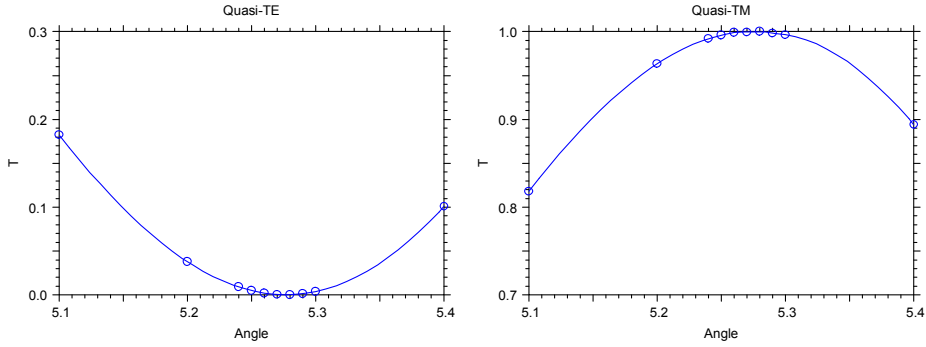
It is worth noting that it has been impossible to achieve a constant level of the total power due to simulation problems, typical for the full-vectorial 3D BPM that currently works only under paraxial approximation [7]. Nevertheless, for our particular waveguides with the small index contrast, this method could be also applied for the near-***Z***-axis waveguides ($\theta < 7°$) but at the expenses of the non constant level of the total power. However, this effect can be corrected by a simple power normalization procedure by means of the correction coefficient K_C to the monitor values for quasi-TM and quasi-TE modes. Results of this power normalization are presented in Fig.2. It is easily seen that, at optimal length L_0 = 7.8 mm, this anisotropic channel waveguide produces a 90° rotation of the incident linear polarization from quasi-TE to quasi-TM (see Fig. 2a) or from quasi-TM to quasi-TE (see Fig. 2b).

The influence of waveguide orientation in the vicinity of the optimum angle θ_0 has been investigated by the power transmittance analysis for quasi-TE and quasi-TM modes passing through the 7.8 mm long anisotropic channel waveguide. This length is close to the optimum for the 90-degree rotation, thus the input polarization has been chosen to have the quasi-TE orientation. As a result, at optimum direction θ_0 of the channel waveguide we have the maximum power transmittance for quasi-TM and the minimum transmittance for quasi-TE mode, respectively. Results of these simulations are presented in Fig. 3.



(a) (b)

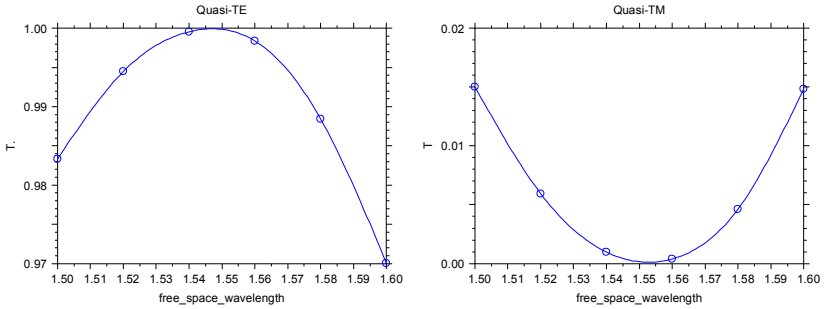
Fig. 2. Normalized results of 3D BPM simulation of power transmittance T in the near-***Z***-axis anisotropic channel waveguide directed at angle $\theta = 5.27°$. $K_C = 1.636$.
Input polarizations: (a) quasi-TE; (b) quasi-TM.



(a) (b)

Fig. 3. 3D BPM simulation of polarization conversion from quasi-TE to quasi-TM mode at different angle θ relative to ***Z***-axis in ***Y***-cut Ti:LiNbO3. $L_0 = 7.8$ mm. (a) quasi-TE; (b) quasi-TM.

One can see that the anisotropic channel waveguide in $LiNbO_3$ is working as the good polarization rotator only within a small angle range, $\Delta\theta \sim 0.1°$, centered around the angle $\theta_0 = 5.27°$ related to ***Z***-axis. For another waveguide parameters, the optimal angle θ_0 is different from this one but the optimum range $\Delta\theta$ is of the same order of magnitude. In general, the larger difference between the effective indices of fundamental quasi-TE and quasi-TM modes (measured along ***Z***-axis), then the larger optimum value of the angle θ_0 and the smaller length of the total polarization conversion.
The proposed optical element for the polarization conversion has the high extinction ratio (larger than -20 dB) in a wide transmitting band ~ 80 nm (see Fig. 4) that is very important for practical applications. For example, this polarization rotator/converter can be applied with the polarization splitter for the polarization diversity of the multiple photonic devices that can be monolithically integrated in lithium niobate substrate.



(a) (b)

Fig. 4. 3D BPM simulation of polarization conversion from quasi-TM to quasi-TE mode at different optical wavelengths in the near-***Z***-axis anisotropic channel waveguide directed at angle $\theta = 5.27°$. $L_0 = 7.8$ mm. (a) quasi-TE; (b) quasi-TM.

3. Conclusions

This paper describes the results of theoretical investigation of the novel passive (without external electric filed) integrated optics polarization rotator/converter based on the near-Z-axis anisotropic graded index Ti-diffused channel waveguide in $LiNbO_3$. The device operation is based on the hybrid nature of guided modes in 3D anisotropic waveguide. The effect of polarization conversion/rotation has been studied by the full-vectorial 3D beam propagation method. It has been found that at particular waveguide direction (about 5° related to ***Z***-axis of ***Y***-cut $LiNbO_3$), the condition of total polarization conversion from quasi-TE to quasi-TM mode (and backward) can be obtained by using a waveguide with index increase 0.015 and total length about 8 mm. This optical element could find the wide applications for the polarization diversity of photonic devices monolithically integrated in the $LiNbO_3$ substrate.

Acknowledgments

The authors thank Company RSoft Design Group, Inc. for providing user license for Rsoft Photonic CAD Suite 8.0 including BeamPROP software [7] for BPM simulations.

References

[1] J. Ctyroky, M. Cada, "Generalized WKB method for the analysis of light propagation in inhomogeneous anisotropic optical waveguides," IEEE J. Quantum Electron. vol. 17, pp. 1064–1070, 1981.

[2] T. Kawazoe, K. Satoh, I. Hayashi, and H. Mori, "Fabrication of integrated-optic polarization controller using Z-propagating Ti-$LiNbO_3$ waveguides," J. Lightwave Technol., vol. 10, pp. 51–56, 1992.

[3] E.M. Zolotov, V.A. Kiselev, V.M. Pelekhaty, A.M. Prokhorov, V.A. Chernykh, E.A. Sherbakov, "A Study of Anisotropic Optical Diffuse Waveguides in LiNbO3," Quantum Electron. (Rus) vol. 5, pp. 1379-1381, 1978.

[4] E.A. Kolosovsky, D.V. Petrov, A.V. Tsarev, I.B. Yakovkin, "An exact method for analyzing light propagation in anisotropic inhomogeneous optical waveguide," Opt. Commun. vol. 43, pp. 21-25, 1982.

[5] J. Ctyroky, "Analysis of polarization effects in near-Z-axis Ti:$LiNbO_3$ devices," J. Opt. Commun., vol. 14, pp. 32-38, 1993.

[6] Andrei V. Tsarev, New compact polarization rotator in anisotropic LiNbO3 graded-index waveguide, Optics Express, vol. 16, pp.1653-1658, 2008.

[7] BeamPROP from RSoft Design Group, Inc , http://www.rsoftdesign.com.

Sm^{3+} doped polymers for planar optical waveguide amplifiers

L.H. Huang, K.C. Tsang, and E.Y.B. Pun

Department of Electronic Engineering, City University of Hong Kong
Tat Chee Avenue, Kowloon, Hong Kong

Abstract *Samarium (Sm^{3+}) doped SU8 polymer materials were synthesized and characterized. Intense red emission at 645nm was observed under 355nm laser light excitation. Spectroscopic investigations show that the doped materials are suitable for the realization of optical waveguide amplifiers.*

Introduction

Organic polymer materials have many advantages over inorganic materials in the fabrication of active and passive optical waveguide devices [1]. Moreover, many polymer materials are transparent across the low-loss visible wavelength windows of polymer optical fibers (POFs) which are being used in local area networks and short-haul communications [2]. These properties make polymer materials attractive for use in optical waveguide devices that can be readily deployed with POFs, e.g. planar waveguide amplifiers to compensate losses in splitters, multiplexers, switches, and so on. The first organic-dye-doped POF amplifier was reported in 1993, however, cw operation has not been demonstrated due to triplet losses [3]. On the contrary, rare earth ions as amplification media do not suffer from triplet loss and exhibit many advantates, such as steady fluorescence and longer metastable lifetimes, making them suitable for cw operations.

The optical properties of $Sm(BTF)_4P$-doped acetone-d_6 [4], $Sm(HFA)_4Net_4$ doped PMMA-d_8 and $Sm(BTF)_4P$ doped PMMA [5], and $Sm(DBM)_3(TPPO)_2$ doped PMMA [6] were studied. Numerical simulations showed that optical gain higher than 20dB can be realized [4,5].

In this paper, spectroscopic investigations on $Sm(TTFA)_3$ doped SU8 polymer films were carried out. Intense red emission at 645nm was observed in the doped polymer films under 355nm Nd:YAG laser light excitation, and doped polymer channel waveguides were fabricated using a simple UV exposure process.

Experimental

SU8 polymers are electron beam and UV light sensitive materials, and were chosen as the host materials due to their high sensitivities and negative tone properties [7]. $Sm(TTFA)_3$ doped polymers were prepared by adding $Sm(TTFA)_3$ organic complexes into SU8 polymers directly, and the complexes dissolve readily at room temperature. Polymers doped with 1, 2, 3, 4 and 6 wt% $Sm(TTFA)_3$ complexes were prepared and spin-coated on quartz substrates, and the film thicknesses were ~2μm. The absorption spectra were recorded using a UV-VIS-NIR Perkin-Elmer λ_{19} spectrophotometer. The emission spectrum and lifetime measurements were carried out using an Acton Research Corporation Spectra Pro 500i, and the excitation source used was a 355nm Nd:YAG 10Hz pulsed laser.

$Sm(TTFA)_3$ doped channel waveguides with a dimension of 2μm high and 50μm wide were also fabricated using simple UV exposure process, and thermally oxidized silicon wafers with ~7μm thick oxide layers were used as substrates.

Results and discussion

The absorption spectra of undoped and $Sm(TTFA)_3$ doped SU8 films are shown in Fig. 1. The absorption bands with peaks at 236nm and 278nm are attributed to the the absorptions of the SU8 polymers, and the absorption band with peak at 346nm corresponds to the ground state to excited state absorption of the organic ligand ($TTFA^{-1}$). The emission spectra of the doped SU8 films under 355nm Nd:YAG laser light excitation are shown in Fig. 2. Intense red emission was observable by naked eyes, and the spectra consist of four emissions, with peaks at 562, 598, 645, and 705nm wavelengths, corresponding to the transitions from the $^4G_{5/2}$ to the $^6H_{5/2}$, $^6H_{7/2}$, $^6H_{9/2}$ and $^6H_{11/2}$ levels, respectively, and the emission at 645nm is the most intense. The emission intensity increases monotonically with increasing $Sm(TTFA)_3$ concentration (up to the 4 wt%), and then decreases.

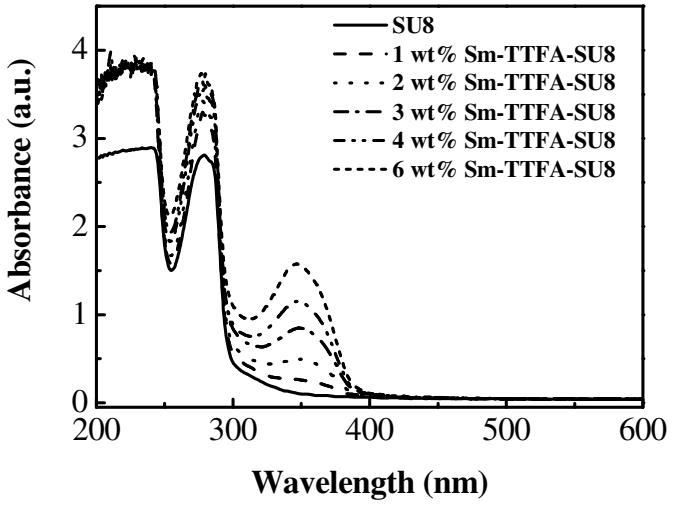


Fig. 1 Absorption spectra of undoped and $Sm(TTFA)_3$ doped SU8 films

From the absorption spectra, the emission spectra and the energy level diagram of Sm^{3+} ions, the luminescence mechanisms of $Sm(TTFA)_3$ doped SU8 films can be explained, as illustrated in Fig. 3. The excitation of the singlet state S_1 from the ground singlet state S_0 occurs in the TTFA ligand after the absorption of UV light. Then, the singlet state S_1 undergoes non-radiative intersystem crossing process to the triplet state T_1. The triplet state T_1 couples with the $^4G_{7/2}$, $^4I_{9/2}$ and $^4M_{15/2}$ energy levels, and transfers energy to these levels. These upper levels relax non-radiatively to the lowest level $^4G_{5/2}$. Finally, the ions in the $^4G_{5/4}$ level relax radiatively to the lower levels $^6H_{5/2}$, $^6H_{7/2}$, $^6H_{9/2}$ and $^6H_{11/2}$, respectively, thereby producing four emissions at 562, 598, 645 and 705nm wavelengths.

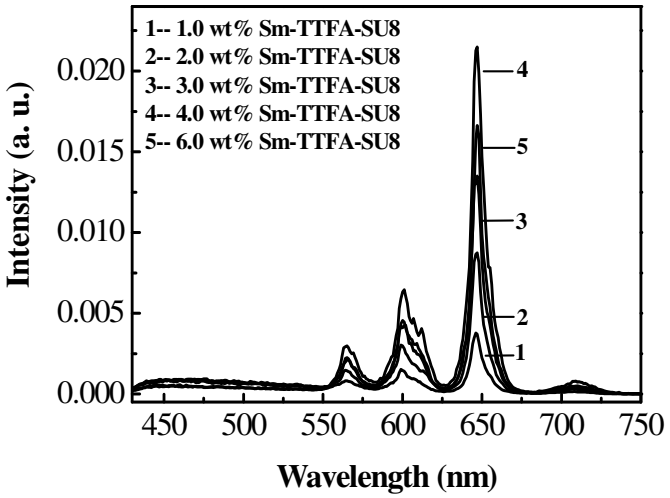


Fig.2 Emission spectra of $Sm(TTFA)_3$ doped SU8 polymer films

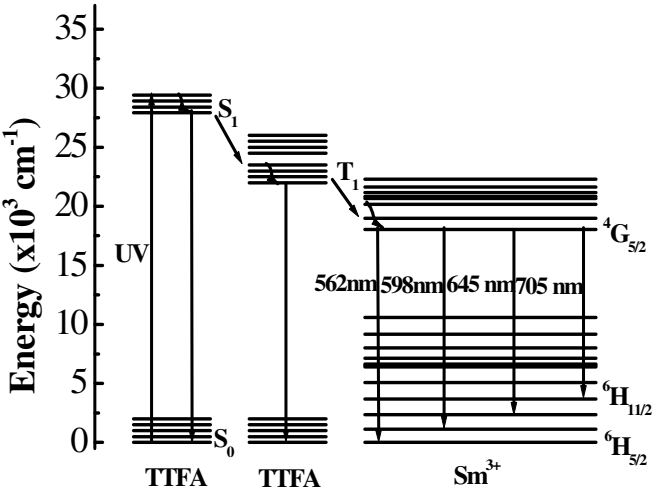


Fig.3 Luminescence mechanisms of $Sm(TTFA)_3$ doped SU8 polymer films under 355 nm UV laser light excitation

The spectroscopic properties of most rare earth ions in solids can be determined quantitatively by the Judd-Ofelt theory [8,9]. Since the waveguide films were only ~ 2μm thick, the absorptions attribute to the Sm^{3+} ions are too weak to be recorded, thus, a 1.47 mm thick 4 wt% $Sm(TTFA)_3$ doped SU8 film was prepared for this purpose. The Judd-Ofelt parameters calculated from the absorption spectra are $\Omega_2 = 14.96\times10^{-20}cm^2$, $\Omega_4 = 11\times10^{-20}cm^2$, and $\Omega_6 = 6.46\times10^{-20}cm^2$. The stimulated

emission cross section (σ_{em}) for the 645nm emission is calculated using the Fuchtbauer-Ladenburg relation [10] and is $2.75\times10^{-21}cm^2$. This value is comparable to reported values for $Sm(BTF)_4P$ doped Acetone-d_6 ($3.3\times10^{-21}cm^2$) [4], $Sm(HFA)_4Net_4$ doped PMMA-d_8 ($4.5\times10^{-21}cm^2$) [5], $Sm(DBM)_3(TPPO)_2$ doped PMMA ($1.58\times10^{-21}cm^2$) [6], and Er^{3+} doped silica optical fiber ($5\times10^{-21}cm^2$) [10]. Hence, $Sm(TTFA)_3$ doped SU8 materials can exhibit efficient amplification at 645nm wavelength under 355nm UV laser pumping. Channel waveguides have been fabricated using direct UV exposure process, and gain measurements are in progress.

Conclusions

Spectroscopic investigations on $Sm(TTFA)_3$ doped SU8 polymer films have been carried out. Intense red emission at 645 nm was observed in the doped polymer films under 355nm Nd:YAG pulsed laser excitation. The J-O parameters of 4 wt% $Sm(TTFA)_3$ doped SU8 film samples are $\Omega_2 = 14.96\times10^{-20}cm^2$, $\Omega_4 = 11\times10^{-20}cm^2$, and $\Omega_6 = 6.46\times10^{-20}cm^2$. The calculated stimulated emission cross section is $2.75\times10^{-21}cm^2$ and is comparable to values reported for Sm doped PMMA polymers. Channel waveguides have been fabricated in the doped materials using simple direct UV direct exposure, and the results indicate that $Sm(TTFA)_3$ doped SU8 polymers are suitable for the fabrication of polymer waveguide amplifiers and lasers in the visible spectrum.

Acknowledgments

This work was supported by a grant from the Research Grants Council of the Hong Kong Special Administration Region, P.R. China [Project No. CityU 1192/06].

References:

[1] H. Ma, A. K. Y. Jen, and L. R. Dalton, "Polymer-based optical waveguides: materials, processing, and devices", Adv. Mater., vol.14, pp.1339-1365, 2002.

[2] J. Zubia and J. Arrue, "Plastic optical fibers: an introduction to their technological processes and applications", Opt. Fiber Technol., vol. 7, pp.101-140, 2001.

[3] A. Tagaya, Y. Koike, T. Kinoshita, E. Nihei, T. Yamamoto, and K. Sasaki, "Polymer optical fiber amplifier", Appl. Phys. Lett., vol. 63, pp.883-884, 1993.

[4] C Koeppen, S. Yamada, G. Jiang, A. F. Garito, and Larry R. Dalton, "Rare-earth organic complexes for amplification in polymer optical fibers and waveguides", J. Opt. Soc. Am. B, vol. 14, pp.155-162, 1997.

[5] R. Gao, R. A. Norwood, C. C. Teng, and A. F. Garito, "Rare earth-doped polymer optical waveguide amplifiers", Proceedings of the SPIE Conference on Organic Photonic Materials and Devices II, 2000, pp.12-16.

[6] F. Xie, Z.Q. Zheng, "Radiative properties of $Sm(DBM)_3$ $(TPPO)_2$ doped poly(methyl methacryate) (PMMA)", Physica B, vol. 39, pp.415-419, 2004.

[7] W. H. Wong, J. Zhou, and E. Y. B. Pun, "Low-loss polymeric optical waveguides using electron-beam direct writing", Appl. Phys. Lett., vol. 78, pp. 2110-2112, 2001.

[8] B. R. Judd, "Optical absorption intensities of rare-earth ions", Phys. Rev., vol. 127, pp.750-761, 1962.

[9] G. S. Ofelt, "Intensities of crystal spectra of rare-earth ions", J. Chem. Phys., vol.37, pp. 511-520, 1962.

[10] W. L. Barnes, R. I. Laming, E. J. Tarbox, and P. R. Morkel, "Absorption and emission cross section of Er^{3+} doped silica fibers", vol. 27, pp.1004-1010, 1991.

Horizontal slot waveguide-based efficient fiber couplers suitable for silicon photonics

J. V. Galan[1], P. Sanchis[1], J. Blasco[1] and J. Marti[1]

[1]Nanophotonics Technology Center, Universidad Politécnica de Valencia, Camino de Vera s/n 46022 Valencia, Spain
jogaco@ntc.upv.es

Abstract. *In this paper, simulation results of high performance grating and inverted taper fiber couplers for horizontal slot waveguides are reported. Maximum 48% and 61% coupling efficiencies are achieved for positive and negative detuned gratings, respectively. Furthermore, 93% coupling efficiency is achieved for the horizontal inverted taper-based coupler.*

Introduction

Silicon-on-Insulator is emerging as a very suitable technology to develop silicon-based photonic integrated circuits. This technology is 100% CMOS compatible, allowing the development of planar optical devices and making possible to achieve very large scale integration (VLSI). However, nonlinear effects in silicon are inefficient. Materials which have superior optical properties, such as alloys of Group III and V elements, are commonly used to make lasers and active devices. These materials are regrettably not CMOS compatible. Slot waveguides have recently been proposed for silicon photonics devices [1]. The main advantages of slot waveguides is the possibility of filling the slot region with an active optical material thus enabling modulation, switching, sensing and many other applications which are not feasible with silicon material. In this paper, we design efficient fiber couplers for horizontal slot waveguides.

Horizontal slot waveguides

The use of silicon nanocrystal (Si-nc) embedded in silica (SiO_2) is one of the most promising approaches to exploit nonlinear effects by means of silicon slot waveguides. In the slot waveguide (see Fig. 1), the light is highly confined in a very small region (slot region) of a low index contrast material (n_s) sandwiched between two high index contrast layers (n_H). Vertical and horizontal slot waveguide configurations, as depicted in Fig. 1, have been recently studied [2]. Optimum parameters of the slot waveguide have been obtained in order to achieve minimum effective area in the slot region thus enhancing the nonlinear effects [2]. However, the horizontal slot waveguide planar geometry offers an easier fabrication compared to the vertical geometry [2]. Regarding the horizontal slot waveguide, light confinement in the slot is achieved for TM polarization, whose main electric field component is in the y-axis direction (see Fig. 1b). Considering that the slot is formed by Si-nc/SiO_2 (n_s=1.6 for λ=1550 nm), it was obtained that the optimum slot waveguide parameters for enhanced nonlinear performance are w=350 nm, h=200 nm and w_s=50 nm λ=1550 nm [3].

Horizontal slot waveguide-based fiber couplers

In Fig. 2 it can be seen both grating coupler and inverted taper slot waveguide-based proposed fiber couplers.

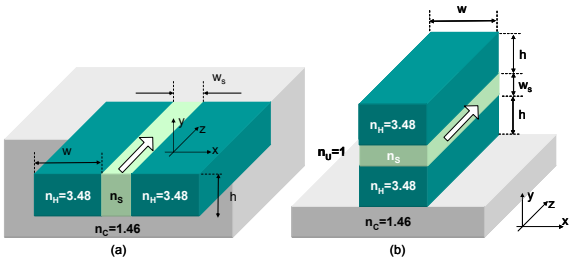


Fig. 1.- (a) Vertical and (b) horizontal silicon based slot waveguide configurations.

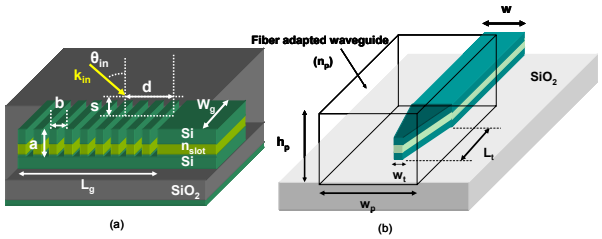


Fig. 2.- (a) Grating coupler and (b) inverted taper horizontal slot waveguide-based fiber couplers.

With respect to the grating coupler in Fig. 2a, the entire grating coupler is surrounded by a silica layer. The slot thickness is 50 nm. The main grating design parameters are the grating period (b), the etching depth (a), the grating width (W_g) and the grating length (L_g). The fiber core is slightly tilted (θ_{in}) to minimize the effect of second order diffraction. The fiber core is also vertically separated from the grating by a distance s, and horizontally by a distance d. The inverted taper-based coupling structure (Fig 2b) is based on a horizontal slot waveguide, on top of a silica cladding layer, which is tapered down by the inverted taper. A fiber-adapted waveguide on top of the inverted taper is used [4] to efficiently guide light from the taper to the fiber (see Fig. 2b). This waveguide can be made by means of a polymer with a refractive index n_p=1.6 equal to the Si-nc/SiO_2 refractive index. The main design parameters are the taper length (L_t), the taper tip width (w_t), and the dimensions of the fiber-adapted waveguide (w_p, h_p).

Grating coupler design

The grating has been designed employing 2D-FDTD simulations. The parameters optimization is based on maximum coupling efficiency for λ=1550 nm and TM polarization. The grating is 20 period long (L_g=20b). The grating width is chosen as W_g=12μm. The fiber is considered vertically separated from the grating by a distance s=1.5μm. A tilt angle of θ_{in}=±8º is chosen for negative and positive detuned gratings. As usual in conventional SOI grating coupler designs [5-6], the filling factor is initially ff=50%. Tab. 1 shows the obtained optimum simulation parameters. 48% coupling efficiency can be achieved for the positive detuned grating coupler. On the other hand, it 61% coupling efficiency can be achieved for the negative detuned grating coupler. For these optimum parameters, the spectral response of the grating coupler has also been calculated. Fig. 3 shows the obtained spectral response. A 35 nm 1 dB-bandwidth spectral response is achieved in both cases.

Parameters @ λ=1550 nm and TM polarization			
Positive detuned grating θ_{in}=8°		Negative detuned grating θ_{in}=-8°	
b	807 nm	*b*	670 nm
a	265 nm	*a*	265 nm
d	3.83 µm	*d*	3.83 µm
t_{BOX}	2.2 µm	t_{BOX}	2.3 µm

Table 1.- Optimum design parameters of the grating coupler.

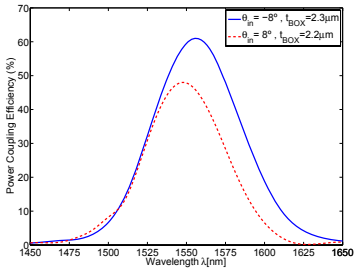


Fig. 3.- Spectral response of the grating couplers with optimum parameters shown in Tab. 1.

Sensitivity to fabrication and alignment tolerances of the structure has also been analyzed. Regarding fabrication tolerances, it is obtained that the coupling efficiency is almost constant for etching depth variations of ±10 nm or filling factor changes of ±5 %. For alignment tolerances, it is obtained that the coupling efficiency is also almost constant for tilt angle variations of ±2º or horizontal fiber position changes of ±3 µm.

Inverted taper design

The inverted taper-based fiber coupler has been analyzed employing 3D BPM simulations. Parameters have been optimized to achieve maximum coupling efficiency for λ=1550 nm and TM polarization. To simplify the design, the dimensions of the fiber-adapted waveguide have been chosen as w_p=h_p=3 µm. For these waveguide dimensions, it has been evaluated the mode mismatch between the fundamental mode of the waveguide and the fiber in the fiber-SiO_2 waveguide interface. To do this, overlap integral [5] between the fiber and the waveguide fundamental modes has been analyzed as a function of the fiber mode field diameter (MFD). It was obtained that if a standard single mode fiber with MFD=2.5µm is chosen, 98% coupling efficiency is achieved at the fiber interface. The design can be optimized for coupling to higher MFD optical fibers by changing the dimensions of the SiO_2 waveguide. For this waveguide section, the mode mismatch in the inverted taper tip interface has also been evaluated by using the overlap integral. Fig. 4a shows the simulation results of the power coupling efficiency as a function of the inverted taper tip width. It can be seen that if a taper tip width of w_t=40nm is chosen, the power coupling efficiency at the taper tip interface increases up to 95%.

Using the taper tip width of w_t=40 nm and the SiO_2 dimensions of w_p=h_p=3 µm, the taper length has been optimized by employing 3D BPM simulations. In Fig. 4b, it can be seen the simulation results of the coupling efficiency as a function of the taper length for w_p=h_p=3 µm and w_t=40 nm. It is obtained that the coupling efficiency remains almost constant for inverted taper lengths longer than 150 µm. For a taper length of

L_t=150 μm a maximum coupling efficiency of 95% is obtained. The final coupling efficiency would then be 93% for TM polarization and λ=1550 nm.

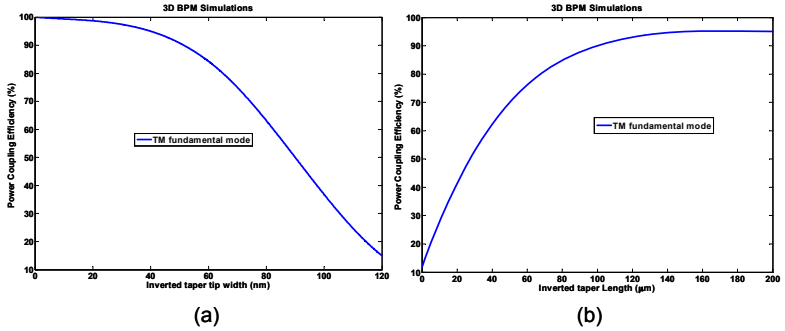


Fig. 4.- (a) Power coupling efficiency as a function of the inverted taper tip width taking into account a SiO_2 waveguide of w_p=h_p=3 μm. (b) Power coupling efficiency as a function of the taper length for a taper tip width of w_t=40 nm.

Conclusion

In conclusion, 48% and 61% coupling efficiencies and a 35 nm-bandwidth spectral response can be obtained for positive and negative detuned slot waveguide-based grating couplers, respectively. On the other hand, coupling efficiency higher than 90% may be achieved with slot waveguide-based inverted taper couplers.

Acknowledgments

Authors acknowledge financial support by EC under project 017158-PHOLOGIC and Spanish MEC and EU-FEDER under contact TEC2005-07830 SILPHONICS. It is also acknowledged the support of Generalitat Valencia under project reference 20070775 EFIDIS.

References

[1] V. R. Almeida, Q. Xu, C. A. Barrios, and M. Lipson, "Guiding and confining light in void nanostructure," Opt. Lett., vol. 29, pp. 1209–1211, 2004.

[2] P. Sanchis, J. Blasco, A. Martinez and J. Martí, "Design of Silicon-Based Slot Waveguide Configurations for Optimum Nonlinear Performance," IEEE J. Ligth. Techn., vol. 25, pp. 1298-1305, 2007.

[3] J.-M. Fedeli, E. Jordana, P. Lyan, J.-P. Colonna, P. Gautier, N. Daldosso, L. Pavesi, Y. Lebour, P. Pellegrino, B. Garrido, J. Blasco, F. Cuesta-Soto and P. Sanchis, "Deep-UV Lithography Fabrication of Slot Waveguides and Sandwiched Waveguides for Nonlinear Applications," 4th Group IV Photonics Conference (GFP), pp. 222-224, 2007.

[4] G. Roelkens, P. Dumon, W. Bogaerts, D. Van Thourhout, and R. Baets, "Efficient silicon-on-insulator fiber coupler fabricated using 248nm deep UV lithography," Photon. Technol. Lett. 17, 2613-2615 (2005).

[5] F. Van Laere, G. Roelkens, M. Ayre, J. Schrauwen, D. Taillaert, D. Van Thourhout, T. F. Krauss, and R. Baets, "Compact and Highly Efficient Grating Couplers Between Optical Fiber and Nanophotonic waveguides," IEEE J. Ligth. Techn., vol. 25, pp. 151-156, 2007.

[6] L. Vivien, D. Pascal, S. Lardenois, D. Marris-Morini, E. Cassan, F. Grillot, S. Laval, J.-M. Fédéli, and L. El Melhaoui, "Light Injection in SOI Microwaveguides Using High-Efficiency Grating Couplers," IEEE J. Ligth. Techn., vol. 24, pp. 3810-3814, 2006.

Surface Plasmon Generation in a Subwavelength Slit in metal: a Palladium-Based H_2 Leak Detection Sensor

M.A. Vincenti[1,2], D. de Ceglia[2], M. De Sario[1], V. Marrocco[1], V. Petruzzelli[1], F. Prudenzano[3], M. Scalora[2], and A. D'Orazio[1]

[1]Dipartimento di Elettrotecnica ed Elettronica, Politecnico di Bari, Via Orabona 4 – 70125, Bari - Italy
vincenti@deemail.poliba.it
[2] Charles M. Bowden Research Center, AMSRD-AMR-WS-ST, Redstone Arsenal, AL 35898-5000, USA
[3] Dipartimento di Ingegneria dell'Ambiente e per lo Sviluppo Sostenibile, Politecnico di Bari, Taranto, Via del Turismo 8, 74100, Italy

Abstract. *We investigated the extraordinary transmission that occurs for subwavelength slits on metallic substrates: the transmission process is driven by several physical mechanisms, whose relative importance depends on the thickness of the metallic substrate and slit size. We show how a Palladium-based device is suitable for H_2-leak-detection exploiting the enhanced transmission phenomenon.*

Introduction

The demand for using hydrogen as a next-generation, clean, and renewable energy source has stimulated considerable efforts toward developing sensitive, reliable, and cost-effective hydrogen sensors for the fast detection of hydrogen below the lower explosive limit (LEL) of 4.65% [1]. Currently, Pd or Pd-based alloys are commonly used as sensing material, due to palladium high sensitivity and selectivity toward hydrogen [2-4]. Manipulation and storage of hydrogen are associated with danger of leakage which leads to an explosive atmosphere if the hydrogen concentration exceeds the LEL. Therefore, the development of sensors for hydrogen detection is important to preserve human beings and equipments. The literature reports several examples of hydrogen sensors based on chemical or electronic approaches [5-9]. Chemical hydrogen sensors measure changes induced by reaction between hydrogen and a corresponding chemical transducer, such as palladium [10-12]. Moreover, optical sensors are highly important for use in dangerous environment where explosive concentration of hydrogen could occur. The detection of very small quantities of hydrogen in the surrounding environment can be operated by monitoring the transmitted field of a subwavelength slit carved on a palladium substrate: the association of resonance cavity effects and surface plasmon generation allows the investigation of a regime of extraordinary transmittance in which the sensitivity to the variation of the optical properties is dramatically increased due to the presence of surface waves inside the nanocavities.

Transmission From a Single Slit

Several theoretical and experimental works report on the ability of subwavelength apertures carved on metal substrates to enhance the transmitted field thanks to the coupling of surface plasmons inside the nanocavities [13-15]. In this paper we investigate the enhanced transmission phenomenon that occurs for a single slit carved on an opaque metal substrate by inspecting two different mechanisms, respectively

driven by two different geometrical parameters: the thickness of the metallic substrate and the aperture size. The device under investigation is depicted in Fig.1-a : it consists of a palladium layer whose key parameters are the metal thickness *w* and the slit size *a*. All the calculations and results reported below are obtained solving Maxwell's equations by means of a proprietary numerical code based on a full-wave, finite-difference, time-domain method (FDTD) [16] and considering a Gaussian shaped incident input tuned at 800nm. Dispersion and absorption of the Palladium layer are considered in all the simulations [17]. Fig.1-b shows the transmission coefficient obtained by changing the metal thickness *w* and the slit size *a* by considering the source input described above and normalizing the transmitted field to the energy that only impinges the slit: the Fabry-Perot-like behavior of such structures is altered respect to previously reported transmittance peculiarities of equivalent perfect electric conductor structure [18], meaning that the presence of a plasmon resonance inside the nanocavity plays a fundamental role in the resonant mechanism as well as in the enhanced transmission phenomenon, resulting in the enhancement of the transmitted field due to the double coupling between the resonant conditions that depend on the metal thickness and on the slit size.

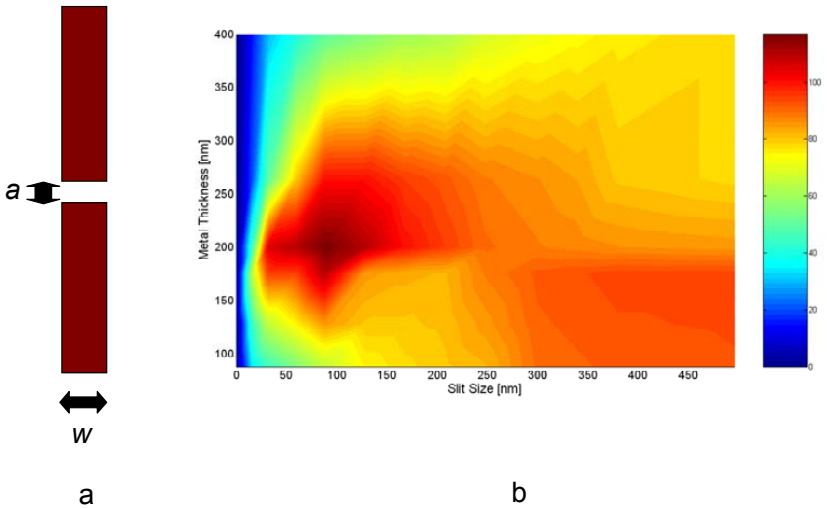


Fig.1: a) Sketch of the palladium substrate: the parameters under investigation are *a* (slit size) and *w* (substrate thickness) b) Transmission coefficient evaluated by varying the metal thickness *w* and the aperture size *a*; The presence of a resonance located for *w*=200nm confirms the Fabry-Perot like behavior of the structure.

The Palladium-Based Sensor: operating principle

As it is well known, the majority of transition metals spontaneously absorb hydrogen, changing their mechanical and optical properties as a function of the hydrogen content in the environment. Palladium, indeed, shows an extraordinary ability of trapping hydrogen molecules in its electrical configuration free states, modifying its Fermi level and changing reversibly its electrical [10] and optical [11] properties. This phenomenon causes the decrease of both the real and the imaginary parts of the complex permittivity

of palladium [17] described by means of a simple function h, that relates the bare palladium permittivity to the hydride palladium one as follows:

$$\varepsilon_{PdH}(\omega) = h(\omega) \times \varepsilon_{PdH}(\omega) \quad (1)$$

where $\varepsilon_{PdH}(\omega)$ is the dielectric permittivity of bare Pd, $\varepsilon_{PdH}(\omega)$ is the dielectric permittivity of hydride Pd, and $h(\omega)$ is a nonlinearly decreasing function that assumes real values between 1 and 0 by increasing the hydrogen concentration [19]. Moreover, to take into account the dispersive properties of both bare and hydride palladium, we consider the Drude model, which remains valid by increasing the hydrogen concentration inside the Pd lattice [6,7,12]. As mentioned in the previous section the peak in the transmission coefficient for a carved metal substrate corresponds to a perfect coupling condition inside the subwavelength aperture, meaning that also a slight variation in the optical properties of the palladium induces a dramatic change in the coupling phenomenon and, as a consequence, in the transmitted field. As depicted in Fig.2 the variation associated to the increase of the hydrogen content in air is remarkable: the sensitivity of the sensor calculated as the ratio between the variation of the transmission coefficient over the hydrogen content variation [6], is equal to S=0.567 %·ppm^{-1} when the hydrogen content goes from 0ppm to 100ppm.

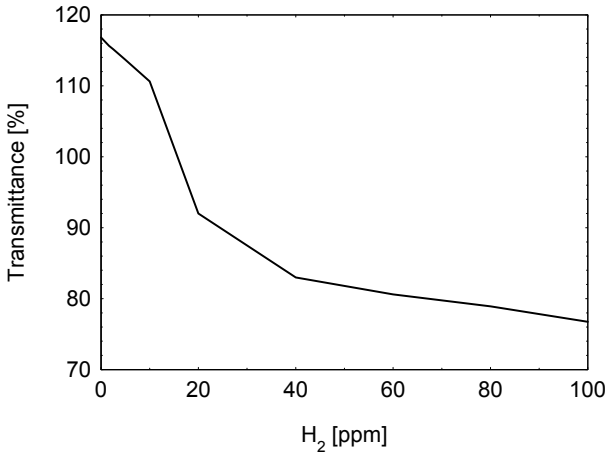


Fig2: Sensor calibration curve: transmittance value decreases as a nonlinear function of the hydrogen content, showing a sensitivity S=0.567 %·ppm^{-1} when the hydrogen content goes from 0ppm to 100ppm.

Conclusions

We theoretically investigated on the extraordinary transmission phenomenon that occurs for sub-wavelength slits carved on opaque metal substrates, i.e. palladium. Due to the dramatic response of palladium to hydrogen presence and to the combination of cavity effects and surface waves inside the slit one can explore the quantity of this gas by simply monitoring the changes in the transmitted field.

Acknowledgments

M.A. Vincenti thanks the U.S. Army European Research Office for partial financial support (contract no. W911NF-07-1-0567).

References

[1] F.A. Lewis, "The Palladium Hydrogen system", New York: Academic, 1967.
[2] P.T. Moseley, J.O.W. Norris and D.E. Williams, "Techniques and Mechanism in gas sensing", Philadelphia, PA: IOP, 1991.
[3] K. Hara and N. Nishida, "H_2 sensor using Fe_2O_3 based thin film", Sens. and Actuators B, vol. 20, pp. 181, 1994.
[4] S. Basu and A. Dutta, "Modified heterojunction based on zinc oxide thin film for hydrogen gas sensor application", Sens. and Actuators B, vol. 22, pp. 83-87, 1994.
[5] M.A. Vincenti, S.Trevisi, D. de Ceglia, N.Cioffi, M. Scalora, M. De Sario, V. Petruzzelli, F. Prudenzano, A. D'Orazio, "Metallo-Dielectric Multilayer Sensor for Hydrogen Detection in Exhaled Breath", ECIO 2007 - 13th European Conference on Integrated Optics, Copenhagen Denmark, 25-27 April 2007, paper ThG12.
[6] M.A. Vincenti, A. D'Orazio, M. De Sario, V. Petruzzelli, F. Prudenzano, D. de Ceglia, M. Scalora, "Fabry-Perot Microcavity Sensor for H_2-Breath-Test Analysis", Jour. of Appl. Phys. vol.102, no.7 074501, 2007.
[7] M.A. Vincenti, S. Trevisi, M. De Sario, V. Petruzzelli, A. D'Orazio, F. Prudenzano, N. Cioffi, D. de Ceglia, M. Scalora, "Theoretical Analysis of a Novel Palladium-Based Metallo-Dielectric Photonic Band Gap Structure for Applications to H_2 sensors", Jour. of Appl. Phys. vol. 103, no. 4, 2008.
[8] V.R. Katti, A. K. Debnath, S.C. Gadkari, S.K. Gupta, and V.C. Sahni, "Passivated thick film catalytic type H2 sensor operating at low temperature" , Sens. and Actuators B, vol. 84, pp. 219-225, 2002.
[9] K. Domansky, A. Rose, W.H. Grover, and G. J. Exharos, " Localized deposition of zinc oxide films by automated fluid dispensing method", Mater. Sci.Eng. B, vol.76, no.2 , pp. 116-121, 2000.
[10] J.C. Barton, J.A.S. Green, F.A. Lewis, "Changes of electrode potential and electrical resistance as a function of the hydrogen content of some Pd + Ni and Pd + Rh alloys", Trans. Faraday Soc., vol.62, pp. 960-970, 1966.
[11] A. Mandelis, J.A. Garcia, "Pd/PVDF thin film hydrogen sensor based on laser amplitude modulated optical transmittance: dependence on H_2 concentration and device physics", Sens. Actuators B, vol. 49, pp. 258-267, 1998.
[12] K. Wyrzykowski, A. Rodzik, B. Baranowski, "Optical transmission and reflection of PdH_x thin films", J. Phys. Condens. Matter, vol. 1, pp. 2269-2982, 1999.
[13] T.W. Ebessen, H.J. Lezec, H.F. Ghaemi, T. Thio and P. A. Wolff, "Extraordinary optical transmission through subwavelength hole arrays", Nature 391, 667-669, 1998.
[14] J. Bravo-Abad, L. Martin-Moreno and F.J. Garcia-Vidal, "Transmission properties of a single metallic slit: from the subwavelength regime to the geometrical optical limit, Phys. Rev. E 69, 026601, 2004.
[15] R. Gordon, "Light in a subwavelength slit in metal: propagation and reflection", Phys. Rev. B 73, 153405, 2006.
[16] R.W. Ziolkowski, "Pulsed and CW Gaussian beam interactions with double negative metamaterials slab", Opt. Express **11**, 662, 2003.
[17] M.A. Ordal, L.L. Long, R.J. Bell, S.E. Bell, R.R. Bell, R.W. Alexander, C.A. Ward, "Optical properties of the metals Al, Co, Cu, Au, Fe, Pb, Ni, Pd, Pt, Ag, Ti, and W in the infrared and far infrared", Appl. Optics **22**, 1099-1120, 1983.
[18] T.W. Ebessen, H.J. Lezec, H.F. Ghaemi, T. Thio and P. A. Wolff, "Extraordinary optical transmission through subwavelength hole arrays", Nature 391, 667-669, 1998.
[19] T. Graham, "On the absoption of dialytic separation of gases by colloid septa", Phil. Trans. R. Soc. Lond., **156**, 399-439, 1866.

Nanorice Chain Waveguides Based on Low and High Order Mode Coupling

Xudong Cui, and Daniel Erni

General and Theoretical Electrical Engineering (ATE), Faculty of Engineering, University of Duisburg-Essen, D-47048, Duisburg, Germany
xudong.cui@uni-due.de, daniel.erni@uni-due.de

Abstract *– We investigate the optical properties of a plasmonic chain waveguide consisting of a linear array of elongated nanoshell particles (i.e. nanorice), where the interaction is based on low and high order mode coupling. Research shows that the propagation length can be improved by this kind of nanorice structures when compared to solid metallic structures with elongated (elliptical) shapes. Furthermore, at high order resonances, the propagation, as well as the energy transfer can be enhanced compared to the propagation at low order mode interactions. These findings allow the design of highly efficient waveguides for guiding light on the nanoscale.*

Introduction

Waveguiding at nanoscale dimensions using metallo-dielectric structures become an active research topic of increasing interest [1]. One promising candidate is the so-called plasmonic chain waveguide made of orderly arranged nanoparticles, which can provide strong 3D mode confinement at still moderate propagation lengths [1]. By changing the building blocks of the chain, the performance of the waveguide can be further improved, when using a more complex geometry for the nanoparticles [2], such as e.g. elliptical nanoparticles similar to a nanoscopic grain of rice [3]. Nanorice chains are essentially set up from a specific kind of (elongated) nanoshells, which consist of a dielectric core and metallic cladding material. The underlying nanorice particles show a wide tuning range of the surface plasmon resonances, reaching from ultraviolet to the near-infrared [3]. Moreover, the modes existing in nanorice particles can be either of low or high order provided the geometric parameters are properly selected. In the following we shall discuss the advantages of plasmonic chain waveguides when consisting of nanorice particles. We investigate energy propagation in the framework of low and high order mode coupling. This study complements our previous research on spherical nanoshell chain waveguides [2].

Numerical modeling considerations

In this paper, we use full wave simulations based on the Finite Element Method (FEM) [4], which is capable to handle the complex geometries, as well as the strong dispersive nature of the materials involved with reasonably small numerical errors. For simplicity, only two dimensional structures are considered in this paper. Since the surface plasmon resonances of most noble metals occur at ultraviolet or optical frequencies, our calculation is then carried our in the wavelength range from $300\,\mathrm{nm} - 900\,\mathrm{nm}$. Considering the polarization dependence of such 2D structures, only *H*-polarization is used here, where the magnetic field (i.e. the H_z component) is oriented out of the plane as depicted in Fig.1.

Results and discussion

The nanoshell chains under consideration are shown in Fig.1. First, the resonances of an isolated nanorice particle are detected while calculating its scattering cross section (SCS). The wavelengths related to the peaks in the SCS's spectral response correspond to the resonance wavelengths, where the interaction of light at an angular frequency ω with the metal nanoparticle is strongest if ω lies in close vicinity to the particle's localized surface plasmon frequency.

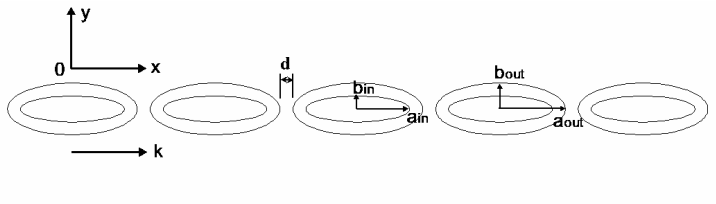


Fig.1. A schematics of the chain waveguide under calculation. The nanorice particle consists of a dielectric core ($n = 1.5$) and a silver shell [5], the overall structure is embedded in air. The coordinate system is indicated in the figure and the wave is incident from the $-x$ direction. The geometric parameters of the nanorice are $a_{in} = 40$ nm, $b_{in} = 10$ nm, $a_{out} = 50$ nm, and $b_{out} = 20$ nm, with a particle separation of $d = 10$ nm.

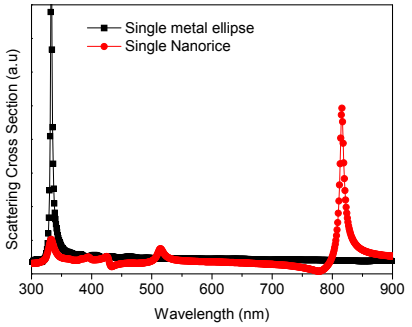


Fig.2. Scattering cross sections of a single nanorice and a solid metallic elliptical particle.

Figure 2 shows the SCSs for single nanorice and a solid silver elliptical particle having the same shape and volume as the nanorice. The resonances for the nanorice are found at 334 nm, 514 nm, 816 nm within our wavelength of interest. The modes in the nanorice at 334 nm and 514 nm are characterized as multipolar modes due to mode hybridization [3, 6], whereas the mode at 816 nm and the mode in the solid elliptical counterpart at 334 nm are identified as low order modes. To investigate the propagation properties we use the resonant modes as an excitation field at the input of the particle chain. For comparison, energy propagation relying on other non-resonant modes will be demonstrated as well.

The chain waveguide under investigation consists of 12 nanorice particles (the spacing between two adjacent particles is 10 nm throughout the paper). In order to numerically estimate the power attenuation of the chain waveguide, first; the field intensity along the

particle chain was computed at a line parallel to the propagation direction which is displaced to the outmost surfaces (y- direction) of the nanorice; second, the attenuation factors are then calculated referring to the Beer-Lambert law (exponential decay of the field intensity with respect to the propagation length). Here we will use the spatial averages of the field intensities. Note that the computed data from the first and the last nanorices in the chain will be excluded, in order to mask out interference effects stemming from impedance mismatch at the far and the near end of the chain waveguide.

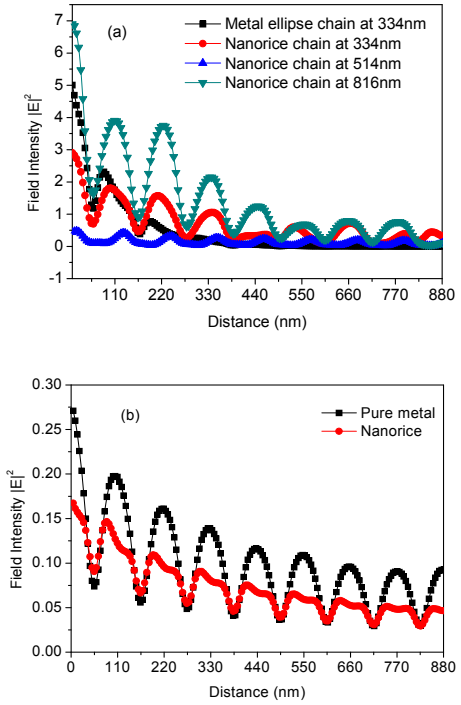


Fig.3. Total electric field intensities along the outer surfaces of the 12-nanorice chain. The starting point (0) is at the outmost surface of the second nanorice particle. (a) The chain waveguides are operated at the single resonance of the underlying particle, namely the nanorice or the solid metallic elliptical particle, including low and high order modes. (b) The chains operated at off-resonance of the structures (at 600 nm).

Figure 3(a) displays the results of the total electric field intensities along the outmost surfaces of a 12-nanorice chain under the operation of low order modes (816 nm) and high order modes of a single nanorice (334 nm, 514 nm). The result of a 12-elliptical solid particle chain is also shown for comparison. The power attenuation factors for the cases as given in Fig. 3(a) are $\alpha_1 = 0.0010488\ \mathrm{nm}^{-1}$(nanorice chain at 334 nm), $\alpha_2 = 0.0011834\ \mathrm{nm}^{-1}$ (nanorice chain at 514 nm), $\alpha_3 = 0.00455\ \mathrm{nm}^{-1}$ (nanorice chain at 816 nm), and $\alpha_4 = 0.0093\ \mathrm{nm}^{-1}$ (elliptical particle chain at 334 nm), which correspond to a $1/e$-propagation length of $L_1 = 953$ nm, $L_2 = 845$ nm, $L_3 = 219$ nm, $L_4 = 107$ nm, respectively. As can be seen from these figures, the propagation length is dramatically enhanced by a factor of 8 when using such nanorice structures instead of the pure metal counterpart even

when the structure is operated on the low order resonance of the single nanorice particle. Since the light matter interaction is strongest at low order resonances, the enhanced propagation of nanorice chain at low order mode arises likely from the large field enhancement in the interparticle space [cf. the behavior of the field intensities in Fig. 3(a)]. Whilst at high order mode resonances, the propagation lengths are generally larger although the light matter interaction is not as strong as before. The enhanced propagation at high order mode coupling is owing to the promising far-field radiation features of the high order modes in nanorice structures, which shows forward radiation features along the chain direction [2], and thus the interaction between particles is supported by far-field contributions. Figure 3(b) shows the results when the chains are operated at off-resonance either of the nanorice or of the solid metallic elliptical particle. As can be seen in Fig. 3(b), there is no big difference for the structure's propagation properties, and high-energy transfer is also possible at off resonances. This is due to the fact that at off-resonances, the nanoparticle acts as a weak dipole, where the weak coupling between adjacent particles leads to a considerable reduction of damping losses. However, there is a well-known trade-off between mode confinement and propagation length: The propagation length is smaller at resonant coupling which is associated to a strong field concentration; the propagation length is larger at off-resonances but with less tight field confinement. It should be noted that the local response of the chain is quite sensitive to the incident light due to interference effects. In particular, the mode coupling becomes more complicated when the nanoshell particle encompasses complex geometries. Under these circumstances mode hybridization is likely to give rise to a considerable amount of novel features that will be investigated in the near future.

Conclusions

In this paper, we investigate the optical properties of a plasmonic chain waveguide consisting of elongated nanoshells, i.e. nanorice. The propagation lengths under resonant and non-resonant conditions of single nanorice particles are analyzed. Studies show that the propagation, as well as energy transfer can be significantly improved by means of the proposed structure. Particularly, high order mode coupling provides enhanced propagation compared to low order mode coupling in the particle chain. This would inspire new design rules for light guiding in the nanoscale range.

References

[1] S. A. Maier and H. A. Atwater, “Plasmonics: Localization and guiding of electromagnetic energy in metal-dielectric structures”, J. Appl. Phys., vol. 98, pp. 011101, 2005.

[2] X. Cui and D. Erni, "Enhanced propagation in a plasmonic chain waveguide with nanoshell structures based on low and high order mode coupling", J. Opt. Soc. Am. A, submitted, 2008.

[3] H. Wang, D. W. Brandl, F. Lei, P. Nordlander, and N. J. Halas, “Nanorice: A hybrid plasmonic nanostructure”, Nano Lett., vol. 6, pp. 827-832, 2006.

[4] www.comsol.com.

[5] P. B. Johnson and R. W. Christy, “Optical constants of the noble metals”, Phys. Rev. B, vol. 6, pp. 4370, 1972.

[6] E. Prodan, C. Radloff, N. J. Halas, and P. Nordlander, “A hybridization model for the plasmon response of complex nanostructures”, Science, vol. 302, pp. 419-422, 2003.

Theoretical study of plasmonic propagation on a chain array

G. Lévêque, E. P. O'Reilly, and B. Corbett[1]

[1] Tyndall National Institute, Lee Maltings, Prospect Row, Cork, Ireland.
gaetan.leveque@tyndall.ie

Abstract *- A chain of gold nanoparticles embedded in a dielectric waveguide is proposed to locally transfer energy from a guided optical mode into a nearby absorbing medium through the excitation of surface plasmon modes. The energy transfer is evaluated placing different absorbers at the end of the chain.*

Introduction

The purpose of this work is to investigate a way to locally transfer energy from a guided optical mode into an absorbing medium using a metallic nanodevice. Plasmonic properties of metallic particles provide both confinement and enhancement of the light, offering the potential for efficient energy transfer [1]. The idea is to use a chain of closely packed gold nanoparticles in order to produce a hot spot at the end of the chain, in a similar way to what was proposed by Ghenuche et al in [2]. For this purpose, a strong coupling between each gold particle is important. This can be achieved in the near-field coupling regime, which occurs when the metallic objects are coupled together through the evanescent waves they scatter under illumination. The interspace between the particles must then be only a few tens of nanometers. We consider a system made of a number N of gold nanoparticles placed inside a dielectric waveguide (Fig. 1). In the following simulations the size of the particles is chosen to be $100 \times 100 \times 20$ nm^3. The period of the chain is 120 nm, which means that the gap between two adjacent particles is 20 nm. The chain is excited by the first TE mode supported by the slab, with the electric field directs as shown in Fig. 1. This can excite a surface plasmon mode which results from the combination of the individual localized surface plasmon mode of each particle.

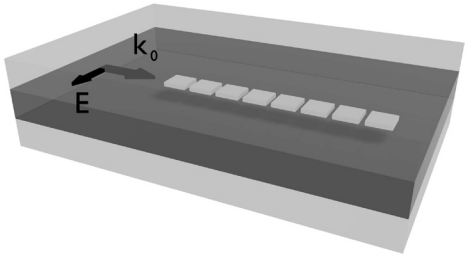
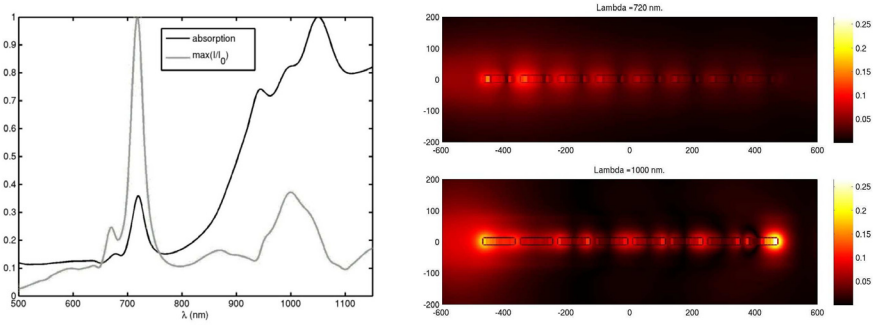


Figure 1: A chain of eight gold particles embedded in a dielectric waveguide and illuminated by a TE-polarized mode.

The electromagnetic field is computed using the Green's tensor formalism. A detailed description of the method can be found in the literature, see for example references [3, 4]. The data for gold susceptibility were taken from Palik [5].

Spectroscopy

As first example, we consider a structure where the waveguide is 150 nm thick, and the refractive index is equal to 2.1. The effective index of the incoming guided TE mode evolves from 1.7 ($\lambda = 720$ nm) to 1.4 ($\lambda = 1000$ nm). Several methods are possible to characterize the response of the structure. Two parameters are plotted in Fig. 2(a): the absorption per volume unit and the maximum of the electric field amplitude inside the gold structure. Absorption is calculated based on the time-averaged Joule power per volume unit ; by electric field amplitude we mean the square root of the time-averaged intensity.



(a) (b)

Figure 2: (a) Absorption and electric-field maximal-amplitude spectra, normalized to their maximum ; (b) Distribution of the electric-field amplitude in the plane perpendicular to the middle of the chain, for the two resonances of the maximal-intensity spectrum.

Both quantities have been normalized to their maximum for easier comparison. The absorption (black curve) and the field maximum (gray curve) show similar responses in the position and number of peaks. Two sets of resonances are observed, respectively around $\lambda = 700$ nm and $\lambda = 1000$ nm. Two peaks are visible around $\lambda = 700$ nm, whereas the broad resonance around $\lambda = 1000$ nm is composed of several different peaks, sometimes hidden in the wings of the main resonance (see $\lambda = 870$ nm). We note that the maximum for the field intensity, around 1000 nm, is not reached at the same wavelength as the one for maximal absorption, around 1050 nm. Figure 2(b) shows the distribution of the time-averaged electric-field amplitude on the plane crossing the middle of the chain, for the two resonance wavelengths of the maximum intensity spectrum (Fig. 2(a), gray curve). At 720 nm, the field amplitude drops rapidly along the chain direction, and is almost zero inside the last gold particle: the energy is completely absorbed and scattered by the chain while the incident guided mode propagates inside the system.
The resonance at 1000 nm has a completely different structure, as both ends of the chain show a strong field enhancement. This results from the coupling between the incident field and the collective mode of the chain. Indeed, as the effective wavelength of the mode supported by the dielectric waveguide is $1000/1.43 \approx 700$ nm, the chain length is about 1.5 times the wavelength. Hence the gold system resonates, and the electric field at the two ends oscillates in phase opposition. In the present case, the maximum is at

the forward end, which is interesting to optimize the energy transfer. The electric field intensity at this location is 26 times the intensity of the incoming electric field at the middle of the waveguide.

Influence of the waveguide parameters

The proposed system has a very large parameter space, as all the dimensions and materials can be modified in order to optimize a chosen property. In the following we focus on the effect of the waveguide thickness. Moreover, we also change the waveguide material to SiO_2 in order to demonstrate that the previous effects can be shifted to different wavelengths ($n = 1.5$).

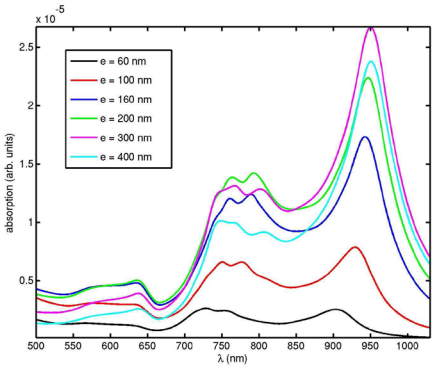
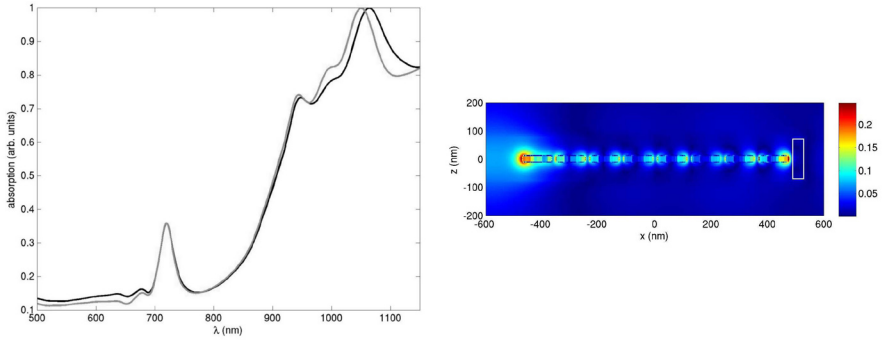


Figure 3: Evolution of the absorption spectra with the thickness of the silica waveguide.

Figure 3 shows the absorption spectra of a chain composed of 10 gold particles, placed in a $n = 1.5$ waveguide of variable thickness e. As in the previous paragraph, two broad peaks are observed. An increase of the waveguide thickness results in a red-shift of the different resonance wavelengths. The longer wavelength peak corresponds here to absorption of the incoming wave by the chain. Similarly, the light intensity decays all along the system (not shown). The shorter wavelength group of resonances corresponds to the excitation of cavity modes: the evaluation of the effective wavelength of the incident guided mode shows that the light couples in this case to the $L = 2\lambda$ cavity mode of the chain. The electric-field distribution (not shown) indicates that the balance between the electric field amplitude at the end and the beginning of the gold chain can be modified by varying on e. Moreover the enhancement in intensity at the end of the chain is about 40 times the incoming intensity in the middle of the waveguide from $e = 60$ nm to $e = 300$ nm.

Effect of an absorbing element

In order to study the energy transfer to a nearby absorbing medium, several geometries and materials has been considered. In the following example, a chromium pad is added 20 nm away from the last gold particle. The block is chosen to be $150 \times 150 \times 30$ nm^3, with the shortest side being set parallel to the chain axis.



(a) (b)

Figure 4: (a) Absorption spectra of the eight-particle chain without (black) and with (gray) chromium block placed 20 nm away from the last particle ; (b) Amplitude of the electric field along the middle of the chain, with the chromium block.

As expected, the absorption spectra computed with and without the absorber are almost identical around the short wavelength resonance, as the incoming wave does not reach the last particle (Fig. 4(a)). The shapes differ somewhat for the wavelengths around 1000 nm, as the last gold particle is then strongly excited: the mode is then more sensitive to the presence of the chromium particle. A shift of 20 nm in the position of the maximum is observed. The distribution of the electric field amplitude (Fig. 4(b)) shows unfortunately that the presence of the chromium particle is unfavorable since it tends to expel the field, which prevents the energy from being transferred efficiently from the guided mode to the substrate. It will be shown that we can change the material of the particle and add an air layer between the chain and the absorbing part to influence the energy transfer.

References

[1] G. Lévêque, and O. J. F. Martin, "Optical interactions in a plasmonic particle coupled to a metallic fi lm", *Opt. Express*, vol. 14, pp. 9971, 2006.

[2] P. Ghenuche, I. G. Cormack, G. Badenes, et al., "Cavity resonances in fi nite plasmonic chains", *App. Phys. Lett.*, vol. 90, pp. 041109, 2007.

[3] O.J.F. Martin, and N. B. Piller, "Electromagnetic scattering in polarizable backgrounds ", *Phys. Rev. E*, vol. 58, pp. 3909-3915, 1998.

[4] M. Paulus, and O. J. F. Martin, "Light propagation and scattering in stratifi ed media: a Green's tensor approach", *J. Opt. Soc. Am. A*, vol. 18, pp. 854-861, 2001.

[5] E. D. Palik, Handbook of optical constants of solids, New York: Academic Press, 1985.

Transfer Matrix Analysis of Spectral Response of Even-Row Microring Resonator Arrays

Xiaobei Zhang[1, 2*], Jose B. Rosas-Fernandez[1], R.V. Penty[1], I.H. White[1], Xinliang Zhang[2] and Dexiu Huang[2]

1: Electrical Engineering Division, 9 J J Thomson Avenue, University of Cambridge, Cambridge, UK

2: Wuhan National Laboratory for Optoelectronics, Huazhong University of Science and Technology, Wuhan, Hubei, P. R. China

*xz259@cam.ac.uk

Abstract: The spectral response of even-row microring resonator arrays is analysed using a transfer matrix model. A simple 2×2 microring resonator array is firstly studied analytically, and the results are found to agree well with the FDTD simulation. Finally, we provide detailed results of complex spectral responses for larger array sizes.

Keywords: Integrated optics, microring resonator, transfer matrix model, finite-difference time-domain method

Introduction

Microring resonators are promising building blocks for future high density optical circuits [1]. To date, many studies have been performed based on multiple microring resonator systems in both series and parallel forms. Recently, microring resonator arrays (MRAs) have been proposed and studied, but these have mainly focused on the odd-row MRAs for filtering [2], pulse repetition rate multiplication and shaping applications [3]. A 4×*N* MRA has been demonstrated for programmable spectral-phase encoding (SPE) and decoding for wavelength-division-multiplexing (WDM)-compatible optical code-division multiple access (OCDMA) systems [4, 5]. In *M* series coupled microring resonators (i.e. an MRA with just one column), the morphology-dependent spectral resonances split into *M* higher-*Q* modes, which are defined as mode splitting [6]. However, there has been less attention on the theoretical study of the even-row MRAs. Hence, in this paper we study even-row MRAs, and show that the spectra are modulated by the presence of the coupled resonators and feedforward waveguides, rather than exhibiting mode-splitting.

Transfer Matrix Model

Figure 1(a) shows an MRA with *M* rows and *N* columns. Each column contains *M* coupled resonators and is connected to each of the other columns in the array via waveguides placed at the top and bottom of the array. Figure 1(b) gives the detailed representation of each column in the MRA. The array is also denoted as MRA(*M*,*N*) or an *M*×*N* MRA.

The transmission spectrum of an even-row MRA is calculated using conventional transfer matrix formalisms [2, 3]. The transverse transfer matrix of the nth column is denoted as U_n, and the transfer matrix of straight waveguides between the nth and (n-1)th columns is V_{n-1} with V_0=(1,0;0,1) assumed. After decompositions and iterations, normalized complex transfer functions at the drop and through ports can be written as (ξ_T; ξ_D) =(P_{22}; P_{12}), where $P=\prod_{n=1}^{N} V_{n-1}U_n$ is the total transfer matrix. $D=|\xi_D|^2$ is the normalized transmission spectrum at the drop port. Significant differences between the even-row and odd-row MRAs can thus be deduced. For example, every column of straight waveguides provides feedback paths for an odd-row MRA but feedforward paths for an even-row MRA. Mathematically, the complex optical propagation coefficient for the straight waveguide l_{n-1} cannot be distilled from V_{n-1} for the odd-row MRA. However, $P=(\prod_{n=1}^{N} l_{n-1})(\prod_{n=1}^{N} U_n)$ for an even-row MRA, where the product of every column of ring resonators is $\prod_{n=1}^{N} U_n$ and the product of every column of straight waveguides is $\prod_{n=1}^{N} l_{n-1}$. Finally, due to the reasons above, the normalized transmission spectrum at the drop port is not affected by l_{n-1} for an even-row MRA, while it is significant for an odd-row MRA.

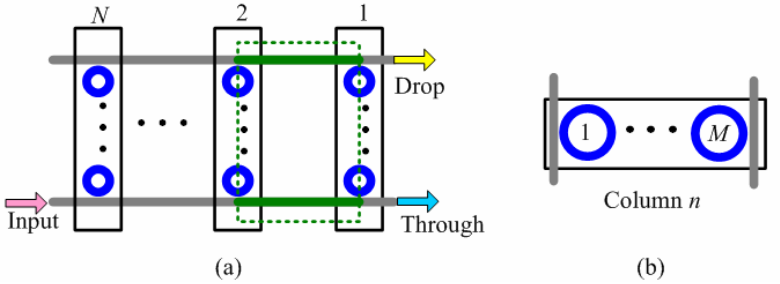


Figure.1 (a) Schematic of an even-row MRA. The solid boxes correspond to each column of M cascaded microring resonators and the dash box corresponds to straight waveguides between two adjacent columns. (b) Each column of M cascaded microring resonators.

Using the transfer matrix model above, transmission characteristics can be calculated for MRAs with arbitrary ring sizes and coupling coefficients. The values of the coupling coefficients are critical for the performance of microring resonators, strongly affecting the spectral shape and the transmission full width at half maximum. In the following investigations, ring sizes are assumed identical and the resonators are lossless. For simplicity, we denote θ and $\Delta\theta$ as the total and normalized round-trip phases in the resonator, respectively, with $\theta = \Delta\theta + 2m\pi$, where m is the resonance order. At resonance, it is assumed that $\Delta\theta = 0$. The relation between θ and radius R is given by $\theta = 4\pi^2 n_{eff} R/\lambda$, where n_{eff} is the effective reflective index of the waveguide and λ is the optical wavelength.

Analytical and Numerical Results

The simplest even-row MRA, i.e., the MRA(2,2), is firstly investigated using both the analytical transfer matrix method and a rigorous finite-difference time-domain (FDTD) simulation. The waveguide-resonator and inter-resonator coupling

spectrum at the drop port is found as $D = 4\rho^2\sigma^2 / \left(\rho^2 + \sigma^2\right)^2$, where $\rho = \cos\theta - (2-k^2)/2$ and $\sigma = k^3/(2\sqrt{1-k^2})$. The solid line in Fig.2(a) is the transmission spectrum of MRA(2,2) with $k = 0.5$. The transmission spectrum of MRA(2,1) is also calculated for comparison. When the two resonators are series coupled as in MRA(2,1), mode splitting is clearly present. However, more complex modulated spectral features appear in MRA(2,2). The resulting zero transmission occurs in MRA(2, 2), where unity transmission occurs for MRA(2,1). 2D FDTD simulation [7] is adopted to validate the accuracy of the analytical model based on the transfer matrix method. A Gaussian pulse at a centre wavelength of 1.5μm is injected into the resonator system. The waveguide is chosen to be high index semiconductor material with air as the cladding. Thus, the refractive index difference is as high as 2.4 to provide a small radius of microring resonators. The radius of microring resonators is chosen to be 2μm with a waveguide width of 0.2μm. The widths of inter-resonator and waveguide-resonator gaps are chosen as 0.05 and 0.10μm, respectively. Fig. 2(b) gives numerical results of the spectral response of the MRA(2,2) structure for wavelengths between 1.4 and 1.6 μm. This response shows good agreement with the results obtained using the analytical model.

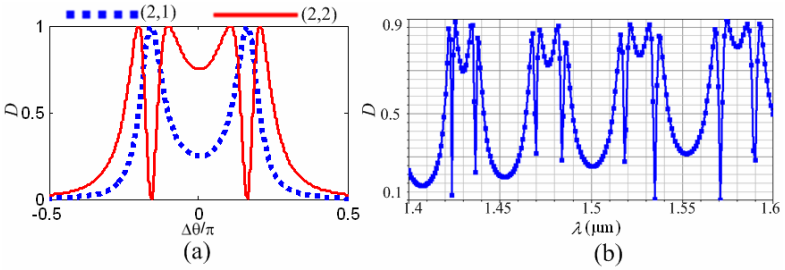


Figure. 2 (a) Transmission spectral of MRAs (2,1) and (2,2), respectively. (b) Transmission spectrum of MRA(2,2) using FDTD simulations.

We further study the spectral performance of even-row MRAs for larger array sizes. The coupling coefficient *k* is firstly assumed to be 0.5 for each coupler. Fig. 3(a)-(e) shows the transmission spectra for MRAs (2,3), (2,5), (2,6), (2,7) and (2,9), respectively. Fig. 3(f) shows the transmission spectral plotted in contour form, where zero transmissions are black. It can be seen that strong modulation of the spectra occurs in the spectral regions where originally mode splitting has occurred, and that the spectral modulation becomes very strong. To characterise this spectral responses, the number of zeros is denoted as M_T. Fig. 3(g) gives the spectral response when *M* is increased to 4, and shows that more zeros appear. Generally, M_T is observed to equal *M*(*N*-1), with *N*-1 zeros near each splitting mode of MRA (*M*,1), as shown in Fig.3(f) when *N* varies from 1 to 5. However, two or more zeros merge when the coupling coefficient is larger than some specific values. The transmission spectra are calculated as a function of the coupling coefficient *k* as shown in Fig. 4. For the case of MRA(2,6), there is just one region at $\Delta\theta = 0$ where zeros merge as shown in Fig.4(a). As *k* increases, the most inner zeros merge when *k*=0.5 and the following inner zeros merge when *k*=0.87. However, for the case of MRA(4,6), there are three

regions where zeros merge as shown in Fig.4(b). Zeros at $\Delta\theta = 0$ merge at the same k as that of the MRA(2,6). Zeros at two outer symmetrical regions merge at k=0.58 and 0.91 sequentially.

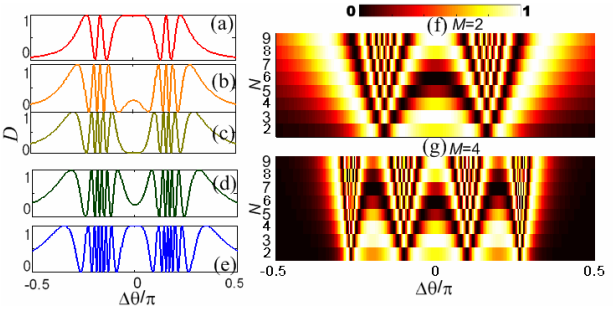


Figure 3. (a)-(e) Transmission spectra of MRAs (2,3), (2,5), (2,6), (2,7) and (2, 9), respectively.
(f) Contour plot of transmission spectra corresponding to MRAs(2,2:9).
(g) Contour plot of transmission spectra corresponding to MRAs(4,2:9).

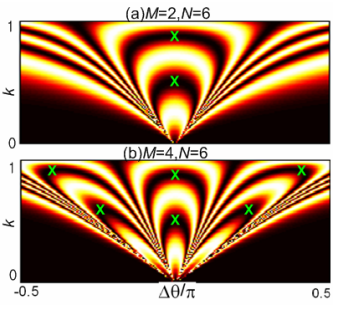


Figure 4. (a), (b)Contour plots of transmission spectra of MRAs (2,6) and (4,6) as a function of the coupling coefficient, respectively. 'x' points correspond to values of k where zeros merge.

Conclusion

To conclude, we have analysed the spectral response of even-row MRAs, and a large number of zeros is found to appear in the spectra. Thus the spectra are modulated, which is caused by combination effects of resonator interactions and waveguide feedforwards, compared to mode-splitting in series coupled microring resonators. This kind of modulated spectra may have potentials in spectrally dependent sub-system applications. By tuning each column's effective index and coupling coefficients, it would be possible to control the response of even-row MRAs, which allow very large numbers of spectral amplitude codes to be generated for OCDMA systems.

References

[1]. B.E. Little, OFC2003, Paper ThD1(2003)
[2]. Y. M. Landobasa, S. Darmawan, and M. Chin, IEEE J. Quantum Electron. 41, 1410-1418(2005)
[3]. B. Xia and L. R. Chen, IEEE Phonton. Technol. Lett. 18, 1999-2001(2006)
[4]. A. Agarwal, P. Toliver, R. Menendez, S. Etemad, J. Jackel, J. Young, T. Banwell, B. E. Little, S. T. Chu, J. Hryniewicz, W. Chen, W. Chen, and P. Delfyett, OFC2005, Paper PDP6(2005)
[5]. A. Agarwal, P. Toliver, T. Banwell, R. Menendez, J. Jackel, and S. Etemad, OFC2007, Paper OMO5 (2007)
[6]. D. D. Smith, H. Chang, K. A. Fuller, J. Opt. Soc. Am. B 20, 1967-1974(2003).
[7]. OptiFDTD, Optiwave Software, Ottawa, Canada

Surface waves on the boundaries of photonic crystals and their coupling

B.A.Usievich, V.V.Svetikov, J.Kh.Nurligareev and V.A.Sychugov

General Physics Institute, Moscow, Russia
borisu@kapella.gpi.ru

Abstract. *Photonic crystal structure supporting the surface wave is considered. It is shown both theoretically and experimentally that two such structures placed close to each other can yield to resonance transmission of light through the structure. This effect is promising for sensor applications.*

Introduction

Recently bounded systems of coupled waveguides attracted attention of researchers because of the surface waves that can exist on its boundaries with the homogeneous medium. Surface waves could be a handy tool for studying the processes taking place at the surface and sensor applications [1, 2]. These wave are somewhat analogous to the surface waves that can be excited on the metal-dielectric surface (surface plasmon polaritons (SPP)), however they are not limited to TM polarization like SPP as they are excited on the boundary of dielectric media. The feature of the considered waves that is common to SPP is the exponential decay of field into the both adjacent media. While the field in the uniform dielectric media is strictly exponential, the field in the stratified media is oscillating inside the exponent envelope. This penetration of the field in the adjacent dielectric media makes possible the design of the structure that supports two surface waves evanescently coupled with each other. Earlier in paper [3] was devoted to experimental study of such waves in the case of metal-dielectric boundaries. In this paper we are demonstrating the same effect for surface waves propagation on the photonic crystal boundary.

1D photonic crystal and the surface wave on it's boundary

We use the following structure supporting the surface wave: 10 pairs of Nb_2O_5-SiO_2 were deposited on the glass substrate ($n_s = 1.52$ at wavelength of He-Ne laser $\lambda = 632.8$ nm). Waveguide system was deposited using high-vacuum ion-beam sputtering setup Aspira 150 [4]. Measured refractive indices of the films at this wavelength are $n_1 = 2.27$ and $n_2 = 1.48$ for Nb_2O_5 and SiO_2 films respectively. Layer thicknesses were chosen to be $h_1 = 110$ nm for Nb_2O_5 and $n_2 = 180$ nm for SiO_2 that correspond to single mode guiding of each

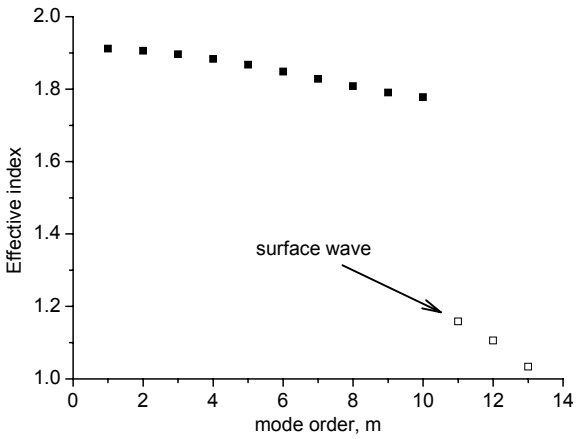


Figure 1: modes of the waveguide structure

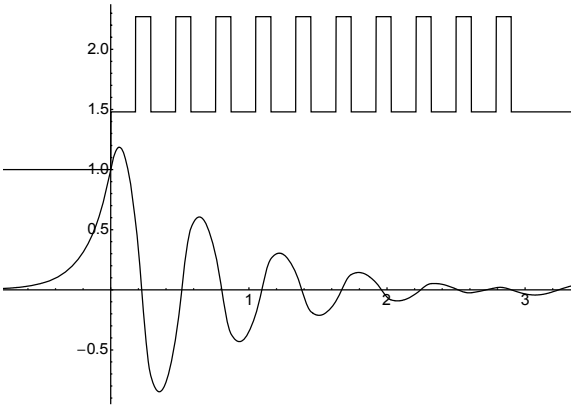


Figure 2: Field distribution of the surface wave

high-index layer. Figure 1 presents the calculated effective refractive indices of TE waveguide modes propagating in the structure in the case when the medium adjacent to the structure is air. The characteristic feature of the shown curve is the sharp drop of effective refractive index from 10^{th} to 11^{th} mode that corresponds to the forbidden zone of the periodic structure. Note that the 11^{th} mode lies inside the forbidden zone that makes this mode a surface wave at the boundary between the periodic photonic crystal and dielectric medium. We confirmed the surface nature of the mode by calculating its field using the method described in [5] (see Figure 2).

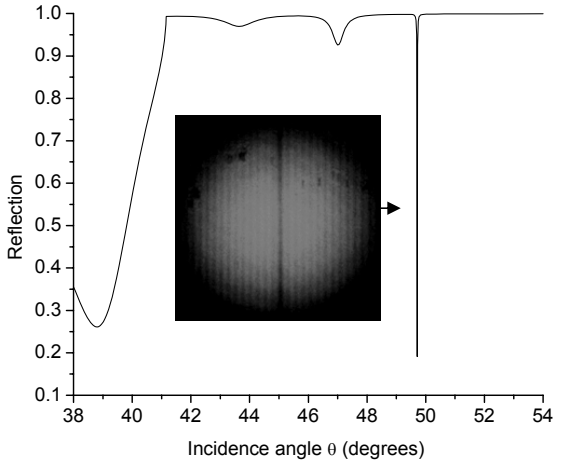


Figure 3: Reflection from the single structure

We used the Kretchmann setup for excitation of the surface wave with the prism attached to the back side of the structure substrate and having refractive index 1.52. Excitation of the surface wave in this scheme occurs due to leak of the wave into the substrate. Number of layers in the structure was chosen so that the leak is high enough to provide a sufficient coupling with the incident beam of He-Ne laser. Figure 3 presents the calculated dependence of light reflection from the structure. Dips correspond to the different modes of the structure. The sharpest dip corresponds to the surface wave. Inset on Figure 3 shows the m-line obtained in the experiment confirming the excitation of the surface wave.

Tunnel coupling of two photonic crystal with surface waves

In our experiment on tunnel coupling of surface waves between two photonic crystals used two glass prisms with substrates carrying waveguide structures attached to their bases. Air gap between the structures was created by sputtering buffer metal stripes on one of the structures. The system was excited by TE-polarized He-Ne laser beam (λ = 632.8 nm). Figure 4 presents the scheme of the experiment. PD1 and PD2 were photodiodes registering the reflected and transmitted light beams. When the air gap was wide (about 2 mkm) we detected only the reflected beam that had one resonance dip

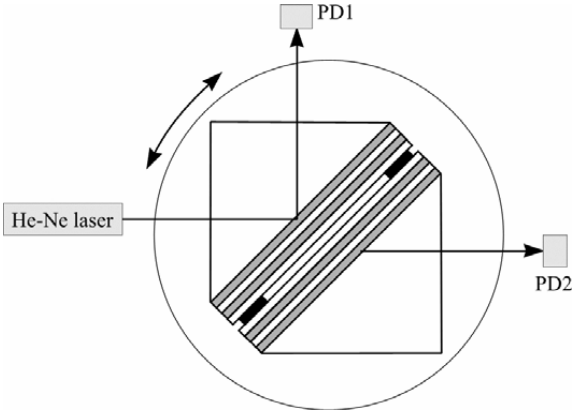


Figure 4: Experimental setup

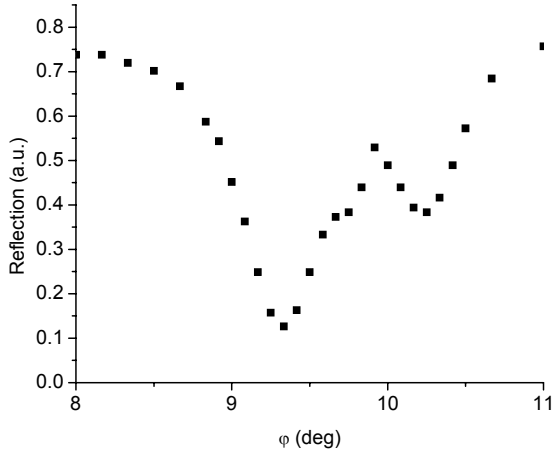


Figure 5: Reflection near the resonance

when the surface wave was excited like in the case of the single structure. At smaller gaps (below 1 mkm) we were able to detect the transmitted signal. Two peaks in this signal correspond to two dips in the reflected signal (see Figure 5). The characteristic feature of this curve is the double resonance that means that two different modes were excited. Angular distance between these two resonances increased when we applied more pressure on the structure reducing the air gap. These are very first results obtained and we will present more detailed results at the conference.

Discussion

As we said earlier paper [3] demonstrated the possibility of coupling between the surface waves propagating in two closely placed planar metallic films. In our case the structure consists of two identical photonic crystals separated by a small air gap. This structure can be considered as Bragg waveguide transmitting the light radiation in the air gap [6] (or in any other material having refracting index lower than that of the waveguides. Two surface modes exist near this gap. One has a symmetric electric field distribution in the gap and the other – anti-symmetric. Existence of these modes leads to the transparency effect that we observed in the experiment. These two modes have different effective refractive indices (see Figure 6) and thus different angles at which the structure transparency exists. Splitting of the resonance allows us to conclude that we are in fact observed tunnel coupling between the surface modes. Dispersion curves presented at Figure 6 shows that the mode parameters depends on the gap width. Effective indices are most sensitive to the gap width at small values of the width. Our calculations show that the loss in the gap (imaginary part of gap material dielectric constant) leads to strong losses in the surface modes and thus to the rapid decrease of the transparency effect. Change in the real part of the dielectric constant leads to angular shift of the resonance transparency peaks.

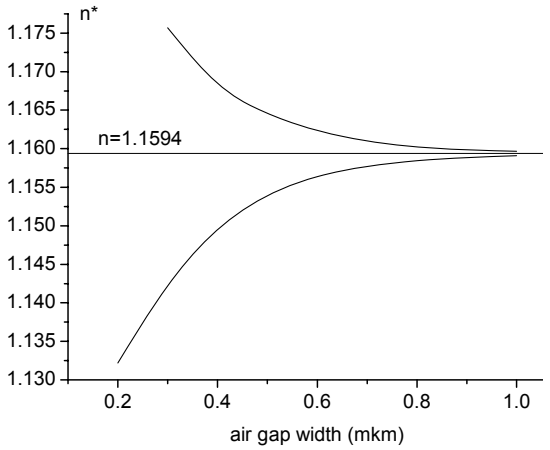


Figure 6: Effective indices of two surface waves

The observed effect of tunnel coupling between the surface waves of two photonic crystals leading to resonance transparency in the region of total reflection can be utilized in various sensor and modulating devices. This kind of waves is more attractive than the plasmonic waves in metal films due to absence of the absorbing medium. It allows to create devices with the larger sensing area and with the better sensitivity due to lower width of the resonace. If we create a cavity between the two photonic crystals like that was shown in [7] for the plasmons then it will have very high quality factor and could be used for high-sensitive sensors. Besides sensor applications it seems feasible to achieve light switching in the structure by adding nonlinearities.

Acknowledgements

This work was supported by Russian Foundation for Basic Research grant N07-02-00064.

References

[1] B.A. Usievich, V.V. Svetikov, D.Kh. Nurligareev and V.A. Sychugov, “Surface waves at the boundary of a system of coupled waveguides”, Quant. Elect., vol. 37, pp. 981-984, 2007.

[2] V.N. Konopsky and E.V.Alieva, “Photonic Crystal Surface Waves for Optical Biosensors”, Anal. Chem., vol. 79, pp. 4729-4735, 2007.

[3] N.M. Lyndin, O. Parriaux, F.A. Pudonin, I.F. Salakhutdinov, V.A. Sychugov and B.A.Usievich, “Long-range plasmons in an asymmetric four-layer metal-dielectric structure”, Quant. Electron., vol. 28, pp. 647-651, 1998.

[4] http://www.izovac.com

[5] P. Yeh, A.Yariv and C.-S. Hong, “Electromagnetic propagation in periodic stratified media. I. General theory”, J. Opt. Soc. Am., vol. 67, pp. 423-438, 1977.

[6] D.F.P. Pile, “Gap modes of one-dimensional photonic crystal surface waves”, Appl. Optics, vol. 44, pp.4398-4401, 2005.

[7] B. Hu, J. Liu, B.-y. Gu, S. Di, X.-d. Sun and S.-q. Wang, “Enhanced effect of local fields in subwavelength metallic series nanocavities from surface plasmon polaritons”, J. Opt. Soc. Am. A , vol. 24, pp. A1-A6, 2007.

Stimulated Raman Scattering in Membrane Silicon Waveguides

F. De Leonardis[1] and V. M. N. Passaro[2]

[1]Photonics Research Group, Dipartimento di Ingegneria dell'Ambiente e per lo Sviluppo Sostenibile, Politecnico di Bari, Taranto, Italy
f.deleonardis@poliba.it
[2]Photonics Research Group, Dipartimento di Elettrotecnica ed Elettronica, Politecnico di Bari, Bari, Italy

Abstract. *An investigation and optimization of silicon rib-membrane waveguides for Stimulated Raman Scattering applications is presented.*

Introduction

In order to develop Silicon Photonics, main areas or building blocks for investigation include selectively guiding and transporting of the light within the silicon, encoding light, detecting light, amplification and generation the light, packaging the devices and intelligent control of these photonic functions. While a wide variety of passive devices were developed in the 1990's, recent activities have focused on achieving active functionality, mostly light amplification and generation, in silicon-on-insulator (SOI) waveguides. In particular, the approach for light generation based on Stimulated Raman Scattering (SRS) in SOI technology has recently met a large interest [1]. More recently, new silicon-based waveguides have been proposed to manage the propagation loss in the near and long-wave infrared region [2]. This work represents a first investigation of SRS effect in silicon membrane waveguides, demonstrating the possibility to increase the Raman amplification by an appropriate design of air membrane.

Theory

When Stokes optical pulses propagate inside a waveguide in sub-picosecond regime, both dispersive and nonlinear effects largely influence their shapes and spectra. Space-time evolution of Stokes waves can be described by the following equation:

$$\begin{aligned}
&\frac{\partial A_\kappa}{\partial z}+\beta_{1\kappa}\frac{\partial A_\kappa}{\partial t}+j\frac{1}{2}\beta_{2\kappa}\frac{\partial^2 A_\kappa}{\partial t^2}=-\frac{\alpha_\kappa^{(prop)}}{2}A_\kappa-\frac{1}{2}\alpha_\kappa^{(FCA)}A_\kappa-\beta^{(TPA)}f_{\kappa,2}\left|A_2\right|^2A_\kappa+\\
&-\beta^{(TPA)}f_{\kappa,1}\left|A_1\right|^2A_\kappa+j2(1-f_R)\gamma_\kappa\left|A_\mu\right|^2A_\kappa+j2(1-f_R)\gamma_\kappa\left|A_{\mu+1}\right|^2A_\kappa+\\
&+j(1-f_R)\gamma_\kappa\left|A_\kappa\right|^2A_\kappa+j2(1-f_R)\gamma_\kappa\left|A_\nu\right|^2A_\kappa+j\frac{2\pi}{\lambda_\kappa}\Delta n_\kappa A_\kappa+\\
&+j2k_{\kappa,\mu,\mu+1,\nu}A_{\mu+1}A_\mu^*A_\nu e^{j(\beta_{0,\mu+1}+\beta_{0,\nu}-\beta_{0,\mu}-\beta_{0,\kappa})z}+j2k_{\kappa,\mu+1,\mu,\nu}A_\mu A_{\mu+1}^*A_\nu e^{j(\beta_{0,\mu}+\beta_{0,\nu}-\beta_{0,\mu+1}-\beta_{0,\kappa})z}+\\
&+jk_{\kappa,\kappa,\nu,\nu}A_\nu A_\kappa^*A_\nu e^{j(2\beta_{0,\nu}-2\beta_{0,\kappa})z}+j2k_{\kappa,\mu+4,\nu,\mu+5}A_\nu A_{\mu+4}^*A_{\mu+5}e^{j(\beta_{0,\nu}+\beta_{0,\mu+5}-\beta_{0,\kappa}-\beta_{0,\mu+4})z}+\\
&+j2k_{\kappa,\mu+5,\nu,\mu+4}A_\nu A_{\mu+5}^*A_{\mu+4}e^{j(\beta_{0,\nu}+\beta_{0,\mu+4}-\beta_{0,\kappa}-\beta_{0,\mu+5})z}+R_p(z,t)+R_s(z,t)-\frac{\gamma_{\kappa,\kappa}}{\omega_\kappa}\frac{\partial\left(\left|A_\kappa\right|^2A_\kappa\right)}{\partial t}
\end{aligned}\tag{1}$$

where $\kappa=3,4$ for quasi-TE and quasi-TM fundamental Stokes pulses and $\kappa=5,6$ state for first order Stokes waves, respectively. In addition, if $\kappa=3,4$, it results $\mu=1$ and $\nu=4,3$, while if $\kappa=5,6$, it results $\mu=3$ and $\nu=6,5$. Meaning of all terms and other details of complete mathematical model can be found in our recent work [3]. The

efficiency of Raman amplification depends on total loss coefficient $\alpha_i^{(tot)} = \alpha_i^{(prop)} + \alpha_i^{(FCA)}$, where $\alpha_i^{(FCA)}$ is the free carrier absorption (FCA) contribution and $\alpha_i^{(prop)}$ is the propagation loss coefficient in the waveguide, depending on material absorption evaluated for the SOI waveguide as [2]:

$$\alpha_i^{(prop)} = \Gamma_{Si}\alpha_{Si}^{(bulk)} + \Gamma_{SiO_2}\alpha_{SiO_2}^{(bulk)} \tag{2}$$

being $\alpha_{Si}^{(bulk)}$ and $\alpha_{SiO_2}^{(bulk)}$ the bulk absorptions of silicon and silica, respectively, and Γ_{Si} and Γ_{SiO_2} the guided-power fractions into silicon and silica, respectively. Eq. (2) suggests that a silicon rib-membrane waveguide, as shown in Fig. 1, could guarantee a significant reduction of optical loss because of absence of any silicon oxide layer. The waveguide is characterized by total rib height H, slab height H_s, rib width W and air cavity H_m.

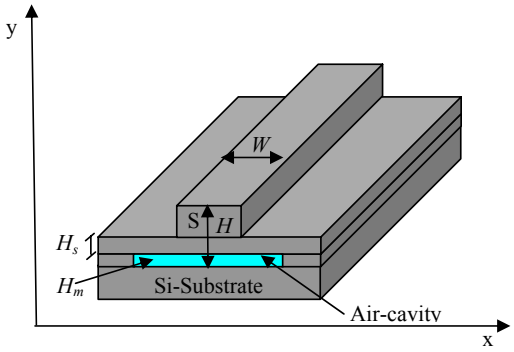
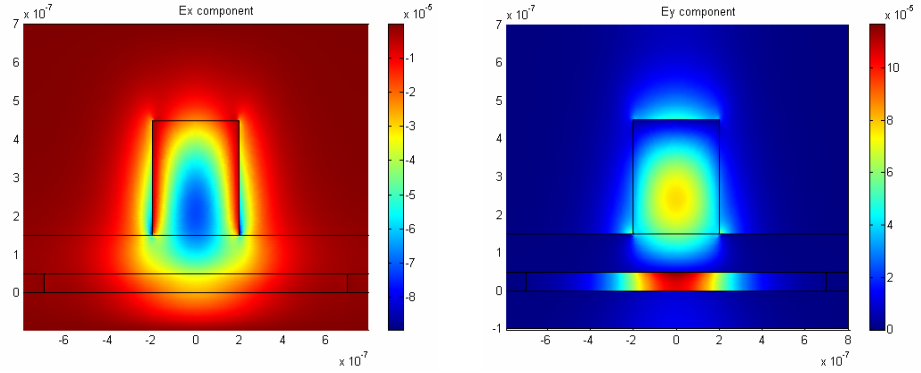


Fig. 1. Schematic diagram of suspended-membrane rib waveguide.

Numerical Results

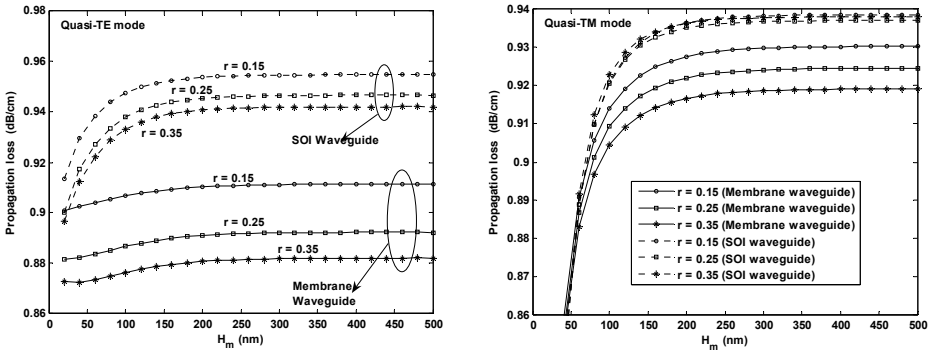
In the optimization of membrane waveguides, the cavity thickness H_m plays a fundamental role. In fact, it must to be large enough to avoid the slot effect into the air layer, but not too much for structural reasons. Fig. 2(a-b) shows the electric field dominant components by full-vectorial finite element method (FEM) [4] for quasi-TE and quasi-TM polarizations, respectively, at λ = 1.55 μm assuming H_m = 50 nm, H = 400nm, W = 400 nm and $r = H/H_s$ = 0.25. For high index contrast interfaces, Maxwell's equations state that, to satisfy the continuity of electric flux density normal component, the corresponding electric field (E-field) must undergo a large discontinuity with much higher amplitude in the low-index material. Thus, thin air cavities induce strong enhancement of light confinement for vertical component of electric field (quasi-TM mode in Fig. 2(b)), compromising Raman amplification in rib waveguides for quasi-TM modes. Fig.3 shows the propagation loss versus parameter H_m for both polarizations, in cases of membrane and SOI rib waveguides. The curves have been obtained by Eq. (2), in which the guided-power fraction in each layer has been again evaluated by FEM, with at least 60,000 mesh elements, λ = 1.55 μm, H = 400 nm, and

$W = 400$ nm. In addition, we have considered $\alpha_{Si}^{(bulk)}$ and $\alpha_{SiO_2}^{(bulk)}$ equal to 1dB/cm (worst case in [2]).



(a) (b)

Fig. 2. Electric field distribution: (a) x-component (quasi-TE mode); (b) y-component (quasi-TM mode).



(a) (b)

Fig. 3. Propagation loss versus H_m for various values of r and for silicon membrane and SOI waveguides: (a) quasi-TE mode; (b) quasi-TM mode.

For both polarizations, the membrane waveguide shows a propagation loss smaller than standard SOI rib waveguide. Moreover, r strongly influences the membrane waveguide with respect to SOI one. In addition, for the quasi-TM modes the curves show a large slope for small values of H_m, as due to light confinement into air cavity (see Fig. 2(b)). The presence of air cavity also influences the dispersion properties of the rib waveguide. Fig. 4 shows the group velocity dispersion (GVD) coefficient spectra for membrane and SOI rib waveguides and both polarizations. The simulations are obtained with H_m=200 nm, H=400nm, $W = 400$ nm, and $r = 0.25$. The membrane waveguides clearly lead to obtain larger GVD coefficients in the anomalous region for both polarizations with respect to SOI waveguides.

Finally, Fig. 5 shows the net Raman gain versus input pump pulse FWHM width, by solving the system of partial differential equations (1) and comparing membrane and SOI rib waveguides. The input pulse is considered aligned as a quasi-TE mode, while both polarizations of Stokes waves are included, with pump peak power $P_0 = 1$ W, pump

wavelength λ_p = 1.434.4μm, Raman gain $g_R = 10.5\,\mathrm{cm/GW}$ [1], and keeping the fundamental Stokes probe power 10 dB below the pump. All optical parameters are calculated by FEM. For both membrane and SOI rib waveguides, the curves related to quasi-TE and quasi-TM modes cross each other for a particular value of FWHM width, namely $\overline{T}_{FWHM}$.

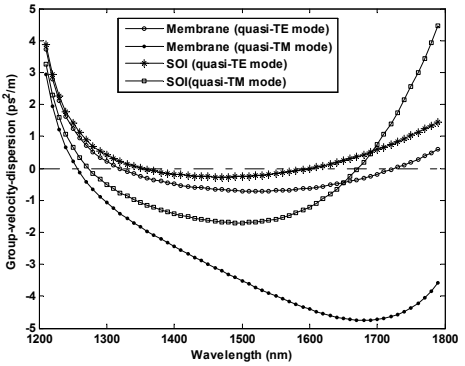


Fig. 4. Group velocity dispersion spectrum

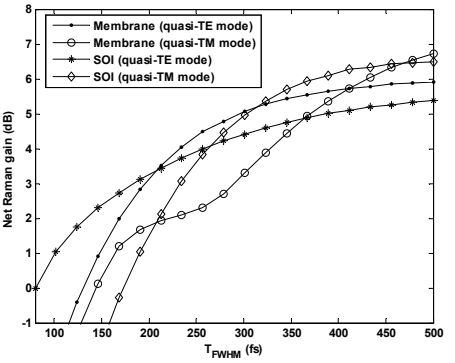


Fig. 5. Raman net gain versus FWHM width

Thus, for both SOI and membrane rib waveguides, when $T_{FWHM} \le \overline{T}_{FWHM}$, quasi-TE modes experience a larger net gain with respect to quasi-TM ones, which have a larger anomalous GVD effect for the designed waveguide. However, the opposite behaviour is revealed for $T_{FWHM} > \overline{T}_{FWHM}$. In fact, larger values of FWHM width induces the quasi-TM dispersion length to be larger than the waveguide length. In this situation, the anomalous GVD effect is not dominant even for quasi-TM modes and then the net gain for TM polarization can increase, becoming larger than for quasi-TE because of its smaller optical mode area. It is worth to note that, if the anomalous GVD effect is not dominant, the membrane waveguides show their advantage in terms of larger net Raman gains with respect to standard SOI waveguides. Our investigations indicate that in dependence of designed cross section, it is possible to find a range of FWHM time widths for which the membrane waveguide shows a larger Raman net gain than SOI waveguide, for both polarizations. This offers the possibility to downscale the waveguide sizes in Silicon Photonics. Moreover, membrane waveguides could induce significant advantages in terms of sizes and power consumption even for SRS effect applied in mid-IR wavelength region.

References

[1] B. Jalali, V. Raghunathan, R. Shori, S. Fathpour, D. Dimitropoulos, and O. Stafsudd, "Prospects for Silicon Mid-IR Raman Lasers", *IEEE J. Sel. Top. in Quantum Electron.*, vol. 12, pp. 1618-1627, 2006.

[2] R. A. Soref, S. J. Emelett, and W. R. Buchwald "Silicon waveguided components for the long-wave infrared region," *J. Opt. A: Pure Appl. Opt.,* vol. 8, pp. 840-848, 2006.

[3] F. De Leonardis and V. M. N. Passaro, "Ultrafast Raman Pulses in SOI Optical Waveguides for Nonlinear Signal Processing", *IEEE J. Sel. Top. in Quantum Electron*., to be published.

[4] Comsol Multiphysics by COMSOL AB, single license, 2005.

Design of a Monolithically Integrated All-Optical Label Swapper for Spectral Amplitude Code Labels Using Cross-Gain Modulation

Christian Habib[1], Pascual Muñoz[1], Lawrence R. Chen[2], and José Capmany[1]

[1] Optical and Quantum Communications Group - iTEAM, Universidad Politécnica de Valencia, Spain
[2] Photonics Systems Group, Electrical & Computer Engineering Department, McGill University, Montréal, QC, Canada
christian.habib@mail.mcgill.ca, pmunoz@gco.upv.es, lawrence.chen@mcgill.ca

Abstract *- We propose a design for an integrated all-optical label-swapper for packet-switched optical networks using Indium Phosphide technology. The proposed topology is a two stage approach that makes use of cross-gain modulation in a semiconductor amplifier used inside a ring laser topology.*

Introduction

Optical packet networks have attracted much attention as a solution for reducing latency and increasing flexibility in next-generation optical networks [1]. One implementation of packet switched optical networks is optical code multi-protocol label switching (OC-MPLS). OC-MPLS makes it possible to process labels in the optical domain, thereby avoiding power-hungry and costly conversions between electrical and optical domains for payload data [2]. Spectral amplitude coding (SAC) is an attractive implementation of OC-MPLS because it promises simple label processing [2, 3]. Using SAC, part of the channel spectrum is allocated to the OC-MPLS label, as shown in Fig. 1a.
A key component in a OC-MPLS network node is the label swapper, which strips the incoming label, attaches a new label, and reinserts it with the payload. Devices using cross-gain modulation (XGM) in ring cavities have previously been demonstrated which have several desirable characteristics for a label swapper; namely, high extinction and contrast ratios [4]. In particular, a proof-of-concept tabletop label-swapper using a two-stage XGM-based fiber-ring laser has been demonstrated [5]. The main drawbacks of this device were cost, size, and low operating frequency due to a lengthy cavity.

Label Swapper Topology and Principle of Operation

The proposed label swapper is shown in Fig. 1b. The device makes use of two cross-gain modulation (XGM) stages to achieve the desired label swap, which is essentially all-optical multi-wavelength conversion. In both cases, the XGM is realized in a semiconductor optical amplifier (SOA). It should be noted that each XGM stage performs a wavelength conversion, while also performing a logical inversion of the signal. As a result, for a dual stage topology, the output has the same polarity as the input signal.
The first stage is used to convert the input label ($\lambda_{in,1}, \lambda_{in,2}$) to an out-of-band intermediate wavelength (λ_{int}). To achieve this, the modulated input label is first injected into a semiconductor optical amplifier (SOA_1) through an arrayed waveguide grating (AWG). Simultaneously, a continuous wave probe beam at λ_{int} is injected into SOA_1 in a counter-propagating configuration relative to the input beam. The counter-propagating configuration of the first stage minimizes the amount of in-band power transmitted to the second

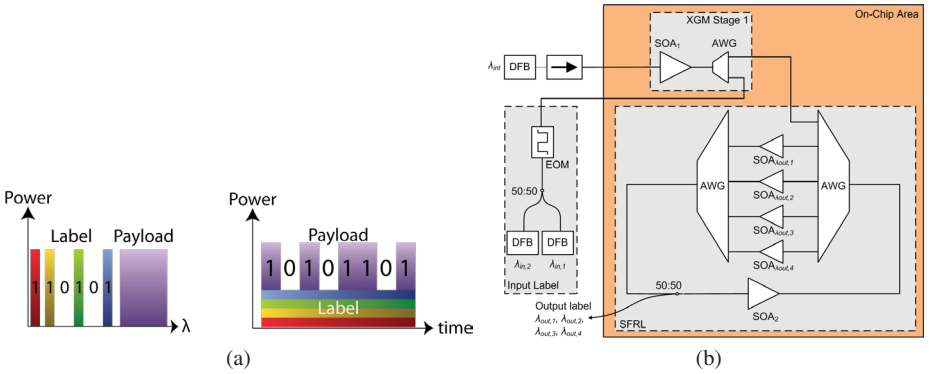


Figure 1: Fig. 1a Time and wavelength domain representations of an optical packet with SAC-label; Fig. 1b Proposed two stage XGM-based integrated label-swapper.

stage without requiring additional filtering. Note that this stage serves the dual purpose of performing the required logical inversion of the signal (λ_{int} is OFF when the input label is on and vice-versa) as well as ensuring that no power enters the ring laser in the SAC label band (this ensures that output label wavelengths have the same power levels regardless of input wavelength).

The second stage uses XGM in SOA_2 which is placed inside a semiconductor ring laser (SRL). The second stage is biased so it operates slightly above the SRL lasing threshold. When λ_{int} is present, the SRL operates below threshold and no output is produced by the SRL. Conversely, when λ_{int} is absent, the SRL produces power at $\lambda_{out,1},\ldots,\lambda_{out,n}$. Note that λ_{int} is injected via an AWG; it is also removed using an AWG. The output wavelengths are selected using the pass-bands of the AWGs inside the ring. The label swapper can be esily reconfigured to output some or all of the available wavelengths by changing the bias conditions on $SOA_{out,1},\ldots,SOA_{\lambda out,n}$; this compares favorably with the table top demonstrator which used mechanical adjustments (stretching of Fiber Bragg Gratings) [5].

Simulation Details and Results

The topology shown in Fig. 1b was implemented using the VPItransmissionMaker software (version 7.6). The parameters for the devices correspond to the targeted fabrication platform, JePPIX [6–9]. Optimal biasing conditions and device parameters were found and are shown in Tables 1a and 1b. Note that the SRL was assumed to contain 5 mm of waveguides (losses were adjusted accordingly). Furthermore, note that all AWGs were assumed to have Gaussian filtering profiles and 100 GHz channel spacing, with a bandwidth of 40 GHz, and total losses of 6 dB (this includes AWG insertion and transmission losses).

Fig. 2a shows the simulated optical spectrum analyzer traces of the input, intermediate and output wavelengths. Note the clearly visible longitudinal modes that exist within each output label. Their spacing is related to the cavity length, as in [9]. For single-mode ring laser operation, the overall cavity length should be properly adjusted, given the AWG passband bandwidth. Fig. 2b shows the static transfer function of the device as the input

Parameter	*Value*
l_{SOA} (all SOAs)	500 μm
I_{bias} (SOA_1)	178 mA
I_{bias} (SOA_2)	110 mA
I_{bias} $(SOA_{\lambda out,N})$	15 mA
$P_{InputLabel}$ (avg.)	0 dBm
$P_{\lambda,int}$	-21 dBm

(a)

Param.	*Value*
$\lambda_{in,1}$	1552.52 nm
$\lambda_{in,2}$	1551.72 nm
λ_{int}	1554.13nm
$\lambda_{out,1}$	1552.52 nm
$\lambda_{out,2}$	1551.72 nm
$\lambda_{out,3}$	1550.92 nm
$\lambda_{out,4}$	1549.32 nm

(b)

Perf. Metric	*Value*
Static CR	41 dB
OSNR	$>$ 60 dB
$t_{rise/fall}$	295 ps
Dynamic CR	25 dB

(c)

Table 1: Tables 1a & 1b, biasing conditions and device parameters of simulated integrated label swapper; Table 1c, simulated integrated label swapper performance

power level is swept. Fig. 2c shows the input and output temporal traces with a wide bandwidth ($>$ 100 GHz) photodetector module with unit responsivity. Finally, Fig. 2d shows the input and output temporal traces with after conversion to an electrical signal using a photodetector with a bandwidth of 1.25 GHz. Note that the simulation software considers the input laser sources to be temporally coherent, resulting in the beating pattern visible for the input label in Fig. 2c & 2d.

Two static performance metrics are used for the label swapper: (1) the static contrast ratio (SCR), which is defined as the ratio of power in the ON to OFF states for the output label wavelengths, (2) the optical signal-to-noise-ratio (OSNR), which is the ratio of the peak output label wavelength in the ON state to the noise floor.

Full transient simulations were then performed using a PRBS input with a frequency of 1.25 GHz. In particular, we consider the rise and fall times, which are defined as the time required for the output to pass from 10%-90% or 90%-10% of the signal levels. We also consider the dynamic contrast ratio (DCR) which is defined as the ratio of the mean power of ON bits to the mean power of OFF bits for the output label wavelengths. Note that all dynamic results are taken using the photodetector with a 2.5 GHz bandwidth.

Analysis and Conclusion

The results in Table 1c show excellent results in terms of CR and OSNR. In addition, however, it should be noted that the device produces a near-single-mode output for each label wavelength, with better than 25 dB suppression of side modes. In order to compare with our previous results in [5], the power values were determined from the OSA traces using similar resolution bandwidth (60 pm), therefore taking into account the power of all the longitudinal modes within one optical label.

Note that this device requires a wide spacing between label wavelengths due to the use of AWGs; for a transparent optical network, the entire SAC label would need to fit in a single 100 GHz ($\approx$ 0.8 nm) band. AWG performance is limited by lithographic technology. Smaller lithographic features will allow for tighter AWG channel spacing; nonetheless, it may be necessary to investigate other filtering mechanisms to reduce spacing between label wavelength slots. Regarding bidirectional lasing, previous work shows lasing only occurs on one direction [9]. In the simulations, the output label was collected from the counter-clockwise direction as it avoids the need to filter the intermediate wavelength

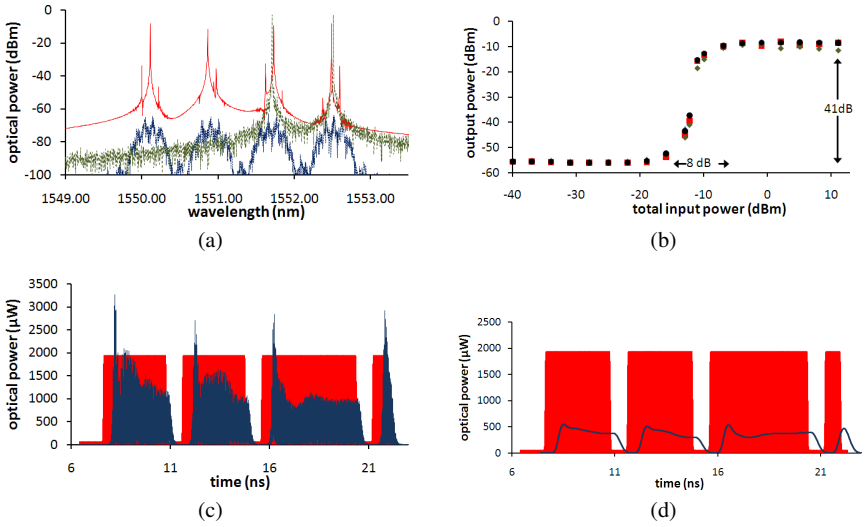


Figure 2: Spectral output, static transfer functions, and dynamic simulations for the label swapper. For 2a, OFF state (blue, dotted), ON state (red, solid), input label (green, dashed). For 2b, $\lambda_{out,1}$ (blue triangles), $\lambda_{out,2}$ (red squares), $\lambda_{out,3}$ (green diamonds), $\lambda_{out,4}$ (black circles). For 2c, the raw output of the label swapper (dark blue) is shown with the input label (red). For 2d the output of the label swapper after a photodetector with limited bandwidth (dark blue) is shown with the input label (red).

from the output signal, but in practice additional filtering should nonetheless be included. In conclusion, the proposed topology shows a marked improvement in frequency response (1.25 GHz), dynamic contrast ratio (25 dB), and reconfiguration speed relative to the previously demonstrated work [5].

References

[1] A. Viswanathan *et al.*, "Evolution of multiprotocol label switching," *IEEE Commun. Mag.*, vol. 36, no. 5, pp. 165–173, May 1998.

[2] N. Wada *et al.*, "Cutting-edge technologies on broadband and scalable photonic network-packet switched networks based on all-optical label processing," *Optical Review*, vol. 11, pp. 106–112, 2004.

[3] P. Seddighian *et al.*, "Low-cost, scalable optical packet switching networks with multi-wavelength labels," in *Proc. OFC/NFOEC '07*. Optical Society of America, 2007, p. OThF5.

[4] R. E. Gordon *et al.*, "Demonstration of all-photonic spectral label-switching for optical MPLS networks," *IEEE Photon. Technol. Lett.*, vol. 18, no. 4, pp. 586–588, Feb. 2006.

[5] C. Habib *et al.*, "All-optical swapping of spectral amplitude code labels using non-linear media and semiconductor fiber ring lasers," *IEEE J. Sel. Topics Quantum Electron.*, (accepted Jan. 2008).

[6] T. DeTemple *et al.*, "On the semiconductor laser logarithmic gain-current density relation," *IEEE J. Quantum Electron.*, vol. 29, no. 5, pp. 1246–1252, May 1993.

[7] T. Durhuus *et al.*, "Detailed dynamic model for semiconductor optical amplifiers and their crosstalk and intermodulation distortion," *J. Lightw. Technol.*, vol. 10, no. 8, pp. 1056–1065, Aug 1992.

[8] M. Hill *et al.*, "Optimizing imbalance and loss in 2 /spl times/ 2 3-db multimode interference couplers via access waveguide width," *J. Lightw. Technol.*, vol. 21, no. 10, pp. 2305–2313, Oct. 2003.

[9] J. den Besten, "Integration of multi-wavelength lasers with fast electro-optic modulators," Ph.D. dissertation, Technische Universiteit Eindhoven, 2004.

High-Q whispering-gallery mode quantum-dot microdisk lasers

K. Solís Trápala, R. W. Smink, J. Molina Vázquez, B. P. de Hon and H. J. S. Dorren

COBRA Research Institute, Eindhoven University of Technology, P. O. Box 513, 5600 MB Eindhoven, The Netherlands
k.s.t.solis.trapala@tue.nl

Abstract. *We compute the whispering-gallery modes for a microdisk laser with an InGaAsP/InP quantum-dot gain medium. We find that whispering-gallery modes in the 1.5 μm telecommunication window with $Q>10^5$ can be sustained in a microdisk laser with a diameter as small as 2.8 μm and a thickness of 200 nm.*

Introduction

To fulfill the demands of increasing speed of fibre-optic-based telecommunications, high speed, integrability and low-power consumption for the constituent devices are needed. Particularly, semiconductor microdisk lasers are attractive because of their small cavity volume, cleavage-free cavities, excellent wavelength selectivity, ultra-low threshold and high cavity quality (Q) factor due to the great confinement of whispering-gallery modes (WGMs) [1]. These characteristics can be enhanced with a quantum-dot (QD) active region offering fast response to external pumping [2] and the possibility for simultaneous excitation of multiple WGMs inside one microdisk over a wide spectral range [3].

At the surface of the microdisk laser, the modes are bound by total internal reflection. These whispering-gallery modes [4] are of special interest due to a very good confinement of the field which can be characterized by the cavity Q factor.

Recently, whispering-gallery modes in microdisk lasers have been theoretically and experimentally investigated [1;2;5-8]. The theoretical models in [5-7] simplify the problem to two dimensions by neglecting the wavevector dispersion in the axial direction. We investigate whispering-gallery modes through a three-dimensional model of a microdisk laser with a QD active region. We solve and compute the lasing modes for a quantum-dot microdisk laser by considering an approximate separation of Maxwell's equations in the axial and transverse directions, subsequently, we compute the Q factor in closed form for disk lasers with different dimensions. We find that large Q factors can be obtained for small disks.

Model

Figure 1 shows the device considered in our study, a disk with a dielectric-air boundary supported by a post with an active region consisting of ten QD layers. We are only interested in modes propagating along the edge of the disk and therefore the coupling of the field into the supporting post can be neglected. These are higher-order modes and correspond to the whispering-gallery modes. We labeled these modes with two numbers. The order of the resonance is N, where $N-1$ denotes the number of nodes in the radial variation of the field and M is the azimuthal-mode number, where $2M$ corresponds to the maxima in the azimuthal variation of the resonant field around the disk's circumference [4].

Due to the symmetry of the problem, we use a cylindrical coordinate system to solve the Maxwell's equations in three dimensions, for transverse-electric (TE) modes, using the

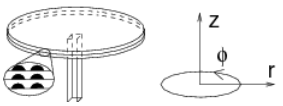


Figure 1: Multiple-layer quantum-dot microdisk laser in a cylindrical coordinate system.

method of Borgnis' potentials [9]. In the angular direction, we assume clockwise and counter-clockwise propagating waves. In the axial direction, the field consists of a cosine solution and decaying exponential functions inside and outside the disk, respectively. Lastly, the solution in the radial direction is expressed in terms of Bessel functions of the first kind and modified Bessel functions of the second kind, both of them of complex order k_φ, inside and outside the disk, respectively. The complex order k_φ, which corresponds to the complex wavevector for the field propagating in the angular direction, is a result of the losses due to the field radiating away from the disk. Simplified solutions consisting of Bessel functions of integer order, found for instance in [5-7], result in an over-estimation of the field confinement. Following the considerations above, we obtain expressions for the electric and magnetic field components inside and outside the disk. Modes are found by solving the continuity conditions at the microdisk radial and axial boundaries. For the QD gain and carrier-induced refractive index spectra we use the linear gain model described in detail in [10;11]. Finally, we compute the Q factor for the *i*-th mode using the following relation [9]:

$$Q = \omega_i \frac{W}{P}, \tag{1}$$

where ω_i denotes the natural angular frequency of the *i*-th mode, W is the time-averaged energy stored in the cavity and P denotes de power loss. Hence, we compute the time-averaged stored energy inside the cavity and we use the Poynting vector to compute the power loss.

Results

We choose a QD gain medium with ten layers having a QD density of 4×10^{10} cm^{-2} and an average dot height of 5 nm. Figure 2 shows the QD gain and carrier-induced refractive index spectra. In our analysis, we consider microdisks with diameters in the range $2\ \mu\text{m} \le D \le 4\ \mu\text{m}$ and thicknesses in the range $50\ \text{nm} \le L \le 350\ \text{nm}$.

In view of the two telecommunication windows, we are interested in modes in the range $1.3\ \mu\text{m} \le \lambda \le 1.7\ \mu\text{m}$. Figure 2 also shows the spectral positions of some of the lasing modes found in a disk with D=3 μm and L=200 nm. In addition, Figure 3 shows the mode wavelength dependence on the disk diameter and on the disk thickness for a fixed L=200 nm and for a fixed D=3 μm, respectively. We found that disks with D<2 μm or L<100 nm can only sustain low-order modes that have a low confinement inside the disk, and thus large losses. In contrast, disk diameters of $D \ge 2.8\ \mu\text{m}$ and thicknesses of $L \ge 200$ nm show lasing of higher-order modes (M>10), i.e. WGMs in the 1.5 μm telecommunication window. We also observe that degenerate modes exist in the cavity. For instance, the modes in the 1.3 μm telecommunication window with M equal to 9 and 12. This situation does not occur in the 1.5 μm telecommunication window unless a thickness larger than 200 nm or a diameter larger than 3.6 μm is used. On the other

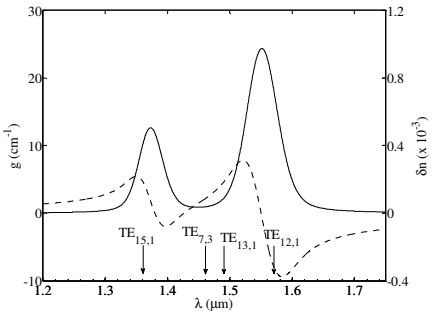


Figure 2: Quantum-dot gain (solid) and carrier-induced refractive index (dashed) spectra. Also shown are some of the lasing modes for a disk with D=3 μm and L=200 nm.

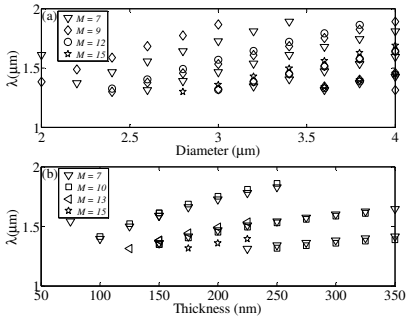


Figure 3: Mode wavelength dependence on the (a) disk diameter for a fixed L=200 nm, and on the (b) disk thickness for a fixed D=3 μm for the 7th, 9th, 10th, 12th, 13th and 15th modes.

hand, from Figure 3 (b), we observe that for $L \geq 250$ one can not sustain modes with M>12 since the cutoff wavelengths of these modes are reached.

We have computed the Q factor for all lasing modes M found during the variation of both the diameter and the thickness of the disk. Figure 4 shows the Q-factor dependence on the mode wavelength for the configuration of Figure 3 (a). We observe that the Q-factor behavior follows that of the QD gain but the other way around. That is, modes whose wavelengths coincide with the low part of the gain spectrum have also lower losses and as a consequence they achieve a higher Q factor (~10^7). On the other hand, modes having more gain are more amplified and consequently the losses, even when they are low, are greater than those in the previous case, resulting in Q factors which are still in the order of 10^5. Hence, we find that even when all of our modes have a positive net gain, only a few of them propagate with a field that is highly concentrated along the edge of the disk. To meet this condition, one should have a higher-order mode lasing at a wavelength with a high gain. It turns out that these modes present only one intensity peak in the radial direction, i.e. N=1. Higher-order modes, lasing at wavelengths with low gain, show more intensity peaks in the radial direction (N>1) which results in propagation along the edge of the disk but also inside the disk. An example of these two situations is illustrated in Figure 5, where the radial dependence of the field |V(r)|, for the 12th mode propagating in two different wavelengths is shown for a disk of D=3 μm and L=200 nm. We observe a similar behavior for the Q-factor dependence on the mode wavelength for the configuration of Figure 3 (b).

Conclusions

We have used a three dimensional model to compute the whispering-gallery modes in quantum-dot microdisk lasers. The model accounts for the radiation of the field in the radial direction. We found that higher-order modes with high Q-factors (~10^5) propagating in the 1.5 μm telecommunication window can be sustained in disks with diameters from 2.8 μm and a thickness of 200 nm. It should be remarked though that the Q factors do not account for scattering losses at the disks edge. Also losses due to surface recombination have been neglected due to the nature of the quantum-dots. Accordingly, mode propagation with a highly concentrated field along the edge of the disk is determined by the quantum-dot gain and by a large azimuthal-mode number M.

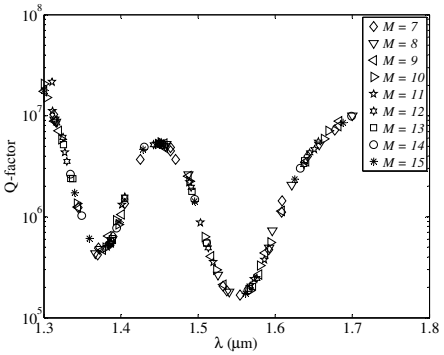


Figure 4: Q-factor dependence on the mode wavelength.

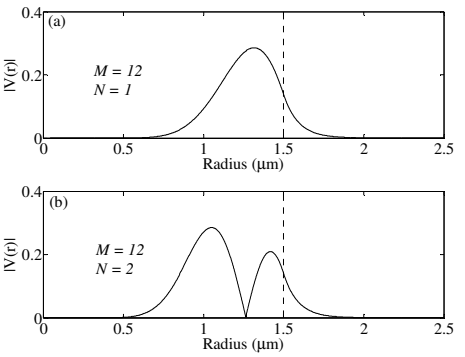


Figure 5: Radial dependence of the field for the (a) $TE_{12,1}$ mode and the (b) $TE_{12,2}$ mode propagating in a disk with D=3 μm (r=1.5 μm) and L=200 nm.

Therefore it is possible to engineer a quantum-dot gain medium having ground and excited state transition peaks centered at the lasing wavelength of the desired modes.

References

[1] M. Fujita, R. Ushigome, and T. Baba, "Continuous wave lasing in GaInAsP microdisk injection laser with threshold current of 40 μA", Electronics Letters, vol. 36, pp. 790-791, 2000.

[2] K. J. Luo, J. Y. Xu, H. Cao, Y. Ma, S. H. Chang, S. T. Ho, and G. S. Solomon, "Ultrafast dynamics of InAs/GaAs quantum-dot microdisk lasers", Applied Physics Letters, vol. 78, pp. 3397-3399, 2001.

[3] H. Cao, J. Y. Xu, W. H. Xiang, Y. Ma, S. H. Chang, S. T. Ho, and G. S. Solomon, "Optically pumped InAs quantum dot microdisk lasers", Applied Physics Letters, vol. 76, pp. 3519-3521, 2000.

[4] S. L. McCall, A. F. J. Levi, R. E. Slusher, S. J. Pearton, and R. A. Logan, "Whispering-gallery mode microdisk lasers", Applied Physics Letters, vol. 60, pp. 289-291, 1992.

[5] N. C. Frateschi and A. F. J. Levi, "The spectrum of microdisk lasers", Journal of Applied Physics, vol. 80, pp. 644-653, 1996.

[6] M. Fujita, A. Sakai, and T. Baba, "Ultrasmall and ultralow threshold GaInAsP-InP microdisk injection lasers: Design, fabrication, lasing characteristics, and spontaneous emission factor", IEEE Journal of Selected Topics in Quantum Electronics, vol. 5, pp. 673-681, 1999.

[7] E. I. Smotrova and A. I. Nosich, "Mathematical study of the two-dimensional lasing problem for the whispering-gallery modes in a circular dielectric microcavity", Optical and Quantum Electronics, vol. 36, pp. 213-221, 2004.

[8] P. Michler, A. Kiraz, L. D. Zhang, C. Becher, E. Hu, and A. Imamoglu, "Laser emission from quantum dots in microdisk structures", Applied Physics Letters, vol. 77, pp. 184-186, 2000.

[9] K. Zhang and D. Li, Electromagnetic theory for microwaves and optoelectronics Berlin: Springer, 1998.

[10] J. Molina Vázquez, H. H. Nilsson, J. Z. Zhang, and I. Galbraith, "Linewidth enhancement factor of quantum-dot optical amplifiers", IEEE Journal of Quantum Electronics, vol. 42, pp. 986-993, 2006.

[11] J. Molina Vázquez, J. Z. Zhang, and I. Galbraith, "Quantum dot versus quantum well semiconductor optical amplifiers for subpicosecond pulse amplification", Optical and Quantum Electronics, vol. 36, pp. 539-549, 2004.

Design of the optical core of an integrated ratiometric wavelength monitor

A. M. Hatta[1], G. Farrell[1], Q. Wang[2] and J. Zheng[3]
[1]Applied Optoelectronics Centre, School of Electronic and Communications Engineering, Dublin Institute of Technology, Kevin Street, Dublin 8, Ireland
agus.muhamadhatta@student.dit.ie
[2]Data Storage Institute, DSI Building, 5 Engineering Drive 1, 117608 Singapore
[3]College of Electronic Science and Engineering, Jilin University, 2699 Qianjin Street, 130012 Changchun, P.R. China

Abstract. *The optical core of an integrated ratiometric wavelength monitor which consists of a Y-branch and two edge filters, with opposite spectral responses, based on a pair of symmetrical multimode interference (MMI) structures is proposed. The designed ratiometric structure demonstrates a suitable spectral response, with potentially a 20 pm resolution over a 100 nm wavelength range.*

1. Introduction

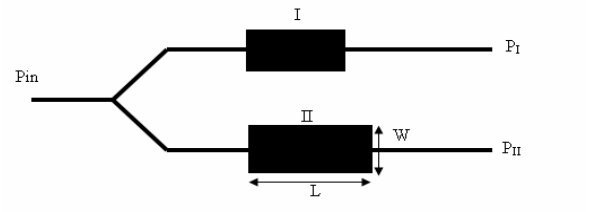
Wavelength monitoring and measurement is required in many optical systems such as multi-channel dense wavelength-division multiplexing optical communication systems and fibre-Bragg-grating-based optical sensing systems. In one wavelength monitoring scheme, the so-called a ratiometric detection scheme, the wavelength of an input signal is determined by the measurement of the ratio of two signal powers. It has a simple configuration and offers the potential for high-speed measurement as compared with wavelength-scanning-based active measurement schemes. A ratiometric wavelength measurement scheme can be implemented with bulk devices, an all-fiber based configuration or integrated optical circuits. Integrated wavelength monitors have a compact size, a fast response, are more robust and have a low fabrication cost compared to bulk optical devices. Examples of the designed and developed integrated wavelength monitors include multimode interference (MMI) couplers, a Y-branch with an S-bend structure and a Y-branch with an MMI structure [1-3].

In [1], the wavelength monitor consists of a central MMI waveguide, two output waveguides, and one input waveguide. For wavelength measurement it offers a 100 nm range and 200 pm resolution. Previously, in [3], we have shown that an MMI structure can be used as an edge filter for a ratiometric wavelength monitor. In [3], the length and width of the multimode section, and the positions of the input and output waveguides are optimised according to a desired spectral response by using the global optimisation algorithm-adaptive simulated annealing. We propose here a further improvement, with a ratiometric scheme which employs two opposite slope edge filters offering a higher resolution compared with the ratiometric scheme with one edge filter and one reference arm [4]. In this paper, two edge filters with opposite slope spectral responses based on a symmetrical MMI are designed and can be used for high resolution wavelength monitoring.

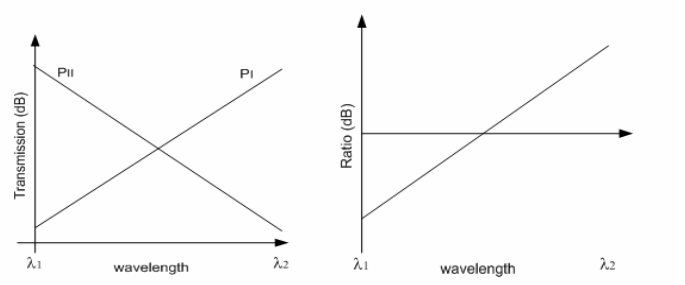
2. Proposed configuration and design method

Fig.1.a shows a schematic configuration of an integrated ratiometric structure. It contains a Y-branch splitter and two edge filter arms, containing symmetrical MMI structures. The desired spectral responses of the two arms are shown in Fig.1.b, while the corresponding ratio of the two outputs over a wavelength range is presented in

Fig.1.c. The wavelength of an input signal can be determined through measuring the power ratio of the output ports at the outputs of the two arms, assuming a suitable calibration has taken place.



(a)



(b) (c)

Figure 1 (a) Schematic configuration of ratiometric structure with two edge filter arms with MMI structures (b) Desired spectral response of two edge filter arms and (c) The output ratio between two arms.

The design steps for each MMI structure are identical. To optimise an individual MMI structure for an edge filter application, the width (W) and length (L) of the MMI are adjusted. The transmission response of the MMI is calculated for each W and L of MMI. A modal propagation analysis (MPA) can be used to calculate the transmission response in the multimode waveguide [5]. It is known that the desired edge filter corresponds to either an increasing or decreasing transmission as the wavelength increases over the wavelength range. Therefore it is necessary to calculate the transmission response between the lower and upper limits [λ_1 and λ_2] of the desired wavelength range over a range the W and L values for the MMI. For each W of the each MMI, we scan the length L in increments of 0.01 L_π (where L_π is the beat length) and determine the transmission value at λ_1, λ_2 as $P(\lambda_1)$, $P(\lambda_2)$ and then calculate the corresponding discrimination range $D = |P(\lambda_1) - P(\lambda_2)|$ (thus $P(\lambda_1)$ and $P(\lambda_2)$ should be in dB). A symmetrical MMI produces a self image at a distance $L = \frac{3}{4} L_\pi$, so we can set the scanning range of L as $0 \le L \le 2\frac{3}{4} L_\pi(\lambda_1)$.

After calculating $P(\lambda_1)$ and $P(\lambda_2)$ for each W and L for an MMI we select some structures as possible candidates. We select the structures based on the constraints that the discrimination, *D,* should be better than 10 dB and that the baseline loss (either $P(\lambda_1)$ and $P(\lambda_2)$ depending on whether the slope is negative or positive) should also be less than 8 dB. Then we calculate the spectral response for each selected structures. An ideal response for the edge filter should give a linear dependence for wavelength versus transmission. We can use a linear curve fitting and get a slope (*m*) of linear function

$(T(\lambda) = m\lambda + c)$ and a norm residual (*nxr*) from a QR decomposition of the Vandermonde matrix [6], as the parameters to choose the best spectral response. The ideal spectral response has high *m* and low *nxr*. The optimal edge filter with positive or negative slope is chosen based on a figure of merit:

$$F = \exp\left[-\left(\frac{c_n nxr}{c_m |m|}\right)\right] \tag{1}$$

where c_n and c_m are weighting coefficients. The best edge filter occurs when $F = 1$ and the worst when $F = 0$.

3. Numerical example and discrimination demonstration

As a numerical example, a buried silica-on-silicon waveguide is chosen where the refractive index of the core and cladding is 1.4553 and 1.4444, respectively. The waveguide cross section is 5.5 μm x 5.5 μm and the multimode section thickness is 5.5 μm. The effective index method is used to simplify the calculation. The wavelength range for this example is taken to be 1500 – 1600 nm. The width of the MMI is chosen to be in the range 30 – 50 μm and the length $0 - 2\frac{3}{4}L_\pi(\lambda_1)$. Based on the above procedure, the optimal edge filters are found to have the dimensions W = 45 μm, L = 3478 μm and W = 46 μm, L = 3250 μm for the positive slope MMI (P_I) and the negative slope MMI (P_{II}), respectively. The spectral responses are plotted in Fig.2.a from which it is clear that the discrimination range (from 1500 to 1600 nm) is 10.97 dB, while the baseline loss is 6.57 dB for the positive slope edge filter. For the negative slope edge filter the discrimination range is 11.39 dB with a baseline loss of 5.96 dB. To calculate the ratio of the whole integrated ratiometric structure, a Pade (1,1) beam propagation method with a GD scheme is used [7]. The ratio of the spectral response is from –10.91 to 11.49 dB and is shown in Fig.3.

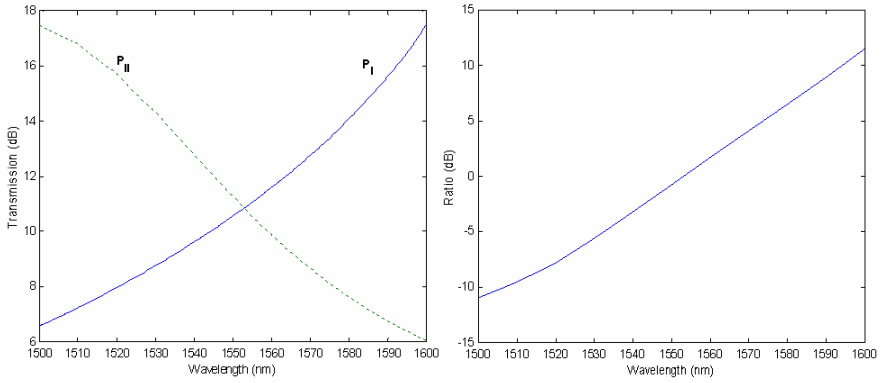


Figure 2 (a) Spectral response of optimised edge filters with opposite slopes (b) Spectral response of the ratiometric

To confirm the wavelength discrimination capability of the designed structure, the ratiometric wavelength measurement process is modelled numerically [8] by taking account of the optical noise of the source signal and the electrical noise of the photodetectors. Assuming the SNR of the input signal is about 55 dB, the best resolution achievable for power measurement is 0.001 dB and the noise generated by

photodetectors and electronic circuitry is equivalent to an uncertainty in the ratio measurement of 0.002 dB. The source wavelength is set to 1550 nm. This wavelength is changed by successively increasing increments of 5, 10, 15 and 20 pm. The photodetector outputs are sampled 100 times and the ratio of the photodetectors outputs is calculated for each wavelength. The wavelength is incremented again and the process of sampling is repeated. Fig. 3 shows the complete time series of the calculated ratio values as a function of sample time and the wavelength increments. From Fig. 3, it is clear that the detectable ratio due to the wavelength tuning has a potential resolution at least better than 20 pm.

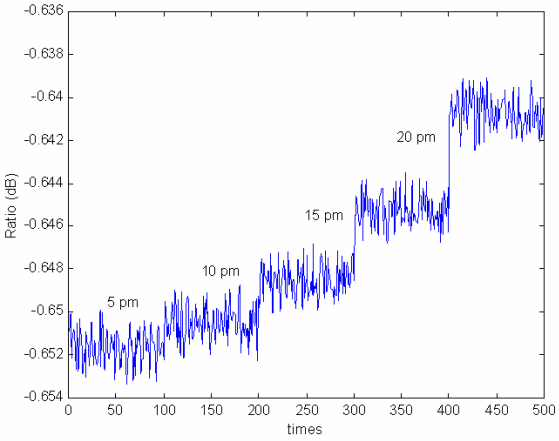


Figure 3 Output ratio as the wavelength is tuned

Conclusion

An integrated ratiometric wavelength monitor based on a pair of MMI structures with symmetrical responses has been presented. The width and length of the two MMI edge filters with opposite slope spectral responses are optimised based on a defined figure of merit. The wavelength discrimination of the designed ratiometric structure has been demonstrated numerically and shows a competitive resolution (20 pm) for wavelength measurement.

References

[1] C. Sookdhis, T. Mei and H. S. Djie, "Wavelength monitoring with low constrast multimode interference waveguide", IEEE Photonic. Technol., Lett., Vol.17, No.4, pp.822-824, 2005.

[2] Q. Wang, G. Farrell and A. M. Hatta, Global optimization of multimode interference structure for ratiometric wavelength measurement, Proc. SPIE Vol. 6619, Third European Workshop on Optical Fibre Sensors 2007.

[3] Q. Wang, G. Farrell, P. Wang, G. Rajan and T. Freir, Design of integrated wavelength monitor based on a Y-branch with an S-bend waveguide, Sensors and Actuators A,134(2), 405-409 (2007).

[4] S. M. Melle, K. Liu, and R. M. Measures, Practical fiber-optic Bragg grating strain gauge system, App. Opt. Vol. 32, No. 19, 1993, 3601-3609.

[5] L.B. Soldano, E.C.M. Pennings, Optical multi-mode interference devices based on self-imaging: principles and applications, J.Ligthwave Technology, Vol.13, No.4, 1995, 615-627.

[6] www.mathworks.com

[7] J. Yamauchi, Propagating Beam Analysis of Optical Waveguides, Research Studies Press, pp.89-97, 2003.

[8] Q. Wang, G. Rajan, P. Wang and G. Farrell, Resolution investigation of a ratiometric wavelength measurement system, App. Opt. Vol. 46, No. 25, 2007, 6362-6367.

Quantum optical effect for switching and slow light applications

G. Manzacca, G. Cincotti

Applied Electronics Department, Roma Tre University, Via della Vasca Navale 84 00146, Rome, Italy
g.manzacca@uniroma3.it

Abstract. *In this paper, the modeling of optically tunable all-optical switching and slow-light device is addressed. We consider cavity-based add-drop and direct-coupled filters as switching elements, and analyze the static and dynamic behaviours; for tunable delay lines, we investigate coupled-resonator optical waveguide (CROW) structures. The tunability of the system under investigation is discussed considering the joint interference effect created by a not excited dipole in a cavity in Purcell regime, and the interference effect in a quantum state by Electromagnetic Induced Transparency (EIT).*

Introduction

One of the main tasks for applications of nanotechnology in Data&Telecom market is the development of innovative devices like lasers with low threshold current, nanocavity laser arrays, add-drop filters for wavelength routing networks, buffers for Optical Burst Switching (OBS) and Optical Packet Switching (OPS) and quantum information devices [1]. The progress in fabrication of 2D Photonic Crystal (PhC) cavity-based structures, achieving recently Q parameters of order of millions [2], gives the opportunity to obtain strong light matter interaction in a small volume V. In particular, by increasing the Purcell factor Q/V, we can design a quantum-based device, and by tuning the decay rate of a dipole through the electromagnetic environment, we can exploit the interaction between a cavity mode and a quantum state [3]. In this paper, we refer to PhC and Quantum Dot technology, and we consider a single quantum dot inside a PhC cavity, analyzing the behavior of side- and direct-coupled waveguides for switching purpose; then we analyze a Coupled Resonator Optical Waveguides (CROW) as a slow light device.

Switching device

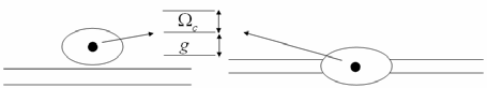
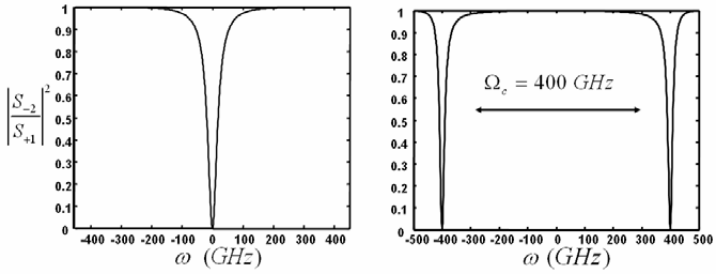


Figure 1: Side and directed coupled PhC cavities

We consider the device of Figure 1, and we suppose that there is a quantum state inside the cavity, composed of three energy levels where one of the two transitions is entangled to a cavity mode through the g parameter [4, 5]. The other transition is driven by a coherent field, not related to any cavity mode, that is described by the Rabi frequency Ω_c . We suppose to work in Purcell regime [6], i.e. the Purcell factor is larger than one

$$F_p = \frac{g^2}{\gamma'\left(\frac{1}{\tau_0}+\frac{1}{\tau_{e1}}+\frac{1}{\tau_{e2}}\right)} \gg 1$$

but there is not strong coupling between the cavity mode and the quantum state. This condition is satisfied for high values of the g parameter, but also if the dipole decay rate γ' is much smaller than the whole decay rate of the cavity, that is related to τ_0, τ_{e1} and τ_{e2}. This situation can be achieved by a suitable design of the cavity, considering the Spontaneous Emission (SE) rate of the dipole in the cavity and by a proper alignment between the cavity mode and the dipole moment matrix elements of the quantum state, but also by reducing the volume of the cavity mode to increase the g parameter [5].
In Figure 2, the power spectral density of the direct-coupled system is shown in two cases: when the pump signal is switched off (Ω_c=0), we observe a sharp transmittance peek and for Ω_c=400 GHz, the so called Rabi splitting is achieved in the quantum state, and the distance between the two symmetric transitions is $2\Omega_c$.



(a) (b)

Figure 2: Power spectral density of a direct-coupled cavity: (a) $\Omega_c = 0$ (b) $\Omega_c = 400$ GHz

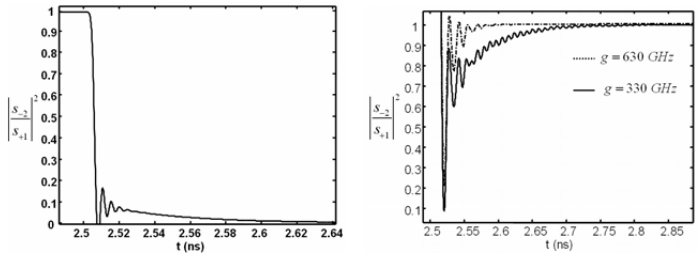
This behavior is similar to that one in a EIT material, where a coherent field cancels the absorption of a probe transition, if the two allowed transitions share a common energy level. In side-coupled system, we have an opposite behavior and the signal is reflected or dropped, depending on the design, when the pump is on [4]. This effect holds in a weak excitation limit, when the photon flux is much smaller than the Purcell factor [3, 7].
We have performed our analysis in both frequency and time domains, and the transient behavior of the side- and direct-coupled systems are shown in Figure 4, for two values of the g parameter. We have considered an input monochromatic field, and it is evident that a large Purcell factors speeds the creation of the dark state in an EIT material; we also observe that a side-coupled system has a larger Q parameter.

Slow-light device

The proposed approach can be used to design a tunable slow-light device based on a CROW. We assume that the whole Hamiltonian of the system is

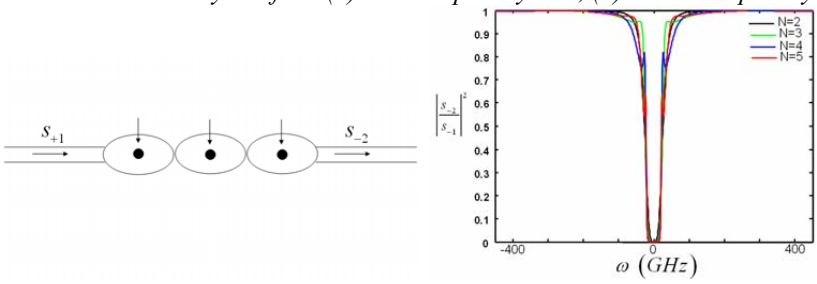
$$H = \sum_R \left(E_1^R |1\rangle\langle 1| + E_2^R |2\rangle\langle 2| + E_3^R |3\rangle\langle 3| \right) + \sum_R \hbar\omega_p a_R a_R^\dagger + \kappa \sum_{R,R'} (a_R a_{R'} + h.c.) - \sum_R \hbar g \left(\sigma_+^R a_R + \sigma_-^R a_R^\dagger \right) -$$

where the first term is the energy level related to the quantum state in each cavity, the second term is related to photon number of the mode in each cavity, the third term is related to photon hopping between neighbor cavities, and the forth and the fifth terms are related to the interaction part in the rotating wave approximation, between each cavity mode and the quantum state inside. The last two terms are related to the modes in the waveguides that are coupled to the first and the last cavity [6]; κ, κ' are the coupling coefficients between neighbor cavities that can be calculated through an overlap integral [7].



(a) (b)

Figure 3: Transient analysis of the (a) side-coupled system, (b) direct-coupled system.



(a) (b)

Figure 4:(a) CROW system under investigation (b) Reflectivity considering $\Omega_c^j = 0$ (in the j-th cavity)

We consider an interaction picture, to eliminate the time dependence of the pump signals, and derive the Heisenberg picture of the system. In Figure 4b the transmittance considering different numbers of cavities N with a resonant dipole is shown, and we observe that the reflectivity bandwidth increases, and the frequency response becomes more flat, by increasing the number of cavities. Figure 5 shows the group velocity, and we observe that the slowing down effect is larger for a small value of the Rabi frequency of the pump, in accordance with the dispersion relation of an EIT material.
N is the number of cavities with a value of the pump signal of 100 GHz in Figure 5 (a) or 500 GHz in Figure 5 (b), and all the remaining cavities have a 2THz pump, that is quite identical to have no pump effect.

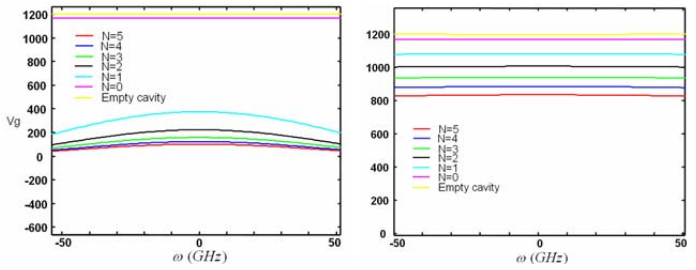


Figure 5: Group velocity for (a) $\Omega_c^j = 100$ *GHz (b)* $\Omega_c^j = 500$*GHz (in the j-th cavity)*

We observe that for N=5 we obtain the maximum group velocity reduction in both case, as expected, and that there are two different behaviours in the two cases. For Ω_c=500 GHz, the light speed reduction varies linearly with N (the curves are equally spaced apart), and it is almost constant over the frequency bandwidth, whereas this is not true for Ω_c=100 GHz.

Conclusions

In this paper, we have analyzed the behavior of different PhC and Quantum Dot system for switching and slow light applications, in the Purcell regime. We have investigated different regimes of EIT material in microcavities [10] to drop or slow down an input monochromatic signal. The EIT effect created in a single quantum dot has been considered, in both static and transient regimes; a CROW device is investigated as an optically tunable buffer, with a large bandwidth.

The work reported in this paper has been funded by the European Sixth Framework Program FP6-2004 IST-NMP-2 "Novel nano-template technology and its applications to the fabrication of novel photonic devices N2T2".

References

[1] T. Aalto et al. “A European roadmap for photonics and nanotechnologies” the MONA (Merging Optics and Nanotecnology) road map, (2005).

[2] M. Notomi, T. Tanabe, A. Shinya, E. Kuramochi, H. Taniyama, S. Mitsugi, M. Morita, "Nonlinear and adiabatic control of high-Q photonic crystal nanocavities", Opt. Exp. vol. 15, no. 26 17458-17481, (2007).

[3] E. Waks, E. Vuckovich , “Dipole Induced Transparency”, Phys. Rew. Lett. Vol. 96, 153601 (2006).

[4] G. Manzacca, G. Cincotti, K. Hingerl, "Ultra fast switching by controlling Rabi splitting", Appl. Phys. Lett. vol. 91, 231920 (2007).

[5] L. C. Andreani, G. Panzarini, J. M. Gérard, “Strong coupling regime for quantum boxes in pillar microcavities: Theory”, Phys. Rev. B vol. 60, no. 19, 13276-13279, (1999).

[6] A. Auffèves-Garnier, C. Simon, J. M. Gérard and J. P. Poizat, “Giant optical nonlinearity induced by a single two level system interacting with a cavity in the Purcell regime” Phys. Rev. A vol. 75, 053823 (2007).

[7] E. Waks, E. Vuckovich, “Dispersive properties and large Kerr nonlinearities using dipole induced transparency in a single sided cavity” Phys. Rew. A vol. 73, 041803 (2006).

[8] M. J. Hartmann, F. G. S. L. Brandão, M. B. Plenio, “Strongly interacting polaritons in coupled array of cavities” Nat. Phys. vol. 2, 849-855 (2006).

[9] J. M. Bendickson, J. P. Dowling, M. Scalora, “Analytic expressions for the electromagnetic mode density in finite, one dimensional, photonic band-gap structures” Phys. Rev. E vol. 53, 4, (1996).

New thin heterogeneous optical waveguides on SOI for reconfigurable optical add/drop multiplexers

A.V. Tsarev

Institute of Semiconductor Physics, Siberian Branch of Russian Academy of Sciences
Prospect Lavrenteva, 13, Novosibirsk, 630090, Russia
tsarev@.isp.nsc.ru

Abstract: *This paper presents the new type of heterogeneous optical waveguide on silicon-on-insulator (SOI) and its application for ROADM. The side p-n-doping of 220 nm×35 μm silicon core provides quasi-single-mode behavior due to small optical losses for fundamental mode with 10 μm mode width and increasing losses for the higher modes.*

1. Introduction

Optical waveguides based on thin silicon-on-insulator (SOI) nanostructures are widely used in various photonic elements [1] whose production technology can be compatible with the standard CMOS technology. On the base of thin SOI one can manufacture photonic crystals, nano-scale two-dimensional (2D) diffraction gratings for coupling light from optical fibers or/and for polarization diversity of photonic devices [2].

However, due to a high contrast of the refractive index of the silicon core (n = 3.478) and surrounding oxide (n = 1.447), it is impossible to fulfill simultaneously incompatible requirements imposed on the optimal geometrical dimensions of the waveguide silicon core that have the best fit with 2D grating. To reduce parasitic signals, the waveguide should be single-mode, i.e. it should have the submicron size. In the direction perpendicular to the waveguide axis, this condition is fulfilled due to the small optical thickness (~ 220 nm) of a high-quality silicon layer. At the same time, the width of such strip waveguides should be large enough (about 10 μm) to provide the acceptable matching with the optical fiber, and hence, these waveguides are necessarily multi-mode, containing tens of modes. Traditional way to eliminate this problem is based on the use of adiabatic waveguide coupler that has to change waveguide width about 20 times (from submicron silicon wire to multi-micron grating region).

In this paper, we describe alternative way, that is based on the use of the new thin heterogeneous SOI waveguides with large transverse dimensions (mode size ~ 10 μm), being at the same time a single-mode. The new design contains additionally heavily doped *p*-*n*-regions on the sides of a multi-mode strip waveguide (with silicon core cross section ~ 220 nm × 35 μm). Such doping provides the quasi-single-mode behavior of the heterogeneous waveguide due to the small optical losses for the fundamental mode and increase in losses for the higher-order modes. This heterogeneous SOI waveguide provides low propagation and waveguide crossing losses and is preferable for jointly use with 2D grating couplers, reconfigurable optical add/drop multiplexers (ROADMs) [2] and multi-reflector filtering photonic devises [3].

New structure design is accomplished by a number of numerical simulations using beam propagation method (BPM) and finite difference time domain (FDTD) method [4]. To have faster simulations, 3D structure has been replaced by its two-dimensional analogy using the effective index method (EIM), which decomposes 3D strip waveguide into two

2D slab waveguides. We use the same width and concentration for p^+ and n^+ - doped regions that provides charge equilibrium of the structure. Besides, the width of *p-n* junction is assumed very small in comparison with the waveguide width that makes possible to use a step shape approximation of the refractive index across the structure.

II. Optical properties of heterogeneous optical waveguide in thin SOI

Recently, we propose heterogeneous optical waveguide that contains p^+- doping of sides of wide silicon core [3, 5]. Here we extend this approach for the more preferable case of *p-n* side doping (see Fig.1) that provides even better results. Optical properties are studied on the base of simple relation obtained from the well-known paper by Soref et al. [6]. It describes the change in refractive index (Δn) and absorption ($\Delta\alpha$) at the wavelength of interest ($\lambda_0 = 1.55$ μm) due to presence of free electron (N_e) and hole (N_h) concentration in silicon [3, 5]:

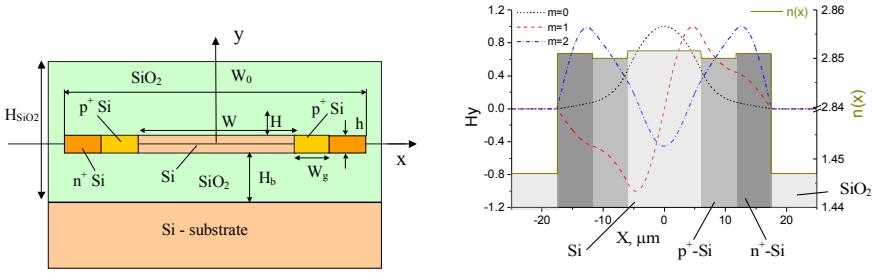
$$\Delta\alpha_e = 0.12 \cdot |\Delta n_e| \qquad (1)$$

$$\Delta\alpha_h = 0.16 \cdot |\Delta n_h|^{5/4}$$

Thus total change of complex refractive index due to the free charge dispersion effect is:

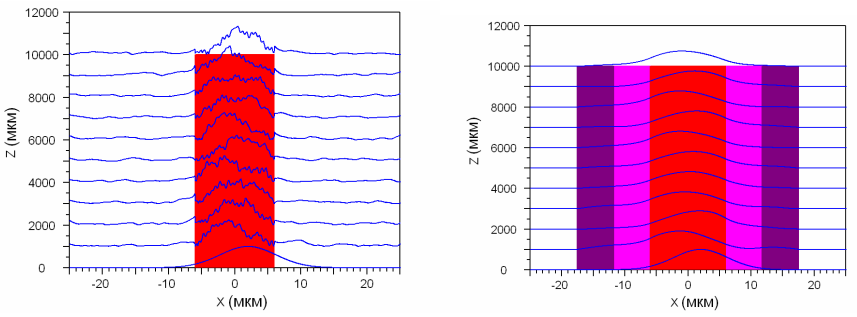
$$\Delta n_c = \Delta n + i \cdot n', \qquad (2)$$

where $n' = \Delta\alpha\lambda_0/(4\pi)$, $\Delta n = \Delta n_h + \Delta n_e$, $\Delta\alpha = \Delta\alpha_h + \Delta\alpha_e$.



a) b)

Fig. 1. Heterogeneous optical waveguide in SOI structure.
a) the structure design; b) distribution of the real part of a refractive index and optical fields of the first three modes ($W=10$ μm, $W_0=35$ μm, $\Delta n = 0.002$); Calculation by 2D BPM.



а) б)

Fig. 2. Propagation of the Gaussian optical beam that is displaced by 2 μm in relation to the axis of wide SOI waveguide. Spatial distribution of a magnetic field of TM polarization (that corresponds to TE in 3D case): a) in standard multi-mode waveguide ($W=12$ μm); b) in heterogeneous quasi-single-mode waveguide ($W = 12$ μm, $W_0 = 35$ μm). 2D BPM simulation.

The principal difference of standard and heterogeneous optical waveguide is illustrated by the Fig.2 that demonstrates propagation of the Gaussian optical beam that is displaced by 2 μm relative to the core center. One can see that heterogeneous optical waveguide suppressed multi-mode interference that disturbs optical field of wide waveguide (compare Fig.2a and Fig.2b).

This positive effect produced by the *p-n* side doping ($N_h = N_e \sim 9.2 \cdot 10^{17}$ cm^{-3}, $|\Delta n_h| \sim 0.002$, see (1)) that changes the field distribution in those manner that the main part of the fundamental-mode energy in concentrated in the central region of the waveguide of width W (see Fig.1b), while only a very small part of this energy occupies the dissipative region with charge carriers. The optical fields of all other modes with effective refractive indices close to the refractive index in the doped region occupy the entire cross section of the waveguide. Therefore, the fraction of energy occupied the dissipative region increases by many times (Fig. 1b) and that produces considerable additional decay (see Fig.3) of these optical modes by free charge absorption. One can see from the data presented in Fig. 3 that fundamental mode of heterogeneous waveguide has negligible losses related to the losses of the high-order modes and that the losses could be controlled by the structure design.

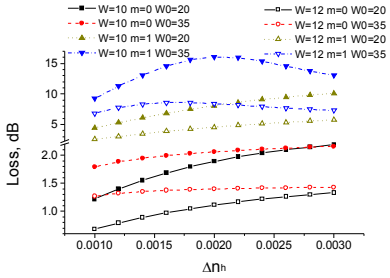


Fig. 3. Additional optical losses by free charge carriers (holes and electrons) in a strip optical waveguide for various modes as a function of real part of refractive index increment in p^+-doped regions. $W = 10$ μm and $W = 12$ μm, $W_0 = 20$ μm and $W_0 = 35$ μm. 2D BPM simulation.

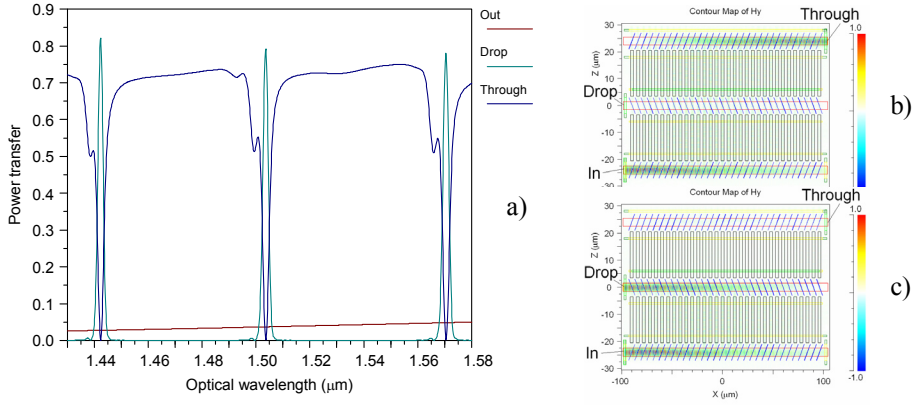


Fig. 4. Simulation by 2D FDTD of multi-reflector ROADM with heterogeneous waveguides with 32 slanted reflectors ($\varphi = 45°$) for TM polarization. $W = 3$ μm, n(reflector) = 1.7, period of reflectors $d_x = 6$ μm, beam expander period $d_z = 24$ μm. Variable reflector width from 40 nm to 90 nm. a) frequency response (FWHM = 2.4 nm, FSR = 67.1 nm); b) field map at through wavelength $\lambda_0 = 1.55$ μm; c) field map at drop wavelength $\lambda_0 = 1.5036$ μm.

Single-mode behavior and wide mode size, small propagation and waveguide crossing losses [3] make heterogeneous waveguides very suitable for multiple photonics applications. For example, they could be used for construction multi-reflector filtering devices [3]. For the illustration Fig.4 presents simulation by 2D FDTD [4] of typical frequency response of multi-reflector ROADM [3] with heterogeneous waveguides. We use variable reflectors width and position to provide proper apodization of the frequency response. The structure could be manufactured by modern nano-photonics technology.
These results show the need to conduct extensive investigation of novel nano-SOI waveguide structures and devices that utilizes *p-n*-doping, nano-grooves, and 2D-grating couplers. These arrangement could provide polarization diversity and better manufacturability of multi-reflector reconfigurable optical add/drop multiplexers [1-3].

Summary

This paper presents the first description and simulation of novel nano-photonic SOI heterogeneous waveguide structures. New structure design includes *p-n* doping on both sides of SOI strip waveguide with 220 nm × 35 μm silicon cross section surrounded by the silica cladding. It provides small crossing and propagation optical losses for fundamental mode and large losses for high-order modes due to different free charge absorption depending on the modes field distribution that is controlled by the structure design. For example, heterogeneous waveguide with equal level of p^+ and n^+ side doping ($N_h = N_e \sim 9.2 \cdot 10^{17}$ cm^{-3}, $|\Delta n_h| \sim 0.002$, $W = 10$ μm, $W_0 = 35$ μm) has the very different losses of fundamental and the first mode -2.1 dB and -20.4 dB, respectively. That is enough for single-mode optical beam propagation. Incorporation of these novel heterogeneous waveguides with 2D nono-grating couplers provides new opportunity for polarization diversity of ROADM. Thin and wide quasi-single-mode SOI heterogeneous waveguide provides better performance and manufacturability of multi-reflector ROADM that utilizes multi-reflector beam expanders. Multiple simulations by FDTD and BMP methods demonstrate the validity of the new SOI design that will be also interesting for implementation in other multiple nano-photonic optical elements.

Acknowledgments

Author would like to thank Company RSoft Design Group, Inc. that provides the FDTD and BMP software [4].

References

[1] W. Bogaerts, R. Baets, P. Dumon, V. Wiaux, S. Beckx, D. Taillaert, B. Luyssaert, J. Van Campenhout, P. Bienstman, D. Van Thourhout, "Nanophotonic waveguides in silicon-on-insulator fabricated CMOS technology," J. Lightwave Technol., vol. 23, pp. 401-412, 2005.

[2] W. Bogaerts, D. Taillaert, P. Dumon, D. Van Thourhout, R. Baets, "A polarization-diversity wavelength duplexer circuit in silicon-on-insulator photonic wires," Opt. Express, vol. 15, pp. 1567-1578, 2007.

[3] A. V. Tsarev, F. De Leonardis, and V. M. N. Passaro, "Thin heterogeneous SOI waveguides for thermo-optical tuning and filtering", Opt. Express, vol. 16, pp. 3101-3113, 2008.

[4] BeamPROP and FullWave from RSoft Design Group, Inc , http://www.rsoftdesign.com.

[5] A. V. Tsarev, "New type of heterogeneous nanophotonic silicon-on-insulator optical waveguides," Quantum Electron. (Rus), vol. 37, pp. 775-776, 2007.

[6] R. A. Soref and B. R. Bennett, "Kramers-Kronig analysis of electrooptical switching in silicon", Proc. SPIE, vol. 704, pp. 32–37, 1986.

BPM Validation of the Modal Gain Measured with the Segmented Contact Method

P. Bardella[1], I. Montrosset[1]

[1]Dipartimento di Elettronica, Politecnico di Torino, Torino, Italy
paolo.bardella@polito.it

Abstract. *We determine, using a Beam Propagation Method technique, the accuracy of the well known method of evaluating the modal gain based on a ratio between the ASE powers obtained injecting current in one and two longitudinal sections of a device. We correlate the method accuracy with the sections length.*

Introduction

Segmented contact method has been widely used since its introduction to measure the gain [1] and loss [2] of active semiconductor materials analyzing the emitted amplified spontaneous emission (ASE) power.

The usual technique requires two equal-length electrodes on the semiconductor device under test [1]: first, amplified spontaneous emission (ASE) power $P(L)$ is measured injecting current only one section; then $P(2L)$ is measured injecting in both sections. In the laboratory set-up, output ASE power is then collected with an optical system to an OSA.

Net modal gain G is then estimated from the measures using the relation

$$G = \frac{1}{L}\log\frac{P(2L)-P(L)}{P(L)}. \tag{1}$$

More complex solutions are also used, which require two electrodes with different lengths [2], or 3 or more electrodes, allowing estimating both the gain and the intrinsic material losses [3].

The aim of this work is to give a quantitative evaluation of the error affecting this measurement technique, and to determine the minimum device length required in order to obtain certain accuracy. We analyzed for simplicity the case of 1D layered structure, $n(y)$, using a two-dimensional BPM simulator. We calculated the ASE radiated power and its coupling with an optical system, and then we calculated the device gain. Results are shown for different modal gain values and different equivalent spot sizes of the collecting optical system.

Simulations procedure

Fig. 1 shows the layout of the device and the numerical discretization grid we used: y and z directions are discretized with step Δy and Δz respectively.

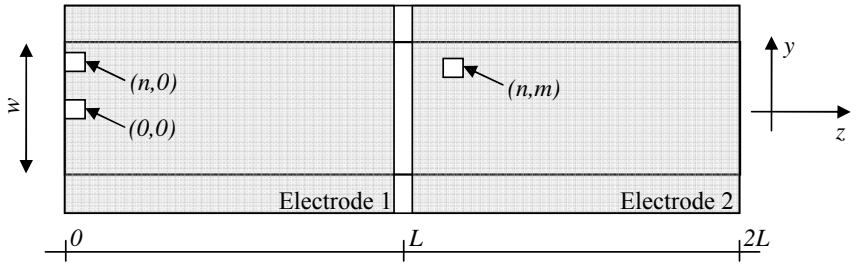


Fig.1 Layout of the device and 2D numerical discretization grid.

In the hypothesis of unsaturated regime of operation, the output ASE coupled to the output optical system can be computed using the following steps:

- We calculate first the field[1] $f(n,m;0)$ in all the structure generated by a point source in the middle of the active section ($y_s = 0$) of the waveguide in the plane $z = 0$ (see Fig. 2);

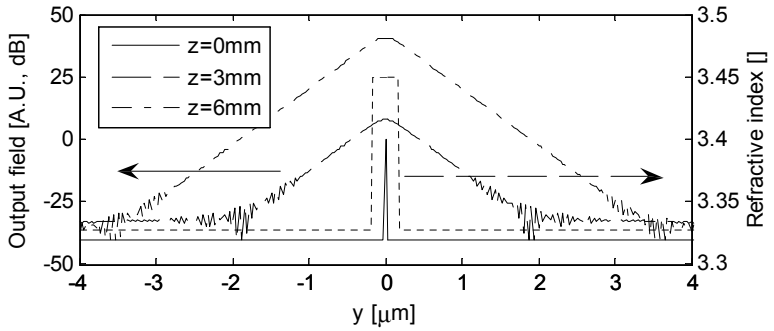


Fig.2 Calculated fields from a SE point source at various longitudinal sections and refractive index profile.

- We repeat this calculation for all the discretization points in the input section ($|y_s = s\Delta y| < w/2, z = 0$), obtaining the fields $f(n,m;s)$;
- From these results the ASE field contribution due to each SE source in the active region can be computed at the output section;
- The Fourier Transform of these fields can then be used to determine the transmitted fields at the output cleaved interface $F(k;m,s)$ from the spontaneous emission source at ($s\Delta y, m\Delta z$);

[1] The first two indices indicate the position of the field sample at the coordinates ($n\Delta y, m\Delta z$), the third defines the position of the SE source which originates the field at ($s\Delta y, 0$).

- The projections of these fields on the Fourier Transform $F_f(k)$ of the equivalent spot size of the receiving optics allow to determine the contribution of each SE source $P(m,s)$; the total contribution from section $m\Delta z$ is therefore calculated as $P(m)=\sum_s\left[\left|\int F_f(k)F(k;m,s)\,dk\right|^2 \Big/ \int\left|F_f(k)\right|^2 dk\right]$.
- Finally, we obtain the gain for a cavity with length $2L=2M\Delta z$ from Eq.1 as $G(2L)=\frac{1}{2L}\left[\log\sum_{m=M+1}^{2M}P(m)-\log\sum_{m=0}^{M}P(m)\right]$.

Results for modal gain and its relative error

In Figs. 3 and 4 we report the modal gain and relative errors obtained from the simulation of an InAs/GaAs QD active waveguide with $Al_{0.25}Ga_{0.75}As$ cladding having a spot size FWHM of 0.6μm.
In the case of Fig.3, we considered a 16cm^{-1} modal gain waveguide. The results dependence with the equivalent spot size of the receiver system clearly appears, and at least 750μm total device length is necessary to obtain a 10% relative error with a 1μm equivalent spot size. Wider spot sizes clearly require longer device in order to obtain the same error.

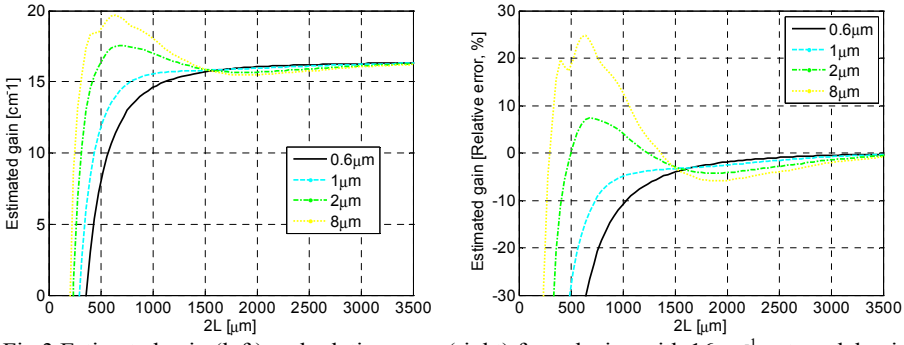


Fig.3 Estimated gain (left) and relative error (right) for a device with 16cm^{-1} net modal gain, for different equivalent spot sizes of the receiver system.

When working with lower gain values, a longer device is also required: for G=5cm^{-1}, at least 1.7mm are necessary to obtain a 10% relative error (Fig.4).
This behaviour clearly shows that segmented contact method gives correct results only when the ASE field coupled to the output optical system is sufficiently filtered from the unguided modal field components. Low modal gain operation and large spot size of the equivalent output optical system risk not guaranteeing a sufficient filtering effect respectively during the propagation in the waveguide or at the end coupling.

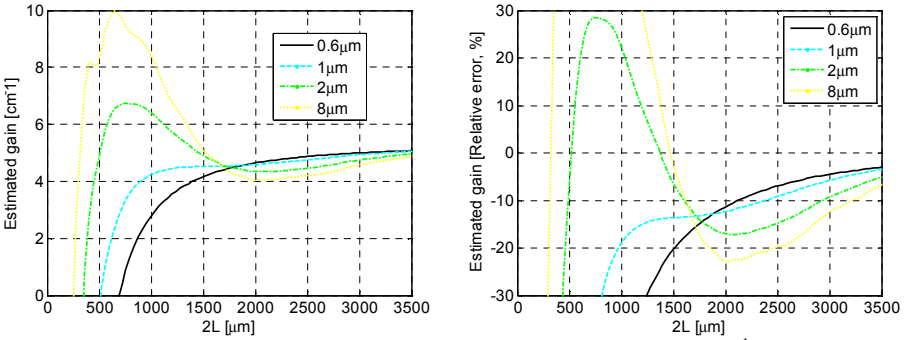


Fig.4 Estimated gain (left) and relative error (right) for a device with 5cm^{-1} net modal gain, for different equivalent spot sizes of the receiver system.

Conclusions

For the first time, to our knowledge, the multistrip modal gain measurement technique has been validated respect to its measurement error. Results from BPM simulation show that the error depends significantly on the ASE filtering capability of the receiving system and on the modal gain itself. Longer strips are necessary in order to measure low modal gain.

This project was supported by the IST NanoUBSources FP6 European Project, contract no. 017128.

References

[1] P. Blood, A. I. Kucharska, J. P. Jacobs and K. Griffiths, "Measurement and calculation of spontaneous recombination current and optical gain in GaAs-AlGaAs quantum-well structures", J. Appl. Phys., vol. 70, pp. 1142-1156, 1991.

[2] S. D. McDougall and C. N. Ironside, "Measurements of reverse and forward bias absorption and gain spectra in semiconductor laser material", Electron Lett., vol. 31, no. 25, pp. 2179-2181, Dec. 1995.

[3] Y.-C. Xin, Y. Li, A. Martinez, T. J. Rotter, H. Su, L. Zhang, A. L. Gray, S. Luong, K. Sun, Z. Zou, J. Zilko, P. M. Varangis and L. F. Lester, "Optical Gain and Absorption of Quantum Dots Measured Using an Alternative Segmented Contact Method", IEEE J. Quantum Electron., vol. 42, no. 7, pp. 725-732, July 2006.

Photonic Crystal Microlasers

Myung-Ki Kim, Min-Kyo Seo, Seo-Heon Kim and Yong-Hee Lee

Department of Physics, Korea Advanced Institute of Science and Technology
yhlee@kaist.ac.kr
373-1 Kusung-dong, Yusung-gu, Taejon, Korea 305-70

Abstract. *Electrically-pumped single-cell photonic crystal lasers are reported. Two possible nondegenerate resonant modes are chosen and investigated in detail. In addition, our recent proposal and demonstration of 'reconfigurable' photonic crystal resonators will be discussed.*

The ability to localize photons into photonic bandgap semiconductor microcavities [1, 2] having wavelength-scale volumes and high quality factors enables us to study the cavity quantum electrodynamics in semiconductor material systems. Various optically-pumped, ultra-small, photonic crystal lasers and electrically-driven light emitting structures based on the concept of photonic crystal have been recently reported. However, the deployable microlasers should be built on the simple electrical pumping scheme. One of the realistic difficulties of the wavelength-scale electrically-driven photonic crystal laser is the electrical contact onto the sub-micron-size semiconductor slab resonator.

In our electrically-driven photonic crystal resonator structure [3, 4], a sub-micron-size semiconductor post is placed at the center of the single-cell photonic crystal resonator where the photon density is almost zero. This small central post functions simultaneously as an electrical wire, a mode selector and a heat sinker. Electrons are supplied laterally from the top *n*-electrode while holes are injected directly through the bottom *p*-post. A *nip* doping structure that is inverted from that of a typical semiconductor laser is used to exploit the high mobility of the electrons that has to travel a longer distance along the top surface. The central *InP* post was size-tuned by changing the temperature of dilute *HCl* solution from 10 degrees to room temperature. We observed single mode lasing operations from two nondegenerate modes, the monopole mode and the hexapole mode, respectively. For the monopole mode, the single modeness comes naturally since this resonance is spectrally well-isolated from the other modes. However, near the hexapole mode, the high-quality factor degenerate quadrupole modes always exist. We suppressed the quadrupole mode by controlling the size of the current post and hence the optical losses. Lasing operation in an intended mode is confirmed through contour finite difference time domain methods, where the structural input data is transferred directly from the digitized scanning electron microscope image of the fabricated sample. Threshold current and voltage are 100~300 A and 0.9~1.1 V, respectively, at room temperature, near 1,550 nm.

Semiconductor quantum dot combined with microcavities is the one of the attractive approaches for the single photon sources. Photons trained by a high *Q/V* resonant mode have a narrow spectral line and a well-defined polarization state. In addition, photon collection can be achieved more efficiently by controlling inner

symmetries of the resonant mode of interest. The successful optical characterizations of PhC microcavities with quantum dots were performed recently. However, these trials employing PhC cavities exposed two critical problems clearly. The first issue is that of the spatial and spectral overlaps of two relevant resonances, the cavity resonance and the quantum dot resonance. In order to answer this question, one needs to control the emission wavelength of a quantum dot on the order of nanometer or better. At the same time, this right quantum dot should be placed at the anti-node of the resonant mode with precision on the order of nanometers. The second issue is that of the efficient collection and delivery of valuable photons to customers. This nontrivial issue requires good understanding of photon out-coupling out of a resonant cavity. Our microfiber-coupled 'reconfigurable' resonator allows the repeatable formation of the cavity's physical position until the quantum dot of 'right' emission spectrum is identified at the 'right' physical position. Efficient out-coupling into the tapered single mode optical fiber follows naturally and easily.

Free-standing 2-D slab *InP* triangular photonic crystals are employed as basic building blocks. The single-row photonic crystal slab waveguide is coupled with a highly-curved tapered fiber as shown in Fig. 2 [5]. Note that the whole real estate over the single-row PhC waveguide is where at least one 'right' quantum dot needs to be found. The beauty of this scheme is that of allowing a large margin of fabrication errors until one constructs the optimized resonant cavity supported by the 'spectrally-right' quantum dot. When a microfiber is placed on the PhC slab waveguide, the effective index near the point of contact increases relative to that of the bare waveguide as calculated in the dispersion curve shown in Fig. 3. With one step further along this logic, one is able to construct a photonic potential well by simply placing a tapered fiber on top of a PhC waveguide, in the proximity of a properly-selected spectral position in the PhC waveguide dispersion curve. As shown in Fig. 4, we confirmed the formation of a 'Gaussian' photonic potential well in the proximity of the contact point of the highly-curved-fiber. Considering that the electric field of the PhC guided mode penetrates into the silica in exponential fashion and the air-gap distance of the curved fiber from the slab has a quadratic dependence, the Gaussian dependence is physically understandable. In this scheme, the physical location and size of a PhC laser resonator can be defined (and redefined) repeatedly by simply relocating the microfiber along the PhC waveguide. Experimentally we confirmed the formation of reconfigurable resonators slightly below the all three available band edges in the form of lasing action.

References

[1] E. Yablonovitch, *Phys. Rev. Lett.* **58,** 2059 (1987).
[2] O. Painter *et al.*, *Science* **284**, 1819 (1999).
[3] H. G. Park *et. al.*, *Science* **305**, 1444 (2004).
[4] M. K. Seo *et. al.*, *Appl. Phys. Lett.* **90**, 171122(2007)
[5] M. K. Kim *et. al.*, *Opt. Express* **15**, 17241 (2007).

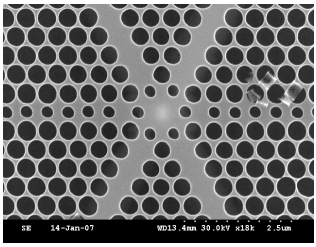


Fig. 1 Hexapole mode resonator with six PhC waveguides.

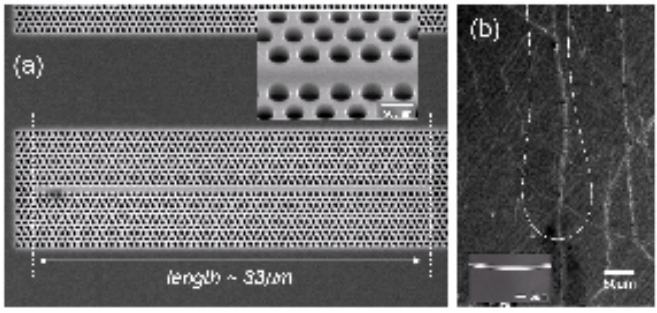


Fig.2 Photonic crystal waveguide and tapered microfiber

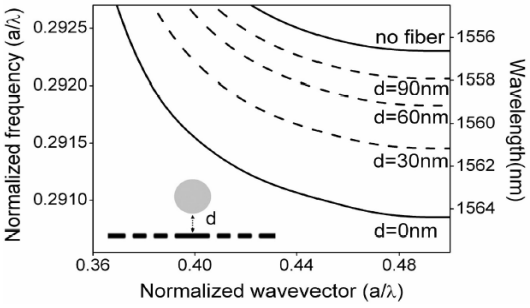


Fig. 3 Dispersion curve of fiber-coupled PhC waveguide.

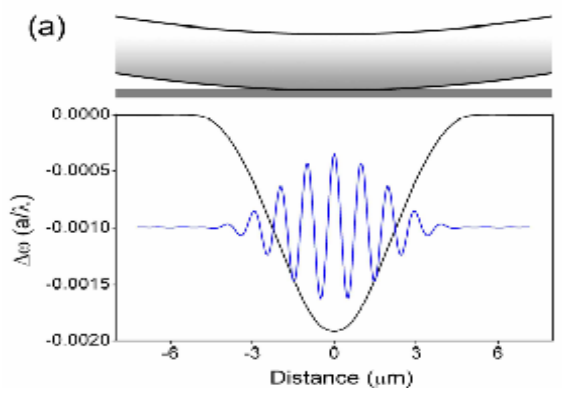


Fig. 4 Photon localization by a reconfigurable Gaussian potential well.

Functional photonic-crystal mini-stopband demux integrated in emitting and detecting devices.

H. Benisty[1], C. Cambournac[1], M. Ayre[1], F. Van Laere[2], D. Van Thourhout[2], R. Baets[2], T. Stomeo[3], T.F. Krauss[3], M. Kamp[4], H. Hofmann[4], A. Forchel[4], D.F.G. Gallagher[5]

[1]Institut d'Optique, CNRS, Campus Polytechnique, RD128, 91127 Palaiseau cedex, France
henri.benisty@institutoptique.fr
[2] Ghent University - IMEC, Department of Information Technology, Belgium
[3] St Andrews University, Physics and Astronomy, Fife, KY16 9SS, Scotland, U.K.
[4]Technische Physik, Am Hubland, Universität Würzburg, Würzburg D-97074, Germany
[5]Photon Design, 34 Leopold Street, Oxford, OX1 4TW, UK

Abstract. *We successfully implement mini-stopband DeMUX – the wavelength-selective routing in multimode photonic-crystal "Wn" n-missing-rows waveguides – in two devices: (i) a tunable laser for wavelength monitoring based on W3 guides with < 20 GHz accuracy; (ii) a membrane-based InP DeMUX receiver, based on W(5+x) guides, with polarization diversity and Coarse WDM capability.*

Introduction

Demultiplexing is a crucial function in integrated telecom devices. Photonic Crystal (PhC) multimode waveguides support anticrossing phenomena, so-called MSB (mini-stopband) that have been exploited to demonstrate a demux action. We show here two devices where integration of such a demux has been made possible, a laser to monitor its wavelength, and a polarization-independent surface coupled receiver, with integrated photodiodes. This work was part of the EU project FUNFOX (IST 04582).

Fig. 1 explains the basics of MSB demux. Fig.1a depicts the typical band structure of a multimode "Wn" photonic crystal waveguide consisting of holes on a triangular array of pitch *a* with n missing rows (here n=7, matrix index n_{eff}=2.7 to 3.3 depends on the layer structure). Higher order modes and the fundamental mode couple together in tiny frequency and wavevector windows [1], ignoring each other elsewhere. The higher-order mode easily tunnels through many rows of PhC (Fig.1d-e), while the fundamental mode cannot. Hence, in Fig.1b, we exploit this difference to produce highly wavelength-dependent photocurrents in two 'side' and 'through' photodiodes. The ratio can be used to monitor in an integrated fashion a tunable laser wavelength, and provide data for feedback, especially along the edges of the spectral response.

Fig.1c shows the demux WDM action, that we shall use rather in a Coarse WDM (CWDM) spirit, according to Refs [2-4]. Thanks to its small footprint and satisfactory response, our device competes well with various approaches (phasar/AWG [5], cut-off waveguides [6], multiple cavities [7]) and has some intrinsic design robustness.

The existing attempts of an MSB-based demux [2-4] were all made in a substrate approach. This will still be the case of the laser monitor of Fig.1b, but we will demonstrate here an MSB-based demux implemented on an InP membrane[8,9], with surface couplers and polarization diversity [10].

Wavelength monitor

The wavelength monitor we implemented was based on the principle of Fig.1b. The basic PhC-tunable laser makes use of two cavities of similar length, and uses two

injection currents to tune the laser monomode emission across several tens of nm around 1550 nm, with good SMSR in general [11-12]. The rear mirror of such a laser was thinned to three rows to allow sufficient signal to leak through. The short taper was simple, its efficiency was not a critical issue, as it had a smooth spectral behaviour.

Several other hurdles had to be tackled. Firstly, electrical cross-talk between diodes and with lasers had to be controlled by means of insulation trenches and grounded guard rings to avoid leakage currents. Next, reflections in the laser had to be tamed, thanks to extensive FDTD simulations [13]. For this, the few rows at the start of the PhC waveguide were made different so as to break coherence of the back reflected beam, as will be detailed. The thinned side was also made with a simple trench instead of one of the rows to diminish the feedback and broaden the response range.

After all these steps, the system looked as shown in Fig.2. The ratio of the photocurrent was monitored as a function of the two laser currents with our home made setup and gave the result of Fig.3a. Compare with the lasing wavelength map of Fig.3b. The impact of the MSB can clearly be seen. Using the ratio to monitor, we obtained the correlation data of Fig.4a,b, which show an unambiguous correlation between lasing wavelength and ratio over several nm.

This particular monitor, with associated electronics, could therefore be of interest to finely lock laser arrays in PICs. The issue of temperature dependence will be discussed.

Integrated receiver with photonic-crystal integrated demux

Thanks to the progresses in surface couplers on membrane [14], we could design a device that gathers three key elements: (i) a polarization diversity surface coupler, (ii) a demux device working as indicated in Fig.1c, and (iii) integrated photodiodes.

The basic system is an InP membrane bonded thanks to BCB onto a holder. A single e-beam-defined mask is defined. It is first used to perform deep etching of PhC holes, while the coupler areas are completely protected by another coarse masking. Then, these area are de-protected, and a shallow-etch step is practised, of no influence for the "through" PhC holes. The photodiode array is included on the back side, as will be described in more detail on slides in correspondence with the BCB bonding procedure.

Several subparts were tested at intermediate steps. They revealed the high performance limits of our approach, notably the polarization diversity performance (Fig.4) and the wavelength demux capabilities (Fig.5, on devices with cleaved optical readout rather than photodiodes).

The overall chip is described in Fig.6 as well as its key demux performances on all but one functional channels. The overall footprint is small and can be shrunk to 100x150 μm with curved grating coupler. Device-wise, 50 MHz operation of the demux will be shown, the photodiodes having a designed 10 GHz cut-off (not measured).

Acknowledgements

Authors acknowledge the FP6 European Project IST-04582 "FUNFOX" (2004-2007).

References

[1] S. Olivier et al. Phys. Rev. B, vol. 63, pp. 113311 (1-6), 2001.

[2] E. Viasnoff-Schwoob et al. Appl. Phys. Lett., vol. 86, pp. 101107, 2005.

[3] L. Martinelli IEEE J. Lightwave Technol., vol. 25, pp. 2385-2394, 2007.
[4] L. Martinelli et al. IEEE Phot. Technol. Lett., vol. 19, pp. 282-284, 2007.
[5] W. Bogaerts et al. "Compact Wavelength-Selective Functions in Silicon-on-Insulator Photonic Wires," IEEE J. Sel. Top. in Quantum Electron., vol. 12, pp. 1394-1401, 2006.
[6] T. Niemi et al. IEEE Phot. Technol. Lett., vol. 18, pp. 226-228, 2006.
[7] Y. Akahane et al. Opt. Express, vol. 13, pp. 2512-2530, 2005.
[8] T. Stomeo et al. "Integration of Grating Couplers with Compact PhC Demux on InP Membrane", submitted to Optics Letters (2008).
[9] G. Roelkens et al., J. Electrochem. Soc., vol. 153, pp.G1015-G1019 (2006).
[10] F. Van Laere, D. Van Thourhout, R. Baets, T. Stomeo, T. F. Krauss, M. Ayre, C. Cambournac, and H. Benisty, "Multifunctional Photonic Crystal Compact Demux-Detector on InP," paper OThM5, presented at OFC/NFOEC 2008, 25-28 Feb., San Diego, 2008.
[11] S. Mahnkopf, M. Kamp, A. Forchel, et al. Optics Comm., vol. 239, pp. 187-191, 2004.
[12] M. Kamp et al. "Nanophotonic integrated lasers" SPIE Proc. Photonics West (San Jose, 2007), Integrated Optics: Devices, Materials, and Technologies X 64750Z (Feb. 14, 2007).
[13] http://www.photondesign.co.uk
[14] See F. Van Laere et al. IEEE Phot. Technol. Lett., vol.19, pp.1919-1921 (2007) and refs therein.

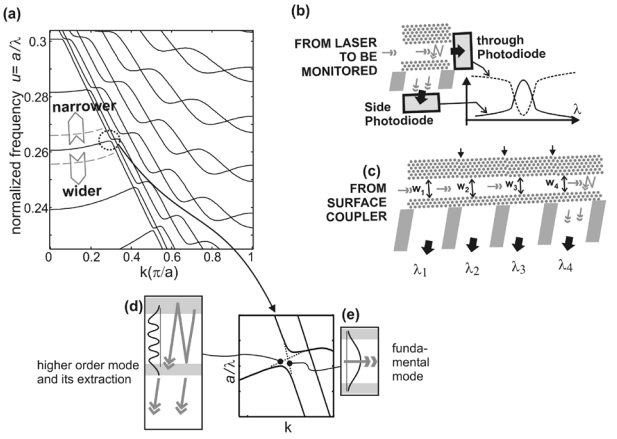


Figure 1 : (a) dispersion relation of a typical Wn PC waveguide (here W7), with highlighted crossing of higher order mode with fundamental mode; (b) use of MSB to get complementary spectral selectivity between the two photo-currents, 'side' and 'through' ; (c) use of variable width to produce a demux ; (d) schematic profile and tunneling of higher-order mode through the thinned cladding ; (e) fundamental mode profile.

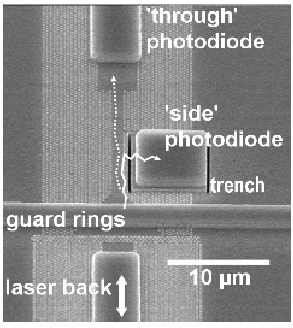
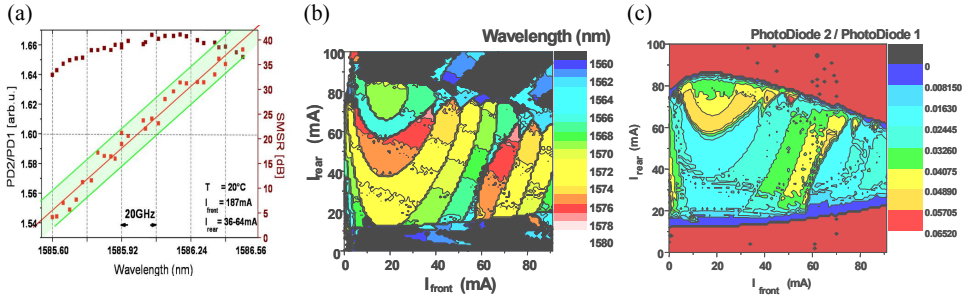


Figure 2 : Micrograph of the wavelength monitor situated at the rear side of a two section PhC laser. The fate of different wavelengths is illustrated by arrows with solid line or dotted line. Note the strong taper just at the entrance of the monitor, partly hidden by the guard ring.

Figure 3 (page 4 top): (a) Correlation of wavelength and ratio along a particular plateau (high SMSR), ensuring 20 GHz potential stability over 110 GHz (dots at the top are the SMSR data, cf. left scale); (b) Tuning map of the laser: wavelength (color) as a function of front and rear section currents. Note well-defined parabola-shaped regions; (c) Map of photocurrent ratio PD2/PD1 as a function of the same parameters. Note the overall similarity with the (b) map. features.



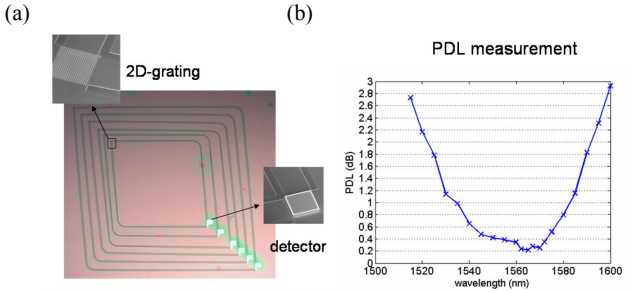


Figure 4 : (a) Grating coupler and integrated detectors for polarization diversity, test layout; (b) Polarisation dependent loss as a function of wavelength (see Fig.5c for the typical coupler spectral characteristics)

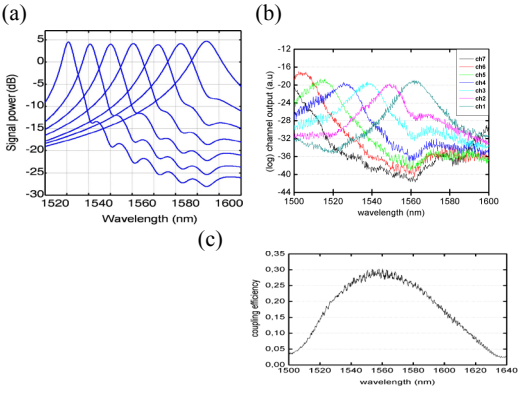


Figure 5 : (a) modeled response of an seven-channel demux based on a wedged W_{5+x} PhC (|x|<0.26), largest wavelength channels are extracted first, hence the trough on the right wing of shorter wavelength channels; (b) experimental data from test device with cleaved edge, dB scale ; (c) spectral response of surface coupler used in this test device for incoupling.

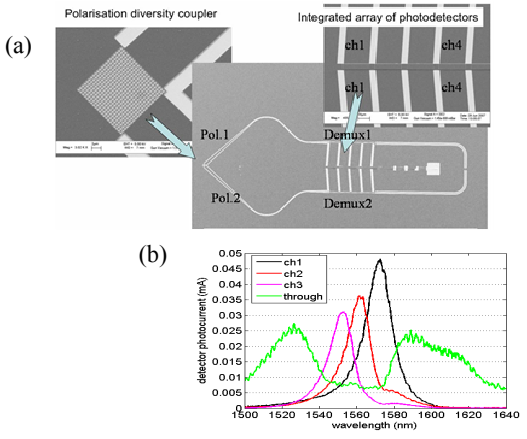


Figure 6 :(a) Overall layout of the compact integrated demux showing the two polarization diversity paths circulating in the pair of demux 1&2, and recombining in the array of photodiodes, including the 'through' one at the right end; (b) Raw spectral response (photo-current, linear scale) of the three rightmost channels and the through detector. Channel4 was damaged.

Photonic Crystal DFB laser array and fine emission wavelength engineering

O. Bouchard[1], A. Larrue[1], A. Monmayrant[1], O. Gauthier-Lafaye[1], S. Bonnefont[1], P. Arguel[1] and F. Lozes-Dupuy[1],
C. Pang[2], A. Bruyant[2] and S. Blaize[2], G. Lérondel[2], P. Royer[2]
F. Pommereau[3], F. Poingt[3], L. Le Gouezigou[3], O. Le Gouezigou[3], O. Drisse[3], E. Dérouin[3] and G. H. Duan[3]

[1]LAAS-CNRS Université de Toulouse, 7 avenue du colonel Roche, 31077 Toulouse Cedex 4, France
antoine.monmayrant@laas.fr
[2]LNIO, ICD CNRS (FRE2848), Université de Technologie de Troyes, 12, rue Marie Curie, BP2060.10010, Troyes cedex, France

[3]Alcatel Thales III-V Lab, Route départementale 128 -91767 Palaiseau Cedex, France

Abstract. *We report on Photonic Crystal DFB laser array under electrical pumping. The 2D geometry of the Photonic Crystal allows precise and fine wavelength spacing. Lasing occurs on the first excited mode, which can be explained by 2D-FDTD calculation showing extremely low loss and high DFB coupling for this mode.*

Introduction

All photonic crystal (PhC) defect waveguide lasers appear as extremely promising for planar optical integration. Indeed they are by nature fully compatible with already reported integrated compact optical systems based on PhC. Moreover, previous works have shown that such lasers can exhibit single-mode DFB-like operation [1] and have also predicted that precise wavelength engineering could be achieved by harnessing the transverse dimension of the 2D PhC [2].
Here we report on integrated arrays of defect waveguide lasers "SW5" where the wavelength spacing is set by altering the transverse period of each waveguide PhC. Both single- and dual-mode DFB lasers were obtained and using planar simulations we can explain most of these lasers' properties.

Sample and geometry

We focused on "SW5" defect waveguides obtained by omitting 5 rows of holes in a rectangular PhC, as shown on figure 1. Such lattice can be described by two periods: a , along the waveguide, and b, transverse to the waveguide. The former is set to a=484 nm for all the lasers in the array and we vary the latter to change the wavelength. In practice, both lattice constants differ by only few percents and we stay close to a square geometry (a~b). Each waveguide can be seen as a square lattice that has been laterally shrinked or expanded by an affine deformation while keeping the hole radius constant. The dimensionless **deformation**, that we define as $\alpha=b/a$, is the key design parameter in this work and all the other parameters remain constant.

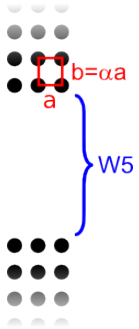


Figure 1: SW5 photonic crystal defect waveguide.

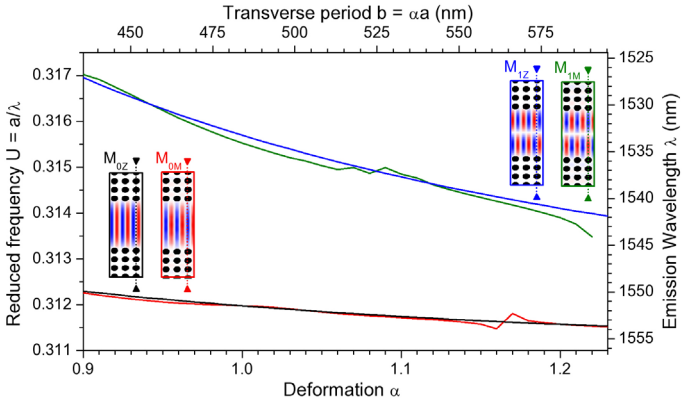


Figure 2:2D-FDTD simulations: wavelength of the first 4 DFB modes: fundamental M_{0Z} (black) and M_{0M} (red) and 1st excited M_{1Z} (blue) and M_{1M}(green). Insets show each mode inside the guide.

For this study, we built arrays of 12 lasers, with a period a=484 nm, hole radius of r=150 nm and deformations ranging from α=0.91 to α=1.23. The waveguides were 370 µm long and both ends were 15 µm away from the cleaved edge. These 15 µm of free propagation help reducing the re-injection from the cleaved edge and ensure a reproducible DFB operation.

Samples were fabricated at "Alcatel Thales III-V Lab" in the InGaAsP/InP material system. We used an InGaAsP planar waveguide on InP substrate with 6 compressively quantum wells. The gain curve of the quantum wells is centered around 1550 nm. The PhC waveguides were defined using e-beam lithography and deep dry etching. The holes depth is around 4 µm, deep enough to achieve 2D like geometry. Metallic contacts were then deposited on the top and bottom surfaces, taking care not to fill the holes so as to preserve the quality of the PhC. A gain region of around 10 µm wide was delimited by proton implantation. Samples were then thinned and cleaved into laser arrays that we reported on an aluminum submount, in turn mounted on a PCB board for characterization.

These structures were simulated using 2D FDTD [3], with an effective index of n_{eff}=3.21 and assuming an infinitely long waveguide (periodic boundaries). The effect of the lateral implant on the guided mode was described using weak perfectly matched layers (PML) in the implanted regions.

Figure 2 shows the evolution of the emission wavelength with the deformation for 4 first DFB modes. The two degenerated fundamental modes are M_{0Z} (black) and M_{0M}(red) and the two degenerated first excited modes are M_{1Z} (blue) and M_{1M}(green). The subscripts "Z" and "M" respectively stand for "zero" and "maximum" and describe the way the mode is phased with the holes, as can be seen on the insets of figure 2: "Z" modes have a zero aligned with the holes column and "M" modes have a maximum aligned with the holes column. "M" modes experience higher losses than "Z" ones and this explains the single-mode operation on the M_{0Z} reported for W1 waveguides [1].

Here, we expected single-mode DFB operation on M_{0Z}, with a central wavelength ranging from 1550 nm to 1554 nm, as can be seen on figure 2 (black line).

Experimental results

Emission spectra of the lasers were measured under pulsed operation using a 1-m focal length monochromator fitted with a cooled InGaAs photomultiplier. Figure 3 shows the DFB lasing wavelength depending on the deformation α (top part) together with a typical spectrum obtained for deformation α=1 (bottom part).
As expected, the lasing wavelength changes slowly and linearly with the deformation.

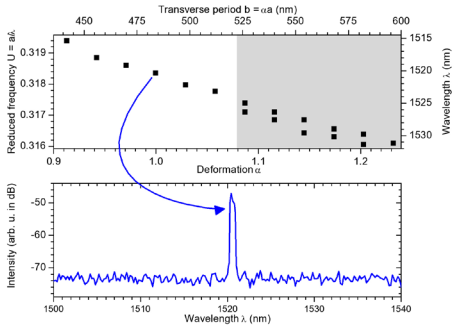


Figure 3:Lasing wavelength depending on the deformation (top) and typical spectrum (bottom). In the gray area (top) lasers are dual-mode.

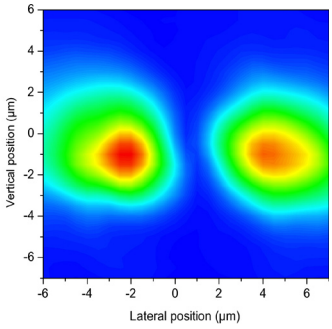


Figure 4: Beam profile measured in the close vicinity of the cleaved edge on a SW5 waveguide for α=1.

However, neither the average lasing wavelength (around 1520 nm) nor the slope of the wavelength evolution ($\Delta\lambda/\Delta b \approx 0.1$) matches what was expected for the fundamentals DFB modes M_{0Z} and M_{0M} (see figure 2). In fact, all these lasers are on the first excited transverse mode. Indeed, the theoretical slope for M_{1Z} and M_{1M} ($\Delta\lambda/\Delta b \approx 0.1$) perfectly matches the experimental results shown on figure 3 (we attribute the small wavelength offset to a slight mismatch in the effective index used in the simulation).
Lasing on the first excited mode was confirmed by near-field probe measurements in the close vicinity of the waveguide exit facet. To avoid distortion of the beam profile over the 15 μm of free propagation, measurements were made on shorter lasers (280 μm long) cleaved inside the waveguide. Figure 4 shows a typical intensity profile obtained for a cleaved SW5 waveguide for α=1 (lasing wavelength around 1520 nm).
Moreover, for deformations higher than α=1.08 (gray area), the lasers are no longer single-mode and both degenerated DFB modes M_{1Z} and M_{1M} are visible.

Analysis and discussion

To understand why these lasers were on the first excited mode and why the single-mode behavior was lost for high deformations, we compared various properties of the different modes obtained from 2D FDTD and complementary 2D plane wave simulations.
First, from the spatial profile of each mode, we estimated the confinement inside the guide and thus the modal gain. We found that all 4 modes experience almost identical modal gain (with a confinement above 98 %).
Then, we extracted from 2D-FDTD the loss level (the imaginary part of the propagation constant) for each mode, which is displayed on figure 5. One of the first excited mode, M_{1Z} (blue), experiences losses orders of magnitude smaller then the other 3 modes excepted for high deformations where the loss level difference tend to shrink.
This low level of losses for M_{1Z} , together with comparable modal gain could explain the single-mode lasing on the first excited mode observed in our experiment.

Moreover, there is a clear reduction in the loss level difference for high deformations, in good agreement with the experimental observation of a dual-mode behavior for the DFB lasers. This reduction could partly explain the dual mode behavior seen experimentally.
However, for high deformations, fundamental modes M_{0Z} (black) and M_{0M} (red) also experience reduced losses, whereas we never see lasing on of these modes. An explanation could lay in the DFB coupling that is way stronger for the first excited modes than the fundamental ones in this region.
Once more, these 2D simulations only account for in-plane losses and 3D FDTD simulations are needed to estimate losses out of the plane that could be different for fundamental and first order modes.

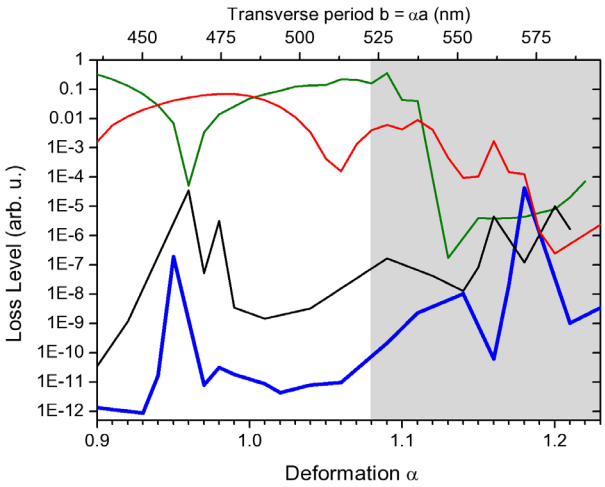


Figure 5:Loss level for the first 4 DFB modes, M_{0Z} (black), M_{0M}(red), M_{1Z} (blue) and M_{1M}(green). M_{1Z} (blue) has lower losses than all the other modes. The gray area corresponds to deformations for which lasers are dual-mode.

Conclusion

We have experimentally demonstrated a new concept for integrated DFB laser arrays based on PhC defect waveguide. The affine deformation of the crystal lattice offers an efficient way to precisely tailor the wavelength spacing between lasers of the array. The peculiar characteristic of these lasers, among which the lasing on the first excited transverse mode, is well described by planar simulations.
A. Larrue acknowledges financial support from DGA under supervision of B. Desruelle.

References

[1] Gauthier-Lafaye O et al.. "Highly monomode w1 waveguide square lattice photonic crystal lasers." *IEEE Photonics Technology Letters* (2005) **17**: pp. 1587-1589.
[2] Gauthier-Lafaye O et al.. Square lattice w1 waveguide photonic crystals lasers for telecommunications. In *Proceedings of spie "photonic materials, devices, and applications"*. 2005.
[3] Farjadpour A et al.. "Improving accuracy by subpixel smoothing in the finite-difference time domain." *Opt. Lett.* (2006) **31**: p. 2972--2974.

CW electrical operation of single-mode all photonic crystal DFB-like laser

O. Bouchard[1], A. Larrue[1], O. Gauthier-Lafaye[1], S. Bonnefont[1], P. Arguel[1], F. Lozes-Dupuy[1]
F. Pommereau[2], F. Poingt[2], L. Le Gouezigou[2], O. Le Gouezigou[2], O. Drisse[2], E. Dérouin[2], G. H. Duan[2]
[1]LAAS-CNRS, Université de Toulouse, 7 Avenue du Colonel Roche, 31077 Toulouse Cedex 4, France
olivier.gauthier-lafaye@laas.fr
[2]Alcatel Thales III-V Lab, Route départementale 128 -91767 Palaiseau Cedex, France.

Abstract. *We present results on room temperature CW electrical operation of an edge emitting, all photonic crystal laser diode. The laser is based on a DFB-like photonic crystal W5 defect waveguide and shows stable single mode emission at 1563 nm. Laser design and performances are discussed.*

Introduction

All photonic crystal (PhC) defect waveguide lasers appear as extremely promising for planar optical integration. Indeed they are by nature fully compatible with already reported integrated compact optical systems based on photonic crystals [1]. In this paper, we present results on the design optimization and CW operation of hexagonal "HW5" defect waveguides lasers showing single mode emission based on 2nd order DFB operation.

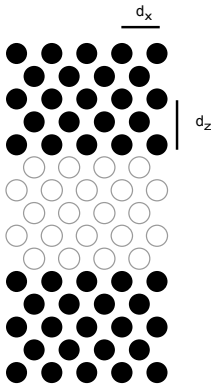


Figure 1: Schematic diagram of the deformed hexagonal lattice used for the "HW5" waveguide.

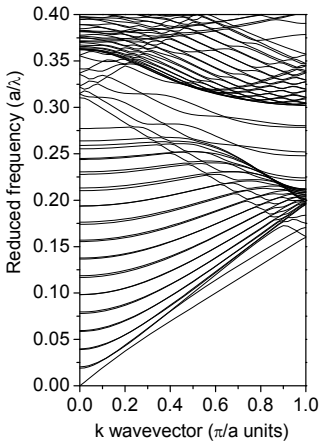


Figure 2: Band diagram of the waveguide with a deformation of -25%. Calculations used 2D PWEM method and an effective index of 3.21.

Laser design

To achieve efficient single mode lasing in the waveguide, we design our PhC waveguide so that the second folding of the first guided mode occurs at the gain peak wavelength. In that way, we plan to achieve stable 2nd order DFB-like emission of our laser [2, 3]. To minimize propagation losses and to minimize the laser threshold, we

tried to minimize possible couplings between the DFB mode and the PhC optical modes [4]. To that effect, we introduce an affine deformation of the hexagonal lattice (figure 1) to move the band gap so that the 2nd folding of the guided mode rests into it (figure 2). The final parameters of the lattice are dx = 494 nm and dz = 642 nm, with a hole radius of 123 nm. These values correspond to a deformation of -25%, as a standard hexagonal lattice with the same dx of 494 nm would require dz equal to 856 nm. Due to the deformation, the waveguide width is reduced from 2.5 µm to 1.9 µm. The waveguide is delimited by a cleaved facet on one end and on the other end by a rear hexagonal PhC mirror in the ΓM direction. The lattice constant of the mirror is 403 nm, and the air filling factor is 30%. We designed the PhC mirror so that the emission wavelength of the laser rests at the center of the band gap, to maximize the reflectivity

Results and discussion

Since the main challenge of electrical pumping is heat dissipation, we use what appears to be the most promising route to manage it, the so called "substrate approach". Samples were fabricated at Alcatel Thales III-V lab in the InGaAsP/InP material system. We use an InGaAsP based planar waveguide on InP substrate with 6 compressively quantum wells. The gain curve of the quantum wells is centered around 1.55 µm. The photonic crystal waveguide was defined using e-beam lithography and deep dry etching. The holes depth is around 4 µm, deep enough to achieve 2D like geometry [5]. Metallic contacts were then deposited on the top and bottom surface of the sample, taking care not to fill the holes so as to preserve the quality of the PhC. A gain region of about 10 µm wide was delimited by proton implantation. Samples were then thinned and cleaved into laser bars that we reported on an aluminum submount, in turn mounted on a PCB board for characterization.

Fabricated samples of different lengths ranging from 80 µm to 330 µm were characterized in the continuous regime. Figure 3 shows a typical light-current curve obtained on a 230 µm long laser at room temperature. There is a clear emission threshold around 22 mA with a slope efficiency of 0.07 W/A. The maximum emitted power is around 3 mW and is limited by temperature. As seen on figure 4, the threshold current increases with laser length, whilst the efficiency slowly decreases.

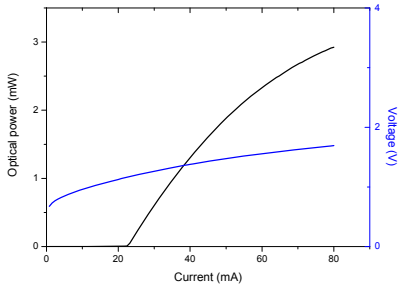


Figure 3: CW Light-current characteristic of a 230 µm long laser at room temperature.

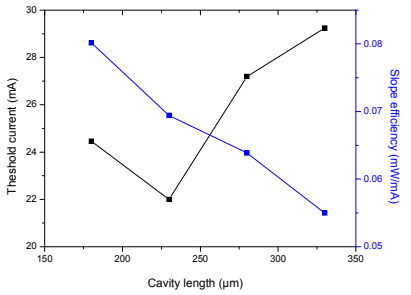


Figure 4: Evolution of the measured threshold current and slope efficiency versus cavity length.

Emission spectra of the lasers were measured using an Ando AQ6315 optical spectrum analyzer. Lasers with lengths ranging from 230 µm to 330 µm showed single mode

emission with a side mode suppression ratio (SMSR) larger than 30 dB. The single mode emission is stable with the bias current, as shown on figure 5. For shorter cavity lengths, the Fabry-Perot emission prevailed due to the influence of the rear PhC mirror. DFB operation would be favored by using an antireflection coating on the front facet and moreover the SMSR would be increased. Indeed a 400 µm long laser designed with a cleaved rear reflector showed SMSR as high as 46 dB (figure 6), with a threshold current of only 28 mA.

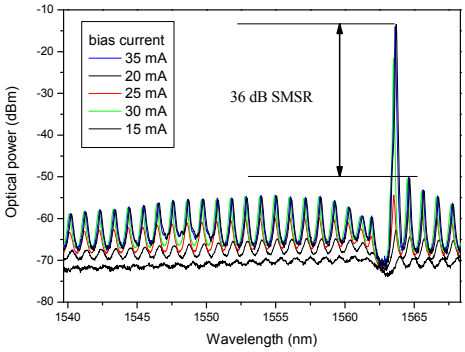


Figure 5: 330 µm long laser spectra for several bias current with a rear PhC mirror.

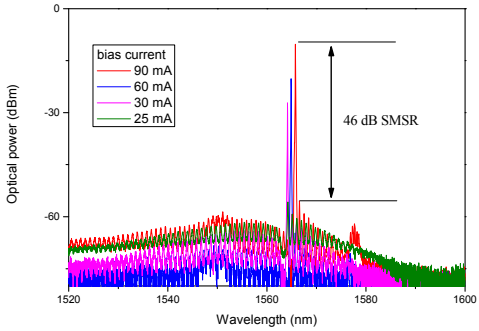


Figure 6: 400 µm long laser spectra for several bias current with a rear cleaved facet.

Similar PhC lasers without affine deformation were fabricated and tested. The crystal lattice constant was 485 nm. Lasers with a rear PhC reflector exhibited threshold current in the same range as deformed lasers and showed multimode Fabry-Perot emission. A 400 µm long laser with a cleaved rear facet presented DFB emission at 1540 nm with a SMSR of about 35 dB, with a high threshold current of 50 mA. These results show the influence of the lateral lattice parameters on the spectral characteristics and the interest in engineering the lateral lattice parameter to design and to achieve a DFB laser with a high SMSR.

Conclusion

We demonstrated CW electrically pumped, 2nd order DFB-like laser emission using an all photonic crystal defect waveguide laser. We introduced an affine deformation to limit the coupling of the DFB mode with the PhC optical modes and to force the emission in the bandgap. Experimental results show that DFB operation is improved by introducing an affine deformation in lateral dimension of the lattice. This approach will allow to achieve DFB lasers operating with high SMSR values.

A. Larrue acknowledges financial support from DGA under supervision of B. Desruelle.

References

[1] H. Benisty, J. M. Lourtioz, A. Chelnokov, S. Combrié, and X. Checoury, "Recent advances toward optical devices in semiconductor-based photonic crystals," *Proceedings of the IEE*, vol. 94, pp. 997-1023, 2006.

[2] X. Checoury, P. Boucaud, J. M. Lourtioz, F. Pommereau, C. Cuisin, E. Derouin, O. Drisse, L. Legouezigou, F. Lelarge, F. Poingt, G. H. Duan, S. Bonnefont, D. Mulin, J. Valentin, O. Gauthier-Lafaye, F. Lozes-Dupuy, and A. Talneau, "Distributed feedback-like laser emission in photonic crystal waveguides on InP substrate," *IEEE Journal of Selected Topics in Quantum Electronics*, vol. 11(5), pp. 1180-1186, 2005.

[3] O. Gauthier-Lafaye, D. Mulin, S. Bonnefont, X. Checoury, J. M. Lourtioz, A. Talneau, and F. Lozes-Dupuy, "Highly monomode W1 waveguide square lattice photonic crystal lasers," *IEEE Photonics Technology Letters*, vol. 17, pp. 1587-1589, 2005.

[4] X. Checoury, P. Crozat, J. M. Lourtioz, C. Cuisin, E. Derouin, O. Drisse, F. Poingt, L. Legouezigou, O. Legouezigou, F. Pommereau, G. H. Duan, O. Gauthier-Lafaye, S. Bonnefont, D. Mulin, F. Lozes-Dupuy, and A. Talneau, "Single-mode in-gap emission of medium-width photonic crystal waveguides on InP substrate," *Optics express*, vol. 13, pp. 6947-6955, 2005.

[5] F. Pommereau, L. Legouezigou, S. Hubert, S. Sainson, J. P. Chandouineau, S. Fabre, G. H. Duan, B. Lombardet, R. Ferrini, and R. Houdre, "Fabrication of low loss two-dimensional InP photonic crystals by inductively coupled plasma etching," *Journal of Applied Physics*, vol. 95, pp. 2242-2245, 2004.

Efficient Injectors for Slow light Photonic Crystal waveguides

L.O'Faolain[1], T. P. White[1], M. V. Kotlyar, D. O'Brien[1]and T.F.Krauss[1]

[1]University of St Andrews
jww1@st-andrews.ac.uk

Abstract. *Efficient coupling in the slow light regime of photonic crystal waveguides is a key prerequisite for many designs. In this paper, we describe an easily implanted injector that promises high coupling efficiency for values of n_g up to 100 and show experimental results demonstrating the usefulness of this technique.*

Introduction

The realization of devices that may control the group velocity of light propagating in photonic waveguides has a number of important applications and is receiving considerable interest among researchers. By reducing the group velocity, the light-matter interaction may be considerably enhanced enabling the creation of devices that perform useful functionalities with lower powers and smaller devices than otherwise possible. Linear interactions, including gain and the electro-optic effect, scale with the slowdown factor (the ratio between the group and phase velocities). Nonlinear interactions then scale with the square of the slowdown, as there is both a phase and an intensity enhancement [1].

Slow light photonic crystal devices promise to be very advantageous for the Silicon on Insulator (SOI) system. Very high quality passive silicon photonic crystals have been reported in the literature [2, 3], however, the absence or weaknesses of many non linearities in silicon have hampered the development of active devices. By using the slow light enhancement, more useful devices may be created, thereby capitalizing on the many advantages of the CMOS compatible SOI system.

There have been a number of promising results on slow light photonic crystals both passive [4] and active [5], but a recurring issue is the low coupling into the slow light regime of the photonic crystal from a photonic wire. Vlasov *et al.* have shown that the termination between the wire and crystal strongly affects the efficiency, with small fabrication errors in this area, having a considerable effect [6]. Recently, Hugonin *et al.* [7] and Marris-Moroni *et al.* [8] have theoretically investigated adding an intermediate photonic crystal region between the slow light photonic crystal and the photonic wire. The principle of this technique is to couple light from the wire into the fast mode of the photonic crystal (in the coupler region) and then from this fast mode into the target slow mode of the main photonic crystal.

In this paper, we fabricate photonic crystal W1 waveguides with intermediate photonic crystal coupling regions (referred to as W') and test the improvement in coupling efficiency using transmission measurements.

Theory and Design

The coupling between a photonic wire and the fast mode of a W1 has been shown to be very good- over 90% [6]- as the modal size and group index are reasonably well matched. This suggests the addition of an intermediate region, W', (with a larger lattice

constant and, thus, a faster mode for a given wavelength) as a solution to coupling to slow W1 modes.
We have considered a number of possible configurations for this region, such as slowly chirping the lattice into the main crystal, rapidly chirping and an abrupt change. Somewhat surprisingly the abrupt termination proved the most successful. Numerical simulations then showed that in spite of the abrupt change, the field actually experiences a transient zone, allowing the light to smoothly build up in intensity (while slowing down), see figure 1a.

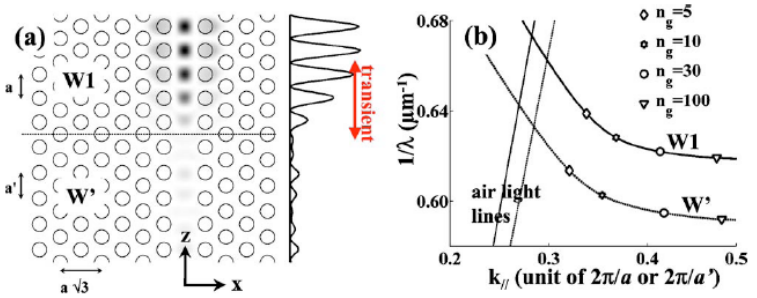


Figure 1: Simulations performed using a Bloch mode Fourier modal method, showing the smooth transition between the injector region and the main crystal (a). Dispersion relations for the W1 and W1 regions are shown on the right (b) [7].

Efficiencies as high as 80% for the coupling into the slow mode at n_g=100 have been predicted with this technique [7].
As this is quite a simple technique, the experimental implementation is straightforward and easily applied in practice. Figure 2 shows how we chose to realize the injector region. For the 10 rows immediately next to the interface with the photonic wire, the hole spacing along the direction of the defect is increased, thus, enlarging the lattice constant and pushing the mode to longer wavelengths, creating the W' region as in figure 1b.

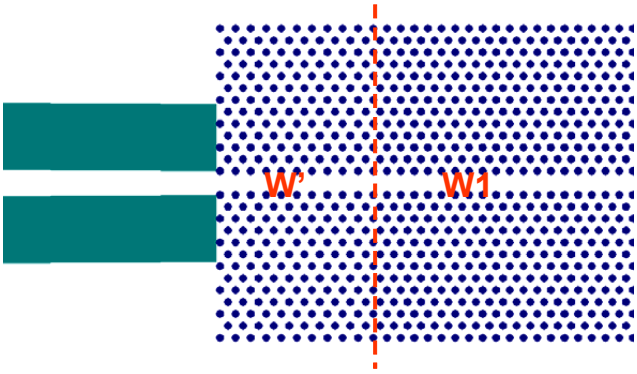


Figure 2: An example of a W1 photonic crystal waveguide with a coupling region (W') between the slow light region (W1) and the access photonic wire. The lattice constant along the direction of the defect is enlarged in the coupler region. For illustrative purposes the enlargement shown here is 50 nm.

Fabrication

The devices were fabricated on a SOITEC Silicon on Insulator wafer comprising a 220 nm thick Silicon layer on 2 μm of silica. The pattern was exposed in ZEP520A electron

beam resist using a hybrid ZEISS GEMINI 1530/RAITH ELPHY electron beam writer at 30 keV with a pixel size of 2 nm and a writing field of 100 μm. The resist was developed using xylene with ultrasonic agitation. Pattern transfer was carried out using Reactive Ion Etching with CHF_3 and SF_6 gases. The silica beneath the photonic crystal was removed using Hydrofluoric acid (the rest of the pattern was protected with photoresist).
The fabrication of these devices was carried out in the framework of the ePIXnet Nanostructuring Platform for Photonic Integration [9] and was very similar to that used in [2]. A propagation loss of 12 db/cm was measured for benchmark W1 waveguides.

Transmission Measurements

The devices were characterized using an endfire setup with a broadband LED source source. Figure 3 shows a comparison between W1s with and without the W' injector region. As the mode cutoff is approached (at a wavelength of approx. 1545nm) and the group velocity of the mode reduces, the improvement due to the injector region becomes very apparent- for example, at a wavelength of 1540nm, the transmission of the W1 with the injector is twice that of the normal W1.

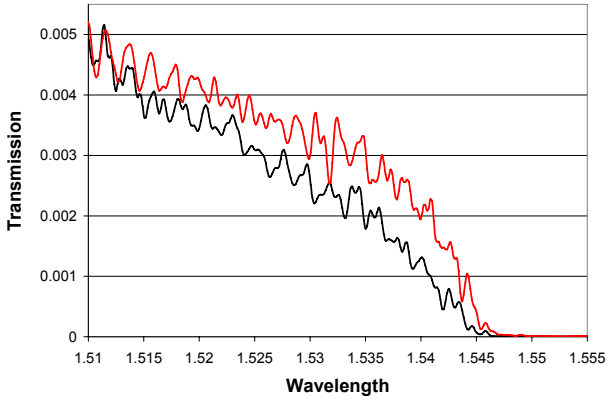


Figure 3: Transmission spectra for a normal W1 (black) and a W1 with 10 period injector regions with a 20 nm period enlargement (red). The nominal lattice constant was 420 nm and the W1 length was 200 μm. The shape of the transmission curves is also influenced by the propagation loss, which is higher in the slow light regime.

The injector region is also expected to improve the tolerances for the fabrication of the interface between the photonic wire and photonic crystal. Normally, nanometer scale imperfections may have significant effects on the transmission but as this region now only affects the coupling from the wire into the fast mode, its significance is much reduced.

Conclusion

An injector region has been implemented that significantly improves the coupling to the slow regime of W1 photonics crystals. This technique may be expected to add to the performance of many slow light photonic crystal designs. Further work will involve the investigation of the more advanced injector proposed in [7], which is predicted to have superior performance in the n_g>100 region.

Acknowledgments

The authors would like to thank George Robb and Steve Balfour for help with experiments and Phillip Lalanne for useful discussions.

References

[1] T.F. Krauss, "Slow light in Photonic Crystal Waveguies", J. of App. Phys D, vol. 40, pp. 2666-2670, 2007.

[2] L. O'Faolain, X. Yuan, D. McIntyre, S. Thoms, H. Chong, R.M. De La Rue and T.F. Krauss, " Low-loss propagation in photonic crystal waveguides", Electron. Lett, vol. 42, pp. 1454-1455, 2006.

[3] E. Dulkeith, S. J. McNab and Y. A. Vlasov, "Mapping the optical properties of slab-type two-dimensional photonic crystal waveguides", Phys Rev. B, vol. 72, p. 115102, 2005.

[4] M. Notomi, K. Yamada, A. Shinya, J. Takahashi, C. Takahashi and I. Yokohama, "Extremely Large Group-Velocity Dispersion of Line-Defect Waveguides in Photonic Crystal Slabs", Phys. Rev. Lett., vol. 87, p. 253902, 2001.

[5] Y. A. Vlasov, M. O'Boyle1, H. F. Hamann and Sharee J. McNab, "Active control of slow light on a chip with photonic crystal waveguides", Nature, vol. 438, pp. 65-69, 2005.

[6] Y. A. Vlasov and S. J. McNab, "Coupling into the slow light mode in slab-type photonic crystal waveguides", Opt. Lett., vol. 31, pp 50-52, 2006.

[7] J. P. Hugonin, P. Lalanne, T. P. White, and T. F. Krauss, "Coupling into slow-mode photonic crystal Waveguides," Opt. Lett., vol. 32, pp. 2638-2640, 2006.

[8] D. Marris-Morini, E. Cassan, D. Bernier, G. Maire and L. Vivien, "Ultracompact tapers for light coupling into two dimensional slab photonic-crystal waveguides in the slow light regime," Opt. Eng., vol. 47, p. 014602, 2008.

[9] http://www.nanophotonics.eu

Low propagation loss photonic wire and ring resonator devices in silicon-on insulator using hydrogen silsesquioxane electron-beam resist

A. Samarelli[1], M. Gnan[1,2], R. M. De La Rue[1], M. Sorel[1]

[1]Glasow University, Glasgow, United Kingdom
[2]Department of Engineering, University of Ferrara, Ferrara, Italy,
antonios@elec.gla.ac.uk

Abstract. *We demonstrate propagation loss as low as 1 dB/cm in photonic wire waveguides based on Silicon-on-Insulator. A high repeatability process based on hydrogen silsesquioxane electron-beam resist (HSQ) is demonstrated with small dispersion of the resonance frequency of coupled micro-ring resonators and optical delay lines.*

Introduction

Silicon-on-insulator (SOI) technology is a promising platform for constructing functional micro-scale optical devices for a high density photonic integration. Sub-micron cross-section waveguides and micrometer-size bend radii are allowed by the high refractive-index contrast between silicon and typical cladding materials such as silica.

The small dimensions also imply the need for stringent manufacturing tolerances and for reduction of the sidewall roughness that is the main source of the propagation losses due to scattering. With optimized etching processes, lithographic pattering becomes the only significant source of imperfection –through sidewall roughness.

In most work to date, electron-beam resists such as PMMA and ZEP together with a transfer mask layer of silica or silicon nitride, have been used to transfer the require device pattern into the substrate. But in the recent years Hydrogen silsesquioxane (HSQ) has proven to be a promising electron-beam resist because it combines high resolution at a moderate sensitivity, with minimal line edge roughness, together with a substantial level of etch resistance. Despite of all these positive characteristics, several papers have shown that HSQ suffers from significant process delay effects that result in a fluctuation of the optimum e-beam dose and pattern size.

In this work we show that very low propagation loss silicon wires and low resonance-frequency dispersion coupled micro-ring resonators can be fabricated by using HSQ e-beam resist. The patterning process was optimized both in terms of its repeatability, accuracy and edge roughness.

Fabrication

A 220-nm silicon core layer on 1-μm buried oxide sample of SOI wafer from SOITEC was spin-coated with a FOX16-HSQ, diluted with MIBK at a ratio of 1:1. All the structures were patterned using a VISTEC VB6 electron-beam lithography (EBL) machine and a SF_6 plus C_4F_8 gas combination in an STS-ICP machine. The cross-

section of the resulting fabricated waveguides is 500 x 220 nm^2 which provides single-mode operation in the third telecommunications wavelength window.

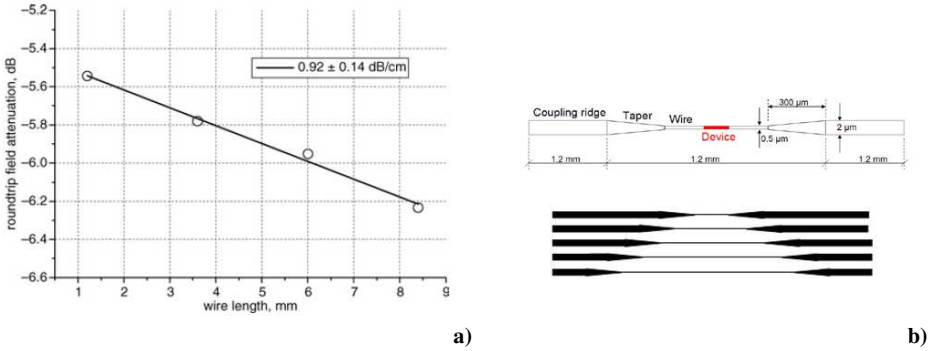
Loss Measurements

Propagation loss reduction is critical for the development of photonic wire based devices in SOI. Given the high quality of the SOI wafers available, the major source of propagation losses is the scattering due to sidewall roughness [1].

Optimizing the HSQ process parameters (baking time and temperature, thickness of the mask layer) and etching conditions (temperature, gas flow rate and pressure), we have achieved substantial improvements in comparison with previous values (~ 2-3 dB/cm) and have measured propagation losses just below 1 dB/cm, with a standard deviation of 0.14 dB/cm [2], for a photonic wire waveguides without silica upper-cladding, as is shown in Fig. 1. To our knowledge this is the lowest value reported for a non-embedded photonic wire.

We extracted the propagation loss value using a combination of Fabry-Perot fringe and cut-back techniques for a set of waveguides with different lengths varying between 1 mm to 9 mm, adiabatically tapered to 2 µm wide coupling ridge waveguides.

The FP fringes generated by the cleaved facets allow the extraction of the round-trip attenuation independently of the input optical power coupled into the system.



a) **b)**

Fig. 1: a) Loss measurements obtained using the combined FP and cut-back technique. **b)** Schematic of the standard waveguide design with the input/output tapered waveguides (top) and device layout for the cut-back loss measurement technique (bottom) [2].

Coupled Ring Resonators

Optical delay lines can be formed by using a cascade of resonant cavities [3] e.g. ring resonators (Fig. 2a) coupled together that slow the propagation of through the combined effects of resonance and increased optical path length.

All-Pass Filters (APF) can be constructed from a series of distinct photonic wire ring-resonators separately coupled to a single photonic wire bus (see Fig. 2b).

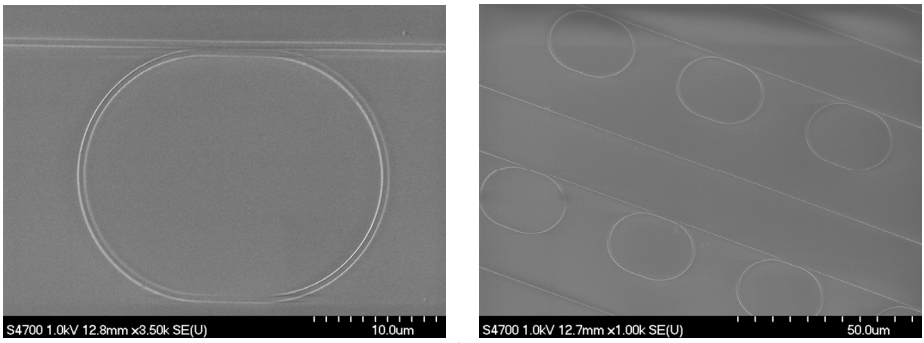


Fig. 2: SEM micrographs of **a)** Singe ring resonator. **b)** All pass filter multiple ring resonators configuration.

Mismatch between the resonance frequencies related to each ring has the additional effect of broadening the spectrum – and such mismatch can compromise the correct operation of the fabricated device structures. The HSQ-based fabrication technology suffers from significant aging effects. In particular, the dose changes significantly with the elapsed time from dilution of the base material, even when the resist is stored in a refrigerator. The resulting expansion or contraction of the written pattern modifies the characteristic properties of the devices produced.

An assessment of the optical resonance of single and cascaded racetrack resonators provides information on both the long-term stability and uniformity of the HSQ e-beam resist [4].

We have fabricated 500 nm wide and 20 μm bend radius ring-resonators, transversely coupled to a bus waveguide in APF configuration. To increase the coupling strength, straight waveguide coupling regions with a length, L, of 10 μm have been introduced into the design. The gap between the bus waveguide and the coupling region of the ring was 150 nm.

A 1 μm thick upper-cladding layer of silica is deposited by PECVD, to reduce the dependence of the device characteristics on the etching depth, all the samples were slightly over-etched and subsequently covered with silica. Antireflection coatings were deposited after the cleaving of the sample section, in order to reduce the Fabry-Perot resonance effects.

We have produced device structures using newly diluted HSQ at different times over a period of several weeks and have obtained more consistent results than those obtained by preparing a single dilution of HSQ to be used over the same period; Fig. 3(a) shows the resonances obtained from two devices fabricated at times separated by five days, from the same batch of diluted HSQ.

A shift in the resonance wavelength of 0.33 nm was observed, corresponding to a change in waveguide width of 0.43 nm.

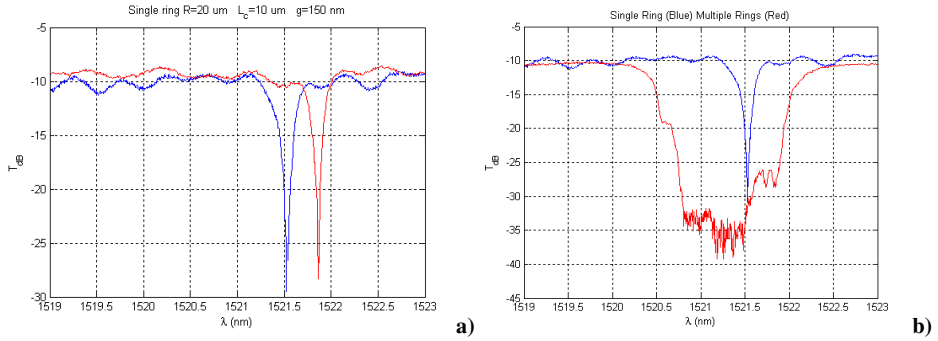


Fig. 3: Measurements of the resonance for (**a**) two different single ring devices fabricated on different days on two different substrates, (**b**) a single ring and 64 rings fabricated on the same substrate.

The results of a second experiment using 64 separate ring resonators along a bus waveguide are shown in Fig 3 (b). From the broadening of the resonance peak, it can be deduced that the average variation of the resonance wavelengths over the cascade of 64 rings is approximately 0.7 nm.
This result also provides a test of the fidelity of the proximity effect correction used in the electron-beam writing process, since the rings at either end of the cascade require different doses to those in the centre.

Conclusions

In conclusion, propagation losses and aging effects of the HSQ were accurately measured in single-mode silicon wire waveguides. Propagation losses as small as 0.92 ± 0.14 dB/cm were measured by a combined Fabry-Perot fringes and cut-back techniques.
Samples made with newly diluted HSQ resist have shown more consistent results than those obtained by preparing a single dilution of HSQ to be used over the same period. This suggests the use of a fresh dilution all the times that the dimensions are critical for the performance of a device e.g. photonic crystals, photonic micro-cavity, waveguide gratings, etc.
These loss figures and the development of HSQ lithographic processes are useful for further development of silicon photonics circuits on SOI technology.

References

[1] K.K. Lee, D.R. Lim, H.C. Luan, A. Agrawal, J. Foresi and L.C. Kimerling, "Effect of size and roughness on light transmission in a Si/SiO2 waveguide: Experiments and model", App. Phys. Lett. 77, pp. 1617-1619, 2000.

[2] M. Gnan, S. Thoms, D.S. Macintyre, R.M. De La Rue and M. Sorel, "Fabrication of low-loss photonic wires in silicon-on-insulator using hydrogen silsesquioxane electron-beam resist", Electronics Letters, vol. 44 n. 2, 2008.

[3] A. Yariv, Y. Xu, R.K. Lee and A. Scherer, "Coupled-resonator optical waveguide: a proposal and analysis", Optics Letters, vol. 24 n. 11, pp. 711-713, 1999.

[4] F. Xia, L. Sekaric and Y. Vlasov, "Ultracompact optical buffers on a silicon chip", Nature Photonics, vol. 1, pp. 65-71, 2007.

High quality optical microring resonators in Si_3N_4/SiO_2

Andrzej Kaźmierczak[1], Laurent Vivien[2], Kristinn B. Gylfason[3], Benito Sanchez[4], Amadeu Griol[4], Delphine Marris-Morini[2], Eric Cassan[2], Fabian Dortu[1], Hans Sohlström[3], Domenico Giannone[1] and Daniel Hill[4]

[1]Applied Photonics Department, Multitel a.s.b.l.. Mons, Belgium
andrzej.kazmierczak@multitel.be
[2]Institut d'Electronique Fondamentale, CNRS UMR 8622, Université Paris-Sud 11, 91405 Orsay, France
[3]Microsystem Technology Laboratory, School of Electrical Engineering, KTH – Royal Institute of Technology, Stockholm, Sweden
[4]Nanophotonics Technology Center, Universidad Politécnica de Valencia, Valencia, Spain

Abstract. *We have experimentally demonstrated high Q-factors strip waveguide resonators using the Si_3N_4/SiO_2 material platform at the wavelength of 1.31μm. The analyzed filters demonstrate high quality factors reaching 133,000. The dependence on resonator radii and coupling gap is also discussed.*

Introduction

The usefulness of integrated microring resonators has been demonstrated in numerous applications, including optical signal filtering [1], switching [2] and modulation [3], as well as biological and environmental sensing [4]. Usually silicon on insulator (SOI) is an attractive platform to make such photonic structures, featuring high index contrast ($\Delta n \approx 2$) between silicon and its oxide and therefore further leading to high integration and possible miniaturization of the photonic devices. However, the high optical index contrast makes the device highly sensitive to fabrication imperfections (e.g. sidewall roughness) [5]. The use of silicon nitride (Si_3N_4) instead of silicon permits reducing index contrast to $\Delta n \approx 0.5$, offering a higher tolerance to fabrication imperfections, while maintaining low cost and a reasonable level of integration [6].
In this paper we analyze silicon nitride microring resonators based on strip waveguides. According to the experimental results, the influence of ring resonator radius as well as the coupling gap is analyzed. Finally the high quality factor of the resonator is shown.

Design of the optical filters

The simplest topology of an optical filter based on a microring resonator is composed of a bus waveguide evanescently coupled to a single ring resonator presented in Fig.1.

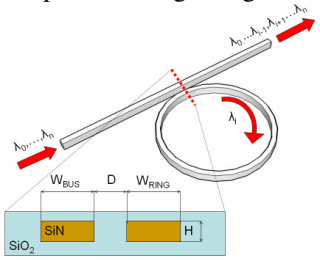


Fig.1. Schematic view of the wavelength selective filter with single bus waveguide side-coupled to the ring resonator

In the presented configuration, the device acts as a wavelength selective stop-band filter, where the resonant wavelengths are dropped to the resonator and do not propagate within the bus waveguide.
The considered geometry of the strip waveguide is the following: height H=300 nm, W_{bus}=W_{ring}=900 nm. The D gap ranges between 400 and 700 nm and the ring radius ranges between 80 and 120 nm.
Fig. 2 presents simulations of the fundamental mode profile of Si_3N_4 strip waveguide. The obtained effective index of a fundamental mode is equal to 1.59 and the group index of the mode equal to 1.913.

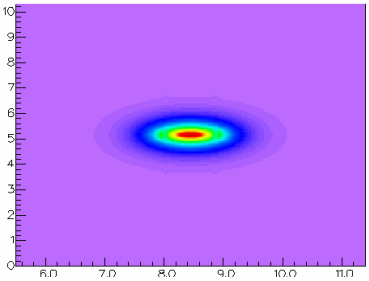


Fig.2: Simulation of a Si_3N_4 strip waveguide TE electrical field profile obtained at the wavelength of 1.31µm

Fabrication of experimental structures

A 3.3 µm thick silicon dioxide bottom cladding was grown on a silicon substrate by wet thermal oxidation at 1100°C. The 300 nm thick silicon nitride core layer was then deposited by LPCVD at 800°C from NH_3 and SiH_2Cl_2 precursors. A hard mask was patterned by electron beam lithography of PMMA, followed by a chromium evaporation and lift-off. The waveguide pattern was then transferred to the core layer by dry etching in a He/CF_4 plasma. Finally, the guides were covered by a 530 nm silicon dioxide top cladding by TEOS LPCVD at 720°C.
Fig.3 shows the SEM micrograph of the coupling section between the bus waveguide and the microring resonator.

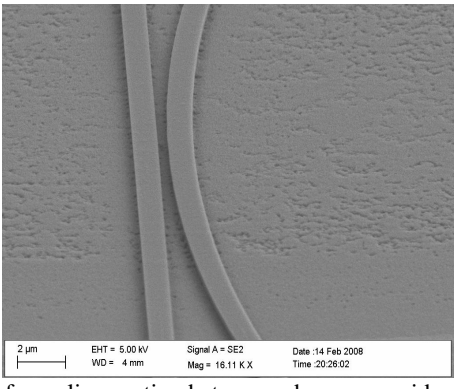


Fig.3. SEM micrograph of coupling section between a bus waveguide and a microring resonator

Experimental validation of test structures

The transmission spectra of fabricated test structures have been experimentally investigated by means of a micrometric optical setup and a tunable laser source.

Fig.4 shows the transmission spectrum of a strip waveguide microring resonator of radius R=90 µm and gap D=700 nm.

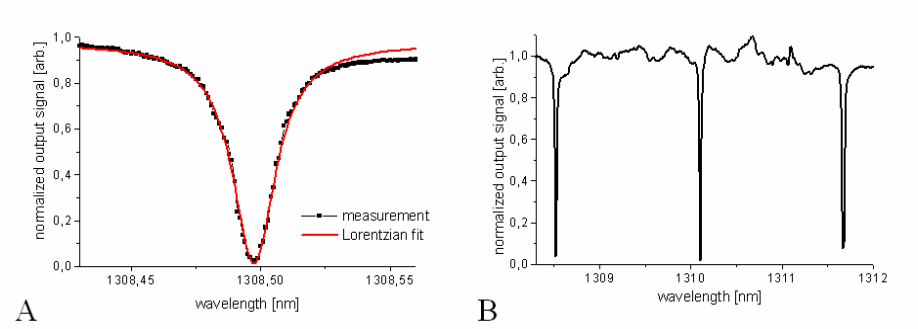
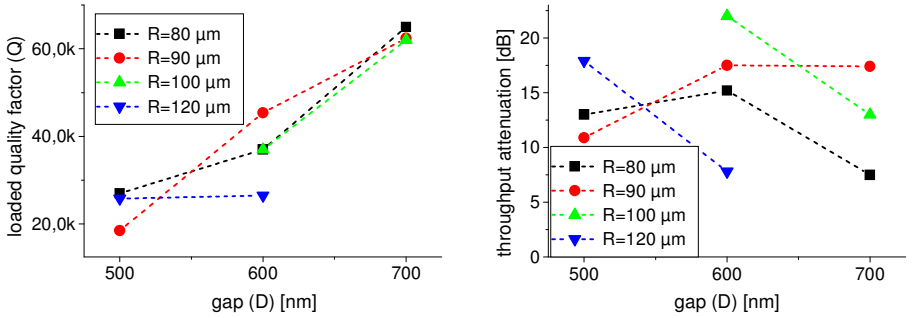


Fig.4. Transmission spectrum of a wavelength selective filter based on Si_3N_4 ring resonator. a) close-up on the resonant peak, b) the free spectral range of the filter

The normalized transmitted power has been measured in the wavelength range 1308.400–1305.570 nm with a step of 1 pm, so as to resolve the extremely narrow resonance peak of the filter (Fig.5a). The peak shows a resonance wavelength of 1308.497nm ± 10^{-3}nm and a full width at half maximum (FWHM) of 17pm, corresponding to a loaded (measured) quality factor (Q) of 77,000 and the intrinsic quality (Q_i) of 133,000. The extinction ratio reaches 15.9 dB. The free spectral range (FSR) of the filter has also been characterized experimentally by enlarging the wavelength range of the measurement to 1308.25–1312.00 nm with a step of 10pm (Fig.5b). Three resonant peaks are observed at 1308.50 nm, 1310.07 nm and 1311.68 nm, respectively, giving an average FSR of 1.59 nm ± 0.01 nm. These measurement results allow calculating the effective group index of the strip waveguide resonator mode that is equal to 1.91 that is in good agreement with the theoretical investigations.

Fig.5 depicts dependence of measured filter parameters on resonator radii and coupling gap between bus waveguide and microring.
In the case of resonators with radius between 80 µm and 100 µm, the loaded quality factor strongly depends on the coupling gap between resonator and bus waveguide. Indeed for the gaps ranging between 500 nm and 700 nm, the quality increases with the gap increment reaching more than 60000. It can be explained with lower coupling losses. In the case of the resonators with 120 µm radius, the quality does not exceed 30000 and only slightly depends on coupling gap. This could be explained by dominating propagation losses being the limitation of quality factor. In contrary for the resonators of radii between 80 µm and 90 µm bending losses dominates as the quality increases with radius increment.
A similar observation can be made when the throughput attenuation of the filters is analyzed. In the case of resonators with radii varying from 80 up to 100 µm it reaches

the highest value (exceeding 15dB) for the coupling gap of 600 nm. In the case of the resonator with 120 µm, where coupling is weaker due to more open bend the highest attenuation is obtained for the smallest analyzed gap of 500 nm.



a) b)

Fig.5. Comparison of the loaded quality factor (a) and throughput attenuation (b), for filters with different resonator radii and coupling gaps

Conclusion

We have demonstrated wavelength selective filters with high quality factors from microring resonators based on silicon nitride strip (Q_i=133,000) waveguides. We discussed the influence of the filter parameters such as resonator radius and coupling gap on the quality factor of the filters.

Acknowledgments

This work is done within the FP6-IST-SABIO project (026554), funded by the European Commission. K.B. Gylfason would like to acknowledge support of the Steinmaur Foundation, Liechtenstein.

References

[1] B. E. Little, J. S. Foresi, G. Steinmeyer, E. R. Thoen, S. T. Chu, H. A. Haus, E. P. Ippen. L. C. Kimerling, and W. Greene, "Ultra-compact *Si–SiO*$_2$ microring resonator optical channel dropping filters," IEEE Photon. Technol. Lett. 10, 549-551 (1998)

[2] A. Kazmierczak, M. Brière, E. Drouard, P. Bontoux, P. Rojo-Romeo, I. O'Connor, X. Letartre, F. Gaffiot,R. Orobtchouk, and T. Benyattou, "Design, simulation, and characterization of a passive optical add-drop filter in silicon-on-insulator technology," IEEE Photon. Technol. Lett. 17, 1447–1449 (2005).

[3] Q. Xu, S. Manipatruni, B. Schmidt, J. Shakya, M. Lipson, "12.5 Gbit/s carrier-injection-based silicon microring silicon modulators", Opt Express 15, 430-436 (2007).

[4] K. De Vos, I. Bartolozzi, E. Schacht, P. Bienstman, and R. Baets, "Silicon-on-Insulator microring resonator for sensitive and label-free biosensing," Opt. Express 15, 7610-7615 (2007)

[5] F. Grillot, L. Vivien, S. Laval, D. Pascal, and E. Cassan, "Size Influence on the Propagation Loss Induced by Sidewall Roughness in Ultrasmall SOI Waveguides," IEEE Photon. Technol. Lett. 16, 1661-1663 (2004).

[6] N. Daldosso, M. Melchiorri, F. Riboli, M. Girardini, G. Pucker, M. Crivellari, P. Bellutti, A. Lui, and L. Pavesi, "Comparison among various Si3N4 waveguide geometries grown within a CMOS fabrication pilot line," J. Lightwave Technol. 22, 1734-1740 (2004).)

Analysis of Raman lasing in integrated small-volume silicon-on-insulator racetrack resonators

M. Waldow, M. Först, and H. Kurz

Institut für Halbleitertechnik, RWTH Aachen, Germany
waldow@iht.rwth-aachen.de

Abstract. *We present a detailed simulation-based analysis of Raman lasing in small-volume silicon-on-insulator racetrack resonators. Continuous-wave Raman lasing in submicron-sized resonant waveguide devices can be expected without the need of additional electronic structures, with a significant improvement in threshold power, device footprint and laser efficiency compared to state of the art integrated Raman lasers on silicon.*

Introduction

One elementary building block within the emerging field of Silicon Photonics is an efficient integrated laser source. In the last years rapid progress in the development of Raman lasers as integrated laser sources has been made [1], [2]. So far, experimentally demonstrated silicon-based Raman lasers comprise low-loss waveguides with large cross-sections above 1.5 μm² and exhibit overall footprints larger than 5.5 mm² [1], [2]. As the stimulated Raman scattering cross section is proportional to the intensity of the pump laser inside the silicon waveguide, it is desirable to use small-size waveguides. Another benefit of small size waveguides is the strongly reduced carrier lifetime compared to large size waveguides [3], as the free carrier lifetime determines the dominating loss mechanism of free carrier absorption in Raman lasers.
By the use of racetrack resonators high quality factors over a large wavelength range can be achieved [4]. These properties make these devices well suited for integrated Raman laser cavities. In the following we will present a model for analyzing the Raman laser characteristics in integrated racetrack resonators on silicon. With this model we analyze for the first time Raman lasing in ultrasmall waveguide resonators on silicon. We show that it is possible to develop a Raman laser with submicron-sized waveguides based on a racetrack resonator with a magnificent improvement in threshold power, laser efficiency, device footprint and without the need of additional electronic structures.

Modeling

Figure 1 shows a schematic view of the racetrack resonator structure studied here. The resonator is pumped with laser light at the pump wavelength λ_p, which is coupled to the resonator and generates the laser signal at the Stokes wavelength λ_s by stimulated Raman scattering. The amount of power coupled to or from the resonator is described by power coupling coefficients κ_p^2 and κ_s^2 at the pump and Stokes wavelengths.
The propagation of pump and Stokes powers (P_p, P_s) per resonator roundtrip can be described by two coupled differential equations [5], [6]. Within our model pump depletion, two photon absorption (TPA) and free carrier absorption (FCA) are included. Here, $\alpha_{p/s}$ are the linear waveguide losses at the pump and Stokes wavelengths, g_R is the Raman gain coefficient and β=0.5 cm/GW is the TPA coefficient of silicon [1], [2].

$$\frac{dP_p}{d\xi} = -\alpha_p P_p - \frac{g_R}{A_{eff}}\frac{\lambda_s}{\lambda_p} P_s P_p - \frac{\beta}{A_{eff}}\left(P_p^2 + 2P_p P_s\right) - \sigma(\lambda_p) N P_p \qquad (1)$$

$$\frac{dP_s}{d\xi} = -\alpha_s P_s + \frac{g_R}{A_{eff}} P_p P_s - \frac{\beta}{A_{eff}}\left(P_s^2 + 2P_p P_s\right) - \sigma(\lambda_s) N P_s \qquad (2)$$

In the last terms of Eqs. (1) and (2), σ represents the wavelength dependent FCA cross section and N is the charge carrier density resulting from TPA.

$$N = \frac{\beta \tau_{eff}}{2E_p A_{eff}^2}\left(P_p + P_s\right)^2 \qquad (3) \qquad \sigma(\lambda) = 1.45 * 10^{-17}\left(\frac{\lambda}{1.55\mu m}\right)^2 cm^2 \qquad (4)$$

In Eq. (3) τ_{eff} is the effective carrier lifetime inside the silicon waveguide and E_p is the photon energy at the pump wavelength, where the assumption $E_p \approx E_s$ is made. For an adequate description of the nonlinear interaction area we use an overlap integral between the mode profiles at pump and Stokes wavelengths based on the definition presented in [7]:

$$A_{eff} = \frac{\mu_0}{\varepsilon_0 n_{Si}^2} \frac{\left|\iint_{Atot} \Re\{\vec{E}_p \times \vec{H}_p\}\vec{e}_z dxdy\right| * \left|\iint_{Atot} \Re\{\vec{E}_s \times \vec{H}_s\}\vec{e}_z dxdy\right|}{\iint_{ASi} \left|\vec{E}_p\right|^2 * \left|\vec{E}_s\right|^2 dxdy} \qquad (5)$$

In order to describe the resonator behavior, the boundary conditions at the coupling region of the resonator have to be included. Inside the resonator the following equations, for pump and Stokes power for the i^{th} roundtrip inside the resonator can be derived:

$$P_s''(i) = t_s^2 P_s'(i-1), \; P_p''(i) = t_p^2 P_p'(i-1) + P_p'(0) + 2t_p\kappa_p\sqrt{P_p'(0)P_p'(i-1)}, \; t_{p/s}^2 + \kappa_{p/s}^2 = 1 \qquad (6)$$

It is assumed, that pump and Stokes wavelengths match precisely a resonance wavelength of the racetrack resonator. Equations (1)-(6) are solved iteratively until a steady state for pump and Stokes power after n iterations is reached. The output power of the Raman laser at the Stokes wavelength is then calculated as $P_{Raman}=\kappa_s^2 P_s'(n)$.

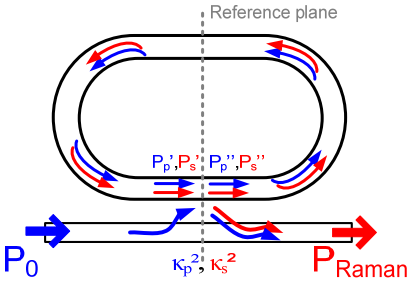


Fig.1: Schematic view of a racetrack resonator. P_0 represents the initial pump power, P_{Raman} the output power of the Raman laser at the Stokes wavelength λ_s. $\kappa_{p/s}^2$ describe the wavelength dependent coupling coefficients between bus waveguide and resonator.

Results and discussion

In order to demonstrate the reliability and performance of our model we apply the equations above to an experimentally demonstrated Raman laser based on a racetrack resonator of large-size SOI rib waveguides [2]. For all presented modeling results in this contribution a pump wavelength of λ_p=1550nm and a Stokes wavelength of λ_s=1686nm is used. All coupling coefficients for the different resonators were also taken from [2].

Used modeling parameters as given in [2] are L_{cav}=3 cm, $\alpha_{s/p}$=0.6±0.1 dB/cm, τ_{eff}=1 ns and g_R=9.5 cm/GW.

Figure 2 shows the Raman laser output power P_{Raman} for different input pump powers P_0. Solid lines represent our numerical simulations and corresponding measured data points are taken from [2]. Obviously, our modeling results are in excellent agreement with the experimental data, demonstrating the suitability of our model to analyze Raman lasing in SOI racetrack resonator structures.

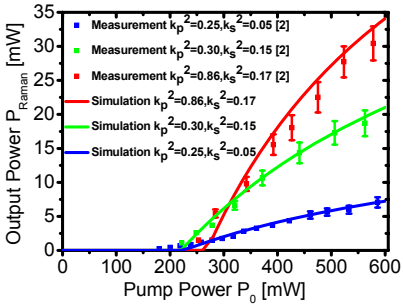


Fig.2: Output power Raman laser over input pump power. Shown are the experimental data taken from Ref. [2] and our simulation results (solid lines) for different coupling coefficients $\kappa_{p/s}^2$.

Subsequently we apply our model to resonator structures with ultrasmall cross sections. We consider SOI waveguides of 400 nm width and 340 nm height. After simulating the mode profiles for pump and Stokes wavelengths with the finite element software HFSS the effective modal area was calculated to A_{eff}=0.15 µm². For the Raman gain coefficient g_R we used the value of g_R=30 cm/GW, which has been experimentally determined for small-size waveguides with comparable cross-sections [8], [9]. We model a ring resonator of 100 µm radius equivalent to about a 24-fold reduction in resonator length compared to Raman lasers on silicon demonstrated up to now.

For this resonator configuration power coupling factors of κ_p^2=0.12 and κ_s^2=0.09 were calculated using coupled mode theory. The value of κ_p^2 is close to critical coupling at the chosen resonator geometry for state of the art waveguide losses of 2 dB/cm [4], [10]. The effective carrier lifetime is determined by interface and surface recombination velocities and can be estimated to τ_{eff}=1.2ns for the given waveguide geometry [3]. Figure 3(a) shows the Raman output power P_{Raman} versus input pump power P_0 for different linear propagation losses $\alpha=\alpha_p=\alpha_s$. The laser threshold power increases with increasing linear waveguide losses and the Raman output power saturates at higher input powers due to TPA induced FCA. An extremely low threshold power level of 6.9 mW for state of the art waveguide losses can be expected. This presents about a threefold reduction in power threshold level compared to the lowest threshold level presented so far for large size rib waveguide resonators [1].

Fig. 3(b) shows the Raman output power P_{Raman} over input pump power P_0 for different effective carrier lifetimes τ_{eff}. It becomes clear, that at shorter effective carrier lifetimes larger laser efficiencies can be reached. Assuming an effective carrier lifetime of τ_{eff}=50ps, which has already been demonstrated using a p-i-n-diode ring resonator in small size waveguides [11], a total laser efficiency of 30.1 % at P_0=100 mW can be achieved. This represents more than twice of the highest efficiency of silicon Raman lasers realized so far .in large size rib waveguides.

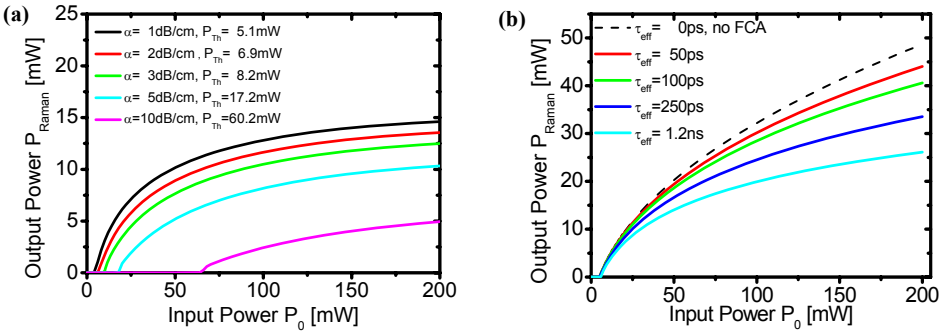


Fig. 3: (a) Raman output power P_{Raman} vs. input pump power P_0 for different linear propagation losses $\alpha=\alpha_p=\alpha_s$ and τ_{eff}=1.2 ns. (b) Raman output power P_{Raman} vs. input pump Power P_0 for different effective carrier lifetimes τ_{eff} and α=2 dB/cm.

Conclusion

An effective model to predict the output characteristics of racetrack resonator based integrated continuous wave Raman lasers on silicon is presented, predicting better performance as reported up to now. The key point is the scalability to ultrasmall SOI waveguides, with small effective core areas and low carrier lifetimes, allowing integrated Raman laser on silicon with higher efficiencies, lower threshold power levels and about a 140-fold footprint reduction compared to state of the art Raman lasers.

References

[1] H. Rong, S. Xu, Y. Kuo, V. Sih, et al., "Low-threshold continuous-wave Raman silicon laser", Nature Photonics, vol. 1, pp. 232-237, 2007.

[2] H. Rong, Y. Kuo, S. Xu, A. Liu, et al., "Monolithic integrated Raman silicon laser", Optics Express, vol. 14, pp. 6705-6712, 2006.

[3] D. Dimitropolous, R. Jhaveri, R. Claps, J. C. S. Woo, and B. Jalali, "Lifetime of photogenerated carriers in silicon-on-insulator rib waveguides", Appl. Phys. Lett., vol. 86, 2005.

[4] J. Niehusmann, A. Vörckel, P. H. Bolivar, T. Wahlbrink, W. Henschel, and H. Kurz, „Ultrahigh-quality-factor silicon-on-insulator microring resonator, Optics Express, vol. 24, pp. 2861-2863, 2004.

[5] M. Krause, H. Renner and E. Brinkmeyer, "Analysis of Raman lasing characteristics in silicon-on-insulator waveguides", Optics Express, vol. 12, pp. 5703-5710, 2004.

[6] F. De Leonardis and V. M. N. Passaro, "Modelling of Raman amplification in silicon-on-insulator optical microcavities", New Journal of Physics, vol. 9, 2007.

[7] C. Koos, L. Jacome, C. Poulton, J. Leuthold and W. Freude, "Nonlinear silicon-on-insulator waveguides for all-optical signal processing", Optics Express, vol. 15, pp. 5976-5990, 2007.A. Liu,

[8] R. L. Espinola, J. I. Dadap, R. Osgood, et al., "Raman amplification in ultrasmall silicon-on-insulator wire waveguides", Optics Express, vol. 12, pp. 3713-3718, 2004.

[9] J. I. Dadap, R. L. Espinola, R. M. Osgood, et al., "Spontaneous Raman scattering in ultrasmall silicon waveguides", Opt. Lett., vol. 29, pp. 2755-2757, 2004.

[10] S. Xiao, M. H. Khan, H. Shen , and M. Qi, "Compact silicon microring resonators with ultra-low propagation loss in the C band", Optics Express, vol. 15, pp. 14467-14475, 2007.

[11] S. F. Preble, Q. Xu, B. S. Schmidt, and M. Lipson, "Ultrafast all-optical modulation on a silicon chip", Opt. Lett., vol. 30, pp. 21, 2005.

Design of a micro-ring resonator electro-optical modulator embedded in a reverse biased PN junction

A. Brimont [1] F.Y. Gardes[2], P. Sanchis[1], D. Marris-Morini[3], P. Dumon[4], J.M. Fedeli[5], L. O'Faolain[6] , W. Bogaert[4], L. Vivien[3], J. Martí[1], G.T. Reed[2], T.F. Krauss[6]

[1]Nanophotonics Technology Center - Universidad Politécnica de Valencia (Spain)
abrimont@ntc.upv.es
[2]Advanced Technology Institute, University of Surrey (UK)
F.Gardes@surrey.ac.uk
[3]Institut d'Electronique Fondamentale, CNRS, Université Paris Sud (France)
[4]Ghent University – IMEC (Belgium)
[5]CEA-Leti (France)
[6]School of Physics & Astronomy, University of St Andrews (UK)

Abstract. *In this paper, the design of a micro-ring resonator electro-optical modulator using a PN junction embedded in a rib waveguide is reported. A reverse bias of 10V is applied to the junction and shows the possibility to achieve a high modulation depth. The figure of merit of this compact depletion modulator is estimated to be Lp.Vp=3.46 V.cm for a loss varying from about 5 dB/cm to 8.6 dB/cm depending on the voltage applied.*

1. Introduction

Silicon photonics aims at scaling down dramatically the dimensions of optical components so electronic and optical functionalities could be integrated monolithically into an all-silicon chip at very low cost. Most of research activities in the field of silicon have been so far focused on passive structures, light emitting devices, detectors and modulators. Significant progress has been made, pushing physical limits of silicon beyond initial expectations. In the field of light modulation in Silicon, the challenging aspect is to alter the refractive index as silicon does not exhibit any linear electro-optic (Pockels) effect, usually used in III-V semiconductors. Alternative ways to alter the refractive index in all-silicon structures have been proposed. So far, the last experimental evidences shown that the only viable mechanism to achieve multi-Ghz modulation in all-silicon devices is proven to be the plasma dispersion effect. This physical effect is basically based on free carrier concentration variation in a semiconductor, which alters both the real and imaginary part of the refractive index, respectively known as electrorefraction and electroabsorbtion. These parameters were derived experimentally by R.A.Soref [1] from the Drude-Lorenz equations at the specific telecommunication wavelengths (1.3 μm and 1.55 μm). His conclusions led to the following empirical equations:

At λ= 1.55 μm:

$$\Delta n = \Delta n_e + \Delta n_h = -[8.8\times10^{-22}\Delta n_e + 8.5\times10^{-18}(\Delta n_h)^{0.8}]$$

$$\Delta \alpha = \Delta \alpha_e + \Delta \alpha_h = 8.5\times10^{-18}\Delta n_e + 6.0\times10^{-18}\Delta n_h$$

Where Δn_e is the change in refractive index resulting from change in free electron concentration; Δn_h is the change in refractive index resulting from change in free hole concentration; $\Delta \alpha_e$ is the change in absorption resulting from change in free electron concentration; $\Delta \alpha_h$ is the change in absorption resulting from change in free hole concentration

Combining these equations with a mode solver it becomes possible to work out the effective index change of a mode and therefore the resulting phase shift for a given voltage. Experimental demonstrations of high speed modulation in free carriers depleted silicon-based structures was demonstrated theoretically by [2,3] and experimentally by [4-7] to work in the multi-GHz regime. However, the need for compactness, the key for VLSI integration motivated researchers to move toward resonating structures among other alternatives. The use of a ring resonator to modulate an optical signal was already shown by [8] to reach bit rates as high as 12.5 Gbit/s under a pre-emphasized voltage driving scheme. In this paper, we propose also the use of a ring resonator modulator, in which modulation is achieved shifting the resonance peaks by means of carrier depletion within a PN junction.

2. Device description

The proposed ring resonator modulator (Fig. 1) is based on a 300nm wide, 150nm etch depth and 200 nm high rib waveguide, which enables to achieve single mode transmission.

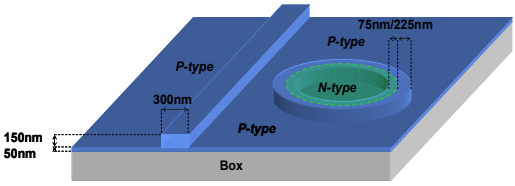


Fig1. Schematic of the proposed ring resonator modulator showing the positioning of the junction inside the ring modulator

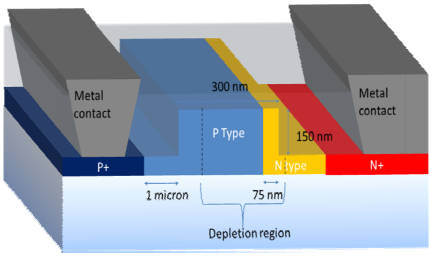


Fig2 : Electrical structure of the modulator

As shown on Fig .2, the PN junction is asymmetrical in size and in doping concentration in order to maximize the holes depletion area overlapped by the optical mode. The n-type region is 75 nm wide and the p type 225 nm wide, the net doping concentration of this particular junction is varying between 6E17/cm3 and 2E17/cm3, for n and p type respectively. The resistive contacts are formed by highly doped regions (1E20/cm3) in order to form a good resistive contact and are placed 1µm away from the junction to minimise interaction with the optical mode and thus absorption losses. The position of the contacting electrodes is a key aspect in the case of a reverse biased PN based-modulator because the RC constant cut off frequency, which results from capacitive effects within the junction, limits the modulation speed.

The modulator performance was simulated using Athena for the process development and ion implantations and Atlas for DC and transient analysis, both part of the

semiconductor CAD software Silvaco. Optical Characteristics for the optical loss, efficiency and transient analysis were calculated using an in house mode solver. Fig. 3 represents the variation of the effective index for different reverse voltages; the loss of the active area is also displayed, and varies from 8.6dB/cm when no bias is applied, to about 5 dB/cm with a reverse bias of 10 volts. The efficiency of this specific modulator is Lp.Vp=3.46 V.cm. meaning that a length of 3.46 mm would be necessary to obtain a π-phase shift with a 10 volt reverse bias in a Mach Zehnder interferometer.

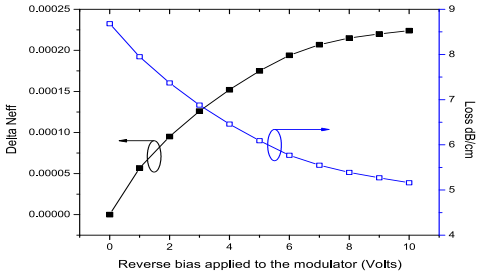


Fig3. Simulated effective index change and loss of due to the carrier for different reverse voltage bias

As the active part of the modulator is inserted in the ring resonator, the response of the ring modulator is calculated by combining the results in figure 3 in the equation below ([9], [10])

$$|b_1|^2 = \frac{K^2 + |t|^2 - 2K|t|\cos\left(\frac{2\pi}{\lambda}NL\right)}{1 + K^2|t|^2 - 2K|t|\cos\left(\frac{2\pi}{\lambda}NL\right)}$$

Where N is the total effective index including dispersion or group index, K is loss factor of the ring (K=1 is lossless), L is total physical length of the ring (nm), t is transfer or coupling coefficient of the coupler, λ is the wavelength.

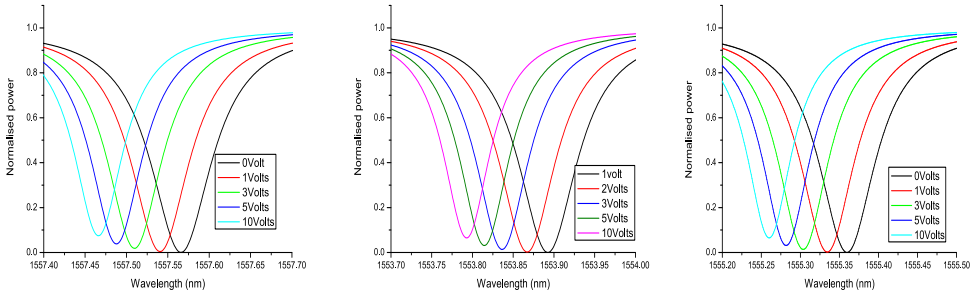


Fig4. Simulated ring response for different radius 10, 30 and 50 µm and reverse bias voltage varying between 0 and 10 volts.

The results are displayed in Fig4 for three different ring radii. Those results are derived from an ideal coupling factor matched to the loss factor of the ring in order to obtain the best response, also only the loss induced by the free carriers inside the waveguide is taken into account. The interesting result here is to show that for a similar PN junction

design, a similar extinction ratio can be achieved regardless of the ring size. This is due to the fact that as the ring decreases in size, the free spectral range (FSR) increases hence a small change in refractive index inside the waveguide will induce a bigger shift in wavelength compared to larger rings where the FSR is smaller. Nevertheless, it is important to note that decreasing the bend radius increases the intrinsic losses inside the ring due to the waveguide wall roughness, hence increasing the loss factor and the extinction ratio of the ring.

Conclusion

This paper shown the theoretical possibilities of modulating efficiently an optical signal propagating through a ring resonator and using a PN junction embedded in rib waveguide. Due to the intrinsic possibilities offered by a PN junction, high speed modulation can then be achieved by shifting the ring resonance peak under a reverse biased voltage, canceling the need of using complicated pre-emphasized voltage driving schemes. Furthermore such a device would be beneficial and a major improvement in terms of power requirements as well as real estate of the device compared to depletion modulators inserted in MZI.

Acknowledgments

Authors acknowledge financial support by EC under NoE ePIXnet.

References

[1] R A. Soref, B.R. Benett, “Electrooptical effects in Silicon*” IEEE J. Quantum Electron*. QE-23, pp. 123-129, 1987.

[2] F. Y. Gardes, G. T. Reed, N. G. Emerson, and C. E. Png, "A sub-micron depletion-type photonic modulator in silicon on insulator," *Optics Express*, vol. 13, pp. 8845-8854, 2005.

[3] D. Marris, E. Cassan, L.Vivien, “Response time analysis of SiGe/Si modulation-doped multiple-quantum-well structures for optical modulation”, *Journal of applied physics*, Vol 96, nº11, pp 6109-6111, 2004.

[4] A. Lupu, D. Marris, D. Pascal, J-L. Cercus, A. Cordat, V. Le Thanh, S. Laval, “Experimental evidence for index modulation by carrier depletion in SiGe/si multiple quantum well structures”, *Applied physics letters*, Vol 85, nº 6, pp. 887-889, 2004

[5] D. Marris-Morini, X. Le Roux, L. Vivien, E. Cassan, D. Pascal, M. Halbwax, S. Maine, S. Laval, J. M Fedeli, and J. F. Damlencourt, "Optical modulation by carrier depletion in a silicon PIN diode," *Optics Express*, vol. 14, pp.10838-10843, 2006.

[6] L. Ansheng, L. Ling, D. Rubin, N. Hay, B. Ciftcioglu, Y. Chetrit, N. Izhaky, and M. Paniccia, "High-speed optical modulation based on carrier depletion in a silicon waveguide," *Optics Express*, vol.15, pp. 660-668, 2007.

[7] D. Marris-Morini, L.Vivien, J.M. Fédéli, E. Cassan, P. Lyan, S. Laval, “Low loss and high speed silicon optical modulator based on a lateral carrier depletion structure”, *Optics express*, vol.16, pp.334-339, 2008.

[8] Q. Xu, S.Manipatruni, J. Shakya, M. Lipson, “12,5 Gbit/s carrier-injection-based silicon micro ring ring silicon modulators”, *Optics express*, vol. 15, pp. 430-436, 2007.

[9] J. M. Choi, R. K. Lee, and A. Yariv, "Control of critical coupling in a ring resonator-fiber application to wavelength-selective switching, modulation, amplification, and oscillation," *Optics Letters*, vol. 26, pp. 1236-8, 2001.

[10] A. Yariv, "Critical coupling and its control in optical waveguide-ring resonator systems," *IEEE Photonics Technology Letters*, vol. 14, pp. 483-5, 2002.

Wavelength routing and dispersion compensation in a narrow-band integrated resonant router

F. Morichetti[1,2], C. Ferrari[1], L. Flaccadori[1] A. Melloni[1]

[1] Dipartimento di Elettronica e Informazione, Politecnico di Milano, 20133 Milano, Italy
[2] CORECOM, via G. Colombo 81, 20133 Milano, Italy
morichetti@corecom.it

Abstract - *We demonstrate that a narrow-band resonant-router made of a matrix of integrated ring-resonators can combine wavelength routing and dispersion compensation operations, with neither significant signal distortion nor inter-channel crosstalk deterioration. The transmission of 10-Gbit/s NRZ data-streams through a* 2×2 *integrated SiON router with 4-GHz bandwidth is reported.*

Introduction

Reconfigurable architectures made of bi-dimensional arrays of ring-resonators (RRs), also known as resonant routers (ReRs) [1], are good candidates for implementing advanced routing and switching operations in a WDM optical network [2]. ReRs combine high flexibility, full reconfigurability and the capability of handling many WDM optical channels in small footprint devices. Recently, ReRs have been also proposed as cost effective solutions in access network applications [3].

One of the major limits of the ReR performance is the intrinsic trade-off between the bandwidth and the off-band rejection, the latter determining the inter-channel cross-talk of the ReR. To increase the ReR bandwidth with no crosstalk deterioration, RRs with a large free spectral range (FSR) can be employed, this approach requiring waveguides with a suitably high index contrast. On the other side, to reduce the crosstalk without narrowing the bandwidth, each ReR node can include several coupled RRs; besides a larger footprint, this solution increases the complexity of the RER configuration and management.

In this contribution, we demonstrate that the bandwidth of a ReR can be significantly narrowed with respect to the signal bandwidth, while corrupting neither the signal quality nor the crosstalk. To this aim, a small frequency detuning between the signal carrier and the ReR's frequency response is introduced. In this condition, the frequency chirp provided by the RRs dispersion can be also exploited to make the transmitted signals more robust against fiber chromatic dispersion. The routing of two intensity modulated 10 Gbit/s NRZ channels through a 2×2 integrated ReR with 4 GHz bandwidth is reported and the signal quality after propagation through several spans of optical fiber is evaluated.

Fabrication and characterization of a 2×2 integrated ReR

Fig. 1(a) shows a 2×2 ReR fabricated in 4.5% index-contrast silicon oxynitride technology [4]. It comprises a crossbar matrix of four identical racetrack RRs, which are side-coupled with four orthogonally-crossing straight bus-waveguides. The optical waveguide has 2.2×2.2 μm^2-wide cross-section and 0.35 dB/cm propagation loss at 1550 nm. The bending radius of the RRs is 570 μm, corresponding to a FSR of 50 GHz. The resonance of each RR is independently controlled by means of a metallic heater deposited onto the waveguide, so that the ReR spectral response can be fully reconfigured.

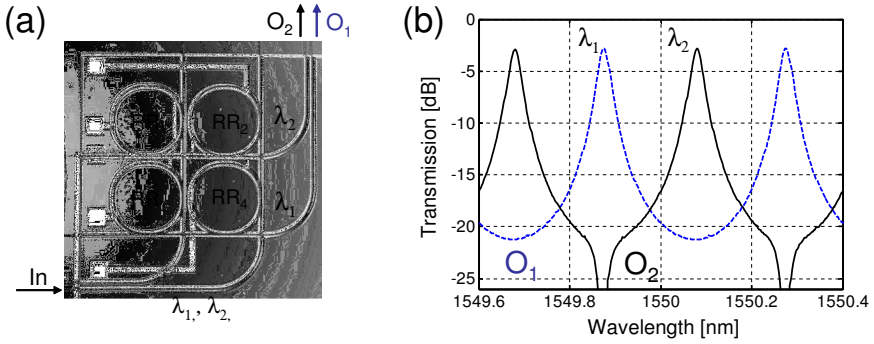


Figure 1: (a) Photograph of a 2×2 λ-ReR fabricated in SiON technology. (b) Measured frequency-domain response of the λ-ReR shown in (a) at the output ports O_1 (dashed line) and O_2 (solid line) when the signal is provided at the In port.

Fig. 1(b) shows the measured transmission from the input port (In) to the output port O_1 (dashed line) and O_2 (solid line). The bell-shaped passbands in O_1 and O_2 are the drop-port responses of RR_4 and RR_2, respectively. The deep notch in O_2 is due to the through-port contribution of RR_4. The measured 3-dB bandwidth is 4.1 GHz ($\pm$0.1 GHz) and the overall insertion loss at the transmission maximum is 2.9 dB ($\pm$0.1 dB). This insertion loss partially comes from fibre-to-waveguide coupling, amounting to 0.2 dB/facet when small-core fibers with 3.6 μm mode field diameter are used. The round-trip loss of each 4-mm-long RR is about 0.2 dB/turn, where 0.15 dB come from propagation loss and the remaining 0.05 dB from bending loss and directional couplers' excess loss. The loss at each waveguide-crossing is 0.4 dB, but it can be reduced by tapering the waveguides profile at the crossing-sections. The unbalance between the peak transmission at the two output ports is below 0.3 dB. Thanks to the high finesse of the RRs, the off-band isolation exceeds 18 dB over more than 8 GHz at both the ReR output ports.
The fabricated ReR can operate either as wavelength router (λ-ReR) in a WDM system with 25 GHz spaced channels or as an optical cross-connect, if the channel spacing is 50 GHz. In the experiment reported in the following the operation as λ-ReR is discussed.

Two-channel wavelength routing at 10 Gbit/s

Fig. 2 shows the experimental setup used for the time-domain measurements of the 2×2 ReR of Fig. 1(a). Two optical sources λ_1 and λ_2, spaced by 25 GHz, are modulated by two intensity modulators, MOD_1 and MOD_2, in order to generate two 10 Gbit/s NRZ optical data-streams. The two signals, sharing the same pseudo-random bit sequence (PRBS), are decorrelated by making λ_1 propagate through few kms of optical fiber while a variable optical attenuator (VOA) is placed on the λ_2-path to compensate for fiber loss. Two polarization controllers are employed to control the polarization state of each channel at the ReR input. A 3dB coupler is used to couple λ_1 and λ_2 into the In port of the ReR. For back-to-back measurements (B2B), the signal outgoing the ReR output O_2 is directly supplied to an EDFA pre-amplifier followed by a VOA, which is employed to control the received power level. A small portion (10%) of the received signal is sent to an optical spectrum analyzer (OSA) for monitoring the ReR frequency response. The signal quality

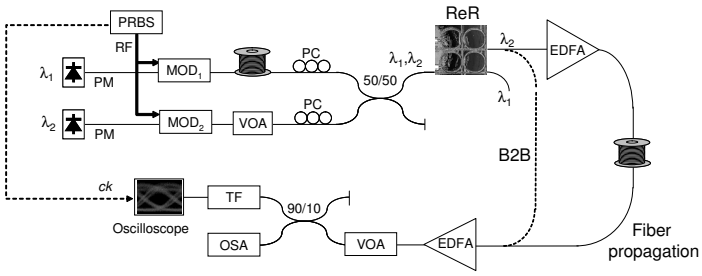


Figure 2: Experimental setup.

is evaluated by measuring the eye-diagram opening (system Q-factor) by means of an optical sampling oscilloscope. A tunable optical filter (TF) with 1-nm-wide bandwidth is placed before the detector to remove the off-band ASE noise produced by the EDFA. For propagation measurements, an EDFA booster is added at the ReR output and several spans of SMF fiber are inserted before the receiver apparatus.

The Q-factor of the received signal was measured for different detuning $\Delta\lambda = \lambda_R - \lambda_2$ between the ReR spectral response and the signal carrier λ_2, as shown in Fig. 3(a). Fig. 3(b) shows the measured Q in B2B transmission, when the received power is kept at a constant level. When $\Delta\lambda = 0$ the eye diagram is completely closed ($Q < 2$), because of the large intersymbolic interference introduced by the narrow ReR bandwidth. As the detuning increases, the Q-factor improves symmetrically with respect to λ_R. As shown in the insets of the figure, the eye-diagrams measured at $\Delta\lambda = \pm 28$ pm are almost indistinguishable. We observed also that if $\Delta\lambda < 30$ pm, the eye-opening is almost independent of the presence of the interfering channel λ_1, demonstrating that the crosstalk level is not significantly affected by the small detuning. This result is a direct consequence of the high off-band rejection of the narrow-band ReR.

The symmetry of the Q curve versus $\Delta\lambda$ disappears when propagation through an optical SMF fiber is added. As shown in Fig. 4(a), fiber propagation makes the Q factor increase on the upper wavelength side of the RR's resonance ($\Delta\lambda > 0$), whereas the Q factor de-

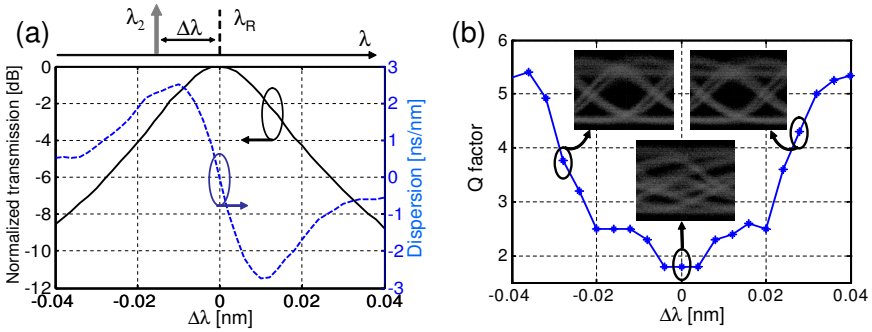


Figure 3: (a) Transmission (solid line) and dispersion (dashed line) of the ReR in the neighborhood of the O_2 port maximum; (b) measured Q-factor versus the detuning $\Delta\lambda$ in B2B measurements. The reported eye-diagrams are measured at $\Delta\lambda$ = -28 pm, 0 pm and +28 pm.

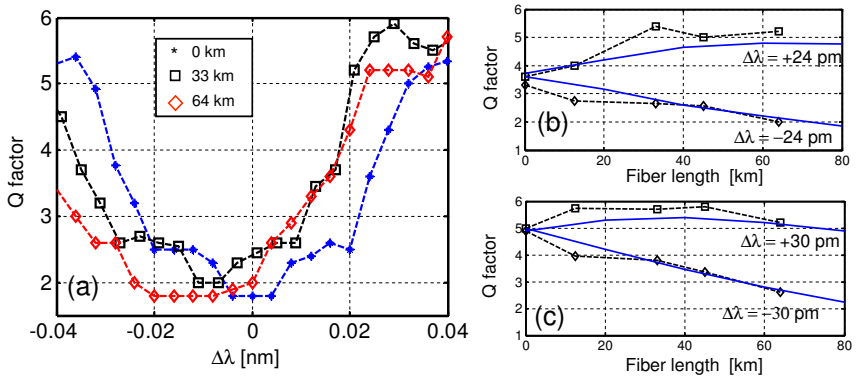


Figure 4: (a) Measured Q-factor versus the detuning $\Delta\lambda$ for increasing propagation length; measured (squares) and simulated (solid line) Q-factor versus the propagation length for $\Delta\lambda = \pm 24$ pm (b) and $\Delta\lambda = \pm 30$ pm (c).

creases for $\Delta\lambda < 0$. The minimum of the Q curve shifts towards shorter wavelengths. This effect is due to the combination of the fiber and the ReR dispersion, the latter assuming an opposite sign at the two sides, as shown in Fig. 3(a). For $\Delta\lambda > 0$ the ReR introduces a normal chromatic dispersion, which compensates for the anomalous fiber dispersion, so that the Q improves with propagation. Fig. 4(b) and (c) show the simulated (solid lines) and the measured (squares) Q versus the propagation length for $\Delta\lambda = +24$ pm and $\Delta\lambda = +30$ pm, respectively. The distance L_{max} at which the Q-factor reaches its maximum value (chirp-free signal) is 65 km (-1050 ps/nm ReR dispersion) in (b) and 40 km (-650 ps/nm ReR dispersion) in (c). The Q-factor decreases to its original value at $2L_{max}$. Since L_{max} depends on $\Delta\lambda$, the quality of the received signal can be optimized for a variable range of fiber lengths. On the other side of the RR frequency response, where the ReR dispersion is positive, the Q-factor monotonically decreases.

Conclusion

Our results demonstrate that wavelength routing and dispersion compensation can be both accomplished by a narrow-band λ-ReR. The control of the wavelength detuning between the signal and the device enables the optimization of the signal quality for a variable range of propagation lengths, with no significant deterioration of the ReR crosstalk level. The device can be usefully exploited either in a node or at the receiver side of a WDM network.

References

[1] A. Melloni et al., Analysis of the Resonant Wavelength Router, *in Proceed. of the 11th European Conference on Integrated Optics*, Prague, April 2003.

[2] R.A. Soref et al., "Proposed N-wavelength M-fiber WDM crossconnect switch using active microring resonators," *IEEE Phot. Technol. Lett.*, vol. 10, no. 8, pp. 1121-1123, Aug. 1998.

[3] E.J. Klein et al., "Densely integrated microring resonator based photonic devices for use in access networks," *Opt. Express*, vol. 15, pp. 10346-10355, 2007.

[4] F. Morichetti et al., "Integrated optical receiver for RZ-DQPSK transmission systems". *in Proced. of the Optical Fiber Communication Conference*, vol.2, Los Angeles, CA, 2004.

High-quality-factor micro-ring resonator in amorphous-silicon on insulator structure

Ziyang Zhang[1], Matteo Dainese[2], Marek Chacinski[1], Lech Wosinski[1], and Min Qiu[1*]

[1]Laboratory of Optics, Photonics and Quantum Electronics, Department of Microelectronics and Applied Physics, Royal Institute of Technology (KTH), Electrum 229, 164 40 Kista, Sweden
[2]Replisaurus AB, Electrum 229, 164 40 Kista, Sweden
*Email: min@kth.se

Abstract. *Micro-ring resonators have been fabricated in hydrogenated amorphous silicon on silica structure. The intrinsic quality factor is estimated as 56,000 and the notch depth is ~ 30dB. The intrinsic loss per unit length is 15.3dB/cm, comparable to 9.16dB/cm in the single-crystalline silicon ring of the same geometry.*

Introduction

Micro-ring resonators have found wide applications in optical filtering, add-drop multiplexing, dispersion compensation and bio-sensing [1-4]. Q values larger than 10^5 have been demonstrated in single-crystalline silicon-on-insulator (SOI) structure [5-6]. There have been some reports on amorphous silicon rings [7], but the results are not well-comparable to single-crystalline silicon rings. From fabrication aspects, amorphous silicon (α-Si:H) can be readily deposited using low temperature plasma enhanced chemical vapour deposition (PECVD) with good uniformity. The thickness can be varied flexibly. Commercial SOI wafers, on the other hand, are fabricated using expensive wafer-bonding technology and usually the silicon thickness cannot be chosen freely. The common belief is that α-Si:H exhibits much higher material loss. In this work, we fabricate micro-rings in both α-Si:H and single-crystalline SOI of the same lateral and vertical geometry during the same process. By comparison we show that the performance of the α-Si:H ring resonator is at least comparable to that of the single-crystalline ring and α-Si:H is a promising platform for high quality photonic devices.

Theory

Time-domain coupled mode theory is applied to analyze the filter consisting of a single waveguide side-coupled to a ring [8-9]. The schematic is shown in Fig. 1. We assume that wave coming from the waveguide excites only one of the travelling modes in the ring, which in turn generates the other counter-travelling mode. We allow the mutual coupling between the two ring modes because we have introduced some nanometre-scaled periodic roughness on the ring sidewalls. This periodic roughness works as gratings. The period and amplitude can be tuned during the fabrication process. In the optimal case, it only improves the mutual mode coupling and does not significantly deteriorate the intrinsic Q. The presence of mutual mode coupling makes it easier to reach deep transmission notches for detection [10].

We study the steady-state solution and assume $e^{j\omega t}$ time dependence for the resonator and waveguide modes. The transfer function can be derived as

$$T(\omega) = \frac{|S_{-2}|^2}{|S_{+1}|^2} = \left|\frac{D}{C}\right|^2 \qquad (1)$$

where $C = AB + u^2$, $D = C - |\kappa_a^2|B$, $A = j(\omega - \omega_a) + \frac{1}{\tau_a}$ and $B = j(\omega - \omega_b) + \frac{1}{\tau_b}$.

For power conservation, the mutual coupling coefficient u is a real number. $\omega_{a,b}$ are the resonant frequencies for the ring resonator modes, τ is the photon life time, and κ is the coupling coefficient between the ring and the waveguide. The reciprocal of photon life time is the decay rate $1/\tau$, which is related by power coupling to the waveguide ($1/\tau_e$) and power dissipating due to intrinsic losses ($1/\tau_i$). Thus, $1/\tau = 1/\tau_e + 1/\tau_i$. The quality factor (Q) is decided by the photon life time, i.e., $Q = \omega_0\tau/2$. The waveguide/ring coupling coefficient and the power decay rate are related by $|\kappa|^2 = 2/\tau_e$.

From Eq. (1), the transfer function in general is not of Lorentzian shape. The Q value of the system cannot be estimated from the division of resonance frequency by 3dB bandwidth. The transmission spectrum has to be fitted to obtain the Q factors numerically.

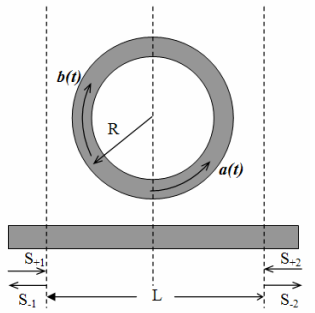


Fig. 1 Schematic of a ring resonator side coupled to a waveguide.

It is convenient to define a mutual coupling Q factor Q_u. Assume $\omega_a = \omega_b = \omega_0$, $Q_u = \frac{\omega_0}{2|u|}$. Q_u is not related to any power loss in the system. It is merely a figure that manifests the mutual coupling rate for the two travelling modes in the ring.

In practice it is difficult to guarantee the conventional critical coupling, when $Q_{ai} = Q_{ae}$, for complete channel drop. However, with the help of mutual coupling, the notch depth improves and it is possible to reach new critical coupling. When u further increases, the resonance notch will split [10].

Fabrication

α-Si:H is deposited by PECVD (STS). The refractive index variation is less than 1.0×10^{-3}. From atomic force microscope, the root mean square of the surface roughness is measured as 7.5 Å for the chamber deposition temperature 250 °C. The device sample has a top α-Si:H layer of 250 nm and silica buffer layer 3 μm.

The waveguide and ring pattern is first defined in electron beam (E-beam) lithography (Raith 150, 25kV) with negative resist ma-N 2405. During the E-beam scan, the ring area is broken down into concentric polygons. By varing the E-beam scan step size, dose factor and resist developing time, the period and amplitude of the grating can be tuned.

Reactive ion plasma etching (ICP DRIE, STS) is then performed to transfer the pattern to the silicon layer. The bending radius of the ring is 40 μm and the cross-section is 400

nm (wide) by 250nm (thick). The width of the air gap between the ring and waveguide is ~ 100 nm to ensure good coupling with the waveguide and thus $Q_{ae} < Q_{ai}$.

Results

The SEM photos and measurement results of α-Si:H ring resonator are shown in Fig. 2. The resonance at 1540.05 nm is split due to mutual mode coupling. Eq. (1) is used to fit the experimental curves. The estimated intrinsic Q value for the notch in Fig. 3(c) is 5.6×10^4.

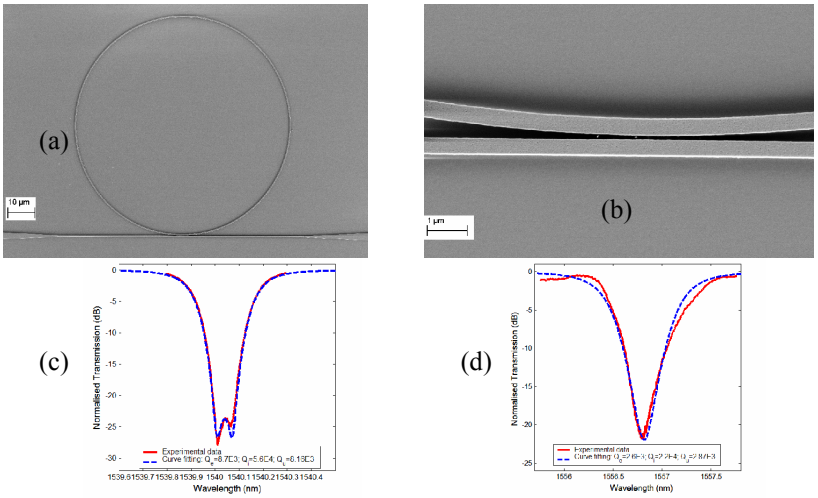


Fig. 2 (a)-(b) SEM photos of the amorphous ring resonator. (c)-(d) Measured transmission spectra (solid) and fitted curves (dashed) using Eq. (1). The resonance at 1540.05 nm is slightly split with intrinsic Q ~ 5.6×10^4 and notch depth ~ 30 dB. The resonance at 1556.57 nm has intrinsic Q ~ 2.2×10^4 and notch depth ~ 22 dB.

To make a comparison, we have fabricated and analyzed the device of the same lateral and vertical geometry in the single-crystalline silicon sample during the same process. The results are shown in Fig. 3. The best notch occurs at 1574.6 nm with intrinsic Q estimated as 9.1×10^4.

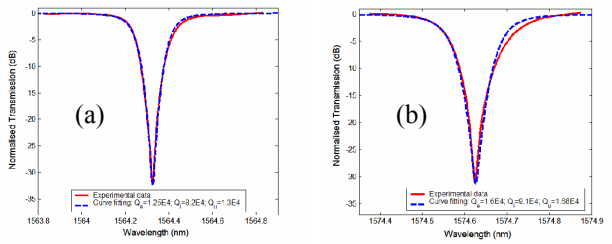


Fig. 3 Measured transmission spectra (solid) for the 40-μm-radius single-crystalline micro-ring and fitted curves (dashed) using Eq. (1). (a) The resonance at 1564.32 nm has intrinsic Q ~ 8.2×10^4 and notch depth ~ 33 dB. (b) The resonance at 1574.62 nm has intrinsic Q ~ 9.1×10^4 and notch depth ~ 31 dB.

Note that the intrinsic Q values of α-Si:H and single-crystalline silicon ring resonators are on the same order of magnitude. For α-Si:H, the intrinsic loss per unit length in the ring is calculated as 15.30 dB/cm and for single-crystalline silicon the loss is 9.16 dB/cm.

Summary

To summarize, we have fabricated and analysed micro-ring resonators in the hydrogenated amorphous silicon on silica structure. The intrinsic Q value is estimated as 5.6×10^4. The loss per unit length is calculated to be 15.30 dB/cm. A control device with the same structure but fabricated in single-crystalline silicon on silica structure during the same process gives intrinsic Q of 9.1×10^4 and loss per unit length 9.16 dB/cm. This indicates the fact that ring resonators fabricated using α-Si:H are at least comparable to those fabricated using single-crystalline silicon. With PECVD as a convenient and cheap solution for SOI wafer deposition, α-Si:H is well-suited for high-quality photonic devices.

Acknowledgments

This work is supported by the Swedish Foundation for Strategic Research (SSF) through the INGVAR program, the SSF Strategic Research Center in Photonics, and the Swedish Research Council (VR).

References

[1] B. E. Little, J. S. Foresi, G. Steinmeyer, E. R. Thoen, S. T. Chu, H. A. Haus, E. P. Ippen, L. C. Kimerling, and W. Greene, "Ultra-compact Si/SiO2 microring resonator optical channel dropping filters," IEEE Photon. Technol. Lett. **10**, 549-551 (1998).

[2] Q. Xu, V. R. Almeida, and M. Lipson, "Micrometer-scale all-optical wavelength converter on silicon," Opt. Lett. **20**, 2733 (2005)

[3] F. Xia, L. Sekaric, and Yu. A. Vlasov, "Ultra-compact optical buffers on a silicon chip," Nature Photon. **1**, 65-71 (2007).

[4] K. De Vos, I. Bartolozzi, E. Schacht, P. Bienstman, and R. Baets, "Silicon-on-Insulator microring resonator for sensitive and label-free biosensing," Opt. Express **15**, 7610-7615 (2007)

[5] J. Niehusmann, A. Vörckel, P. H. Bolivar, T. Wahlbrink, W. Henschel, and H. Kurz, "Ultrahigh-quality-factor silicon-on-insulator microring resonator," Opt. Lett. **29**, 2861 (2004).

[6] S. Xiao, M. H. Khan, H. Shen, and M. Qi, "Compact silicon microring resonators with ultra-low propagation loss in the C band," Opt. Express **15**, 14467 (2007)

[7] S. Selvaraja, E. Sleeckx, W. Bogaerts, M. Schaekers, P. Dumon, D. Thourhout, and R. Baets, "Low loss amorphous silicon photonic wire and ring resonator fabricated by CMOS process," The 33rd European Conference and Exhibition on Optical Communication (ECOC2007), 16th - 20th September 2007, Berlin, Germany.

[8] B. E. Little, S. T. Chu, H. A. Haus, J. Foresi, and J. P. Laine, "Microring resonator channel dropping filters," IEEE J. Light. Tech.. **15**, 998 (1997).

[9] C. Manolatou, M. J. Khan, Shanhui Fan, Pierre R. Villeneuve, H. A. Haus, and J. D. Joannopoulos, "Coupling of Modes Analysis of Resonant Channel Add-Drop Filters," IEEE J. Quantum Electron. **35**, 1322 (1999).

[10] Z. Zhang, M. Dainese, L. Wosinski, and M. Qiu are preparing a manuscript to be called "Resonance-splitting and enhanced notch depth in SOI ring resonators with mutual mode coupling."

Ultrafast tracking of slow photonics and plasmons

K. Kuipers
Center for Nanophotonics, AMOLF, AMSTERDAM, The Netherlands

Widely tunable mid-infrared difference frequency generation using apodized $\chi^{(2)}$ grating and its application to gas spectroscopy

T. Umeki, M. Asobe, T. Yanagawa, O. Tadanaga, † Y. Nishida, K. Magari and ‡ H. Suzuki

NTT Photonics Laboratories, NTT Corporation
3-1 Morinosato Wakamiya Atsugi, Kanagawa, 243-0198 Japan
umeki@aecl.ntt.co.jp
Present affiliation † NTT Electronics Corporation, Ibaraki, Japan
Present affiliation ‡ ATR International, Kyoto, Japan

Abstract. *We have proposed a new device structure to achieve apodization in a quasi-phase-matched (QPM) wavelength converter. Widely tunable 3 μm-band difference frequency generation was realized using an apodized QPM $LiNbO_3$ waveguide. We have demonstrated the simultaneous detection of the absorption lines of CH_4 and C_2H_4 using the widely tunable source.*

Introduction

Mid-infrared light sources have attracted a lot of attention because they are useful for sensing environmental gases. A 3 μm-band light source is particularly important for sensing hydrocarbons because there is much strong absorption in this wavelength range [1] [2]. However, no practical laser source has been developed that can emit a continuous wave at room temperature. On the other hand, quasi-phase-matched (QPM) difference frequency generation (DFG) is an attractive technique for generating mid-infrared light because we can utilize well-established telecom laser diodes as pump and signal sources. Recently, we demonstrated 3 μm-band laser light generation in periodically poled $LiNbO_3$ (LN) ridge waveguides using a direct bonding technique. Direct bonding is especially suitable for generating mid-infrared light because it avoids any undesired absorption by hydroxyl and other groups [3]. We achieved a high conversion efficiency of 40 %/W by making best use of the advantages of direct bonding [4]. However, the narrow bandwidth of the current waveguide, yielded by quasi-phase matching, limits its application to a multiple-gas sensor. So there is a strong need for a broadband QPM device if we are to realize a widely tunable mid-infrared light source. In this paper, we present the basis for the apodization of a $\chi^{(2)}$ grating that yields an arbitrary degree of band broadening and a flat phase-matching response, as well as a high conversion efficiency. We use the method to obtain widely tunable high-efficiency 3 μm-band DFG in a $LiNbO_3$ ridge waveguide. Moreover, we apply the result to demonstrate multiple hydrocarbon gas detection. We detect the absorption lines of CH_4 and C_2H_4 simultaneously.

Concept of apodized QPM $LiNbO_3$ device

In a uniform QPM-grating device, we can increase the bandwidths by reducing the interaction length. This is because the bandwidth scales inversely with length. However, since the conversion efficiency scales quadratically with length, this approach leads to a marked decrease in conversion efficiency. Another common broadband device technology is the chirped $\chi^{(2)}$ grating [5]. This grating makes it possible to obtain a linear tradeoff between conversion efficiency and bandwidth. However, attempts to obtain a high conversion efficiency with a moderate bandwidth have resulted in large ripples in the tuning curve owing to interference arising from various phase-matching conditions of the grating. Apodization is widely used to suppress the ripples produced by Bragg gratings in semiconductors and fibers [6]. However, QPM structures are formed by reversing the spontaneous polarization, which has only two states, namely the up state (0°) and down state (180°). That means that, unlike a refractive index, it is

impossible for a nonlinear coefficient to have an intermediate state. Therefore, apodization has never been demonstrated in a QPM grating.

We found that it is possible to control the effective nonlinearity by changing the duty ratio [7]. And we exploited this characteristic to apodize a QPM grating. Figure 1 is a schematic of an apodized $\chi^{(2)}$ grating structure. To reduce unwanted ripples in the phase matching curve, we change the duty ratio at both ends of the device. The duty ratio in the center section is conventionally uniform. In addition, to increase the bandwidth, we invert the sign of the nonlinear coefficient aperiodically. Here, we define the duty ratio *f(z)* as the ratio of a non-inverted domain to one poling period. In this work, we employed the following duty ratio function [8]:

$$f(z) = \frac{1}{2}\tanh\left[\frac{2az}{L}\right], \qquad \frac{L}{2} \le z \le L \qquad (1)$$

$$= \frac{1}{2}\tanh\left[\frac{2a(L-z)}{L}\right], \qquad 0 \le z \le \frac{L}{2}$$

where *a* is an apodization parameter that adjusts the duty ratio variation, and *L* is the total length of the device. For the unapodized grating, *f(z)* is equal to 0.5. In addition, to increasing the bandwidth, we chirped the poling period linearly.

Widely tunable high-efficiency 3 μm-band DFG

We demonstrated 3 μm-band DFG with a large bandwidth and high conversion efficiency. We fabricated ridge waveguides by employing the direct-bonding technique [3]. We used a 3-inch z-cut non-doped $LiNbO_3$ wafer and a 3-inch z-cut $LiTaO_3$ wafer for the waveguide layer and substrate, respectively. First, we formed QPM gratings on the LN wafer and then directly bonded the two wafers together. We reduced the thickness of the waveguide layer to 11 μm by lapping and polishing. Finally, we fabricated 17 μm-wide ridge waveguides using a dicing saw. Since we did not use ion exchange or adhesives in the fabrication, there was no unwanted absorption by, for instance, hydroxyl and/or hydrocarbon groups. This makes the technique very suitable for the generation of mid-infrared light. Figure 2 shows the measured tuning curve as a function of signal wavelength. The corresponding idler wavelength is shown on the upper horizontal axis. For comparison, we have also plotted the theoretical tuning curves for apodized and linear chirped gratings.

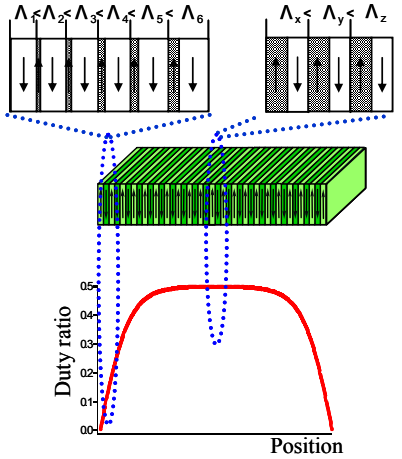


Fig. 1. Schematic of apodized grating structure

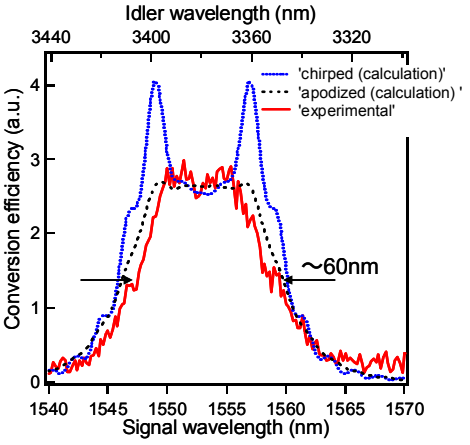


Fig. 2. Measured and calculated DFG tuning curves

The experimental and calculated tuning curves agree well. Apodization clearly suppresses the ripples in the phase-matching curve to about ±0.5 dB. The residual ripples are mainly caused by Fresnel reflection. These ripples can largely be eliminated by reducing the reflection at the end of the waveguide. We obtained a bandwidth as large as 60 nm in the 3.4 μm band and a DFG efficiency of 2 %/W. The 3 dB bandwidth for the apodized grating is 7 times larger than that of a device of the same length with a uniform grating, while the peak conversion efficiency only decreased by a factor of ~10 [4]. This technology enables us to examine the mid-IR absorption spectrum precisely over a wide range, and can be employed, for instance, in the detection of multiple gases by using a mature tunable laser diode for the 1.55 μm band.

Detection of multiple hydrocarbon gases

We demonstrated the simultaneous detection of the absorption lines of CH_4 and C_2H_4. Figure 3 shows the experimental gas detection setup. We used a 1.05 μm laser diode as a pump source. We also used a 1.55 μm band external-cavity laser diode (ECLD) and an erbium-doped fiber amplifier (EDFA) as a signal source. The pump and signal beams were combined with a fiber coupler injected into the QPM-LN WG. Pump, signal, and idler beams radiate from the QPM-LN WG output facet, and the input beams are separated from the DFG idler output beam with a dichromatic mirror. The input light was measured with a powermeter. The pump and signal powers at the output facet of the QPM-LN WG were measured and found to be approximately 600 μW and 100 mW, respectively. The DFG output beam passed through a Ge filter and was divided by a beam splitter into two parts, namely a gas-absorption detection beam and a reference beam. Both beams passed through gas cells or reference cells and were detected by a PbSe photoconductive detector. Each of the idler outputs was independently measured with the lock-in amplifier. The QPM-LN WG temperature was set at 25 °C. All the gas cells that we designed and used were made from the same fused-silica cylinder and had anhydrous silica windows, which were tilted to prevent reflection. There were two hydrocarbon gas cells and two reference cells. One cell was filled with CH_4 at 9 Torr and the other cell contained C_2H_4 at 5 Torr and buffer gas at 495 Torr. The CH_4 and C_2H_4 cells had path lengths of 20 and 10 cm, respectively.

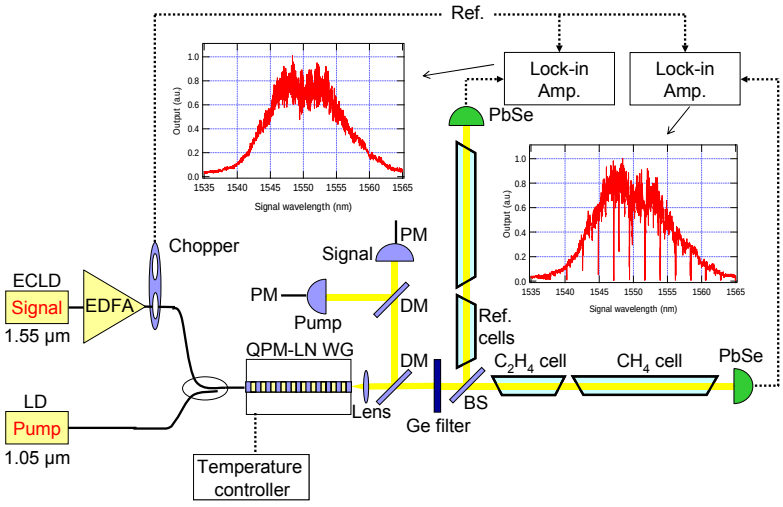


Fig. 3. Experimental setup for measuring hydrocarbon gas absorption lines

Figure 4(a) shows the absorption spectrum that resulted when CH_4 and C_2H_4 were observed simultaneously. The spectrum was provided by a single scan of the signal with a wavelength resolution of 0.01 nm/step. We obtained the absorption spectrum by dividing the transmission spectrum through the gas cells by the transmission spectrum through the reference cells, as shown in Fig. 3. Figure 4(b) shows other experimental data. A gas-absorption measurement was performed for each gas cell and the reference cell. The absorption spectrum agrees with that in the HITRAN database. We successfully demonstrated the detection of multiple gases using the broadband DFG technique.

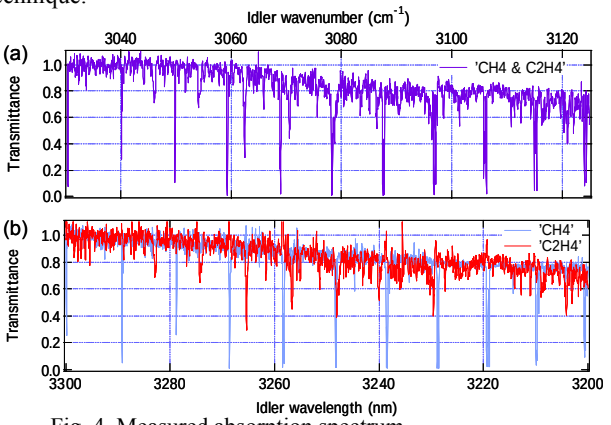


Fig. 4. Measured absorption spectrum.
(a) Simultaneously observed spectra for CH_4 and C_2H_4
(b) Superimposed individual spectra for CH_4 and C_2H_4

Conclusion

We succeeded in using apodization in a QPM wavelength converter by changing the duty ratio of a $\chi^{(2)}$ grating. This technique provides a large bandwidth and a flat phase-matching response, as well as a high conversion efficiency. We employed the technique to fabricate a DFG device based on $LiNbO_3$ waveguides. We demonstrated 3 μm-band DFG with a bandwidth of over 60 nm. These results agreed well with the theoretical predictions. We also demonstrated the simultaneous detection of the absorption lines of CH_4 and C_2H_4 and obtained a broadband absorption spectrum over 100 nm in the 3 μm region.

References

[1] Th. Toepfer, K. P. Petrov, Y. Mine, D. Jundt, R. F. Curl, and F. K. Tittel, "Room-temperature mid-infrared laser sensor for trace gas detection," Appl. Opt. vol. 36, pp. 8042-8049 ,1997.

[2] T. Yanagawa, O. Tadanaga, Y. Nishida, H. Miyazawa, K. Magari, M. Asobe, and H. Suzuki, "CH_4 monitoring in ambient air by communication band laser diode based difference frequency generation in a quasi-phase-matched $LiNbO_3$, " Appl. Phys. Lett. , vol. 89, 221115, 2006.

[3] Y. Nishida, H. Miyazawa, M. Asobe, O. Tadanaga, and H. Suzuki," A direct-bonded QPM-LN ridge waveguide with high damage resistance at room temperature," Electron. Lett., vol. 39, pp. 609-610, 2003.

[4] O. Tadanaga, T. Yanagawa, Y. Nishida, H. Miyazawa, K. Magari, M. Asobe, and H. Suzuki," Efficient 3-μm difference frequency generation using direct-bonded quasi-phase-matched $LiNbO_3$ ridge waveguides," Appl. Phys. Lett., vol. 88, 061101, 2006.

[5] T. Suhara and H. Nishihara" Theoretical analysis of waveguide second-harmonic generation phase matched with uniform and chirped gratings," IEEE J. Quantum Electron, vol. 26, pp. 1265-1276, 1990.

[6] M. M. Fejer, G. A. Magel, D. H. Jundt, and R. L. Byer, " Quasi-phase-matched second harmonic generation: Tuning and tolerances," IEEE J. Quantum Electron, vol. 28, pp. 2631-2654, 1992.

[7] R. Kashyap," Fiber Bragg Gratings," Academic Press, pp. 195-223, 1999.

[8] K. Ennser, M. N. Zervas, and R. I. Laming," Optimization of apodized linearly chirped fiber gratings for optical communications," IEEE J. Quantum Electron, vol. 34, pp. 770-778, 1998.

Semiconductor Quantum Dots

Andrea Fiore[1]

[1]COBRA Research Institute, TU Eindhoven, Eindhoven, The Netherlands
a.fiore@tue.nl

Abstract. *In this tutorial the physics of semiconductor quantum dots and their application to optoelectronic devices will be presented.*

The three-dimensional electronic confinement in semiconductor nanostructures ("quantum dots", QDs) produces discrete energy levels, much like in atoms. This gives rise to unique physical properties, with potential advantages over well-established bulk or quantum well active regions for lasers and other optoelectronic devices. Defect-free, nanometer-sized QDs with excellent optical properties are routinely obtained by self-assembled growth methods, using the strain in lattice-mismatched heterostructures as the driving force for nucleation (e.g. in the InAs/GaAs and InAs/InP material systems). High-performance and reliable lasers have been demonstrated in the entire 800-1600 nm wavelength range. Nevertheless, QD lasers have fallen short of original predictions in terms of gain, modulation frequency and temperature characteristics. In this tutorial, after a brief overview of growth methods and physical properties, the state-of-the-art of QD lasers will be presented. The main limiting factors in the laser modulation bandwidth and temperature performance will be analysed. Additionally, it will be shown that the unique features of QDs can find application in other optoelectronic devices, such as amplifiers, superluminescent diodes, mode-locked lasers and single-photon sources.

Scalable Quantum Dot Amplifier Based Optical Switch Matrix

A. Albores-Mejia, K.A. Williams, T. de Vries, E. Smalbrugge, Y.S. Oei, M.K. Smit, S. Anantathanasarn, R. Nötzel

TU Eindhoven, Eindhoven, The Netherlands

a.a.m.albores.mejia@tue.nl

Abstract. *A quantum dot active layer is used in a novel, highly scaleable monolithic optical switch matrix architecture. Electronically paired semiconductor optical amplifiers gates are implemented in a four-input four-output configuration to reduce the electrical connections and control complexity. Low power penalty 10Gb/s routing at a wavelength of 1555nm is demonstrated.*

Increasingly high-capacity data transfer in storage area networking, high performance computing, and server networks is driving research into increasingly elaborate photonic switched interconnect test-beds [1-4]. The need for low-latency, high capacity, scalable switch fabrics with low driver complexity, excellent crosstalk and the broad gain bandwidth has lead to a particular focus on semiconductor optical amplifier (SOA) based switches. However, considerable integration is required to remove complex packaging-related restrictions such as the high numbers of fibre pigtails, power consuming cooler circuits, and the complex electronic control circuits.

To date, integrated SOA based switch designs have focused on gate arrays in a broadcast and select architecture. The gates and inputs are connected via splitters and combiners utilising fibre [4] and waveguides with hybrid integration [5] and epitaxial regrowth [6]. The latter has lead to the smallest circuits with 20mm^2 footprints. The bulk active layer amplifier designs implemented have however lead to low saturation powers. The resulting low distortion threshold necessitates a lower number of photons per bit and thereby impairs signal to noise ratio and data capacity. The broadcast and select architecture requires a high number of waveguide crossings and exhibits a square law scaling in the required electrical control signals with the number of optical inputs. This already leads to 16 independent controls for a four input four output switch.

In this work, we present the first implementation of a four input, four output quantum dot based switch matrix. The design is based on a new crossbar element design which both integrates the waveguide crossing within the gate and is implemented with common electrodes to halve the required numbers of electrical connections. The use of complementary electrical signals further halves the number of independent control signals to four. Integration of the crossing within the gate also allows a reduced size for the shuffle network, and in combination with low loss, low distortion, quantum dot epitaxy, this allows an all-active implementation in a reduced chip area of only 3mm^2.

Integration Architecture

Figure 1i shows a photograph of the fabricated circuit. Four parallel input and output waveguides on a 250µm pitch are shown on the left and right hand side of the image. At the centre, a reduced shuffle network is implemented to interconnect the four crossbar switches. This therefore allows any optical input to be pathed to any optical

output by means of electronic addressing, although not necessarily simultaneously. Non-blocking operation may be implemented with a third stage of crossbars, but contention may also be more efficiently addressed with a packet-time-scale media access protocol.

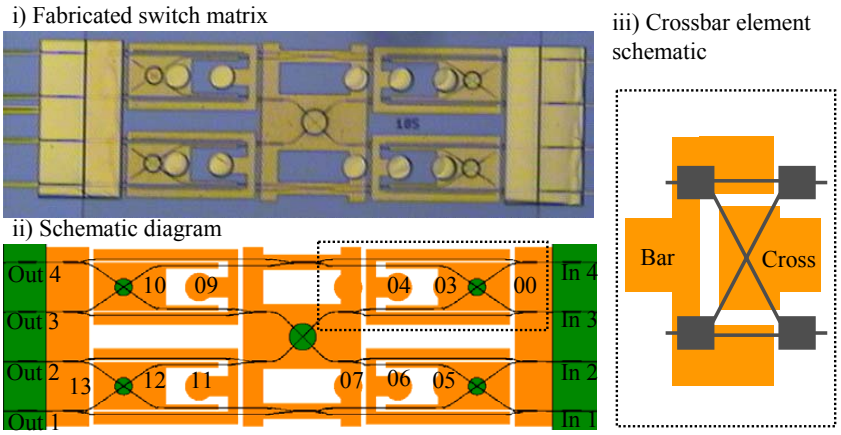


Figure 1: i) Photograph of switch matrix prior to bonding.
ii) Schematic layout showing waveguides and metallisation in correct proportion.
iii) Logical representation for one crossbar element.

The paths are implemented with a combination of multimode interference splitters and combiners located within the input, shuffle and output regions (pads 00, 07 and 13 in figure 1ii). These are interconnected by two stages of cascaded SOA gates (pads 03-06 and 09-12) which are also electronically configured. A crossing is implemented within the gates themselves using tight bend radius 100µm curves in combination with shallow-etched orthogonal crossings. This allows the area required for the remaining crossings and connections to be significantly reduced. The metallisation is common between the paths for the input, output and central shuffle region (pads 00, 07, 13). Within the crossbar matrix element, pairs of gates are electronically coupled to each other to reduce the off-chip wiring. One such crossbar matrix element is highlighted by the dashed box in figure 1ii with its logical equivalent alongside. For the two logical operational states required: cross and bar, this leads to a requirement for only one control input per crossbar switch, further reducing the operational complexity. Only four independent control signals are required for the four input, four output matrix.

The switch matrix is fabricated from a five stack quantum dot active plane embedded in a Q1.15µm InGaAsP separate confinement heterostructure [7]. A single step all-active epitaxy is used. The lower schematic in Figure 1ii shows the connections for the switch matrix. Three of the mask layers are shown including the SOA waveguide layer in black, p-metallisation denoted by the light shading, and regions with shallow SOA waveguides denoted by the dark shading. While the mask layer for the electrical isolation is not shown, the InGaAs capping layer is removed between the metal areas for this purpose. Planarisation is performed prior to gold evaporation and plating. Devices are mounted as-cleaved, epoxy bonded to patterned ceramic tiles, and wire bonded.

Circuit element performance

The switch is assessed using a multi-probe to the ceramic tile in combination with a reconfigurable electronic multiplexer. Forward series resistance values between 4-6Ω are measured depending on the addressed waveguides with one electrical fail at pad 5. Electrical isolation is measured to be in excess of 100kΩ for all electrode combinations. Initial characterisation is performed without electrical bias as the quantum dot epitaxy is sufficiently low loss to enable such characterisation and this is expected to provide clearer insight into on-chip component performance. Photocurrent measurements were performed for each circuit element with a continuous wave optical input of -13.7dBm in-fibre. Figure 2 shows the photocurrent generated at each electrical connection with the remaining connections left open circuit. Both forward and reverse directions through the circuit are overlaid with separate axes to show responses to all eight optical inputs. The data indicate a relatively uniform optical performance throughout the circuit. Predicted photocurrent values are also shown for the circuit with a solid line in figure 2 assuming the designed de/multiplexing gain and 4dB combiner losses.

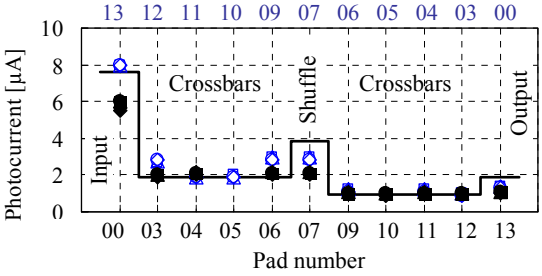


Figure 2: Measured photocurrent for -13.7dBm in-fibre injected power for each input (open symbols) and output (filled symbols). The solid line shows the predicted values.

A mean photocurrent reduction of 9dB is observed from the input pin to the output pin. The mean fibre coupling loss is estimated to be 8dB per facet from photocurrent measurements and this includes an estimated loss of 1.5dB through the cleaved facet. Including a 6dB adjustment to account for the four optical outputs gives a predicted fibre to fibre loss of 31dB for the unbiased circuit. This may be compared with direct power measurements at the input and output fibres where best case fibre coupled measurements give a 36dB off-state loss. More typical values of around 40dB are also measured for the majority of paths. A discrepancy is expected from difficulties in precisely estimating fibre coupling loss and from output waveguide losses which are unaccounted for in the photocurrent measurements.

Continuous wave currents are subsequently applied to combinations of five electrodes to form the switch paths. The input, output and shuffle pins are each operated at 200mA. The crossbar electrodes are selected according to the required state and are biased at 100mA. When one crossbar element is switched from on to off state, crosstalk values of over 10dB are typically observed. Local heating is believed to compromise the available gain and therefore crosstalk. Improved confinement layer design and longer gate length in the crossbar elements is expected to directly enhance performance. Optical saturation properties have also been studied, with the dependence of the gain on input fibre coupled power being negligible up to +11dBm.

10Gb/s Routing

To assess the integrity of routed data, optical eye diagrams and bit error rate measurements were performed at a data rate of 10Gb/s with a pattern length of 2^{31}-1. A fibre-coupled input power of +11dBm is used to study stressed performance. The switch matrix is polarisation sensitive and the injected state is optimised for minimum path loss. The bias conditions are the same as for the previous crosstalk assessment. Measurements are shown for the path from input 3 to output 4 to give a 0.4dB power penalty. Eye diagrams before and after the matrix remain clearly open.

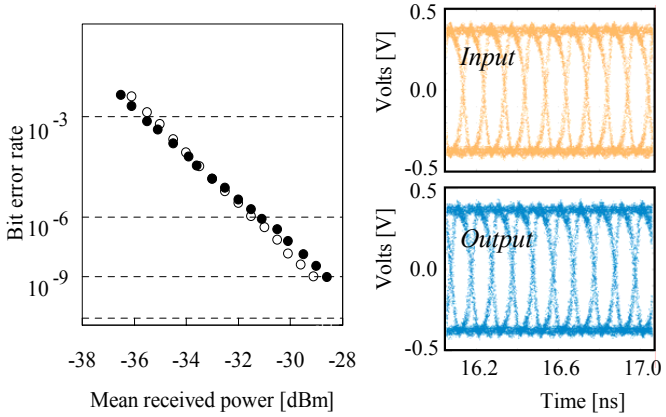


Figure 3: Bit error rate at 10Gb/s as a function of received power with (solid symbols) and without (open symbols) the switch matrix and corresponding eye diagrams.

Conclusions

The first quantum dot SOA based crossbar switch matrix design is proposed, fabricated and demonstrated. The monolithic circuit exploits the low loss and low distortion properties of the epitaxy to enable a compact, all-active, four input, four output switch fabric. The architecture leads to a marked reduction in electrical connections and control complexity compared to previously published SOA based switch arrays. A low optical power penalty of only 0.4dB is observed when routing 10Gb/s data.

References

[1] A. Shacham, B. A. Small, O. Liboiron-Ladouceur, and K. Bergman, J. Lightwave Technol. 23, 3066–3075 (2005).

[2] R. Luijten, C. Minkenberg, R. Hemenway, M. Sauer, and R. Grzybowski, Proceedings of the 2005 ACM/IEEE Conference on Supercomputing, p. 18.

[3] T. Lin, K. A. Williams, R. V. Penty, I. H. White, M. Glick, J. Lightwave Technology, 25 (3): 655-663 2007

[4] G. Soulage, A. Jourdan, P. Doussiere, M. Bachman, J. Y. Emery, J. Da Loura, and M. Sotom, European Conference on Optical Communication (1996), vol. 4, p. 145, paper ThD.2.1.

[5] J. Sasaki, H. Hatakeyama, T. Tamanuki, S. Kitamura, M. Yamaguchi, N. Kitamura, T. Shimoda, M. Kitamura, T. Kato, and M. Itoh, Electron. Lett. 34, 986–987 (1998).

[6] W. van Berlo, M. Janson, L. Lundgren, A.C. Moerner, J. Terlecki, M. Gustavsson, P. Granestrand and P. Svensson, IEEE Photonics Technology Letters, 7, 11, 1291-1293, 1995

[7] R. Nötzel, S. Anantathanasarn, P.J. van Veldhoven, F.W.M. van Otten, T.J. Eijkemans, A. Trampert, B. Satpati, Y. Barbarin, E.A.J.M. Bente, Y.S. Oei, T. de Vries, E.J. Geluk, E. Smalbrugge, M.K. Smit, and J.H. Wolter, (Review Paper), Jpn. J. Appl. Phys. 45, 6544-6549 (2006).

Integrated Quantum Dot 2x2 Switch for Uncooled Switching Applications

H. Wang[1], E.T. Aw[1], M.G. Thompson[1], A. Wonfor[1], A.R. Kovsh[2], R.V. Penty[1] and I.H. White[1]

[1]Department of Engineering, University of Cambridge, 9 JJ Thomson Avenue, Cambridge CB3 0FA, UK
hw288@cam.ac.uk
[2]Innolume GmbH, Konrad-Adenauer-Allee 11, 44263 Dortmund, Germany

Abstract. *This paper demonstrates the uncooled operation of an integrated 2x2 quantum dot switch and investigates the feasibility of an uncooled 32x32 optical switch constructed using QD monolithic crosspoint switches.*

Introduction

The increasing commercial demand for next generation services such as video on demand, voice over IP, and IP television has placed a requirement for highly reconfigurable optical cross-connects (OXC) for implementation as both core and edge switches in the next generation optical networks [1]. Optical switching technologies such as optical MEMS have been of interest, but they have slow switching speeds and are relatively lossy [2]. High speed switching is considered advantageous as it would improve network efficiency and provide greater flexibility, while lossless switching would negate the need of additional amplifiers in the link. As a result, there has been increasing interest in quantum dot (QD) semiconductor optical amplifiers (SOAs) for high speed optical switching applications as they demonstrate broad gain bandwidth, low noise performance, ultra-fast gain recovery, high saturation output power and low crosstalk performance [3]. A further issue arises from the need for high port count switch fabrics to operate uncooled over a large temperature range to reduce package complexity and cost by the removal of the thermoelectric cooler (TEC) used for temperature stability. QD-SOAs have been believed for some time to have the potential for enhanced temperature performance compared with multi-quantum well (MQW) SOAs owing to their improved carrier confinement.

In this paper, we present the performance of uncooled integrated 2x2 QD-SOA switches and consider their potential for scalability to switch sizes of up to 32x32. The basis of the analysis draws from the presented measurements of high gain, low penalty switching operation in an integrated 2x2 QD SOA switch at temperatures up to 70°C [4].

Monolithic 2x2 QD Switch

The layout of the 2x2 QD SOA switch is shown in Figure 1. The switch incorporates a QD active structure which is grown on a GaAs(100) substrate using molecular beam epitaxy. The active layer comprises a ten-fold stack of $In_{0.15}Ga_{0.85}As$ QDs, separated by 33nm GaAs buffer layers, embedded in an $Al_{0.35}Ga_{0.65}As$ waveguide. Standard photolithography and ICP dry etch processes are used to fabricate the ridge waveguide structures. Each of the four input ridge waveguides has a width of 3µm which expands linearly to a 6µm width, over a length of 150 µm. At this point, a focused ion beam etched 45° TIR mirror (inset Figure 1) is used to realise an integrated beamsplitter element, which allows 50% of the signal to pass to each of the following straight and perpendicular SOA gates. For ‘through’ path switching, bias current is applied to the

QD SOAs in sections 1, 2, and 3. Alternatively, bias current is applied to sections 1, 4, and 6 for the 'drop' path. The switch has an overall chip area of only 2.55x0.85 mm^2.

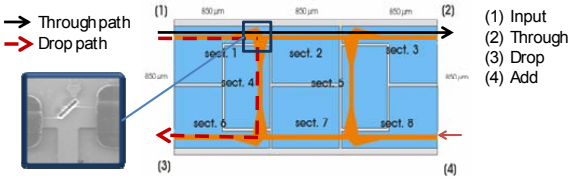


Figure 1: Schematic of switch structure showing the inputs, outputs, waveguides, splitters and SOA sections. Labels (1) to (4) denote the inputs and outputs of the switch. The solid and dotted arrows show the 'through' and 'drop' paths respectively. The TIR mirror used to route the light to drop and through path is shown in the inset.

The switch architecture considered in this analysis is based on a recently published Benes-Tree hybrid architecture [5]. This switch is similar to the Benes architecture, but with its middle cores replaced by a tree broadcast & select (B&S) architecture of corresponding size. A NxN switch designed using this architecture is shown in Figure 2A (with N as the number of inputs and outputs). It consists of N/2 2x2s in the input stage, two N/2xN/2s in the middle stage and N/2 2x2s in the output stage. Figure 2B shows how a 2x2 switching element can be augmented to a 4x4, 8x8 and 16x16 middle switching stage. Therefore, it can be seen for example that the 32x32 switch can be built using 160 2x2 switches, with each routing path traversing three cascades of 2x2 QD-SOA switches. As shown in Figure 2B, each step of switch augmentation requires an addition of one splitter at the inputs and one combiner at the output. The total number of splitters at the input and combiners at the output, as well is the corresponding net loss assuming 3.5dB passive loss for each splitter and combiner, is summarized in Table 1.

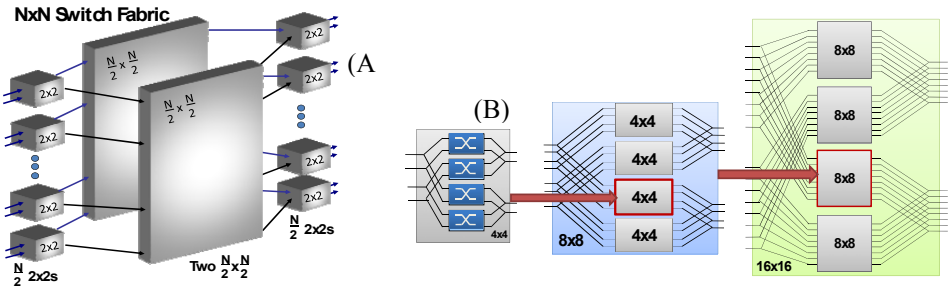


Figure 2: (A) A rearrangeably non-blocking 32x32 switch using the Benes-Tree hybrid architecture [2]. The 32x32 switches can be built using 192 2x2 switches. Each routing path would transverse three cascades of 2x2 switches. (B) Shows how a 2x2 switching element can be create successively larger 4x4, 8x8 and 16x16 switch fabric. Each step of switch augmentation requires an addition of one splitter at the inputs and one combiner at the output.

Table 1: Summary of number of input splitters and output combiner for a given switch size using 2x2 switching element and building blocks.

Switch Size for N/2 x N/2 middle stage	Number of Input Splitter	Number of Output Splitter	Total Input Splitting loss	Total Output Combiner loss
4x4	1	1	3.5dB	3.5dB
8x8	2	2	7.0dB	7.0dB
16x16	3	3	10.5dB	10.5dB

Uncooled Operation of 2x2 QD SOA Switch

Figure 3 shows the performance of the switch operating under temperature conditions between 20°C to 70°C. In figure 3A we show the gain vs. wavelength for a range of temperatures for the through path of the switch. The gain of the drop path is 3dB less owing to the excess loss of the additional mirrors to route the signal to the drop path. In general, the peak gain is higher when temperature is low, and the peak gain wavelength increases with temperature, as expected. For a 5nm optical bandwidth (1285-1290nm), there is only a ±3dB gain variation in the temperature range from 20°C to 70°C, which is shown in figure 3B.

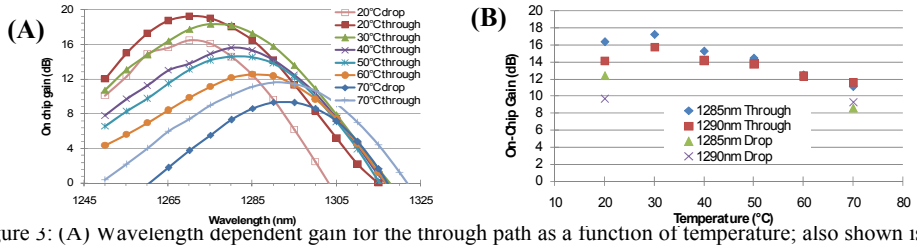


Figure 3: (A) Wavelength dependent gain for the through path as a function of temperature; also shown is the drop path at 20°C and 70°C. (B) highlights a region where gain is above 8.5dB for all temperature and ports .

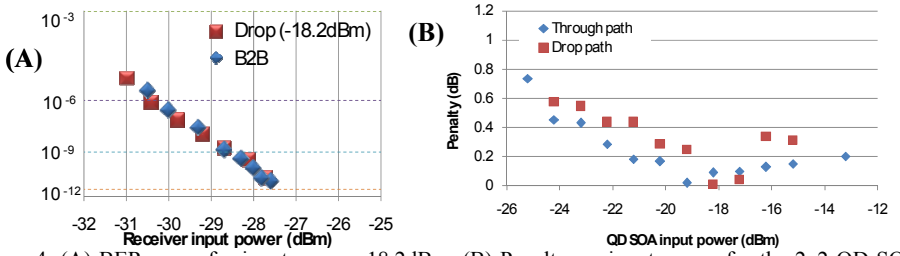


Figure 4: (A) BER curve for input power -18.2dBm. (B) Penalty vs. input power for the 2x2 QD-SOA switch at 70°C at 1290nm.

An optical signal at 1290nm wavelength, modulated with 10Gb/s PRBS sequence of 2^{31}-1, is transmitted to the 'input' power of the switch to assess the bit error rate (BER) performance from the 'through' and 'drop' output ports. The BER curve for input power -18.2dB is shown in Figure 4A, showing error free operation. The power penalty vs. input power curve for both the through and drop ports of the switch at operation of 70°C is shown in Figure 4B. A dynamic range of 11dB, restricted by measurement limitation, is obtained at power penalties of <0.6dB. No output power saturation is observed within the IPDR measurement range. A switching time of 1ns at 70°C has been measured [4], limited by the parasitics of the switch driver circuit.

Power Budget Analysis and Discussion

From Figure 3(A), it can be seen that for wavelength region of 1285 to 1290nm, a gain higher than 8.5dB can be obtained for both through and drop for all temperatures between 20°C and 70°C. It can be seen that for power penalties of <0.6dB, the input power dynamic range into the switch ranges from -13dBm to -24dBm. Hence, the power budget analysis would be based on each 2x2 switch giving a worst case gain of 8.5dB, with the maximum incurred power penalty for each stage of 0.6dB. Together

with the inter-stage switch loss information in Table 1, the evolution of power budget with the specified constraints is plotted in Figure 5.
It can be seen from Figure 5 that the estimated input power dynamic range of 11dB, 11dB and 7dB are obtained for switch sizes 8x8, 16x16 and 32x32 respectively. However, as calculations are based on IPDR measurements carried out using experimentally measured parameters for 1290nm wavelength, 70°C temperature and 100mA bias current, several assumptions have to be made. Overshoot of the 'IPDR max' region is considered acceptable as the gain of the QD-SOA can be reduced to operate within the IPDR margin by using a lower bias current. The reduction of gain is assumed not to incur additional penalties over the region of interest as lower bias current would contribute less amplified spontaneous emission (ASE) noise to the signal. As for the changes in temperature, similar IPDR measurements of a QD 2x2 SOA have been previously carried out at 20°C and penalties of <0.2dB have been measured over the region of interest [6].

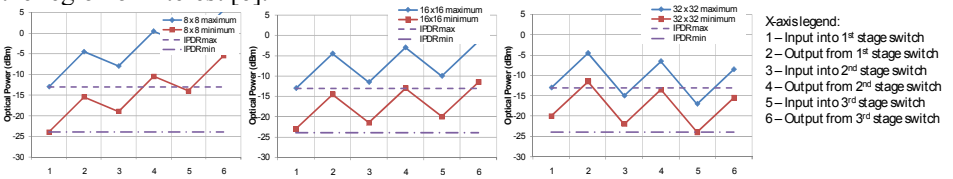


Figure 5: Figure shows the power budget evolution for switch sizes of 8x8, 16x16 and 32x32. The numbers (1 to 6) x-axis of the graph corresponds to the point of the signal within the switch, as shown in the top sub-figure.

Conclusion

This paper investigates the potential to realise high speed optical switches of size up to 32x32, operating uncooled over a temperature range of 20 to 70°C, using cascades of integrated 2x2 QD SOA switches. This analysis is derived from uncooled static and dynamic measurements of a fully integrated QD-SOA switch, which in the wavelength region of 1285 to 1290nm has a maximum of 17dB and minimum of 8.5dB gain, and an IPDR of 11dB (restricted by measurement limitations) at temperatures up to 70°C for power penalties of <0.6dB. The estimated input power dynamic range of the switches are 11dB for 8x8, 10dB for 16x16 and 4dB for 32x32 for cumulative power penalties of 1.8dB and below. These results show the significant potential of QD SOA technology in uncooled optical switched networks.

References

[[1] A. Jourdan, et al., "The perspective of optical packet switching in IP-dominant backbone and metropolitan networks", IEEE Commun. Mag., vol. 39, no. 3, pp. 136-141, Mar 2001
[2] X. Ma, G.S. Kuo, "Optical switch technology comparison: optical MEMS vs. other technologies", IEEE Commun. Mag., vol. 41, no. 11, pp. 16-23, Nov 2003
[3] T. Akiyama et al., "An ultrawide-band semiconductor optical amplifier having an extremely high penalty-free output power of 23 dBm achieved with quantum dots", IEEE Photon. Technol. Lett., vol. 17, no. 8, pp1614-1616, Aug 2005
[4] E.T. Aw et al., "Uncooled 2x2 Quantum Dot Semiconductor Optical Amplifier Based Switch", in CLEO 2008, accepted
[5] E.T. Aw et al., "Large Dynamic Range 32 x 32 Optimized non-blocking SOA based Switch for 2.56Tb/s Interconnect Applications", in ECOC 2007, We 4.3.2
[6] E. T. Aw et al., "Monolithic 2x2 Quantum Dot Switch for Optical Interconnect Networks ", in ECIO 2007.

ECIO-08: Polymer Devices in Integrated Optics

Author: [1]Dr. Terry V. Clapp (principle contact), [2]Dr. Jon V. DeGroot, Jr.

Affiliation: [1]Dow Corning Ltd. embedded researcher and Director of the Cambridge Integrated Knowledge Centre in Advanced Manufacturing Technologies for Photonics and Electronics (Exploiting Molecular and Macro-Molecular Materials). [2]Dow Corning Corporation, Midland, MI USA.

1 Abstract

Polymers have many applications in Photonics. Over the last 20-30years they have provided revolutions in the base technology (e.g. polymer coatings for silica fibres and plastic optical fibre) and in advanced applications (e.g. liquid crystal based filters and switching devices). This presentation offers a vision of the future

2 Polymers and Molecular Materials in Photonics

For a polymer to find application in optical systems it is essential to understand what physical form the polymer will take and what best fits the application. In contrast to most crystalline systems or oxide glasses, the naming of a polymer, for example polyethylene, is no guide to its physical nature nor its full property set. To understand the full gamut of its properties it is necessary to know, for illustration,

- Molecular size as specified by the molecular weight and molecular weight distribution of the polymer
- Polymer topology – is the polymer cross-linked (covalently bonded), branched, or are the molecules separable,
- Mechanical and Thermal phase behavior - is it glassy, elastomeric or crystalline (or a mixture of many "phases"), and if so its relevant thermal parameters,
- Chemical composition - is it a single monomer,
- a co-polymer,
- Monomer distribution – is it random, blocky, etc.,
- etceteras.

This list is many pages long and not readily answered except in a few highly studied systems and each parameter may be subject to change within any single embodiment, from batch-to-batch or from different manufacturers of notionally the 'same' material.

Thus, the down-selection of an individual material is not trivial and should properly be done via an exacting specification and verification exercise. Sadly many market deployments of polymeric materials failed to grasp this issue, or perhaps took expedience before good engineering! Unfortunately this has seriously damaged the credibility of these materials and they have had a troubled history, and now carry a baggage of suspicion as to their "fitness-for-purpose" in critical applications.

For most applications in optical technology, especially integrated optics, the principle requirements are for a baseline performance as an optical material (low loss at the wave-band of interest; preferably a suitable refractive index of low dispersion; good thermal performance; good process-ability) and additionally engineering quality assurance. This latter has been the most substantial challenge for optical quality polymers.

3 Contemporary Developments

Plastic optical fibres have had a long gestation, struggling for many years to demonstrate value against an incumbent glass fibre of mostly superior metrics, lower cost and greater supporting technology. However, with an improved specification, and the emergence of volume optical system deployment wherein ease of termination and flexibility, linked to easy alignment and a non-exacting application specification, has opened many new opportunities; plastic optical fibre has definitely found volume applications suited to the performance it offers.

Typically based on acrylates or perfluoro polymers, there are now several vendors of plastic optical fibre. This is supported by the emergence of cost effective VCSEL based transceiver technology, and RCLED. Plastic fibre for intra-office equipment and automotive applications (e.g. MOST) seem likely to continue to expand the opportunities for POF. From the perspective of integrated optics this is driving new developments for integrated optic modules and components and these will continue to grow the ECU50 Billion photonics market in Europe. (See ref.1 and ibid)

Cambridge University and Dow Corning have been developing planar waveguide technology using siloxane based polymers. A key target market is board level optical interconnect. The expectation is that optical technology will penetrate to every level of electronics systems and be the back-bone for all high data-rate channels for signalling. A recognition that siloxanes provide a preferred materials class for waveguide developments had been advanced for some years but the development of acceptable polymers, and proving the full-spectrum of process and performance specifications for circuit-board deployment has taken skill and persistence. This work provides an excellent example of the required program of research required if a polymer based optical interconnects is to be fit for commercial deployment.

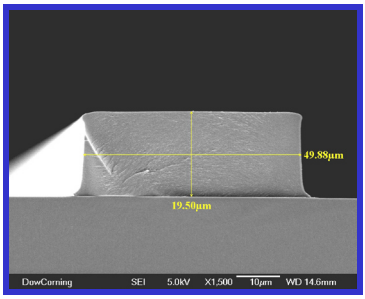
The requirements of this application illustrate the technical complexity of the problem The material has to be deployable into manufacturing of boards with complex metallic interconnects; quite possibly needing to be processed via large area patterning; it must certainly survive lead-free solder reflow temperatures (>250^{o}C); it must provide low enough loss for low-cost transceiver link budgets in realistic systems scenarios; it must be agnostic with respect to wavelength selected.

The challenge is to select hierarchical classes of device element that can be combined effectively to demonstrate functions that might then be integrated as single devices similar to the “Spice” models for the functional elements in electronics. Foundry practice can then permits exchange of design rules and the designer can then parameterise the selected design against a target foundry.

Additionally the various waveguide geometries required by differing applications must be explored. The companion proofs of process variables, process methods and quality engineering (reliability in service and tolerances to manufacturing of total systems, for example thermal excursions in solder re-flow etceteras) are also demonstrated.

To begin an emulation of this design practice the polymer wave-guide program within Dow Corning and CAPE has taken a step-wise approach to the full technology expression of optical waveguide components and systems. The first parts made were

simple traces rendered as short straight sections and longer spirals. Later devices, typical of standard needs (such as splitters, combiners and couplers), were fabricated in multi-mode and single mode designs. Thus the demonstration of the technology allows a level of abstraction sufficient to allow end-users clear paths to realise designs of merit in a variety of applications. (Refs: 2,3).



Adoption of a polymer waveguide technology for optical interconnect applications on circuit boards requires that every facet of the design and deployment is plausibly enabled to future proof the developments. Thus adherance to the design framework above coupled with verification engineering and quality engineering disciplines is vital. In Dow Corning's development we see a very clear demonstration of the conjoining of the materials science with process engineering that has enabled market relevant proofs of fitness-for-purpose.

The development of electro-optic devices based on polymeric and/or molecular materials is not new. In more recent times many have recognised the potential of molecular engineering to provide superior electro-optic coefficients and faster operational performance than is possible from the traditional materials. The difficulty has always been that any real application of such devices has deployment specifications and operational demands which the highly specialised molecules have thus far proven unable to survive. This does not detract from their potential and has not stopped researchers from continuing to seek improved systems, but even the best-in-class have yet to prove their fitness-for-purpose.

It is worth noting that inorganic, electro-optic crystals typically have a rising dielectric loss as the frequency operation increases. They may or may not have inconvenient damage thresholds (for optical flux or electric field). For the vast majority of available crystals the relevant electro-optic coefficient will lie in a range between 25 and 50pm/V. This contrasts with the best in class polymeric, or dye guest-host systems which have shown peak electro-optic coefficients greater than 200pm/V (see L. Dalton e.g. ref.11). Furthermore, typical molecular design targets utilise a non-resonant electro-optic response dependent on "Chi2" which is determined by the transition dipole moment magnitude in the aromatic charge transfer system. This means that contrary to their metal oxide or semiconductor crystalline competitors these materials have a lower dielectric constant and low dielectric loss which may be low to extremely high frequency, greatly in-excess of 100GHz.

Liquid crystal materials in integrated optics have also been studied, designs from the planar waveguide community for electric field driven phase control in Mach-Zehnder (MZ) devices are typical (ref. 12). Herein the relatively slow but either analogue or digital response of the LC is used to introduce a field initiated phase shift in one arm of a MZ structure and thus cause switching of optical power from one branch of the device to the other. In principle such optical elements can then be combined in parallel and in series to produce filter structures of arbitrary complexity. As yet the optical integration offered out of such elements has yet to be exploited widely, but the feasibility proofs have shown the promise.

Thus there are still opportunities for these materials but the technical and scientific challenge should not be underestimated.

The development of low cost CMOS back-planes for projection display applications has driven commodity costing of so-called liquid-crystal-on-silicon technology. Several groups world-wide have seen the potential herein to produce a new class of integrated optical system.

In principle, since an LC can control phase, the pixel circuitry of an LCoS back-plane can address upwards of 4Million phase controllers. This array of controllers thus becomes an arbitrarily programmable phased array (or holographic optical element). These have been shown to allow not only beam steering, but also point-to-point interconnection, multi-cast and broad-cast array switching capability. Using the intrinsic capability to write gratings then extends this capability to dispersive devices and LCoS has been adopted by several groups to demonstrate wavelength selective add-drop devices suitable for deployment in telecommunications as Reconfigurable Optical Add-Drop Multiplexers (ROADM).

This technology is still in its infancy but the direct coupling of the power of CMOS, with capability to place over a billion gates of processor power, with the power of computer generated holograms, via the liquid crystal phase control, is a staggering example of integrated optics far exceeding the previous generations of study.

4 Conclusions: The Potential Future

It is clear that polymers and molecular materials will play an every increasing role in integrated optics. Their complexity brings with them challenges as well as exciting opportunities. We believe to be the most exciting opportunities for advancement are

Self Assembly - the ability of molecular materials to self assemble and, either as polymers or as mesoscopic supramolecular systems, it is this capability which suggests manifold photonic integration applications. The future is for device structures to be created wherein the assembly of the photonics crystal or ordered array is entirely pre-determined by molecular design and process environment control. Example applications are: Polymer Modulators; Quantum Information Processing; Ubiquitous Integrated Optics. For high performance polymer modulators and, conceptual nano-scale gain devices, the ability to create polar order and thus have exceptional hyper-polarisability tensor values is already being demonstrated. Taking the next steps to create these effects in systems which replicate nature's ability to sequester and protect the reactive, functional, molecular entities is being attempted and will surely occur in the next decades. Having mastered polar order the next challenge beyond this is to control the spin environment and manipulate directly the quantum density of states. This leads one to contemplate the next great revolution... that of Quantum Information Processing, wherein we will finally see the complete fusion of "electronics" and "optical physics". The concept of ubiquitous integrated optics has been a currency of our community for many years. Even today this is true to a degree un-imaginable when Charlie Kao and George Hokham invented the optical fibre in the latter half of the 1960s. However, the process has a long way to run still.

5 References

[1.] Plastic Optical Fiber Trade Organisation; www.pofto.com

[2.] DeGroot, J., et al., "Highly transparent silicone materials", Proc. SPIE Vol. 5517, p. 116-123, Linear and Nonlinear Optics of Organic Materials IV; Robert A. Norwood, Manfred Eich, Mark G. Kuzyk; Eds., Oct. 2004.
[3.]Ingham, J. et al., "Multimode Siloxane Polymer Waveguides for Robust High- Speed Interconnects", Waveguides and Processing (CThS), CLEO, Long Beach, California, May 21, 2006.
[4.]Norris, A., et al., "Silicone polymers for optical films and devices," Proc. SPIE Vol. 4798, p. 79-86, Linear and Nonlinear Optics of Organic Materials II; Manfred Eich, Mark G. Kuzyk; Eds., Dec. 2002.

[5.] DeGroot, J., et al., "Highly transparent silicone materials," Proc. SPIE Vol. 5517, p. 116-123, Linear and Nonlinear Optics of Organic Materials IV; Robert A. Norwood, Manfred Eich, Mark G. Kuzyk; Eds., Oct. 2004.

[6.] Clapp, T. et al., "Dow Corning photonics: the silicon advantage in automotive," Proc. SPIE Vol. 5663, p. 208-215, Photonics in the Automobile; Thomas P. Pearsall; Ed., Feb. 2005.

[7] Su, K. et al., "Siloxane materials for optical applications," Proc. SPIE Vol. 6029, 60291C, ICO20: Materials and Nanostructures; Wei Lu, Jeff Young; Eds., Jan. 2006.

[8] Clapp, T. et al., "Dow Corning photonics: the silicon advantage in automotive," Proc. SPIE Vol. 5663, p. 208-215, Photonics in the Automobile; Thomas P. Pearsall; Ed., Feb. 2005.

[9] Su, K. et al., "Siloxane materials for optical applications," Proc. SPIE Vol. 6029, 60291C, ICO20: Materials and Nanostructures; Wei Lu, Jeff Young; Eds., Jan. 2006.

[10] Bamiedakis, N. et al., "Low-Loss, High-Uniformity 1x2, 1x4, and 1x8 Polymer Multimode Y-Splitters Enabling Radio-over-Fibre Multicasting Applications," submitted to OFC 2007.
[11.]Larry Dalton et al., "Terahertz all-optical modulation in a silicon-polymer hybrid system", Nature Materials, 5(9), p703, Sept. 2006
[12.] DeGroot et al., "Hybrid integration of silicone PDLC into a planar light circuit" Proc. SPIE Vol. 5222, pp163-170, Nov. 2003

Er:Ta_2O_5 waveguide optimization & spectroscopy

Ananth Subramanian[1], Claudio J. Oton[1], Robert[2] and James S. Wilkinson[1]

[1]Optoelectronics Research Centre, University of Southampton, Southampton, UK
ans@orc.soton.ac.uk
[2]School of Chemistry, University of Southampton, Southampton, UK

Abstract. *The optimization of erbium-doped Ta_2O_5 thin film waveguides deposited by magnetron sputtering is described. Background losses below 0.4dB/cm have been obtained before post-annealing. A broad photoluminescence spectrum centered at 1534nm is obtained, and the photoluminescence power and fluorescence lifetime increase with post-annealing, yielding promising results for compact amplifiers.*

1. Introduction

Optical amplifiers are key components in optical telecommunications and in fully-integrated optical systems. Erbium doped materials are of particular importance in optical communications technology, due to their excellent performance as gain media for amplifiers and lasers at the telecommunications wavelength of 1.5 microns. Low-cost, compact erbium doped waveguide amplifiers (EDWAs) are essential for local-loop optical systems, and fully-functional densely integrated planar lightwave circuits (PLCs) will rely upon gain as electronic integrated circuits do at present. Erbium-doped high index contrast materials have generated great interest [1-4], and will allow strong confinement of light, ultra compact photonic devices, and non-linear processes at moderate power levels. Tantala (Ta_2O_5) has already been used as a host for rare earth ions [5-7], with lasing being achieved only in Nd:Ta_2O_5 to date [5]. This, combined with high refractive index (>2.0), moderate phonon energy for high radiative efficiency [8], a large third order non-linearity [9], and high photosensitivity [10], makes it an ideal material for realising multifunctional PLCs. In this paper, the deposition and optimisation of erbium-doped Ta_2O_5 (Er:Ta_2O_5) thin films using magnetron sputtering is presented. The photoluminescence and fluorescence lifetime characterisation of these Er:Ta_2O_5 films annealed at different temperatures are also presented to evaluate this material's potential as a high index contrast host for erbium and as an EDWA.

2. Waveguide fabrication & characterization

Slab waveguides were fabricated by magnetron sputter deposition of a powder pressed, Er:Ta_2O_5 target onto an oxidised silicon substrate (oxide thickness ~ 2.1 μm). The target was doped with 1 wt. % of Er_2O_3 (~2.5 x 10^{-20} ions/cm^3). The deposition was carried out in a vacuum chamber pumped to a base pressure of 10^{-8} Torr and backfilled with an Ar:O_2 ambient. In order to obtain high-quality as-deposited films, substrate temperature, magnetron power and O_2 gas flow rate were optimised to yield low-loss films. The deposition rate was determined by measuring the film thickness for various sputtering times, using a stylus profilometer. Figure 1a shows the thickness plotted against time, for the deposition conditions optimised below, with the average deposition rate found to be ~ 2 nm.min^{-1}.

The slab waveguide losses were measured at 633nm (He-Ne laser) by prism coupling and measuring the propagation decay length. The losses were estimated at several different places on a sample to check the homogeneity of the sample, and averaged. The optical loss variation with substrate temperature is shown in Figure 1b. The sample sputtered at 200^oC gave the lowest losses (~0.4 dB/cm), so this was chosen as the

optimum substrate temperature. Losses are expected to be substantially lower at wavelengths near 1550nm.

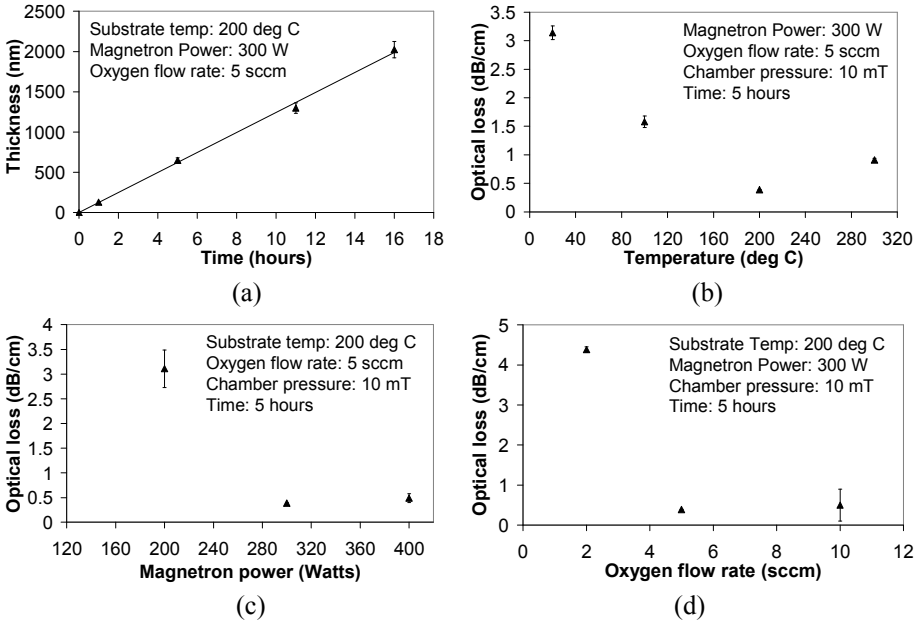


Fig 1 Er:Ta_2O_5 waveguide optimization a) Er:Ta_2O_5 deposition rate. b) Loss vs. substrate temperature, c) Loss vs. magnetron power, and d) Loss vs. oxygen flow rate.

Figure 1c shows the variation of optical loss with magnetron power, with low loss being achieved at 300W. Argon is used to start and maintain the plasma discharge and thus its flow rate is not critical, but the oxygen flow rate plays an important role in achieving low loss films as shown in figure 1d. With the increase in the O_2 flow rate, the film approaches its stoichiometric composition and hence lowest possible loss, but a further increase will lead to increased oxidisation of the target surface and an unacceptably low deposition rate. For our samples, a flow rate of 5sccm achieved the lowest loss value and a reasonable deposition rate. Ellipsometry measurements were performed on the sputtered Er:Ta_2O_5 samples to determine the thin film refractive index at various wavelengths in the visible region. Figure 2 shows the results for the fully optimized Er:Ta_2O_5 film.

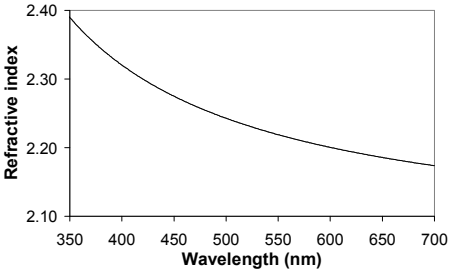
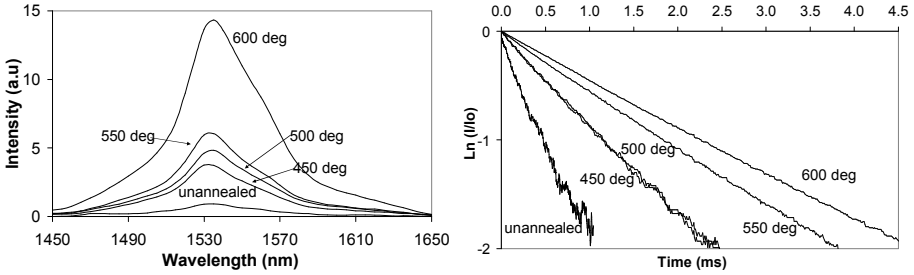


Fig 2.Refractive index of magnetron sputtered Er:Ta_2O_5 in the visible wavelength region.

2. Photoluminescence characterization

Photoluminescence measurements were performed at room temperature by pumping erbium ions into their $^4I_{11/2}$ level using a Ti:Sapphire laser emitting at 980nm. The thickness of the sample was approximately 2 microns. The power density was of the order of 1kW/cm^2 (180mW total power), and was chopped at 25Hz. The luminescence was collected perpendicular to the sample, sent to a 30cm focal monochromator, and detected with an InGaAs photodiode through a lock-in amplifier. The resolution of the spectra was 10nm. Lifetime measurements were also performed with 0.2ms resolution.The photoluminescence spectra of annealed and non-annealed magnetron sputtered Er:Ta_2O_5 samples are shown in Figure 3a. Four samples were annealed at 450,500,550 and 600°C, respectively, in a tube furnace for one hour in oxygen. Higher temperatures were not employed as annealing above 600°C is expected to result in a lossy polycrystalline film [11].



(a) (b)

Fig 3 a) Photoluminescence spectra (bottom: unannealed, topmost: 600 °C) and b) Luminescence decay (leftmost: unannealed, rightmost: 600 °C) for annealed and unannealed samples.

The emission spectra correspond to the transition between the $^4I_{13/2}$- $^4I_{15/2}$ levels of the Er^{3+} ion and peak at 1534nm. The bandwidth of the spectrum (FWHM) was measured to be 50nm which is substantially broader than those obtained from non-telluride glasses (~30nm) [12] and comparable to high index contrast hosts such as telluride glasses (n~2.1, 65nm) [13] and alumina (n~1.69, 55nm) [14] and shows potential for broadband applications. The photoluminescence intensity increases with annealing temperature to about 14 times that of the unannealed sample, at 600°C. The luminescence lifetime of the erbium ions is shown in Figure 3b and was found to increase from 0.53ms for the as-deposited sample to 2.4ms for the sample annealed at 600°C, where I/I_o is the intensity normalized with respect to the maximum intensity. The relationship between the intensity and lifetime can be explained in terms of the decrease in the non radiative decay rate when annealed at higher temperatures. The 2.4ms lifetime decay is smaller than those obtained from non-telluride glasses (10-15ms) [12] and alumina (6ms) [14] but comparable to high refractive index hosts such as telluride glasses (3.5ms) [15] and zirconia (n~2.04, 1.8ms) [2].

3. Conclusions

The deposition of Er:Ta_2O_5 by magnetron sputtering has been optimized to yield low loss slab waveguides (<0.4 dB/cm at 633nm) without annealing and losses can be expected to reduce further upon annealing at high temperatures, and with use at longer wavelengths. The refractive index of the thin film was determined over the wavelength range from 350nm to 700nm. A relatively broad photoluminescence spectrum

(FWHM~50nm) peaking at 1534nm was obtained, and a luminescence lifetime of 2.4ms was measured for the erbium ions in the Er:Ta_2O_5 film for optimised sputtering and annealing conditions. The results obtained for the losses and radiative lifetime are promising, for realizing erbium-doped integrated amplifier/laser and multifunctional photonic circuits based on Er:Ta_2O_5.

4. Acknowledgements

The authors would like to thank Neil Sessions, David A. Sager and Dr G. Senthil Murugan for their invaluable help and advice on optimising the sputtering process.

References

[1] G.N. van den Hoven, R.J.I.M. Koper, A. Polman, C. van Dam, J.W.M. van Uffelen and M.K. Smit, "Net optical gain at 1.53 microns in Er-doped Al_2O_3 waveguides on silicon," Appl. Phys. Lett., vol. 68, pp. 1886-1888, 1996.

[2] R. Schermer, W. Berglund, C. Ford, R. Ramberg and A. Gopinath, "Optical amplification at 1534 nm in erbium doped Zirconia waveguides," IEEE J. Quantum Electron., vol. 39, pp. 154-159, 2003.

[3] C.C. Baker, J. Heikenfeld, Z. Yu and J. Steckl, "Optical amplification and electroluminescence at 1.54 micron in Er-doped zinc silicate germanate on silicon," Appl. Phys. Lett., vol. 84, pp. 1462-1464, 2004.

[4] P. Nandi and G. Jose, "Erbium doped phospho-tellurite glasses for 1.5 micron optical amplifiers," Opt. Commun., vol. 265, pp. 588-593, 2006.

[5] B. Unal, M.C. Netti. M.A. Hassan, P.J. Ayliffe, M.D.B. Charlton, F. Lahoz, N.M.B. Perney, D.P. Shepherd, C.Y. Tai, J.S. Wilkinson and G.J. Parker, "Neodymium doped tantalum pentoxide waveguide lasers," IEEE J. Quantum. Electron., vol. 41, pp. 1565-1573, 2005.

[6] H. Rigneault, F. Flory, S. Monneret, S. Robert and L. Roux, "Fluorescence of Ta_2O_5 thin films doped by kilo-electron-volt Er implantation: application to microcavities," Appl. Opt., vol. 35, pp. 5005-5012, 1996.

[7] N. Maeda, N. Wada, H. Onoda, A. Maegawa, K. Kojima, "Preparation and optical properties of sol–gel derived Er^{3+}-doped Al_2O_3–Ta_2O_5 films," Opt. Mater., vol. 27, pp. 1851-1858, 2005.

[8] P.S. Dobal, R.S. Katiyar, Y. Jiang, R. Guo and A.S. Bhalla, "Raman scattering study of a phase transition in tantalum pentoxide," J. Raman Spectrosc., vol. 31**,** pp. 1061-1065, 2000.

[9] C.Y. Tai, J.S. Wilkinson, N.M.B. Perney, M.C. Netti, F. Cattaneo, C.E. Finlayson and J.J. Baumberg, " Determination of nonlinear refractive index in a Ta_2O_5 rib waveguide using self-phase modulation," Opt. Exp., vol. 12, pp. 5110-5116, 2004.

[10] C.Y. Tai, C. Grivas and J.S. Wilkinson, "UV photosensitivity in a Ta_2O_5 rib waveguide Mach-Zender interferometer," IEEE Photon. Tech. Lett., vol. 16, pp. 1522-1524, 2004.

[11] P.C. Joshi and M.W. Cole, "Influence of postdeposition annealing on the enhanced structural and electrical properties of amorphous and crystalline Ta_2O_5 thin films for dynamic random access memory applications," J. Appl. Phys., vol. 86, pp. 871-880, 1999.

[12] P.M. Peters, D.S. Funk, A. P. Peskin, D.L. Veasey, N.A. Sanford, S.N. Houde-Walter, and J.S. Hayden, "Ion-exchanged waveguide lasers in Er^{3+}/Yb^{3+} codoped silicate glass," Appl. Opt., vol. 38, pp. 6879-6886, 1999.

[13] R. Rolli, M. Montagna, S. Chaussedent, A. Monteil, V.K. Tikhomirov and M. Ferrari, "Erbium-doped tellurite glasses with high quantum efficiency and broadband stimulated emission cross section at 1.5 μm ," Opt. Mater., vol. 21, pp. 743-748, 2003.

[14] G.N. van den Hoven, E. Snoeks, A. Polman, J.W.M. van Uffelen, Y.S. Oei, and M.K. Smit, "photoluminescence characterization of Er-implanted Al_2O_3 thin films," Appl. Phys. Lett., vol. 62**,** pp. 3065-3067, 1993.

[15] H. Yamauchi, G.S. Murugan, and Y. Ohishi, "Optical properties of Er^{3+} and Tm^{3+} ions in a tellurite glass," J. Appl. Phys., vol. 97, pp. 043505-1 -043505-8, 2005.

Fabrication of Uniform Photonic Devices Using 193nm Optical Lithography in Silicon-on-Insulator

S. K. Selvaraja, W. Bogaerts, D. Van Thourhout and R. Baets
Gent University-IMEC, Department of Information Technology, Gent, Belgium
shankar@intec.ugent.be

Abstract: *We report sub-nanometer linewidth control in high index contrast photonic devices using CMOS fabrication tools. A linewidth uniformity of 20pm and 0.1nm is achieved over a distance scale of 25μm and 10,000μm respectively. Over a 200mm wafer, we have achieved linewidth uniformity of 99.55% for a 450nm photonic wire.*

Introduction

High index contrast material technology is an attractive platform for making compact and high density photonic integrated circuits[1]. However, the spectral characteristics of these high index contrast devices, especially SOI based circuits, are very sensitive to very small dimensional variations. This does not only hold for circuits as a whole but also for parts of devices, such as an individual ring in a multi-ring demultiplexer [2]. Making identical photonic circuits or devices is a technological challenge in high-index contrast systems. Each step in the fabrication process can give rise to dimensional variations. Starting from mask fabrication till device measurement small variations in dimensions and material properties can induce a change in the spectral response of the device. The device dimensions - width and layer thickness - have to be controlled in the order of few nanometers (or even below 1nm), which requires a high resolution fabrication process. Fortunately, advanced CMOS fabrication processes allows for such high resolution and stable fabrication process.

In this paper, we present our recent results on device uniformity achieved using 193nm optical lithography and dry etching. All the processes were carried out using 200mm CMOS high volume manufacturing tools. Over a 200mm wafer, we have achieved a linewidth uniformity of 99.55% and 99.44% after optical lithography and dry etching respectively, for isolated lines. This high uniformity encouraged us to fabricate wavelength selective devices such as ring resonators and mach-zehnder interferometers. For these devices, we obtained a fabrication accuracy better than 20pm for short range device-to-device separations (25μm) and 0.1nm for long range device-to-device separations (10,000μm).

Design and fabrication

To test the uniformity within a die and between dies, identical wavelength selective components were arranged in a particular fashion (Fig. 1a). We use all-pass racetrack ring resonators and 1X1 mach-zehnder interferometers (MZI) as wavelength selective test devices for characterizing the device uniformity over short (25μm) and long distance range (1700μm). Each device was repeated 4 times in pairs of 2 (twins). The racetrack ring resonators were designed with a wire width of 450nm, coupling gap of 180nm, coupling length of 4μm and a ring radius of 4μm. The MZI's were designed with a delay length of 50μm in one of the arms.

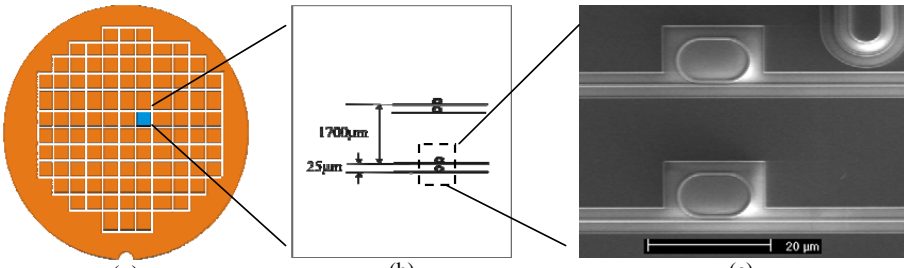


Fig. 1 (a) Die layout in a 200mm wafer , (b) Device layout in a die and (c) SEM picture of the ring pair

A 200mm SOI wafer was patterned with the mask containing the test devices described above (Fig. 1a). The fabrication was done in a CMOS pilot line at IMEC, Leuven, Belgium. We used 193nm optical lithography (ASML/1100) and dry etching to define our circuits. For comparison, we have also used 248nm optical lithography [3] and etching to compare the process with our new 193nm lithography process [4]. Fig.1b depicts one of the fabricated pairs of ring resonators. During the fabrication process the linewidths were measured at two stages, first, the resist linewidth after optical lithography and then the silicon wire width at the end of the fabrication process. Accurate linewidths were measured using critical dimension scanning electron microscope (CD-SEM). The linewidth measurement was done at 175 locations in a 200mm wafer. For a 450nm photonic wire, a standard deviation (1σ) of 2nm and 2.6nm was obtained after optical lithography and etching respectively. Table 1 summarizes the linewidth measurements statistics. A 15nm increase in the mean linewidth value after etch is due to the sloped sidewalls obtained after etching, which increase the photonic wire linewidth measured from the top. There is also a slight increase in the standard deviation after etch, which is associated with a non-uniform plasma distribution over the wafer, which subsequently increases the linewidth non-uniformity.

Table 1
Linewidth statistics after 193nm optical lithography and dry etch
Target linewidth = 450nm

	After Lithography	After Etch
Mean linewidth (nm)	450.92	464.77
Intra wafer stand. deviation (nm)	2.01	2.59
Intra wafer range (nm)	5.50	7.50
Intra wafer stand. deviation (%)	0.45	0.56
Intra wafer range (%)	1.22	1.61

Device characterization

The fabricated devices were optically characterized by coupling in TE polarized light from a broadband light source and measuring the output from the devices through a spectrum analyzer with a resolution of 0.12nm. Grating fiber couplers [5] were used for in and out coupling of light. The measurement spectrum was limited to the 1550nm telecom wavelength range (1520nm-1600nm). The spectral response of the ring resonators and MZI's was obtained to analyze intra (within) die and die-to-die uniformity.

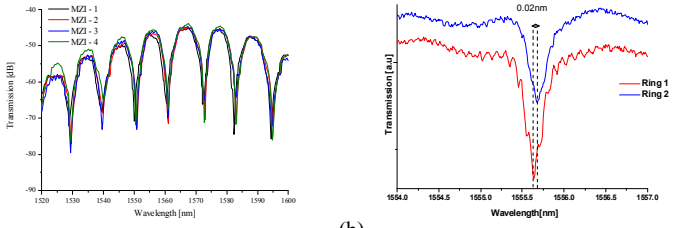
Intra Die Uniformity

Each die contains two pairs of ring resonators and MZI's as shown in Fig.1. Fig 2a shows the spectral response of four MZI's within a die, which were separated by 25μm (MZI-1,2 and MZI-3,4) and 1700μm (MZI-1,3 and MZI-2,4). Similarly, ring resonators were characterized (Fig. 2b). The measurements are summarized in Table 2. It can be clearly seen from Table 2 that the wavelength shift increases with an increase in the distance between the devices. This shift is more apparent when using 248nm lithography. Even though we used the same mask for 193nm and 248nm illumination, the linewidth variation using 248nm lithography is much higher than for 193nm lithography. These measurements clearly demonstrate the need for high resolution optical lithography for fabricating photonic devices.

From the measurements, we observed that the wavelength shift in the short distance range (25μm) ring resonator was below the resolution of our spectrum analyzer (0.12nm). Therefore, a tunable laser was used to characterize the resonance wavelength shift. With a sampling period of 10pm, we observed a peak shift of 20pm. This indicates an average linewidth offset of 20pm between the two ring linewidths. Fig.2b depicts the spectral response of two closely placed ring resonators. This short range linewidth uniformity achieved is comparable with matched ring resonators fabricated in SiN using e-beam lithography [2].

Table 2
Within Die/Chip device uniformity

Distance between the devices (Within Die)	Average resonance wavelength shift obtained using 193nm litho		Average resonance wavelength shift obtained using 248nm litho	
	Ring resonator	MZI	Ring resonator	MZI
25μm	0.15nm	0.2nm	0.3nm	0.7nm
1700μm	0.55nm	0.6nm	7.8nm	7.3nm



(a) (b)

Fig. 2 (a) Spectral response of 4 MZI's within a die,
(b) Spectral response of two racetrack ring resonators which are 25μm apart.

Die-to-Die Uniformity

Die-to-die or chip-to-chip uniformity is the device uniformity between two normally identical chips within a wafer. Die-to-die uniformity falls under long distance scale uniformity, at least few 10's of millimeter. Thus device uniformity is more complex than within a die. There are various factors (lithography tool etch, resist thickness, Si layer thickness, etc) contributing to the device non-uniformity and discriminating the contribution requires a detailed study of the different factors.

Table 3 shows the summary for 3 dies of the die-to-die measurements on ring resonators and MZI's. The average wavelength shift was calculated from 12 ring resonators and 12 MZI's (Fig. 3). A wavelength shift as low as 0.1nm was observed for ring resonators on

immediately adjacent dies and 1.5nm for the next farthest die. From these measurements, we observe a strong correlation of wavelength shift over each die (not shown here), which could be related to the mask or the lithography tool. More extensive experiments and analysis are necessary to draw further conclusions however.

Table 3
Die-to-Die device uniformity using 193nm optical lithography

Distance between the devices (Die-to-Die)	Average resonance wavelength shift obtained		Smallest resonance Wavelength shift obtained	
	Ring resonator	MZI	Ring resonator	MZI
10,000µm	1.3nm	1.08nm	0.1nm	~0nm
20,000µm	1.8nm	1.73nm	1.5nm	1nm

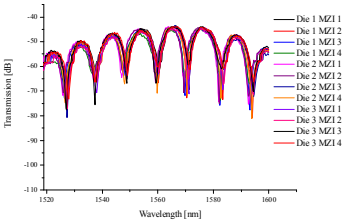


Fig.3 Spectral response of 12 MZI's from 3 different Dies

Conclusion

Highly uniform high index contrast silicon-on-insulator photonic devices were demonstrated. Device uniformity within die and die-to-die showed linewidth uniformity as low as 20pm and 1.5nm respectively. The results obtained are a good indication of the high resolution fabrication possible using CMOS fabrication tools. An extensive study on the non-uniformity is necessary to understand and improve the accuracy further.

Acknowledgments

We acknowledge the Smartmix Memphis and the ICT WADIMOS projects for supporting this work

Reference

[1] P. Dumon, W. Bogaerts, V. Wiaux, J. Wouters, S. Beckx, J. Van Campenhout, D. Taillaert, B. Luyssaert, P. Bienstman, D. Van Thourhout, and R. Baets, "Low-loss SOI photonic wires and ring resonators fabricated with deep UV lithography," *IEEE Photon. Technol. Lett.,* vol.16, pp. 1328-1330, May 2004.

[2] T. Barwicz, M. A. Popovic, M. R. Watts, P. T. Rakich, E. P. Ippen, and H. I. Smith, "Fabrication of add-drop filters based on frequency-matched microring resonators," *J. Lightw. Technol.,* vol. 24, pp. 2207-2218, 2006.

[3] W. Bogaerts, R. Baets, P. Dumon, V. Wiaux, S. Beckx, D. Taillaert, B. Luyssaert, J. Van Campenhout, P. Bienstman, and D. Van Thourhout, "Nanophotonic waveguides in silicon-on-insulator fabricated with CMOS technology," *J. Lightw. Technol.,* vol. 23, pp. 401-412, 2005.

[4] S. K. Selvaraja, P. Jaenen, S. Beckx, W. Bogaert, P. Dumon, D. Van Thourout, and R. Bates, "Silicon nanophotonic wire structures fabricated by 193nm optical lithography," in *Proc. 20th Annual Meeting of the IEEE* LEOS, 2007, pp. 48-49.

[5] D. Taillaert, F. Van Laere, M. Ayre, W. Bogaerts, D. Van Thourhout, P. Bienstman, and R. Baets, "Grating couplers for coupling between optical fibers and nanophotonic waveguides," *Jpn. J. Appl. Phys. Part-1,* vol. 45, pp. 6071-6077, Aug 2006.

Thermally stable ultra thin metal transparent electrodes

L. Martínez[1], S. Giurgola[2], P. Vergani[2] and V. Pruneri[1,3]

[1] ICFO - Insitut de Ciències Fotòniques, 08860 Castelldefels, Spain
Valerio.Pruneri@icfo.es
[2] Avanex Corp. - Via Fellini 4, 20097 San Donato Milanese, Italy
[3] ICREA - Institució Catalana de Recerca i Estudis Avançats, 08010 Barcelona, Spain

Abstract *- Transparent electrodes made of ultra thin metal films are highly competitive with respect to Transparent Conductive Oxides, e.g. ITO. We report on thermally stable nickel transparent electrodes.*

Introduction

Wide band gap semiconductors with heavy doping have been widely investigated as transparent electrodes. They are known as Transparent Conductive Oxides (TCOs) with Indium Tin Oxide (ITO) probably the most used of them. The trade-off between low electrical resistivity and high optical transmittance that can be achieved in TCOs has led to their use in many electro-optic devices such as solar cells, photo-detectors and Organic Light Emitting Diodes (OLEDs)[1]. TCOs deposition is, however, far from being a straightforward process. The influences of oxygen pressure, substrate temperature or post-deposition treatments on electrical resistivity and optical transparency of the film have been widely studied and regarded as potential drawbacks.
We have shown in previous works that Ultra Thin Metal Films (UTMFs) can possess higher electrical conductivity than TCOs while still having similar optical transparency [2, 3]. In addition, they can be grown through a single step deposition process, such as ultra high vacuum sputtering. In this paper we investigate the temperature stability of nickel-based UTMFs. We show that the electrical resistivity of films with thicknesses ≥ 3 nm does not change significantly for annealing temperatures $\leq 90^{o}$C. Also, in the case of film thickness ≥ 5 nm, the electrical resistivity does not change significantly for temperatures up to 145^{o}C.

Experimental results

Ultra thin nickel films were sputtered onto glass substrates at room temperature using a *Kenosistec Dual Chamber* DC sputtering machine in a pure argon (Ar) atmosphere. We used 8 mTorr Ar pressure and 200 W DC Power. Resulting deposition rate was 1.6 Å/s. Fig.1(a) and Fig.1(b) show respectively AFM images of blank BK7 substrate and a 3.4 nm Ni film taken five weeks after deposition with a *Digital Instrument D3100* AFM and associated software *WsXM* [4]. Surface roughness has to be kept below the thickness of the layer, otherwise films could be discontinuous and thus non-conductive. In our case, 3.4 nm film's RMS roughness is measured to be 0.36 nm using the *WsXM* software.
The electrical measurements were carried on using a *Cascade Microtech* 44*/7S* 2791 four point probe connected to a *Keithley* 2001 multimeter while a *Cary* 500 *Fourier Transform scan spectrometer* was used for optical transmittance measurements.
Five weeks after deposition UTMFs show electrical resistivity and optical transparency levels similar to ITO as shown in Fig.2(a) and Fig.2(b) respectively but slightly larger

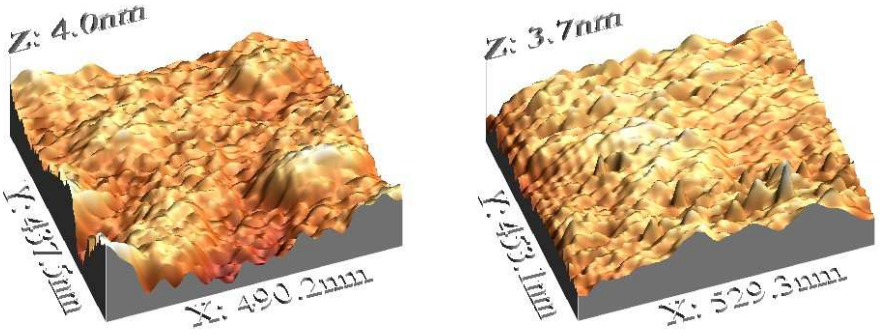


Figure 1: AFM images: (a) Blank BK7 substrate with a surface RMS roughness of 0.56 nm (b) 3.4 nm Ni film with a RMS roughness of 0.36 nm. Surface roughness levels of the substrate lower than deposited thickness are required for continuous films.

electrical resistivity when compared to previous works [2, 3] where it was measured straight after deposition. The difference is attributed to the advance in the oxidation process of the films. Note that the substrate's absorption is taken into account in the optical transmittance measurements as $T_f = T_t/T_s$ where T_t is the total optical transmittance (film and substrate), T_f and T_s are the film's and substrate's optical transmittance respectively.

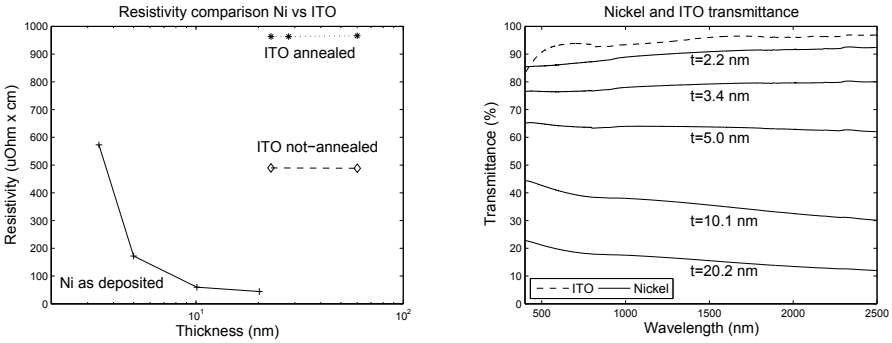


Figure 2: Comparison between UTMFs and ITO: (a) Electrical resistivity of ultra thin Ni films (solid line) 5 weeks after deposition. ITO annealed (dotted line) and non-annealed (dashed line) films are given as TCO reference. (b) Ultra thin Ni films (solid line) and ITO (dashed line) optical transmittance in the 400-2500 nm range. Two nanometer Ni film shows approximately the same optical transparency as ITO layers. The measurements were obtained five weeks after deposition.

The cumulative annealing treatments described in Table 1 were performed inside a *Selecta Hightemp* 2001406 oven and temperature was measured using a *Fluke thermometer* 52 *II*

Treatment name	Time	Temperature°C
H1	2h	90
H2	2h 45 min	105
H3	2h 30 min	112
H4	2h 30 min	145
H5	2h 30 min	90
H6	X	-40 to 85

Table 1: Time and temperature of the annealing treatments applied to the nickel films. These treatments were performed cumulatively. Treatment H6 corresponds to temperature cycles ranging from -40 to 85°C at 1.4°C per second.

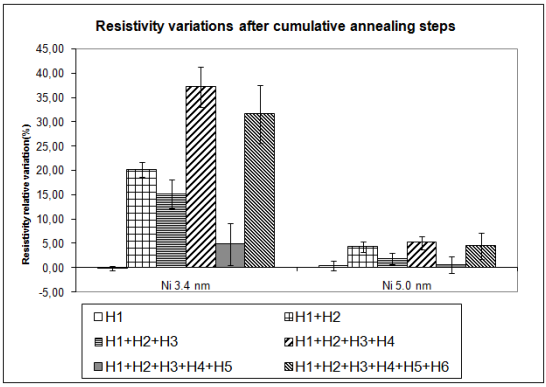


Figure 3: Electrical resistivity variation after cumulative annealing treatment.

thermometer and 80 *PK*-1 thermocouple. The first annealing treatment - labeled as H1 - was performed five weeks after the films had been deposited.
Electrical resistivity variations were measured after each annealing step on the same samples of different thicknesses. The values reported in Fig.3 are an average among 6 measurements. The formation of a natural oxide film due to oxygen indiffusion reduces the effective metallic layer, thus leading to higher electrical resistivity as shown in Fig.3, this effect being more significant for thinner films. Electrical resistivity variations of layers thicker than 5.0 nm are found to remain within 5% for all the annealing treatments whereas thinner films show larger variations. Accordingly, Fig.3 presents only the relative electrical resistivity variations for 3.4 nm and 5.0 nm films. Harder conditions, i.e. higher temperature, lead to larger electrical resistivity variations. The effect upon the 5.0 nm film is significantly reduced, with all variations within 6% meaning thus this film maintains similar conductivity along all the annealing process. In addition, also for films if 3.4 nm the variations are negligible below 90°C.

Conclusions

Ultra thin Ni films have been deposited using ultra high vacuum sputtering on glass substrates. The deposited films show continuity despite their very small thickness. The observed temperature stability together with the optical transmittance and electrical resistivity performances confirm that Ultra Thin Metal Films are serious competitors to Transparent Conductive Oxides, such as ITO, for those applications where transparent electrodes are required.

Acknowledgements

This work was partly supported by the Spanish National Program Plan Nacional no. TEC 2007-60185.

References

[1] G.G. Granqvist, "Transparent conductors as solar energy materials: A panoramic review", *Solar Energy Materials & Solar Cells*, vol. 91, pp. 1529, 2007.

[2] S. Giurgola, P. Vergani, V. Pruneri, "Ultra thin metal films as an alternative to TCOs for optoelectronic applications", *Nuovo Cimento B*, vol. 121, pp. 887, 2007.

[3] S. Giurgola, A. Rodriguez, L. Martinez, P. Vergani, F. Lucchi, S. Benchabane, V. Pruneri, "Ultra thin nickel transparent electrodes", *Journal of Materials Science: Materials in Electronics*, Published online: 22 December 2007.

[4] Horcas I, Fernandez R, Gomez-Rodriguez JM, Colchero J, Gomez-Herrero J, Baro AM (2007) Rev Sci Instrum

Trimming of silicon ring resonator by electron beam induced compaction

J. Schrauwen, D. Van Thourhout, R. Baets

Photonics Research Group, Department of Information Technology, Ghent University - IMEC, Gent, Belgium

jonathan.schrauwen@intec.ugent.be

Abstract *- We present a technique to trim the resonance of silicon ring resonators. The cladding oxide is compacted by electron beam bombardment, causing strain in the silicon lattice, which leads to a 5 nm resonance shift.*

Introduction

Silicon-on-insulator (SOI) is gaining interest as preferable material system for future ultra-compact integrated photonic components. The main advantages of this material system are firstly the high refractive index contrast between silicon (core) and oxide or air (cladding) enabling small bend radii and dense integration, and secondly mature fabrication facilities thanks to the electronics industry. One of the applications aimed at by the telecom industry is optical filtering for wavelength (de)multiplexing. SOI is the ideal platform to make these filters compact and low-cost. Several geometries, such as ring resonators [1] and photonic band gap materials [2] have good filtering characteristics. However, most of the demonstrated filters were fabricated with electron beam lithography, which is a serial fabrication technique and therefore unattractive for mass fabrication. In previous work we have demonstrated that these filters can also be fabricated in a parallel way, with 248 nm or 193 nm Deep-UV lithography (DUV) in a standard Complementary Metal Oxide Semiconductor (CMOS) facility [3]. However, variations of the critical dimensions of devices fabricated by optical lithography are inevitable. These variations can be caused by wafer non-uniformity, by e.g. varying layer thicknesses on wafer edges, or by non-uniformity within one chip, mainly caused by lithography imperfections near mask edges. A way to assess critical dimension variations in a photonic circuit is to evaluate the resonance wavelength shift of identically designed ring resonators, dispersed over a wafer. These resonators are fabricated with Q-factors of about 10^4 [1], or a 3 dB bandwidth of 0.15 nm. In practice the resonance wavelength shifts exceed 1 nm, which is unacceptable for many applications. The most common solution for this is active thermal tuning [4], however, when many resonators have to be integrated on a single chip, this would lead to high power consumption and important device complexity. Another approach to circumvent these process variations is trimming of the devices after fabrication. In this paper we present a technique to locally and independently trim the resonances of ring resonators on a silicon chip. This allows for complete compensation of resonance wavelength variations on silicon photonic integrated components.

Experiment

The resonance wavelength of a ring resonator is trimmed by changing the optical path length of the resonator, in our case by varying the effective index of the guided mode and

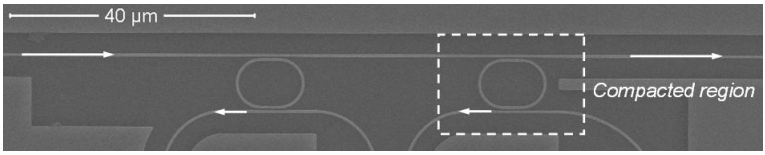


Figure 1: Overview of the experiment: the right ring is trimmed by electron beam compaction; the left one is kept original as a reference to exclude temperature or ambient variations.

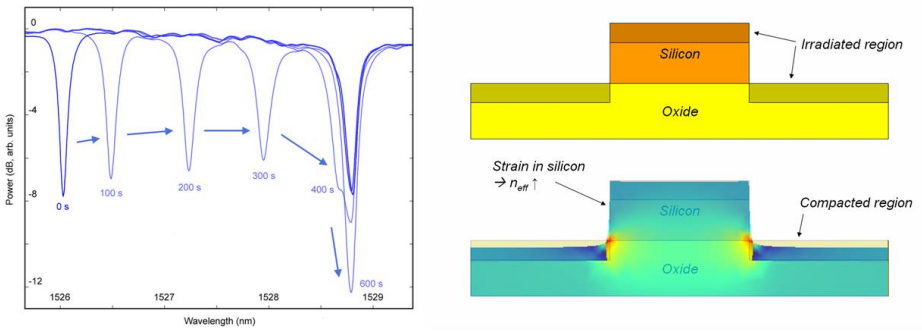


Figure 2: Left: The resonance wavelength of a ring is red shifted to equate that of the reference ring. One can notice a slight decrease of the Q factor. Right: Cross-section of the 220 nm thick silicon ring resonator. The 2 keV electrons penetrate 70 nm into silicon and oxide, and lead to volume compaction only in the oxide. This effect generates a tensile strain in the silicon, parallel to the substrate. The effect of silicon strain dominates the refractive index change. In the bottom drawing the first principal strain obtained from a finite element simulation was overlaid.

not the length of the ring. An increase in effective index causes a red shift of the resonance wavelength. This was demonstrated in several (low to medium index contrast) material systems such as silica glass [5] and SiN/SiON [6]. In SOI, the preferable material system for future industrial deployment, the core material is silicon, which can not be compacted by either UV or electrons. Only the SiO_2 cladding is susceptible to compaction. Due to the imaging capabilities and the ease to precisely control the irradiation dose and energy we have used an electron beam (from an FEI Nova 600 scanning ion/electron microscope) to compact the SiO_2 cladding layer. The resonance frequency of silicon ring resonators is extremely sensitive to changes of temperature and of the surrounding medium; rings are therefore attractive as sensors. However, in this experiment we want to exclude all external factors and investigate the resonance shifts caused only by electron beam irradiation. Therefore we have fabricated a sample with two rings, with different resonance wavelengths, serially connected to the same waveguide, as depicted in Figure 1. Only one of these rings is irradiated by imaging it with a scanning electron beam. The transmission spectrum features two superimposed ring spectra. By evaluating only relative peak shifts between the two ring spectra the external influences are excluded.
The experiment was performed in situ, inside the vacuum chamber of a scanning elec-

tron microscope, by providing it with vacuum fiber feedthroughs. The optical input and output signals are transported by single mode fibers, glued (with UV-curable glue) in a near-vertical position above grating couplers. The optical circuit, with grating couplers, waveguides, tapering sections, and ring resonators, was fabricated by DUV lithography in a CMOS pilot line [3]. Light was generated by a super luminescent LED with center wavelength at 1530 nm and detected by a spectrum analyzer with a resolution of 60 pm. The graph in Figure 2 shows part of the experiment. The left transmission dip - belonging to the right ring from Figure 1 - is trimmed to equate the resonance of the other ring. In this graph a resonance wavelength red shift of about 3 nm is shown. This part of the experiment was performed with a 0.84 nA beam, by scanning it over the ring resonator for 400 s. Figure 2 shows a slight decrease of the Q factor. The original position of the resonance was around 1523.9 nm, so in the complete experiment a total resonance shift of 4.91 nm was obtained.

Discussion

Two distinct physical processes cause the effective index change of the mode in the silicon ring resonator, as depicted in Figure 2. The first is a larger refractive index of the oxide cladding due to volume compaction; the second is the stress this oxide compaction induces in the silicon lattice. In our experiment we have worked with 2 keV electrons, which have a penetration depth of about 70 nm in Si and SiO_2 (this was calculated with Monte Carlo simulations, and confirmed by [7]). The silicon ring is 220 nm thick, on top of a 2 μm oxide layer; therefore the electrons can not penetrate the silicon. The mode overlap with the compacted oxide is lower than 1.5%, as was calculated with a mode expansion tool. From [7, 8] we have estimated the maximum amount of refractive index change lower than 3% (i.e. for a compaction of about 10%), with a total irradiation dose of 2.8 x 10^{23} keV/cm^3 (the total dose in our experiment). This can not lead to more than 0.5 nm shift in resonance wavelength. We can thus conclude that the largest fraction of the observed resonance wavelength shift is caused by strain in the silicon lattice. Finite elements simulations were used to evaluate this effect, as is shown in Figure 2. The overlay picture illustrates the deformed mesh (with a scale factor of 2) and the first principal strain in the case of a 10% compacted oxide layer with a thickness of 70 nm. Since a complete study was beyond the scope of this work, we have chosen to estimate the influence of compaction induced stress on the effective index of the supported modes without detailed simulations of the optical mode profile in the strained lattice. We have therefore calculated the average silicon strain in the dominant direction: perpendicular to the waveguide propagation direction and in the plane of the substrate surface. The resonance wavelength shift was calculated by using only the p_{11} component of the silicon elasto-optical tensor. This shift is calculated for varying oxide compaction rates and for different compacted layer thicknesses. The results of this simulation support the fact that tensile strain in the silicon waveguide can account for the observed resonance wavelength shift of more than 5 nm. Although all experiments in this report were performed with an electron beam, they can in principle be repeated with UV since the penetration depth at wavelengths between 200 nm and 400 nm is sufficiently low to create compaction induced strain. Ring resonators in other semiconductor materials can be compacted in a similar way, as well as other kinds of cavities, such as photonic crystal cavities. It can be argued that this method is too slow for mass fabrication purposes. However, we believe that it can be accelerated

by using higher beam currents. Furthermore, realistic shifts will not often exceed 1 nm. This makes that a typical trim will be performed in seconds. Specifically in combination with vertical grating couplers and in situ readout, this technique is suited for rapid and automatic trimming of devices before packaging and on wafer scale.

Conclusion

We report on the trimming of a silicon ring resonator by electron beam irradiation. The oxide cladding is subject to volume compaction, causing tensile strain in the silicon lattice. Both effects generate an increase in refractive index, generating a red shift in resonance wavelength. The dominant effect is the tensile strain in silicon. In our experiment we have measured a maximum resonance wavelength red shift of 5 nm, which would be sufficient to compensate for variations on wafer scale and on chip scale due to optical lithography imperfections.

Acknowledgements

This work was partly supported by the European Union through the Network of Excellence ePIXnet, by the Belgian IAP-PHOTON network and the Fund for Scientific Research (FWO).

References

[1] P. Dumon, W. Bogaerts, V. Wiaux, J. Wouters, S. Beckx, J. Van Campenhout, D. Taillaert, B. Luyssaert, P. Bienstman, D. Van Thourhout, and R. Baets, "Low-loss SOI photonic wires and ring resonators fabricated with deep UV lithograph", *IEEE Photonics Technology Letters*, vol. 16, pp. 1328-1330, 2004.

[2] Y. Akahane, T. Asano, B. S. Song, and S. Noda, "High-Q photonic nanocavity in a two-dimensional photonic crystal", *Nature*, vol. 425, pp. 944-947, 2003.

[3] W. Bogaerts, D. Taillaert, B. Luyssaert, P. Dumon, J. Van Campenhout, P. Bienstman, D. Van Thourhout, R. Baets, V. Wiaux, and S. Beckx, "Basic structures for photonic integrated circuits in silicon-on-insulator", *Optics Express*, vol. 12, pp. 1583-1591, 2004.

[4] I. Kiyat, A. Aydinli, and N. Dagli, "Low-power thermooptical tuning of SOI resonator switch", *IEEE Photonics Technology Letters*, vol. 18, pp. 364-366, 2006.

[5] Y. Nasu, M. Kohtoku, M. Abe, and Y. Hibino, "Birefringence suppression of UV-induced refractive index with grooves in silica-based planar lightwave circuits", *Electronics Letters*, vol. 41, pp. 1118-1119, 2005.

[6] H. Haeiwa, T. Naganawa, and Y. Kokubun, "Wide range center wavelength trimming of vertically coupled microring resonator filter by direct UV irradiation to SiN ring core", *IEEE Photonics Technology Letters*, vol. 16, pp. 135-137, 2004.

[7] C. B. Norris, and E. P. Eernisse, "Ionization Dilatation Effects in Fused Silica from 2 to 18-Kev Electron-Irradiation", *Journal of Applied Physics*, vol. 45, pp. 3876-3882, 1974.

[8] T. A. Dellin, D. A. Tichenor, and E. H. Barsis, "Surface Compaction in Irradiated Vitreous Silica", *Bulletin of the American Physical Society*, vol. 21, pp. 296-296, 1976.

Subwavelength Structures in Silicon-on-Insulator Waveguides for Modification of Facet Reflectivity and Efficient Fiber-Chip Coupling

J. H. Schmid, P. Cheben, S. Janz, J. Lapointe, E. Post, A. Delâge, A. Densmore, B. Lamontagne, P. Waldron and D.-X. Xu

Institute for Microstructural Sciences, National Research Council, Ottawa, Ontario, Canada, K1A 0R6
jens.schmid@nrc-cnrc.gc.ca

Abstract. *First implementations of subwavelength gratings in silicon-on-insulator waveguides are discussed and demonstrated by experiment and simulations. The subwavelength effect is exploited for making antireflective and highly reflective waveguide facets as well as efficient fiber-chip coupling structures for photonic wire waveguides.*

Introduction

Subwavelength gratings (SWGs), i.e. gratings with a pitch that is sufficiently small to suppress all but the 0^{th} order diffraction, have been known and used for many years [1], most commonly as an alternative to antireflective (AR) coatings on bulk optical surfaces. Since diffraction is suppressed, the light propagating through a SWG structure is influenced by the average optical properties of the SWG medium. This SWG effect allows one to engineer artificial materials with refractive indices that are intermediate to those of the constituent materials of the SWG. In the context of high index contrast (HIC) integrated planar waveguide circuits, SWG patterns can be used to alleviate some of the fundamental problems intrinsic to HIC waveguides. Here, we demonstrate by experiment and simulation the first implementations of SWG structures in silicon-on-insulator (SOI) waveguides. We show that both AR and highly reflective (HR) waveguide facets as well as highly efficient fiber-chip couplers for photonic wire waveguides can be made using SWGs fabricated by standard lithography and etching processes.

Modification of Facet Reflectivity by SWGs

The AR effect of SWG structures formed on waveguide facets, such as those shown in Fig. 1, is analogous to the same effect on bulk optical surfaces and can be described using the effective medium theory (EMT) [2]. According to EMT, a composite medium comprising two different materials interleaved at the subwavelength scale can be approximated as a homogeneous medium with a refractive index expressed as a power series in (Λ/λ), where Λ is the pitch of the SWG and λ is the wavelength of the light. From this theory a gradient-index AR effect is expected for gratings with a triangular shape while square SWGs can be used to mimic the effect of a single layer AR coating. The duty cycle of the grating controls the effective index and the modulation depth corresponds to the thickness of the equivalent thin film. Examples of square and triangular SWG patterns on ridge waveguide facets in 1.5 μm thick SOI are shown in Fig. 1. In both cases, samples are fabricated with a two-step patterning process. The facets are formed by electron beam lithography and reactive ion etching.

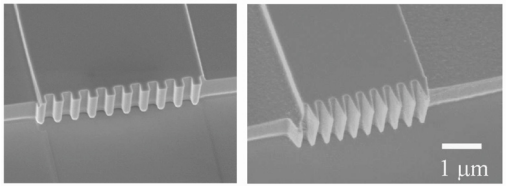


Fig. 1: Scanning electron micrographs of SOI waveguide facets patterned with square (left) and triangular (right) SWGs.

To measure the facet reflectivity, transmittance of fabricated waveguides was measured as a function of wavelength near λ=1.55 μm and the reflectivity was inferred from the depth of the Fabry-Pérot fringes observed in the transmission spectrum. Results of these measurements for triangular SWGs are shown in Fig. 2 as a function of the grating modulation depth. An efficient AR effect is observed, with facet power reflectivities as low as 2.0% for transverse electric (TE) and 2.4% for transverse magnetic (TM) polarization for a modulation depth of 0.7 μm [3]. The single layer AR effect of square SWGs is also demonstrated experimentally. Unlike the case of the triangular SWGs, the reflectivity of square SWGs is strongly polarization dependent. For example, the lowest experimental facet reflectivity for a square SWG obtained is 3.6% for TE polarized light; however, the same facet has a reflectivity of 23% for TM polarization. The experimental results for both triangular and square SWG facets are in good agreement with EMT.

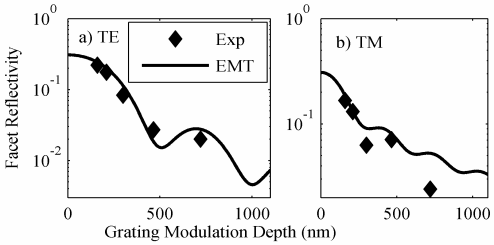


Fig. 2: Experimental data and theoretical results from EMT for the reflectivity of facets with triangular SWGs as a function of the grating modulation depth (corresponding to the length of the gradient-index section).

When the pitch of a square SWG is increased to the point where diffraction becomes possible on the silicon side, but is still suppressed on the air side of the grating, i.e. $\lambda/n_{Si} < \Lambda < \lambda$, an interesting effect is observed. The grating parameters can be chosen such that a waveguide mode incident on the patterned facet from the silicon side experiences a high reflectivity, whereas light incident from the air is almost completely diffracted into the +1 and -1 diffraction orders inside the silicon, with the 0^{th} order transmission and reflection being suppressed. Finite-difference time domain (FDTD) modeling is used to demonstrate this effect. The layout of a 2D FDTD simulation is shown in Fig. 3a. It is a 7 μm wide Si waveguide (n_{Si} = 3.476) with SiO_2 lateral claddings (n_{SiO2} = 1.44), terminated at the facet with a square grating. The grating period

is 0.7 μm, the duty cycle is 54% and the grating modulation depth is 485 nm. The external medium is air (n = 1). A continuous-wave field excitation of a TE (electric field in the plane of the drawing) waveguide fundamental mode of free space wavelength λ = 1.55 μm propagating in the waveguide towards the facet was assumed. The mesh size used was 10×10 nm^2 and the simulation was run for a total of 10,000 time steps of $\Delta t=2.2\times10^{-17}$ s. The calculated TE electric field map is shown in Fig. 3b. The excitation plane for the waveguide mode source is indicated in the figure by a blue line, including the mode propagation direction (arrow). It can be seen that the transmittance through the grating structure is efficiently suppressed, creating the mirror effect. Between the excitation plane and the facet, the forward propagating and the reflected light form a standing wave interference pattern. To the left of the excitation plane, the reflected mode propagates unperturbed in the waveguide. A reflectivity value of 97% is obtained for this 2D structure. Figure 3c shows the simulation of light coupling from an external optical fiber to the Si waveguide. In this case, a light source with Gaussian intensity profile with a $1/e^2$ full width of 10.4 μm (SMF-28 fiber mode), is located at the excitation plane (white line in Fig. 3c). The calculated field in the waveguide reveals a strong transverse modulation with a period half of the grating pitch, which persists almost unperturbed for several micrometers as the light propagates in the waveguide. This intensity pattern stems from the superposition of the -1 and +1 diffraction orders, while the 0^{th} order is suppressed. Rigorous coupled wave theory (RCWT) of plane waves incident on silicon surface gratings corroborates the FDTD results described above. For example, reflectivities >99% for light incident from the silicon side are calculated from RCWT.

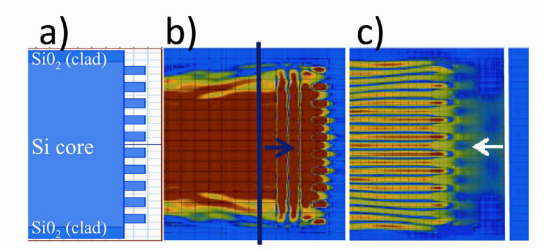


Fig. 3: FDTD simulations of HR SOI facets: a) Simulation layout. b) FDTD simulation for a TE waveguide mode launched at the plane indicated in the figure. c) TE field map for an external optical fiber mode coupling into the waveguide.

Waveguide transmission measurements similar to the ones we have discussed for the AR facets have been carried out for the HR structures. The results confirm the HR subwavelength grating concept; however, it is found that the reflectivity depends strongly on mode confinement. This was confirmed by 3D FDTD simulations, which showed that the maximum facet reflectivity for a 1.5 μm thick SOI waveguide is 80%, whereas 94% reflectivity can be achieved for a waveguide thickness of 5 μm.

Fiber-Chip SWG Couplers

An original application of SWGs for fiber-to-waveguide coupling and mitigating losses due to the mode size mismatch of optical fibers and SOI waveguides of submicrometer dimensions has been proposed recently [4]. The principle of this fiber-chip coupler is based on a gradual modification of the waveguide mode effective index by the SWG

effect. In this scheme the waveguide is transformed into a longitudinal subwavelength waveguide grating, as shown in the scanning electron micrographs of a fabricated coupler structure in Fig. 4a. As the mode travels along the SWG, the waveguide mode effective index is altered by chirping the SWG duty ratio $r(z) = a(z)/\Lambda(z)$, where $a(z)$ is the length of the waveguide core segment and $\Lambda(z)$ is the pitch. Figure 4b depicts the same coupler structure closer to edge of the chip, where the fiber is coupled to the SWG. Both the duty ratio and the width of the segments are reduced to optimize the overlap of the fiber mode with the mode of the segmented waveguide. Coupling efficiencies as large as 76% (1.35 dB loss) were calculated for coupling from a standard SMF-28 optical fiber using 2D FDTD simulations of SOI waveguides with a Si core thickness of 0.3 μm. The first fabricated SWG waveguide couplers shown in Fig. 4 are for SOI photonic wire waveguides with dimensions of 0.45 μm (width) × 0.26 μm (height). The minimum pitch of the grating is 0.2 μm and the smallest gaps are nominally 50 nm. In first experiments, the lowest coupling loss of approximately 4 dB was achieved for a coupler length of 50 μm, compared to 11 dB loss for photonic wires without couplers. Preliminary experimental results indicate that the coupling loss can be further improved by optimization of the SWG parameters, in particular by tapering the width.

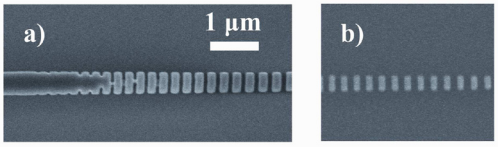


Fig. 4: Scanning electron micrographs of a fabricated SOI photonic wire waveguide with a SWG coupler (top view): a) The SWG coupler joining the photonic wire waveguide. b) Mid-section of the SWG coupler.

Conclusions

We have presented results of experiments and simulations of first SWG structures in SOI waveguides. Three types of structures have been discussed, namely AR and HR waveguide facets and fiber-chip couplers, all fabricated using standard fabrication techniques. The AR facets were demonstrated exploiting either a single layer AR effect from square SWGs or a GRIN effect from triangular SWGs with a minimum measured reflectivity of 2%. HR SWG facets employ a similar structure to that of square AR SWG waveguide facets but with different grating parameters, namely pitch, modulation depth and duty ratio. Finally, the principle, design and first experimental results on SWG fiber-chip couplers were reviewed, demonstrating a fiber-to-photonic wire coupling loss of ~4 dB.

References

[1] H. Kikuta, H. Toyota and W. Yu, "Optical elements with subwavelength structured surfaces", Opt. Rev., vol. 10 (2), pp. 63-73, 2003.

[2] S. M. Rytov, "Electromagnetic properties of a finely stratified medium", Sov. Phys. JETP, vol. 2 (3), pp. 466-475, 1956.

[3] J. H. Schmid, P. Cheben, S. Janz, J. Lapointe, E. Post and D.-X. Xu, "Gradient-index antireflective subwavelength structures for planar waveguide facets", Opt. Lett., vol. 32 (13), pp. 1794-1796, 2007.

[4] P. Cheben, D.-X. Xu, S. Janz and A. Densmore, "Subwavelength waveguide grating for mode conversion and light coupling in integrated optics", Opt. Expr., vol. 14 (11), pp. 4695-4702, 2006.

Ultrafast all optical switching in AlGaAs photonic crystal waveguides

D.M. Szymanski[1,2], B.D. Jones[1], David O'Brien[2], M.S. Skolnick[1], A.M. Fox[1], T.F.Krauss[2]

[1]Department of Physics and Astronomy, University of Sheffield, UK S3 7RH
d.szymanski@sheffield.ac.uk
[2]School of Physics and Astronomy, University of St Andrews, Fife, UK KY16 9SS

Abstract. *We have demonstrated all optical switching using photonic crystals integrated into an AlGaAs Mach Zehnder interferometer (MZI). Enhanced phase modulation efficiency together with fast carrier recovery times of 4 ps and high nonlinearities of the AlGaAs material make this design suitable for ultra fast all optical switching applications.*

Ultrafast all optical switching

Nowadays telecommunication networks rely on electro – optic components that limit the network's performance. Only full optical control of light by light can meet the demands of increased bandwidth. Optical components are not limited by the RC constants like their electronic counterparts and allow generation of much shorter pulses which allow higher network speeds. However still some work must be done to fulfil all the requirements for optical devices. The most important are low power consumption, high S/N ratio, and high repetition speed. It is very hard to meet all of these criteria at once so the device should be carefully chosen. All optical elements rely on the refractive index change. This optically induced change is limited by the material nonlinearity and the required π phase change entails that the size of the device be in the range of millimetres. Proper device design, material choice and the optical nonlinearity used can significantly increase the device performance. High repetition rates can be achieved using nonresonant optical nonlinearities. The main disadvantage of that approach is the high power required to utilize the full material nonlinearity. Power consumption and the speed can be enhanced by utilizing resonant coherent effects. Coherent effects are not limited by real carrier relaxation. The pulse width of the laser should be shorter than the carriers' relaxation times, if not, real carrier generation occurs and limits device speed. Even if the laser pulse width is shorter real carrier generation can still mask coherent effects. Carriers are generated then via multiple photon absorption. From a practical point of view it is easier to work with incoherent effects because the device can be operated at low powers. In this experiment we show a way to decrease carrier relaxation time utilizing TPA (two photon absorption).

Experimental methods

We have investigated all optical switching using photonic crystals integrated into a GaAs/AlGaAs Mach Zehnder interferometer (MZI). The MZI employs multimode interference (MMI) optical power splitters and photonic crystal waveguides in the functional area of each arm. Optical switching can be achieved by optically pumping the photonic crystal sections of one of the arms causing a carrier induced refractive index change in this arm of the MZI.
A compact 3dB 1x2 power splitter operating at 950nm centre wavelength was designed by selecting correct position along MMI's and waveguides configurations.

The imaging length of the MMIs was optimised using FDTD simulation and $3/8L_{\pi}$ was found to get 1x2 power splitting. A refractive index of 3.29 was used during simulation. This refractive index represents the effective index of the waveguide slab which was calculated separately.
The optical bandwidth of the splitter is inversely proportional to the square of the MMI's width so 6μm width was chosen as optimal for the sake of device performance and fabrication purposes [1]. As an output waveguides separation was design to be 3μm hence further decreased in device size could cause outputs overlapping.
Optimal geometry was found to be: 6μm MMIs width, 64μm MMIs length, 1.5μm width of the input and output waveguides. S-bend type waveguides were added to separate MZ arms of 25μm.
Photonic crystal waveguides are the most critical part of the all optical MZ switch. Their function is not only decreasing the functional area of the device but, importantly increasing the operation speed of device. The holes patterned in a semiconductor host system play the role of recombination centres and hence relaxation time of the excited carriers is reduced. Samples were fabricated with three different types of photonic crystal waveguides. The first two types rely on engineered defects in the triangular lattice PhC. Rows of the one and three holes were removed to create W1 and W3 type waveguides. The third type utilizes self-collimation phenomena in a square PhC lattice. The main advantage of this type of structure is that the guiding does not rely on the photonic bandgap, so no defect need to be introduced into lattice. The fraction of etched holes and thus surface recombination is increased in that type of lattice. The self-collimation regime of the square lattice was found using PWE and FDTD method.
Light propagation in the photonic crystal is governed by its dispersion surface and it is perpendicular to it. Non patterned semiconductor slab exhibits circular shape of EFC (equi-frequency contour) so propagated light is diverged. Different dispersion properties of the photonic crystals at different frequency give rise to different EFC contours shapes. One can obtain a square shape of EFC contours and hence collimation of the beam by carefully choosing the geometry and frequency operation range for the square lattice. Square lattice has two possible self-collimation regions [2].

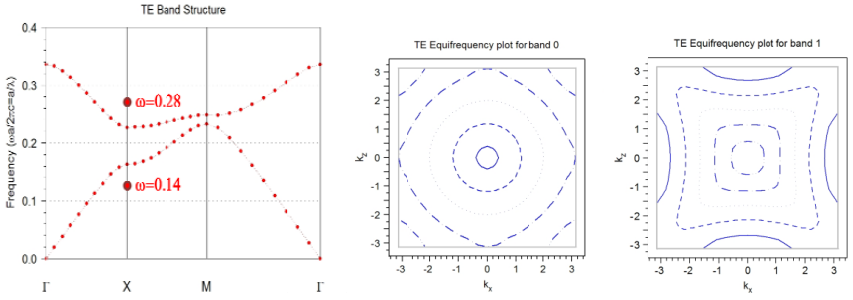


Figure 1. Dispersion diagram for PhC comprising an AlGaAs slab patterned with air holes in a square lattice (top left). PWE method was used with effective refractive index of the slab 3.29. EFC contours for a first two bands: band 0 (left) and band 1 (right) show variety of shape for different frequencies.

Figure 1 shows EFCs for first two bands. First band has a square shape of the EFC for a gamma – M direction of the lattice and frequency in the range of 0.2096. In the second band self-collimation takes place in gamma – X direction. One can obtain the same self-collimation properties in the second band by simple rescaling and rotating the geometry by 45^{o}. This has one important consequence in fabrication of self-collimation based

device in the near infrared region. The rescaling factor of √2 makes the lattice larger and easier to fabricate. FDTD calculation was performed to confirm proper frequency range for the device operating in the gamma – X direction.

Sample fabrication and characterisation

Devices were patterned on asymmetric AlGaAs/GaAs heterostructure slab system. The sample consists of an $Al_{0.2}Ga_{0.8}As$ core layer of thickness d = 400nm and lower $Al_{0.6}Ga_{0.4}As$ cladding layer with thickness d_{cl}=1500nm. A 200nm thick SiO2 layer was deposited on the top of the heterostructure and acts as a hard mask during dry etching steps. Patterns were written into 400 nm PMMA electron beam resist then transferred into silica mask via fluorine – based chemistry CHF3. The resist was then removed and the patterned oxide mask transferred to the semiconductor layers with Cl_2/Ar chemistry. This type of system is characterized by low index contrast $\Delta\varepsilon=n^2_{co}- n^2_{cl}= 1.6$. That low contrast system needs deeply etched holes to decrease scattering of the light at the bottom of the holes. The sample was etched with an aspect ratio of 8:1 (depth >1 um for period 260 nm, r/a=0.26). Figure 2 shows integrated MZ switch with photonic crystal waveguides in functional area of each MZ arms.

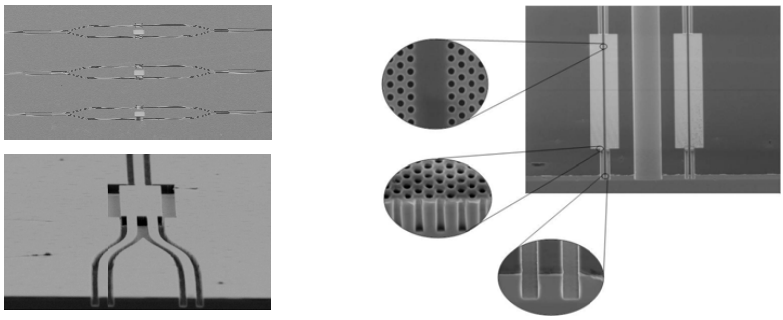


Figure 2 Scanning electron micrograph of the fabricated MZ switch (top left). Cross section of the central part of MZ switch (top right) and the MMIs splitter (bottom left).

The dynamics of the excited carriers were measured by pump probe techniques. Experiments were performed using 130fs pulses from a frequency mode-locked Ti–Sapphire laser. An 800nm wavelength pump beam of 1kHz repetition rate was focused onto the top surface of one of the PhC regions. The weaker probe beam is transmitted through the device and the pump induced transmission change is registered by single channel Si detector. The main advantage of this low repetition frequency is very high peak intensity meaning the material nonlinearity can be fully utilized. The pump beam was focused to 8μm in diameter giving a fluence of 0.1 mJ/cm^2.

The maximum change in the transmission occurs near zero delay time τ=0. A rapid decrease and recovery of the transmission dependent on geometry used is observed near zero delay (fig.3). This modulation of the transmission was a result of a change in the real part of the refractive index induced by injected carriers. Free carriers are generated by the two photon absorption in AlGaAs core layer.

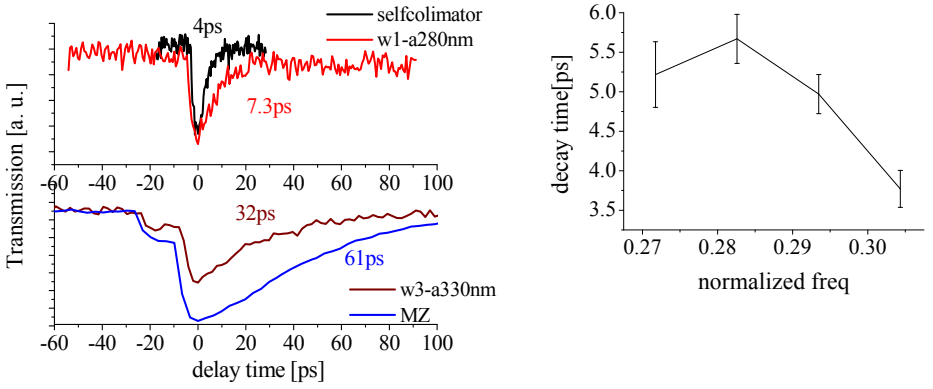


Figure 3 Time dependence of the transmission spectra (left).Clearly visible difference of the decay time for different type of waveguides used in active switch area. **Right:** Relationship between measured decay time and normalized frequency for self-collimator based MZ switch. Decay time was measured for different periods at 920nm wavelength and average pump power 2.25 uW.

The carrier decay time is highly dependent on the geometry of the photonic crystal waveguides used in the experiments. A non patterned MZ switch shows a decay time of 61 ps which is about a factor of 2 faster than in bulk AlGaAs material [3]. Introduction of a photonic crystal in the active area of the switch changes the mean distance of the carriers from the surface hence increasing surface recombination. The self-collimator based MZ switch has a larger fraction of etched holes in comparison to W1 and W3 waveguides, so the recombination of optically excited carriers is further enhanced. A time decay of 4 ps was measured for a self-collimator based MZ switch with a period of 280nm. A decay time has been measured for a range of periods close to the self collimation region. Figure 3 shows a decrease of the decay time with an increase of normalized frequency. This implies that the probe beam is more collimated for normalized frequency 0.304 and undergoes higher modulation by the pump beam. Modulation depth was calculated using:

$$m = \frac{(Am-A)}{(Am+A)} \qquad (1)$$

where Am is a peak-peak value of the modulated beam and A is peak-peak value of the unmodulated beam. The self-collimator based device showed a modulation depth of 34%. The estimated switching energy is 2.82nJ (for average absorbed power 2.25μW).

References

[1] P.A. Besse, M. Bachmann, H. Melchior, L. B. Soldano, and M. K. Smit, "Optical Bandwidth and Fabrication Tolerances of Multimode Interference Couplers", Journal of Lightwave Technology, vol.12, no.6, June 1994

[2] J. Witzens, M. Loncar, and A. Scherer "Self-Collimation in Planar Photonic Crystals". IEEE Journal of Selected Topics in Quantum Electronics, Vol. 8, no 6, November/December 2002

[3] M. J. LaGasse, K. K. Anderson, C.A. Wang, H.A Haus and J.G. Fujimoto, "Femtosecond measurements of the nonresonant nonlinear index in AlGaAs," Appl. Phys. Lett. 56, 417 (1990).

Design and fabrication of a photonic crystal directional coupler for use as an optical switch

D. M. Beggs[1], T. P. White[1], L. O'Faolain[1] and T. F. Krauss[1]

[1]School of Physics and Astronomy, University of St Andrews, St Andrews, Fife, KY16 9SS, UK
daryl.beggs@st-andrews.ac.uk

Abstract. *We have designed and fabricated closely spaced photonic crystal waveguides in the silicon-on-insulator material system for use as an optical switch. By providing a slow-light region, the switch can have a total length of just 5μm. The design incorporates a silica overlayer, thus providing a robust solution suitable for integration.*

Introduction

Directional couplers are made up of two optical waveguides that are brought close enough together for their respective optical modes to interact. This interaction splits the modes into odd and even symmetry supermodes and allows the transfer of power between the waveguides. Light in the directional coupler is split between the odd and even supermodes of the coupled system, and the difference in propagation constants of the two supermodes is equivalent to a difference in the optical path length – a relative phase difference accumulates as light propagates through the directional coupler.

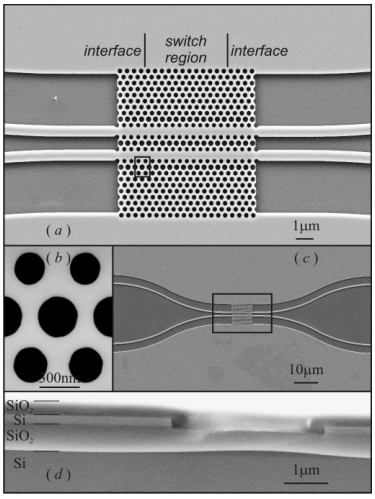


Figure 1: (a-c) Scanning electron micrographs of photonic crystal directional coupled etched into the silicon, before silica infilling. (a) shows the design of the switch, which has a length of 12a = 4.9 μm (the central region, as marked). At the input/output, interface regions of a stretched photonic crystal lattice with a slightly different bandstructure to the central switching region are used to couple light from the slab waveguides into the switching regions. (b) shows detail of the three hole sizes used for engineering the bandstructure. (c) shows the on-chip layout: s-bends are used in order to separate the slab waveguides to prevent interaction between them. (d) A cross-section of the SOI wafer after etching and silica infilling.

An optical switch requires a relative phase difference of π between the two supermodes of the coupled system, equivalent to the requirement $\Delta n\, L = \lambda/2$, where Δn is the index change needed to actuate the switch, L is the length of the switch and λ is the wavelength of light. Usually, values of Δn achievable in linear materials are small – for example, the thermo-optic effect in silicon will provide $\Delta n = 1.8\times10^{-4}$/K – and hence L must be large. However, by using closely spaced photonic crystal waveguides as the directional coupler, the dispersion of the coupled waveguide system can be engineered. Providing a slow region adds a new dimension to the problem – the effective interaction can be increased whilst maintaining a small footprint.

We recently demonstrated a compact, low-power optical switch based on a photonic crystal directional coupler in silicon [1]. In [1], the dispersion of the supermodes of the coupled system where engineered through a control of the hole sizes in the photonic crystal waveguides. Switching was demonstrated using the thermo-optic effect, with a 30 dB discrimination ratio between the output states achieved with an index shift of only 4×10^{-3}. The engineered slow-light region meant that the switch had a length of just 5 μm, or only a few wavelengths of the light, and the switching energy was estimated to be less than 200 pJ. The switch in [1] was based on a membrane slab geometry, where the substrate is selectively etched away from beneath the photonic crystal regions to form an air-bridge; this provides a vertically symmetric structure required for the decoupling of orthogonal polarisation states in the photonic crystal waveguides, and it also increases the contrast between the photonic crystal slab and its cladding, providing stronger index confinement. This contribution considers similar photonic crystal directional couplers to those in [1], but rather than use the membrane geometry, we have designed and fabricated the photonic crystal to be infilled with a silca overlayer. The silica overlayer provides a vertically symmetric structure and is a more robust solution compared to the membrane geometry. The post-photonic-crystal-etch processing of other device components (for example, electrical contacts or integrated microheaters) needed to drive the switch is simplified, as they can be placed directly over the photonic crystal regions with no increase of the optical losses.

Design and fabrication

The device presented here uses a photonic crystal directional coupler to switch light. The concept is based on that given in [2] – the sizes of several sets of holes are modified in order to engineer the dispersion properties of the waveguides. The geometry is shown in fig. 1. The holes in the rows of circles immediately adjacent to the waveguides have a smaller radius $r_1 = 0.31a$, whereas those in the rows immediately adjacent to this have the larger radius $r_2 = 0.39a$. All other holes have a radius $r_0 = 0.34a$. Ridge waveguides provide access to the interface regions, which consist of four periods of a "stretched" photonic crystal lattice, where the lattice constant in the direction along the waveguides is increased. This increase provides a slightly different dispersion in the interface regions as compared to the central region, which is designed to enable the efficient injection of light into the device; especially important in the slow light regime where large coupling losses can occur.

The switching length – the length at which the π phase change occurs – depends on the splitting of the odd and even modes: $L_{switch} = \pi/\Delta k$, where Δk is the difference in propagation constants of the two modes. The task is to provide a dispersion diagram that maximizes the change in L_{switch} for a minimum change in frequency – such a condition is met by providing a slow light region in the even mode. We have designed the directional coupler described above to provide such a region – the dispersion of the modes are shown in fig. 2(a), calculated by a 3D bandstructure method using the MIT Photonic-Bands Package [3].

The fabrication of the devices proceeds as follows. A 350 nm thick layer of ZEP-520A is spun onto a SOI wafer supplied by SOITEC (220 nm ± 5 nm thick Si layer, 2 μm SiO_2 buffer) to act as a resist and etch mask. The patterns were generated by electron

beam lithography, and, following development of the resist, transferred directly into the Si layer using low-power, low-DC bias reactive ion etching in a CHF_3/SF_6 gas mix, a process known to yield very low-loss photonic crystal waveguides [4]. A silica overlayer and the infilling of the etched structures is provided by a spin-on flowable oxide, which is hard-baked at 400°C for 3 hours. Figure 1 (d) shows an SEM of the cross-section of a slab waveguide after this process.

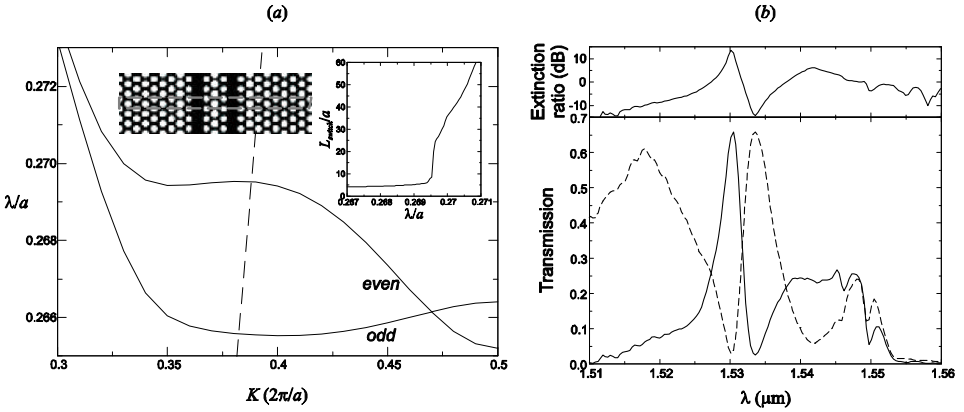


Figure 2: (a) Dispersion curves of the modes of the central section of the directional coupler switch, calculated using a 3D bandstructure method. The dashed line indicates the position of the lightline of the silica cladding. (Inset) The switching length, directly calculated from the bandstructure using the equation $L_{switch} = \pi/\Delta k$. (b) Measured transmission spectra (bottom) of the through port (dashed) and the cross port (solid) for the photonic crystal directional coupler after silicon infilling. The transmission axis is normalized to the mean transmission of several 3 μm wide slab waveguides on the same chip. Also shown (top) is the extinction ratio.

Results and discussion

In order to test our fabricated devices, we characterized them using an end-fire setup with a broadband LED source. Figure 2(b) shows the transmission spectra of both the through (dashed line) and cross (solid line) ports of the device, normalized to the mean transmission of several 3 μm wire waveguides on the same chip. Figure 2(b) also shows the extinction ratio of the output ports (top), defined as the ratio of power in the cross-port to that in the through-port. This extinction ratio varies from 14 dB at $\lambda = 1530$ nm to −14 dB at $\lambda = 1533$ nm. Such a spectral response makes the device an excellent prospect for switching applications, as it could be activated with a refractive index change of just 7×10^{-3}, which corresponds to a temperature shift of 38 K where the thermo-optic effect to be used.

Whilst the thermo-optic effect could be used to actuate the switch by using integrated microheaters, we believe that electronic tuning is more suitable for real applications [5], where switching speed is an important parameter. With suitably designed contacts, the small size of our device would afford an extremely low capacitance, which is essential for high-speed operation. As an example, the carrier-depletion type modulator recently

demonstrated by Liu *et al* [6] affords effective refractive index changes in the low 10^{-4} range. Larger changes are predicted for our device due to the strong confinement of the optical mode in photonic crystal waveguides and the corresponding increased overlap with the depletion layer. Values of $\Delta n = 10^{-3}$ have, in fact, already been demonstrated with carrier-injection type devices based on photonic crystals [7]. Further optimisation of the switch design is required in order to access these small index changes, but the control over the dispersion offered by the photonic crystal directional coupler gives the flexibility of design in order to meet this requirement (the current design traded index change required for a greater bandwidth).

The on-chip insertion efficiency is around 65%, corresponding to an insertion loss of ~2dB. The insertion loss of this device is interesting: as can be seen from fig. 2 (a), much of the dispersion curves of the relevant modes of the switch lie above the silica lightline, and hence the index confinement in the silicon slab is lost and the modes become "leaky". This could be expected to significantly increase the insertion loss as compared to an equivalent membrane or air-bridge device. However, it can be seen that the insertion loss reported here is similar to the membrane devices in [1]. We attribute this to the ultra-short length of the device; losses above the lightline are proportional to the propagation length in the device. More devices would need to be tested in order to see if there is a statistically significant difference of the insertion loss between the two classes of device.

Conclusions

We have designed and fabricated a photonic crystal directional coupler for use as an optical switch. The design is for the SOI material system, and includes a silica overlayer and infilling of the etched pattern, which provides a robust solution suitable for post-processing steps. We have demonstrated that excess optical losses due to the lower silica lightline are small, and also that our device has good spectral characteristics for use in optical switching: a port to port extinction ratio which varies from ± 14 dB for a wavelength shift of 3 nm. Such a switch requires a temperature shift of 38K to be actuated by the thermo-optic effect.

References

[1] D. M. Beggs, T. P. White, L. O'Faolain, and T. F. Krauss, "Ultracompact and low-power optical switch based on silicon photonic crystal", Optics Letters, vol. 33 (2), pp. 147-149, 2008.

[2] N. Yamamoto, T. Ogawa, and K. Komori, "Photonic crystal directional coupler switch with small switching length and wide bandwidth," Optics Express, vol. 14 (3), pp. 1223-1229, 2006.

[3] S. G. Johnson and J. D. Joannopoulos, "Block-iterative frequency domain methods for Maxwell's equations in a planewave basis", Optics Express, vol. 8 (3), pp. 173-190, 2000.

[4] L. O'Faolain, X. Yuan, D. McIntyre, S. Thoms, H. Chong, R. M. De la Rue, and T. F. Krauss, "Low-loss propagation in photonic crystal waveguides," Electron. Lett., vol. 42 (25), pp. 1454-1455, 2006.

[5] W. M. J. Green, M. J. Rooks, L. Sekaric, and Y. A. Vlasov, "Ultra-compact, low RF power, 10 Gb/s silicon Mach-Zender modulator," Optics Express, vol. 15 (25), pp. 17106-17113, 2007.

[6] A. Liu, L. Liao, D. Rubin, H. Nguyen, B. Ciftcioglu, Y. Chetrit, N. Izhaky, and M. Paniccia, "High-speed optical modulation based on carrier depletion in a silicon waveguide," Optics Express, vol. 15 (2), pp. 660-668, 2007.

[7] L. Gu, W. Jiang, X. Chen, L. Wang, and R. T. Chen, "High speed silicon photonic crystal waveguide modulator for low voltage operation," Appl. Phys. Lett., vol. 90, 071105, 2007.

Successful fabrication and integration of multifunctional photonic-crystal devices on bonded InP membrane chip

T. Stomeo[1*], T. F. Krauss[1], F. Van Laere[2], D. Van Thourhout[2], R. Baets[2], C. Cambournac[3], M. Ayre[3], H. Benisty[3]

[1]School of Physics and Astronomy, University of St. Andrews, Fife, KY16 9SS, St. Andrews, U.K.
*present address: tiziana.stomeo@unile.it
[2]Department of Information Technology (INTEC), Ghent University-IMEC, 9000, Gent, Belgium
[3]Institut d'Optique, CNRS, Campus Polytechnique, RD 128, 91127 Palaiseau Cedex, France

Abstract. *An ultra-compact photonic-crystal DeMUX for coarse-WDM applications is successfully integrated with a polarization-independent surface coupler on bonded InP membrane. The optimized technology allows to integrate the DeMUX with photodetectors as well, showing that both active and passive functionalities are implemented in III-V materials, without combining different material systems.*

Introduction

Nowadays, low-cost and small-footprint integrated optical devices for metropolitan optical network are actively demanded. One of the requirements for photonic integrated circuits is the need for system-oriented multi-functionality, *i.e.* the ability to perform different operations desired by system engineers, under the same materials technology simply by adjusting the geometry of the structure itself and by joining several devices together to form a complete integrated sub-system. This multi-functionality —a core concept of the EU project FUNFOX (IST-04582)— is addressed here by implementing two kinds of photonic-crystal (PhC) structures in bonded InP membranes.

The fabrication of these PhCs is typically carried out using electron-beam lithography and dry etching, and the precise fabrication of the 2D structure is always a critical issue for achievement of low-loss and high-quality components in photonic integrated circuits. Well-controlled pattern features are necessary in order to get a PhC device exhibiting the desired functions. There are various kinds of fabrication errors that might cause deviation from perfect photonic-crystal structures, such as the deviation of the periodicity due to the hole misplacement, hole size non-uniformity due to errors in the e-beam writing, proximity-effect-induced non-uniformity in the e-beam lithography, or systematic hole size change due to imperfect sidewall features formed during the dry etching process.

The variation of hole size due to fabrication errors could have a significant impact on the photonic bandgap. In this work, special attention is given to the electron-beam lithography (EBL) process for making the PhC patterns with well-controlled size, in order to integrate PhC DeMUX devices with 1D grating coupler without spectral mismatch. We also report on a highly controlled EBL approach to align different structures, which allows us to successfully fabricate efficient polarization diversity couplers integrated with photodetectors on bonded InP-membrane.

1D Grating Coupler integrated with 2D PhC DeMUX

The integrated device we implemented consists of 1D grating-coupled [1-2] PhC-based demultiplexer on bonded InP membrane, for application in coarse-WDM systems operating at 1500-1560 nm wavelength window. The DeMUX action is based on the anticrossing phenomenon, so-called mini-stopband (MSB) [3-4], supported by PhC multimode waveguides.

The basic heterostructure consists of a 300 nm-thick InP membrane sandwiched between air and benzocyclobutene (BCB, a low-index polymer, $n = 1.54$ at 1.55 μm) on a host substrate. The 1D coupler and the seven-channel DeMUX consisting of a W_{5+x} 2D PhC waveguide ($|x| < 0.26$) were written in a single step using a hybrid LEO Gemini 1530/RAITH ELPHY e-beam lithography tool operating at 30 kV. The ZEP520-A resist thickness of 400 nm was chosen to ensure sufficient durability as a mask for the RIE transfer of the pattern into an underlying SiO_2 layer and at the same time, to ensure good resolution of e-beam writing. The key issue in the fabrication process is to achieve PhC devices with well-controlled patterns size. A proximity error correction (PEC) had to be applied to reach this target. Moreover, in order to achieve smoother and circular holes and faster exposure, the EBL system was used in "circular mode". In this mode, every circular hole is exposed by the deflection of the beam along concentric circles.

High-quality grating coupler (660 nm period and 50 % duty cycle) and PhC DeMUX (362 nm hole diameter and 540 nm period) with well-controlled sizes were achieved after the resist development. The other demux-device's fabrication steps are described in [5]. In Fig. 1 are shown SEM pictures of the devices prior to bonding. The demultiplexing operation of the PhC device is demonstrated by the experimental data of Fig. 2. Note the precise 10 nm spacing, and the non-next-channel cross-talk of ~ –10 dB.

Polarization diversity grating-coupled 2D PhC DeMUX integrated with photodetectors

Thanks to the progresses in surface couplers on InP membrane [6-8], we could fabricate a complete integrated device consisting of (i) a polarization diversity surface coupler, (ii) a MSB-based DeMUX , and (iii) integrated photodiodes.

The basic system is always a BCB-bonded InP membrane. Also in this case a single e-beam process was performed, but it required a highly controlled approach to align the 2D polarization diversity coupler integrated with 2D PhC DeMUX to the photodetectors. The process is based on a two-step procedure: (i) First detector mesas and alignment marks have been defined using optical lithography and etching until the InP-membrane layer is reached; (ii) In a following step, 2D coupler, waveguides, and 2D PhC DeMUX have been aligned to the detector mesas using a controlled EBL process carried out by means of a hybrid LEO Gemini 1530/RAITH ELPHY e-beam lithography system. The approach is reproducible and widely applicable allowing tight alignment accuracy.

A complete layout of the device after e-beam alignment process and mask etch is shown in Figure 3. It involves a 2D polarisation diversity coupler on the input side, tapering down to single mode waveguides and bends, entering into the 2D PhC demultiplexer section. The subsequent detection of each wavelength is achieved by an integrated detector. The overall footprint is small but can be significantly shrunk to 100×150 μm with curved grating couplers and much shorter tapers. Figure 4 shows the

spectral response (photo-current, linear scale) of the three rightmost channels and the through detector (Channel 4 was damaged). These results highlight that very high standards of fabrication accuracy need to be met in order to integrate high-quality multifunctional PhC devices.

Acknowledgements

Authors acknowledge the FP6 European Project IST-04582 “FUNFOX” (2004-2007).

References

[1] D. Taillaert et al., Jpn. J. Appl. Phys. 45, 6071-6077, 2006.

[2] F. Van Laere et al., IEEE J. Lightwave Technol. 25, 151-156, 2007.

[3] S. Olivier et al., Phys. Rev. B 63, 113311 (1-6), 2001.

[4] L. Martinelli et al., IEEE J. Lightwave Technol. 25, 2385-2394, 2007.

[5] T. Stomeo et al., “Integration of Grating Couplers with Compact PhC Demux on InP Membrane”, submitted to Optics Letters (2008).

[6] F. Van Laere et al., IEEE Phot. Technol. Lett. 19, 1919-1921, 2007

[7] F. Van Laere et al., IEEE Phot. Techn. Lett. 20, 318-320, 2008

[8] F. Van Laere, D. Van Thourhout, R. Baets, T. Stomeo, T. F. Krauss, M. Ayre, C. Cambournac, and H. Benisty, "Multifunctional Photonic Crystal Compact Demux-Detector on InP," paper OThM5, presented at OFC/NFOEC 2008, 25-28 Feb., San Diego, 2008.

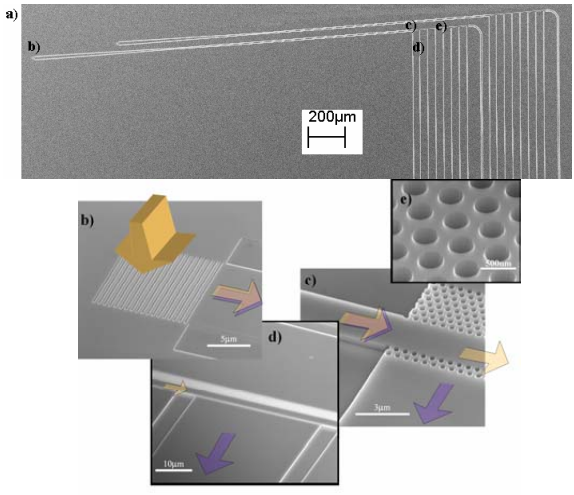


Figure 1:
(a) Complete device layout: 1D Grating Coupler integrated with PhC DeMUX.
(b) Input 1D grating coupler (shallow etch).
(c) Entrance of the PhC waveguide.
(d) Channel1, at DeMUX entrance.
(e) PhC holes (deep etch).

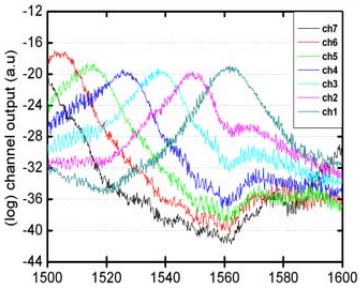


Figure 2: Experimental data from seven-channel demux with cleaved edge. A good separation of 7 optical channels with a spectral resolution of 10 nm nearly suitable for coarse WDM at 20 nm spacing is achieved.

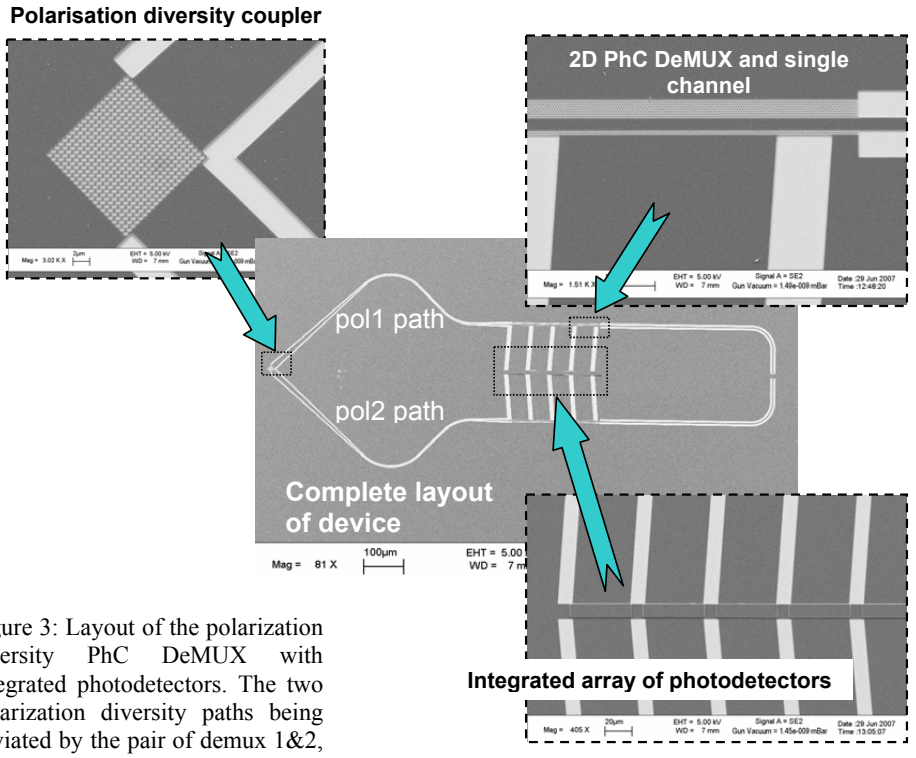


Figure 3: Layout of the polarization diversity PhC DeMUX with integrated photodetectors. The two polarization diversity paths being deviated by the pair of demux 1&2, and recombined in the array of photodiodes, including the 'through' waveguide.

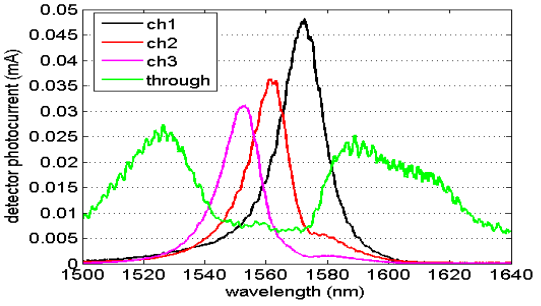


Figure 4: Spectral response (photo-current, linear scale) of the three rightmost channels and the through detector. Channel 4 was damaged.

Photonic crystals (PC) in diamond: Ultra-high-Q nanocavity design, analysis and fabrication

Igal Bayn[1], Boris Meyler[1], Alex Lahav[1], Joseph Salzman[1], B.A. Fairchild[2], S. Prawer[2], Felix L. Martinez[3]

[1]Department of Electrical Engineering and Microelectronics Research Center, Technion Haifa, 32000, Israel
eebayn@techunix.technion.ac.il
[2]Centre for Quantum Computing Technology and Micro Analytical Research Center, School of Physics, The University of Melbourne
[3]Department of Electrical Engineering, Polytechnic University of Cartagena

Abstract. *We present an ultra-high-Q nanocavity design on diamond. The 3D FDTD analysis of mode volume compensation technique in a double heterostructures produces a $Q \approx 2.6\times10^5$. The highest $Q \approx 1.3\times10^6$ with $V_m = 1.77\times(\lambda/n)^3$ in a local width modulation design is derived. The fabrication of mono-crystalline diamond planar PC devices is introduced.*

Introduction

2D Photonic Crystal Structures in diamond are being considered as an attractive architecture for the control and manipulation of atom-photon dressed states [1]. This implementation requires the capability to couple the optical emission of a diamond color center (NV center) to a cavity with a sharp spectral resonance. Photonic crystal (PC) architecture provides integral scalability, which is very important for the quantum information applications. In diamond reaching the high-Q PC cavities is challenging due to low refractive index (*2.4*). Recently, several designs for the PC high-Q cavities on diamond were reported [2-4], while the best $Q\sim1.3\times10^5$ is obtained for the double heterostructure (DH) [4]. It is based on the mode compensation technique, where the cavity quality factor (Q) is increased with the increase in the mode volume (V_m). In this talk we discuss this technique limitation and present a design with a one order of magnitude higher Q, with a similar DH mode volume.

The PC cavities considered are formed of a membrane suspended in air and periodically modulated by a triangular array of air holes. The implementation of such devices is very challenging, due to extreme chemical resistance of diamond, and the lack of developed micro-fabrication technology. Following the high Q design, we present the manufacturing process of 2D PC devices realized on mono-crystalline diamond membrane, and relocated to a silicon substrate for further optical characterization. To the best of our knowledge, this is the first report of mono-crystalline diamond photonic crystal fabrication.

Ultra-high Q cavity design

Cavities are formed as spatial modulation of a PC waveguide providing mode localization, which in previous works, demonstrated the best Q values in both silicon [5-7] and diamond [4]. The PC waveguide (*W1*) is defined by a *ΓJ* directed linear defect into the PC slab, with one filled row of holes. Since diamond refractive index (*2.4*) is lower than that of silicon (*3.4*), the diamond light cone is much higher than in silicon. This light cone mismatch results in exponentially increase in Q_{Si}/Q_D as the function of

mode widths in x and z directions (σ_x and σ_z). Taking the Ideal Gaussian envelope cavity [6] as an analytic model for the high-Q design, we have shown that the increase in diamond mode volume compensates the higher vertical losses and provides $Q_D=Q_{Si}$ [4]. This model has been checked for the modified DHs, where the mode is localized by the two step change of the lattice constant in the x direction ($a<a_{21}<a_2$) see Fig. 1a, while the lattice constant in z direction is left intact. In this design, the increase in mode volume is governed by the number of a_{21} lattice periods (N_{21}). The *1.2* times increase in the V_m results in the *4* times higher Q ($Q(N_{21}=0\rightarrow4)=6.4\times10^4\rightarrow2.53\times10^5$). Further increase in N_{21} results in saturation of Q ($Q(N_{21}=8)\approx2.6\times10^5$), regardless of the higher V_m. This saturation contradicts the Ideal Gaussian model prediction, since the model and the DH exhibit different distributions in the k-space. As a result, the increased mode volume cavities ($N_{21}=4\div8$) do not support further decrease in the vertical power losses, while these losses prevent the improvement in Q.

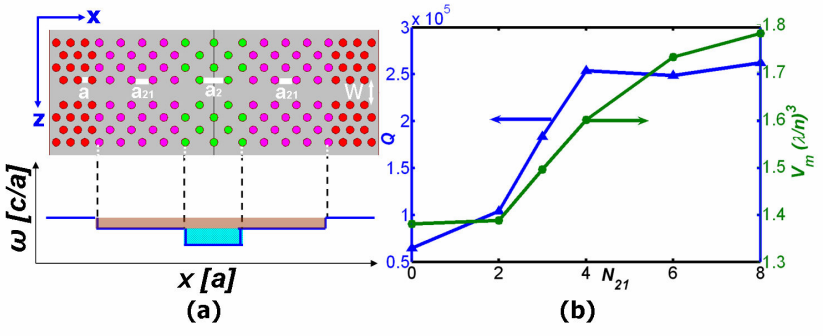


Fig. 1. Modified Double Heterostructure cavity: (a) Geometrical parameters for $N_{21}=4$ cavity, with schematic of waveguide confinement dawn below. (b) Q, V_m vs. N_{21}.

To achieve a higher Q, we utilize the local width modulation design [7]. This is a waveguide based cavity, as well, where the adjacent holes are z-shifted away from the waveguide. These holes are divided in 3 groups: *A, B, C* and each is shifted by D_A, D_B, D_C, respectively (see Fig. 2a, b(inset)). In this way, a more gentle mode confinement is obtained in the xz plane. The hole's radii are $r_A=0.2875a$, $r_{B,C}=r=0.275a$. The slab thickness is $h=0.96a$.

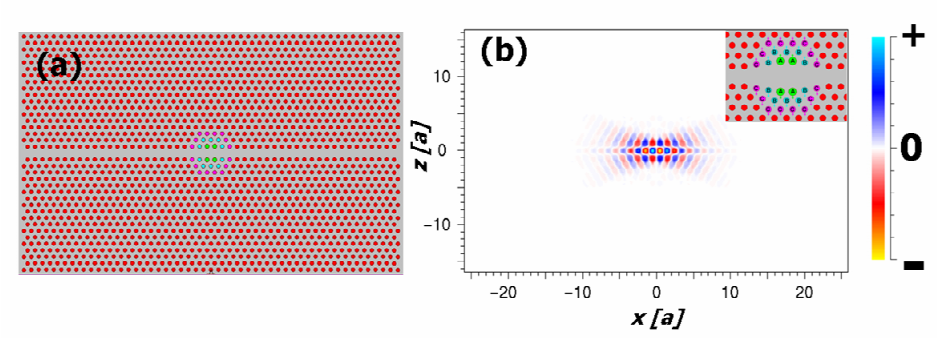


Fig. 2. Local width modulation cavities (A1): (a) A1 cavity computational domain. (b) H_y in the plane $y=0$. In the inset the detailed geometry is shown. The holes *A, B, C* are shifted by D_A, D_B, D_C.

The cavity Q is optimized by the variation of the shifts D_A, D_B, D_C. The best quality factor $Q \approx 1.3 \times 10^6$ is obtained for $D_A=0.056a$, $D_B=0.031a$, $D_C=0.019a$, and exhibit $V_m=1.775\times(\lambda/n)^3$. Its magnetic field profile (H_y) at the plane $y=0$ is shown in Fig. 2(b). Note, that the Q is nearly ~5 times higher than that in the DH design, while the mode volume is very similar. This shows that in order to achieve a high Q, we do not have to compromise the V_m.

This cavity design is a "near optimal", since it exhibits the best k-space distribution. Further work in the diamond high-Q cavity design might improve the Q, but will require sub-nanometer precision in the device fabrication for the NV center wavelength.

Fabrication

The thin diamond membrane is formed by two consecutive implantations of a high dose He^+, producing amorphized layers, that after annealing and etching [8] form membranes *3.3* and *0.3*μm thick (Fig. 3a). Removal of the *3.3μm* membrane allows focused-ion-beam patterning of the PC structure on the thin membrane. Since the air-gap under this membrane is *~50nm*, the mode leakage into the substrate prevents any practical use of this PC. To prevent this leakage, the membrane is "welded" to an omni-probe tip (Fig. 3b), cut out and relocated from the diamond (Fig. 3c) onto the Si substrate. It is welded to initially prepared Si and Pt posts by Pt deposition. This scheme provides sufficient separation from the substrate, to allow efficient mode confinement. In Fig. 3d we show 1.55μm PC transmission structure, while in Fig. 2e A1 cavity for 637nm is demonstrated.

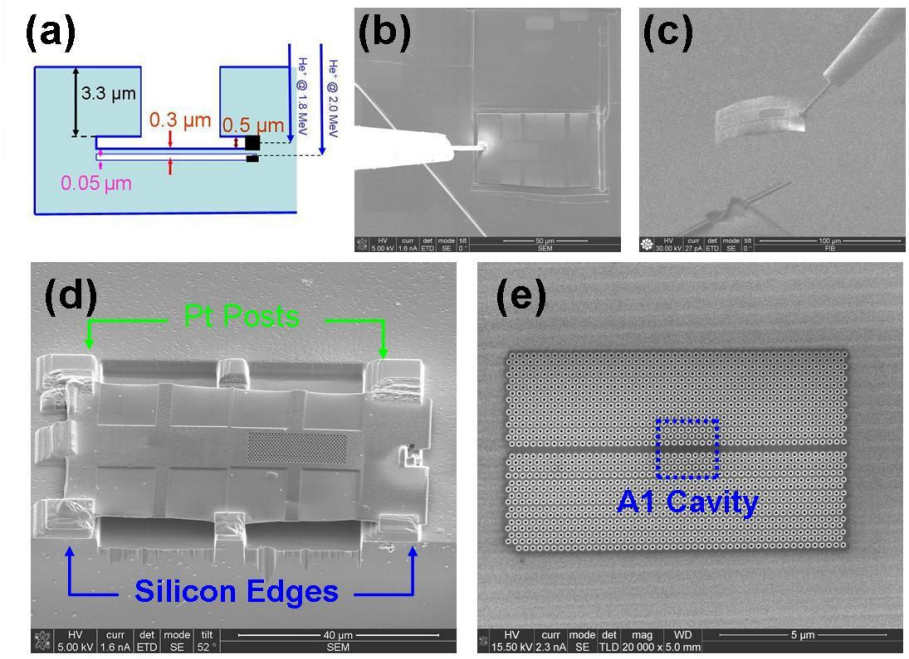


Fig. 3: (a) Membranes thickness vs. Implantation energy. (b) Omni-probe Pt welding to the thin membrane. (c) Thin membrane relocation. (d) *1.55μ* transmission set-up (PC with I/O ridge waveguides) welded on Si and Pt posts above 4μm Si substrate. (d) *637nm* A1 PC cavity.

Summary

In this talk we show that the achievement of ultra-high-Q cavities in diamond is possible. The fabrication process of mono-crystalline diamond PC is demonstrated. The micro-photo-luminescence experiments are undergoing and progress in this direction will be presented.

References:

[1]. A.D. Greentre, J. Salzman, S. Prawer, and L.C. Hollenberg, "Quantum gate for Q-switching photonic band-gap cavities containing two level atoms" Phys. Rev. A73, 013818 (2006).

[2]. S. Tomljenovic-Hanic, M. J. Steel, C. M. de Sterke and J. Salzman, "Diamond based photonic crystal microcavities", Optics Express 14, 3556 (2006).

[3]. I. Bayn and J. Salzman, "High-Q photonic crystal nanocavities on diamond for Quantum Electrodynamics", Eur. Phys. J. Appl. Phys. 37, 19 (2007).

[4]. I. Bayn and J. Salzman, "Photonic Crystals (PC) in Diamond: Cavity Q-Mode Volume Influence on the Design", CFH6, CLEO (2007).

[5]. B. Song, S. Noda, T. Asano and Y. Akahane "Ultra-high-Q photonic double heterostructure nanocavity", Nature, Vol.4, March (2005).

[6]. D. Englund, I. Fushman, J Vuckovic, "General recipe for designing photonic crystal cavities", Optics Express 12, 5961 (2005).

[7]. E. Kuramochi, M. Notomi, S. Mitsugi, A. Shinya, T. Tanabe and T. Watanabe "Ultrahigh-Q photonic crystal nanocavities realized by the local width modulation of a line defect", Appl. Phys. Let. 88, 041112, (2006).

[8]. B.Fairchild et. al., "Material issues in the micro-fabrication of sub micron layers in single-crystal diamond", 17th Biennial Congress of the Australian Institute of Physics, Brisbane, (2006).

Investigation of photonic crystal cavities sandwiched in a grating structure

K. Van Acoleyen[1] and M. Qiu[1]

[1] Department of Microelectronics and Applied Physics, Royal Institute of Technology (KTH), Electrum 229, 16440 Kista, Sweden
karelva@kth.se
min@kth.se

Abstract *- By sandwiching a high Q photonic crystal cavity in a grating structure, the Q can be increased with about 150% compared to a silica background, since certain Fourier-components inside the leaky light cone are now resonating in the vertical resonant structure.*

Introduction

Design of high Q cavities, together with a small modal volume, is crucial for photonic integration. High Q values of the order 10^5 - 10^6 have already been designed in the air-bridge structure. The methodology used is nearly always the same. As proved in [1], the Q values can be very high, by shifting holes or reducing the hole size so that the reflection coefficient is not steep, but gradual. The abrupt change introduces a lot of leaky components while when having a gradual reflection these components are shifted out of the light cone and are no longer leaky.
In the present paper, this methodology is used again and furthermore a vertical cavity is designed to increase the Q value. In a first stage an attempt is made to increase the Q factor by putting a SiO_2-SiN grating around the cavity. This grating results in forbidden regions for which light can not propagate. The effect of changing the gap-center frequency of the grating is investigated. In a later stage, the first SiO_2 layer is increased in thickness resulting in a resonant cavity. Afterward the effect of a SiO_2-Si grating is investigated.
The Q cavities are simulated with the FDTD software and the Q-values are calculated with a Padé approximation [2]. The refractive index of Si, SiO_2 and SiN are 3.6, 1.45 and 2 respectively. The air holes in the photonic crystal slab have a radius of 0.3a and the slab thickness is 0.6a. All the distances given in the present paper are normalized to a, the lattice constant of the photonic crystal.

Investigation of the vertical structure

The vertical structure is investigated by first changing the grating surrounding the photonic crystal slab. The grating will be specified by its gap-center frequency. Afterward the first SiO_2 layer of the grating is tuned. This is visualized in Fig. 1. The vertical structure is analyzed by means of the Transfer Matrix Method in which the starting point is the center of the photonic crystal slab. For the SiO_2-SiN grating 10 grating periods are taken, for the SiO_2-Si grating 5 grating periods are sufficient for the saturation of the Q value.

M1 cavity

The structure under investigation is the M1 cavity, one missing hole with H_z even in the x, y and z-direction. This cavity supports one high Q mode in the air-bridge structure

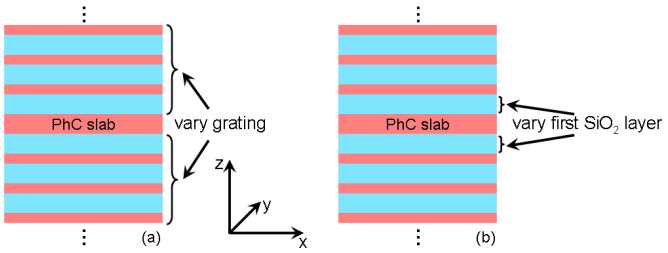


Figure 1: Design procedure of the vertical structure: (a) the gap-center frequency of the grating is tuned, (b) the thickness of the first SiO_2 layer is tuned.

of 37000 for shifted holes of 0.20a with a frequency of 0.292c/a. The field profile is shown in Fig. 2(a). When having a silica background on both sides, in order to keep the symmetry, the Q reduces to 2800 at a hole shift of 0.23a at a frequency of 0.286c/a.

The structure is now surrounded by a grating for a hole shift of 0.22a and 0.25a with a

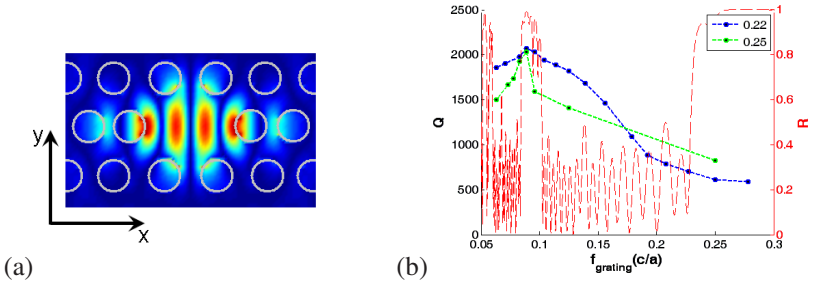


Figure 2: (a) Field profile of $|E_y|$ for the M1 cavity in air for a hole shift of 0.20a. (b) Q values of the M1 cavity for a hole shift of 0.22a and 0.25a when shifting the gap-center frequency of the surrounding grating. The reflection coefficient at the center of the PhC slab for a frequency of 0.292c/a and an in plane k_{xy} of 0.4π/a is shown in the red graph.

corresponding mode frequency of about 0.296c/a and 0.292c/a respectively. The resulting Q factors are shown in Fig. 2(b). When the gap-center frequency of the grating equals the frequency of the mode, the Q is rather low ($\sim$ 500). This is due to the fact that the SiN slab is rather close to the photonic crystal slab and so part of the light that decays exponentially into the silica will be guided again in the SiN resulting in increased losses. When lowering the gap-center frequency of the grating, the grating layers increase in thickness and the first SiN layer is further away from the silicon slab resulting in an increase in the Q value. The Q value stays however below that of the structure with a silica background. A maximum can be seen around a grating gap-center frequency of 0.089c/a. This can be explained due to the fact that the gap-center frequency of the grating is then about one third of the mode frequency, so the grating is again highly reflective. If the effect that the mode does not radiate at perpendicular incidence but at small angles is taken into account, it can be seen in Fig. 2(b) that for an in plane Fourier component k_{xy} of 0.4π/a, the high reflectivity of the grating corresponds with the maximum in Q value. The Fourier transform of the M1 mode surrounded by a grating with a gap-center frequency of 0.089c/a is shown in Fig. 3(a). Since the mode will only feel the surrounding silica,

the silica light cone is depicted instead of the effective index light cone of the grating. The above result suggests that it is important for the grating to reflect at approximately the mode frequency while keeping the first higher index slab far enough from the PhC slab. When having a lower gap-center frequency of the grating, other k-components are forbidden to propagate into the grating, but this does not imply that this light will reflect back into the mode volume. The band diagrams of the gratings are shown in Fig. 4. For the grating with $f_{gap-center} = 0.089$c/a the forbidden region near $k_{xy} = 0.4\pi$/a is visible for which we saw (Fig. 2(b)) the structure was highly reflective. The first forbidden region in 4(a) however extends much further and it is only due to the fact that the SiN is so close to the PhC slab that losses occur.

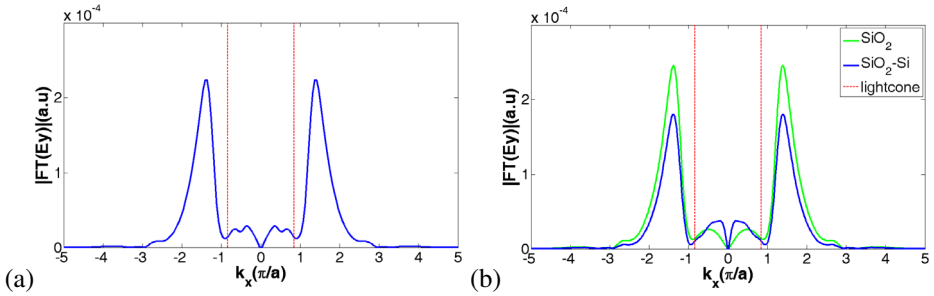


Figure 3: 2D Fourier transforms of the M1 mode in a grating structure along the k_x axis. The red dashed line denotes the silica light cone: (a) grating structure with gap-center frequency of 0.089c/a, no tuning of the first SiO_2 layer (hole shift 0.24a). (b) SiO_2 background (hole shift 0.23a) and 0.6207a SiO_2 - 0.250a Si grating (hole shift 0.25a) with first SiO_2 layer thickness of 2.3a.

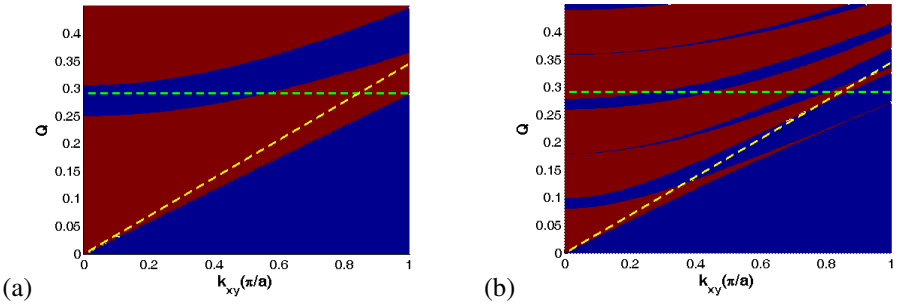


Figure 4: Band diagram of the gratings. Blue areas are forbidden regions. The green dashed line denotes the mode frequency, the yellow dashed line denotes the silica light cone. (a) grating 0.6207a SiO_2, 0.450a SiN: $f_{gap-center}$=0.278c/a, (b) grating 1.9130a SiO_2, 1.400a SiN: $f_{gap-center}$=0.089c/a.

The only possibility to effectively increase the Q is by having an extra resonance in the vertical structure. Therefore not only high reflection is needed, but the phase condition should be met as well. For this the first SiO_2 layer is shifted as denoted in Fig. 1(b). For the following, focus is pointed to a hole shift of 0.25a. The results are shown in Fig. 5. It can be seen that the highest Q values appear when the reflected light is in phase with

the original field. The phase shown is for perpendicular incidence since the only way to improve the Q is to have an extra resonance in the vertical direction and as can be seen in Fig. 3(b), the main k-components inside the light cone are near $k_x = 0$. The maximum Q values obtained are 3000 and 4000 for the SiO_2-SiN and SiO_2-Si grating respectively. The SiO_2-Si grating gives a higher Q than the SiO_2-SiN grating since the former is more broadband and will be highly reflective for more k-components inside the light cone. The first maximum is lower than the second since for this maximum the higher index SiN/Si slab is too close to the PhC slab. In Fig. 3(b) the 2D Fourier transform of the M1 mode

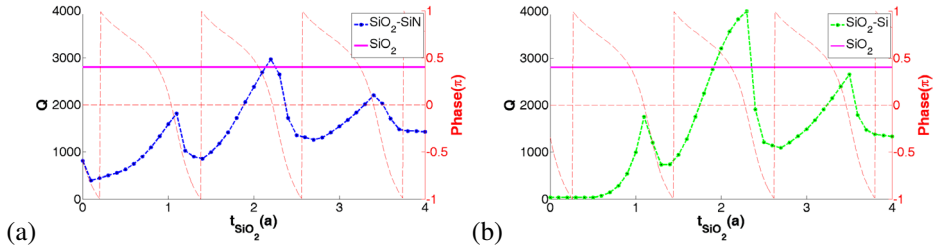


Figure 5: Optimization by shifting the thickness of the first silica layer. The red graph shows the corresponding phase of the light reflected back from the center of the photonic crystal slab for perpendicular incidence, $k_{xy} = 0$; the solid magenta line shows the Q value in the case of a silica background: (a) 0.6207a SiO_2 - 0.450a SiN grating, (b) 0.6207a SiO_2 - 0.250a Si grating.

along the k_x-axis is shown when the PhC slab is surrounded by silica and when it is surrounded by the SiO_2-Si grating with tuned first SiO_2 so that the Q is maximal. This graph clearly shows that the k-components are not decreased within the light cone, but they are on the contrary bigger. The light near $k_x = 0$ is however resonating in the vertical direction and therefore stays confined.

Conclusion

The effect of putting a PhC slab inside a grating structure is investigated for microcavities. By using a SiO_2-Si grating and ensuring phase match in the vertical direction, the Q value could be increased compared to a silica surrounding. This is mainly due to the fact that, instead of reducing light leakage, part of the leaky light resonates in the vertical cavity.

Acknowledgement

This work is supported by the Swedish Foundation for Strategic Research (SSF) through the future research leader (INGVAR) program, the SSF Strategic Research Center in Photonics, and the Swedish Research Council (VR).

References

[1] Y. Akahane, T. Asano, B. S. Song, S. Noda, "High-Q photonic nanocavity in a two-dimensional photonic crystal", *Nature*, vol. 425, pp. 944-947, 2003.

[2] W. H. Gua, W. J. Li, Y. Z. Huang, "Computation Resonant Frequencies and Quality Factors of Cavities by FDTD Technique and Padé Approximation", *IEEE Microwave and Wireless Components Letters*, vol. 11, pp. 223-225, 2001

Deeply inside tunable CROW delay lines

A. Melloni[1], F. Morichetti[1,2], A. Canciamilla[1], C. Ferrari[1]
[1] *Dipartimento di Elettronica e Informazione, Politecnico di Milano*
Via Ponzio 34/5, 20133 Milano, Italy
[2] *CORECOM, via G. Colombo 81, 20133 Milano, Italy*
E-Mail: melloni@elet.polimi.it

A chip-scale continuously tunable delay-line is presented and both experimental and numerical results are discussed. The focus of the work is mainly on the open issues, involving both theoretical and practical aspects to take care of or still to solve.

Summary

A slow-wave coupled-resonator optical waveguide (CROW) has been successfully employed to realize a tunable delay line able to introduce a continuously controllable delay of several bits on optical signals modulated at several Gbit/s [1]. Experimental results obtained with thermally activated rings fabricated in 4.5% index contrast silicon oxynitride (SiON) technology demonstrated a continuously tuneable fractional delay from 0 to 8 bits at 10 Gbit/s (overall delay 800 ps) and 25 Gbit/s (320 ps). Thanks to the high storage efficiency, exceeding 1 bit/RR, the device reconfiguration can be easily handled and the device footprint is below 7 mm^2. System performance and signal degradation were also investigated, showing a fractional loss below 1 dB/bit and error-free operation (BER < 10^{-9}) at 10 Gbit/s for fractional delays up to 3 bits.

This device is an excellent demonstration of the optimal trade-off achieved between all the variables and parameters of the structure and the synergy between the optical circuit, the technology constraint and the management of the reconfigurability. There are several critical points to tackle with and to optimize: the choice of the technology and the architecture, the impedance matching (or apodization) impacts on backreflections, the slow down factor should be high enough to increase the storage efficiency but not too high to reduce the technological sensitivity to tolerances, the limitations imposed by the index contrast, mainly the minimum bending radius, the effect of waveguide roughness, the impact of coupling coefficient disorder and phase disorder, the tuning mechanism and its management, thermal cross-talk and so on. Moreover, one has to face with waveguide losses, chromatic dispersion and impedance matching, the three main limiting factor of the ultimate performances of this architecture, and find the right trade-off to achieve acceptable system performance.

In the talk we will highlight the main features and limits, the open issues and the tricks for proper operation with a brief overview on the possible applications.

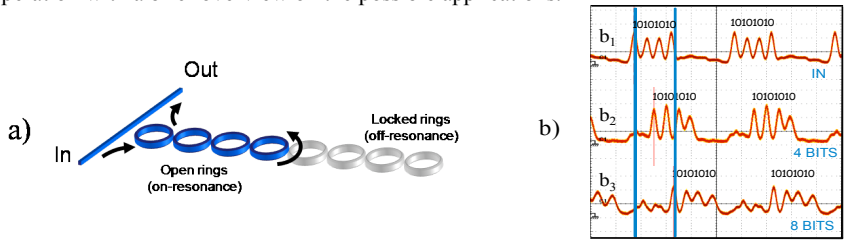


Fig. 1. a) Schematic of a tunable CROW delay line; b) Time traces of the delayed 25 Gbit/s sequence 10101010-00000000 at the output of the CROW delay line: (b_1) zero delay, (b_2) 4-bit 160 ps delay and (b_3) 8-bit 320 ps delay.

References

[1] F. Morichetti et al., "*A reconfigurable architecture for continuously variable optical slow-wave delay lines*," Opt. Express **15**, 17273, Dec. 2007.

Closed-loop Modeling of Silicon Nanophotonics: From Design to Fabrication and Back Again

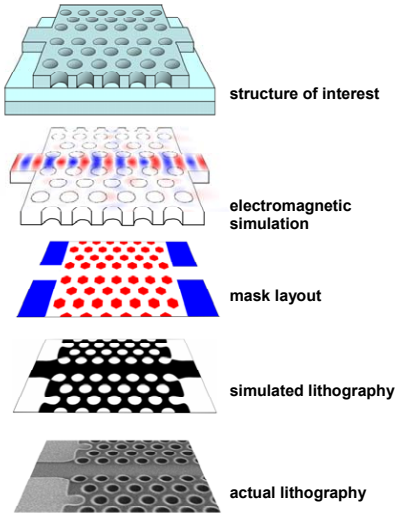
(invited paper)

Wim Bogaerts, Lieven Vanholme, Paul Bradt and Peter Bienstman
Ghent University, Department of Information Technology, Sint-Pietersnieuwstraat 41, 9000 Gent, Belgium
Wim.Bogaerts@UGent.be

We present a system for closed-loop modeling of silicon nanophotonics, where the properties of the fabrication process are taken into account in the design and optimization of nanophotonic components.

Summary

When fabricating nanophotonic components, several aspects come into play. There is the detailed electromagnetic simulation of the component, the generation of the mask layout, and the properties of the fabrication process which make that the fabricated structure is often not exactly identical to the one that was originally designed. We present a framework where all of these aspects are integrated in such a way that the properties of the fabrication can be taken into account during the design phase.



The framework is held together with Python, a flexible programming language especially suitable for scientific applications [1]. Currently, the framework has a python interface to an electromagnetic simulator based on eigenmode expansion [2], a library for mask layout design, and a simulator for optical projection lithography. This last library is calibrated against actual fabrication processes using the 248nm and 193nm steppers used by IMEC for the fabrication of nanophotonic waveguide circuits [3].
In addition, python makes it exceptionally easy to include new interfaces to existing software tools (commercial and free), including advanced optimization routines such as genetic algorithms.
To demonstrate this framework we optimize an in-line DBR reflector in a photonic wire. A design with rectangular grating teeth will be deformed by the optical lithography, because for submicron features the lithography acts as a spatial low-pass filter, rounding sharp corners. Therefore, while an optimization routine on the rectangular design might yield an efficient component, the actual fabricated structure would be very different. Thus, we included the lithography in the optimization loop. Starting from a mask design, we perform a virtual lithography, and the resulting pattern is fed to CAMFR. The result is used to modify the mask layout, taking into account design rules such as minimal spacing. This whole cycle is then managed by an optimization routine, in this case a relatively simple steepest descent method.

References

[1] Special issue on Python of *Computing in Science & Engineering*, vol. 9(3) (2007)
[2] P. Bienstman and R. Baets, *Opt. Quantum. Electron* 33(4/5), p.327 (2001)
[3] W. Bogaerts et al. *J. Lightwave Technol.* 23(1), p.401 (2005)

Design of a Waveguide-Type Polarization Beam Splitter Incorporating Trenches Filled with Low-Refractive Index Material

Jiro Ito[1], Kenji Iwamoto[1] and Hiroyuki Tsuda[1]

[1]Department of Electronics and Electrical Engineering, KEIO University
jiro-i.23@tsud.elec.keio.ac.jp

Abstract. *We propose a waveguide-type polarization beam splitter (PBS) incorporating trenches filled with low-refractive index material, which exhibits a low insertion loss of less than 2 dB and a high polarization extinction ratio of more than 20 dB over a wide wavelength range from 1525-1630 nm.*

Introduction

The concept of a waveguide-type polarization beam splitter (PBS) is very promising because such a device could be easily integrated with other circuits. A silica-based waveguide-type PBS which utilizes waveguide birefringence and which is dependent on the core-width has been reported [1]. This device exhibited low-insertion loss and a high polarization extinction ratio. Silica-based waveguides have been very popular in the field of passive optical components because they offer low fiber-to-chip coupling losses and low propagation losses. However, these devices require the use of long waveguide arms because the waveguide birefringence is low. PBS devices fabricated using silicon-on-insulator waveguides have also been studied [2]. Since they feature large waveguide birefringence which depends on the rib width, the size of these devices can be more compact than silica-based designs. However, it is difficult to achieve a high polarization extinction ratio and a low coupling loss between single mode fibers without mode-size conversion when using a silicon-based waveguide-type PBS.

We have proposed and fabricated a compact silica-based PBS [3] by including trenches filled with low-refractive index material with a refractive index of 1.3335. This device exhibited a high polarization extinction ratio around the center wavelength. In this paper, we have optimized such a PBS structure which incorporates trenches in order to obtain a high polarization extinction ratio over a wide wavelength range, and we have confirmed the transmission characteristics of the PBS that we designed by using simulations based on the beam propagation method (BPM).

Design of PBS

Our proposed PBS structure with trenches filled with low-refractive index material is shown in Fig. 1. It has a Mach-Zehnder interferometer (MZI) configuration, and consists of two 3-dB couplers and two waveguide arms with trenches of different lengths. We used multimode interference (MMI) devices as a 3-dB coupler, and the trenches were introduced along both sides of the core. Because of the local laterally-enhanced optical confinement, the propagation constants of the embedded waveguides containing low-refractive index material strongly depend on the polarization. Therefore, the size of such a PBS can be reduced. To balance the light intensities in both waveguide arms, we inserted trenches into both of them. The straight trenches were

inserted gradually into the core to reduce the junction loss between the conventional waveguide and the low-refractive index material embedded waveguide.

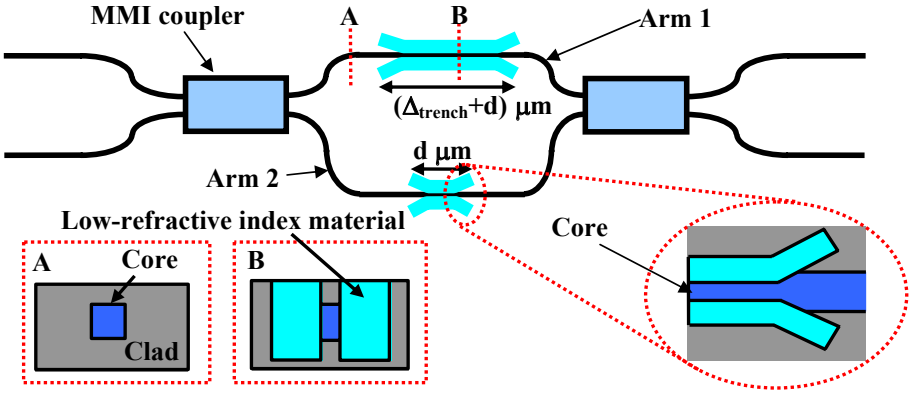


Fig. 1. Schematic configuration of our proposed PBS

The wavelength dependences of the effective refractive indices for both the conventional waveguides and the low-refractive index material embedded waveguides are shown in Fig. 2. The value of the difference in optical pass-length between the two waveguide arms *Δ(nL)* changes according to the wavelength because the effective refractive index of a low-refractive index material embedded waveguide depends on the wavelength. Therefore, we can't obtain a high polarization extinction ratio over a broad wavelength range with this configuration.

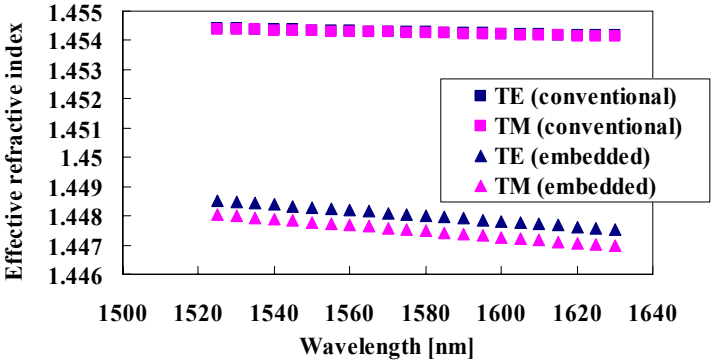


Fig. 2. Wavelength dependences of the effective refractive indices of both conventional waveguides and low-refractive index material embedded waveguides with mesa widths of 3.0 μm.

We solved this problem by taking the wavelength dependence of the effective refractive index into account. From Fig. 2, we can assume that the wavelength dependence of the effective refractive index decreases almost linearly as a function of wavelength. The conditions in which the PBS has a broad bandwidth are expressed by

$$n1_{TE}(\lambda)(\Delta_{trench}+\Delta L)-n2_{TE}(\lambda)\Delta_{trench}=m\lambda, \quad (1)$$

$$n1_{TM}(\lambda)(\Delta_{trench}+\Delta L)-n2_{TM}(\lambda)\Delta_{trench}=\left(n+\frac{1}{2}\right)\lambda, \quad (2)$$

where $n1_{TE(TM)}$ and $n2_{TE(TM)}$ respectively express the effective refractive indices of TE(TM) mode for a conventional waveguide and a low-refractive index material embedded waveguide (whose values depend on the wavelength), Δ_{trench} is the difference in length between the trenches in the two waveguide arms, ΔL is the difference in length between the two waveguide arms, λ is the wavelength of the incident light, and m and n are integers. From (1) and (2), the optimum values for Δ_{trench} and ΔL can be determined. However, it is difficult to set the parameters in order to completely satisfy (1) in relation to (2) because the slopes of the effective refractive indices of TE and TM mode as a function of wavelength for a low-refractive index material embedded waveguide do not share the same values. Although we can adjust these by changing the mesa width, they are not independently controllable. Therefore, we obtained a wide bandwidth by making a small sacrifice in terms of the extinction ratio by designing the parameters such that the values of m and n almost become integers.

Simulation results

We optimized the parameters and confirmed the characteristics of the wavelength dependence by using a two dimensional (2D) beam propagation method (BPM). ΔL was 3.59 μm. The mesa width was 3 μm. The birefringence of a waveguide fabricated using trenches filled with low-refractive index material is shown in Fig. 3, and it can be seen that it depends strongly on the mesa width. Smaller mesa widths exhibit larger birefringence; therefore, this enables the use of shorter waveguide arms. However, the difference between the slopes of the effective refractive indices between TE and TM modes as a function of wavelength for a low-refractive index embedded waveguide becomes larger and therefore narrows the working bandwidth. Moreover, narrow mesa widths are difficult to fabricate. Therefore, we determined that the mesa width should be 3 μm, Δ_{trench} was 764 μm, and the straight length of the shorter trench, d was 10 μm. The length of the longer trench, including the taper parts, was less than 1130 μm. The transmission characteristics are shown in Fig. 4.

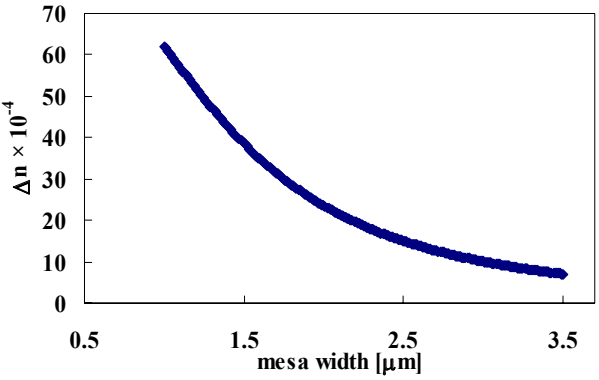


Fig. 3. Birefringence of a low-refractive index material embedded waveguide as a function of mesa width.

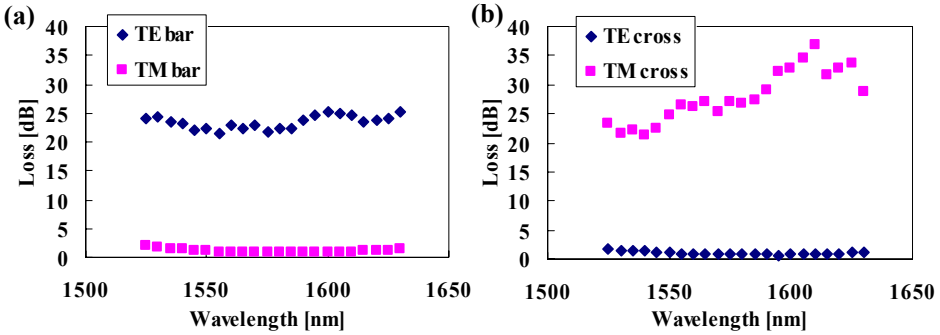


Fig. 4. Wavelength dependence of transmission characteristics.
(a) through-path. (b) cross-path.

The insertion loss was less than 2 dB. The polarization extinction ratio was greater than -20 dB over a wide wavelength range from 1525-1630 nm for both polarizations. Although the trench length becomes longer, higher polarization extinction ratios can be obtained by widening the mesa width.

Conclusion

We improved the wavelength-dependence of a PBS incorporating trenches filled with low-refractive index material by taking the wavelength-dependence of the effective refractive index into account. We confirmed that a PBS fabricated using our proposed design method exhibited a low insertion loss of less than 2 dB and a high polarization extinction ratio of more than 20 dB over a wide wavelength range from 1525 to 1630 nm by making 2D BPM simulations.

References

[1] Y. Hashizume, R. Kasahara, T. Saida, Y. Inoue and M. Okano, "Integrated polarization beam splitter using waveguide birefringence dependence on waveguide core width," Electron. Lett., vol. 25, no. 25, pp. 1517-1518, 2001.

[2] T. K. Liang and H. K. Tsang, "Integrated polarization beam splitter in high index contrast silicon-on-insulator waveguides," IEEE Photon. Technol. Lett., vol. 17, no. 2, pp. 393-395, 2005.

[3] J. Ito, Y. Ikuma, K. Iwamoto and H. Tsuda, "Compact polarization beam splitter using trenches filled with low-refractive index material," in Proceedings of the APLS 2008, 2008, pp.181.

Temperature Insensitive Silicon Slot Waveguides with Air Slot

Ken Kashiwagi[1], Shinji Yamashita[1], Katsunari Okamoto[2], S. J. Ben Yoo[2]

[1]Department of Electronic Engineering, Graduate School of Engineering, The University of Tokyo
kasiwagi@sagnac.t.u-tokyo.ac.jp
[2]Department of Electrical and Computer Engineering, University of California, Davis

Abstract. *We report numerical simulation about thermal stabilities of silicon slot waveguide. A polymer cladding, which has negative thermo-optic(TO) coefficient, was used to compensate positive TO coefficient of silicon and silicon-dioxide(SiO_2). We found athermal waveguide can be realized with air slot, and even with SiO_2 slot.*

Introduction

High index contrast waveguides are very attractive, with the advantage of small footprint and large nonlinearity due to their high optical density because of their sub-micron sized dimensions. Novel nonlinear devices have been proposed and demonstarated by using sub-micron sized silicon (Si) waveguides. Si has, however, high thermo-optic (TO) coefficient which is one magnitude larger than that of silicon-dioxide (SiO_2) which is utilized for various photonic applications in industry. Very accurate and power consumable temperature controller should be used to stabilize the device performance, especially the devices which have wavelength dependent characteristics, such as arrayed waveguide gratings (AWGs), ring resonators, Bragg gratings, Mach-Zehnder interferometers.

Recently, a novel design of high index contrast waveguide, called slot waveguide, have been proposed[1],[2]. Since it can confine a light in low index region, we can employ various materials as optical nonlinear materials by filling the slots with them. High optical intensity in the slot enhances their optical nonlinearity. One of the advantages of the slot waveguides is the design flexibility. Slot width can be another design degree of freedom additional to the height and width of the waveguides. However, when we use Si as a host material of a waveguide, thermal stability should be suffered from the large TO coefficient of Si. A thermally stable ring resonator based on Si slot waveguide was proposed and experimentally demonstrated using a polymer as over cladding and slot region[3]. In this paper, we investigate on thermal stability of Si slot waveguides focusing on slot materials. We found that filling slot regions with polymer materials is not necessary to achieve temperature insensitive slot waveguides.

Athermal silicon slot waveguides with polymer slot

Fig. 1 shows a schematic cross-sectional structure of a slot waveguide. The slot waveguide has a slot region which is embedded with two high index regions, and the structure is surrounded by under cladding and over cladding which have lower refractive index comparing to that of high index region. A material of slot region can be the same with those of over cladding or under cladding as far as the material has lower refractive index comparing to that of high index regions. In this paper, we assume symmetric waveguides, or two high index regions have the same width.

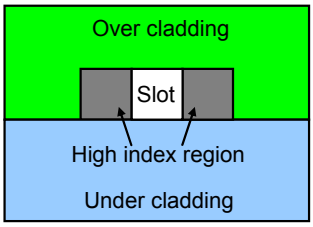


Fig. 1 Cross-sectional schematic structure of a slot waveguide

In this section, we assume slot waveguides which consist of SiO_2 under cladding, Si high index region, and slot region and over cladding polymethyl methacrylate (PMMA). In the simulation, the refractive indecies of Si, SiO_2 and PMMA were 3.48, 1.46 and 1.481[4], and their TO coefficients were 1.84×10^{-4}, 1.0×10^{-5} and -1.0×10^{-4}, respectively. We fixed the waveguide heights as 250 nm, and calculated effective refractive index (n_{eff}) with changing Si and slot width using finite different method based modesolver. Only TE mode was considered in this paper since light confinement in the slot region appears only in TE modes.

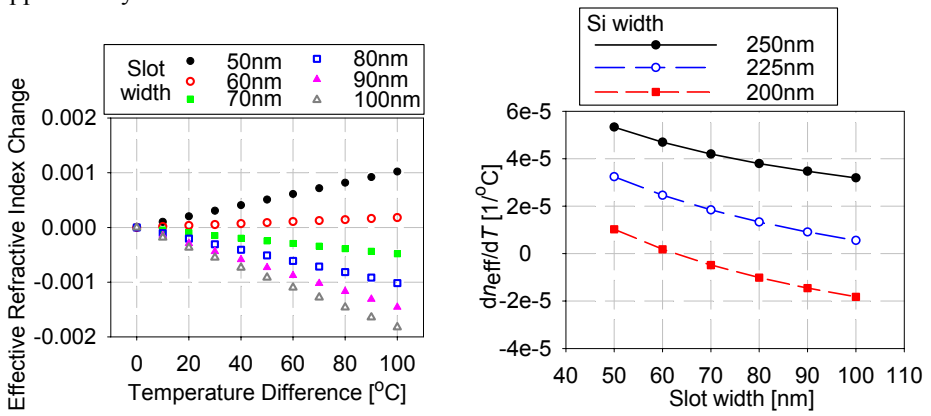


Fig. 2(a) Simulated temperature dependence of effective indecies with several slot width

(b) Simulated effective index change slope as a function of slot width, 250nm height

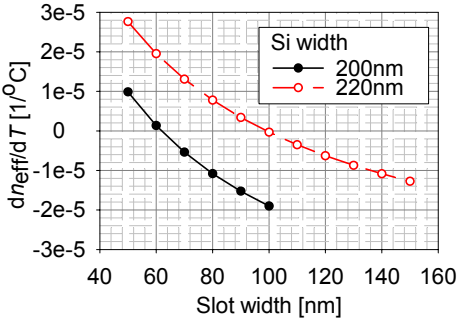


Fig. 3 Temperature insensitivity design with different Si width without changing waveguide heights (250nm)

Fig. 2(a) and (b) show the simulated temperature dependence of effective index of the waveguide with several slot widths and the slot width dependence of effective index slope (dn_{eff}/dT) with three different Si widths, respectively. In the case that a waveguide is temperature independent, effective refractive index change stay zero at any temperature. Widening slot width decreased dn_{eff}/dT from positive to negative slope shown in Fig. 2(a). A zero-crossing point in Fig. 2(b) are the temperature insensitive waveguide structure, and ~62 nm slot width was the optimum for Si width of 200 nm.
Temperature independence can be achieved in various waveguide designs without changing their heights. Fig. 3 shows temperature dependence of the Si slot waveguides with two different Si widths. Waveguide heights were 250 nm. 100 nm slot width was the optimum size for Si slot waveguides whose Si width is 220 nm.

Athermal silicon slot waveguides with air slot

In practical fabrication process, it is difficult to fill the slot region with a material, such as PMMA. However, temperature insensitive slot waveguides can be realized without filling any materials in the slots, or with air slots. Fig. 4 shows the effective index slope of slot waveguides as a function of slot width. The refractive index and TO coefficient of air were assumed as 1.0 and 0, respectively. The waveguide heights were fixed at 250nm. Under cladding were SiO_2. For the case of Si width of 200nm and 220nm, athermal Si slot waveguides could be achieved with the slot width of ~65nm and ~125nm, respectively.
The refractive index of air is much smaller than that of PMMA and the light is much highly confined inside the slot region. Since the TO coefficient of air is zero, temperature insensitivity could be realized with air slot, covering slot structures was sufficient to compensate the TO coefficient of Si and SiO_2.

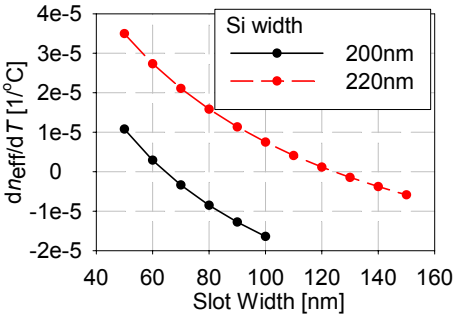


Fig. 4 Effective refractive index slopes of Si slot waveguides with air slots, 250nm heights, TE modes

Athermal silicon slot waveguides with SiO_2 slot

We reported the athermal Si slot waveguide filled with air in previous section. While the waveguides are easier to fabricate than the PMMA slot waveguides, we cannot utilize the advantage of slot waveguides, enhancement of optical nonlinearity due to the high optical concentration inside the slots. To use the advantage, the slots must be filled with a material. In this section, we report simulation results of athermal Si slot waveguides which had SiO_2 slot and PMMA over cladding.

The simulation results of Si slot waveguides with SiO_2 slots are shown in Fig. 5. Their heights were 250nm, same as the waveguides in the previous sections. Under cladding was SiO_2. For the case of Si width of 200nm and 210nm, athermal Si slot waveguides could be achieved with the slot width of ~103 nm and ~145 nm, respectively.
The SiO_2 slot itself cannot compensate the positive TO coefficients of Si and under cladding SiO_2. For this reason, the wider slot and narrower Si width were necessary than those of PMMA and air slot. Narrow Si width and wide slot width decrease the optical component inside the Si region. This permits the compensation of positive TO coefficient mainly comes form Si part, by PMMA over cladding. By using a polymer material which has larger negative TO coefficient than that of PMMA, athermal slot waveguides can be realized by narrower slot and wider Si width.

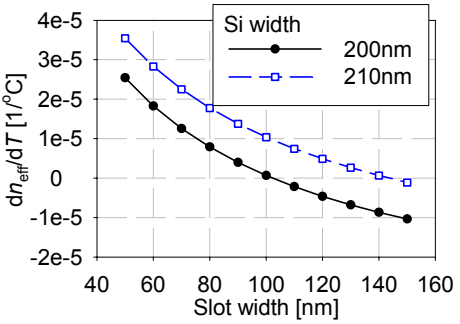


Fig. 5 Effective refractive index slopes of Si slot waveguides with SiO_2 slots, 250nm heights, TE modes

Summary

We reported the numerical simulation of temperature insensitive Si slot waveguide to achieve thermally stable optical devices. The positive TO coefficients of Si and SiO_2 can be compensated using PMMA, whose TO coefficient is negative, as an over cladding material of Si slot waveguides. We showed temperature insensitive design of Si slot waveguides whose slot regions were filled with PMMA. Temperature insensitive waveguides with air slots were proposed for easy fabrication. SiO_2 was employed as an example of slot material to use the advantage of slot waveguides, the enhancement of optical nonlinearity.

References

[1] Vilson R. Almeida, Qianfan Xu, Carlos A. Barrios, and Michal Lipson, "Guiding and confining light in void nanostructure, " Optics Letters, vol. 29, pp.1209-1211, 2004.

[2] Qianfan Xu, Vilson R. Almeida, Roberto R. Panepucci, and Michal Lipson, "Experimental demonstration of guiding and confining light in nanometer-size low-refractive-index material, " Optics Letters, vol. 29, pp.1626-1628, 2004.

[3] Jong-Moo Lee, Duk-Jun Kim, Gwan-Ha Kim, O-Kyun Kwon, Kap-Joong Kim, and Gyungock Kim, "Controlling temperature dependence of silicon waveguide using slot structure," Optics Express, vol. 16, pp.1645-1652, 2008.

[4] Y. Kokubun, S. Yoneda and S. Matsuura, "Temperature-insensitive optical filter at 1.55μm wavelength using a silica-based athermal waveguide," Electronics Letters, vol. 34, pp.367-369, 1998.

A Demultiplexer with Blazed Waveguide Sidewall Grating

A. Delâge[1], P.J. Bock[1,2], P Cheben[1], J.H. Schmid[1], D.-X. Xu[1], S. Janz[1], and T.J. Hall[2]

[1]*Institute for Microstructural Sciences, National Research Council Canada, Ottawa, K1A 0R6 Canada*
Andre.Delage@nrc-cnrc.gc.ca
[2]*University of Ottawa, Centre for Research in Photonics, Ottawa, Canada*

We propose a new type of waveguide diffraction grating demultiplexer with a very small footprint, designed for the silicon-on-insulator platform.

Summary

Integrated waveguide de-multiplexers as AWG's and etched echelle gratings (EEG) have been designed in the last decade to accommodate the specifications of telecommunication for narrow channel spacing. Now, with new applications with relaxed specifications (such as FTTH, optical sensing, etc.), new designs have emerged for compact coarse WDM devices. Among them we have been interested in the performance of the dispersive waveguide grating recently published by Hao et al [1], and we propose the use a sub-wavelength antireflection structure to improve its design.

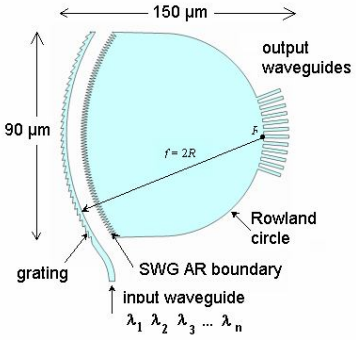


Fig 1: Waveguide grating demultiplexer

The device is presented in Fig. 1; it consists essentially of a curved waveguide on the left of the picture, in which the external wall is etched as a first order grating in order to diffract the light, originally in the waveguide, towards the output waveguides at the right. The arrangement is based on a Rowland circle (RC) configuration, with the radius of curvature of the waveguide equal to twice the Rowland radius. The focus point of the diffracted light is expected to lie on the RC in front of the output waveguides. The light is confined in the vertical direction, justifying the 2D simulations that are used to describe the device. To be efficient, this demultiplexer should also include an anti-reflection boundary that could be provided by a sub-wavelength grating as described in reference [2]. Contrary to AWG and EEG, the size of the focused spot in front of the output waveguides is not related to the input waveguide nor the grating waveguide width or mode profile; but rather to the total span of the grating and to the apodisation brought to the shape of the grating. This paper will present the properties of this device and its performance as a coarse wavelength de/multiplexer.

These properties have been studied by two different approaches: a two dimensional Kirchhoff-Huygens diffraction integral and by FDTD to account for more specific details. The first method is particularly adequate to establish the fundamental properties and limits of an ideal device. For R=70 um in silicon, it indicates the possibility of more than 10 channels separated by 25 nm with cross-talk of -40 dB. More realistic results have been then obtained with a 2D-FDTD technique that includes the grating shape and the AR-layer. This model uses a straight waveguide on a 100 µm × 3 µm calculation window from which the far-field is calculated using a standard Fourier transform. Our present design produces a 15 channel configuration with 25 nm spacing with only a supplementary penalty of –10 dB in cross-talk compared to the ideal case.

References

[1] Y. Hao, Y. Wu, J. Yang, X. Jiang and M. Wang, *Opt. Express* **14**, 8630-8637 (2006).
[2] J. H. Schmid, P. Cheben, S. Janz, J. Lapointe, E. Post and D.-X. Xu, *Opt. Lett*. **32**, 1794-1796 (2007).

Integrated optical source of polarization entangled photons at 1310 nm

A. Martin[1,*], V. Cristofori[3,1,*], P. Aboussouan[1], D.B. Ostrowsky[1], A. Thomas[2], H. Herrmann[2], W. Sohler[2], O. Alibart[1], and S. Tanzilli[1]

[1] LPMC, Université de Nice Sophia-Antipolis, CNRS UMR 6622, France
[2] Angewandte Physik, Universitat-GH-Paderborn, Postfach 1621, D-4790 Paderborn, Germany
[3] Dipartimento EIS, Universita di Bologna, Viale Risorgimento 2, I 40136 Bologna, Italy

Abstract *- We report the realization of a new polarization entangled photon-pair source based on a titanium-indiffused waveguide on periodically poled lithium niobate. The paired photons are emitted at the telecom wavelength of 1310 nm within a bandwidth of less than 1 nm. The related quantum properties are demonstrated to be of high quality.*

Introduction

Quantum communication often relies on the use of single quantum systems, such as photons, to carry the quantum analog of bits, usually called *qubits*. To do so, individual photons merely serve as carriers and quantum information is encoded on their quantum properties, like polarization or time-bins of arrival [1]. Selecting two orthogonal states spanning the Hilbert space, for instance $|H\rangle$ and $|V\rangle$ when polarization is used, allows encoding the 0 and 1 values of the qubit, and quantum superposition makes it possible to create any state $|\psi\rangle = \alpha|0\rangle + e^{i\phi}\beta|1\rangle$, provided the normalization rule $|\alpha|^2 + |\beta|^2 = 1$ is fulfilled. Entanglement is a generalization of the superposition principle to multiparticle systems. Polarization entangled photon-pairs can be described by states of the form

$$|\psi^{\pm}\rangle = \frac{1}{\sqrt{2}}\left[|H\rangle_1|V\rangle_2 \pm |V\rangle_1|H\rangle_2\right], \tag{1}$$

where the indices 1 and 2 label the two photons, respectively. The interesting property is that neither of the two qubits carries a definite value. But as soon as one of them is measured, the associated result being completely random, the other one will be found to carry the opposite value. There is no classical analog to this purely quantum feature [2].
In today's quantum communication experiments, spontaneous parametric down-conversion (SPDC) in non-linear bulk crystals is the common way to produce polarization entangled photons [3]. However, since such experiments are getting more and more complicated, they require more and more efficient sources together with narrower photon bandwidths [4, 5]. In addition, as soon as long-distance quantum communication is concerned, the paired photons have to be emitted within one of the telecom windows.
The aim of this work is to gather all of the above mentioned features in a single source based on a titanium (Ti) indiffused periodically poled lithium niobate (PPLN) waveguide. We report for the first time the efficient emission of narrowband polarization entangled photons at 1310 *nm*, showing the best quality of two-photon quantum interference ever reported for a similar configuration [6, 7]. In the following, we will first describe the essential aspects of the source. Then, we will focus on classical characterization enabling the choice of the desired SPDC interaction. Finally, we will move on to an interferometric setup designed to evaluate the quantum quality of the source and discuss the results.

*Both authors contributed the same.

Principle of the entangled photon-pair source

To date, the creation of entangled photon-pairs is usually ensured by SPDC in non-linear bulk or waveguide crystals [1]. In this case, the interaction of a pump field (p) with a $\chi^{(2)}$ non-linear medium leads, with a small probability, to the conversion of a pump photon into so-called signal (s) and idler (i) photons. Naturally, this process is subjected to conservation of energy $\omega_p = \omega_s + \omega_i$ and momentum $\vec{k}_p = \vec{k}_s + \vec{k}_i + \frac{2\pi}{\Lambda} \cdot \vec{u}$, where Λ represents, in the case of a PPLN waveguide, the poling period. Note that the latter equation is also known as quasi-phase matching (QPM). In our case, we choose this condition such that, starting with a pump laser at 655 nm, we expect the generation of pairs of photons centered at the telecom wavelength of 1310 nm.
From the quantum side, since we want to generate cross-polarized entangled photons, the waveguide device has to support both vertical and horizontal polarization modes. Therefore, the well-established Ti-indiffusion technology can be applied for waveguide fabrication and a type-II SPDC process, taking advantage of the non-linear coefficient d_{24} of the material, can be used [6]. This leads, at degeneracy, to the generation of paired photons having strictly identical properties, but showing orthogonal polarizations. As depicted in FIG. 1, the paired photons are emitted simultaneously and, after filtering out the remaining pump photons, separated at a 50/50 beam splitter (BS) whose outputs are labelled a and b. At this stage, when the pairs are actually separated, the two possible outputs, $|H\rangle_a|V\rangle_b$ et $|V\rangle_a|H\rangle_b$, have equal probabilities. Furthermore, provided the two photons are indistinguishable for any observable but the polarization, it is possible to describe them by the entangled state of equation Eq. 1. Two steps are therefore cascaded for obtaining such a state configuration, $|H\rangle_p \overset{NLO}{\longmapsto} \eta |H\rangle_s|V\rangle_i \overset{BS}{\longmapsto} \eta^\star \frac{1}{\sqrt{2}} [|H\rangle_a|V\rangle_b + |V\rangle_a|H\rangle_b]$, where η and η^* stand for the efficiencies of the non-linear process and of the entire source, respectively.

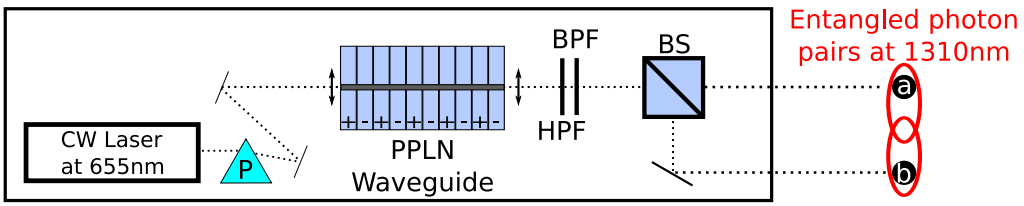
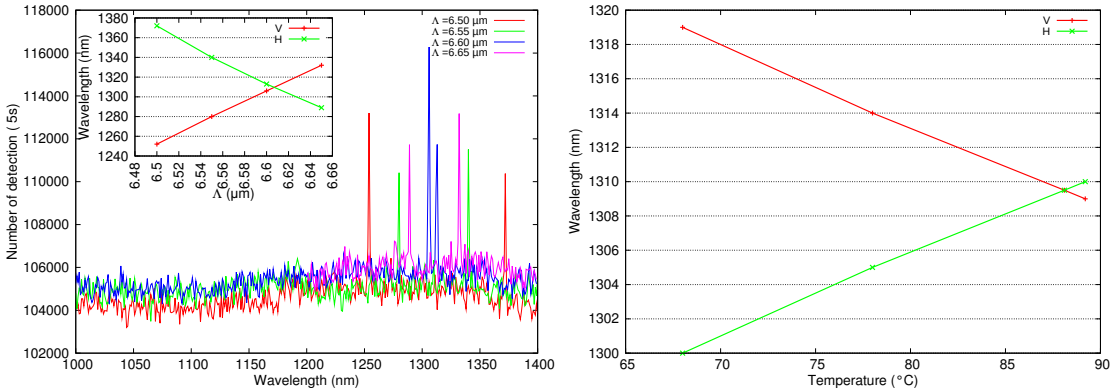


FIG. 1: Schematic of polarization entangled photon-pair source based on an H-polarized CW laser at 655 nm pumping a titanium-indiffused PPLN waveguide; A prism (P) is used to remove the infrared light coming from the laser. The association of a high-pass filter (HPF, cut-off at 1000 nm) and a bandpass filter (BPF, 1310 nm, $\Delta\lambda = 10\,nm$) allows removing the residual pump photons; Finally, a 50/50 beam-splitter (BS) is employed to separate the paired photons, revealing entanglement when coincidences are regarded.

Fabrication and classical characterization of the PPLN waveguide

The required poling period for the generation of photon-pairs at the degenerate wavelength of 1310 nm was calculated to be around 6.6 μm. Therefore, we fabricated a sample containing various waveguides widths (5, 6, and 7 μm) together with different poling periods (6.50 to 6.65 μm with a step of 0.05 μm). Experimentally, we got near-degeneracy photon-pair emission for a temperature of 80° in a 6 μm-wide waveguide for the predicted period. A fine tuning of the temperature up to 88° allowed us to get exactly both signal and idler photons at the degenerate wavelength of 1310 nm, as shown on FIG. 2. The measured bandwidth of those photons is less that 1 nm for a 3.6 cm-long sample. Note

here that the measured value of the bandwidth is very close to the resolution of our optical spectrum analyzer. The theoretical value has been estimated to be $0.6\,nm$ which corresponds to a coherence length of about $2.8\,mm$.

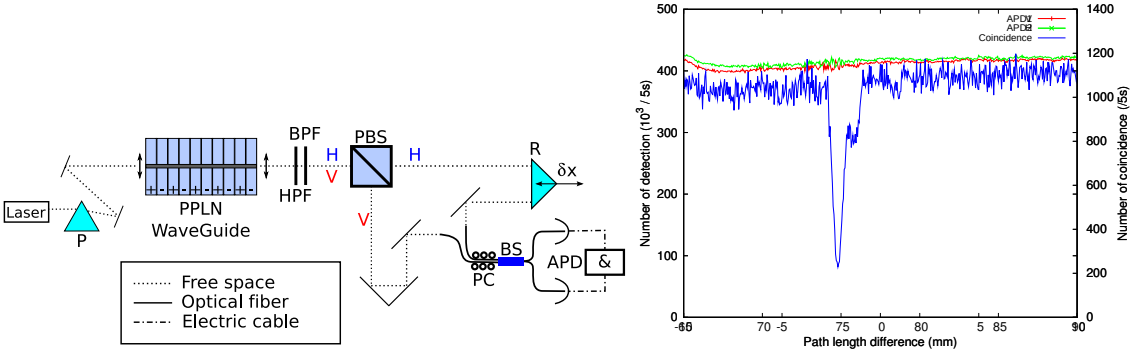


(a) (b)

FIG. 2: (a) Fluorescence spectra, obtained in the single photon counting regime, for various poling periods associated with a $6\,\mu m$-wide waveguide heated to $80^{\circ}C$ when pumped at $655\,nm$. (b) QPM curve as function of the temperature for $\Lambda = 6.60\,\mu m$; The degeneracy point can be reached by fine tuning of the temperature up to $88^{\circ}C$.

Quantum characterization of the source

Obtaining polarization entangled photon-pairs (see Eq. 1) requires these two photons to be indistinguishable for any degree of freedom, but the polarization, before they reach the beam-splitter of FIG. 1. To demonstrate the indistinguishability, we performed a non-classical two-photon interference experiment. Contrary to FIG. 1, this now consists of separating the paired photons into two spatial modes regarding their polarization state (H,V) using a polarization beam-splitter (PBS), and then recombining them at a standard fiber optic 50/50 BS. This interferometric apparatus, depicted in FIG. 3-a, permits characterizing the quantum properties of the pairs. Since photons are bosons, and provided the two photons are strictly indistinguishable, we expect them to exit the BS through the same output arm, leading to a dip in the coincidence rate, when two detectors are placed at each output. Such a destructive interference effect, first demonstrated by Hong, Ou, and Mandel (HOM) requires, in our case, to rotate one of the photon polarization states. This is ensured by the polarization controllers placed before the BS. Therefore, indistinguishability means in this case that the two photons have to show the same wavelength, bandwidth, polarization state, spatial mode, and time of arrival for obtaining a perfect overlap at the BS where the interference occurs [8]. Changing the path length difference of the two arms allows scanning over the coherence length of the single photons and leads to the so-called HOM-dip in the coincidence rate. The more indistinguishable the photons are, the better the visibility of the dip is. This figure of merit allows inferring the quality of the entangled state produced by the source (see FIG. 1 and related text).
FIG. 3-b exhibits the coincidence rate as a function of the path length difference between the two arms and shows the obtained HOM interference while single photon detection remains constant in both APDs. In our case, the associated net visibility and FWHM are of about 84% and $1.5\,mm$, respectively. Work is in progress towards understanding the origin of the reduction of visibility. Energy-time entanglement or other phase-matched



(a) (b)

FIG. 3: (a) Two-photon interference experiment. PBS: polarizing cube; R: retroreflector; PC: polarization controller; BS: fiber optics 50/50 beam-splitter; APD: avalanche photodiode; &: coincidence analyzer. (b) Coincidence rate at the output of the 50/50 beam-splitter as function of the relative length of the two arms. The width of the dip is related to the coherence length of the single photons.

interactions, such as Cerenkov, in our non-linear waveguide can be seen as sources of visibility degradation. In any case, the obtained visibility is, to our knowledge, the best ever reported in a similar configuration, i.e. cross-polarized photons at telecom wavelength generated by a Ti-indiffused PPLN waveguide. This is also a clear signature that a high quality of entanglement can be expected from the setup of Fig. 1.

Conclusion

Using a type-II PPLN waveguide, we have demonstrated a narrowband and bright source of cross-polarized paired photons since we estimated the production rate to be on the order of $10^5\,/s/GHz/mW$, which is one of the best ever reported in such a configuration [6, 7]. Using a HOM-type setup, we obtained an anti-coincidence visibility of 84% indicating a good level of photon indistinguishability. These preliminary results permits expecting our source to be an efficient, compact, and reliable key element providing narrow and high-quality polarization entangled photon-pairs for the first time at $1310\,nm$. Finally, this work clearly highlights the potential of integrated optics for long-distance quantum communication protocols.

The work is funded by the EU ERA-SPOT program WASPS. V. Cristofori acknowledges the ERASMUS program for her travelling grant. The authors thank P. Baldi and M.P. De Micheli for fruitfull discussions.

References

[1] G. Weihs *et al.*, *Quant. Inf. Comp.* **1**, pp. 3–56 (2001).
[2] J.F. Clauser *et al.*, *Phys. Rev. Lett.* **23**, pp. 880–884 (1969).
[3] P.G. Kwiat *et al.*, *Phys. Rev. A* **60**, pp. R773–R776 (1999).
[4] N. Gisin *et al.*, *J. Mod. Phys.* **74**, pp. 145–195 (2002).
[5] M. Halder *et al.*, *Nature Phys.* **3**, pp. 692–695 (2007).
[6] T. Suhara *et al.*, *IEEE Phot. Tech. Lett.* **19**, pp. 1093–1095 (2007).
[7] G. Fujii *et al*, *Opt. Exp.* **15**, pp. 12 769–12 776 (2007).
[8] C. Hong *et al.*, *Phys. Rev. Lett.* **59**, pp. 2044–2047 (1987).

Near field properties of vertical emitting laser based on 2D photonic crystal heterostructures

L. Ferrier, G. Le Gac, O. El Daif, P. Rojo-Romeo, X. Letartre, S. Callard and P. Viktorovitch

Université de Lyon, Institut des Nanotechnologies de Lyon, INL, UMR CNRS 5270,
Ecole Centrale de Lyon, 36 avenue Guy de Collongue, F-69134 Ecully Cedex
Lydie.Ferrier@ec-lyon.fr

Abstract. *Vertical emitting µlasers based on 2D photonic crystal heterostructures constituted by a square lattice of µpillars bonded on a vertical Bragg mirror have been realized at 1.5µm. Near field properties show the slow Bloch mode confinement inside the heterostructure.*

1. Introduction

2D photonic crystal properties, especially at band edges of the dispersion curves where the group velocity tends to zero, allow a wide range of micro-photonic devices that require slow light. To achieve vertical emission, Slow Bloch Modes (SBM) located above the light line are of great interest. Indeed, they have the ability to couple with free space modes. Especially at Γ-point of the dispersion characteristic, strong lateral confinement is expected and very compact structures can be designed. It is thus possible to finely tune the temporal (quality factor) and spatial (SBM confinement and emission characteristic) properties of SBM located at Γ-point to achieve low threshold vertical emitting µlasers.
Based on the concept we developed in ref [1], we fabricated and characterized 2D PC photonic heterostructures constituted by a square lattice of Indium Phosphide (InP) pillars bonded on a Si/SiO2 Bragg mirror. Particularly, we study the near field properties of the first SBM located at Γ-point.

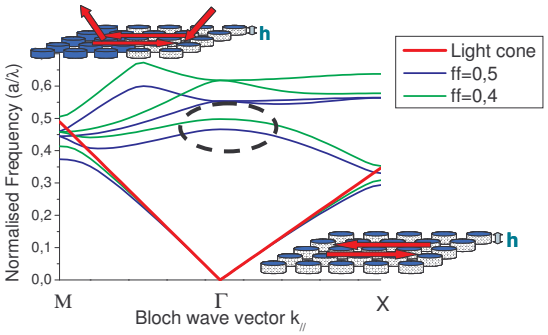


Figure 1. 2D band diagram of a square lattice of dielectric pillars for two InP filling factor: 0.4 and 0.5 in TE polarization. The SBM of interest is circled.

2. Sample design and fabrication

We focused on the first Γ-point SBM in a square lattice of Indium Phosphide (InP) pillars, as shown in the band diagram of the Fig. 1. This mode does not couple to free space modes for symmetry reasons [2] and exhibits a very flat band curvature. 3D FDTD calculations show that quality factors around 1500 can be achieved at 1.5µm in a 21x21 pillar lattice having period of 0.7µm and filling factor of 50%. To increase the quality factor of this SBM without increasing the mode volume, we use a photonic heterostructure as defined in [1]. The heterostructure principle is to slightly increase the radius of the outer pillars to

inhibit the lateral leakages leading to a strong lateral photon confinement. Indeed, by increasing the InP filling factor of the outer rows, we create a barrier for the photons located inside the cavity (see band diagram in figure 1).
The studied heterostructure consists of an inner 11x11 pillar cavity having a filling factor (ff) of 50% surrounded by 5 rows with ff=51.6% and same period, which yields to a difference between the pillar radii of the cavity and the barrier of 5nm. The quality factor of the SBM in the heterostructure calculated using 3D FDTD is thus 3000 whereas it reaches a few hundreds without any row. The photon lifetime is then only limited by vertical losses. These losses can however be reduced by associating the 2D PC heterostructure with a vertical Bragg mirror, as depicted in figure 2. The silica gap between the 2D PC and the Bragg mirror is 790nm which yields to a significantly increase of the quality factor [3]. Quality factors as high as 10000 can then be reached.
The device was fabricated by patterning an InP membrane containing 4 InAsP quantum wells bonded on a silicon/silica Bragg mirror using e-beam lithography and reactive ion etching (RIE). SEM images of the fabricated structures are shown in figure 2.
We fabricated uniform 2D PC as well as heterostructures to compare the two PC structures and their efficiency in terms of laser threshold and field confinement. The uniform PC structures are constituted by 30x30 pillars (≈25x25µm). For the heterostructure, the cavity is constituted by 10x10 pillars (≈8x8µm) surrounded by 5 rows having a slightly higher pillar radius.

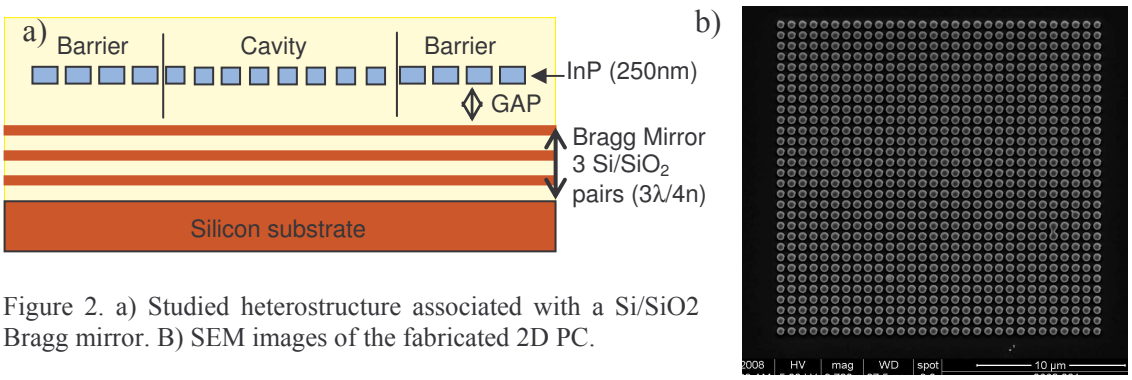


Figure 2. a) Studied heterostructure associated with a Si/SiO2 Bragg mirror. B) SEM images of the fabricated 2D PC.

3. Photoluminescence properties

The samples are first characterized at room temperature by photoluminescence using a pulsed laser diode emitting at 800nm as optical pump. The duty cycle is 1.7% and the pulse width is 6ns. The pulsed diode is focused under normal incidence on the structures using an achromatic objective (numerical aperture of 0.4) onto a surface of around 10µm in diameter. The emitted PL signal by the structure is then collected through the same objective lens and analyzed by a monochromator and a cooled InGaAs photodetector array.
We obtained laser emission for a uniform 2D PC and a 2D PC heterostructure around 1.5µm. Figures 3 a and 3 b shows the Light-in/Light-out curves for each kind of structures. The laser threshold for the uniform structure is about 8mW in terms of peak pump power which is of the order of the obtained threshold for a 2D PC structure constituted by a hole graphite lattice bonded on the same Bragg mirror with the same silica gap between the 2D PC and the Bragg mirror [3]. The laser threshold for the heterostructure is about 12.5mW.

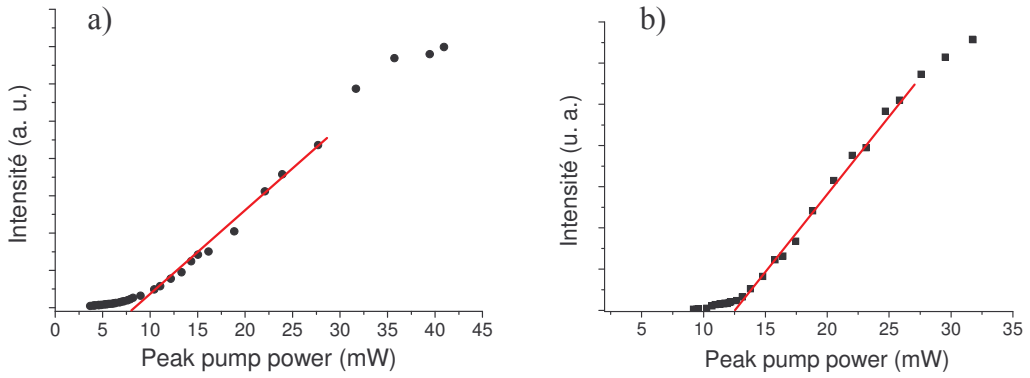


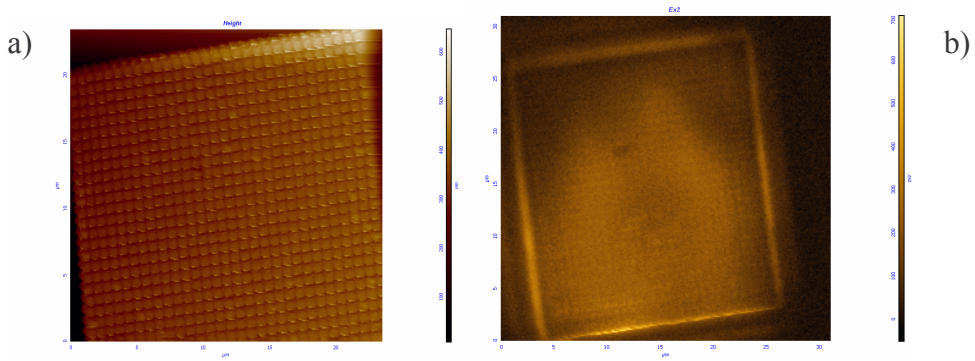
Figure 3. Lin-Lout curves for the uniform PC (a) and the PC heterostructure (b).

The filling factor of the cavity and the barrier are very close to each other. This is almost indistinguishable using SEM observations. A way to know precisely if the confinement of the SBM is achieved inside the heterostructure is to use near field scanning optical microscopy (NSOM) [4]. Indeed, using NSOM characterizations we can access directly to the field distribution inside the 2D PC that is the evanescent components of the SBM which is impossible with a far field experimental set-up. This will give a clear insight into the PL structuration of the SBM inside the PC cavity and the SBM confinement due to the heterostructure.

4. Near field characterizations

In the NSOM experimental set up, the pump beam, which is the same pulsed laser diode as in the far field experiment, is focused on the structure with an objective lens. The PL signal is collected in the near field of the structure (<20nm) by an uncoated, chemically etched optical silica fiber tip. Thus, the near field probe does not perturb notably the SBM spatial distribution. The signal is then guided to a monochromator and detected by a cooled InGaAs photodetector array. The distance between the near field probe and the sample is controlled by a shear force feedback. In this configuration, topographic images as well as PL images can be recorded at the same time.

Figure 4 a shows the topography of a uniform 2D PC constituted by a square lattice of pillars. The near field PL map recorded simultaneously to figure 4 a at 1517nm is given in figure 4 b. Figure 5 presents the near field distribution in the 2D PC heterostructure studied in section 3. The SBM confinement inside the heterostructure is clearly visible. In the case of the uniform 2D PC the field leaks laterally as expected from 3D FDTD calculations [2]. NSOM characterizations demonstrate the confinement of a SBM located above the light cone.



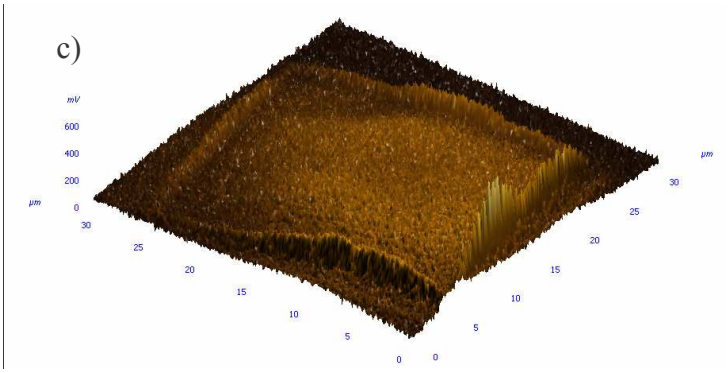


Figure 4. Topography of the uniform square lattice of InP pillars (a) Near field PL map of the SBM inside the uniform 2D PC, 2D (b) and 3D (c) image

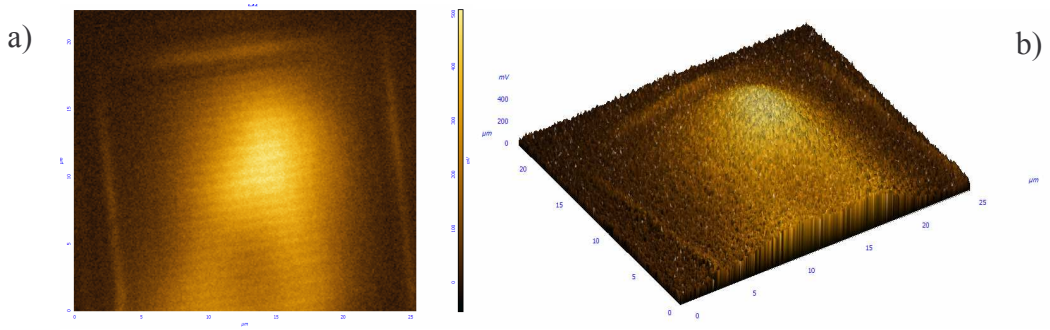


Figure 5. Near field map of the SBM inside the heterostructure, 2D (a) and 3D (b) image

4. Conclusion

We fabricated and characterized vertical emitting µlasers at 1.5µm and at room temperature constituted by 2D PC structures bonded on a silicon/silica Bragg mirror. Laser emission is achieved in a uniform 2D PC as well as in a PC heterostructure. In a 2D heterostructure, the SBM is laterally confined inside the cavity. Near field optical microscopy allowed us to demonstrate experimentally the SBM confinement by mapping the spatial distribution of the intensity in the evanescent tail of the field, at 20nm above the PC slab.

Acknowledgement

This work was partly developed into the frame of 6th PCRD "ePiXnet" European network of excellence. The authors would like to thank Christian Seassal for providing the Bragg mirror structure and the region Rhône-Alpes for supporting this work.

References

[1] L. Ferrier, P. Rojo-Romeo, E. Drouard, X. Letartre, and P. Viktorovitch, "Slow Bloch mode confinement in 2D photonic crystals for surface operating devices", Opt. Express **16**(5), pp. 3136-3145 (2008).

[2] T. Ochiai and K. Sakoda, "Dispersion relation and optical transmittance of a hexagonal photonic crystal slab," Phys. Rev. B **63**, 125107 (2001).

[3] B. Ben Bakir, Ch. Seassal. X. Letartre and P. Viktorovitch, "Surface-emitting microlaser combining two-dimensional photonic crystal membrane and vertical Bragg mirror," Appl. Phys. Lett. **88**, 081113 (2006).

[4] N. Louvion, A. Rahmani, C. Seassal and S. Callard, "Near-field observation of subwavelength confinement of photoluminescence by a photonic crystal microcavity", Opt. Letters, **31**(14), pp. 2160-2162 (2006)

High-Quality Factor Suspended-Wire 1D Photonic Crystal Micro-cavity in Silicon-on-Insulator

A.R. Md Zain, N.P. Johnson, M Sorel and R.M. De La Rue

Optoelectronics Research Groups, Department of Electronics Engineering, Rankine Buildings, University of Glasgow, Glasgow G12 8LT, United Kingdom
amdzain@elec.gla.ac.uk

Abstract. *We present a comparison of high Q-factor tapered membrane-type one-dimensional photonic crystal micro-cavities embedded in photonic wire waveguides based on silicon-on-insulator (SOI). Q-factor values as large as 24,000 have been measured, together with normalized transmission of 67%: an improvement in the Q-factor value in comparison with previous results obtained on structures with silicon cores supported by a silica buffer layer. Simulation using a 3D FDTD approach shows close agreement with measurements.*

Introduction

High quality factor waveguide micro-cavity structures have been a topic of research interest for several years. Hole-based one-dimensional photonic crystal (PhC) micro-cavities embedded in photonic wire waveguides, with a Q-factor value of around 500, were described in [1]. We now report achievement of an experimental Q-factor value as large as 24,000 in an air-suspended photonic-wire waveguide micro-cavity structure - a value that is, to our knowledge, the highest achieved in this particular format.

High Q-factor values have been reported for several different device designs [2,3], but the requirement of achieving high Q-factor values, together with large optical transmission and small modal volumes, has become increasingly important [4]. Recent work based on photonic-wires combined with 1D PhC micro-cavities having silicon waveguide cores supported by a silica buffer layer has achieved Q-factor values in excess of 100,000. Air-suspended membrane-type photonic crystal structures [5], including micro-cavities, have been successfully fabricated and have demonstrated very high cavity Q-factor values, but there are still issues of mechanical stability, robustness and fabrication complexity. The motivation of our work on designing and producing suspended-membrane PhC/PhW waveguide microcavities has been to investigate the impact of increased optical confinement within the waveguides, as well as the effect of possible reductions in the propagation losses.

Design considerations and FDTD simulation approach

Planar one-dimensional photonic crystal micro-cavities embedded in 500 nm wide photonic wire waveguides have been realized recently with Q-factor values of approximately 18,500 - and normalized transmission of nearly 85% [4]. This performance combination was achieved in structures in which the silicon guiding layer was supported by a silica lower cladding or buffer layer. The devices produced are useful for telecommunications applications such as dense wavelength division multiplexing (DWDM) and optical signal processing more generally. Detailed descriptions of the devices can be found in reference [4]. Figure 1 shows an SEM image

of a particular device in which the silica cladding underneath the silicon core has been removed - creating an air-bridge type of structure (see the inset in Fig. 1).

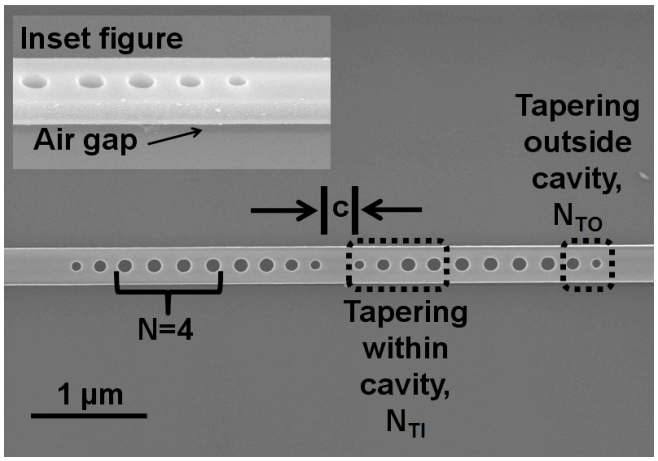


Figure 1: SEM image of an air bridge type of tapered single-row PhC/PhW waveguide with cavity length, c, four hole tapers within the cavity - and two hole tapers outside the cavity. Inset is a bird's eye view (angle ~ 25°) of the suspended PhC/PhW micro-cavities.

The structure consists of two mirrors with four period hole structures separated by a micro-cavity spacer section. Four-hole and two-hole aperiodic tapered structures were inserted within and outside the cavity on each mirror to reduce the modal mismatch between the un-patterned photonic-wire sections and the periodic hole mirror sections. 3D FDTD simulations have been carried out on similar device structures in reference [4] - but with the silica buffer layer having been removed. This device has an N = 4 periodic mirror with hole diameters of 182 nm and periodic spacing between the holes of 350 nm.

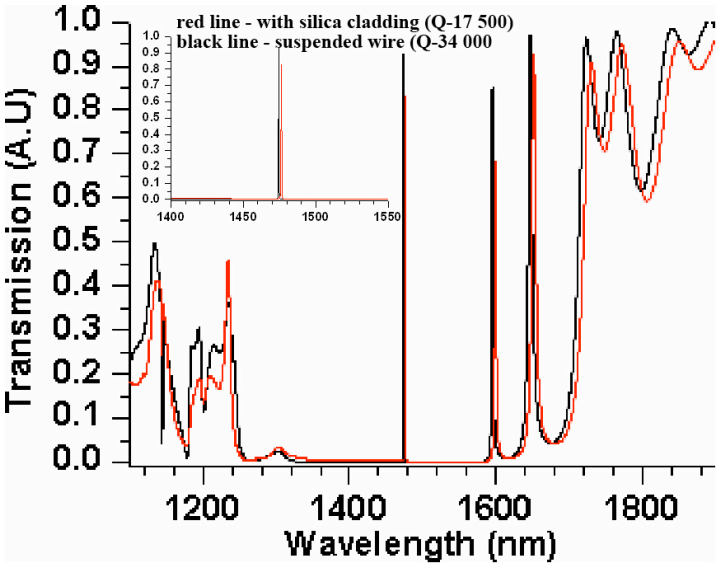


Figure 2: 3D FDTD computed for tapered one-dimensional PhC/PhW micro-cavities embedded in 500 nm photonic wire waveguides with cavity length, c ~ 425 nm for suspended wire (red line) and without removal of the silica buffer lower-cladding layer (black line).

Figure 2 shows a comparison of the transmission spectra for tapered photonic crystal micro-cavities embedded in 500 nm photonic wire waveguides obtained using the 3D finite-difference time-domain (FDTD) approach for both suspended wire structures and ones supported by a silica buffer layer. Our comparison is based on structures in which all of the parameters for the patterning of the silicon waveguide core are the same, i.e. wire width, hole diameters and spacings. The simulations show an increase in the Q-factor value from 17,500 to 34,000 for the suspended wire, in comparison with the value for the structure in which the silica buffer layer remains below the silicon guiding layer. A shift in the resonance frequency, in going from the supported structure to the suspended structure, by approximately -3 nm was also measured for this design arrangement - together with an increase in optical transmission by almost 10%. The shift is due, in particular, to a *reduction* in the effective refractive index of the guided light - thus shifting the resonance towards a shorter wavelength when the silica support layer is removed.

Experimental results

The devices were fabricated using direct-write electron-beam lithography on a Vistec VB6 machine, together with reactive ion-etching. They were characterized using a tunable laser covering the range from 1457 nm to 1580 nm. The TE polarized light was end-fire coupled into and out of the waveguides and was detected using a germanium photo-detector.

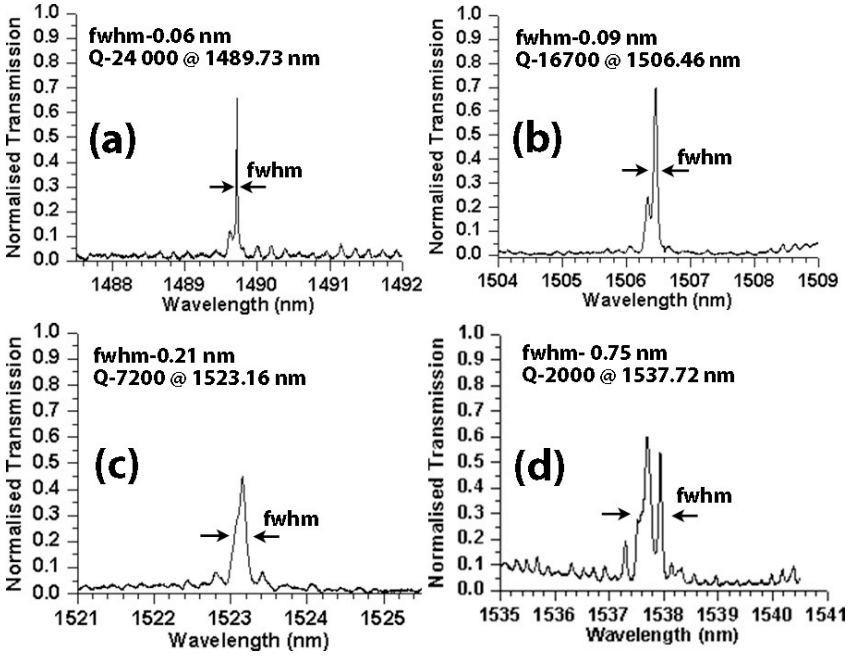


Fig 3:Measurement result for suspended PhC/PhW micro-cavities in a suspended wires with cavity lengths, c (a) 390 nm (b) 415 nm (c) 440 nm (d) 465 nm

Experimental results corresponding to the simulation results obtained using the 3D FDTD approach given in Fig. 2 are shown in Fig. 3.The best experimental Q-factor value - approximately 24 000 - was obtained for a cavity length, c, of 390 nm and at a normalized transmission level of 65%.

Cavity length, c/(nm)	With silica buffer cladding		Suspended wire waveguides	
	Q	*Normalized Transmission*	*Q*	*Normalized Transmission*
390	18 500	0.85	24 000	0.67
415	16 600	0.82	16 700	0.71
440	9 000	0.71	7 200	0.45
465	5 900	0.83	2 000	0.58

Table 1: Comparison of the measured results for the suspended wire waveguides and the one with silica cladding still exist underneath the wire waveguides

As the cavity length was increased from 390 nm to 465 nm, the Q-value decreased to 2000, together with a reduction in the normalized optical transmission level. Table 1 gives the results for the structures shown in Fig 1, in comparison with our previous results – obtained without removal of the silica buffer layer.

Conclusions

We have successfully demonstrated a further enhancement of the PhC/PhW cavity Q-factor value, from 18,500 to approximately 24,000, using the membrane type of structure - at a cavity length of 390 nm - for one of our design arrangements. This value is somewhat lower than the value of 34,000 predicted in the corresponding simulation. Discrepancies between simulation and measurement are probably attributable to imperfections in the fabrication processes. We believe that high Q-factor values, possibly up to more than 500,000, will be achievable if the correct combination of the number of periodic mirror holes, cavity length and aperiodic hole tapering within and outside the cavity is used. The enhancement in the Q-value in this particular design is due to the increase in the optical confinement – thus enhancing the field intensity of the mode confined within the micro-cavity. The effective refractive index changes due to the air gap underneath the silicon guiding layer have also produced a shift in the resonance frequency by approximately 3 nm. The 3D FDTD approach used to simulate the devices has shown reasonably close agreement with the measured results.

References

[1] J.S.Foresi, P.R.Villeneuve, J.Ferrera, E.R.Thoen, G.Steinmeyer, S.Fan, J.D.Jonnopoulos, L.C.Kimmering, H.I.Smith and E.P.Ippen,"Photonic-bandgap micro-cavities in optical waveguides",Nature 390, 143 (1997).

[2] T.Asano, B.S.Song, S.Noda," Analysis of the experimental *Q* factors (~1 million) of photonic crystal nanocavities", Optics Express **14**, 1996-2002 (2006)

[3] P. Velha, E. Picard, T. Charvolin, E. Hadji, J. C. Rodier, P. Lalanne and D. Peyrade, 'Ultra-High Q/V Fabry-Perot microcavity on SOI substrate', *Optics Express*, **15** (24), 16090-16096, 26th November (2007).

[4] Ahmad Rifqi Md Zain, Marco Gnan, Harold M. H. Chong, Marc Sorel and Richard M. De La Rue, "Tapered Photonic Crystal Microcavities Embedded in Photonic Wire Waveguides With Large Resonance Quality-Factor and High Transmission', *IEEE Photonics.Technology Letts*, **20**(1), 6 – 8, 1st January (2008).

[5] L.O.Faolain, X.Yuan, D.Mcintyre, S.Thoms, H.M.H.Chong, R.M. De La Rue and T.F.Krauss,"Low loss propagation in photonic crystal waveguides", Electronics Letters, 42 (25), December (2006).

InP-based Monolithic Integrated Colorless Reflective Transceiver

L. Xu, X.J.M Leijtens, P.J. Urban, E. Smalbrugge, T. de Vries, R. Nötzel,
Y.S. Oei, H. de Waardt, M.K. Smit

COBRA Research Institute, Technische Universiteit Eindhoven
Postbus 513, 5600 MB Eindhoven, The Netherlands
l.xu@tue.nl

A colorless monolithic integrated transceiver based on InP is presented. This transceiver consists of a wavelength duplexer, a reflective SOA (RSOA), and a short photodetector, suitable for the application at the user side to download and upload information carried by two different wavelengths spaced 200 GHz near 1.55 μm. The reflective SOA is 750 μm long, offers 5 dB fiber-to-fiber gain, and 1 Gbit/s dynamic operation at different wavelengths after wire bonding. The integrated 60 μm long photodetector shows 0.25 A/W external responsivity and up to 14 GHz 3 dB bandwidth after wire bonding.

Introduction

With the ever-increasing demands on the data rate at the user side to exchange information, fiber-to-the-home (FTTH) has been shown to be one of the most promising solutions. Currently the maximum widely available bitrate of installed optical network units (ONU) at the user side is 156 Mbit/s for upstream data carried by 1310 nm Fabry-Pérot laser, and 656 Mbit/s downstream data carried by 1550 nm in a TDM-BPON system in Japan [1]. This system uses wavelength-specific optical transceivers which will finally hinder the large-scale deployment of FTTH system due to cost and difficulty in maintenance. A colorless transceiver may be a more cost-effective and flexible alternative. A number of groups have demonstrated colorless upstream operation up to 1 Gbit/s with different methods, such as self-seeding, injection locking, spectral seeding or laser injected reflective SOA [2, 3, 4, 5]. However, most demonstrations were realized with discrete commercial components, which are costly and not practical in the user access network.

In this paper, a monolithic integrated colorless transceiver based on butt-joint active-passive regrowth on InP is presented, and it is one of the key devices developed for Broadband Photonics Architecture [6]. It consists of a wavelength duplexer, a reflective SOA, and a photodetector, Fig. 1. The device works as follows. Two wavelengths (λ_1 and λ_2) come from the network into the transceiver from the left side. They are spatially separated by the wavelength duplexer and guided to the photodetector (λ_1) and to the reflective SOA modulator (λ_2). The downstream data, carried by λ_1, is detected by the photodetector, while λ_2 is a continuous wave (CW) light and is guided to the RSOA where it is modulated, amplified and reflected back to the network.

The wavelength duplexer is a Mach-Zehnder (MZ) interferometer, composed of a 1×2 and a 2×2 3-dB MMI splitter/combiner, connected by two waveguides with different lengths. Due to the large 3-dB optical gain bandwidth of the SOA, it can be operated in a large wavelength range for a colorless operation by modulating the electrical current. A high reflectivity coating (HR) is applied at the SOA side of the chip, causing the light

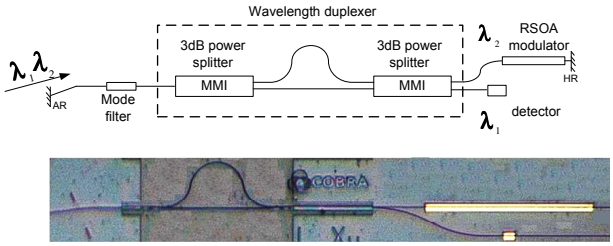


Figure 1: (Up) The layout of the integrated transceiver consisting of a wavelength duplexer, a reflective SOA modulator and a detector. (Below) The fabricated transceiver used for characterization.

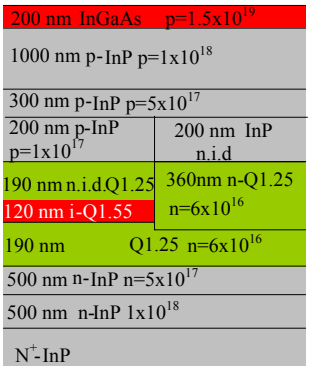


Figure 2: Active-passive butt-joint layerstack with specifications based on N-InP substrate.The unit for the doping level is cm^{-3}.

to be reflected back. The SOA is shallowly etched, 2 μm wide and 750 μm long. The photodetector is shallowly etched, 2 μm wide and 60 μm long. To avoid lasing and to reduce the coupling loss, the facet of the chip where the light is coupled into and out of the device, is provided with an anti-reflection coating (AR). To further reduce any residual reflections, the input waveguide is placed at an angle of 7° toward the chip facet [7], and a mode filter is inserted to suppress propagation of the first-order mode.

Fabrication

The device was fabricated in material grown on an N-type InP substrate by three-step low pressure metal-organic-vapor-phase epitaxy (MOVPE). The first epitaxy finished with a 120 nm thick SOA active InGaAsP layer (Q1.55, $\lambda_{\mathrm{gap}} = 1.55\,\mu$m), embedded between two quaternary confinement layers (Q1.25) with different doping levels, covered by a 200 nm thick p-InP layer. Next, the active sections were defined by lithography and reactive ion etching (RIE) using a SiN_x layer as etching mask. In the second epitaxy step, a Q1.25 InGaAsP layer was selectively grown for the passive sections with the SiN_x mask protecting the active sections[8]. In the third epitaxy step, the p-doped InP cladding layers with graded doping level and the p-InGaAs contact layer were grown with a total thickness of 1300 nm, Fig. 2. All the waveguides were fabricated by reactive ion etching (RIE). Polyimide was spun for passivation and planarization. By etching back the polyimide, the p-InGaAs contact layer was exposed and Ti/Pt/Au metal layers were evaporated to form the electrodes on the top and the ground (n-InP) at the backside. To improve the conductivity, the device was annealed at 325°C for 30 seconds, and electro-plated with gold. The HR coated facet has about 90% reflectivity, and AR coated facet has about 0.1% reflectivity. The device was glued and wire bonded on a AlN RF submount with coplanar waveguide design, Fig. 3, to enable measurements with a GSG RF probe. The measured 3-dB bandwidth for such a RF submount is more than 20 GHz. The bonded wire has 20 μm radius, and is approximately 2 mm long. During the characterization, the chip was stabilized on a copper chuck and cooled by a Peltier element.

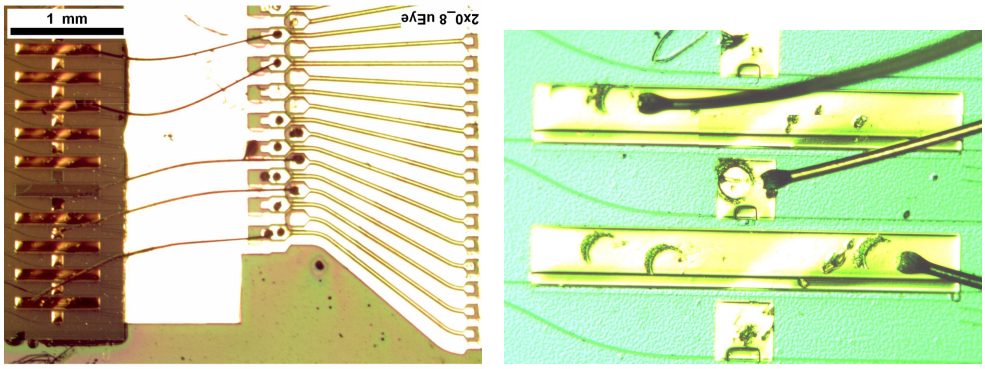


Figure 3: Bonded chip on a AlN RF submount (left) and bonded RSOA and the photodetector (right).

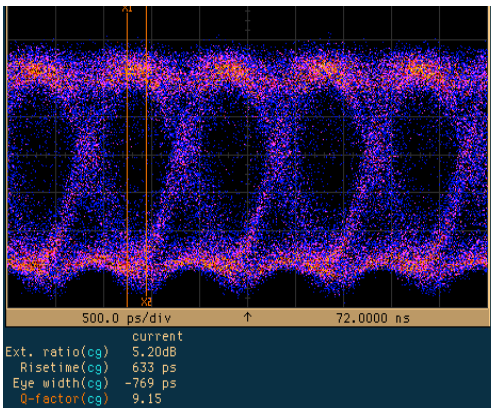


Figure 4: 1 Gbit/s eye diagram at $\lambda = 1541.9$ nm with input optical power $P_{\text{in}} = -11$ dBm, 80 mA injection current and 0.78 V modulation depth.

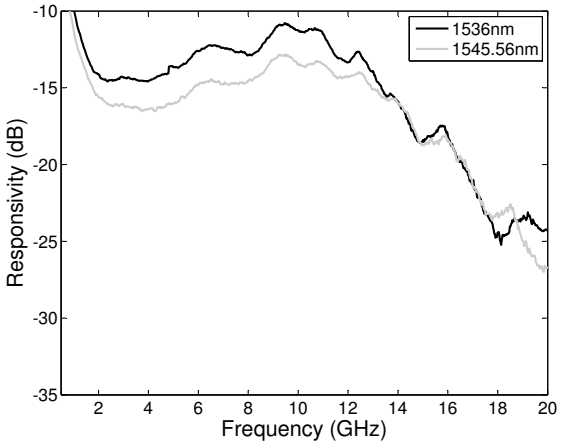


Figure 5: The measured frequency response of the wire bonded photodetector at -6 V when $P_{\text{in}} = -20$ dBm.

Characterisation

The reflective SOA is operated by modulating the electrical current. Because of residual reflections, the RSOA of the bonded device starts to lase at an injection current of 110 mA. The device gain peak is near 1530 nm, and the RSOA achieved about 5 dB fiber-to-fiber gain when injecting 100 mA. This fiber-to-fiber gain can be increased by reducing the fiber-chip coupling loss, which in our case is around 2×5 dB. To measure the bitrate of the SOA, we use a pulse pattern generator to produce 1 GHz PRBS code with $2^{31} - 1$ word length. The bias current was set at 80 mA, the modulation amplitude is 0.78 V over 50 Ω impedance. The input optical power is -11 dBm, and the recorded eye-diagram is presented in Fig. 4, showing a quality factor of 9, and an extinction ratio of 5.2 dB. The measurement has been done on four different upstream wavelengths from 1532.3 nm to 1541.9 nm, and the results are similar.

The photodetector was characterized by performing on-wafer S-parameter measurements in the range of 130 MHz to 20 GHz with a lightwave component analyzer HP8703A and a 50 GHz RF-probe. The photodetector was biased at -6 V through a 65 GHz bias tee,

and the injected wavelengths are 1536 nm and 1545.56 nm with −20 dBm optical power before fiber chip coupling. The measured small signal frequency response is given in Fig. 5. The measured 3 dB frequency response is 14 GHz for a 60 μm long wire bonded photodetector, and the external responsivity shown in Fig. 5 includes the extra loss from the polarization controller and two fiber connectors. The measured static photoresponsivity is up to 0.25 A/W over a large wavelength range, which corresponds to about 64% on chip quantum efficiency (including the loss of the wavelength duplexer) when the chip fiber coupling loss is taken as −5 dB.

Conclusion

We presented a monolithic integrated transceiver that operates up to 1 Gbit/s for upstream data (modulated RSOA) and around 14 Gbit/s for downstream data (reversely biased photodetector). The reflective SOA offers up to 5 dB fiber-to-fiber gain for 100 mA bias current at 1532.3 nm, which is mostly limited by the fiber-chip coupling efficiency. The bonded photodetector has a high external responsivity up to 0.25 A/W within large wavelength range.

This work is partly funded by the Dutch National Broadband Photonics Access project (http://bbphotonics.freeband.nl) and the Dutch National Smartmix project Memphis.

References

[1] H. Shinohara, "Broadband access in Japan: rapidly growing FTTH market," *IEEE Comm. Magazine*, vol. 43, no. 9, pp. 72–78, Sept. 2005.

[2] E. Wong, K. Lee, and T. Anderson, "Low-cost WDM passive optical network with directly-modulated self-seeding reflective SOA," *Electron. Lett.*, vol. 42, no. 5, Mar. 2006.

[3] L. Chan, C. Chan, D. Tong, F. Tong, and L. Chen, "Upstream traffic transmitter using injection locked Fabry-Perot laser diode as modulator for WDM access network," *Electron. Lett.*, vol. 38, no. 1, pp. 43–45, Jan. 2002.

[4] M. Zirngibl, C. Doerr, and L. Stulz, "Study of spectral slicing for local access applications," *IEEE Photon. Technol. Lett.*, vol. 8, no. 5, pp. 721–723, May 1996.

[5] S.-J. Park, G.-Y. Kim, T. Park, E.-H. Choi, S.-H. Oh, Y. Baek, K.-R. Oh, Y.-J. Park, J.-U. Shin, and H.-K. Sung, "WDM-PON system based on the laser light injected reflective semiconductor optical amplifier," in *Proc. 31th Eur. Conf. on Opt. Comm. (ECOC '05)*. Glasgow, Sept. 25–29 2005, p. We3.3.6, postdeadline Paper.

[6] P. Urban, E. Klein, L. Xu, E. Pluk, A. Koonen, G. Khoe, and H. de Waardt, "1.25-10 Gbit/s reconfigurable access network architecture," in *International Conference on Transparent Optical Networks (ICTON '07)*. Rome, Italy, July 1–5 2007, pp. 293–296.

[7] R. Broeke, "A wavelength converter integrated with a discretely tunable laser for wavelength division multiplexing networks," Ph.D. dissertation, Delft University of Technology, Delft, The Netherlands, 2003.

[8] Y. Barbarin, E. Bente, C. Marquet, E. Leclère, T. de Vries, P. van Veldhoven, Y. Oei, R. Nötzel, M. Smit, and J. Binsma, "Butt-joint reflectivity and loss in InGaAsP/InP waveguides," in *Proc. 12th Eur. Conf. on Int. Opt. (ECIO '05)*. Grenoble, France, April 6–8 2005, pp. 406–409.